

Behaviour of carbon/epoxy composite sandwich panels
with sustainable core materials subjected to intermediate
velocity impacts.

by

Edgar Arturo Gomez Meisel

A dissertation submitted by in partial fulfilment of the requirements for
the degree of Doctor of Philosophy (PhD) in

Mechanical Engineering and Industrial Organization

Universidad Carlos III de Madrid

Advisor(s):

Prof. Dr. Enrique Barbero
Prof. Dr. Sonia Sánchez Sáez

March 2022

This thesis is distributed under license “Creative Commons **Attribution – Non Commercial**
– **Non Derivatives**”.



*To God Almighty,
my parents Alfonso & Ines
and my wife Nana*

The love and light of my life

ACKNOWLEDGMENTS

I would like to acknowledge the government of Spain and especially the Ministry of Economy and Competitiveness for its financial support in this research project. To the University Carlos III of Madrid, my home during the last four years and the place where I lived life-changing experiences. To the Department of Continuum Mechanics and Structural Analysis and the research group in mechanics of advanced materials for their support during my research activities.

I want to thank my supervisor Prof. Dr Enrique Barbero and Prof. Dr Sonia Sanchez for their guidance, unconditional support, willingness to share their research experience and for empowering me during this project.

To my lovely wife Nana Sanikidze who has been my shield-maiden during this journey and for whom all her love and sacrifices I am forever thankful - დიდი მადლობა. To my mother Ines Meisel who with her cheerful charisma and unconditional support always made me feel that difficult times are temporary. To my father Alfonso Gomez, my guardian angel. To my aunt Vir, my cousin Pili and the rest of my family who is always attentive to my achievements.

To all the wonderful people I have met in Spain during the last four years: Daniel, Abdel, Claudia, Julian, Angela, Fernando, Jose, Filippo, Shirley, Ines, Luis, Montoya, Marco, Liu, Ramon, Alberto y Sara.

PUBLISHED AND SUBMITTED CONTENT

In peer reviewed scientific journals:

- **A. Gomez**, S. Sanchez-Saez, E. Barbero, Modelling of carbon/epoxy sandwich panels with agglomerated cork core subjected to impact loads, *International Journal of Impact Engineering*, June 2021, DOI: 10.1016/j.ijimpeng.2021.104047 [↗](#). Role of the author: Formal analysis, Validation, Writing – original draft, Writing – review & editing.

Article partially included in the thesis in chapter 3 to 6. The material from this source included in this thesis is not singled out with typographic means and references.

- **A. Gomez**, S. Sanchez-Saez, E. Barbero, Compression impact behaviour of agglomerated cork at intermediate strain rates, *European Journal of Wood and Wood Products*, Jan 2020, DOI: 10.1007/s00107-020-01638-2. [↗](#)

Role of the author: Formal analysis, validation, writing – original draft, writing – review & editing.

Article partially included in the thesis in chapter 4. The material from this source included in this thesis is not singled out with typographic means and references.

In scientific congresses:

- **A. Gomez**, S. Sanchez-Saez, E. Barbero, Intermediate velocity impact damage on carbon/epoxy sandwich panels with agglomerated cork, 23rd International Conference on Composite Structures (ICCS23), Porto, Portugal, September 2020

Role of the author: Presentation, formal analysis, validation, writing, review & editing. Partially included in the thesis in chapters 3 to 6. The material from this source included in this thesis is not singled out with typographic means and references.

- **A. Gomez**, S. Sanchez-Saez, E. Barbero, Compressive behaviour of a natural core, XIII National congress of composite materials, Vigo, Spain, July 2019. Role of the author: Presentation, formal analysis, validation, writing, review & editing. Partially included in the thesis in chapter 4. The material from this source included in this thesis is not singled out with typographic means and references.

ABSTRACT

Sandwich composite structures are made of two strong and stiff face-sheets separated by a lightweight core material. They are used in lightweight structures for load-carrying applications in the aerospace, marine, railway and wind-energy industry as a way to increase the bending stiffness and buckling resistance while maintaining a low weight. During their lifetime these structures are subjected to impact events such as the accidental drop of tools during assembly, bird strikes, hailstone impact, or even Foreign Object (FO) impact of stones, debris, etc.... Damage produced by impacts can compromise the integrity of a structure reducing its residual strength and stiffness, causing premature failure of a component under service loads.

This PhD thesis studies the mechanical response, impact process, and damage mechanisms taking place in an Intermediate Velocity Impact (IVI) over a sandwich composite panel made of woven carbon/epoxy face-sheets with either agglomerated cork core or PET foam core. This is done by applying a numerical-experimental methodology based on the building block approach used for aircraft certification in which results obtained from numerical models are directly compared with results obtained in the experimental test. In this context, the thesis is divided into three main parts.

In the first part of this thesis, the face-sheet and core are treated independently to understand their unique dynamic response and select appropriate constitutive material models for the FEA model implementation. Continuous damaged models are used to model the inter-laminar and intra-laminar fracture behaviour in the face-sheets. The suitability of these models is assessed through the implementation of independent FEA models for fracture tests (modes I & II) and ballistic impact which are validated with experimental experiments from the literature. In the case of the core, the compressive and tensile response of the core materials (agglomerated cork and PET foam) is studied by performing static and dynamic characterization tests. The collected data is then used for the validation of the non-linear material models by implementing an FEA model for dynamic compression.

The second part of this thesis studies the IVI event of the whole sandwich panel. This is done by performing a set of experimental impact tests and implementing a detailed explicit/nonlinear FEA model, which is validated against experimental results. The experimental tests are performed using a gas gun together with a different state of the art measuring techniques such as high-speed video recording, 3D Digital Image Correlation

(DIC) and Computed X-ray Tomography (CT). The FEA model is successfully validated and it is used to study the phases and mechanisms of damage evolution present during the impact process, something that is not possible to obtain experimentally and provides a valuable tool to understand the phenomenon. At the most general level, the impact process is dominated by different interacting physical mechanisms such as elastic deformation of the panel, inter-laminar and intra-laminar fracture of the face-sheets, non-linear core deformation, multi-axial core failure and core-face-sheet debonding. Different impact phases are observed and their physical mechanisms explained in detail. The FEA model is also used to perform a comparative analysis of different impact parameters (e.g. impact velocity, core thickness, impact angle, and axial preload) analysing their influence in the mechanical response of the sandwich panels under IVI.

The third part of this thesis studies the hailstone impact over the sandwich panels using the developed FEA model of the sandwich panel together with a particles model for the hailstone. The interaction between the dominant physical mechanisms in the sandwich panel (e.g. elastic response, face-sheet damage, core failure, etc...) and the fragmentation of the hailstone are explained in detail together with some failure modes expected in this kind of event and the severity of the impact extended for two different hailstone sizes.

RESUMEN

Las estructuras tipo sándwich están compuestas a partir de dos placas rígidas y resistentes separadas por un núcleo liviano. Se utilizan en estructuras ligeras en industrias como la aeroespacial, marina, ferroviaria y eólica como una forma de aumentar la rigidez a la flexión y la resistencia al pandeo, manteniendo un peso reducido. Durante su vida útil, estas estructuras están sujetas a eventos de impacto, como la caída accidental de herramientas durante el montaje, impactos de pájaros, impactos de granizo o incluso impactos de objetos extraños (piedras, escombros, etc...). Los daños producidos por impactos pueden comprometer la integridad de una estructura reduciendo su resistencia y rigidez residuales, provocando la falla prematura de un componente bajo cargas de servicio.

Esta tesis doctoral estudia la respuesta mecánica, el proceso de impacto y los mecanismos de daño que tienen lugar en un impacto de velocidad intermedia (IVI) sobre un panel sándwich fabricado a partir de laminados de tejido de carbono/epoxi con núcleo de corcho aglomerado o núcleo de espuma PET. El estudio se realiza mediante la aplicación de una metodología numérico-experimental basada en el enfoque de bloques de construcción utilizado típicamente para la certificación de aeronaves en el que los resultados obtenidos de los modelos numéricos se comparan directamente con los resultados obtenidos en la prueba experimental. En este contexto, la tesis se divide en tres partes principales.

En la primera parte, el laminado y el núcleo se tratan de forma independiente para comprender su respuesta dinámica única y seleccionar modelos de materiales constitutivos apropiados para la implementación del modelo FEA. Se utilizan modelos de daño continuo para modelar el comportamiento de fractura inter-laminar e intra-laminar en las laminados. La idoneidad de estos modelos se evalúa mediante la implementación de modelos FEA independientes para ensayos de fractura (modos I y II) e impacto balístico que se validan con datos experimentales de la literatura. En el caso del núcleo, se estudia la respuesta a compresión y tracción de los materiales del núcleo (corcho aglomerado y espuma PET) mediante la realización de ensayos de caracterización estática y dinámica. Los datos recopilados se utilizan para validar los modelos de materiales no lineales mediante la implementación de un modelo FEA para compresión dinámica.

La segunda parte de esta tesis estudia el evento IVI del panel sándwich completo. Se ha realizado un conjunto de pruebas de impacto experimentales e implementando un modelo FEA explícito/no-lineal detallado que se valida con resultados experimentales. Para las

pruebas de impacto se utiliza un cañon de gas empleando diferentes técnicas de medición de última generación como grabación de video de alta velocidad, la correlación de imágenes digitales (DIC) en 3D y tomografía de rayos X computarizada (CT). El modelo FEA se valida satisfactoriamente y se utiliza para estudiar las fases y mecanismos de evolución del daño que ocurren durante el impacto; algo que no es posible experimentalmente y que proporciona una valiosa herramienta para comprender el fenómeno. A nivel general, el proceso de impacto está dominado por diferentes mecanismos físicos que interactúan entre si como la deformación elástica del panel, la fractura inter-laminar e intra-laminar de los laminados, la deformación no lineal del núcleo, la falla multiaxial del núcleo y el despegue entre núcleo y laminado. Se observan diferentes fases de impacto y se explican en detalle sus mecanismos físicos. El modelo FEA también se utiliza para realizar un análisis comparativo de diferentes parámetros del problema (por ejemplo, velocidad de impacto, espesor del núcleo, ángulo de impacto y precarga axial) analizando su influencia en la respuesta mecánica de los paneles sándwich bajo IVI.

La tercera parte de esta tesis estudia el impacto del granizo en los paneles sándwich utilizando el modelo FEA desarrollado del panel sándwich junto con un modelo de partículas para el granizo. Se explica en detalle la interacción entre los mecanismos físicos dominantes en el panel sándwich (por ejemplo, respuesta elástica, daño en la cara frontal, falla del núcleo, etc.) y la fragmentación del granizo así como algunos modos de falla esperados en este tipo de evento y la severidad de la extensión de daño asumiendo dos tamaños diferentes de granizo.

CONTENT

ACKNOWLEDGMENTS	v
PUBLISHED AND SUBMITTED CONTENT	vii
ABSTRACT.....	ix
RESUMEN	xi
CONTENT	xiii
NOMENCLATURE	xix
1 INTRODUCTION	1
1.1 Overview and motivation	1
1.2 Objective and scope	3
1.2.1 General objective	3
1.2.2 Specific objectives	4
1.3 Methodology and thesis structure	4
2 BACKGROUND	7
2.1 Sandwich panels.....	7
2.1.1 Sandwich panel stiffness.....	8
2.1.2 Sandwich panel strength	8
2.1.3 Fibre-reinforced Composites	11
2.1.4 Carbon Fibre Reinforced Plastic (CFRP)	13
2.1.5 Cellular solid materials.	14
2.1.6 Agglomerated cork.....	15
2.1.7 Polyethylene terephthalate (PET) foam	16
2.2 The problem of impact vulnerability.....	17
2.2.1 Damage tolerance.....	17
2.2.2 Impact categories	21
2.3 Model validation and the building block approach.....	22

References of the chapter.....	24
3 BUILDING A RELIABLE MODEL FOR THE FACE-SHEETS.....	29
3.1 Modelling woven CFRP laminates	29
3.1.1 Fracture mechanics in laminate composites.	32
3.1.2 The Continuum Damage Mechanics (CDM) approach	34
3.1.2.1 Damage variable.	34
3.1.2.2 Damage activation function.	35
3.1.2.3 Damage evolution equation	35
3.1.3 Intra-laminar CDM for fabric reinforced composites.....	36
3.1.3.1 Fibre damage.....	36
3.1.3.2 Shear response	37
3.1.3.3 Element deletion	38
3.1.4 Inter-laminar CDM for fabric reinforced composites (Delamination)	39
3.1.4.1 Cohesive zone model (CZM) – pure mode.....	39
3.1.4.2 Cohesive zone model (CZM) – mixed mode.....	40
3.2 Modelling inter-laminar and intra-laminar failure	42
3.2.1 Intra-laminar fracture Mode I – Compact tension (CT).....	43
3.2.2 Inter-laminar Mode I – Double Cantilever Beam (DCB)	45
3.2.3 Inter-laminar Mode II – End notch flexure (ENF).....	46
3.2.4 Material.....	47
3.2.5 Fracture test results	49
3.3 Ballistic impact over CFRP laminates	55
3.3.1 FEA model.....	57
3.3.1.1 Mesh.....	57
3.3.1.2 Materials	58
3.3.1.3 Interactions and boundary conditions	58
3.3.2 Ballistic impact results.....	58

References of the chapter.....	60
4 BUILDING A RELIABLE MODEL FOR THE CORE	63
4.1 Cellular materials	63
4.1.1 Compressive behaviour of cellular materials.....	63
4.1.2 Agglomerated Cork.....	66
4.1.3 PET foam	67
4.2 Quasi-static and dynamic characterization test of core materials	69
4.2.1 Core materials	69
4.2.2 Quasi-static and dynamic compression test procedure	71
4.2.3 2D Digital image correlation (DIC) procedure.....	75
4.2.4 Data reduction method.....	76
4.2.5 Quasi-static tensile test procedure	78
4.2.6 Result of quasi-static and dynamic compression of agglomerated cork.....	79
4.2.7 Result of quasi-static and dynamic compression of PET foam.	91
4.2.8 Results of quasi-static tension of agglomerated cork and PET foam	107
4.3 Modelling the core materials in FEA	108
4.3.1 Agglomerated cork constitutive material model.....	109
4.3.1.1 Mullins Effect	110
4.3.2 PET foam constitutive material model	112
4.3.3 Validation of the FEA model for dynamic compression	114
4.3.4 Agglomerated cork.....	115
4.3.5 PET foam	120
References of the chapter.....	127
5 INTERMEDIATE VELOCITY IMPACT TEST ON SANDWICH PANELS.....	131
5.1 Introduction	131
5.2 Materials and Methods	135
5.2.1 Materials	135

5.2.2	Intermediate impact test procedure	136
5.2.3	Digital Image Correlation (DIC) Procedure	140
5.2.4	X-ray Computed Tomography (XCT)	143
5.3	Results and discussion.....	144
5.3.1	Damage and failure morphology	154
5.3.1.1	Visual inspection of cut-sectioned specimens	154
5.3.1.2	X-ray computed tomography (XCT) inspection	159
	References of the chapter.....	161
6	FEA MODEL OF IMPACT ON SANDWICH PANELS	165
6.1	Introduction	165
6.2	Model description.....	168
6.2.1	Mesh.....	168
6.2.2	Interactions.....	169
6.2.3	Boundary conditions and initial conditions	171
6.2.4	Materials	171
6.3	Results	171
6.3.1	Impact phases in sandwich panels with an agglomerated cork core.....	173
6.3.1.1	Phase I.....	173
6.3.1.2	Phase II.....	175
6.3.1.3	Phase III	179
6.3.2	Impact phases in sandwich panels with PET foam core	179
6.4	Validation.....	183
6.4.1	Panel perforation.....	183
6.4.2	Cross-section displacements	184
6.4.3	Damage morphology.....	187
6.5	Comparative analysis of parameters	189
6.5.1	Impact velocity.....	190

6.5.2	Core thickness	196
6.5.3	Impact angle	203
6.5.4	Axial preloading	211
	Reference of the chapter	221
7	HAILSTONE IMPACT OVER COMPOSITE SANDWICH PANELS	223
7.1	The hail impact vulnerability problem	223
7.1.1.1	Hailstone impact	223
7.1.2	Mechanical behaviour of ice	228
7.2	Modelling Hail impact using FE analysis	229
7.2.1	Smooth Particle Hydrodynamics (SPH)	231
7.2.2	Modelling hailstone plasticity	234
7.2.2.1	Mises Yield Criteria	234
7.2.2.2	Hardening and strain rate dependency	236
7.2.2.3	Dynamic failure model	237
7.2.3	FEA validation of the hailstone impact	237
7.2.3.1	Material model	239
7.2.3.2	Mesh sensitivity	241
7.2.3.3	Results of the hailstone model validation	243
7.3	Hailstone impact over CFRP sandwich panels	247
7.3.1	FEA model	247
7.3.2	Results of the largest hailstone (D=50.8 mm)	249
7.3.3	Results of a common hailstone (D=25.4 mm)	261
	References of the chapter	266
8	CONCLUSIONS AND FUTURE WORK	269
8.1	General conclusion	269
8.2	Conclusions by chapters	271
	<u>Chapter 3: Building a reliable model for the face-sheets:</u>	271

<u>Chapter 4: Building a reliable model for the core</u>	271
<u>Chapter 5: Intermediate velocity impact test on sandwich panels</u>	274
<u>Chapter 6: FEA model of impact on sandwich panels</u>	276
<u>Chapter 7: Hailstone impact over composite sandwich panels</u>	279
8.3 Future work	281
APPENDIX A.RELEVANT CONCEPTS IN FINITE ELEMENT ANALYSIS	283
A.1 Explicit time Integration.....	283
A.2 Energy conservation	285
A.3 Continuum shell elements and hour-glassing.....	288
A.4 Reduced integration and hour-glassing	290
APPENDIX B.IMPLEMENTATION OF THE TSAI-WU FAILURE CRITERIA FOR ELEMENT DELETION	293
B.1 Tsai-Wu failure criteria	293
B.2 VUSDFLD user subroutine	295
APPENDIX C. FUNDAMENTALS OF DIGITAL IMAGE CORRELATION (DIC) ..	297
C.1 Basics of camera optics.	297
C.2 Point image transformations	300
C.3 Fundamentals of distortion and calibration.	303
C.4 2D and 3D computer vision.....	305
C.5 Image matching	308
C.6 Shape functions.....	311
References of the appendices.....	313

NOMENCLATURE

A	Scalar of vector field
C_d	Drag coefficient
CFRP	Carbon Fibre Reinforced Plastics
CT	Computed X-ray tomography
d_{\max}	Maximum displacement
$d_{0\max}$	Maximum displacement for a perpendicular impact
D	Characteristic size
D	Distortion displacement vector
D_α	Damage variable in direction α .
DOF	Depth of Field
E_i	Young's modulus in direction i
E_{abs}	Absorbed energy
E_i	Kinetic impact energy
fps	Frames per second
FEA	Finite Element Analysis
FOV	Field of view
F	Deformation gradient
\bar{f}	Focal length
g	Gravity acceleration
G_{ij}	Shear modulus in i - j
G	Pixel intensity field
G_{f_i}	Intra-laminar critical fracture energy release rate ($i=1^+, 1^-, 2^+, 2^-$)
G_{i_c}	Inter-laminar critical fracture energy in mode i ($i=I, II, III$)
GFRP	Glass fibre reinforced plastic
I_i	i th strain invariant
IVI	Intermediate Velocity Impact
J_{el}	Elastic volume strain
\bar{m}	Pinhole model position
p	Hydrostatic pressure stress

PVC	Poly Vinyl Chloride
$P_{ij}^x, P_{ij}^y, P_{ij}^z$	Forces exerted by a neighbouring particle in x, y, z direction
Q_{ij}	Artificial viscosity
q	Deviatoric stress components
\vec{r}	Position vector
R	Yield stress ratio
[R]	Rotation tensor
ROI	Region of Interest
RPUF	Rigid Polyurethane Foam
S	Fracture shear strength
[S]	Compliance matrix. Inverse of the stiffness matrix
SAN	Styrene Acrylonitrile
t	time
\vec{t}	Translation vector
[T]	Transformation matrix
V	Volume
V_i	Impact velocity
V_r	Rebound velocity
U	Strain energy function
W	Strain energy density
W	Smoothing kernel function
W'	Deviatoric strain energy
X, X'	Tensile and compressive fracture strength
x, y, z	Orthogonal Cartesian coordinates
x', y'	Transformed orthogonal coordinates
α	scale factor of the perspective projection
θ	Angle
Φ	Damage function
η	Damage variable (Mullis effect)
ϵ_{yy}	Local longitudinal strain
ϵ_{hyd}	Hydrostatic strain tensor

ε'	Deviatoric strain tensor
ε_{eff}	Effective Von Mises strain
ε_n	Engineering strain
$\bar{\varepsilon}_{yy}$	Nominal longitudinal strain
$\dot{\varepsilon}_x, \dot{\varepsilon}_y, \dot{\varepsilon}_z$	Normal strain rates
$\bar{\varepsilon}^{pl}$	Plastic strain
γ	Image distance
γ	Engineering shear strain
$\dot{\gamma}_{xy}, \dot{\gamma}_{xz}, \dot{\gamma}_{yz}$	Shear strain rates
σ_e	Effective Von Mises stress
σ_e	Mean stress
σ_c	Collapse stress
σ_p	Plateau stress
σ_{true}	True stress
$\hat{\sigma}$	Equivalent stress
σ_i	Normal stress component
σ_{Hyd}	Hydrostatic stress tensor
σ'	Deviatoric stress tensor
σ_{VM}	Von Mises stress
σ^0	Yield stress at zero strain rate
τ_i	Shear stress component
$\beta_x, \beta_y, \beta_z$	Normalizing factors
ρ_{hail}	Hailstone density
ρ_{air}	Air density
η_i	Calibration camera parameters
χ	Cost function
ξ	Shape function
ν_{ij}	Poisson ratio in i-j
$\hat{\lambda}_1, \hat{\lambda}_2, \hat{\lambda}_3$	Principal stretches

Note: All variables and acronyms are properly presented in each chapter. This table only includes the most frequently used terms.

1 INTRODUCTION

1.1 Overview and motivation

Composite materials are used by multiple industries to build lightweight structures due to their high specific strength and stiffness and the possibility to customize their properties for different design requirements. At the structural level, other benefits are high fatigue, corrosion resistance, and low life cycle cost. At the manufacturing level, composite material structures can be formed into complex shapes and produced in fewer pieces than conventional structures. For all these advantages, the aerospace industry has largely benefited from their use in multiple applications, ranging from small general aviation aeroplanes to commercial airliners and spacecraft. Likewise, other high-performance industries such the wind-energy, automotive, railway and maritime industries use large amounts of composite materials in the development of wind turbine blades, sport-cars, high-speed trains and high-speed boats, just to name a few.

Among composite structures, sandwich construction is an efficient way of increasing the bending stiffness while maintaining a low weight. Sandwich panels are made of two strong and stiff face-sheets separated by a lightweight core material. The face-sheet panels are often made from laminates of Carbon Fibre Reinforced Plastic (CFRP), a material that can be produced in thin plies of woven fabrics mixed with a polymeric matrix like epoxy. CFRP laminates are stronger, stiffer and lighter than most steel alloys. However, they are usually brittle and prompt to damage internally when subjected to out-of-plane impact loads.

The sandwich core can be a cellular solid in which the base material is selected according to the specific application. For load-carrying applications rigid foams cores are made from polymers such as Polyvinyl chloride (PVC), Polyurethane (PU), Polyethylene terephthalate (PET) and styrene-acrylonitrile copolymer (SAN), nevertheless natural cellular materials like balsa wood and agglomerated cork are also employed.

Engineering structures are subjected to different kinds of impact during their life, including the accidental drop of tools during assembly, bird strikes, hailstone impact, or even Foreign Object (FO) impact such as stones, debris, etc....

Damage produced by impacts can compromise the integrity of a structure reducing its residual strength and stiffness, causing premature failure of a component under service

loads. During early design phases, certification or even during operation, engineers are often required to assess and mitigate this impact vulnerability issues. However, studying the response of a composite sandwich structure and its damage is not an easy task. At the experimental level, the short duration of the impact constrains the data acquisition in the laboratory and makes it necessary to use expensive equipment and long test preparation. At the analytical level, the complexity of the physical mechanisms interacting in the impact process makes it necessary to use very involving mathematical models that require strong assumptions that sometimes are difficult to apply in practical situations. An alternative is to use the Finite Element Analysis (FEA) method, which has shown to be successful in the past, to study in detail the behaviour of sandwich composite panels under impact loads. The development of an FEA model to study the impact behaviour of composite sandwich panels requires the introduction of numerous experimental data during the definition of the model. It also requires experimental validation of the model, to ensure the reliability of the results for the intended use. If successful, a validated FEA model allows engineers to accurately predict the impact behaviour of a sandwich structure within a few days or even hours. This is ideal for iterative design phases, in which structural components need to be quickly modified and analysed, but also when the structure is already in service and unforeseen impact threats need to be analysed.

In the past decades, there have been many studies in the area of sandwich composite structures subjected to impact loads, some using purely experimental, analytical or numerical approaches or a combination of them. However, at this date, most of them have focused on Low-Velocity Impacts (LVI) on sandwich panels with metallic or composite face-sheets and metallic honeycomb cores. The response of sandwich panels subjected to Intermediate Velocity Impacts (IVI) has been little explored, despite it encompasses a broad range of impact events such as bird strikes, hailstone impacts, and FO impact that could affect general aviation aeroplanes, wind turbine blades, and high-speed trains. At the fundamental physical level, IVI can be categorized as a transition region between Low-Velocity Impacts (LVI) and High-Velocity Impacts (HVI) in which the physical mechanisms taking place are a combination of those encountered separately in LVI and HVI events. There is still limited understanding of the physical process occurring during an IVI on composite sandwich panels and multiple questions are still in debate in the scientific community. Among them are the identification of the dominant physical mechanisms, the damage morphology and the influence of different impact parameters.

These factors are relevant not just from a theoretical perspective but their understanding could bring advances in practical engineering applications.

In this context, this research is aimed to study sandwich panels made of woven CFRP face-sheets and two different core materials: agglomerated cork and PET foam using a numerical and experimental approach. The selected face-sheet material is studied due to its widespread use in industry and because its brittle behaviour makes it highly susceptible to impact damage, limiting its use in applications where impacts loads are expected.

The selection of two different types of core materials is motivated by the following reasons. First, to study the difference in the mechanical response of the sandwich panel using two very different core materials. A semi-rigid and highly elastic naturally derived cellular material as agglomerated cork and a rigid polymeric foam with an elastic-plastic behaviour as PET foam. The second reason is the increased public interest in environmental awareness and the demand for scientific research on more sustainable materials that could substitute conventional core materials in particular applications. In this regard, agglomerated cork and PET foam are potential candidates, as both can be produced by the residuals of other industries. Therefore, the analysis of sandwich panels made of woven CFRP face-sheet with agglomerated cork or PET foam subjected to IVIs is of interest, since little research is available in the open scientific literature.

Finally, on the practical level, this thesis is also aimed to develop a validated FEA model that can predict the penetration threshold, damage extend and elastic response of sandwich panels serving engineers to study practical vulnerability hazards such as hailstone impact.

1.2 Objective and scope

1.2.1 General objective

The general objective of this thesis is to study the mechanical response, impact process, and damage mechanisms taking place in an intermediate velocity impact over a sandwich composite panel made of carbon/epoxy face-sheets with either agglomerated cork core or PET foam core. This objective is accomplished by implementing a detailed dynamic FEA model validated with experimental testing.

1.2.2 Specific objectives

In order to accomplish the general objective the following specific objectives are proposed:

- i. Implement a validated FEA model that can reproduce the response of the carbon/epoxy face-sheets and its dominant damage mechanisms when subjected to intermediate velocity impacts.
- ii. To study the behaviour of agglomerated cork and PET foam subjected to dynamic compression and perform the required characterization of the material properties required for FEA model implementation and validation.
- iii. Implement an FEA model that is able to reproduce the non-linear response of agglomerated cork core and PET foam under dynamic compression.
- iv. To study the impact phenomenon by performing experimental impact tests of a complete sandwich panel using a gas cannon and perform destructive and non-destructive inspections to assess the damage after impact. This includes the design, preparation and execution of the tests, the adjustment of the techniques used in the test (e.g. 3D DIC, video-tracking, high-speed recording, etc...) as well as the data processing and analysis of the results.
- v. To study the impact phenomenon by developing a validated FEA model for the complete sandwich panel analysing the impact process, impact damage and the influence of different impact parameters in the response of the sandwich panels.
- vi. Developing scripting tools that provide automation for FEA model generation, data processing and results comparison.
- vii. Apply the developed FEA model for the complete sandwich panel to study the phenomenon of hailstone impact over sandwich panels.

1.3 Methodology and thesis structure

This thesis work employs a qualitative and quantitative approach to study the phenomenon of intermediate velocity impact over sandwich panels made of carbon-epoxy face-sheets with two diverse core materials (agglomerated cork and PET foam). The methodological design is based on the building block approach used for aircraft certification in which both experimental and numerical methods are used in a complementary manner to fulfil the proposed objectives. The main numerical method employed is the Finite Element Analysis method (FEA) in Abaqus 6.14 particularly the dynamic/explicit solver. This technique can predict the response of a sandwich panel subjected to impact loads and capture the

INTRODUCTION

evolution of different variables during short periods, something that is rather difficult to achieve at the experimental level. The complexity of the modelling approach requires the use of advanced modelling techniques such as explicit integration, non-linear material behaviour, continuum damage models, surface interactions, and particle methods that will be properly addressed in the document.

At the experimental level, the study of a dynamic event can be challenging due to the short impact duration and the complexity to record relevant test data. For this reason, multiple techniques and equipment are applied, starting from drop test towers for dynamic material characterization to gas cannons for impact tests. The capabilities to study these events have been augmented by the use of state of the art techniques such as high-speed video recording, Digital Image Correlation (DIC) and Computed X-ray Tomography (CT). The obtained experimental data has been used not only for analysis purposes but also for calibration and validation of the FEA models.

The thesis structure is presented in chapters so each chapter addresses the state of the art, methods, and results related to one or more specific objectives giving the reader a logical sequence to interpret the research process. Chapter 1 provides an overview of the motivation for the research together with the objectives and scope of the thesis. Chapter 2 presents a brief introduction of key concepts and terminology used across the thesis as well as an introduction to the impact vulnerability problem. Chapter 3 discusses the modelling approach for woven CFRP laminates with its validation (objective i). Chapter 4 is devoted to the experimental study of the mechanical response of the core materials under dynamic compression and its numerical implementation and validation (objectives ii and iii). Chapter 5 presents the intermediate velocity impact tests carried out while chapter 6 discusses the FEA model for the whole panel together with the analysis of different impact parameters (objectives iv and v). Finally, chapter 6 is a practical application of the developed FEA model that studies the phenomenon of hailstone impact over composite sandwich panels.

A set of appendices are also included to guide the reader in important concepts such as dynamic/explicit FEA modelling or digital image correlation technique, which are not usually though in a Bachelor engineering degree in mechanical engineering or similar.

2 BACKGROUND

This section presents a brief background of some fundamental concepts and key terminology that are widely employed in the following chapters. The concept of a composite sandwich panel is introduced together with some remarks about the materials treated in this thesis. Subsequently, the concept of impact vulnerability and impact damage are discussed in order to highlight their importance in industrial scenarios. Finally, the concept of the building block approach is presented to show its importance in creating reliable models to analyse the behaviour of sandwich composite structures subjected to impact.

2.1 Sandwich panels

A sandwich panel is a type of lightweight structure made by two strong and stiff face-sheets separated by a lightweight core (Figure 2.1). The separation between the face-sheets increases the moment of inertia what in turn increases the resistance of the structure against bending and buckling. Since the core separating the face-sheets is usually made of lightweight cellular materials the increase in moment of inertia is associated with very little increase in total weight [1]. The use of sandwich structures covers a broad spectrum of engineering applications such as satellites, aircraft, cars, ships, trains, wind turbines, bridges, etc... Most of the materials available in the form of a thin plate can be used as a face-sheet in a sandwich panel this includes metallic and non-metallic materials. The core, on the other hand, is usually made from either corrugated materials, balsa wood, honeycombs of different materials or cellular foam cores.

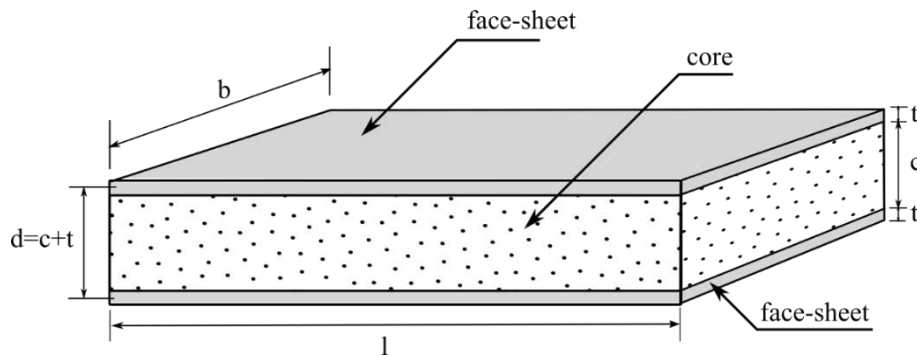


Figure 2.1. Sandwich panel with a core of cellular material

2.1.1 Sandwich panel stiffness

For structural application, sandwich panels are required to have a specified minimum stiffness and not fail under a predetermined load. For this reason, the design of the sandwich panels is tailored to the specific application based on the size of the panel and the mechanical properties of face-sheets and core.

The stiffness of the panel depends mainly on geometrical parameters such as the face-sheet thickness (t), the core thickness (c), and the panel width (b) but also on material properties such as the Young modulus and shear modulus of the face-sheet material (E_f) and core (E_c, G_c^*). The equivalent flexural rigidity $(EI)_{eq}$ and equivalent shear rigidity $(AG)_{eq}$ are two useful values to quantify the stiffness of a sandwich panel [1]:

$$(EI)_{eq} = \frac{E_f b t^3}{6} + \frac{E_c b c}{12} + \frac{E_f b t d^2}{2}$$

$$(AG)_{eq} = \frac{b d^2 G_c^*}{c}$$

2.1.2 Sandwich panel strength

Compared to other types of structures, strength in sandwich panels is more complex since they are subjected to multiple failure modes [1]: face-sheet yielding or fracture, face-sheet wrinkle, core failure (shear failure, although compressive and tensile failure are possible), debonding of the face-sheet and core (Figure 2.2).

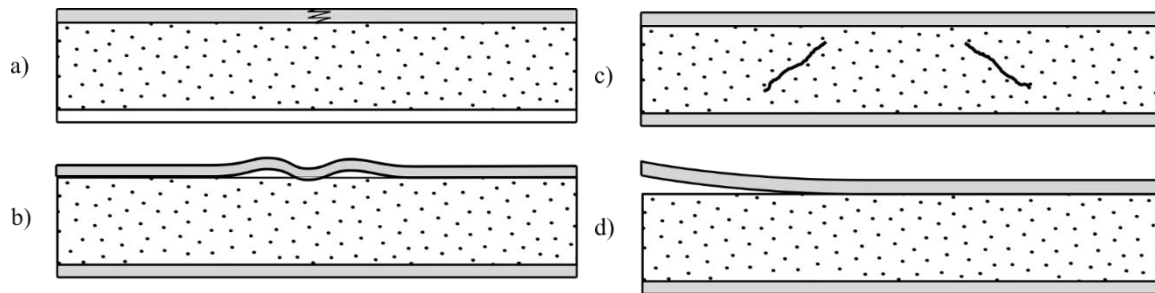


Figure 2.2. Typical failure modes in a sandwich panel. a) face-sheet yielding or fracture, b) face-sheet wrinkle, c) core failure, d) debonding.

The concept of modern sandwich construction dates back to Aachen (Germany) in 1924 where Theodore Von Karman and P. Stocks presented a patent for a glider fuselage having a wood sandwich skin with a core made of spruce and balsa wood. In England, during WWII the Mosquito bomber used sandwich construction in the fuselage with plywood in the face-sheets and balsa wood in the core [2]. In the same period, the Americans designed

BACKGROUND

and manufactured fuselages for the BT-15 using fibreglass reinforced polyester in the face-sheet and both glass-fibre honeycomb and balsa wood in the core.

Supersonic aeroplanes developed during the cold war implemented new kinds of sandwich structures. This is the case of the Convair B-58 a light supersonic bomber in which sandwich construction was used for its wings. The sandwich was made from aluminium face-sheets and a core made of a phenolic resin fibreglass cloth honeycomb. The XB-70 is another example, this aeroplane incorporated stainless steel honeycomb and face-sheet of the same material to provide the thermal insulation required for supersonic flight [2]. The famous supersonic aeroplane Concorde that flew the first time in 1968 was provided with an aluminium sandwich for the rudder and CFRP face-sheet sandwich for ailerons.

Due to safety and certification considerations, the implementation of sandwich construction in civil aviation has occurred gradually starting from non-structural components to secondary structures and finally to primary structures. By 1969 the Boeing 747 had around half of its wing surface made of glass fibre and Nomex honeycomb. In 1988 the ATR-72 aeroplane famous for being the first commercial aircraft to have a certified CFRP wing-box structure incorporated sandwich panels with multiple skins such as glass, Kevlar and carbon. Similar solutions have been implemented by Airbus in the A320, A330 and A340 however in recent projects like the A380 and B-787 the proportion of sandwich structures have decreased since self-stiffened monolithic structures provide economic advantages [2].

Despite this, sandwich composite structures are now well established in primary structures for business aircraft. The most famous case is the Beechcraft Starship designed by Burt Rutan in which 72% of its structures is built in sandwich panels of carbon/epoxy face-sheets and Nomex honeycomb. Other aeroplanes designed by Rutan for Scaled Composites such as the Voyager, the Pond racer and NASA AD-1 are built using CFRP/foam sandwich construction. Other big companies in the sector have followed the example with similar aircraft such as the Cirrus 20, the A500 the Lancair Legacy and more recently the Elixir Aircraft in La Rochelle (France).

Nowadays in aeronautical applications, the material combinations have been partially restricted due to certification concerns being cores made of Nomex and aluminium honeycomb and high-quality polymeric foams the most common choice. Similarly, in this industry face-sheets are usually made from aluminium alloys and composite laminates such as GFRP and CFRP [2].



Figure 2.3. Applications of sandwich composite structures in aviation.
 a) ATR-72, b) Airbus A320, c) Beechcraft Starship, d) Cirrus 20

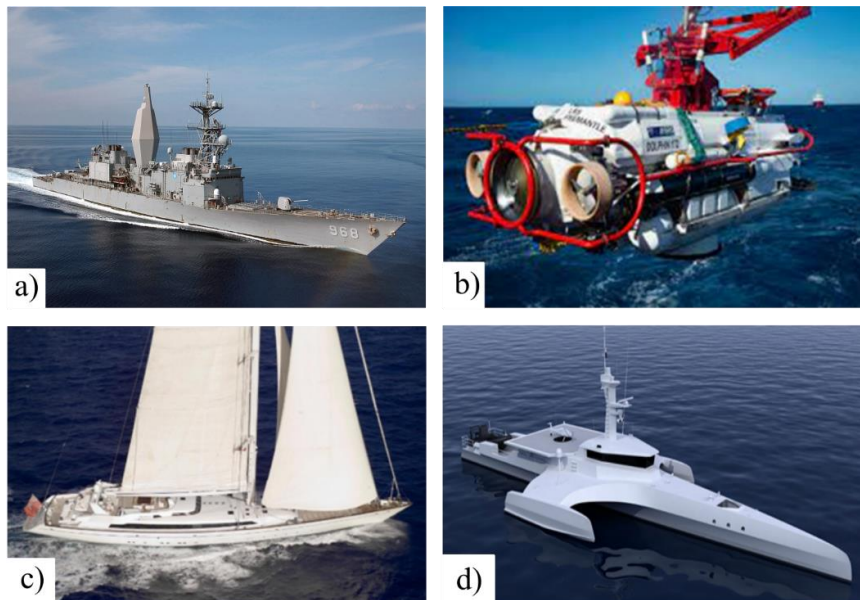


Figure 2.4. Applications of sandwich composite structures in the marine industry.
 a) USS Arthur W. Radford, b) LR5 Submersible submarine rescue vessel,
 c) M5, with a 75 metres sandwich hull, d) Ocean Eagle 43 ocean patrol vessel

During the 1970s the Swedish ship industry began replacing the traditional steel hulls with fibre-glass sandwich composite structures. One of their newest ship the YP2000 Visby is a stealth optimized vessel made of graphite/epoxy that uses sandwich construction. Recently the US Navy used core sandwich construction in the large hexagonally shaped mast of the destroyer ship USS Arthur W. Radford [3]. Other less obvious applications of sandwich composite structures in the marine sector include marine renewable energy systems, offshore oil and gas exploration and exploitation structures, dock infrastructure, submarines

BACKGROUND

and submersibles, lifeboats, naval vessels, fast ferries, power-boats, yachts, stern-gear (propellers and rudders), canoes, kayaks, surfing and fish farms.

Modern wind turbine blades are manufactured using sandwich construction with GFRP face-sheets and balsa wood or polymeric foams (PVC, BMI and PET). Due to the rapid scaling of new wind turbine blades, the use of CFRP is increasing to reduce weight [4]. In wind turbine blades sandwich panels are usually observed in the main spar box and the outer shell (Figure 2.5). Additionally, some other parts such as the hub-spinner are also built from sandwich construction.

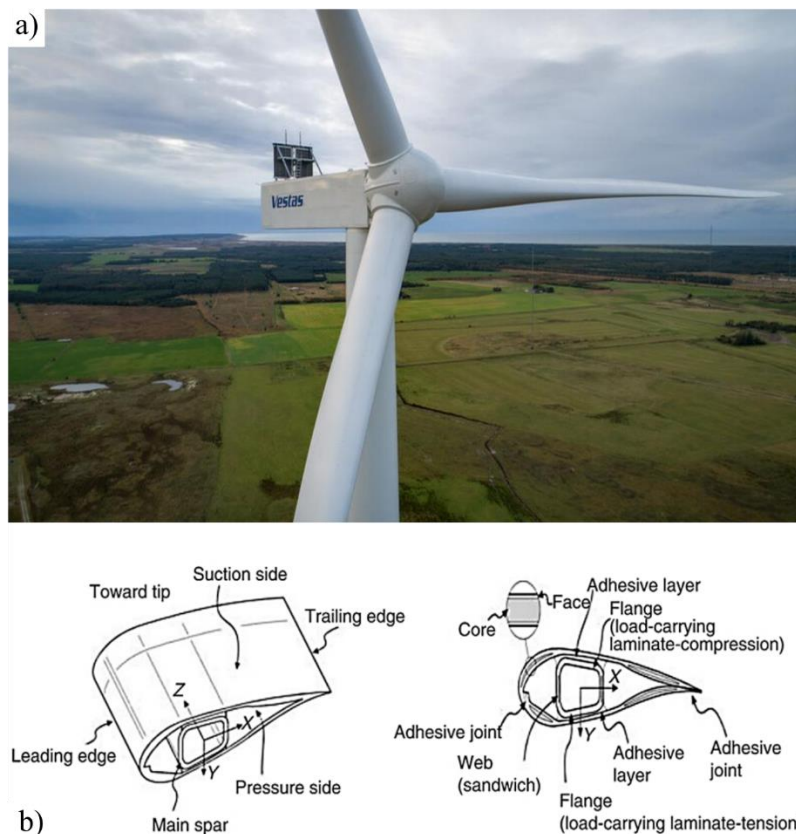


Figure 2.5. Applications of sandwich structures in the wind energy industry. a) Vestas wind turbine V150, b) design details of a wind turbine blade. Source: [4]

2.1.3 Fibre-reinforced Composites

Fibre-reinforced composites are one of the most common types of materials used as face-sheet in sandwich structures. These materials use strong, stiff fibres to reinforce a weaker and less stiff matrix to improve the specific strength and stiffness in what is known as a lamina or ply.

The fibre reinforcement is the main one responsible for the strength and stiffness of a ply. Fibres are efficient load-carrying components since they are stronger than the bulk material they are made from. This occurs mainly due to two reasons: First, fibres contain fewer sub-microscopic flaws due to their reduced size. As a result, smaller fibres are associated with higher strength. Second, the manufacturing processes used to produce fibres encourage the alignment of the atomic structure along the fibre direction.

The matrix on the other side is responsible for transferring the loads to the fibres. They also prevent the failure of adjacent fibres by separating them and protecting them from the environment.

The stiffness and the strength of a ply in the fibre direction are usually estimated by a law of mixtures that is dependent on Young's modulus, the failure strain (or stress) of the constituents and the fibre/matrix volume fraction. Some mechanical properties of the ply are matrix dominated, this is the case of the longitudinal compression strength, transverse tensile strength (in unidirectional plies), and the inter-laminar shear strength [5]. During manufacturing when a group of different plies are stacked in different orientations and bonded together to tailor the stiffness and strength of the material this receive the name of laminate [5].

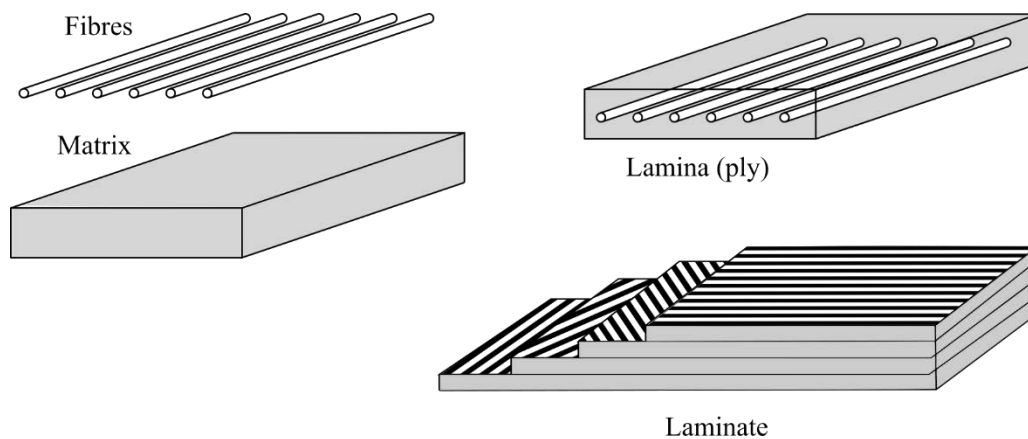


Figure 2.6. Simplified representation of a laminate with unidirectional plies.

Instead of using unidirectional fibres in a ply, textile technology allows woven yarns of fibres to produce a wide variety of fabrics being plain weave and satin weave cloths (Figure 2.7) the most common types. In a plain weave, each warp yarn crosses over (or under) a weft yarn (1x1), while in the case of satin weave yarns go over (or under) multiple warp yarns.

BACKGROUND

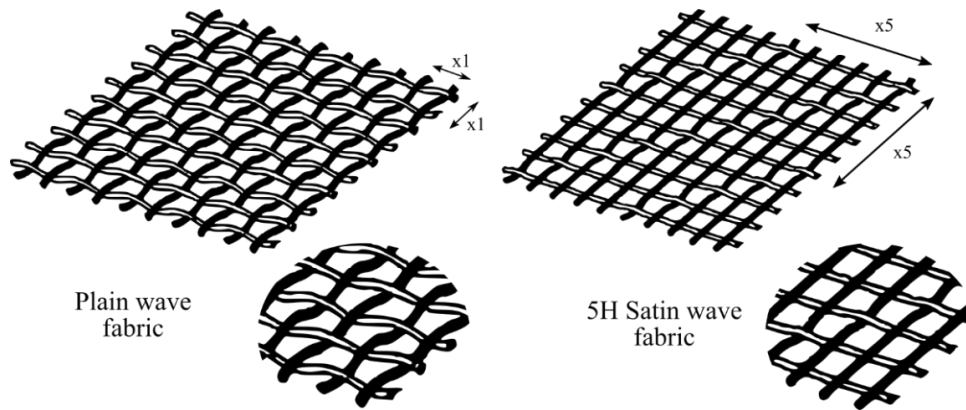


Figure 2.7. Common types of woven fabric

In certain specific applications woven fabrics might be preferred over unidirectional fabrics due to the following reasons [6]:

- a) Reduced cost savings during manufacturing due to reduced layup labour.
- b) Higher toughness against delamination and increased damage tolerance due to fibre interlocking.
- c) Single-ply laminates with balanced properties can be produced with woven fabrics
- d) In woven fabric, there is no weak transverse direction.
- e) Woven fabrics constrain the lateral movement of fibres what improves thickness uniformity. Additionally, woven fabrics have higher drape-ability what enhances manufacturing processes.

2.1.4 Carbon Fibre Reinforced Plastic (CFRP)

CFRP composites are made from a polymer matrix reinforced with carbon fibres. This composite material is one of the most widely used for high-performance sandwich structures and it is the main composite material discussed in this work.

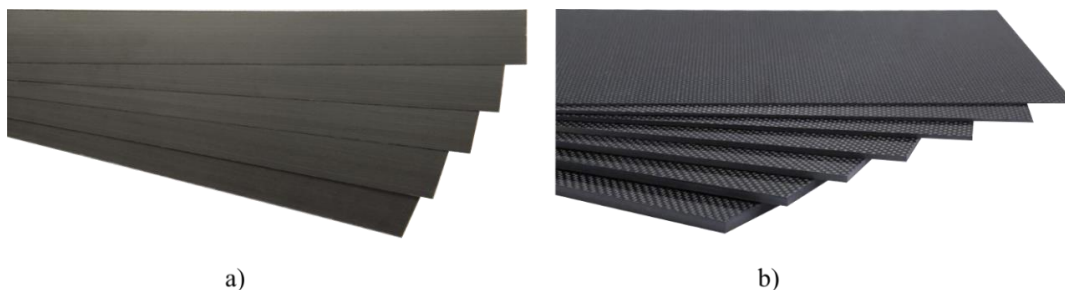


Figure 2.8. CFRP laminates. a) Unidirectional, b) Woven fabric

Carbon fibres are made from organic precursors such as polyacrylonitrile (PAN) fibres by the process of wet or dry spinning. The PEN fibres are subjected to carbonization to remove nitrogen, oxygen and hydrogen. The heat treatment produces a network of mainly carbon

atoms with basal planes aligned with the fibre axis. The strength and stiffness of carbon fibres depend on how perfect is the structure and alignment of the ribbons of basal planes with the fibre axis [5].

The matrix used in CFRP composites can be either a thermoset or a thermoplastic polymer, each with its specific advantages and disadvantages. Thermoset polymers for example are processed at relatively low processing temperature and pressure due to a low viscosity stage before polymerization and cross-linking. On the other side, thermoplastic polymers are processed at higher temperatures and pressure but allow short processing times and they can be post-formed after production.

Carbon fibres reinforced with a thermoplastic matrix such as polyethylene, polyamide, polyetheretherketone (PEEK) or polyetherketone (PEK) are state of the art research fields and the reader is encouraged to follow pioneering projects in the aerospace industry such as Clean Sky 2 (European Commission). However, to this date, thermosetting resins and particularly epoxy resins are the most widely used matrix in CFRP composites for low-temperature applications (-53°C to 82°C) and therefore are the main focus of this work.

Epoxy resins are created by reacting polyphenols (usually bisphenol A) with epichlorohydrin. They have good mechanical and chemical properties, have low shrinkage during curing, and adhere well to most fibres. Due to their low-viscosity stage during cure, they are ideal for processes such as resin transfer moulding (RTM) and can be cured at temperatures between 120°C to 180°C . In their natural state epoxy resins are brittle and can damage internally when impacted so they are usually “toughened” by different means [5], [6].

2.1.5 Cellular solid materials.

Sandwich structures are commonly used in applications where weight is critical, for this reason, cellular solid materials are usually used in the core. As explained by Gibson et al. [1] a cellular solid material is made from an interconnected network of cells. Each cell is formed from struts and plates (or membranes) that constitute the cell edges and faces. Cellular materials can be two-dimensional and being defined by polygonal shapes (honeycombs) or can be three dimensional with polyhedral cells (foams). Due to their porosity cellular materials are usually characterized by their relative density (ρ^*/ρ_s) that is the ratio between the density of the cellular material and the density solid material from which it is made. Relative densities can vary from 0.001 for ultra-low density foams to 0.4

for some soft-woods. Practically all materials can be foamed with current manufacturing techniques including metal and ceramics, but polymers are still most common. Cellular materials are also present in nature, this is the case of wood, cancellous bones or even bread [1].

The mechanical properties of foams are controlled by the properties of the base material. For this reason, they are usually classified into the following categories [7]:

- **Elastomeric foams:** They are soft and flexible and are usually produced from ethylene–vinyl acetate (EVA), polyurethane (PU), and thermoplastic polyurethane (TPU). Due to their excellent cushion response, and hysteresis they are preferred in the sports, leisure and furniture industries.
- **Rigid foams:** They are strong and stiff and are produced from polymers like PVC, PU, PET and styrene–acrylonitrile copolymer (SAN). Due to their characteristics, they are preferred in structural applications as core material in sandwich panels for the aerospace, marine, wind energy, and construction industries [8], [9].

The increasing use of plastics, the inconvenience of their disposal methods (landfill, incineration) and the limitation of current recycling techniques (energy consumption, low-value products) are creating awareness about their environmental sustainability [10]. In this regard agglomerated cork and polyethylene terephthalate (PET) foam are sustainable substitute of conventional polymeric foams are for certain specific applications [11], [12], [9], [13], [14], [7], [15].

2.1.6 Agglomerated cork

Cork is the bark of the oak, a popular tree in Mediterranean countries such as Portugal, Spain, Italy, and France. Cork is a cellular material with a polygonal structure (heptagonal, hexagonal, or pentagonal) made from thin walls analogous to the honeycomb with lateral cell walls running parallel to the radial direction of the tree [1]. Cork is transversally isotropic therefore its mechanical properties perpendicular to the radial direction (axial and tangential) are analogous [16]. In the axial and tangential direction, the cork has a cellular structure similar to a brick wall. Cork cells are closed and hollow containing air inside. Cork is harvested from the tree every 9 to 12 years and boiled to reduce the corrugation of the walls and to open its cells, increasing its volume and making it smoother.

Due to their fast regrow, this material is a potential sustainable substitute for polymeric foams in specific applications due to its mechanical properties. [8], [9].

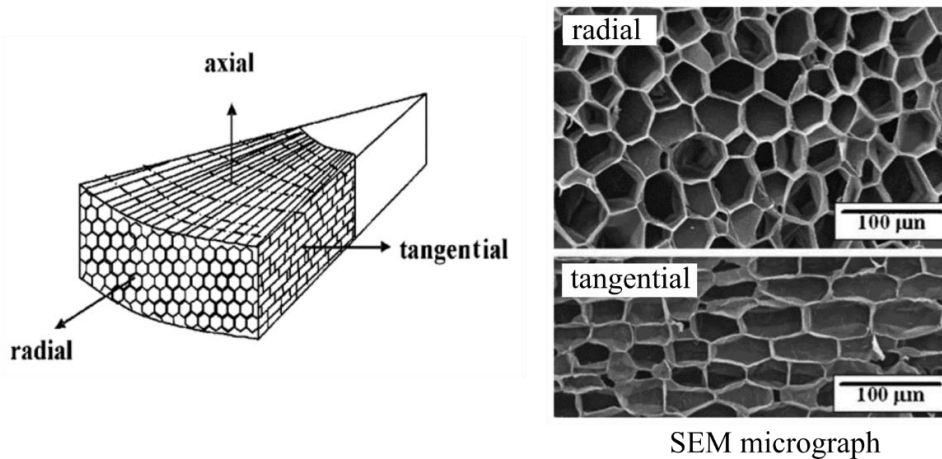


Figure 2.9. The cellular structure of natural cork. Source: [16]

Agglomerated cork is made from triturated granules of cork mixed with a polymeric binder (as polyurethane) and cured under heat and pressure in a mould. This material has an advantage over natural cork since it uses the residuals from the production of cork items such as wine stoppers. Additionally, it can reduce the variability in characteristic properties of natural material, such as anisotropy by mixing granules with random alignment [11], [17]. For those reasons agglomerated cork is often proposed as an alternative to the natural cork [16], [18], [19]. Among the properties of agglomerated cork are hyperelasticity, low permeability, low thermal conductivity, chemical stability, good energy absorption properties, and vibration damping. [16], [20].



Figure 2.10. Agglomerated cork produced from residuals of wine stoppers.

2.1.7 Polyethylene terephthalate (PET) foam

PET is a thermoplastic polymer of the polyester family that can be either amorphous (transparent) or semi-crystalline (opaque/white). PET is made from mono ethylene glycol (MEG) and purified terephthalic acid (PTA) or dimethyl terephthalate (DMT). A prepolymer (bis-HET) is formed and subsequent polymerization forms the polymeric PET.

BACKGROUND

Most of the PET produced around the world is used for synthetic fibres (60%) and bottle production (30%) [21].



Figure 2.11. PET foam produced from recycled plastic bottles.

Extruded PET foam are receiving more attention as a new alternative to structural core materials. This is the case of the wind industry where PET foam core is widely used in the construction of the turbine blades. Some of the advantages of this material are:

- PET is recyclable and can be made from recycled parts such as PET bottles [22].
- PET foam is manufactured by extrusion providing better control in density and mechanical properties [23].
- PET foam is suitable for different manufacturing processes such as infusion, pre-preg and press bonding. It can be cut by either a hotwire or a laser process. It can be re-melted and can be fused with most face-sheet laminates during heated cure, without the use of an adhesive
- It has an extraordinary resistance to fatigue, is chemically stable and has negligible water absorption [22]

2.2 The problem of impact vulnerability

2.2.1 Damage tolerance

The concept of damage tolerance is associated with the ability of a structure to maintain its integrity under a certain state of damage in such a way that damage never propagates to failure before detection. This is particularly important in principal structural elements in

which failure would lead to catastrophic failure. Damage can occur from different sources including manufacturing defects, accidental damage during assembly and handling, or due to service operations such as lightning strikes or foreign object damage (FOD) [24].

The structural damage created by foreign object impact is usually defined as impact damage. The study of impact damage in sandwich composite structures is complex since it involves not just penetration and delamination (as in conventional laminates) but other modes such as core crushing and face-sheet debonding. The damage varies across the sandwich thickness and in some cases it may affect one face-sheet while the other is still intact. Aeronautical structures for example are very sensitive to impact what in turn can generate damage in the core and face-sheet decreasing the residual strength of the structure [2]. The induced damage depends on multiple factors such as face-sheet layup, thickness, core material, core thickness, indenter velocity and shape, as well as boundary conditions, just to name a few [24].

Diverse experimental studies have demonstrated that impact damage in sandwich structures reduces the residual strength in tension, compression, shear and bending. This reduction in residual strength occurs once the impact energy exceeds a threshold after which there is an important difference from the intact state [24]. The term Barely Visible Impact Damage (BVID) has been widely used in the aerospace industry and in particular in composite structures to categorize the damage that sometimes cannot be detected by the naked human eye but that can have a drastic detrimental effect on the structure performance. As stated by McGowan et al. [25] there are two critical challenges in the study of impact damage tolerance in sandwich structures. First, a reliable criterion to predict the appearance of visible impact damage and second the residual strength in a preloaded structure.

The problem of impact vulnerability has concerned the aerospace industry and has called the attention of the public for decades (Figure 2.12) due to infamous accidents such as the one experienced by the Air France Flight 4590 in which debris from a tyre impacted the fuel tank of the Concorde [26]. Another not less shocking case is the accident of the space shuttle Columbia in which one large piece of insulated foam separated from the external fuel tank and struck the underside of the left-wing [27].

BACKGROUND

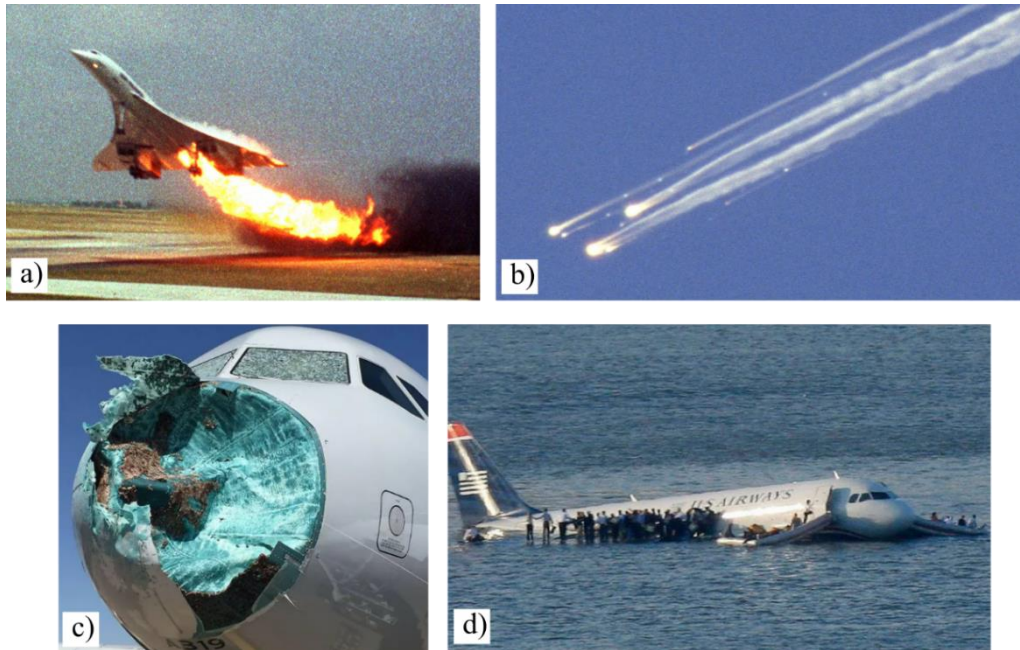


Figure 2.12. Examples of accidents/incidents due to impact vulnerability. a) Concorde AFR-4590, b) Space shuttle Columbia, c) emergency landing of AA-1897 after hailstone impact, d) emergency landing of UA-1549 after a bird strike.

The problem of impact damage is that critical that the airworthiness certification standards for large aeroplanes EASA CS-25 [28] state different scenarios in which appropriate damage tolerance levels must be ensured.

- An aeroplane must be able to safely complete a flight in which structural damage occurs due to the impact of a 4 lb (1.81 Kg) bird at a relative speed equal to the aeroplane cruise speed (CS.25.631). This impact must not cause penetration in the pilot windshield or put in danger the pilots from flying windshield fragments due to bird impact.
- Another consideration accounts for ice thrown by the rotating propellers in the aircraft (CS.25.875). In this case, the airframe must be properly reinforced to withstand the most severe ice impacts to occur.
- The hazard of a blade released by a hub failure must also be considered during the design to minimize the damage to the structure and critical systems (CS.905)
- Fuel tank access cover must minimize deformation and penetration by tyre fragments and other debris to avoid loss of hazardous fuel that could subsequently ignite (CS.25.963).
- The fatigue response of some components must be evaluated under expectable impact damage levels expected during fabrication, assembly, and service. It should

be demonstrated that the stiffness of the component doesn't change under acceptable levels.

In general aviation aeroplanes (EASA CS-23) the standards for impact vulnerability are less severe since this kind of aeroplane fly at a limited speed and impacts can rarely cause a total loss. However, bird strikes penetrating through the pilot windshield, wing airfoil, antennas, pitot tube or hydraulic lines are still a subject of concern [29].



Figure 2.13. Example of bird impact in general aviation. Source: [29]

Due to their stricter safety standards, the aerospace industry has been in the lead of the analysis of impact vulnerability. However, other transport industries are affected as well. For example, in the railway industry, impacts generated by flying track-ballast can damage the train floor [30], [31] and bird strikes are also a hazard for the aerodynamic wind-brake of high-speed trains since they can generate substantial damage to the brake and the subsidiary structure [32].



Figure 2.14. Train damage due to track-ballast impact. Source: [31]

In the wind industry, turbine blades are usually designed for 20 years of operation in which the impact of particles, rain, sand, hail, insects or birds can damage the turbine blade. This damage is usually mild creating small coating cracks that might affect the smoothness of the blade and reduce the gross annual energy production but on some occasions, it can

compromise the integrity of the structure. The subject of impact vulnerability has also gained recently more interest in high-speed marine vessels due to the interest to establish criteria to evaluate collisions with floating and submerged objects as well as berthing impact [33]. In marine vessels, the damage is associated not just with the detrimental structural capacity but also with the danger that a breach may lead directly to a loss of the structure at sea [34].

2.2.2 Impact categories

The impact response is usually classified into low velocity (large mass), intermediate velocity, high velocity or ballistic (small mass) and hypervelocity regimes. Low-velocity impact (LVI) is frequent during tool drops in which the impact velocity is below 10 m/s [35]. In an LVI, the stress waves generated during impact reach the edges of the structure and are reflected before the impact ends. In this kind of impact, structure response is global and is influenced by geometry and boundary conditions [36].

Intermediate velocity impact (IVI) falls in the middle of low-velocity and high-velocity impacts. It occurs at impact velocities near 50 m/s, usually with a blunt impactor. It is characterized by the short duration of impact and a response dominated by flexural and shear waves. Some examples of typical IVI include impacts of road debris, hail impact, impacts of a projectile with low velocity or even a tennis racket hitting a ball. The energy absorbed in the system is divided into two parts: energy absorbed generating damage and energy dissipated by the system through vibrations, heat, and elastic response.

The high-velocity impact (HVI) is controlled by the propagation of waves across the thickness. In this kind of impact, the material is unable to respond globally, causing localized damage. Boundary conditions play a minor role due to the short duration of impact that is not enough for the stress wave to reach the boundaries. It is commonly accepted that HVI occur in a velocity range between 50 m/s and 1000 m/s [35]. The ballistic limit is a useful parameter in the study of HVI. This is simply the maximum velocity reached by the projectile after complete perforation of the structure and it is usually determined in probabilistic terms and adjustment curves. Impacts at higher velocities, particularly above 4000 m/s are usually called hypervelocity impacts. In this kind of impact the projectile velocity is higher than speed of sound in the impacted material therefore the shockwave that propagates across the material is reflected by the surfaces of the target,

inverting its direction of propagation. This kind of impact is of high interest in the to study of debris and meteorite impact against space equipment.

2.3 Model validation and the building block approach.

During the product development cycle, engineers are sometimes challenged to assess the capabilities of different materials and predict the damage and residual strength of a composite structure. Experimental test campaigns are expensive and not practical due to the high number of test articles that will be required to analyse all critical conditions. This has increased the reliance on modelling techniques such as the Finite Element Analysis (FEA) method that must be properly verified and validated against test data [37].

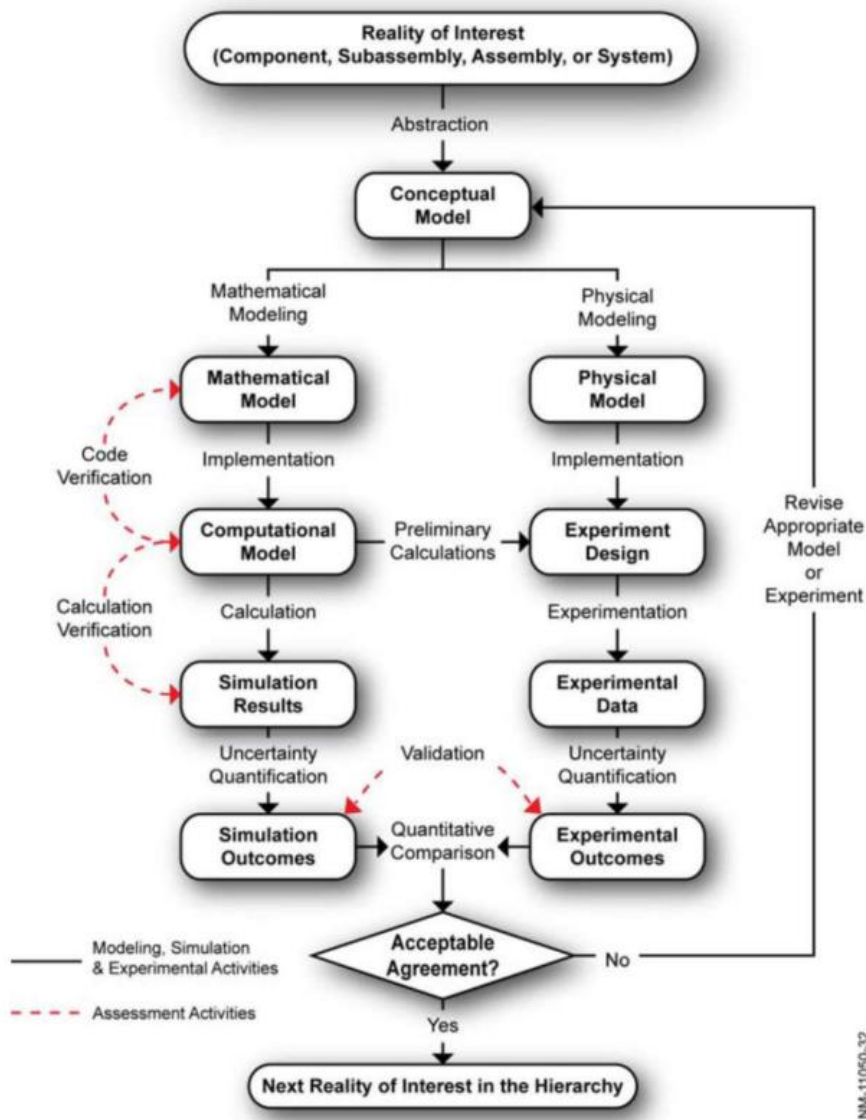


Figure 2.15. Verification and validation process against experimental testing. Source: [37]

BACKGROUND

Figure 2.15 shows the usual parallel process carried out to verify and validate a computational model against experimental testing. The verification phase establishes that the mathematical model and solution algorithms are properly implemented and working properly. Since most users employ commercially available software, they are normally not involved in the code verification process. However, in cases where the users develop in-house tools, the user/developer is expected to carry out the appropriate code verification.

The validation phase is intended to determine how accurate is the model compared to the real world keeping the perspective of its intended use. This is carried out by direct comparison of the numerical results and experimental results. The building block approach is a methodology that unifies physical testing with virtual testing from the early design phases. The building block approach is a step by step series of physical and virtual tests of increasing complexity that serves to create reliable simulation models that support the design of composite structures. This approach is usually related to a testing pyramid in which different levels are addressed sequentially starting from coupon level testing up to structure level testing (Figure 2.16). This approach should ensure that the phenomena under analysis is properly understood and should be able to isolate erroneous output [37]. From the experimental side, this methodology requires collecting as much high-quality data as possible using equipment such as strain gauges, accelerometers, load cells, high-speed cameras and/or techniques such as Digital Image Correlation (DIC). The subject of model validation is very wide to be covered in this chapter. The reader is encouraged to follow reference [37] for further details about different methods of comparing test data with analysis results.

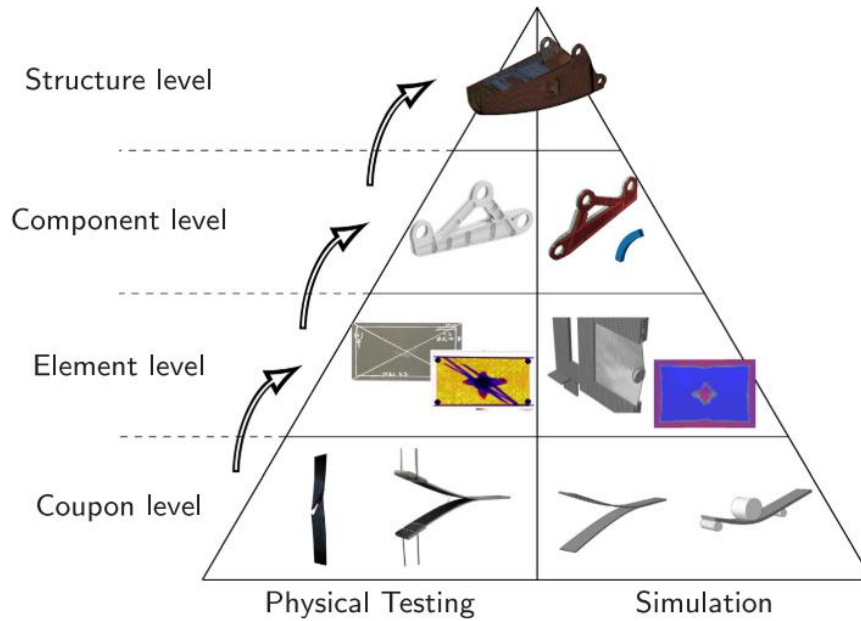


Figure 2.16. Building block approach pyramid. Source: [38]

References of the chapter

- [1] Gibson LJ, Ashby MF. Cellular solids. 2nd ed. Cambridge University press; 1997.
- [2] CASTANIE B, BOUVET C, Ginot M. Review of composite sandwich structure in aeronautic applications. Compos Part C Open Access 2020;1. <https://doi.org/10.1016/j.jcomc.2020.100004>.
- [3] Baxter R, Hastings N, Law A, Glass EJ. Sandwich Structures 7: Advancing with Sandwich Structures and Materials. vol. 39. 2008.
- [4] Thybo Thomsen O. Sandwich Materials for Wind Turbine Blades-Present and Future n.d. <https://doi.org/10.1177/1099636208099710>.
- [5] Baker A, Dutton S, Kelly D. Composite materials for aircraft structures. Blacksburg, Virginia, United States: American Institute of Aeronautics and Astronautics; 2004.
- [6] Niu M. Composite Airframe Structures: Hong Kong: Hong Kong Conmilit Press Ltd; 1992.
- [7] Fathi A. Mechanical Properties of Strand PET Foams at Different Length Scales. ProQuest LLC, 2018.
- [8] Jardin RT, Fernandes FAO, Pereira AB, Alves de Sousa RJ. Static and dynamic mechanical response of different cork agglomerates. Mater Des 2015;68:121–6.

- <https://doi.org/10.1016/j.matdes.2014.12.016>.
- [9] Ptak M, Kaczynski P, Fernandes FAO, de Sousa RJA. Assessing impact velocity and temperature effects on crashworthiness properties of cork material. *Int J Impact Eng* 2017;106:238–48. <https://doi.org/10.1016/j.ijimpeng.2017.04.014>.
- [10] Ashby MF. Materials and the environment. *Mater Environ* 2012;i–iii. <https://doi.org/10.1016/b978-0-12-385971-6.00016-6>.
- [11] Fernandes FAO, Jardim RT, Pereira AB, Alves De Sousa RJ. Comparing the mechanical performance of synthetic and natural cellular materials. *Mater Des* 2015;82:335–41. <https://doi.org/10.1016/j.matdes.2015.06.004>.
- [12] Lakreb N, Boudjema Bezzazi, Pereira H. Mechanical strength properties of innovative sandwich panels with expanded cork agglomerates. *Eur J Wood Wood Prod* n.d. <https://doi.org/10.1007/s00107-015-0908-y>.
- [13] Sergi C, Sarasini F, Barbero E, Sanchez-Saez S, Tirillò J. Assessment of agglomerated corks and PVC foams cores crashworthiness under multiple-impact events in different loading conditions. *Polym Test* 2021;96. <https://doi.org/10.1016/j.polymertesting.2021.107061>.
- [14] Sergi C, Tirill J, Sarasini F, Pozuelo EB, Saez SS, Burgstaller C. The Potential of Agglomerated Cork for Sandwich Structures: A Systematic Investigation of Physical, Thermal, and Mechanical Properties 2019.
- [15] Yang W, Dong Q, Liu S, Xie H, Liu L, Li J. Recycling and Disposal Methods for Polyurethane Foam Wastes. *Procedia Environ Sci* 2012;16:167–75. <https://doi.org/10.1016/j.proenv.2012.10.023>.
- [16] Silva M Da, Oleskovicz M, Coury D V. Cork: properties, capabilities and applications. *Int Mater Rev* 2005;50:345–58. <https://doi.org/10.1179/174328005X41168>.
- [17] Le Barbenchon L, Girardot J, Kopp J-B, Viot P. Multi-scale foam: 3D structure/compressive behaviour relationship of agglomerated cork. *Materialia* 2019;5:100219. <https://doi.org/10.1016/j.mtla.2019.100219>.
- [18] Sasso M, Mancini E, Chiappini G, Sarasini F, Tirillò J. Application of DIC to Static and Dynamic Testing of Agglomerated Cork Material. *Exp Mech* 2018;58:1017–33. <https://doi.org/10.1007/s11340-017-0369-9>.

- [19] Castro O, Silva JM, Devezas T, Silva A, Gil L. Cork agglomerates as an ideal core material in lightweight structures. *Mater Des* 2009;31:425–32. <https://doi.org/10.1016/j.matdes.2009.05.039>.
- [20] Silva JM, Gamboa P V, Nunes C, Paulo L, Franco N. Cork: Is It a Good Material for Aerospace Structures? n.d. <https://doi.org/10.2514/6.2011-2159>.
- [21] Li-Na J. Study on preparation process and properties of polyethylene terephthalate (pet). *Appl Mech Mater* 2013;312:406–10. <https://doi.org/10.4028/www.scientific.net/AMM.312.406>.
- [22] Airex. Airex T92 DATA SHEET 04.2018. 2018.
- [23] Core for composites: Winds of change: *CompositesWorld* n.d. <https://www.compositesworld.com/articles/core-for-composites-winds-of-change> (accessed February 24, 2019).
- [24] Tomblin J, Lacy T, Smith B, Hooper S, Vizzini A, Lee S. Review of Damage Tolerance for Composite Sandwich Airframe Structures. *US Dep Transp Fed Aviation Adm* 1999;71. <https://doi.org/DOI/FAA/AR-99/49>.
- [25] McGowan DM, Ambur DR. Damage characteristics and residual strength of composite sandwich panels impacted with and without a compression loading. 39th AIAA/ASME/ASCE/AHS/ASC Struct. Struct. Dyn. Mater. Conf. Exhib., Long Beach, CA, U.S.A: 1998. <https://doi.org/10.2514/6.1998-1783>.
- [26] Bureau Enquêtes-Accidents. Accident on 25 July 2000 at La Patte d’Oie in Gonesse (95) to the Concorde registered F-BTSC operated by Air France 2000.
- [27] National Aeronautics and Space Administration. Columbia Accident Investigation Board 2015;I:74.
- [28] European Aviation Safety Agency. Certification Specifications for Large Aeroplanes CS-25. 2007.
- [29] EGAST. Bird strike , a European risk icities Edition 1 – Germany GA 6 2013:1–24.
- [30] Sakly A, Laksimi A, Kebir H, Benmedakhen S. Experimental and modelling study of low velocity impacts on composite sandwich structures for railway applications. *Eng Fail Anal* 2016;68:22–31. <https://doi.org/10.1016/j.engfailanal.2016.03.001>.
- [31] Önder A, Robinson M. Harmonised method for impact resistance requirements of

BACKGROUND

- E-glass fibre/unsaturated polyester resin composite railway car bodies. *Thin-Walled Struct* 2018;131:151–64. <https://doi.org/10.1016/j.tws.2018.06.041>.
- [32] Jianyong Z, Xiaoyu Z, Mengling W. Numerical simulation of a bird impact on a composite aerodynamic brake wing of a high-speed train. *Proc Inst Mech Eng Part F J Rail Rapid Transit* 2015;229:223–36. <https://doi.org/10.1177/0954409713508109>.
- [33] Sutherland LS. A review of impact testing on marine composite materials: Part I – Marine impacts on marine composites. *Compos Struct* 2018;188:197–208. <https://doi.org/10.1016/j.compstruct.2017.12.073>.
- [34] Sutherland LS, Guedes Soares C. Impact behaviour of typical marine composite laminates. *Compos Part B Eng* 2005;37:89–100. <https://doi.org/10.1016/j.compositesb.2005.09.001>.
- [35] Abrate S. *Impact engineering of composite structures*. SpringerWi. 2011.
- [36] Buitrago Pérez BL. *Comportamiento de estructuras de material compuesto sometidas a cargas impulsivas*. University Carlos III of Madrid, 2012.
- [37] EASA. *Notification of a Proposal to issue a Certification Memorandum: Modelling and Simulation – CS-25 2020:1–55*.
- [38] Wagner T, Heimbs S, Franke F, Burger U, Middendorf P. Experimental and numerical assessment of aerospace grade composites based on high-velocity impact experiments. *Compos Struct* 2018;204:142–52. <https://doi.org/10.1016/j.compstruct.2018.07.019>.

3 BUILDING A RELIABLE MODEL FOR THE FACE-SHEETS

An effective FEA model for a whole sandwich panel is built from the piecewise validation of its components. This chapter discusses the modelling approach of the woven CFRP laminates, which are used in subsequent chapters to model the sandwich face-sheets. It includes a brief overview of the assumptions and mathematical formulations used in the FEA model together with the introduction of the concept of continuum damage mechanics. The constitutive material model for intra-laminar and inter-laminar damage is presented and validated using results available in the scientific literature. For this purpose, three independent FEA models of standard fracture tests are implemented: one for intra-laminar fracture (mode I) and two for inter-laminar fracture (mode I and II). The material model is then used in the implementation of an FEA model of a laminate subjected to ballistic impact which is further validated with experimental results from the literature.

3.1 Modelling woven CFRP laminates

Modelling laminated composite materials is different from conventional engineering materials because the constitutive equation of each ply in the laminate is orthotropic. In this case, there are three mutually perpendicular planes of symmetry represented by three characteristic directions: fibre direction (x_1), thickness direction (x_3) and a perpendicular direction to the last two (x_2).

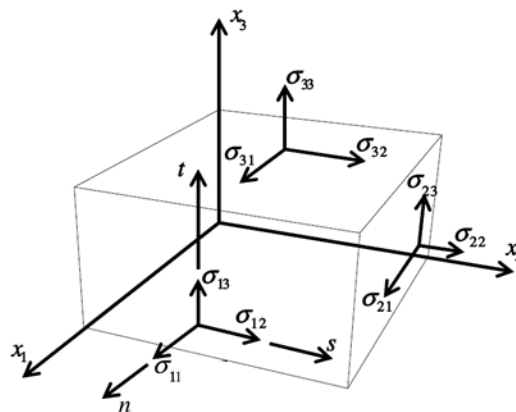


Figure 3.1. Stress components. Source: [1]

Continuous mechanics are used to describe the strain in the ply using the following tensor notation:

$$\boldsymbol{\varepsilon} = \begin{bmatrix} \varepsilon_{11} & \varepsilon_{12} & \varepsilon_{13} \\ \varepsilon_{12} & \varepsilon_{22} & \varepsilon_{23} \\ \varepsilon_{13} & \varepsilon_{23} & \varepsilon_{33} \end{bmatrix} \quad (3.1)$$

Similarly, the stress tensor can describe completely the state of stress at a point.

$$\boldsymbol{\sigma} = \begin{bmatrix} \sigma_{11} & \sigma_{12} & \sigma_{13} \\ \sigma_{12} & \sigma_{22} & \sigma_{23} \\ \sigma_{13} & \sigma_{23} & \sigma_{33} \end{bmatrix} \quad (3.2)$$

Similarly in Voigt notation, both tensors can be expressed as ε_{ij} and σ_{ij} respectively.

Applying Hook's law, orthotropic materials are fully described by the following relation [1]:

$$\begin{pmatrix} \varepsilon_{11} \\ \varepsilon_{22} \\ \varepsilon_{33} \\ \gamma_{23} \\ \gamma_{13} \\ \gamma_{12} \end{pmatrix} = \begin{bmatrix} S_{11} & S_{12} & S_{13} & 0 & 0 & 0 \\ & S_{22} & S_{23} & 0 & 0 & 0 \\ & & S_{33} & 0 & 0 & 0 \\ & Sym & & S_{44} & 0 & 0 \\ & & & & S_{55} & 0 \\ & & & & & S_{66} \end{bmatrix} \begin{pmatrix} \sigma_{11} \\ \sigma_{22} \\ \sigma_{33} \\ \sigma_{23} \\ \sigma_{13} \\ \sigma_{12} \end{pmatrix} \quad (3.3)$$

Where $\gamma_{ij} = 2(\varepsilon_{ij})$ and the multiplying matrix [S] is the compliance matrix which is the inverse of the stiffness matrix. In this case, only 9 independent constants are required to describe an orthotropic material.

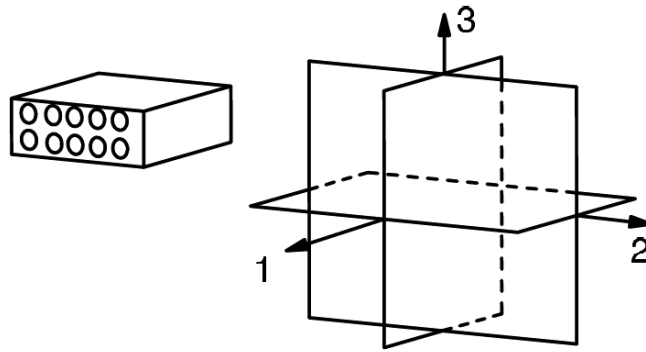


Figure 3.2. Plane of symmetry in an orthotropic material. Source: [1]

The constants in the matrix [S] can be related to the engineering materials constants of an orthotropic material:

$$[S] = \begin{bmatrix} \frac{1}{E_1} & -\frac{\nu_{21}}{E_2} & -\frac{\nu_{31}}{E_3} & 0 & 0 & 0 \\ & \frac{1}{E_2} & -\frac{\nu_{32}}{E_3} & 0 & 0 & 0 \\ & & \frac{1}{E_3} & 0 & 0 & 0 \\ & Sym & & \frac{1}{G_{23}} & 0 & 0 \\ & & & & \frac{1}{G_{13}} & 0 \\ & & & & & \frac{1}{G_{12}} \end{bmatrix} \quad (3.4)$$

Where E_i is the Young modulus in direction i , G_{ij} is the shear modulus in i - j and ν_{ij} is the Poisson ratio in i - j . Composite laminates are usually modelled as assemblies of plates and shells with the constitutive equations of the elements depending on kinematic assumptions of the shell theory used [1]. Plane stress approximates the stresses in thin laminates when fibres are parallel to the plane 1-2 and the laminate is loaded by forces parallel to the same plane that are uniformly distributed over the thickness. For a plane stress formulation, one of the normal stresses is zero ($\sigma_{33} = 0$) and both out-of-plane stresses are zero ($\sigma_{23} = 0$ and $\sigma_{13} = 0$). As a result therefore the third row and column of the matrix $[S]$ are not used simplifying the problem to [1]:

$$\begin{pmatrix} \varepsilon_{11} \\ \varepsilon_{22} \\ \gamma_{12} \end{pmatrix} = \begin{pmatrix} \frac{1}{E_1} & -\frac{\nu_{12}}{E_2} & 0 \\ -\frac{\nu_{21}}{E_2} & \frac{1}{E_2} & 0 \\ 0 & 0 & \frac{1}{G_{12}} \end{pmatrix} \begin{pmatrix} \sigma_{11} \\ \sigma_{22} \\ \sigma_{12} \end{pmatrix} \quad (3.5)$$

The same can be expressed in terms of the stiffness matrix $[Q]$:

$$\begin{pmatrix} \sigma_{11} \\ \sigma_{22} \\ \sigma_{12} \end{pmatrix} = \begin{pmatrix} \frac{E_1}{D} & -\frac{\nu_{12}E_2}{D} & 0 \\ -\frac{\nu_{12}E_2}{D} & \frac{E_2}{D} & 0 \\ 0 & 0 & G_{12} \end{pmatrix} \begin{pmatrix} \varepsilon_{11} \\ \varepsilon_{22} \\ \gamma_{12} \end{pmatrix} \quad (3.6)$$

Where $D = 1 - \frac{E_2}{E_1} \nu_{12}^2$

A woven ply is considered orthotropic when it has the same amount of fibres oriented in the $+\theta$ direction as in $-\theta$ direction. To obtain the stiffness matrix of a woven ply it is

necessary to compute the elements of the stiffness matrix applying a transformation of the fibre oriented by an angle of $\pm\theta$.

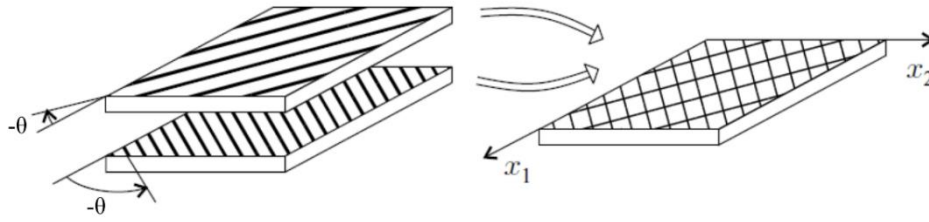


Figure 3.3. A ply made of fibres in the $+\theta$ and $-\theta$ directions. Source: [2]

The elements of the stiffness matrix of a woven ply can be estimated from the elements of the stiffness matrix of the unidirectional ply by applying the following transformation [2]:

$$Q_{11}^{woven} = c^4 Q_{11} + s^4 Q_{22} + 2c^2 s^2 (Q_{12} + 2Q_{66}) \quad (3.7)$$

$$Q_{22}^{woven} = s^4 Q_{11} + c^4 Q_{22} + 2c^2 s^2 (Q_{12} + 2Q_{66}) \quad (3.8)$$

$$Q_{12}^{woven} = c^2 s^2 (Q_{11} + Q_{22} + 4Q_{66}) + (c^4 + s^4) Q_{12} \quad (3.9)$$

$$Q_{66}^{woven} = c^2 s^2 (Q_{11} + Q_{22} - 2Q_{12}) + (c^2 - s^2) Q_{66} \quad (3.10)$$

$$Q_{16}^{woven} = 0 \quad (3.11)$$

$$Q_{26}^{woven} = 0 \quad (3.12)$$

Where $c = \cos(\theta)$ and $s = \sin(\theta)$

3.1.1 Fracture mechanics in laminate composites.

The theory of Linear Elastic Fracture Mechanics (LEFM) allows predicting crack growth assuming that the non-linearities of the material are neglected and the initial position of the crack is known. This theory initially developed by Grifin et al. [3] in the 1920s is based on an energy balance approach between the changes in the mechanical and surface energies of the solid under the influence of an applied stress level. In other words, the decrease of potential energy in the system (due to the displacement of the external boundaries and the change in the stored elastic energy) must compensate for the increase of surface energy due to crack extension.

Similarly in the 1950s Irwin [3] and Orowan [4] proposed a way to characterize a “driving force” for fracture in cracked elastic solids by the introduction of the concept of “energy release rate (G)” that is the rate of change of the potential mechanical energy W_p over the crack area A . This definition of G applies for both linear and nonlinear materials and is a

function of the load and crack length and it is independent of the boundary conditions (i.e. type of loading).

$$G = - \frac{dW_p}{dA} \quad (3.13)$$

They suggested that the advance of a crack under monolithic quasi-static loading occurs when the strain energy is released at a rate sufficiently high to satisfy all energy “sinks” such as the energy required to open new surfaces and plastic flow near the crack tip. They called this parameter “critical strain energy release rate” denoted by G_c .

Solid subjected to stress are usually studied assuming three basic modes of crack propagation (Figure 3.4). Mode I, or opening mode, in which the face open in a direction perpendicular to the plane of the crack. Mode II, or sliding mode, in which the faces of the crack are sheared in the direction of the crack. Finally Mode III or tearing mode in which the faces of the crack are sheared in a direction parallel to the crack front.

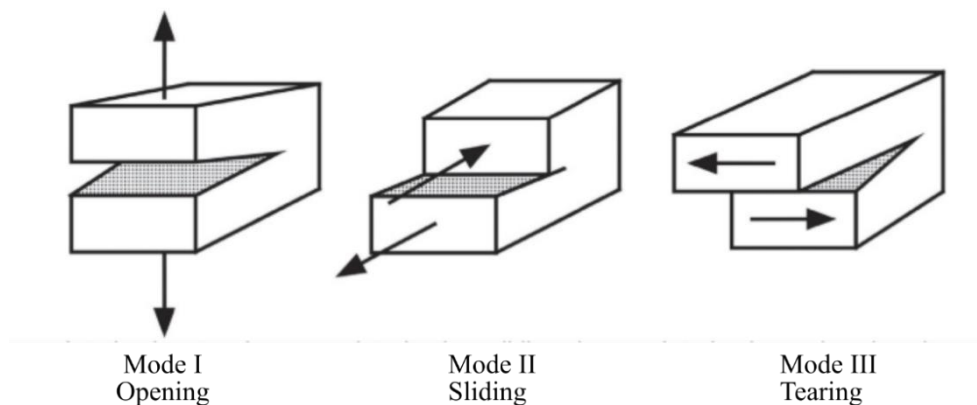


Figure 3.4. Fracture modes. Source: [5]

In practice, in composite materials, the state of stresses to which the laminate is subjected can lead to the appearance of one of these modes, or a combination of them. In addition, the brittle nature of composite materials is associated with sudden crack growth.

In composite laminates, there are two main categories of damage modes: inter-laminar and intra-laminar damage. Inter-laminar damage is related to the separation of two adjacent plies. This mode is acknowledged as one of the most important since it can occur at low load level (compared to ultimate fibre failure) but still compromise the structural load-carrying capability of the laminate. This occurs since conventional composite laminates have no fibre reinforcement through the thickness so properties are dominated by the weak matrix material. Intra-laminar damage, on the other hand, occurs in the plane of the plies

and it is related to different mechanisms such as fibre breakage, fibre pull-out, fibre buckling, matrix cracking and fibre-matrix splitting [5].

3.1.2 The Continuum Damage Mechanics (CDM) approach

CDM is one of the techniques currently used to model fracture and damage in solids mainly since it is easy to implement in FEA software. Additionally, it can predict the initiation of fracture in a structure without a pre-existing sharp notch. CDM models are used to predict the evolution of different damage modes at the mesoscale level and calculate the degradation of the ply stiffness in terms of continuum damage variables. Damage evolution is predicted in terms of empirical equations that are a function of parameters that need additional experimentation. CDM models require three major components [6]:

- a) Damage variable
- b) Damage activation function
- c) Damage evolution equation

3.1.2.1 Damage variable.

It is a state variable to keep track of the amount of damage. The damage variable can be interpreted in the following two alternative ways. First, as a reduction of the area due to the presence of microcracks.

$$D = 1 - \frac{A}{\tilde{A}} \quad (3.14)$$

Or the associated loss of the stiffness in the material

$$D = 1 - \frac{E}{\tilde{E}} \quad (3.15)$$

Where A and E are the area and Young modulus after damage and \tilde{A} and \tilde{E} are the same but at the initial (virgin) state. Since the nominal area \tilde{A} is known, the nominal stress is given by:

$$\sigma = \frac{P}{\tilde{A}} \quad (3.16)$$

The effective stress acting in the remaining area is given by:

$$\tilde{\sigma} = \frac{P}{A} \quad (3.17)$$

Therefore the relation between effective stress $\tilde{\sigma}$ and nominal stress σ is:

$$\sigma = \tilde{\sigma}(1 - D) \quad (3.18)$$

A thermodynamic force Y drives the growth of the variable D . This force can be any physical independent quantity such as stress, strain, the energy release rate, etc...

3.1.2.2 Damage activation function.

The elastic domain is bounded by a load threshold. Below this threshold, no damage occurs in the material; however, if the load exceeds this threshold then damage increases. At higher load levels, the elastic domain changes its threshold due to hardening or softening.

The elastic domain is defined by a damage activation function of the form [6]:

$$g = \hat{g} - \hat{\gamma} \leq 0 \quad (3.19)$$

Where \hat{g} is a positive function that depends on an independent variable and $\hat{\gamma}$ is the threshold for hardening. The updated damage threshold is given by:

$$\hat{\gamma} = \gamma(\delta) + \gamma_0 \quad (3.20)$$

Where γ_0 is the threshold of the virgin material and $\gamma(\delta)$ is the hardening function that depends on a hardening variable.

3.1.2.3 Damage evolution equation

The rate of damage accumulation is:

$$\dot{D} = \dot{\lambda} \frac{dg}{dY} \quad (3.21)$$

Where $\dot{\lambda} \geq 0$ is the damage multiplier that gives consistency between the damage and hardening evolution. The values of $\dot{\lambda}$ and g are used to distinguish between two possible scenarios given by the Kuhn-Tucker conditions:

$$\dot{\lambda} \geq 0; g \leq 0; \dot{\lambda}g = 0 \quad (3.22)$$

a) Loading in the elastic region or unloading without damage growth:

$$g < 0; \dot{\lambda} = 0; \dot{D} = 0 \quad (3.23)$$

b) Loading with damage growth:

$$\dot{\lambda} > 0; g = 0; \quad (3.24)$$

3.1.3 Intra-laminar CDM for fabric reinforced composites

This subsection describes the CDM model for fabric reinforced composites developed by Johnson [7] based on the continuum damage formulation formulated by Ladeveze et Le-Dantec [8]. This model is implemented in Abaqus/explicit through the built-in VUMAT subroutine ABQ_PLY_FABRIC.

The ply is modelled as an orthotropic elastic material that can sustain progressive damage due to fibre/matrix cracking and plastic deformation under shear load. The elastic stress-strain relations are given by:

$$\begin{pmatrix} \varepsilon_{11} \\ \varepsilon_{22} \\ \varepsilon_{12}^{el} \end{pmatrix} = \begin{pmatrix} \frac{1}{(1-D_1)E_1} & -\frac{\nu_{12}}{E_2} & 0 \\ -\frac{\nu_{21}}{E_2} & \frac{1}{(1-D_2)E_2} & 0 \\ 0 & 0 & \frac{1}{(1-D_{12})2G_{12}} \end{pmatrix} \begin{pmatrix} \sigma_{11} \\ \sigma_{22} \\ \sigma_{12} \end{pmatrix} \quad (3.25)$$

Where D_1 and D_2 are the damage variables related to fibre fracture in the 1 and 2 directions respectively, whereas D_{12} is related to matrix micro-cracking due to shear deformation.

3.1.3.1 Fibre damage

The model can differentiate between tensile and compressive failure by activating the corresponding damage variable:

$$D_1 = D_{1+} \frac{\langle \sigma_{11} \rangle}{|\sigma_{11}|} + D_{1-} \frac{\langle -\sigma_{11} \rangle}{|\sigma_{11}|} \quad (3.26)$$

$$D_2 = D_{2+} \frac{\langle \sigma_{22} \rangle}{|\sigma_{22}|} + D_{2-} \frac{\langle -\sigma_{22} \rangle}{|\sigma_{22}|} \quad (3.27)$$

Knowing that the damage variable is a function of effective stress:

$$D_\alpha = D_\alpha(\tilde{\sigma}_\alpha) \quad (3.28)$$

The thermodynamic force driving damage is:

$$Y_\alpha = \frac{1}{2} \frac{\tilde{\sigma}_\alpha^2}{E_\alpha} \quad (3.29)$$

Combining the previous equations, it can be noticed that the damage variable only depends on the corresponding thermodynamic force. The elastic domain is given by the activation function:

$$g_\alpha = \hat{g}_\alpha - \hat{\gamma}_\alpha \leq 0 \quad (3.30)$$

Being \hat{g} the fibre failure criteria and $\hat{\gamma}$ the damage threshold that is initially set to one. X_α is the uniaxial strength in the fibre directions.

$$\hat{g}_\alpha = \frac{\tilde{\sigma}_\alpha}{X_\alpha}; \quad (\alpha = 1_+, 1_-, 2_+, 2_-) \quad (3.31)$$

After damage activation, ($\widehat{g}_\alpha = 1$) the damage threshold increases. This ensures that the damage threshold is not decreasing to enforce the Kuhn-Tucker conditions.

$$\hat{\gamma}_\alpha = \max \hat{g}_\alpha(t) \quad (3.32)$$

The evolution of the damage variables are a function of the fracture energy (per unit area) G_f^α and the damage threshold. The damage evolution is given by the equation:

$$D_\alpha = 1 - \frac{1}{\hat{\gamma}_\alpha} e^{-A_\alpha(\hat{\gamma}_\alpha - 1)} \quad (3.33)$$

Where:

$$A_\alpha = \frac{2g_0^\alpha L_c}{G_f^\alpha - g_0^\alpha L_c} \quad (3.34)$$

Here, L_c is the characteristic length of the element in the mesh, G_f^α is the fracture energy (per unit area) under uniaxial loading, and g_0^α is the elastic energy density (per unit volume) at the point of damage initiation.

$$g_0^\alpha = \frac{X_\alpha^2}{2E_\alpha} \quad (3.35)$$

This formulation creates a restriction in the maximum element size that can be used to estimate the right amount of energy dissipation during fracture:

$$G_f^\alpha - g_0^\alpha L_c > 0; L_{max} = \frac{G_f^\alpha}{g_0^\alpha} \quad (3.36)$$

3.1.3.2 Shear response

The shear behaviour is non-linear and includes both plasticity and stiffness degradation due to matrix microcracking. The elastic effective (undamaged) stress is given in terms of the elastic strain:

$$\tilde{\sigma}_{12} = \frac{\sigma_{12}}{(1 - D_{12})} = 2G_{12}(\varepsilon_{12} - \varepsilon_{12}^{pl}) \quad (3.37)$$

The plastic behaviour is described through a yield function:

$$F = |\tilde{\sigma}_{12}| - \tilde{\sigma}_0(\bar{\varepsilon}^{pl}) \leq 0 \quad (3.38)$$

And a hardening function

$$\tilde{\sigma}_0(\bar{\varepsilon}^{pl}) = \tilde{\sigma}_{y0} + C(\bar{\varepsilon}^{pl})^p \quad (3.39)$$

In shear, the elastic region is similarly defined from damage activation function than in the case of fibre damage:

$$g_{12} = \hat{g}_{12} - \hat{\gamma}_{12} \leq 0 \quad (3.40)$$

The criteria for initiation of shear damage is:

$$\hat{g}_{12} = \frac{\tilde{\sigma}_{12}}{S} \quad (3.41)$$

Being $\tilde{\sigma}_{12}$ the effective shear stress and S the shear stress for initiation of matrix damage

$$\tilde{\sigma}_{12} = \frac{\sigma_{12}}{1 - D_{12}} \quad (3.42)$$

The damage threshold $\hat{\gamma}_{12}$ is set to one and increases after damage activation ($\hat{g}_{12} = 1$):

$$\hat{\gamma}_{12} = \max \hat{g}_{12}(t) \quad (3.43)$$

The evolution of the shear damage variables increases with the logarithm of $\hat{\gamma}_{12}$ until a maximum damage (D_{12}^{max}) is reached:

$$D_{12} = \min(\alpha_{12} \ln(\hat{\gamma}_{12}), D_{12}^{max}) \quad (3.44)$$

The shear damage parameter α_{12} can be determined experimentally by measuring the ratio of the unloading stiffness to the initial elastic stiffness in a cyclic tensile test at ± 45 .

3.1.3.3 Element deletion

The ABQ_PLY_FABRIC subroutine provides two conditions for element deletion that can be chosen by the user:

- 1) When any tensile/compressive damage variable in the fibre directions reaches a maximum specified value $D_1 = D_{max}$ or $D_2 = D_{max}$ or when the plastic shear strain reaches a maximum specified $\bar{\varepsilon}^{pl} = \bar{\varepsilon}_{max}^{pl}$
- 2) When the damage variables along both fibre directions reach a maximum specified value $D_1 = D_2 = D_{max}$ or when the plastic shear strain reaches a maximum specified $\bar{\varepsilon}^{pl} = \bar{\varepsilon}_{max}^{pl}$

In addition, an element deformation criterion can be used for element deletion. This criterion is based on the maximum ($\hat{\epsilon}_{max} > 0$) and minimum ($\hat{\epsilon}_{max} < 0$) principal logarithmic strain that the element can sustain.

3.1.4 Inter-laminar CDM for fabric reinforced composites (Delamination)

Delamination occurs due to the separation of one or more plies in a laminate. The interface of adjacent plies offers a low resistant path for crack growth since it is dominated by matrix properties that are usually weak. Delamination can be analysed using fracture mechanics theory or continuum damage mechanics (CDM) models. In this section, the CDM approach also called the cohesive zone model (CZM) is discussed since this is the approach used in FEA models in this and subsequent sections. The reader is encouraged to refer to [9] for further details about other methods to model delamination in composite materials.

3.1.4.1 Cohesive zone model (CZM) – pure mode

CZM works under the assumption that a cohesive zone (interface) has a linear elastic behaviour until a critical level of stress σ_i^0 (and separation δ_i^0) is reached.

$$\sigma_i = K_i \delta_i a = b + c \quad (3.45)$$

Once this level is reached, the stress transfer capacity is still maintained but the damage is initiated with a progressive degradation of the stiffness. Depending on the load state the initially coincident nodes can either open or slide (mode I: opening, mode II: shear, mode III: tier). The stiffness of the damaged material K_i are then given in terms of the undamaged stiffness values (\tilde{K}_i) and the damage variables for each mode (D_i).

$$K_i = (1 - D_i) \tilde{K}_i \quad (3.46)$$

The undamaged stiffness values (\tilde{K}_i) are different from Young's modulus E and the shear modulus G and they should be estimated experimentally. CZM uses the classical assumption of elastic damage when there is no permanent deformation upon unloading (line AF).

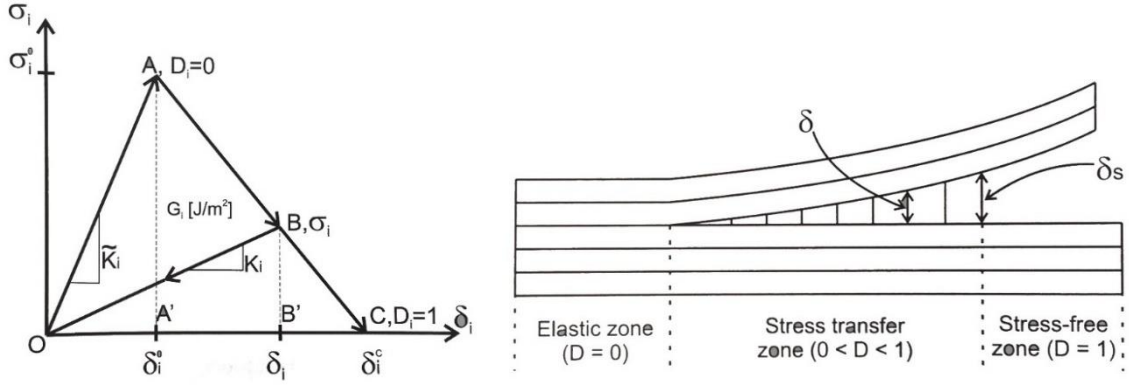


Figure 3.5. Cohesive model for crack growth. Source: [1]

When the fracture is reached there is a complete loss of cohesive stress transfer. The separation at fracture is correlated with the critical energy release rate G_{ic} in each mode by considering the area under the curve (σ - δ).

$$\delta_i^c = \frac{2G_{ic}}{\sigma_i^0} \quad (3.47)$$

CDM requires the experimental estimation of nine material values G_{ic} , σ_i^0 , \tilde{K}_i (three for each crack propagation mode).

Rearranging some terms it can be found that the damage variable can be given in terms of the relative separation between the faces in the cohesive zone [6]:

$$D_i = \frac{\delta_i^c (\delta_i - \delta_i^0)}{\delta_i (\delta_i^c - \delta_i^0)} \quad (3.48)$$

3.1.4.2 Cohesive zone model (CZM) – mixed mode

When the cohesive zone is under multiple modes simultaneously all stresses ($\sigma_I, \sigma_{II}, \sigma_{III}$) and separation components $\delta_I, \delta_{II}, \delta_{III}$ are active. Although the modes occur simultaneously, they are assumed uncoupled.

It is necessary to define mixed mode ratios to characterize the mixed-mode state.

$$\beta_{\delta_{II}} = \frac{\delta_{II}}{\delta_I}; \beta_{\delta_{III}} = \frac{\delta_{III}}{\delta_I} \quad (3.49)$$

$$\beta_{G_{II}} = \frac{G_{II}}{\sum_1^3 G_i}; \beta_{G_{III}} = \frac{G_{III}}{\sum_1^3 G_i} \quad (3.50)$$

A mixed-mode separation is defined as the norm of the mode separations:

$$\delta_m = \sqrt{\sum_1^3 \delta_i^2} \quad (3.51)$$

The single-mode initiation criteria are replaced by a quadratic stress criterion:

$$\sum_1^3 \left(\frac{\sigma_i}{\sigma_i^0} \right)^2 = 1 \quad (3.52)$$

With this, it is possible to estimate the mixed-mode separation at damage onset (δ_m^0). For the case of only mode, I and II acting simultaneously the separation at damage onset are:

$$\delta_m^0 = \sqrt{(\delta_I^0)^2 (\delta_{II}^0)^2 \frac{1 + \beta^2}{(\delta_{II}^0)^2 + \beta^2 (\delta_I^0)^2}} \quad (3.53)$$

The crack propagation for a mixed-mode is given in terms of the energy release rate with a power criterion:

$$\sum_1^3 \left(\frac{G_i}{G_{ic}} \right)^\alpha = 1 \quad (3.54)$$

Each of the single-mode components of the energy release rate (G_i) are calculated by considering only the unrecoverable energy represented by the area A_{OAB} in figure Figure 3.5.

$$A_{OAB} = A_{OAC} - A_{OBC} \quad (3.55)$$

Knowing that A_{OAC} is equivalent to the critical energy release rate (G_{ic}) for a single-mode it is found that the energy release rate at the moment of mixed fracture is given by:

$$G_i = G_{ic} - \frac{1}{2} K_i \delta_i^0 \delta_i^c \left(\frac{\delta_i^c - \delta_i}{\delta_i^c - \delta_i^0} \right) \quad (3.56)$$

Finally, the mixed-mode damage variable is expressed as:

$$D_m = \frac{\delta_m^c (\delta_m - \delta_m^0)}{\delta_m (\delta_m^c - \delta_m^0)} \quad (3.57)$$

With this, the stiffness degradation is estimated in the same manner as the single-mode case [6].

3.2 Modelling inter-laminar and intra-laminar failure

Conventional fracture mechanics have shown to be successful to study homogeneous, isotropic materials however, its use in anisotropic materials has been rather limited and it is still an active subject of research. Modelling composite structures under loading conditions where fracture propagation is expected requires a detailed characterization of the fracture toughness. It is important to characterize the intra-laminar toughness energy to evaluate the structure performance when fibre failure is the dominant failure mechanism but also the inter-laminar toughness against delamination.

One of the most complete studies about intra-laminar fracture in laminated composites was carried out by Pinho et al. [10]. In this study, the fracture toughness of unidirectional carbon/epoxy laminates was investigated in tensile and compressive failure modes. Compact tension (CT) and Compact Compression (CC) tests were performed following the ASTM E399 standard. However, the authors proposed a new geometry for the test specimens and a new data reduction approach since FEA models showed that the stress intensity factor method used for isotropic materials can lead to inaccurate results for laminate composite materials. Finally, after measuring fracture toughness for crack initiation and propagation in CT and CC using FEA analysis (J-integral and VCCT) the authors concluded that fracture toughness is layup dependent.

One of the phenomena that complicate the fracture characterization of composite laminates is fibre bridging. In fibre bridging, adjacent plies bridge the delamination plane and act as crack arrestors increasing the fracture toughness [11]. Fibre bridging has also been recently associated as a toughening mechanism for intra-laminar fracture and the dependency of intra-laminar toughness to laminate thickness [12].

Cohesive elements formulation has been used recently to model delamination in composite laminates. The accuracy of this technique depends on the parameters used for its definition such as fracture toughness, penalty stiffness and interfacial strength. The fracture toughness can be determined from experimental tests while the interfacial strength and penalty stiffness are numerical parameters difficult to obtain experimentally due to the fast initiation and propagation of the crack-tip opening [13], [14]. Lu et al. [14] studied the sensitivity of the last two parameters on the damage process for fracture and coupon tests in CFRP laminates. From their extensive literature review, it is observed that values for penalty stiffness and interfacial strength are commonly assumed or calibrated to obtain a

better correlation with experimental data or even sometimes to improve computational efficiency. The values used in previous FEA analysis over CFRP laminates are sometimes not reported and when reported they might vary substantially from one to another. This study concluded that delamination fracture significantly depends on the interface strength for those simulation cases where stress concentrations are not obvious. On the other hand, the penalty stiffness has an important influence on the model since low values lead to models with low overall structural stiffness and delayed initiation of fracture while too high values may lead to higher computational costs and numerical difficulties [14].

When an FEA with a continuum damage model (CDM) is used, the experimental determination of the fracture toughness energy is not enough to fully describe the fracture behaviour of the model. Additional parameters such as the undamaged (or penalty) stiffness and the stress (or strain) for damage onset must be calibrated from the experimental testing. The purpose of this section is to reproduce the experimental tests carried out by Sandip et al. [15] using the reported fracture toughness and calibrating the remaining CDM model parameters. In their work, the authors studied the fracture behaviour of three different kinds of carbon fibre reinforced composites including woven AS4/8552 (AGP193 PW/8552) in intra-laminar mode I and inter-laminar model I and II. The intra-laminar fracture in a model I was characterized by a Compact Tension test (CT) while inter-laminar fracture in mode I and II by a Double Cantilever Beam (DCB) test and End Notched Flexure (ENF) respectively.

Three independent FEA models are proposed to validate the fracture behaviour of woven CFRP laminates: the first model for intra-laminar fracture in mode I, the second model for inter-laminar fracture in mode I and the third model for inter-laminar fracture in mode II. Additionally, the cohesive law parameters are validated with results obtained through experimental testing [15]. The software Abaqus_v6.14 is employed using standard and explicit solver schemes. To allow correlation of the results the same material properties are used for all modelling approaches. The stress and stiffness parameters in the cohesive law (σ_i, \tilde{K}_i) are established by trial and error while the critical energy release rate (G_i) is obtained directly from [15].

3.2.1 Intra-laminar fracture Mode I – Compact tension (CT)

In their work, Sandip et al. [15] characterized the intra-laminar fracture in mode I through a Compact Tension test (CT) initially proposed by Pinho et al. [10]. This experiment

consists of a notched monolithic specimen eccentrically loaded under tension through the pins inserted into the specimen holes. The notch is cut in two steps first with a disc cutter and second by a wire cutting machine to get a sharp edge (Figure 3.6). The laminate layup used in this experiment is $[90]_{16}$.

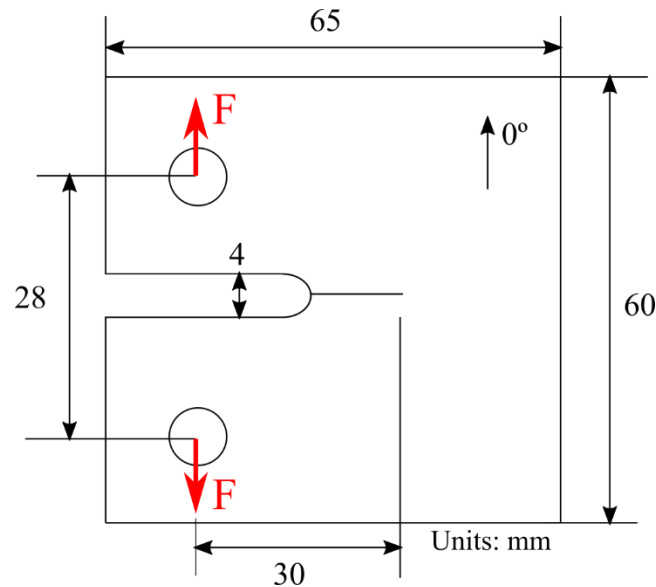


Figure 3.6. CT test specimen

The specimen is modelled as a single deformable shell with the same geometry and lay-up as in the experimental test. The mesh is based on quadrilateral shell elements with reduced integration, hourglass control and three integration points across the thickness for each ply. The geometry was partitioned to create mesh transition regions to improve computational efficiency. The element size is 0.5mm in the vicinity of the crack tip along the expected crack growth direction. For the rest of the specimen, the element size varies from 0.5 to 2 mm. The mesh size is refined in the pinhole region to ensure the proper distribution of the vertical forces (Figure 3.7). Two reference points are coupled to the pinhole edge. One for the top pinhole and the other for the bottom pinhole. A vertical displacement is applied on the top reference point while this displacement is restrained by a pinned constrain is applied to the bottom reference point.

Since the material model is implemented through a VUMAT subroutine an explicit/dynamic procedure had to be used in this model. Mass scaling was used to increase the time increment and improve computational efficiency. The kinetic energy of the whole model was monitored verifying that its magnitude was negligible compared to the internal energy ($<1\%$). This is to ensure that inertial effects are minimum and that the test can be considered as quasi-static.

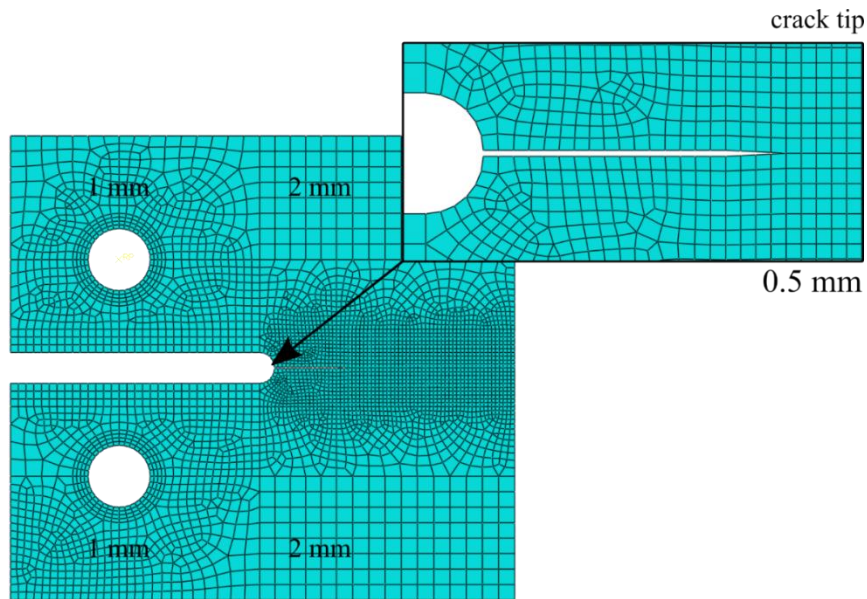


Figure 3.7. FEA model - CT specimen mesh

3.2.2 Inter-laminar Mode I – Double Cantilever Beam (DCB)

For inter-laminar fracture (Mode I) Sandip et al. [15] employed a Double Cantilever Beam (DCB) test following the ASTM D5528 standard [16] and its industrial equivalents AITM 1.0005 (Airbus standard) [17].

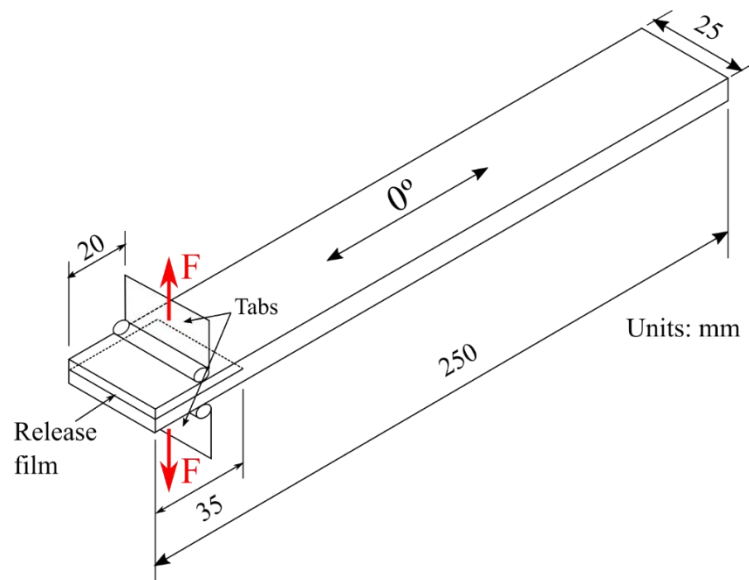


Figure 3.8. DCB test specimen

In this test, a pre-cracked specimen is loaded by peel-forces to propagate the crack. An initial crack of 35 mm is introduced at the end of the specimen by incorporating a release film at the mid-plane of the laminate. Two hinged tabs are located 20 mm from the free edge (Figure 3.8). One of them used to apply the vertical load while the other restrain the

specimen. A conventional DCB specimen of 250x25 mm² made of a monolithic woven (3K) Hexcel AS4/8552 is employed. The layup is [0]₂₄ with a cured ply thickness of 0.2mm giving a total thickness of 4.8mm.

The specimen is modelled as two deformable parts (sub-laminates) attached with a cohesive interaction in the midplane except in the region of the initial crack. The mesh is based on hexahedral solid with continuum shell elements (SC8R) with 3 integration points, reduced integration and first-order accuracy. The mesh distribution is even through the specimen with an element size of 1 mm. The hinge tabs are represented through two reference points coupled to the top and bottom surface where the boundary conditions are applied (vertical displacement and simple support), see Figure 3.9.

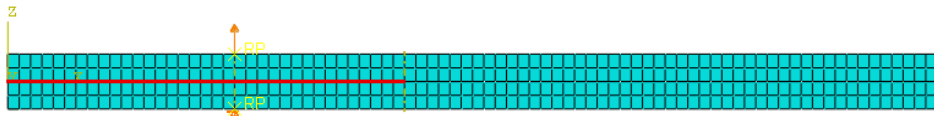


Figure 3.9. Detail of the mesh and Boundary conditions DCB (free edge section)

For the Explicit model, a general contact algorithm (explicit) is applied to model the interlaminar cohesion between both sub-laminates. A cohesive behaviour with maximum stress damage criteria and exponential softening is used. In the case of the Standard model a surface to surface contact with small sliding formulation and damage stabilization.

3.2.3 Inter-laminar Mode II – End notch flexure (ENF)

For the Inter-laminar fracture toughness (Mode II) Sandip et al. [15] performed an End Notch Flexure (ENF) test following the ASTM D7905 [18] and AITM 1.0006 (Airbus standard) [19].

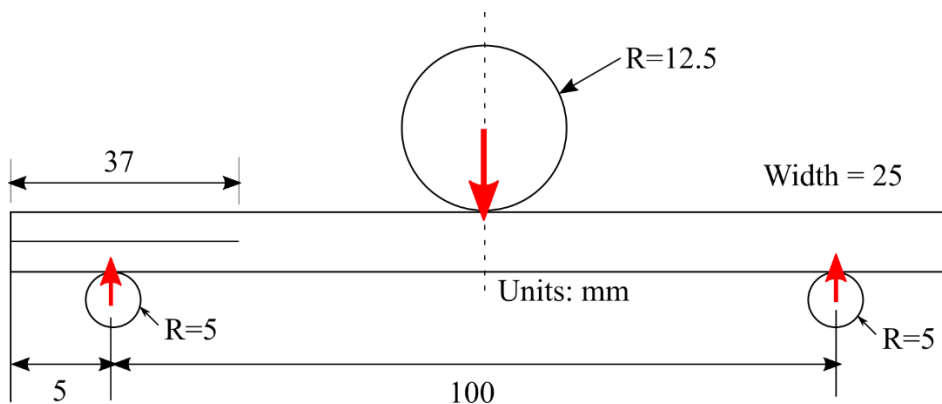


Figure 3.10. ENF test flexure

In this test, a pre-cracked specimen is loaded in a three-point bending test to foster crack propagation. The test specimen is cut from the residual (DCB) specimen tested ensuring that the crack front remains perpendicular to the longitudinal direction. On this occasion, the final specimen geometry used in this experiment is given in Figure 3.10. Three cylindrical supports are located equidistant from the centre line as shown in Figure 3.10. The upper cylinder “called loading nose” is used for the loading application while the bottom supports are used for reacting the specimen.

The ENF specimen is modelled as two deformable parts (sub-laminates) attached with a cohesive interaction in the midplane except in the region of the initial crack. The mesh is based on hexahedral solid with continuum shell elements (SC8R) with 3 integration points, reduced integration and first-order accuracy. The cylindrical supports and the loading nose are modelled independently using rigid shell elements (R3D4). The element size is the same throughout the whole model (1 mm). The cylindrical supports are fixed in all DOF while the loading nose is used to apply the vertical displacement.

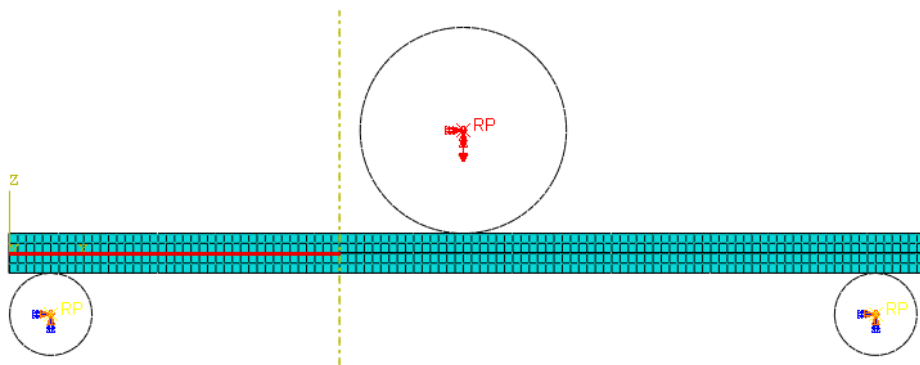


Figure 3.11. Mesh and Boundary conditions ENF

For the Explicit model, the general contact algorithm (explicit) is used for the interaction between the loading nose and the specimen. In the case of the Standard surface contact with small sliding. For both cases, normal and tangential behaviour is used with a skin friction coefficient of 0.2.

The cohesive interaction between the sub-laminates is the same as explained in the DCB case.

3.2.4 Material

The material of the laminate (AS4/8552 woven carbon/epoxy) is modelled using the built-in VUMAT subroutine ABQ_PLY_FABRIC. This subroutine is specifically developed for fabric reinforced composites. The elastic mechanical properties of the material are

extracted from [20] and summarized in Table 3.1. Damage parameters are not included since the laminate is not expected to show intra-laminar damage during the simulation.

ρ (Kg/m ³)	1570
E_{1+} (MPa)	66052
E_{2+} (MPa)	66603
ν_{12+}	0.046
G_{12} (MPa)	5957
E_{1-} (MPa)	76118
E_{2-} (MPa)	74546
ν_{12-}	0.0552
X_{1+} (MPa)	769
X_{1-} (MPa)	1012
X_{2+} (MPa)	753
X_{2-} (MPa)	937
S (MPa)	67

Table 3.1. Mechanical properties AS/8552 carbon/epoxy plain-weave [20]

Besides the widespread use of this material, reported values of its inter-laminar energy release are scarce and previous numerical models can vary substantially from one another. The present work uses the values shown in Table 3.2. is based on CT tests carried out by Sandip et al [15]. In their work only the G_{f1+} is evaluated ($G_{f1+}=50$ N/mm) and this value is taken as a reference to scale the remaining energy terms based on the strain energy at damage onset. As will be shown later the accuracy of this value, as well as the material strength and stiffness, are verified to fit the experimental results obtained in the CT test.

G_{f1+} (N/mm)	50
G_{f1-} (N/mm)	72
G_{f2+} (N/mm)	47
G_{f2-} (N/mm)	67

Table 3.2. Intra-laminar energy release rate AS/8552 carbon/epoxy plain-weave [15].

The inter-laminar parameters for the cohesive law used in this work are presented in Table 3.3. The energy release rate values (G_{ic}) for fracture in mode I and II were extracted from previous ENF and DCB experiments in [13], [15]. The stress and stiffness parameters for

the cohesive law (σ_i, \tilde{K}_i) are established through a sensitivity analysis from the same experiments [15] using a mixed mode power law with an exponent of 2.

K_I (N/mm ³)	2
K_{II} (N/mm ³)	800
K_{III} (N/mm ³)	800
σ_I (MPa)	1.56
σ_{II} (MPa)	23
σ_{IIIc} (MPa)	23
G_{Ic} (N/mm)	0.62
G_{IIc} (N/mm)	2.61
G_{IIIc} (N/mm)	2.61

Table 3.3. Inter-laminar CZM parameters for AS/8552 carbon/epoxy plain-weave.

3.2.5 Fracture test results

Figure 3.12 shows the comparison between the force vs displacement curve for the CT test obtained by the FEA model and the one reported in Sandip et al [15] for the experimental test. The initial part of the curve show the characteristic linear-elastic region where the crack length remains constant. This region is followed by a segment of reduced tangent stiffness due to damage around the crack tip. The maximum peak force denotes the threshold for crack propagation that is followed by a sharp decrease in the stiffness due to rapid crack propagation. From the figure it is clear that the model can predict with accuracy the initial linear elastic response and the onset of damage. Additionally, the CDM model is also able to capture the peak force reached by the specimen during the test and the progressive decrease in the stiffness generated by the damage growth. The region after the peak load shows an unstable crack growth dominated by multiple peak peaks, this behaviour was also observed in the experimental testing. As expected the tensile damage (d_1^+) is highly localized in the crack tip due to the dominant tensile axial stresses in this region. Figure 3.13 show different instants of the test at different loading nose positions. The direction of growth is perfectly aligned to the initial crack something that is required to ensure full mode I fracture. As a result, the intra-laminar tensile behaviour of the material is correctly reproduced by the applied CDM model.

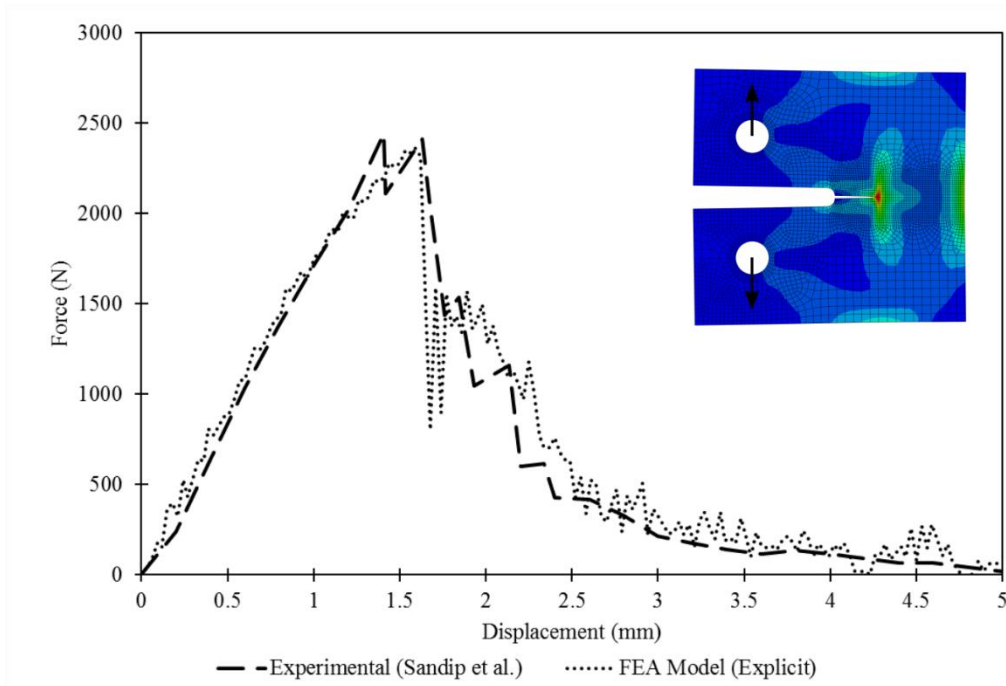


Figure 3.12. Force vs displacement curve for CT test. Comparison between experimental and FEA model

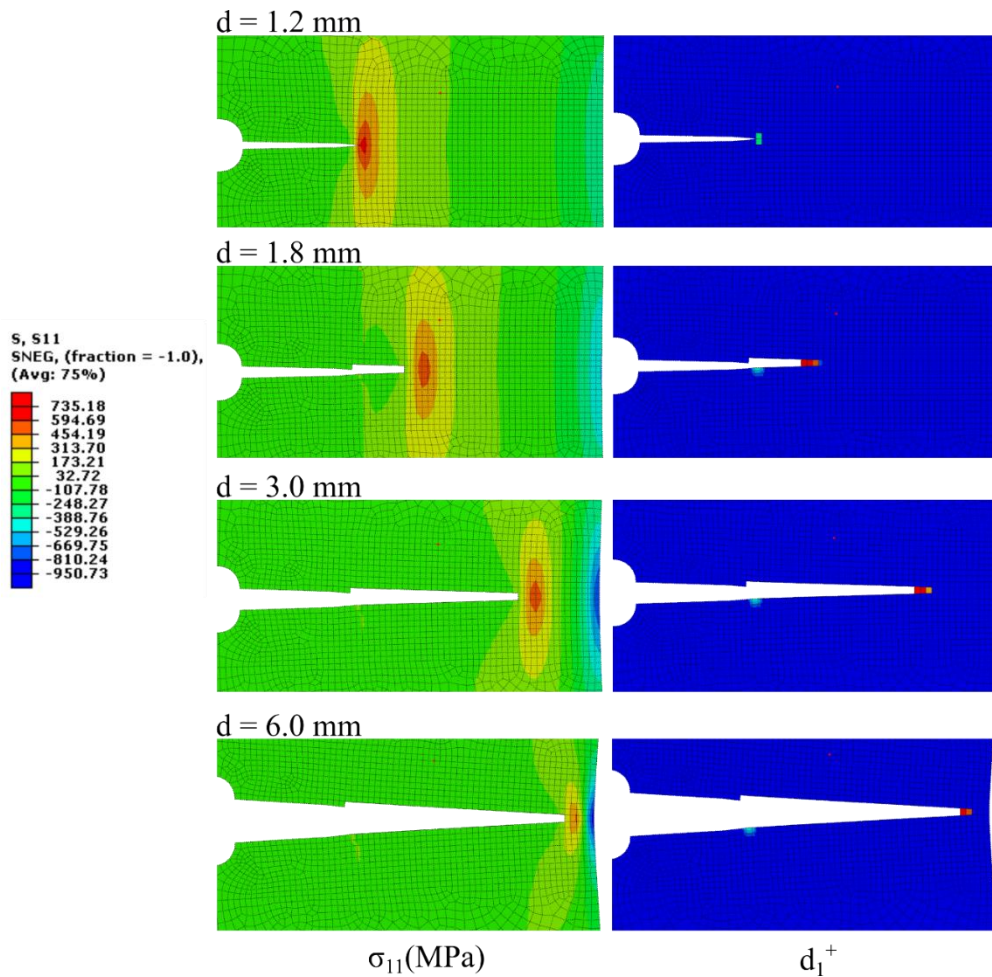


Figure 3.13. Crack growth at different loading nose displacements for CT test (stress along fibre direction σ_{11} and damage variable d_1^+).

Figure 3.14 shows the force/displacement curve of the hinge tabs obtained from the DCB models using standard and explicit solver schemes. The results are compared with the experimental testing from [15]. It can be noticed that both FEA models can predict with high accuracy the damage initiation and damage propagation. Additionally, both models can predict the unstable crack growth described in the experimental testing. For the case of the explicit model, there is a considerable degree of noise in the region of unstable crack growth, this can be associated with the explicit integration method and a large time increment.

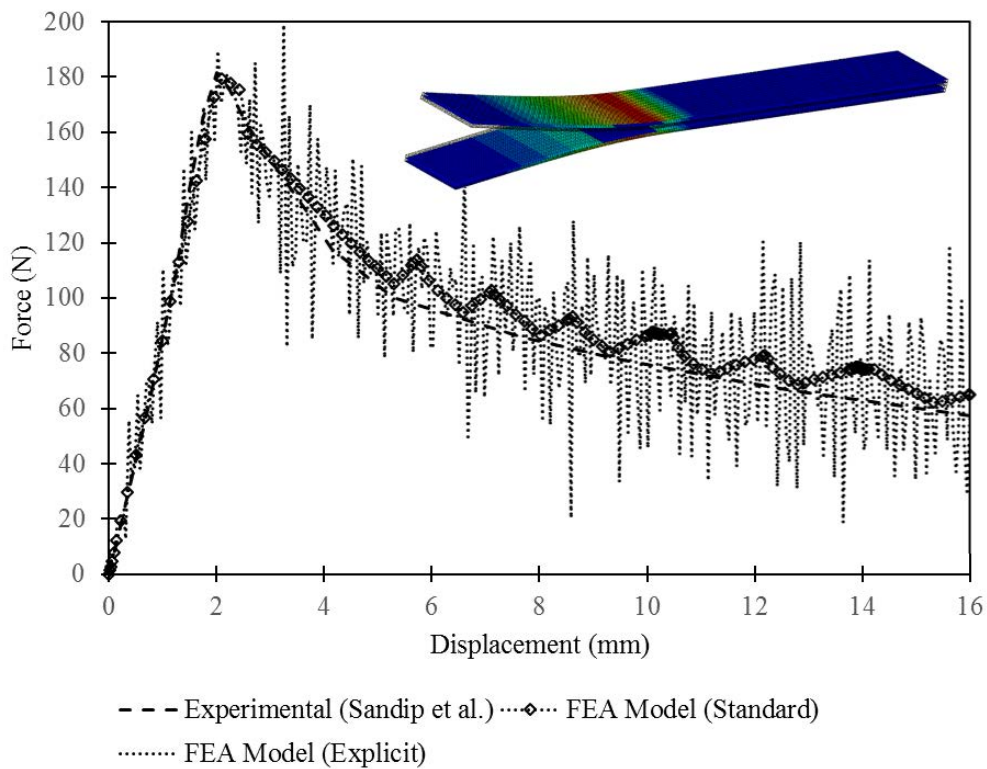


Figure 3.14. Force vs displacement curve for DCB test. Comparison between experimental and FEA models.

The crack growth and damage area monitored for both models at different displacements through the damage variable D . As shown in Figure 3.15 the damage initiation and the cohesive damaged area at three different displacements are almost identical for standard and explicit models.

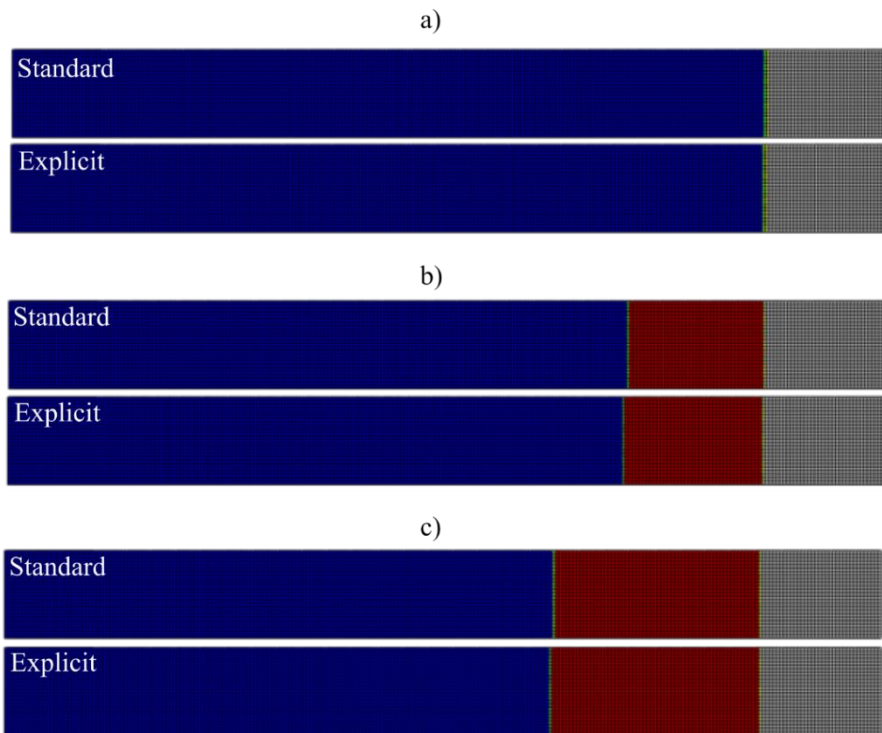


Figure 3.15. Damaged area in DCB model using different FEA solvers.
Tab displacement: a) 2 mm, b) 10 mm, c) 16 mm

A sensitivity analysis is carried out to determine the cohesive law parameters K_{II} and σ_{II} . The chosen parameters are found by trial and error trying to fit at best the results from the experimental testing. Values of K_{II} in the range of 3 to 800 N/mm³ are evaluated and the results are plotted in Figure 3.16. As can be seen the slope in the linear part of the force/displacement curve is highly sensitive to K_{II} . This slope increases with higher values of K_{II} reaching an asymptotic value that corresponds to the ENF with fixed crack length. A value of $K_{II}=800$ N/mm³ seems to fit very well the experimental results in the linear region before cohesive damage.

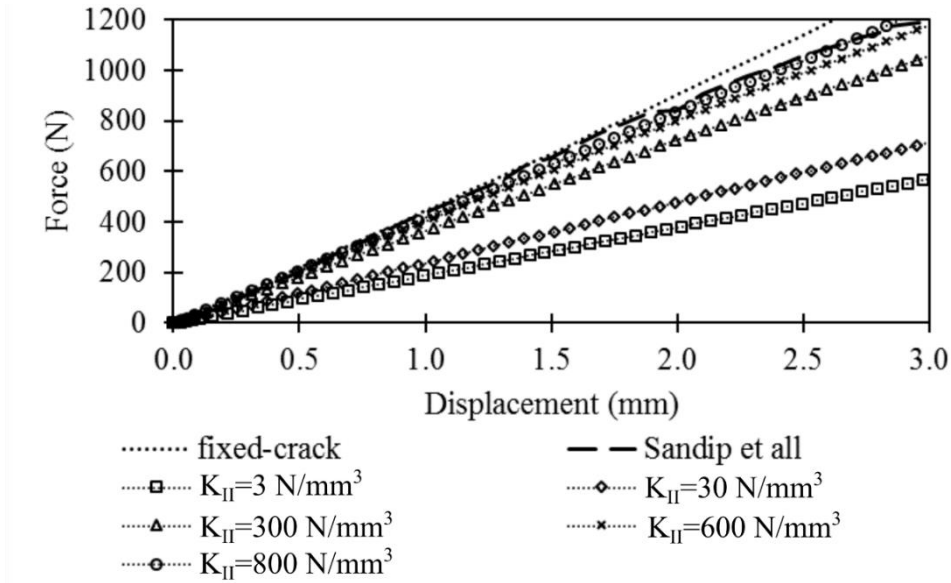


Figure 3.16. Sensitivity for K_{II} (ENF) with $\sigma_{II} = 2$ MPa (standard solver).

A similar sensitivity analysis is carried out for σ_{II} . From Figure 3.17 it can be noticed that the slope of the curve is not sensitive to σ_{II} . However, this value plays a major role in the damage onset. A value close to 20 MPa seems to be adequate to fit experimental data.

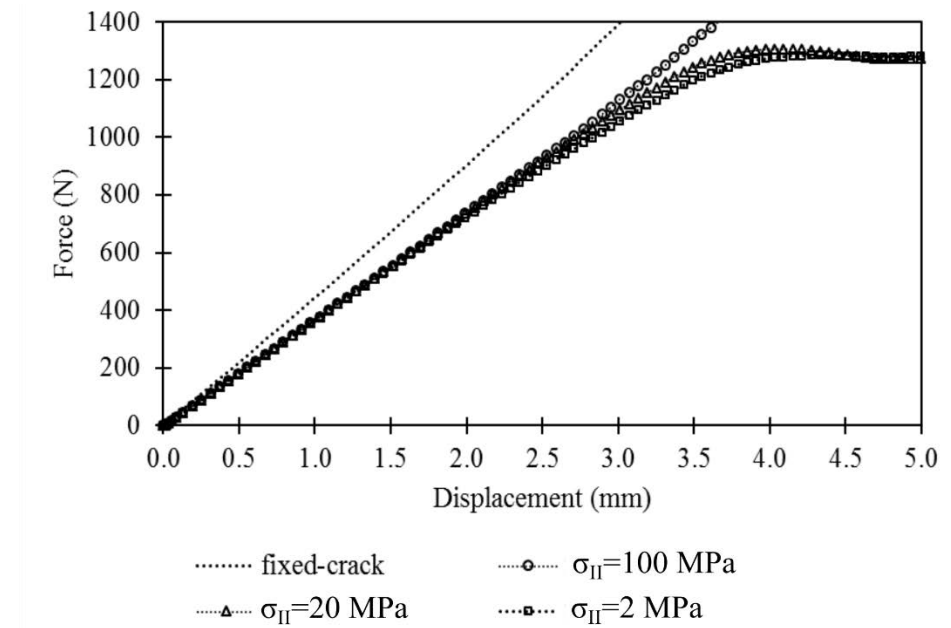


Figure 3.17. Sensitivity for σ_{II} (ENF) with $K_{II} = 300$ N/mm³ (standard solver).

Figure 3.18 shows the force vs displacement curve for the ENF testing for the standard and explicit FEA model, additionally, results are compared with experimental testing from [15]. It can be noticed that the model can predict with high accuracy the linear-elastic portion of the curve. The damage initiation and damage growth are also well predicted however there are small discrepancies with the experimental results in this region.

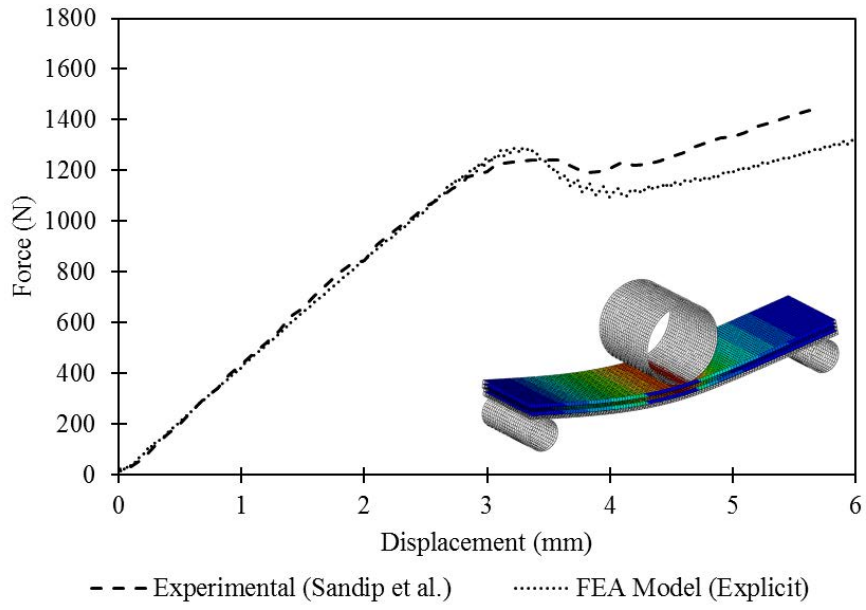


Figure 3.18. Force vs displacement ENF

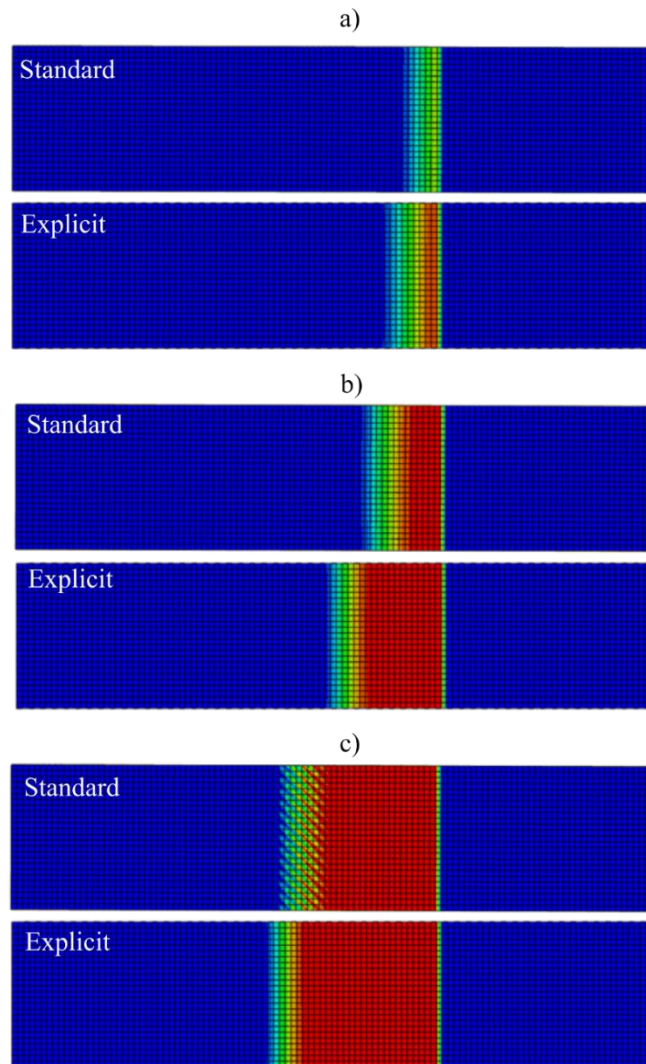


Figure 3.19. Damaged area in ENF model using different FEA solvers. Loading nose displacement: a) 3 mm, b) 4 mm, c) 6 mm

The crack growth is also monitored and a comparison between the standard and explicit model is carried out. As can be noticed from Figure 3.19 the damage initiation and crack growth is well predicted by both models showing small discrepancies that can be produced due to the difference in the contact algorithm used for both cases. It can be also noticed that at maximum displacement (6 mm) the crack extension presented by both models is almost the same with a difference of 3.5%.

3.3 Ballistic impact over CFRP laminates

Lopez-Puentes et al. [21] studied high-velocity impacts on woven CFRP laminates applying an FEA model in Abaqus that implemented the Chang-Chang failure model through a user subroutine. This failure model intrinsically includes damages and failure modes such as fibre failure, and delamination. The laminate is modelled with 3D hexahedral elements with reduced integration and element removal is defined through maximum longitudinal strain criteria to avoid excessive distortions. This study found that the numerical model can reproduce the “rhombus” petal-shaped failure observed in experimental testing. Additionally, the authors compared the damaged area predicted by the numerical model with the measurements obtained using C-Scan ultrasound inspection. The FEA model is able to capture predict similar values of the damaged area as well as the trend of how damage area varies with the impact velocity. The residual velocity of the projectile was also estimated from the FEA model and compared to analytical estimations showing an agreement between both values.

A similar approach was taken by Varas et al. [22] by modelling the high-velocity impact of steel cylinders over CFRP woven laminates. However, in this case, inter-laminar damage and failure are modelled with cohesive elements applying traction-separation laws in which delamination is primarily triggered by normal and shear stresses in the cohesive elements. The authors of this study decided to model only intra-laminar failure in the middle of the laminate instead of at each ply interface to reduce computational costs. The numerical model was able to predict with accuracy the residual velocity of the projectile as well as the damage area trends.

A simplified FEA model was proposed by Buitrago et al. [23] to study ballistic impact in different composite laminates (including woven CFRP). This model uses the Abaqus built-in Hashin criteria for matrix and fibre failure and the laminate is modelled through

conventional shell elements. Beside the simplicity of this model and the fact of not accounting for delamination, the author obtained good correlation in the ballistic limit and the residual velocity.

Heimbs et al. [24] also used the stress-based Chang-Chang failure criteria to model the low-velocity impact of preloaded CFRP laminates in LS-DYNA. In their formulation, once the failure stress criteria are met the stress level is kept constant until the failure strain is reached instead of setting it to zero. The laminate was modelled as a layered shell meaning that one shell element contains multiple sub-layers across the thickness. Intra-laminar damage and failure are considered by applying a tiebreak contact that allows imposing a failure condition between separate shell elements. The model showed a good correlation with the impact force and energy plots recorded in the experiments. Additionally, this model showed the importance of delamination in impact simulation and highlights that neglecting it increases unrealistically the obtained intra-laminar damage.

At DLR institute Johnson [7] developed a continuum damage model for fabric reinforced composites based on the methods previously developed by Ladeveze and Le Dantec [8] for unidirectional ply materials. This model was applied in an explicit FEA model to study CFRP laminates subjected to impact with a hemispherical impactor. The laminate was modelled by layered shell elements and critical parameters for the damage model were obtained from in-plane tensile and cyclic shear tests. The model was able to predict the penetration of the laminate however, it showed some discrepancies with the measured impact forces. In this regard, the authors blame the non-neglecting effect of delamination, which was not modelled in this study.

Wagner et al. [25] performed a study of laminates made of different aerospace-grade composites laminates (including woven CFRP) subjected to high-velocity impacts. The numerical implementation of the FEA model was carried in Abaqus/Explicit using hexahedral continuum shell elements (SC8R) with enhanced hourglass and element deletion. For the fabric material, the built-in VUMAT subroutine ABQ_PLY_FABRIC is used with mechanical properties obtained by the authors directly from tensile and compressive tests. The inter-laminar behaviour of the laminate was modelled using a cohesive contact formulation in which the cohesive behaviour was validated using DCB and ENF tests. The proposed model was able to reproduce the impact behaviour as well as the ballistic limit. Additionally, delamination shape and size agree with experimental observations with the estimation of delamination area being slightly conservative.

After considering all the aforementioned approaches the following FEA modelling is chosen in order to provide a good compromise between modelling complexity, accuracy and data information for the material definition.

3.3.1 FEA model

The precision of the FEA model to predict the perforation of the laminate is validated using the ballistic impact tests carried out Buitrago et al. [23], [26]. To this purpose, a nonlinear dynamic/explicit FEA model in Abaqus v6.14 is proposed. A rectangular laminate (120x120 mm²) of the same woven CFRP material is impacted with a spherical steel projectile of 7.5 mm of diameter and 1.725 g of mass at impact velocities between 45 to 560 m/s. The laminate is 2 mm thick with 10 plies of woven (3K) Hexcel AS4/8552 each one with a cured ply thickness of 0.2 mm.

3.3.1.1 Mesh

The laminate is modelled as a series of independent plies (3D deformable bodies) to create an independent mesh for each ply and allow the definition of the cohesive interaction. Each ply is modelled individually using continuum shell elements with reduced integration (SC8R) and five integration points across the thickness.

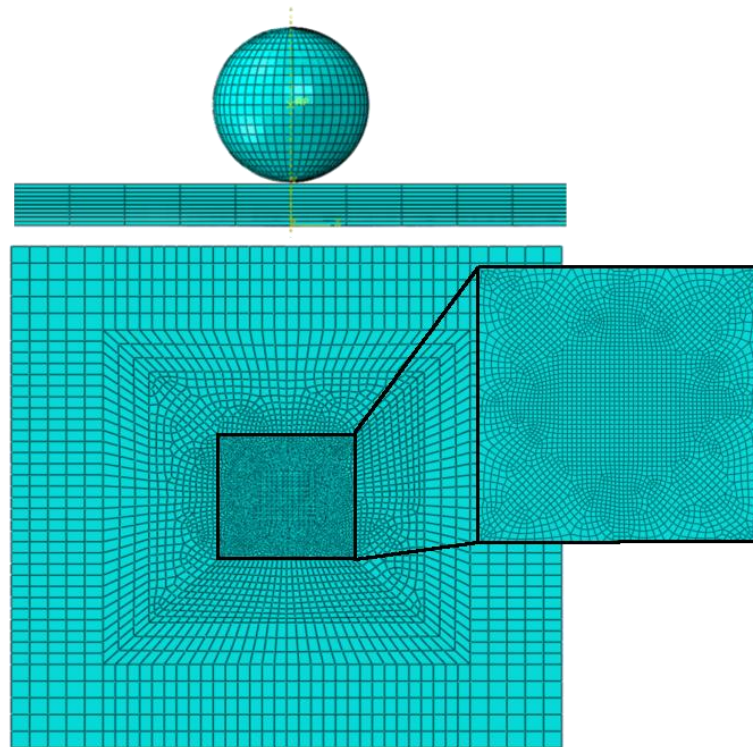


Figure 3.20. Mesh of the laminate and projectile.

The mesh is dominated by hexahedral elements and it is partitioned into five transition regions around the impact zone to improve computational efficiency. The smallest element size at the impact region is 0.5 mm while the largest element size is 4 mm at the free edges. Second-order accuracy, enhanced hourglass control and element deletion are active to avoid excessive deformations. The projectile is modelled with a 3D deformable solid and it is meshed with hexahedral 3D solid elements with an element size of 0.5mm

3.3.1.2 Materials

The material of the projectile is steel with density $\rho=7850 \text{ kg/m}^3$ that follows an isotropic linear-elastic behaviour with a Young Modulus $E=200 \text{ GPa}$ and Poisson ratio $\nu=0.25$.

The material of the laminate (AS4/8552 woven carbon/epoxy) is modelled as orthotropic elastic material with progressive intra-laminar damage applying the built-in VUMAT subroutine ABQ_PLY developed by Jhonson [7] based on the Ladeveze et Le-Dantec model [8]. The intra-laminar and inter-laminar material properties are tabulated in the preceding section (Table 3.1, Table 3.2, Table 3.3) together with detailed information about its validation.

3.3.1.3 Interactions and boundary conditions

The general (explicit) contact algorithm is used to model the interaction between the projectile and the laminate as well as the inter-laminar cohesion between the plies. Normal and tangential behaviour is used for projectile/laminate contact with a skin friction coefficient of 0.55 [27]. A cohesive behaviour with linear softening is used to model the cohesive damage (see section 3.1.4). The complexity of the interactions required the manual selection of all surface pairs (master/slave) that are initially in contact or that can be in contact during the impact. The laminate external edges are fully constrained in all DOF and the initial velocity of the projectile is defined with a predefined field in the initial calculation step.

3.3.2 Ballistic impact results

The residual velocity is estimated for the impact conditions in which there is complete perforation of the laminate. As observed in Figure 3.21 the residual velocity of the projectile shows a good correlation between the experimental and FEA results. In addition, the ballistic limit calculated from the FEA simulations ($V_i= 105 \text{ m/s}$) is an acceptable

estimate of the value obtained in the experimental test ($V_i=100$ m/s). At the qualitative level, the model can capture the perforation process across the laminate including the formation of petal-shaped cracks which has been reported in the literature for impact testing over similar woven CFRP laminates.

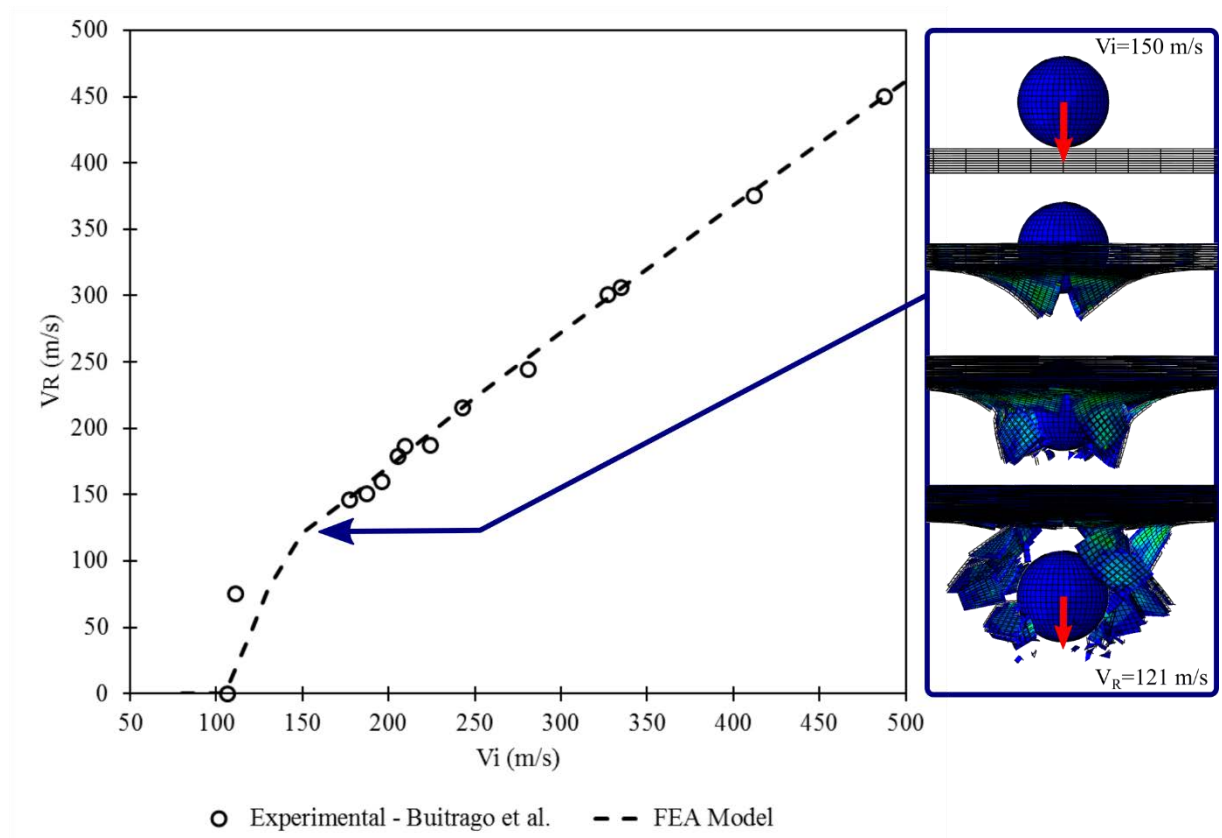


Figure 3.21. Projectile residual velocity vs impact velocity. Monolithic Laminate 2 mm thick. Comparison FEA model and experimental tests (Buitrago et al. [23])

The inter-laminar damage predicted by the FEA model is also compared to the delamination area measured with ultrasound inspection reported by Buitrago et al. [23]. The damaged area in the FEA model is measured as the projected area of all plies in which the cohesive damage variable is greater than one. As observed in Figure 3.22 the measurements from the experimental test show a decrease in the projected delamination area at higher impact velocities. This tendency is also predicted by the FEA model however it does an overestimation of the magnitude of the damaged area.

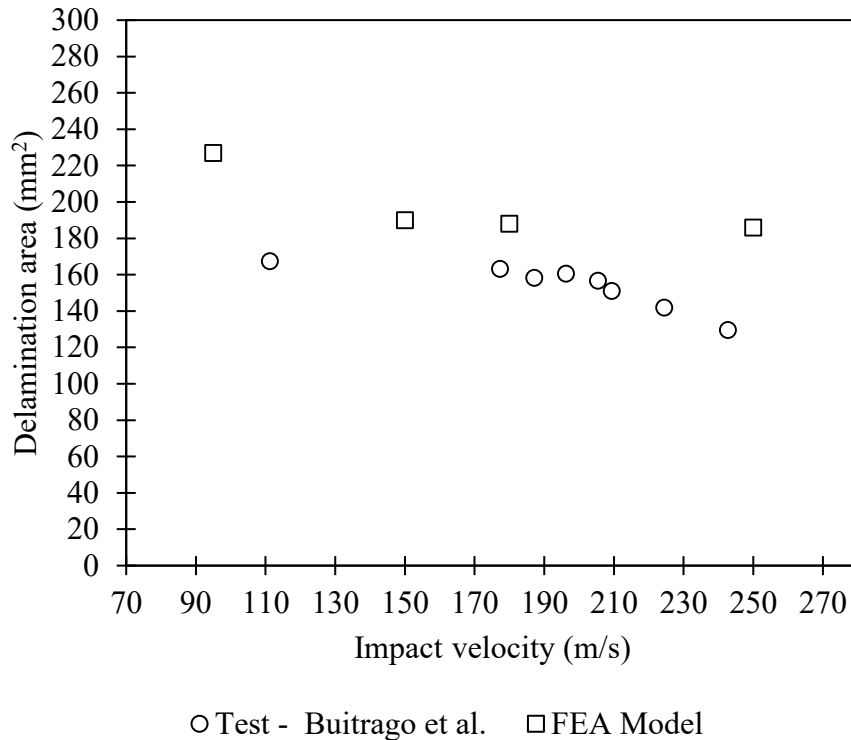


Figure 3.22. Projected delamination area in the laminate. Comparison FEA model and experimental tests (Buitrago et al. [23])

References of the chapter

- [1] Barbero EJ. Finite Element Analysis of Composite Materials with Abaqus. Boca Raton, Florida: 2013.
- [2] Kollar LP, Springer GS. Mechanics of composite structures. New York: Cambridge University press; 2003.
- [3] Griffiths AA. The phenomena of rupture and flow in solids. *Philosophical Trans R Soc* 1920;C:9–14. <https://doi.org/10.1098/rsta.1921.0006>.
- [4] Orowan E. Fracture and Strength of Solids. *Rep Prog Phys* 1949.
- [5] Camanho PP, Hallett SR. Numerical Modelling of Failure in Advanced Composite Materials. Elsevier Inc.; 2015. <https://doi.org/10.1016/C2014-0-02677-9>.
- [6] Barbero EJ. Finite element analysis of composite materials using Abaqus. CRC press; 2013.
- [7] Johnson AF. Modelling fabric reinforced composites under impact loads. *Compos*

- Part A Appl Sci Manuf 2001;32:1197–206. [https://doi.org/10.1016/S1359-835X\(00\)00186-X](https://doi.org/10.1016/S1359-835X(00)00186-X).
- [8] LADEVEZE P, LEDANTEC E. Damage modelling of the elementary ply for laminated composites. *Compos Sci Technol* 1992;43:257–67. [https://doi.org/10.1016/0266-3538\(92\)90097-M](https://doi.org/10.1016/0266-3538(92)90097-M).
- [9] Camanho PP, Hallett SR. Numerical Modelling of Failure in Advanced Composite Materials. 2015. <https://doi.org/10.1016/B978-0-08-100332-9.09987-4>.
- [10] Pinho ST, Robinson P, Iannucci L. Fracture toughness of the tensile and compressive fibre failure modes in laminated composites. *Compos Sci Technol* 2006;66:2069–79. <https://doi.org/10.1016/j.compscitech.2005.12.023>.
- [11] Khan R. Fiber bridging in composite laminates: A literature review. *Compos Struct* 2019;229. <https://doi.org/10.1016/j.compstruct.2019.111418>.
- [12] Pappas G, Botsis J. Intralaminar fracture of unidirectional carbon/epoxy composite: Experimental results and numerical analysis. *Int J Solids Struct* 2016;85–86:114–24. <https://doi.org/10.1016/j.ijsolstr.2016.02.007>.
- [13] Fanteria D, Lazzeri L, Panettieri E, Mariani U, Rigamonti M. Experimental characterization of the interlaminar fracture toughness of a woven and a unidirectional carbon/epoxy composite. *Compos Sci Technol* 2017;142:20–9. <https://doi.org/10.1016/j.compscitech.2017.01.028>.
- [14] Lu X, Ridha M, Chen BY, Tan VBC, Tay TE. On cohesive element parameters and delamination modelling. *Eng Fract Mech* 2019;206:278–96. <https://doi.org/10.1016/j.engfracmech.2018.12.009>.
- [15] Haldar S, Lopes CS, Gonzalez C. Interlaminar and Intralaminar Fracture Behavior of Carbon Fiber Reinforced Polymer Composites. *Key Eng Mater* 2016;713:325–8. <https://doi.org/10.4028/www.scientific.net/kem.713.325>.
- [16] ASTM International. ASTM D 5528 Standard Test method for Mode I Interlaminar Fracture Toughness of Unidirectional Fiber-Reinforced Polymer Matrix Composites 2007.
- [17] Airbus Industries. AITM Determination of interlaminar fracture toughness - Mode I 2006:1–8.

- [18] International A. ASTM D7905 / D7905M-19e1, Standard Test Method for Determination of the Mode II Interlaminar Fracture Toughness of Unidirectional Fiber-Reinforced Polymer Matrix Composites. West Conshohocken, PA: 2019.
- [19] Airbus Industries. AITM Determination of interlaminar fracture toughness - Mode II 2006:1–8.
- [20] Marlett K. Hexcel 8552S AS4 Plain Weave Fabric Prepeg 193 gsm & 38% RC Qualification Material Property Data Report 2011:268.
- [21] López-Puente J, Zaera R, Navarro C. High energy impact on woven laminates. *J Phys IV JP* 2003;110:639–44. <https://doi.org/10.1051/jp4:20020765>.
- [22] Varas D, Artero-Guerrero JA, Pernas-Sánchez J, López-Puente J. Analysis of high velocity impacts of steel cylinders on thin carbon/epoxy woven laminates. *Compos Struct* 2013;95:623–9. <https://doi.org/10.1016/j.compstruct.2012.08.015>.
- [23] Buitrago Pérez BL. Comportamiento de estructuras de material compuesto sometidas a cargas impulsivas. University Carlos III of Madrid, 2012.
- [24] Heimbs S, Heller S, Middendorf P, Hä Hnel C F, Weiße J. Low velocity impact on CFRP plates with compressive preload: Test and modelling 2009. <https://doi.org/10.1016/j.ijimpeng.2009.04.006>.
- [25] Wagner T, Heimbs S, Franke F, Burger U, Middendorf P. Experimental and numerical assessment of aerospace grade composites based on high-velocity impact experiments. *Compos Struct* 2018;204:142–52. <https://doi.org/10.1016/j.compstruct.2018.07.019>.
- [26] Buitrago BL, García-Castillo SK, Barbero E. Influence of shear plugging in the energy absorbed by thin carbon-fibre laminates subjected to high-velocity impacts. *Compos Part B Eng* 2013;49:86–92. <https://doi.org/10.1016/j.compositesb.2013.01.005>.
- [27] Mihiu G, Mihalache I, Graur I, Ungureanu C, Bria V. Comparative study regarding friction coefficient for three epoxy resins. *IOP Conf Ser Mater Sci Eng* 2017;174. <https://doi.org/10.1088/1757-899X/174/1/012024>.

4 BUILDING A RELIABLE MODEL FOR THE CORE

4.1 Cellular materials

From the building-block approach discussed in previous chapters, it is stated that a validated FEA model should be an accurate representation of the real-world. This assessment is carried out by the direct comparison of the numerical results and the experimental test at the corresponding level of the analysis-test pyramid [1]. In this context, the purpose of this chapter is to study the compressive and tensile response of the same cellular materials used as a core in the sandwich panels. These experimental results are used to understand the specific physical mechanisms interacting in the response of each material and allow the author to select an adequate constitutive material model that reproduces their real-world behaviour. A FEA model is proposed to validate the compressive dynamic response of the core materials using the data collected in the experimental test.

4.1.1 Compressive behaviour of cellular materials

The mechanics of cellular materials is a complex subject in which the physical mechanisms interacting are still in debate, part due to their geometrical complexity and because the multiple parameters that influence their properties (e.g. material, porosity, type of cellular structure, cell size distribution and defects). The mechanics of cellular materials are usually explained from the simple ideas extracted in the study of different kinds of foams since they seem to explain the behaviour of other non-synthetic materials such as wood, cork and cancellous bones [2].

The compressive behaviour of cellular materials is non-linear and is characterized by three regions in the stress-strain curve. At low strain, the material has an elastic behaviour dominated by bending and stretch/contraction of the cell edges as well as stretching of the face membranes (for closed-cell foams) what increase the axial stiffness. At higher strain, a region of almost constant strain appears in what is called plateau region and is characterized by a collapse stress (σ_c). This region is occurs due to the collapse of the cells. In the case of elastomeric foams, the collapse is caused by elastic buckling whilst in the case of plastic foams is caused by the formation of plastic hinges in which the strain is no longer recoverable. For closed-cell foams, the plateau region presents a progressive

increment in the stiffness produced by the compression of the gas inside the cells and the stretching of the face membranes [2]. The third region occurs at higher strain, and is characterized by an increment in the slope of the stress-strain curve. This region is known as densification region, and the increment of the stress is triggered by the contact between collapsed cells of the material as compression progresses.

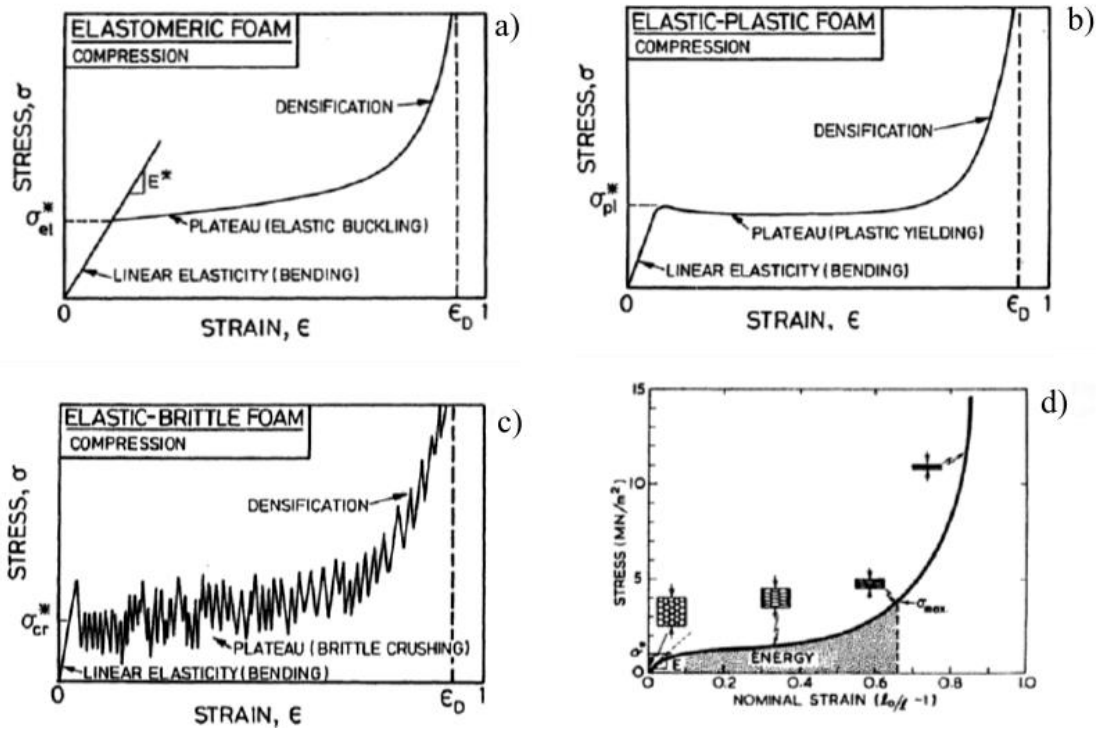


Figure 4.1. Compression stress vs. strain curve of different types of cellular materials.
a) Elastomeric foam, b) elastic-plastic foam, c) elastic-brittle foam, d) natural cork.

Source: [2]

Cellular materials are used in high-performance structures for impact protection and energy absorption. In such applications they are subjected to high strain rates that depending on the kind of cellular materials may affect their mechanical properties [3]. For example, plastic and rigid foams lose some of their energy absorption capabilities if loads exceed the elastic region. The permanent deformation produced in the plateau and densification region due to plastic dissipation and fracture decreases their ability to absorb energy in subsequent impacts. Another factor influencing the energy absorption performance of foam materials is the strain rate dependency. This dependency is complex and it is directly related to the strain rate dependency of the material from which the foam is made, as well as the fluid entrapped inside the cells. For example, for semi-rigid foams both the stiffness and strength properties increase with strain rate while for elastomeric foams they are almost

independent of strain rate. This variability is explained since at ambient temperature some polymeric foams are near to their glass temperature and have viscoelastic behaviour that increases their dependency on strain rate.

The plastic collapse of a foam is proportional to the yield strength of the material from which is made; as a result, the foam inherits its strain rate and temperature dependency. The equation proposed by Ashby et al. [2] presents a linear increase in the yield strength with an increase in $\log \dot{\epsilon}$:

$$\sigma_{pl}^* = (\sigma_{pl}^*)^0 \left(1 - \frac{AT}{T_g} \ln \frac{\dot{\epsilon}_0}{\dot{\epsilon}}\right) \quad (4.1)$$

Where $(\sigma_{pl}^*)^0$ is the plastic collapse stress at 0 K that is directly proportional to the yield strength, A and $\dot{\epsilon}_0$ are material constants and T_g is the glass transition temperature.

In addition to the aforementioned phenomena at very high strain rates, inertial effects create a dynamic crushing effect that influences the overall force-displacement curve increasing the compression strength even further.

The physical mechanisms of dynamic crushing are summarized below [8], [11]

- Localization: Cells are more tightly compressed along with a thin layer adjacent to the loading face creating a change in the cell shape leading to local strain rates that are much larger than the apparent strain rate.
- Micro-inertia: Micro inertia arises from the acceleration of individual cell walls and struts. This phenomenon suppresses the cell-wall buckling increasing the crushing stress. This mechanism is sensitive to the structural characteristics of the cell.
- Densification: When cells come into contact in the localization region they cause a shock that raises the stress.

Strain rate dependence is also caused by the fluid contained inside closed-cell foams. The deformation of a closed-cell change the pressure of the contained fluid affecting the modulus and the collapse strength of the material.

Although there has been extensive research on the strain-rate effect on the plastic properties of cellular materials there is still a lack of consensus on its sensitivity. Conflicting observations can be caused by the limitations of the experimental method or by the inherent behaviour of each cellular material. For example, the strain-rate hardening is evident for balsa wood and steel foam as well as most polymeric foams, however low-density PVC

foams and open-cell aluminium foams are strain-rate insensitive [4]. A different conclusion about aluminium foams was obtained by Tan et al. [5] whom studied the dynamic compressive behaviour of aluminium foams using a direct impact technique. They found that the plastic collapse stress changes significantly with the compression rate as a result of the inertia effects associated with the dynamic localisation of crushing. The reader is encouraged to follow a deeper discussion about the phenomenon and mechanisms in dynamic compression in [4].

4.1.2 Agglomerated Cork

Agglomerate cork shows the well-known compressive behaviour of cellular materials characterized by three regions in the stress-strain curve [3], [14], [15], [16]. The main difference between conventional polymeric cellular materials and agglomerated cork is the mechanism for energy dissipation. Plastic and rigid foams lose their energy absorption capability if loads exceed the elastic region. The permanent deformation produced in the plateau and densification region due to plastic dissipation and fracture decreases their ability to absorb energy in subsequent impacts. In this regard, agglomerated cork can recover almost completely its initial shape. Previous research [9], [17] show that agglomerated cork maintain its energy absorption capabilities under multiple impacts giving this material advantage over synthetic foams.

The compression of agglomerated cork has been previously studied by [18], [19], [20], [11], [21] at the quasi-static and dynamic regime. Research in [18] showed that, apart from density and grain size, other parameters such as binder type or its quantity may also affect the mechanical properties of agglomerated cork in quasi-static compression.

Jardin et al. [7] studied the quasi-static compressive behaviour of seven different agglomerated cork and expanded cork using a universal testing machine. Additionally, it analyses the response of the materials under double impact using a drop weight tower with a hemispherical impactor. The results of this study show a clear correlation between the density and grain size of the material on the resulting mechanical properties. Although this study gives clear hints about the impact behaviour of the material the results could differ from a true dynamic compression experiment due to the shape of the impactor and the methodology used to estimate the stress-strain curves (accelerations measured).

Dynamic compression tests over agglomerated and micro-agglomerated cork were carried out in [19] using Split-Hopkinson Pressure Bar (SHPB) at strain rates from 200s^{-1} to 600s^{-1}

¹. From their observations, the plateau stress in dynamic compression is larger than in the quasi-static case. However, no significant variation of the mechanical behaviour is observed in the dynamic range 200s^{-1} to 600s^{-1} . A similar conclusion was obtained in [20] for agglomerated cork of three different densities at strain rates between 90s^{-1} to 238s^{-1} . Additionally, this study found a correlation between small increments in the strain rate sensitivity and material density. Ptak et al. [8] obtained a similar finding studying the crushing behaviour of different kinds of agglomerate cork at strain rates between 85 s^{-1} and 225 s^{-1} using a drop weight tower with a hemispherical impactor.

Recent studies [11], [21] use digital image correlation (DIC) to evaluate the actual strain distribution of agglomerated cork during dynamic compression showing a heterogeneous strain distribution is found among the test specimens. Local accelerations and inertial stresses were also studied and diverse hypotheses about the influence of inertial effects are proposed. At this point there is still a lack of available data for dynamic compression at strain rates lower than 90s^{-1} . Study of the behaviour at strain rates in this intermediate range are interesting because are representative of some situations as the impact on a helmet [15]. Previous studies in compression of agglomerated cork [10], [11], [18], [19], [20], [21] are focused on the longitudinal behaviour while there is still little knowledge in its behaviour in the transversal direction and particularly in the Poisson effect. Some authors assure that the Poisson ratio in quasi-static conditions is near zero or have a constant value [19],[2],[10]. However, test over natural cork [22] found that there is anisotropy in the Poisson effect particularly at large strains. Other tests carried out over agglomerated cork of different densities agree that there is a dependency between the Poisson ratio and the applied strain in static conditions [7].

4.1.3 PET foam

PET foam also shows the typical compressive behaviour of cellular materials characterized by three regions in the stress-strain curve [27], [28], [29]. Despite its broad use in industry, research about the compression behaviour of PET foam is scarce. Fathi et al. [27] carried out a very complete experimental analysis of the quasi-static compression of strand PET foams along three orthogonal directions. This research found that the compressive modulus and the strength in the out-of-plane direction is significantly higher than in-plane direction. In the direction of extrusion (out-of-plane), the material shows a post-yield softening in the in-plane direction the material shows a smoother behaviour similar to the encountered in

honeycomb materials. This study [27] also analysed the full field compressive strain and Poisson ratio using Digital Image Correlation (DIC). The obtained results suggest that when loading in the extrusion direction the deformation is highly localized near the loading surface and in shear bands. In contrast when loading in the in-plane direction the strain field is regular with hexagonal features proper of the foam strands [27].

A similar study was carried out by Rajput et al. [29] where the quasi-static uniaxial compression behaviour of three different closed-cell polymeric foams (including PET foam) was evaluated using a universal testing machine. This study focused on the significantly different results for the compressive modulus depending on the methodology used to measure the longitudinal strain. The authors evaluated different extensometer techniques and DIC as well as different support conditions. The results of this study indicate that the compressive strain should be measured only over the interior part of the specimen to avoid local effects at the loaded boundaries.

Pyrzowski et al. [30] conducted uniaxial and hydrostatic compressive testing on PET foams of three different densities and their observations showed that both uniaxial and hydrostatic compressive yield strength increases at higher material densities.

Loredana et al [28] carried out uniaxial compression tests and thermo-mechanical memory-recovery cycles over PET foam of two different densities. The measurement was carried out along three orthogonal axes showing higher elastic modulus and compressive strength along the extrusion direction. Additionally experimental results showed that PET foams have the ability to recover at least 90% of their shape after three thermos-mechanical cycles. This memory recovery capability makes PET foam a promising material for self-repairing structures.

Despite the broad use of PET foam in the industry, the behaviour of this material in dynamic compression is still unknown. Therefore, the purpose of this work is to study the mechanical response of PET foam subjected to quasi-static and dynamic compression in the range of 40 and 125 s⁻¹. The effect of strain rate is assessed in the global response (nominal stress-strain curve) and the mechanical properties are determined. The effect of dynamic crushing is also analysed and related to the global response of the material. The deformation field is measured through the specimen using Digital Image Correlation (DIC) to obtain the strain field in the longitudinal and transversal direction, allowing the estimation of the Poisson ratio. Special attention is given to this property and how it varies

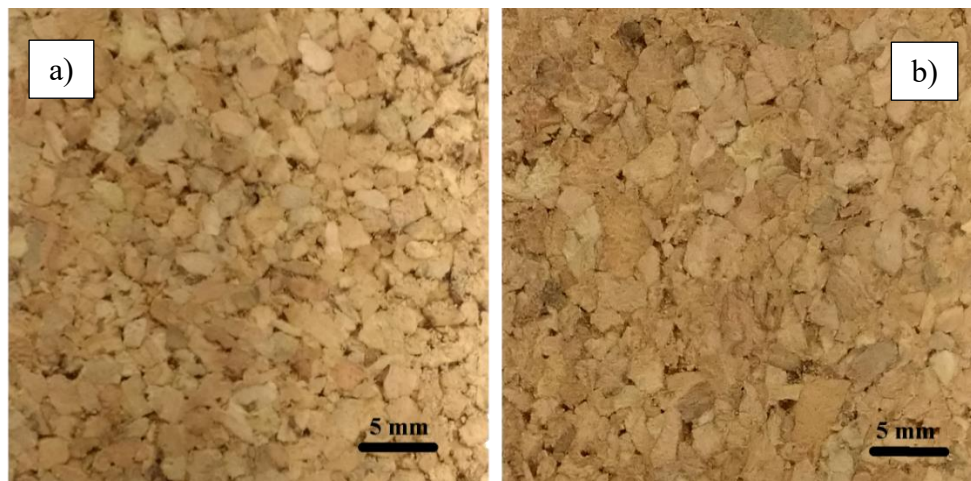
at different strain and strain rate levels.

4.2 Quasi-static and dynamic characterization test of core materials

The purpose of this section is to study the mechanical response of agglomerated cork and PET foam subjected to quasi-static and dynamic compression.

4.2.1 Core materials

Two different types of agglomerated cork are tested, NL-10 (average density $\rho=170 \text{ kg/m}^3$) and NL-20 (average density $\rho=215 \text{ kg/m}^3$), manufactured by Amorim Cork Composites under the commercial name of CORKCORE. These materials are made from cork granules agglomerated with a polyurethane binder. A visual inspection of both agglomerated corks shows a heterogeneous distribution of amorphous granules. Surface analysis is conducted to determine the average size of the granules in each agglomerated cork. Due to its amorphous geometry, the average characteristic length of each granule is estimated from the projected area. From Figure 4.2 it can be noticed that the size of the granules is smaller for the NL-10 than for NL-20 with an average length of 1.7 mm for the NL-10 and 2 mm for the NL-20. The standard deviation is relatively large for both agglomerated being 0.5mm and 0.7mm for the NL-10 and NL-20 respectively. A comparison in the statistical distribution of the average length is shown in Figure 4.2.c.



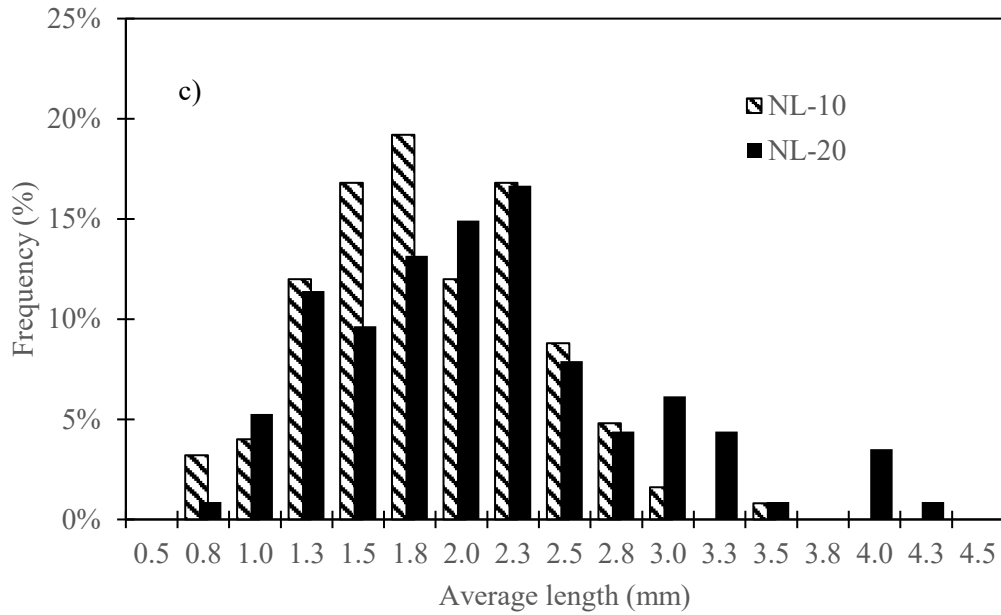


Figure 4.2. Granules in the agglomerated corks used in this work a) NL-10, b) NL-20, c) Statistical distribution of the granulate length.

The other core material is PET foam (average density, $\rho=211 \pm 12 \text{ kg/m}^3$) manufactured by the company Airex under the commercial name of Airex T92.200 [25]. The material's cellular structure is visually inspected using an optical microscope applying black ink over the surface to avoid excessive brightness (Figure 4.3). Observations reveal that the material is composed of polygonal closed cells for which the projected area is measured. The mean characteristic length of the cells is 0.51 mm but it can vary from 0.25 mm up to 0.84 mm.

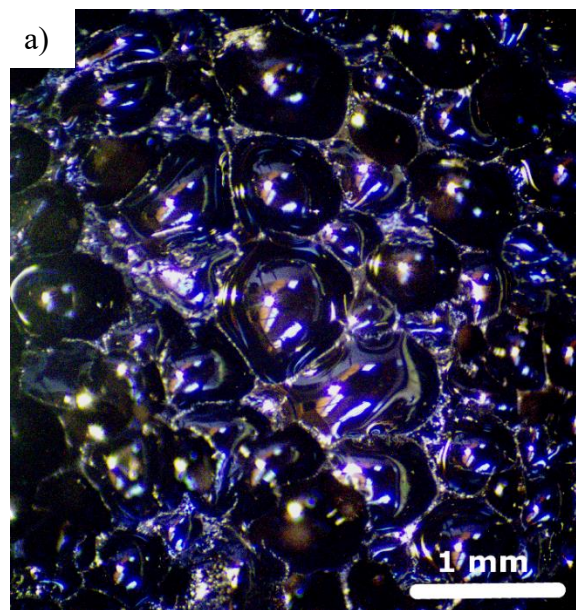


Figure 4.3. The cellular structure of PET foam

4.2.2 Quasi-static and dynamic compression test procedure

Quasi-static (QS) compression tests are carried out for all core materials following ASTM 1621 standard test method [31] using a universal testing machine INSTRON 8516 (Figure 4.4.a). Three specimens of each material are tested at a speed of 5 mm/min (equivalent to a strain rate: $2.38 \times 10^{-3} \text{ s}^{-1}$). From each test, a record of force versus displacement is obtained. The load is measured with a load cell of 5kN while the machine crosshead displacement sensor is used to measure the applied displacement. A uEye digital camera records each test at 10 fps. The video frames are later used to estimate the lateral strain using DIC.

The geometry of the specimens is the same for quasi-static and dynamic compression testing: $40 \times 40 \times 35 \text{ mm}^3$. Three specimens are tested for each material and test condition. All specimens are manufactured from the same batch and all tests were carried out under the same conditions of temperature and humidity.

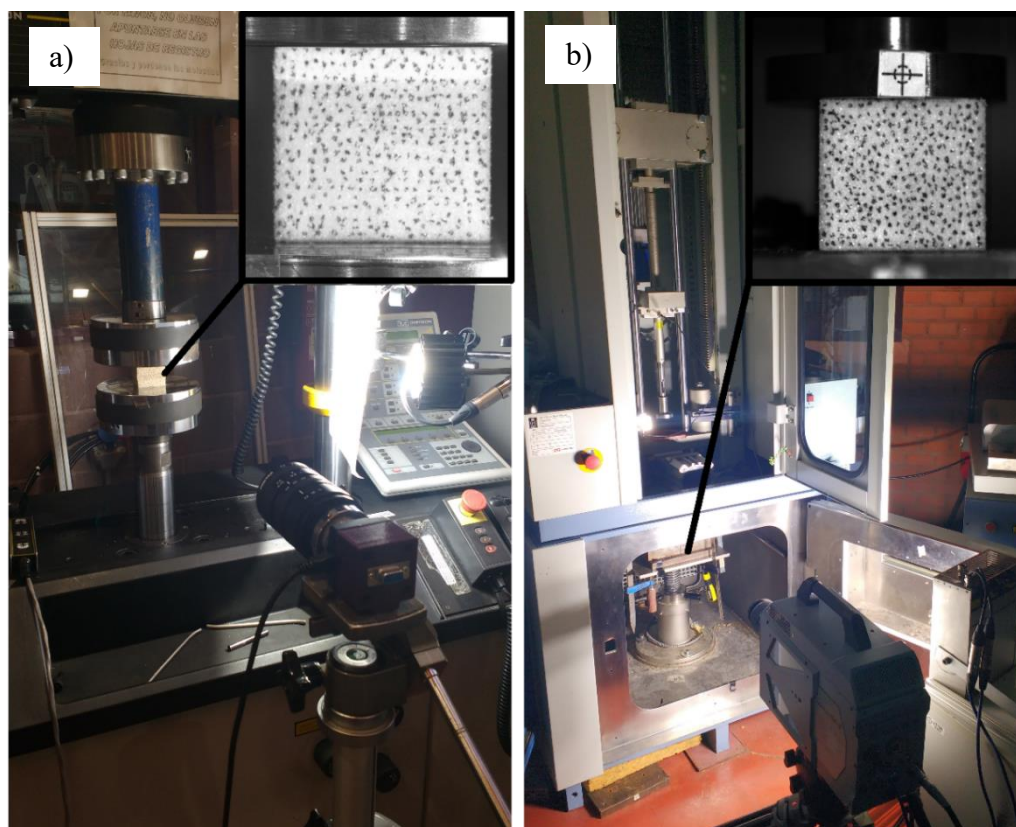


Figure 4.4. Experimental set-up. a) Quasi-static compression b) Dynamic compression

Dynamic compression tests are performed for all core materials using a Ceast-Fractovis 6785 drop-weight testing machine (Figure 4.4.b). The test specimens are simply supported

on the bottom surface and the impactor is cylindrical with a flat impact surface of 50 mm in diameter.

One of the main goals is to achieve a large range of deformations to capture the three regions of compression (linear-elastic, plateau, and densification) therefore the impactor height is adjusted to achieve different impact energy levels. For agglomerated cork experiments are carried out using an impactor with a mass of 9.134 kg reaching nominal impact energies of 10 J, 20 J, 30 J, 40 J, 50 J, 60 J, 70 J, 86 J at impact velocities between 1.4 m/s to 4.3 m/s (average strain rates from 25 s^{-1} to 85 s^{-1}). In the case of PET foam due to its higher stiffness and the maximum height that can be reached in the drop-weight machine, it is necessary to use two different impact masses (9.134 kg and 16.13 kg). With the 9.13 kg mass the impact energies reached are 10 J, 20 J, 30 J, 40 J, 60 J, 70 J, 80 J, 90 J while for the 16.13 kg the impact energies are 60 J, 70 J, 80 J, 90 J, 100 J, 110 J, 130 J, 150 J, and 156 J. The impact velocities achieved in the case of PET foam varied between 1.4 m/s to 4.4 m/s (average strain rates from 40 s^{-1} to 125 s^{-1}).

A PHOTRON FASTCAM SA-Z high-speed camera is located perpendicular to the front face of the test specimen and is used to record the testing at 20000 fps. The contact force between the impactor and specimen is measured through a dynamic digital acquisition system (DAS4000) recording data with a sample time of $9 \mu\text{s}$. This instrumented impactor measures the contact force while the impact velocity is measured using two laser position detectors. Each specimen received a single impact and rebound is prevented by an anti-rebound system. From this initial velocity and the force record, the impactor displacement and energy can be calculated by an integration process whose detailed description has been previously described in [32,33].

Since the method for estimating the dissipated energy requires the impact velocity as initial data, it is relevant to determine the accuracy of the velocity measurement provided by the data acquisition system of the drop weight tower. For this reason, the impact velocity and the residual velocity after impact are measured using automated image tracking software and the video frames from the high-speed camera. Figure 4.5 shows an example of the displacement and velocity history estimated by both techniques. A good correlation between both techniques is found.

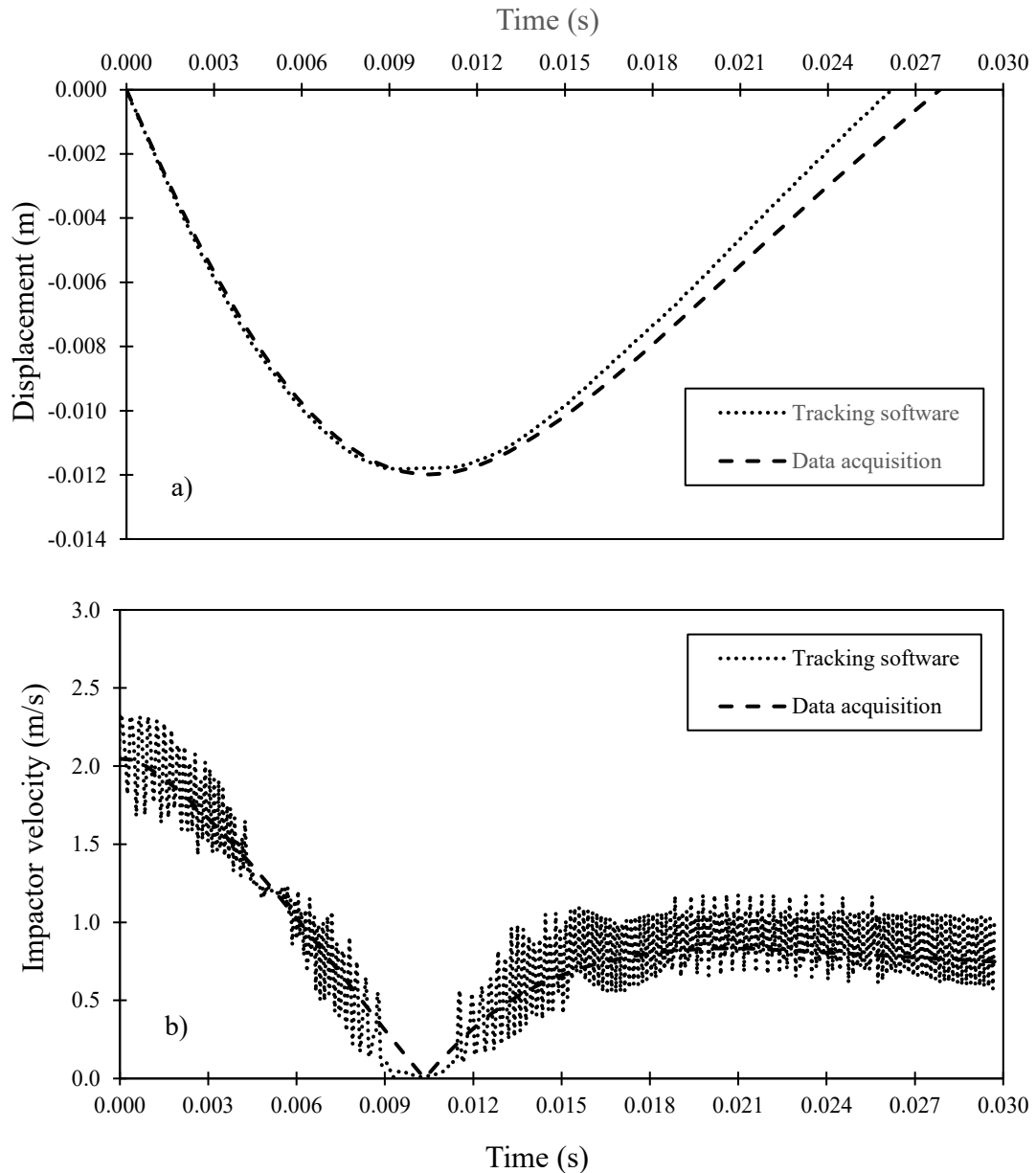


Figure 4.5. Dynamic compression test of NL-20 at 20 J. Data estimated from the data acquisition system of the drop weight tower and the tracking software. a) Impactor displacement history and b) impactor velocity history.

The velocity history measured by the tracking system has a high degree of noise due to the image identification algorithm. However, it is possible to obtain the initial impact velocity by averaging the velocity in the region before the impact. Figure 4.6 shows the comparison in the impact velocity measured by the laser detector of the drop weight tower and the tracking system for NL-20 agglomerated cork. There is good agreement between the measurements obtained by both methods showing a relative error of 3.6% in the worst scenario.

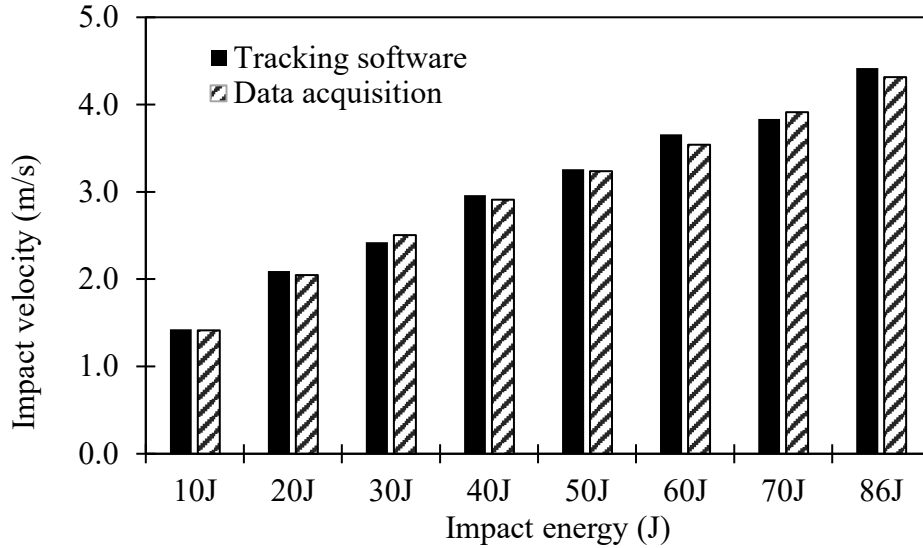


Figure 4.6. Dynamic compression tests of NL-20. Example of impact velocity estimated from the data acquisition system of the drop weight tower and the tracking software.

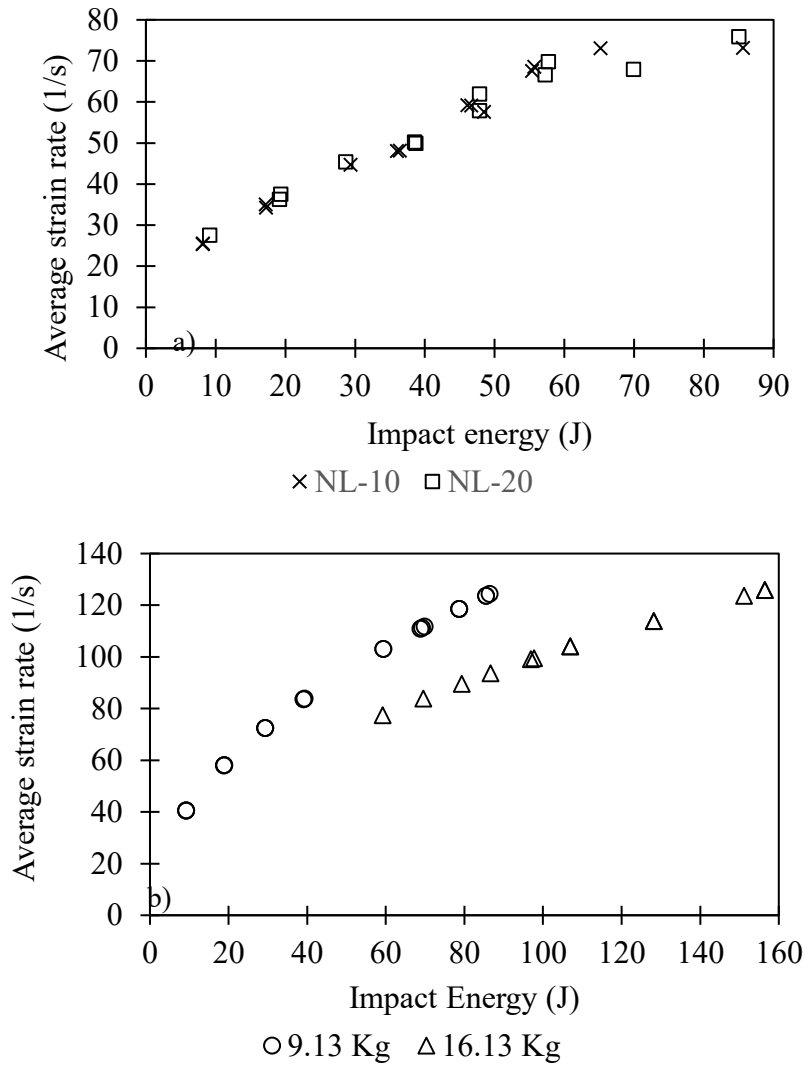


Figure 4.7. Average strain rate vs. impact energy. a) Agglomerated cork ($m=9.13$ kg), b) PET foam (two different impactor masses 9.13 kg and 16.13 kg).

The relationship between impact energy and strain rate is shown in Figure 4.7 for agglomerated cork and PET foam. Strain rates between 25 s^{-1} and 75 s^{-1} are achieved for agglomerated cork (Figure 4.7.a). There is a linear relationship between strain rate and impact energy in both agglomerated corks at low impact energies when the materials do not achieve densification. The slope of the fitting curve is similar, being in the NL-20 a 1.79% higher than in NL-10, thus no significant influence of density was found in the relationship between strain rate and impact energy. Once densification is achieved, a loss of linearity is observed in both materials.

4.2.3 2D Digital image correlation (DIC) procedure

2D-DIC is used to measure the longitudinal and transversal strain distribution in each specimen during the tests. This method provides accurate identification of changes among the video frames taken in the test correlating them at the pixel and subset level to find the displacement and strain field. (for further information about this method, please refer to chapter 5). The lateral surface of all specimens is marked with a random black dot speckle pattern using a fine marker pen with an approximate feature size of 1mm. In the case of agglomerated cork specimens, no white background is applied since the natural granulate texture of the material provides additional randomness to the speckle as well as enough contrast to allow correlation. In the case of PET foam, the natural white colour of the material is used as background. The software used in this analysis is Digital Correlation Engine V.2. developed by Sandias National Laboratory in the U.S. The subset size is chosen depending on the speckle size, ensuring that at least three speckle features are covered by a single subset (Figure 4.8). Additionally, the step size is chosen to compromise enough spatial resolution and low computational time. The difference in the image size between the quasi-static frames (2048×1536 pixels) and the dynamic frames (1024×1024 pixels) requires that both tests be evaluated with different subsets and step sizes. In the case of quasi-static compression, a subset size of 81 pixels and a step size of 5 pixels are used. For the dynamic tests, the subset size is 39 pixels with a step size of 4 pixels. With this subset size, a match confidence of 0.01 pixels is achieved.

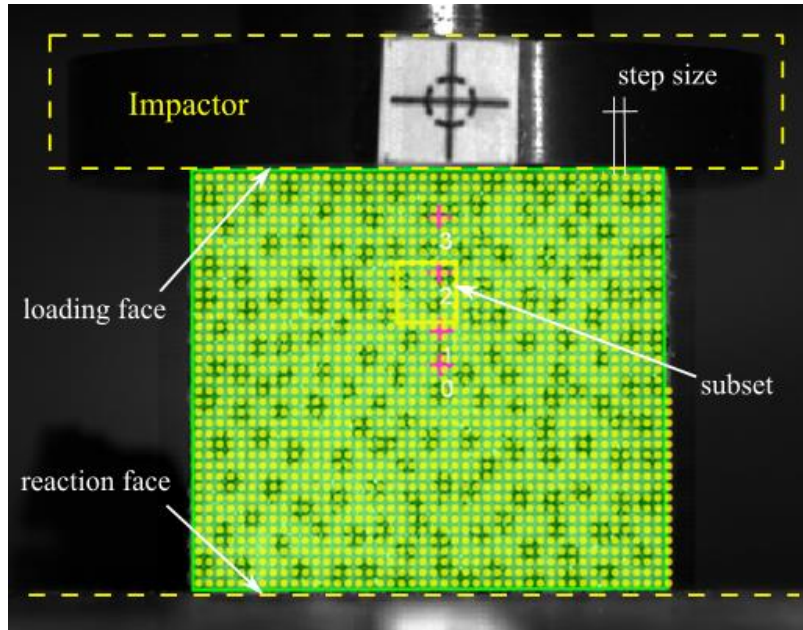


Figure 4.8. Digital image correlation speckle sub-set and step size (PET foam specimen)

4.2.4 Data reduction method

From each test, in both static and dynamic conditions, a record of force versus displacement is obtained. These curves allow the estimations of some material parameters as Young modulus, plateau stress, densification strain, and maximum efficiency. Additionally, the Poisson ratio is obtained from the longitudinal and transversal strains measured by DIC.

In the stress-strain curves, the linear-elastic region can be estimated accurately by a linear fitting curve until 4% applied strain. The Young modulus for each test can be computed from the slope of the linear function. It is also customary in cellular materials to provide a stress value in the plateau region at 20% strain what allows direct comparison of the plateau stress of different materials or test conditions.

Densification strain is the level of applied strain where densification of a cellular material starts. An unambiguous method to determine the transition between the plateau and densification region is based on the evolution of the energy absorption efficiency (η) which is defined in [33], and [34] as follows:

$$\eta = \frac{1}{F(\delta)} \left(\frac{1}{h_0} \right) \int_0^{\delta} F(\delta) d\delta \quad (4.2)$$

Where F is the contact load, h_0 is the specimen thickness, and δ is the displacement.

The maximum efficiency is estimated as the maximum numerical value in the efficiency vs. displacement plot during the loading phase. From the specimen velocity, the strain rate can be estimated. As can be seen in

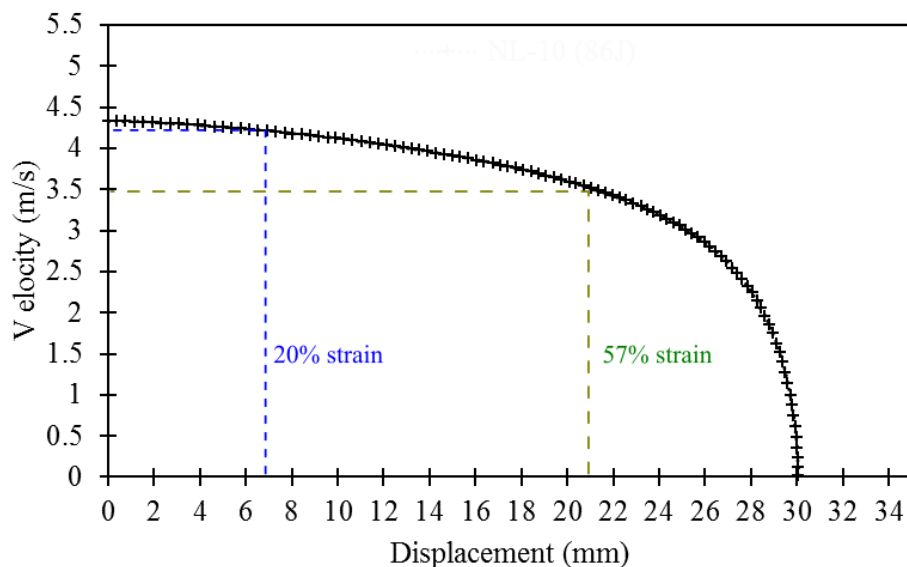


Figure 4.9, the instantaneous velocity varies during a test and therefore the strain rate is not constant. In the agglomerated corks studied in this work, the drop in velocity is small in a broad range of strain. For example, at 20% applied strain the velocity drop is smaller than 5% for both materials. Even at very high-applied strains such as the densification strain, the velocity drop is close to 18% for the NL-10 and 26% for the NL-20.

To allow direct comparison among different tests, an average strain rate is defined for each impact energy. This strain rate is calculated based on the average of the impact velocity and the velocity of the impactor at the maximum impact force. This method is considered the most realistic to estimate the strain rate if compared with other alternatives as using the impact velocity as suggested in other works [34].

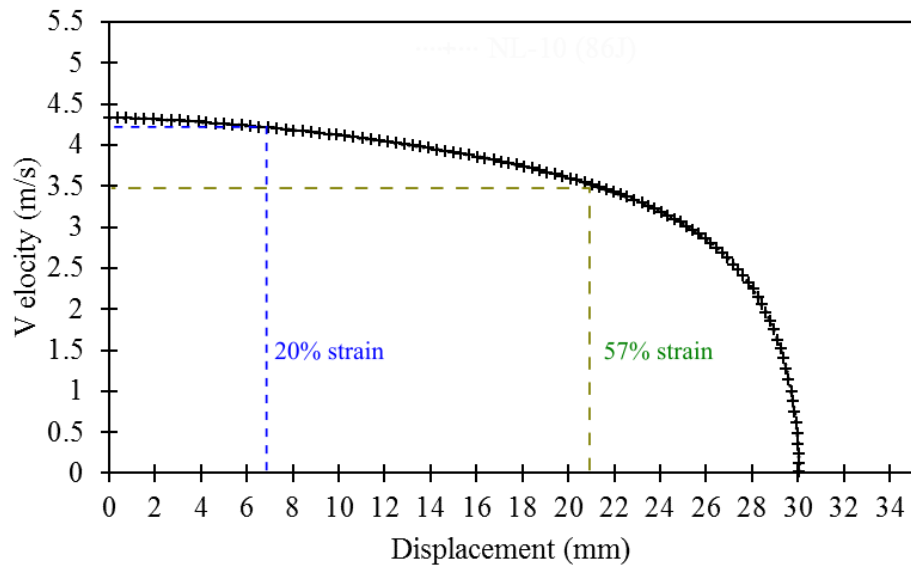


Figure 4.9. Instantaneous velocity of the impactor vs. displacement for Agglomerated cork (NL-10). Impact energy: 86 J.

4.2.5 Quasi-static tensile test procedure

All core materials are tested in tension in order to obtain their nonlinear stress-strain response and fracture strength. Rectangular specimens of 250x35x8 mm are tested at a deformation speed of 0.9 mm/s using a Servosis ME-401/1 universal testing machine with a load cell of 1 KN. A uEye digital camera recorded each test at 10 fps. The video frames were used later to estimate the lateral strain using DIC.



Figure 4.10. Experimental set-up of quasi-static tensile testing (agglomerated cork)

4.2.6 Result of quasi-static and dynamic compression of agglomerated cork

The force vs. displacement curves (Figure 4.11 and Figure 4.12) show the typical behaviour of cellular materials with closed cells characterized by a non-constant plateau region that slightly increase until reaching densification. It can be noticed that there is a considerable difference in the curves for quasi-static and dynamic conditions, a behaviour well-identified in previous research ([19], [18], [11], [20]). The force-displacement relationship is almost the same for all dynamic cases at small strain ($< 7\text{mm}$ or 20% strain) despite the variation in the impact energy and strain rate. Since the strain rate is the highest at small deformations, no significant influence of strain rate in the mechanical properties in a range of 25 s^{-1} to 75 s^{-1} is observed. This complements previous observations in [11] where it is shown that there is not considerable strain rate sensitivity in the range between 90 s^{-1} and 400 s^{-1} . Additionally, this confirms the results in [19] where it is found a no strain-rate dependency in the plateau region for different types of agglomerated cork with different densities.

From the discharge region of the curve, it is noticed that although most of the material presents immediate elastic recovery there is certain remaining deformation after impact. This remaining deformation can be associated with permanent strains due to damage and delayed strains due to viscoelastic effects (creeping). It is also noticed that NL-20 has higher strength and stiffness than NL-10 for both quasi-static and dynamic compression. Similar behaviour has been previously observed for pure cork and polymeric foams [15], [35].

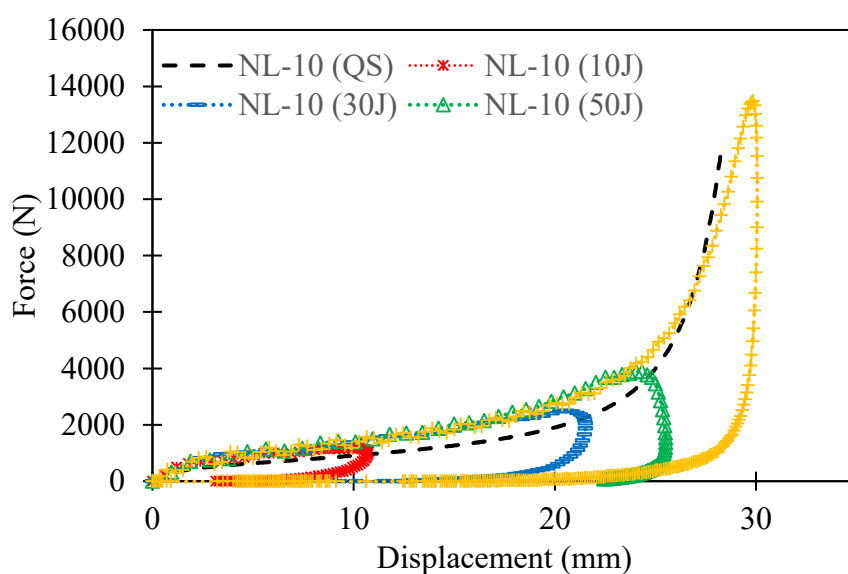


Figure 4.11. Agglomerated cork NL-10. Force vs. displacement.

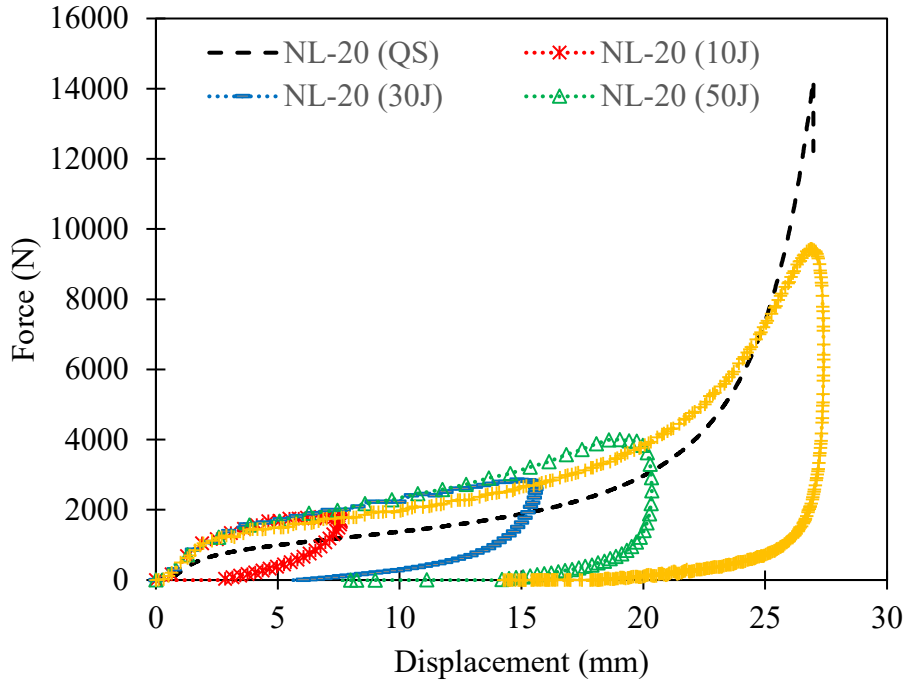


Figure 4.12. Agglomerated cork NL-20. Force vs. displacement impactor.

From the force-displacement plots, it is possible to obtain the engineering stress vs. strain curve. Figure 4.13 shows the comparison between NL-10 and NL-20 agglomerated cork materials for quasi-static compression and dynamic compression at the highest strain rate reached.

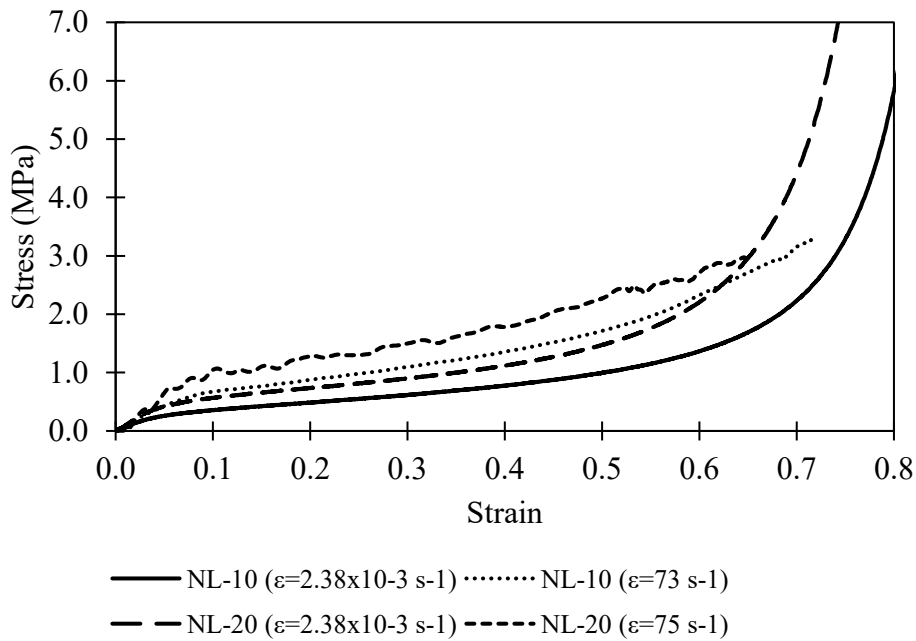
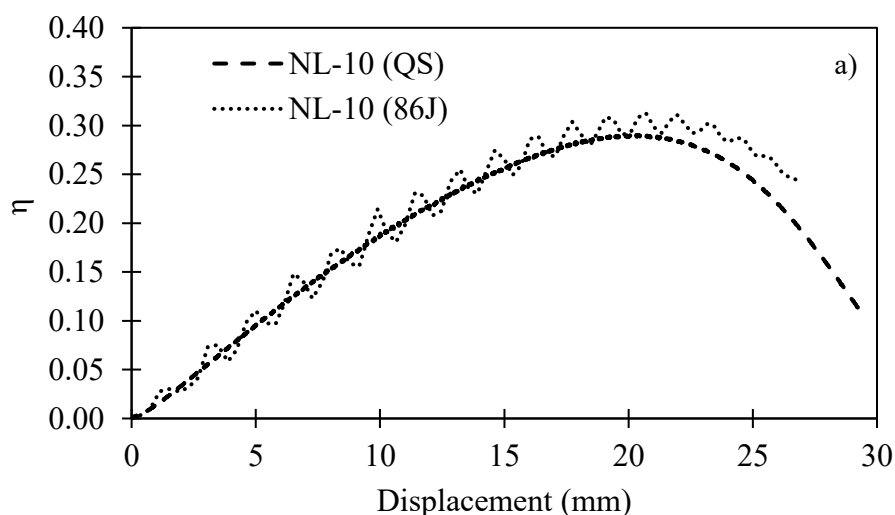


Figure 4.13. Stress vs. strain curve for NL-10 and NL-20 for quasi-static and dynamic compression.

Figure 4.14 plots the energy absorption efficiency vs. displacement for both agglomerated cork materials at quasi-static and dynamic compression. It is observed that η increases with deformation reaching a maximum value (η_{\max}) at the densification onset. These curves are different from those of polymeric foam, due to the existence of a more constant stress plateau in those materials.

In specimens impacted at energies of 40J for NL-10 and 60J for NL-20, no densification is observed. When a specimen is impacted at higher energies, contact between some of the cell walls of the cork granules initiates and densification begins. By increasing the impact energy, a greater strain is achieved and a greater number of walls enter in contact.

The maximum efficiency is estimated as the maximum numerical value in the efficiency vs.. displacement plot during the loading phase (Figure 4.14). At quasi-static compression, both materials show a maximum efficiency close to 0.29 with densification at 57% strain for the NL-10 and 54% strain for the NL-20 (Table 4.1). In dynamic compression, for impact energies that produce densification, a slight shift in the densification onset is observed. In dynamic conditions, densification takes place at 60% strain for the NL-10 and 57% strain for NL-20, this implies an increase of 4.2% in NL-10 and of 4.4% in NL-20. Despite the difference in density (from 170 kg/m^3 to 215 kg/m^3), there is only a slight difference in the onset of densification for both materials, around 5%. This small dependency on density can be explained since densification onset is mostly dependent on the cell's geometry (porosity) which is similar for both agglomerates. The above bears in mind that differences in density in agglomerated cork are created by the amount of binder used and not by the change in the porosity as in a conventional synthetic foam.



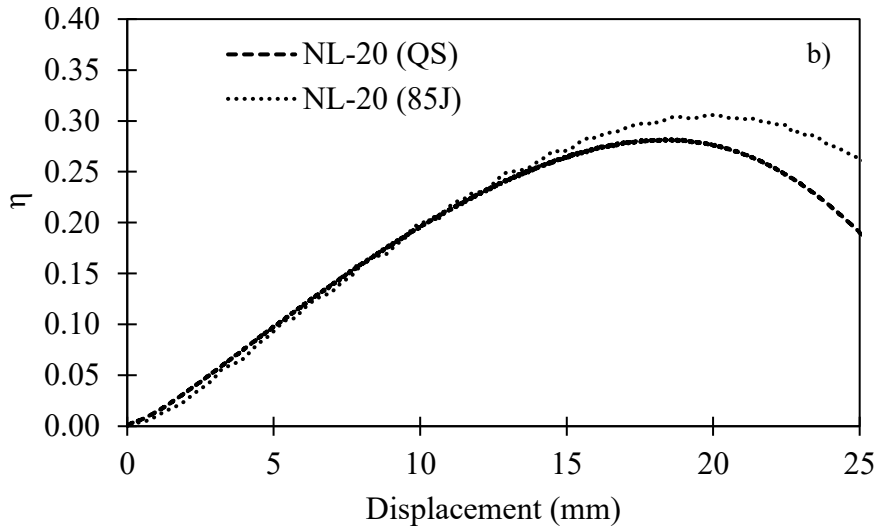


Figure 4.14. Energy absorption efficiency vs. displacement at static and dynamic conditions: a) NL-10, b) NL-20.

From the curves force-displacement (Figure 4.11 and Figure 4.12), the maximum contact force, dissipated energy and maximum displacement are calculated.

The maximum contact force at different impact energies for both agglomerated corks increases linearly with impact energies before densification takes place (Figure 4.15). For high impact energies where densification takes place ($E_i > 60$ J), there is a sharp increase in the impact force. The loss of linearity is observed in impact energies for which the maximum strain that appears produces a large number of contacts between cell walls.

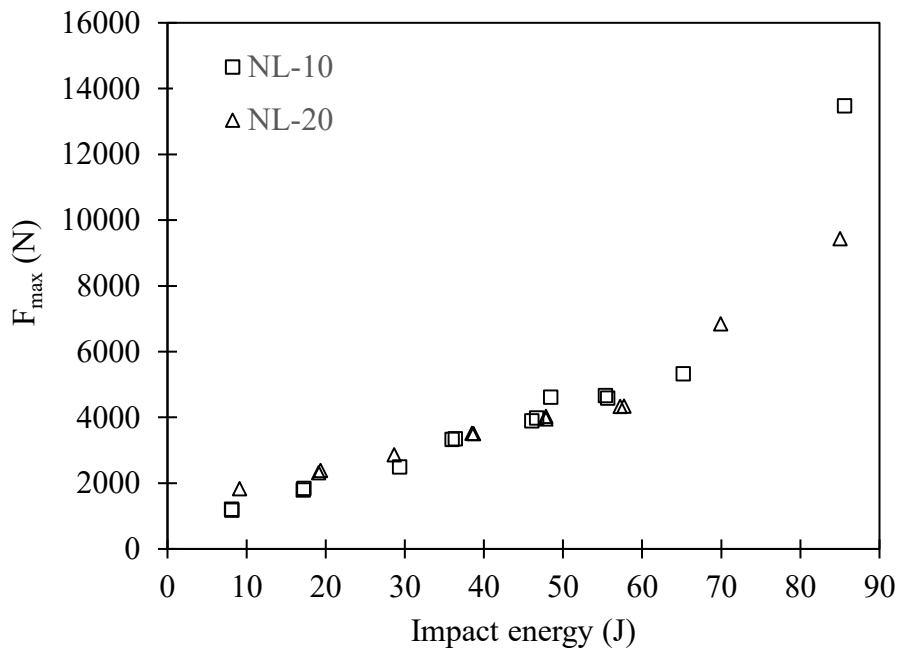
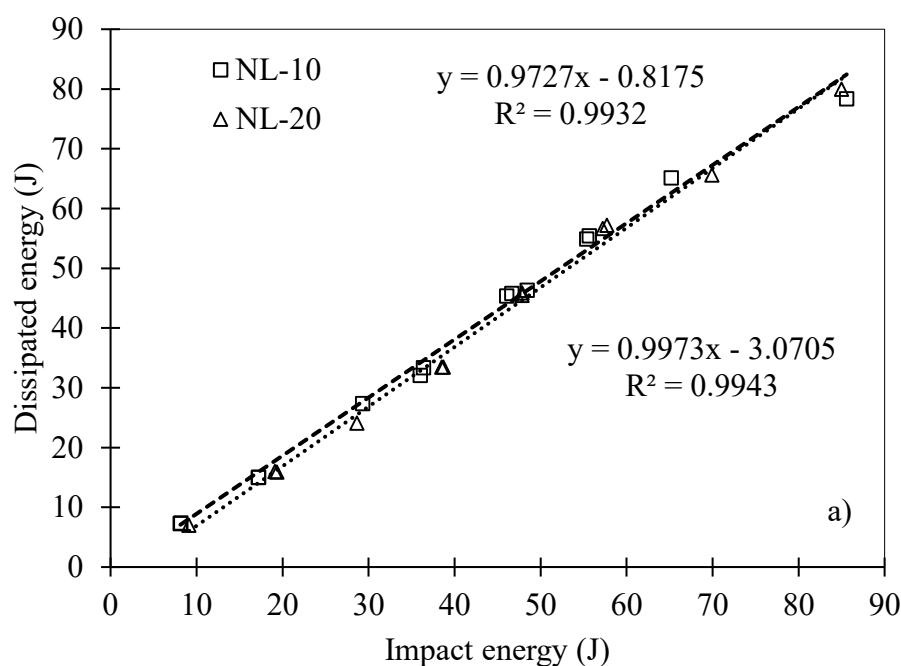


Figure 4.15. Maximum force vs. impact energy in agglomerated cork specimens

Considering that the velocity and displacement measurements obtained by the acquisition system are enough accurate (as demonstrated in the previous section), the dissipated energy is determined from the kinetic energy after impact calculated by numerical integration of the force vs.. displacement curve. The remaining kinetic energy obtained by the numerical integration is compared with the kinetic energy measured with the image track obtaining a good correlation between the two techniques.

From Figure 4.16.a) it is noticed that in both materials the dissipated energy is a linear function of the impact energy. The correlation to a linear fitting curve is very high ($R^2 > 0.99$) and both materials present almost the same slope. Also, the ratio between dissipated energy and the impact energy is calculated (Figure 4.16.b). This curve shows that both agglomerated corks can absorb from 77% to 99% of the initial impact energy. This figure also shows that the energy absorption ratio is slightly higher for the NL-10 than NL-20. This difference can vary from 1% up to 13%.



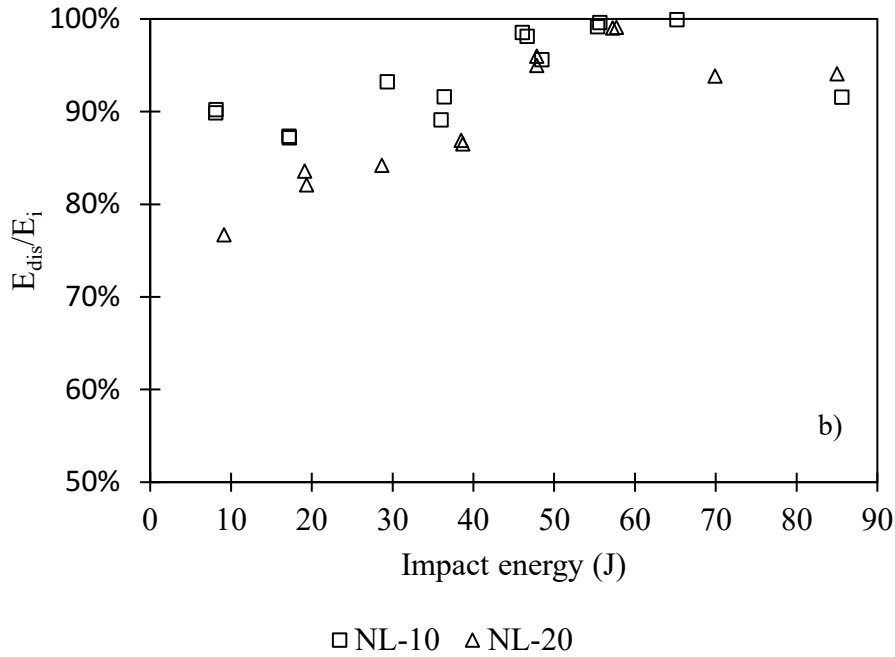


Figure 4.16. a) Dissipated energy vs. impact energy. b) Energy dissipated ratio E_{dis}/E_i (agglomerated cork)

The maximum displacement of the impactor is also studied. Figure 4.17 shows a series of pictures taken at the exact instant of time in which maximum displacement occurs for diverse impact energies over NL-10 specimens.

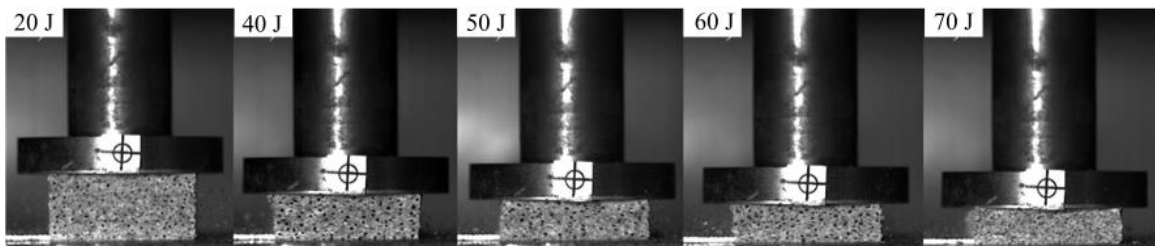


Figure 4.17. NL-10 maximum displacement at various impact energies.

From Figure 4.18 it is noticed that at the same impact energy level the maximum displacement is higher in the less dense material (NL-10). Results also show that there is a quadratic dependency between the maximum displacement and the impact energy across the entire range of impact energies. The correlation to a quadratic fitting curve is high for both cases ($R^2 > 0.96$) For energies that do not produce densification in both materials, there is a clear linear trend. This behaviour is similar to that observed with force.

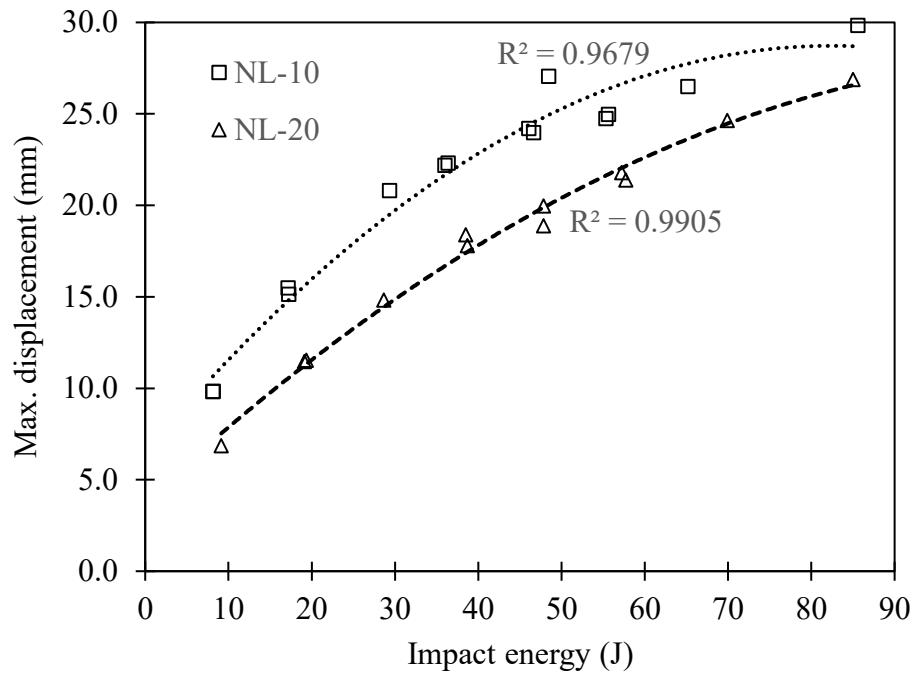


Figure 4.18. Maximum displacement vs. impact energy (agglomerated cork).

From DIC measurements, a non-uniform distribution in the strain field is observed in the test specimens for both agglomerated cork materials. Figure 4.19 and Figure 4.20 show the variation in the longitudinal strain ϵ_{yy} and lateral strain ϵ_{xx} at different points in the specimen for quasi-static compression and dynamic compression at 40 J, and 70 J.

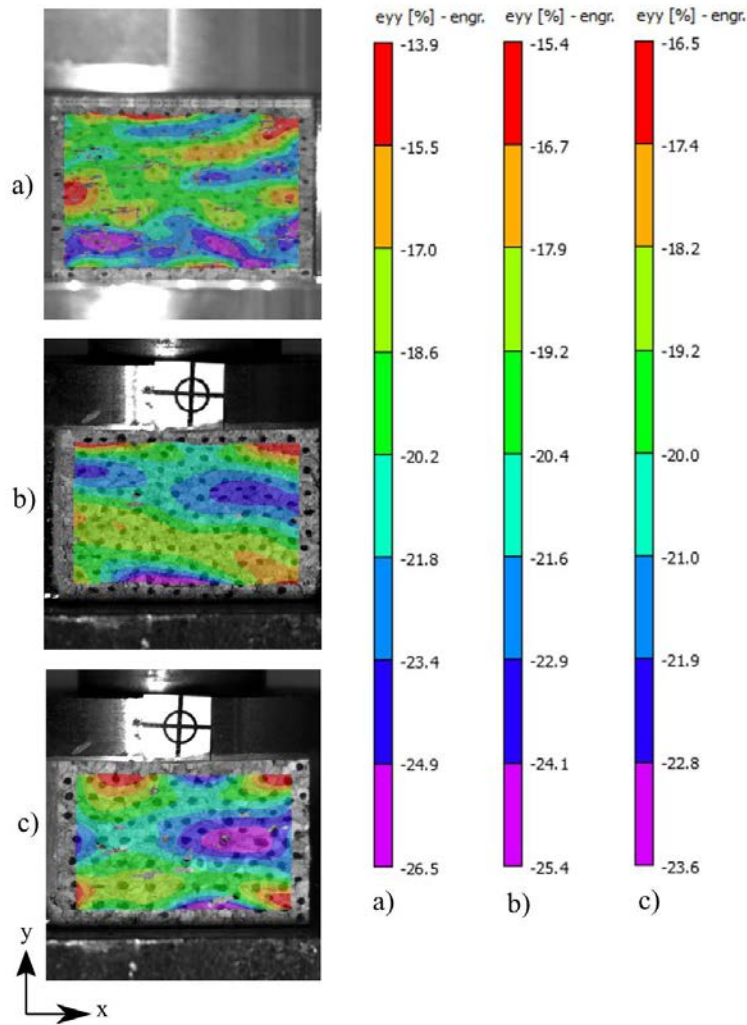


Figure 4.19. Longitudinal local strain of NL-20 at different impact energies (mean longitudinal strain 20%). a) Quasi-static, b) 40 J, c) 70 J.

The strain at a given point or local strain (ϵ_{yy} and ϵ_{xx}) is obtained from the DIC analysis as the ratio of the local displacement to the initial dimensions of the test specimen ($\epsilon_{yy} = \Delta y/h_0$ and $\epsilon_{xx} = \Delta x/w_0$), where Δy and Δx are the longitudinal and transversal displacement of each point, h_0 is the initial thickness and w_0 is the initial width. The axes used to define these strains are shown in Figure 4.19 and Figure 4.20. Due to the anisotropy of the material, it is convenient to estimate a mean longitudinal strain of the whole specimen ($\bar{\epsilon}_{yy}$). The mean strain is calculated as the average value considering all points inside the specimen. An analysis of the variation of local longitudinal strain in all points of the specimens is carried out. Figure 4.21 shows, as an example, the evolution of the longitudinal strain for the NL-20 material in static and dynamic conditions (only three impact energies are shown for the sake of simplicity).

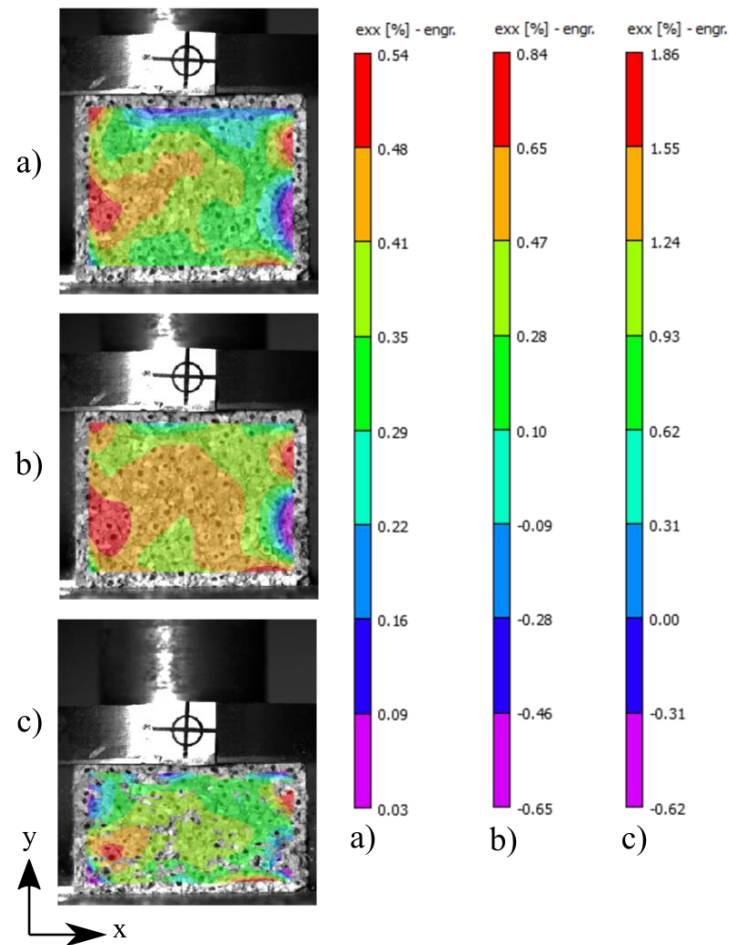


Figure 4.20. Lateral local strain from DIC analysis of NL-10 under a 50J impact. a) 5% longitudinal strain, b) 10% longitudinal strain, c) 30% longitudinal strain.

From these curves, it is possible to quantify the level of heterogeneity in a specimen during quasi-static and dynamic compression at the different strain levels. The vertical axis shows the range on the local strains ε_{yy} encountered inside the specimen whilst the horizontal axis shows the mean strain $\bar{\varepsilon}_{yy}$ of the whole specimen. It is clear from this figure that the local strain along the specimen can differ significantly from the mean strain value showing a relative difference from 23% up to 36% for the dynamic test and variations up to 70% for the quasi-static test.

There is a considerable difference in the strain at different points in the specimen what clearly shows the heterogeneity of agglomerated cork at a small scale. This variation could be attributed among others to the amorphous shape and random allocation of the granules as observed in the surface analysis. Additionally, the random alignment of each granule, as well as the orthotropic nature of the pure cork, could provide an additional source of variability in the local response of the agglomerate. Another possible contribution to this

variability could be the presence of voids or regions of rich binder content. However, a more detailed analysis at the micro-scale and mesoscale level is required and such analysis is beyond the scope of the current study. Other authors working in dynamic compression using Split Hopkinson Bar have reported a non-uniform distribution of strain [11].

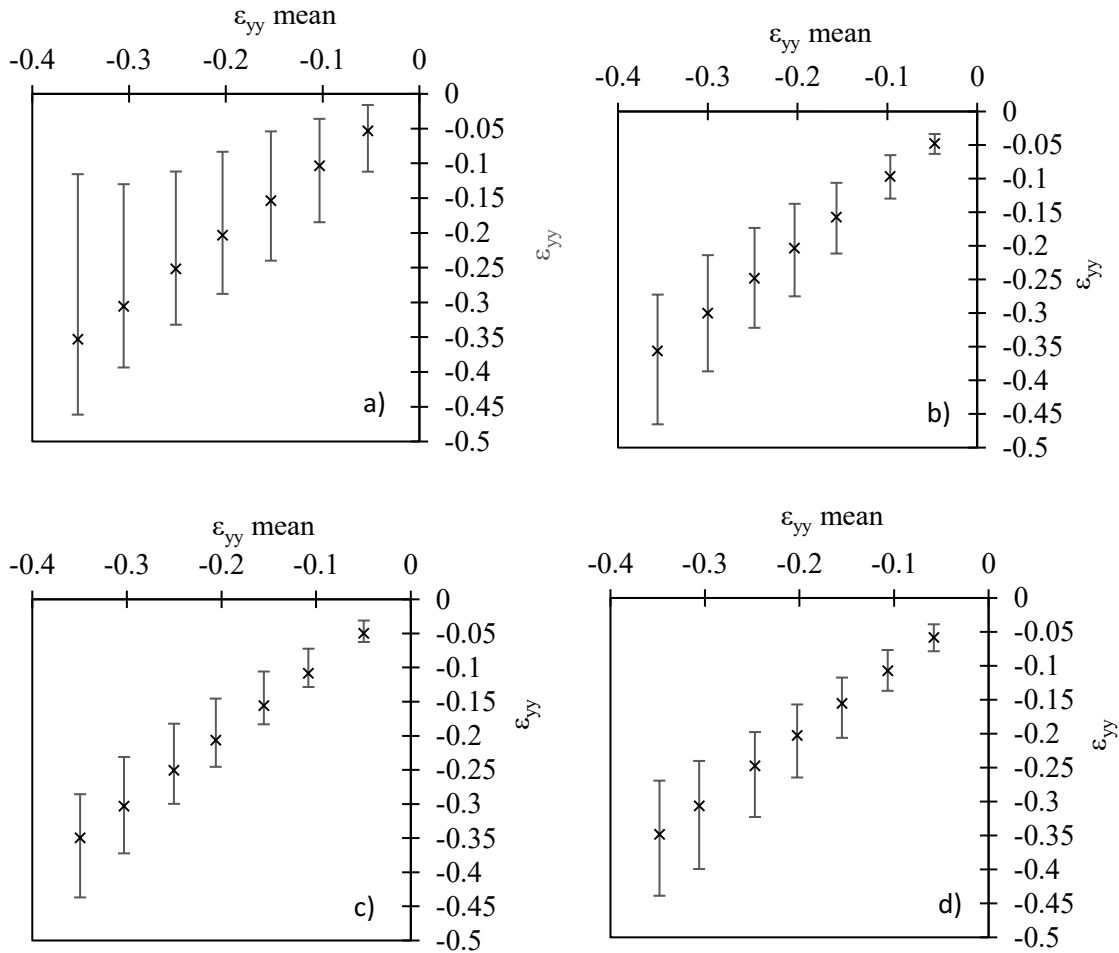


Figure 4.21. Variation on local longitudinal strain vs. mean longitudinal strain (NL-20).
 a) Quasi-static, b) 20 J, c) 40 J, d) 70 J

The mean Poisson ratio is also estimated from the mean longitudinal strain ($\bar{\epsilon}_{yy}$) and mean lateral strain ($\bar{\epsilon}_{xx}$) measured by DIC. Figure 4.22 depicts the average compressive Poisson ratio vs. longitudinal strain for different energy levels. The least-square method with a third-order polynomial is used to obtain the fitting curves. No similar curves have been found in the literature. For both agglomerates, the Poisson ratio decays with the longitudinal strain reaching a plateau at higher strains. It is observed from Figure 4.22 that the plateau region occurs around 12% strain. This approximately corresponds to the beginning of the plateau region in the longitudinal force-displacement curves (Figure 4.11 and Figure 4.12)

and clearly shows that the decay of the Poisson ratio is associated with cell wall buckling. A similar observation was found by Fortes et al. [22] for pure cork.

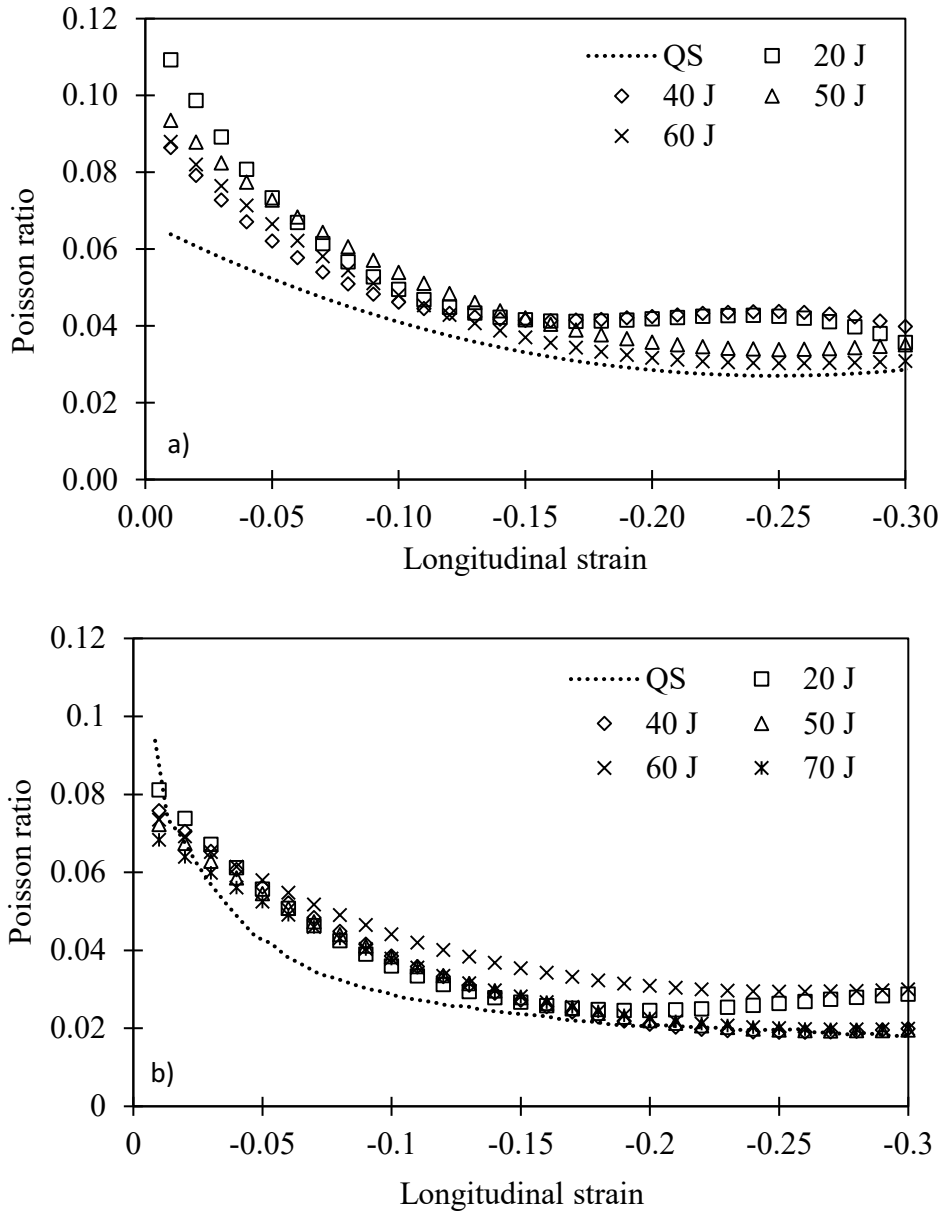


Figure 4.22. Compressive Poisson ratio. a) NL-10, b) NL-20.

The reduction in the Poisson ratio is slightly higher for the more dense agglomerated cork being 59% for NL-10 and around 77% for NL-20. For example under quasi-static compression, for the NL-10 the maximum Poisson ratio is 0.067 and the Poisson ratio in the plateau region is 0.028 while for the NL-20 those values are 0.102 and 0.023 respectively. Similar reductions in the Poisson ratio in agglomerated cork have been previously reported by other researchers in static conditions and at strain rates higher than 90 s^{-1} [11], [7].

Under dynamic compression, agglomerated cork seems to be sensitive to strain rate. Figure 4.22 shows the variation of the Poisson ratio for different impact energies each of them corresponding to an average strain rate given by Figure 4.7.a. In dynamic compression, the average Poisson ratio in the plateau region for NL-10 is 0.038 while in quasi-static compression is 0.028 showing an increment of 33%. This strain rate sensitivity is also visible for the NL-20 although the effect seems less strong and predictable.

At this point, it is important to highlight that using DIC for measuring the Poisson ratio in agglomerated cork at very low applied strains and very large applied strains is a challenging task. At very low applied strains <1% the chosen subset size shows difficulties to provide enough space resolution to accurately measure the very small transversal strains. At very high applied strains (>30%) the excessive distortion of the speckle pattern increases the correlation error causing high dispersion in the measured data. This limitation has been also observed by other researchers using DIC [11].

Table 4.1 summarizes the previously mentioned finding highlighting and some key mechanical properties in quasi-static and dynamic compression. Due to the variability in the mechanical properties, it is convenient to present mean values of each property with their corresponding relative standard error (RSE).

The less-dense agglomerated cork presents a lower Young modulus and stress plateau, both in static and dynamic conditions. This variation has been previously reported by [7], but in dynamic tests with a semi-spherical impactor. The Young modulus increases 62% in static conditions and 61% in dynamic conditions. The increment of the stress plateau is 56% and 58% respectively. By contrast, the increment of density between NL-10 and NL-20 is 26.5%. The variation in the densification strain is different, the NL-20 agglomerated cork shows a slightly lower densification strain, both in dynamic and static conditions. A significant variation between static and dynamic properties is observed in both materials, for example, an increment of 40% in Young modulus is observed in NL-10. As will be seen later in this section a similar behaviour is observed in plateau stress and Poisson ratio at 1% strain. In both agglomerated corks, no relevant influence on mechanical properties is found for the analysed strain rate range. The observed variation of mechanical properties with strain rate in both agglomerated cork has been found in some high-density PU foam and others such as EPS and HDPE [3].

Property	Quasi-static tests		Dynamic tests		Static-dynamic
	Average	Error	Average	Error	Variation (%)
NL-10					
Young modulus E (MPa)	5.14	8.00%	7.2	6.50%	40.10%
Plateau stress (MPa) (at 20% strain)	0.463	3.20%	0.723	2.10%	56.10%
Poisson ratio (at 1% strain)	0.067	0.60%	0.102	4.90%	51.30%
Poisson ratio (at 4% strain)	0.055	2.50%	0.075	3.40%	36.60%
Poisson ratio (at 20% strain)	0.028	10.70%	0.038	5.30%	33.10%
Densification strain	0.57	0.80%	0.6	1.00%	4.20%
Maximum efficiency	0.29	0.20%	0.31	0.60%	8.60%
NL-20					
Young modulus E (MPa)	8.322	15.84%	11.6	4.50%	39.10%
Plateau stress (MPa) (at 20% strain)	0.722	0.66%	1.14	2.40%	58.20%
Poisson ratio (at 1% strain)	0.102	6.72%	0.077	2.60%	-24.30%
Poisson ratio (at 4% strain)	0.062	7.94%	0.059	1.50%	-5.90%
Poisson ratio (at 20% strain)	0.023	17.01%	0.023	7.10%	-0.40%
Densification strain	0.527	0.57%	0.57	1.60%	7.30%
Maximum efficiency	0.281	0.49%	0.3	0.50%	8.50%

Table 4.1. Summary of mechanical properties at quasi-static and dynamic compression of NL-10 and NL-20.

4.2.7 Result of quasi-static and dynamic compression of PET foam.

Quasi-static (QS) and dynamic compression tests at different impact energies are compared. A record of force and displacement is obtained for every test and the corresponding stress-strain curves are estimated. Figure 4.23 and Figure 4.24 show the engineering stress-strain curves for the tests with the impactor mass of 9.13 kg and 16.13 kg respectively. It is observed that under QS conditions the materials shows the conventional behaviour of rigid cellular materials under compression. An initial linear-elastic region ending in plastic collapse stress is followed by almost constant plateau stress and a densification region at high strains. This behaviour has been previously observed in other polymeric foams such as polypropylene and PVC foam [15], [29].

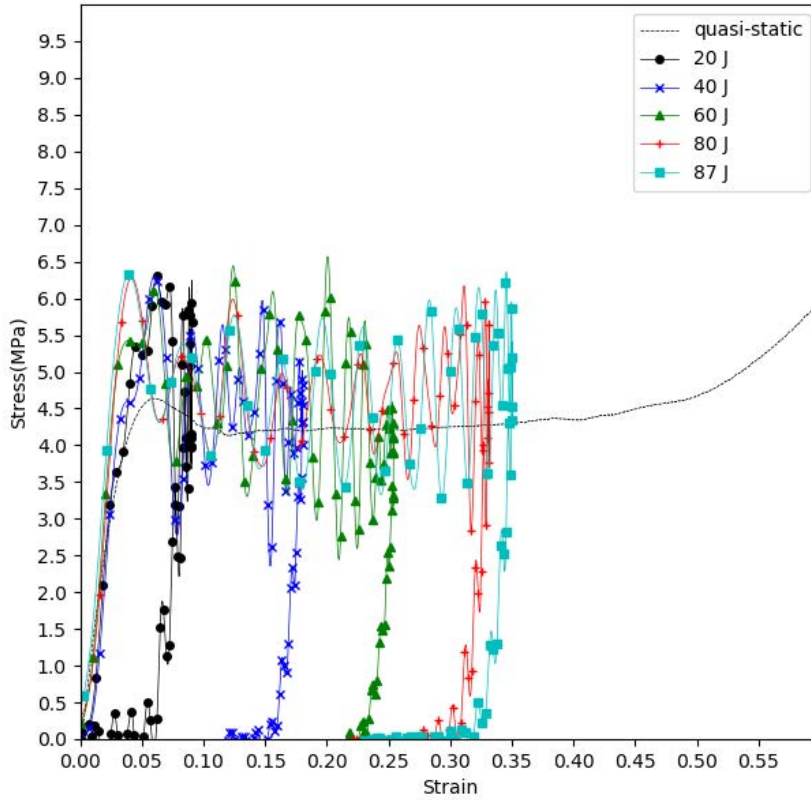


Figure 4.23. Comparison of stress vs. strain curves for quasi-static and dynamic compression. PET foam with impactor mass of 9.13 kg.

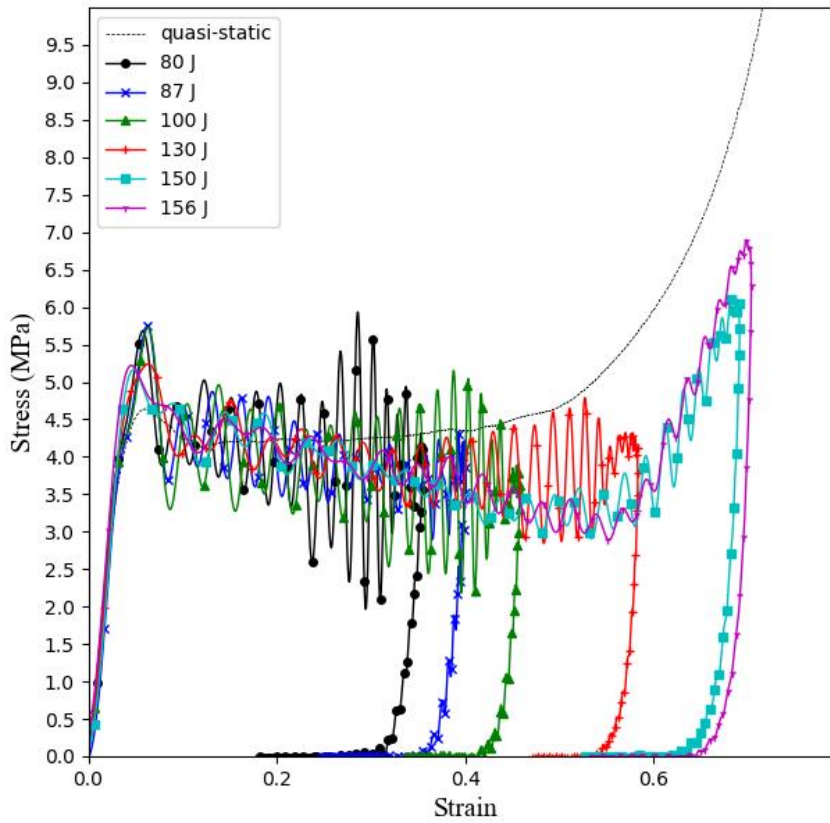


Figure 4.24. Comparison of stress vs. strain curves for quasi-static and dynamic compression. PET foam with impactor mass of 16.13 kg.

Young's modulus for quasi-static and dynamic compression is estimated as the slope of a linear fitting curve up to 3% strain. Under dynamic compression, the material shows a similar stiffness in the linear-elastic region and a significant increase in the collapse stress (Figure 4.23 and Figure 4.24).

In the plateau region, there are significant oscillations of the stress value that can be attributed to the local dynamic crushing of the cell in the layers adjacent to the loading surface. This phenomenon has been previously reported by other authors in metallic foams [5]. High-speed video recording clearly shows the onset and propagation of a “shock” layer of crushed cells that is highly non-homogeneous and unstable. Figure 4.25 shows consecutive video frames of the dynamic compression at 40J and 80J. It can be observed that depending on the test the shock layers appear either on the loading or on the reaction face of the specimen. It is also found that the appearance and propagation of the shock layer are more severe at higher impact energies where the momentum transferred to the layer is higher.

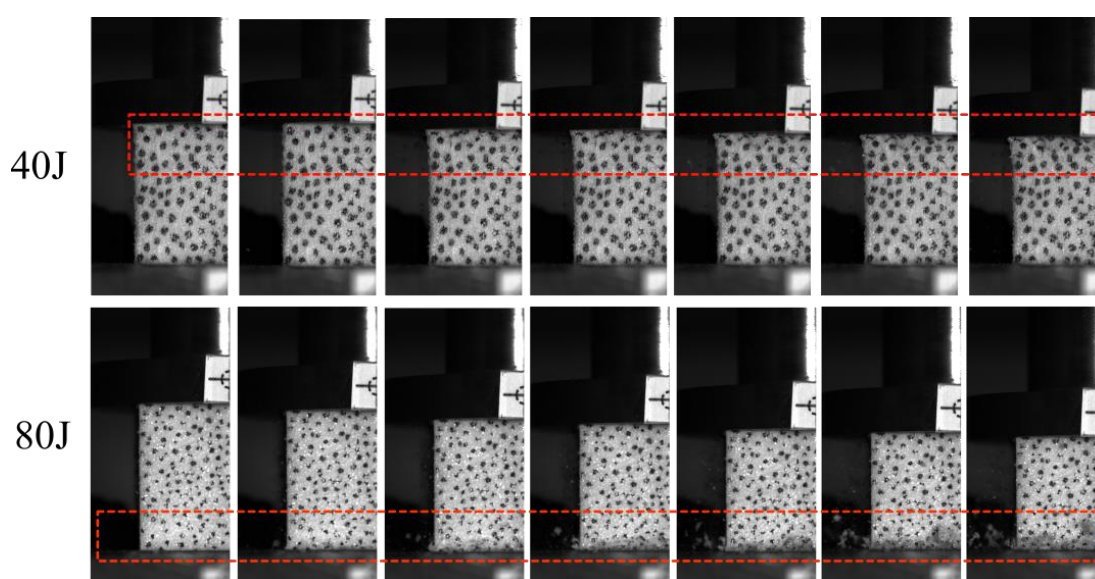


Figure 4.25. Video frames showing the onset and propagation of the dynamic crushing in PET foam.

The high degree of oscillations in the plateau region makes it customary to provide a mean stress value in the plateau region that allows direct comparison of the strength of the material at different strain rates. This value is estimated for each test from the region between the collapse strain and the densification strain in Figure 4.23 and Figure 4.24.

For the test performed with the smallest impactor mass (9.13 kg) despite the high oscillations, the mean plateau stress is almost constant (Figure 4.23). However, dynamic

crushing seems to have an even higher influence on the plateau region for tests performed with the 16.13 kg impactor where the momentum transfer is higher. This can be observed from Figure 4.24 where the plateau region shows stress softening starting from 20% strain up to densification or load removal.

The mean plateau stress shows a small strain rate sensitivity as can be observed from Figure 4.26. The plateau stress tends to slightly increase when the effects of dynamic crushing are minor (low energy impact). In contrast, when dynamic crushing is more relevant (high-energy impact) the mean plateau stress decreases. This last phenomenon can be understood as stress softening in the plateau region associated with the dynamic crushing and can be seen in Figure 4.24 for impact energies above 100J.

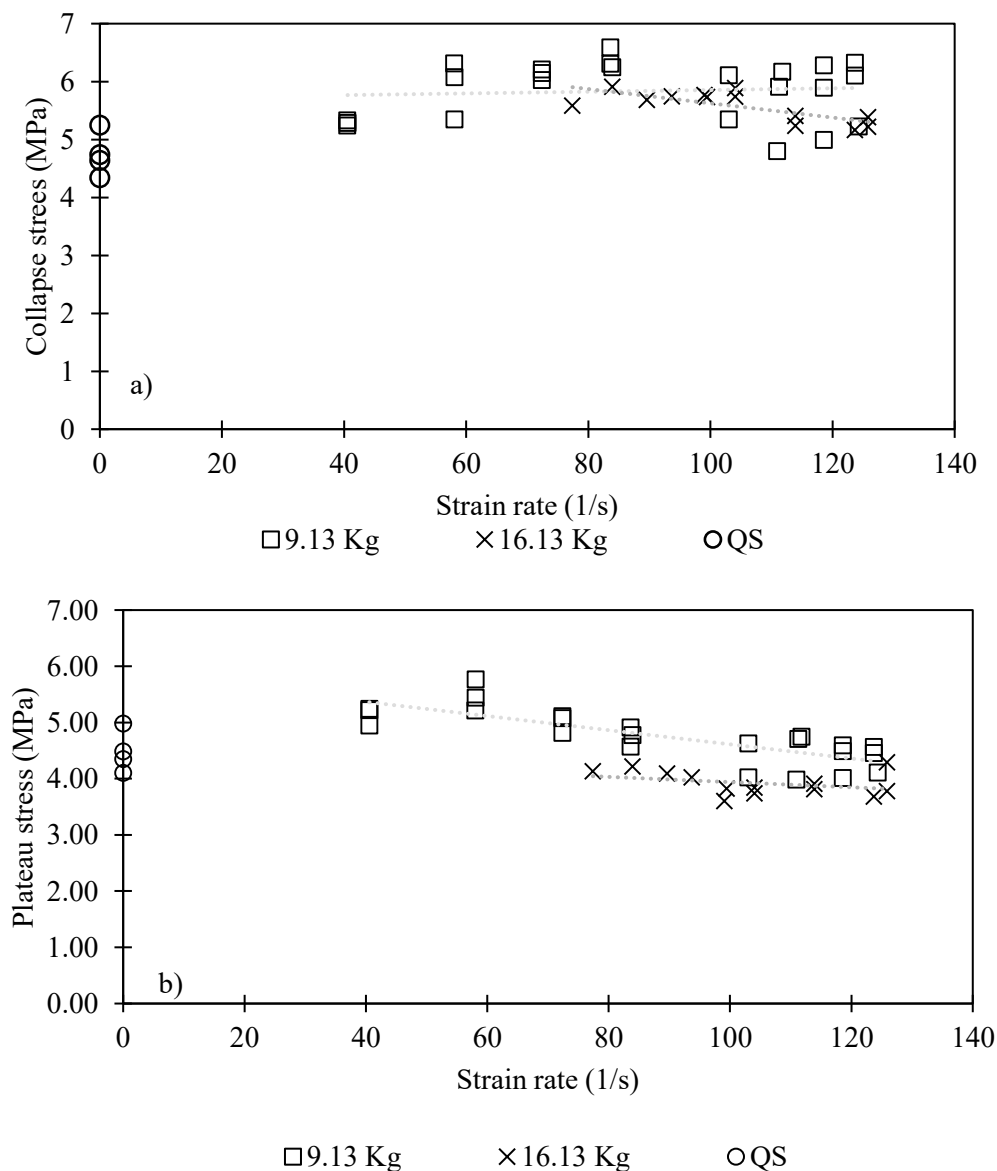


Figure 4.26. a) Collapse stress, b) Mean plateau stress vs. strain rate

Figure 4.27 plots the energy absorption efficiency vs. strain for the test performed with the 16.13 kg impact mass at quasi-static and dynamic compression. It is observed that η increases with strain reaching a maximum value at the densification onset. At quasi-static compression, the material shows a maximum efficiency close to 0.45 with densification occurring at 53% strain. A considerable change is observed in dynamic compression where η_{\max} is 0.69 at 57% strain. The increase in energy absorption efficiency and the delay in the overall densification can be associated with dynamic crushing. This occurs since additional energy is dissipated due to localized damage in the shock layer produced by the brittle fracture of the cell walls. Additionally, the delay in the overall densification of the specimen can be associated with lower strain levels behind the shock layer where the cells are highly deformed due to the dynamic crushing and the localized densification. This effect can be easily observed from the DIC analysis in Figure 4.32 and Figure 4.34.

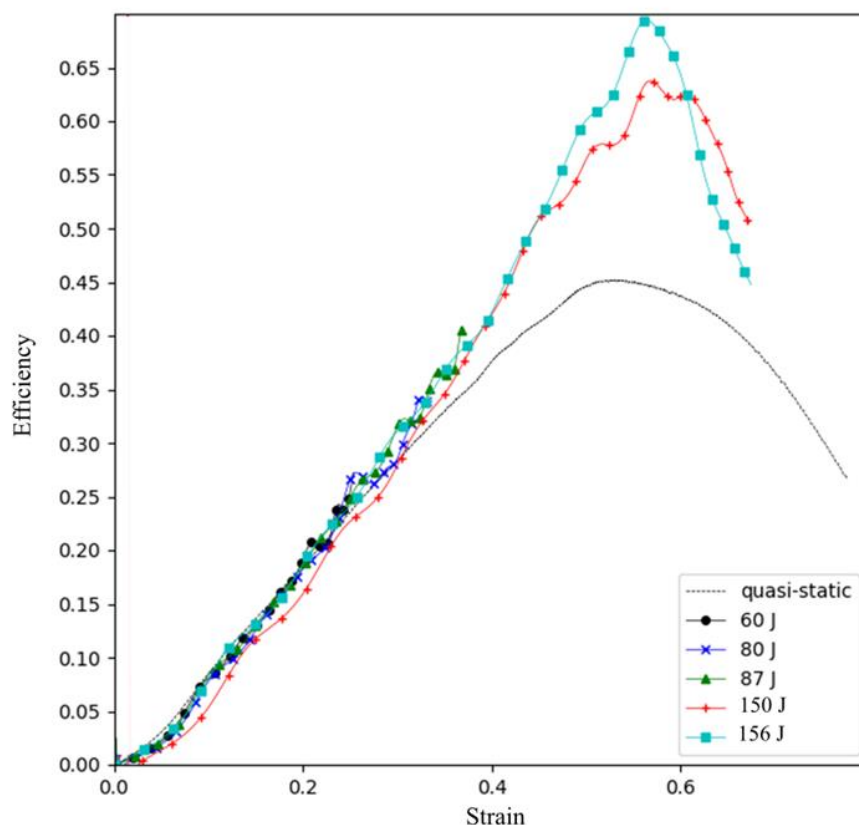


Figure 4.27 Energy absorption efficiency vs. strain quasi-static and dynamic compression.

The maximum displacements estimated by the data acquisition system and the tracker are plotted in Figure 4.28 for the dynamic compression with both impact masses. It can be noticed that the maximum displacement follows a linear relationship to the impact energy even at strain levels beyond densification.

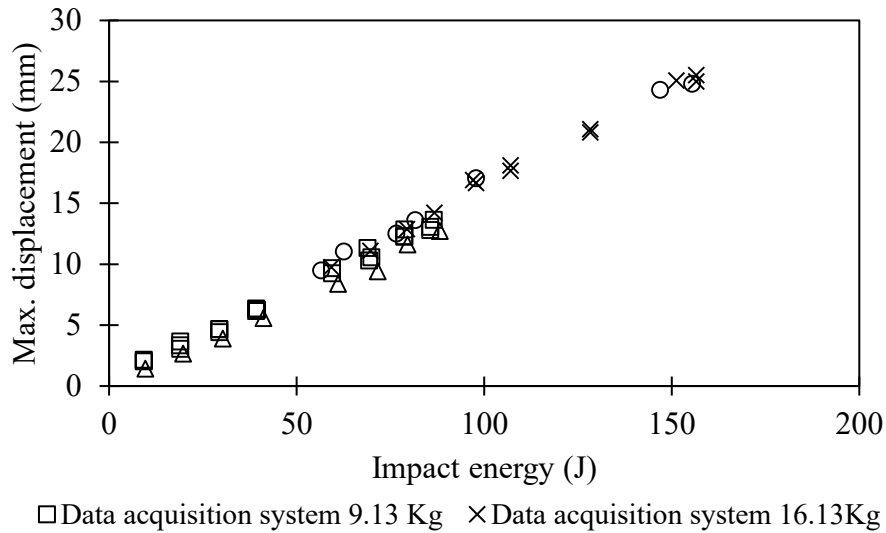


Figure 4.28 Maximum displacement vs. impact energy for dynamic compression of PET foam

Considering that the velocity and displacement measurements obtained by the acquisition system are accurate enough (as demonstrated in the previous section), the dissipated energy is determined as the difference between the kinetic energy before and after impact. Figure 4.29 shows the dissipated energy as a function of the impact energy measured by the data acquisition system and the image tracker.

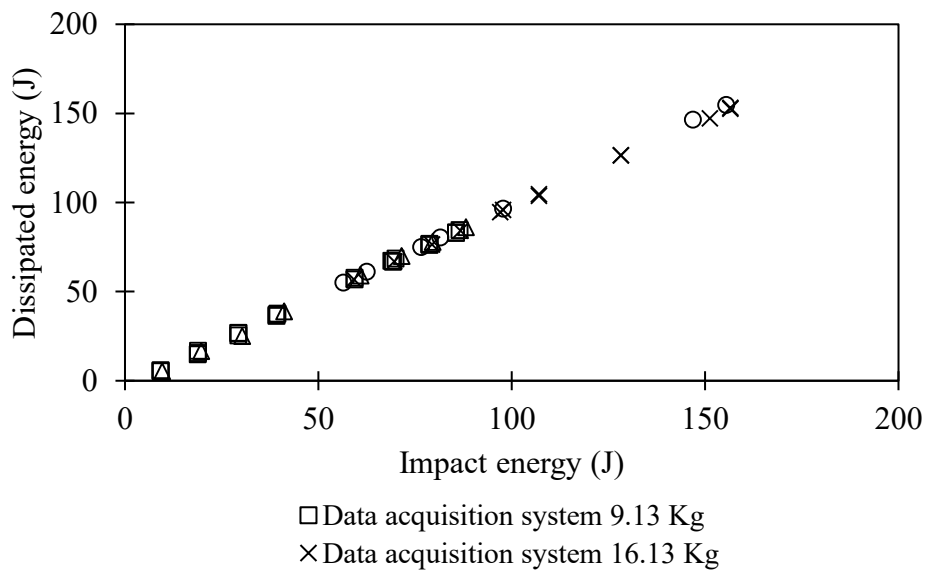


Figure 4.29. Energy dissipated vs. impact energy for dynamic compression PET foam

An interesting observation arises by plotting the energy dissipation ratio (dissipated energy/impact energy) as a function of the maximum displacement. From Figure 4.30 it is observed that the dissipation ratio increases with higher maximum displacements. As a consequence, the dissipation ratio is low when the maximum displacement takes place in

the linear-elastic region or the initial collapse region. However, once the plateau region is reached there is a considerable rise in the dissipation ratio getting values up to 98% once the densification is fully developed ($d_{\max} = 20$ mm).

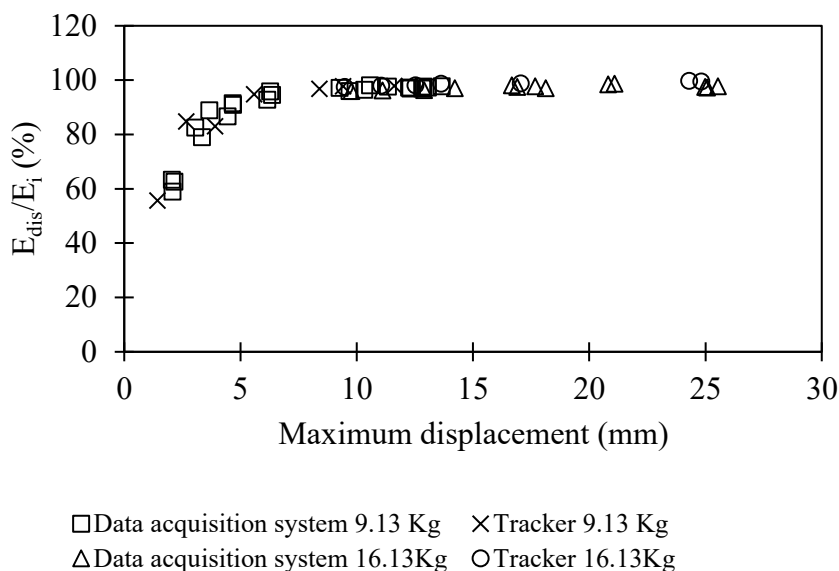


Figure 4.30. Energy dissipation ratio vs. maximum displacement for dynamic compression PET foam

The appearance and evolution of massive cell dynamic crushing near the loading and reaction faces are studied. DIC analysis shows that the local strains field ($\epsilon_{yy}, \epsilon_{xx}, \epsilon_{xy}$) is non-uniform across the test specimen but changes in magnitude as it gets closer to the load surface or the reaction surface. Figure 4.31 shows the evolution of the local longitudinal strain ϵ_{yy} for a dynamic compression test at 40 J (impactor mass of 9.13 kg) for four different vertical locations (Y) along the mid-plane.

For the sake of clarity, the overall strain $\bar{\epsilon}_{yy}$ estimated from the data acquisition system (DAS) is also plotted in a red dotted line highlighting the moment in which the first massive cell collapse appears. During the initial moments after contact (time < 0.5 ms) the local strain at the different vertical locations has a similar magnitude suggesting that the strain field is uniform. After that (time > 0.5 ms) the strain level rises more rapidly in those points near the loading face and the strain field is not uniform anymore. This is followed by a sudden drop in the local strain that can be associated with the first massive crushing of cells along with a thin layer next to the loading face. Fluctuations of the local strain (peaks and valleys) appear at each location every time a new massive cell collapse occurs in the

crushing layer. A detailed observation of the strain level inside the crushing layer next to the loading face is almost impossible to get since correlation in this area is not possible due to the excessively distorted speckle pattern [29].

Figure 4.32 shows the distribution of the local longitudinal strain and local Poisson ratio for the same test at three different instants of time corresponding to -4%, -11% and -16% overall strain. In this figure is also possible to visualize the variation of the longitudinal local strain ϵ_{yy} mentioned in the previous paragraph. It can be also observed that the strain field in the middle of the specimen is almost uniform and the strain magnitude is well below the overall strain computed by the DAS. In contrast, regions close to the loading and reaction faces show a progressive increase in the longitudinal strain and the strain magnitude can reach values closer or even larger than the overall strain (DAS). For example Figure 4.32 (a) shows the strain distribution at $t=5$ ms after impact (overall strain $\bar{\epsilon}_{yy} = -4.1\%$). In the middle of the specimen, the strain is almost constant $\epsilon_{yy} = -2\%$ while in the loading face and the reaction face it can reach values up to -3.5% and -5.1% respectively. This tendency is maintained at larger overall strains Figure 4.32(a) (c) however, the size of the region of constant strain is reduced as the compression progresses.

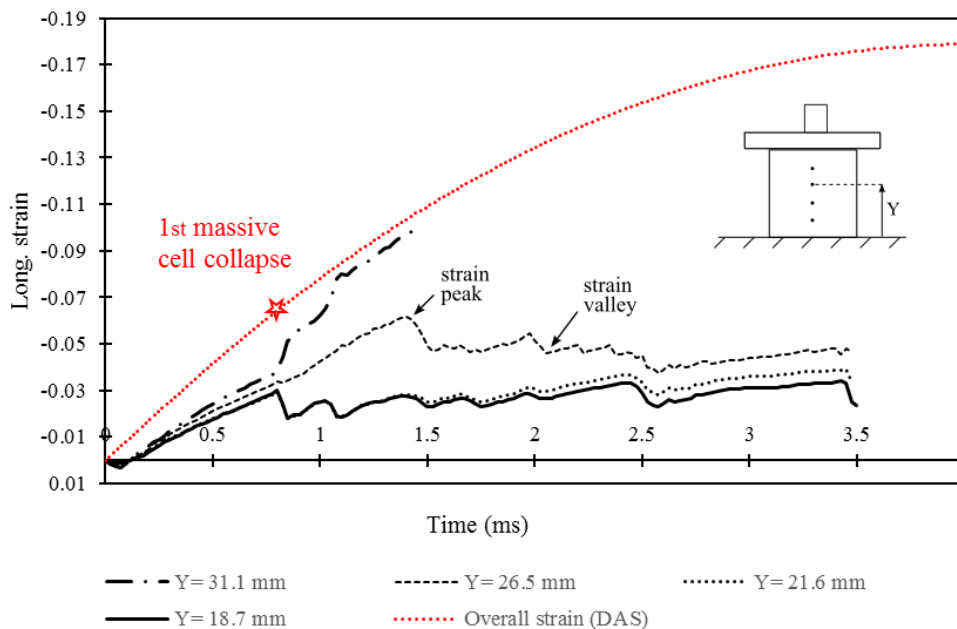
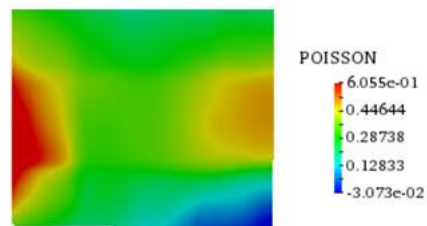
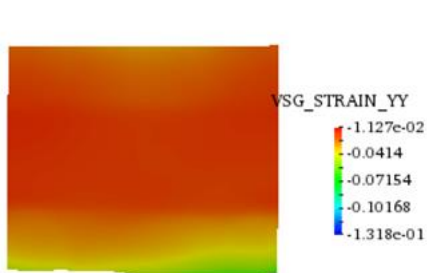
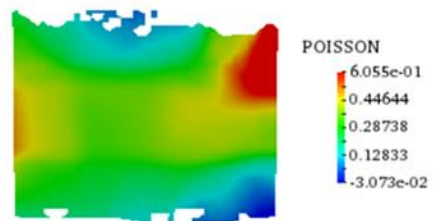
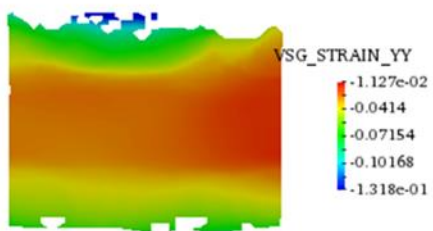
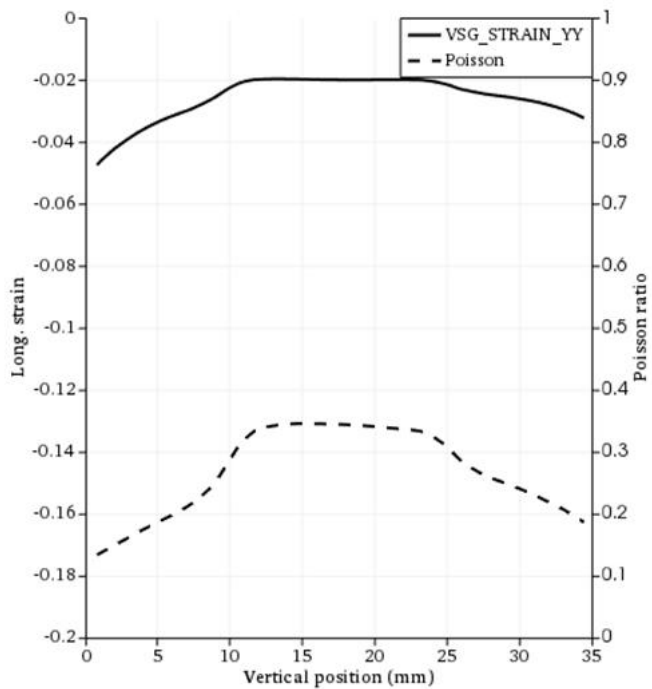


Figure 4.31. Evolution of the local longitudinal strain at different vertical positions, 40 J

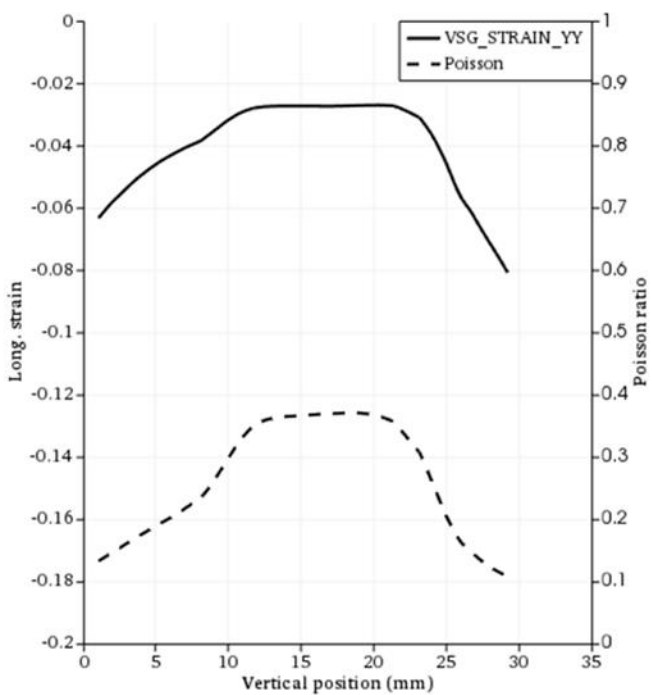
BUILDING A RELIABLE MODEL FOR THE CORE



a)



b)



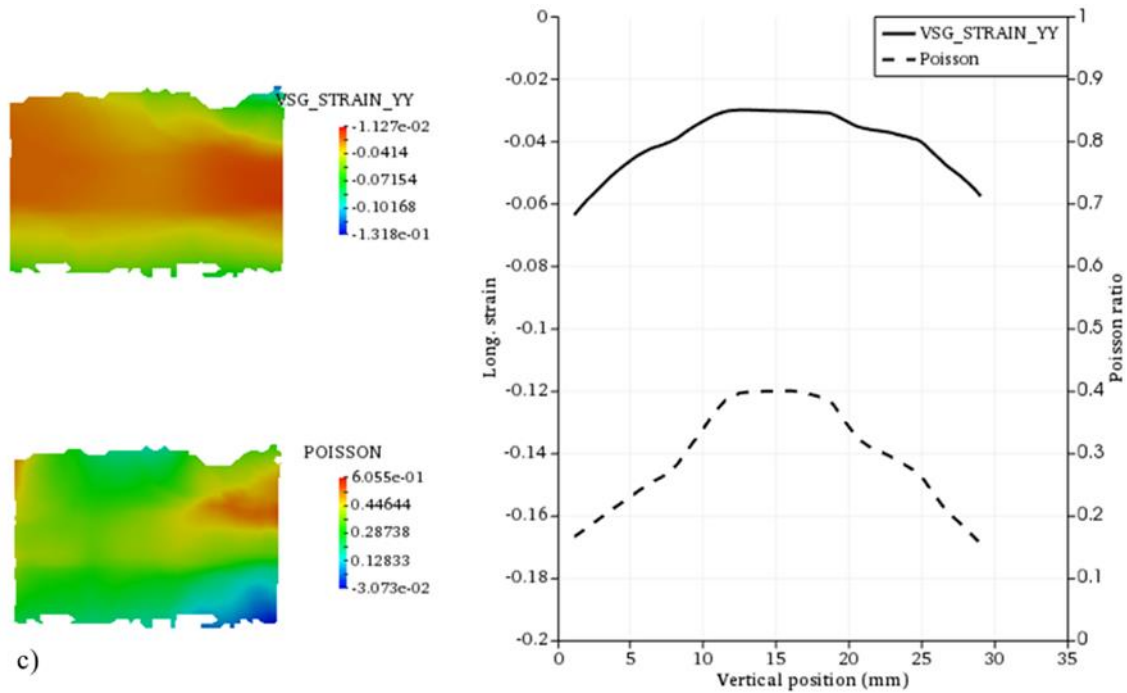


Figure 4.32. Local strain and local Poisson ratio distribution for dynamic compression at 40 J, a) $\bar{\epsilon}_{yy} = -4\%$, b) $\bar{\epsilon}_{yy} = -11\%$, c) $\bar{\epsilon}_{yy} = -16\%$

The local Poisson ratio also shows a similar variation along the longitudinal axis with a region of almost constant value in the middle and higher gradients towards the loading and reaction faces. It is important to notice that in the case of the Poisson ratio the higher values are present in the middle while lower values are next to the loading and reaction face. This can be explained by its inverse relationship with longitudinal strain and the effects of the friction in the loading and reaction faces, which limit the transverse strain creating a “barrel” like deformation.

Another observation is done when analyzing the longitudinal strain field at higher impact energies where localization and dynamic crushing are more relevant. Figure 4.33 shows that local strain evolution for a 150J test is very similar to the 40J case. However, it can be noticed that the strain level along different points along the longitudinal axis seems tighter. This indicates that at this impact energy the strain distribution is more uniform if compared to the 40J compression. This effect is easier to visualize when looking at the strain distribution along the middle plane for three different overall strains -4%, -11% and -16% (Figure 4.34). It is observed that the longitudinal strain remains almost constant across the whole specimen and there is a big gradient just in the vicinity of the shock layer. The order of magnitude of the strain gradient in the vicinity of the shock layer is much higher than dynamic compression at lower impact energies (Figure 4.32).

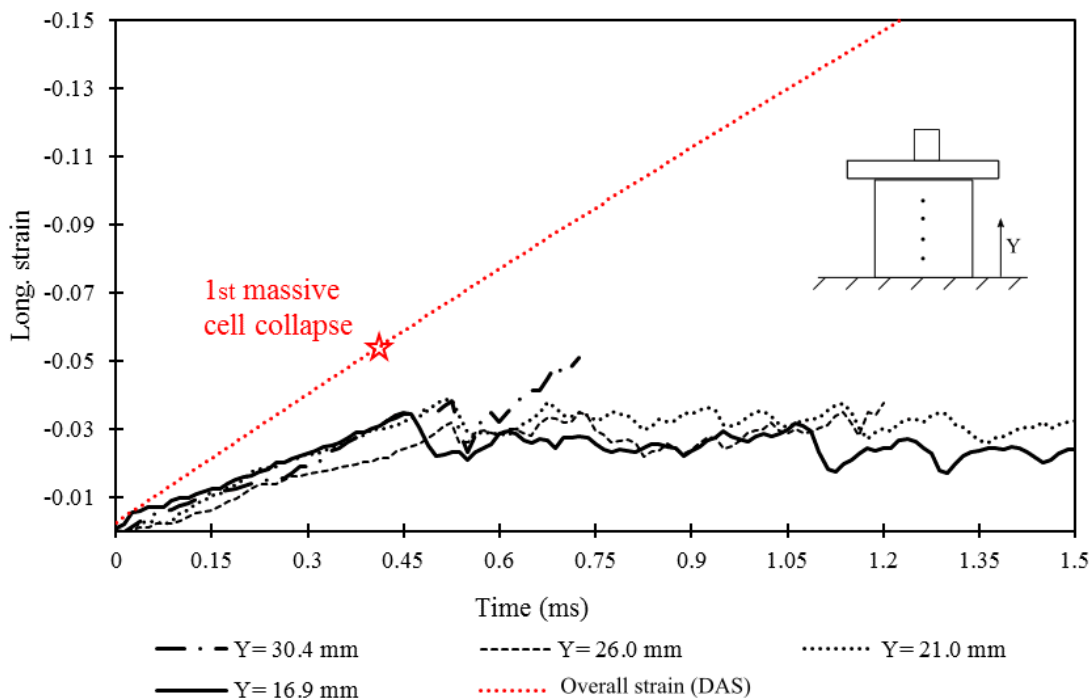
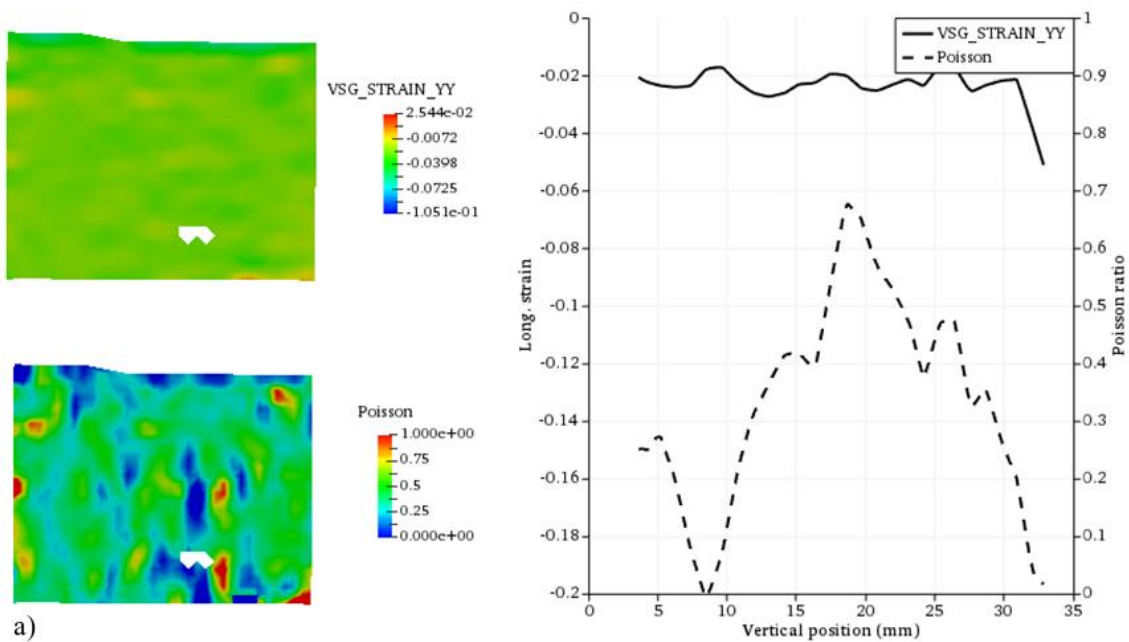


Figure 4.33. Evolution of the local longitudinal strain at different vertical positions, 150 J



a)

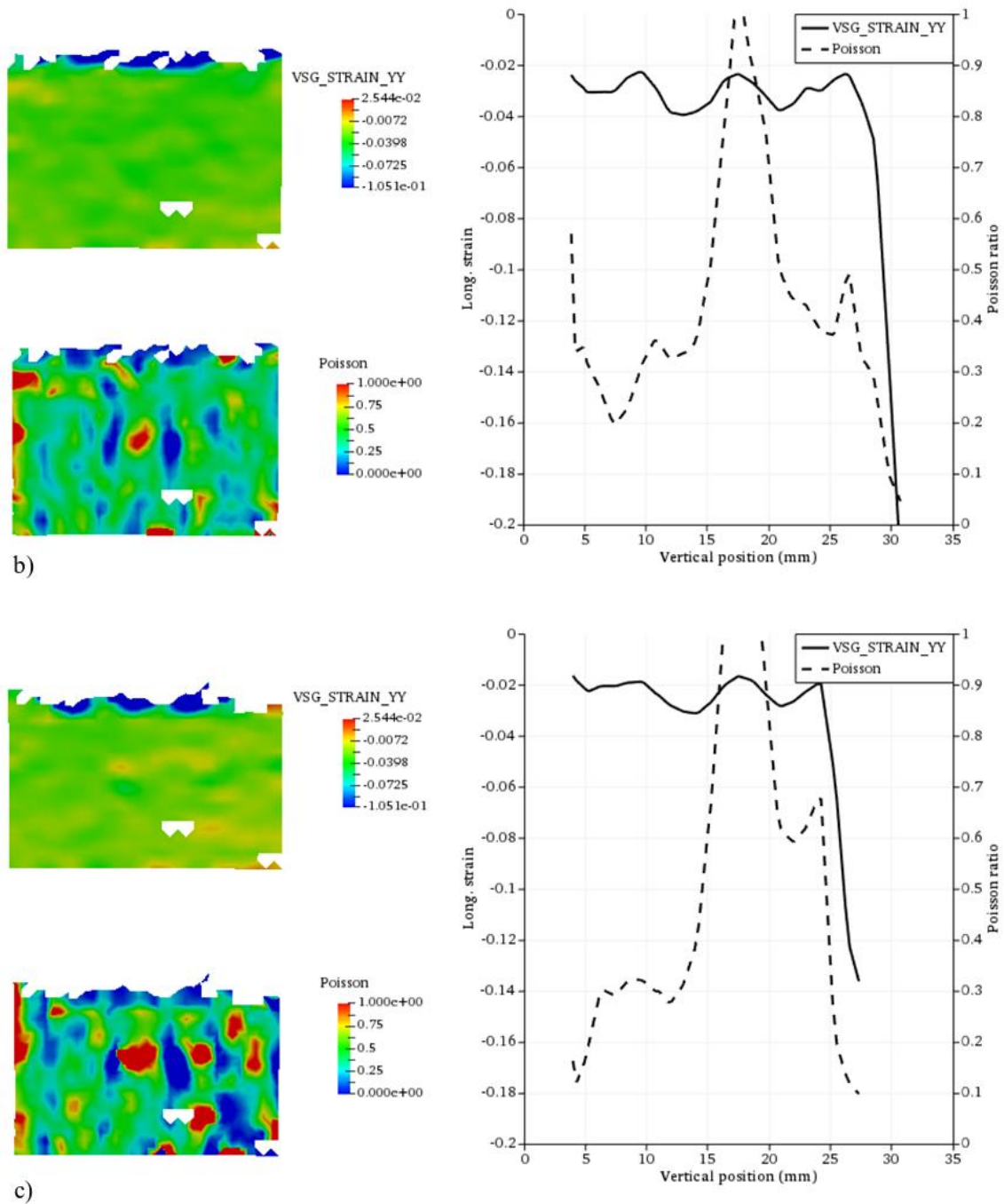
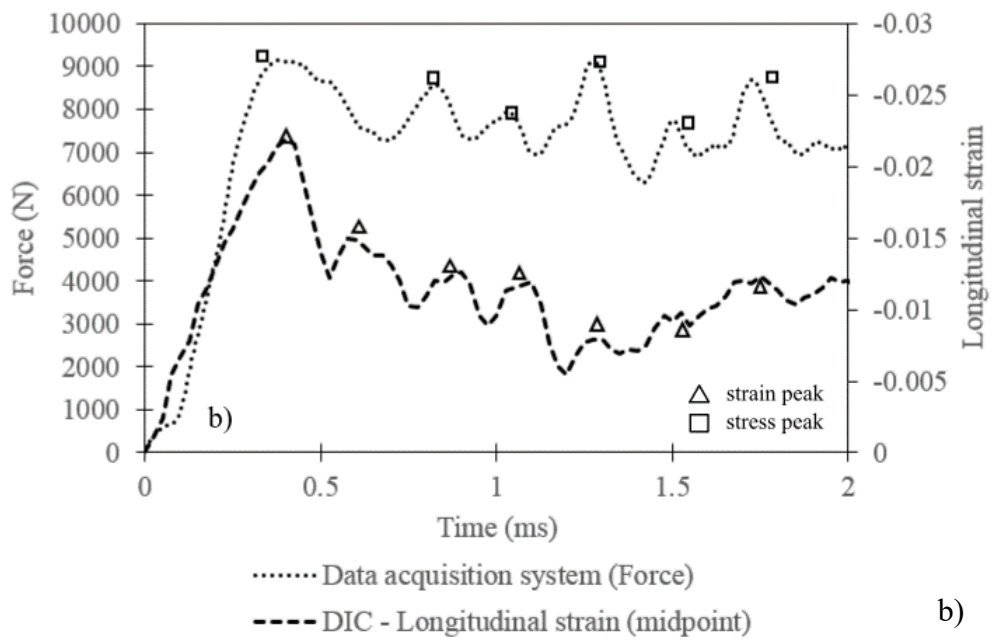
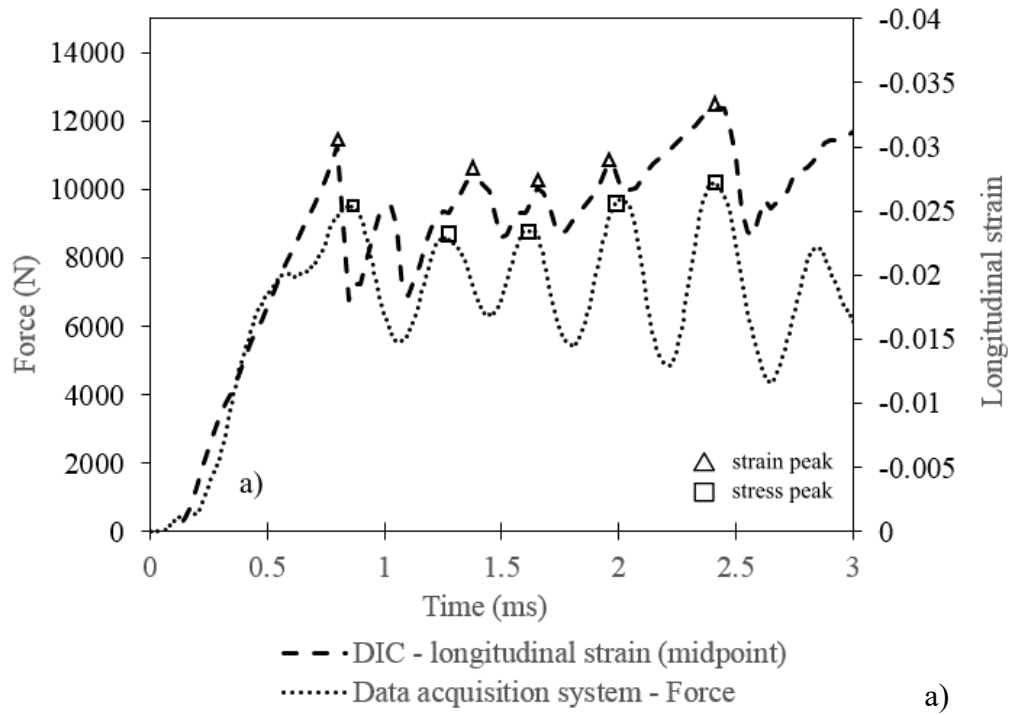


Figure 4.34. Local strain and local Poisson ratio distribution for dynamic compression at 150J, a) $\bar{\epsilon}_{yy} = -4\%$, b) $\bar{\epsilon}_{yy} = -11\%$, c) $\bar{\epsilon}_{yy} = -16\%$

Another observation arises when comparing the evolution of the force signal measured by the (DAS) and the local strain measured by the DIC near the specimen's mid-point. From Figure 4.35 it is noticed that peaks of force and peaks of strain from both independent measurement methods seem to occur at almost the same instant of time. This explains that the presence of stress oscillations in the plateau region corresponds to the dynamic effect of the dynamic crushing and the formation/evolution of the shock layers.

BUILDING A RELIABLE MODEL FOR THE CORE



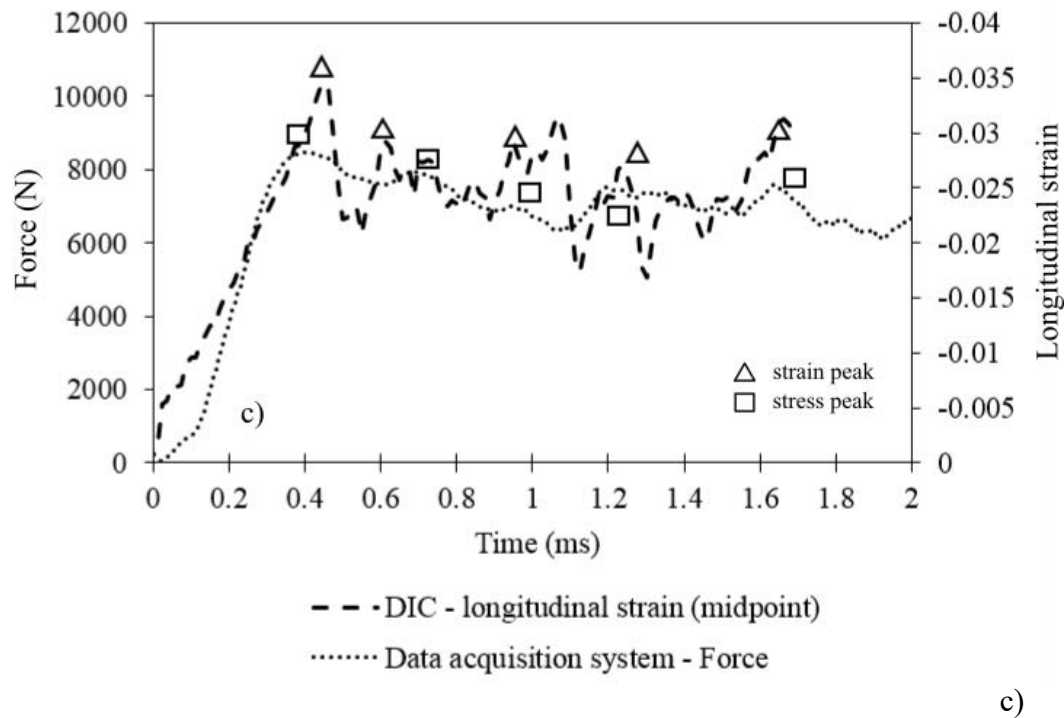


Figure 4.35. Evolution of dynamic crushing (impactor mass = 16 kg) measured by peaks of force (data acquisition system) and peaks in local longitudinal strain ϵ_{yy} (DIC), a) 40 J, b) 80 J, c) 150 J

Figure 4.36 depicts the average compressive Poisson ratio vs. longitudinal strain for different energy levels. Although the data is highly scattered it is possible to identify that the Poisson ratio shows a clear decrement tendency when the compression strain increases.. It is observed that at low strain levels (<3% strain) corresponding to the linear elastic region, the Poisson ratio is maintained in the range of 0.3 to 0.4. For higher strains, the Poisson ratio decays for both quasi-static and dynamic compression. For example, at 10% strain, the Poisson ratio at quasi-static compression reaches a value of 0.22 while in dynamic compression it can reach values in the range of 0.1 to 0.2.

At this point, it is important to highlight that using DIC for measuring the Poisson ratio in PET foam at very low applied strains and very large applied strains is a challenging task. At very low applied strains (<1%) the chosen subset size shows difficulties to provide enough space resolution to accurately measure the very small transversal strains. At very high applied strains (>15%) the excessive distortion of the speckle pattern increases the correlation error causing high dispersion in the measured data. This limitation of the DIC method for measuring strain fields over polymeric foams has also been observed by other researchers [11]. The estimation of the average Poisson ratio requires a very precise measure of the transversal strain, which due to its small magnitude requires high spatial

resolution. A limiting factor to achieving enough resolution is the porosity of the material and the difficulty to plot an optimal speckle pattern in the specimen surface. Other factors that might contribute to the large observed scattering in the Poisson ratio are the intrusion of de-attached foam debris during the crushing of the specimen and the propagation of cracks inside the analysis region. Both conditions disrupt the visibility of the region of interest and induce error in the measured strain field that can be considerable particularly at high impact energies.

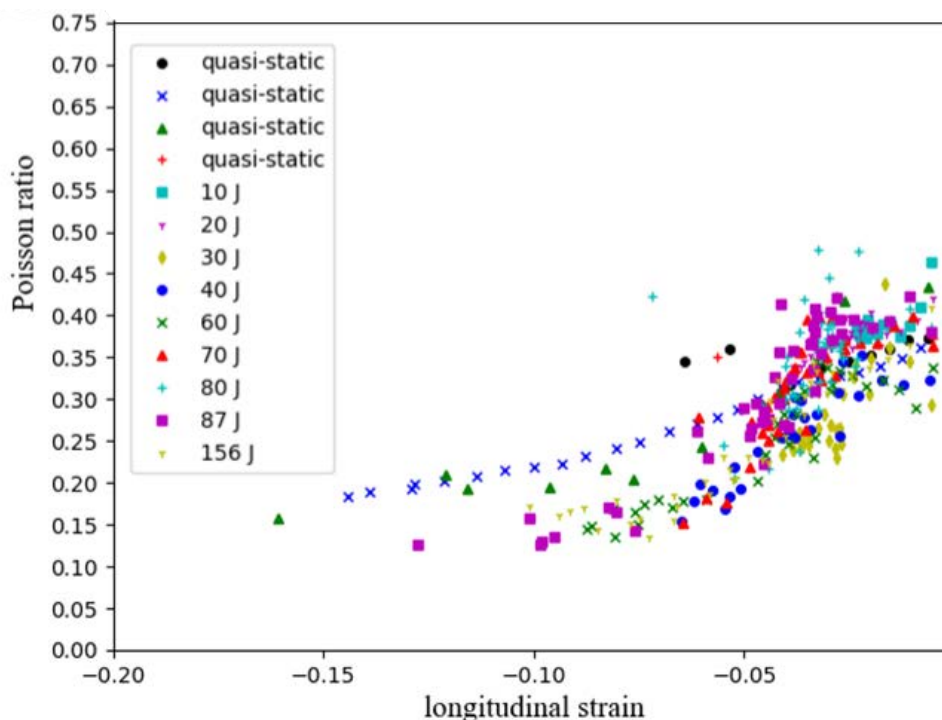


Figure 4.36. Mean Poisson ratio for PET foam under quasi-static and dynamic compression.

Table 4.2 and Table 4.3 shows a summary of some mechanical properties obtained through the quasi-static and dynamic compression tests. Some general remarks are discussed as follows:

- The measured properties show a certain degree of dispersion even in quasi-static test conditions where the relative standard deviation (RSD) could reach values up to 13%.
- The linear elastic Young's modulus and the collapse stress are higher in dynamic compression than in quasi-static compression.
- As discussed previously the mean plateau stress is highly influenced by dynamic crushing. With the lowest impactor mass ($m=9.13$ kg) the plateau stress is larger than the quasi-static case (variation = 6%) while for the largest impact mass ($m=16.13$ kg) the plateau stress is lower than in the quasi-static condition (variation = -12 %).

Property	Quasi-static tests		Dynamic tests Impactor mass = 9.13 kg		Static- dynamic
	Average	error (%)	Average	error (%)	Variation (%)
Young's modulus E (MPa)	112.47	9.35	176.79	15.17	57.19
Collapse stress (Mpa)	4.74	6.88	5.83	8.41	23.01
Plateau stress (Mpa) (at 20% strain)	4.48	7.14	4.76	9.43	6.21
Poisson ratio (at 1% strain)	0.38	3.84	0.43	8.43	13.79
Poisson ratio (at 4% strain)	0.32	3.49	0.30	13.15	-7.99
Poisson ratio (at 10% strain)	0.25	12.90	0.10	83.10	-58.38

Table 4.2. Summary of mechanical properties at quasi-static and dynamic compression (mass=9.13kg)

Property	Quasi-static tests		Dynamic tests Impactor mass = 16.13 kg		Static- dynamic
	Average	RSD (%)	Average	RSD (%)	Variation (%)
Young's modulus E (MPa)	112.47	9.35	139.13	9.87	23.71
Collapse stress (Mpa)	4.74	6.88	5.57	4.49	17.54
Plateau stress (Mpa) (at 20% strain)	4.48	7.14	3.92	5.26	-12.49
Poisson ratio (at 1% strain)	0.38	3.84	0.40	4.25	6.11
Poisson ratio (at 4% strain)	0.32	3.49	0.38	17.86	16.19
Poisson ratio (at 10% strain)	0.25	12.90	0.34	48.58	38.78

Table 4.3. Summary of mechanical properties at quasi-static and dynamic compression (mass=16.13kg)

4.2.8 Results of quasi-static tension of agglomerated cork and PET foam

Quasi-static tensile testing shows that both kinds of materials (agglomerated cork and PET foam) show the typical tensile nonlinear behaviour of cellular materials that includes a

small initial linear region followed by a progressive reduction in the tangent stiffness of the material until failure (Figure 4.37). PET foam shows a much stiffer linear response than agglomerated cork with Young's modulus equal to 110 MPa (measured at 2% strain) with respect to the 12.5 MPa and 20 MPa measured for the NL-10 and NL-20 respectively. Additionally, PET foam is also stronger than agglomerated cork reaching a failure strength of 2.95 MPa while for agglomerated cork this value is 0.46 MPa for NL-10 and 0.96 MPa for NL-20. It can be noticed that there is considerable variability in the peak stress for both NL-10 and NL-20 being 14% and 12% respectively. It is also clear that the failure stress and the failure strain are very sensitive to the material density since for both cases the NL-20 presents higher maximum values.

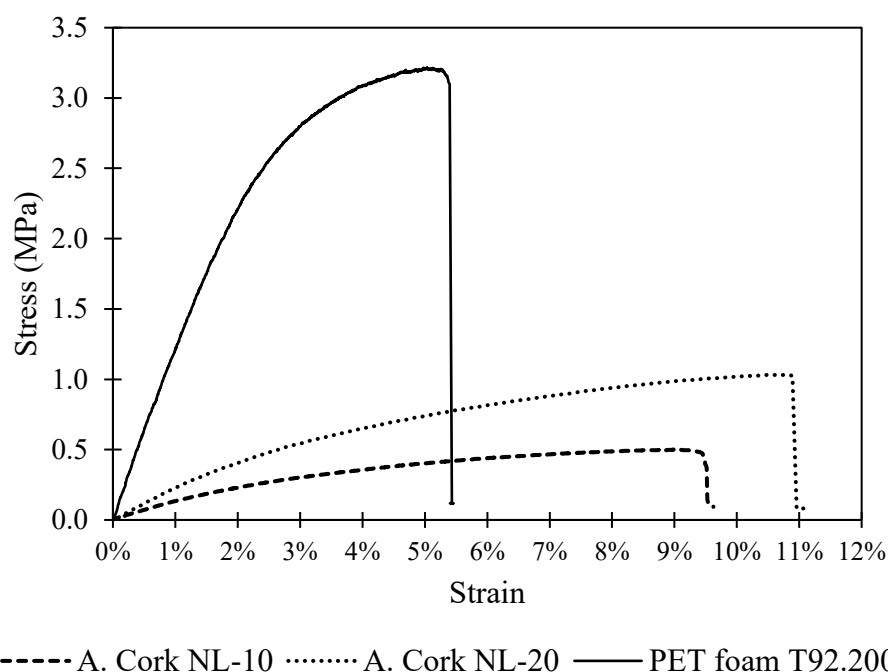


Figure 4.37. Quasi-static tensile stress-strain curve for agglomerated cork and PET foam.

4.3 Modelling the core materials in FEA

The previous section studied in detail the compressive and tensile behaviour of agglomerated cork and PET foam based on the experimental test carried out as part of this work. In this section independent FEA models are proposed for each material to capture with accuracy their dynamic compressive response. The constitutive material models are explained and the validation of each of them is presented.

4.3.1 Agglomerated cork constitutive material model

As explained in detail in the previous section the mechanical behaviour of agglomerated cork is complex. Although this material is quasi-isotropic, it has a non-linear mechanical behaviour and a variable Poisson ratio. Additionally, its stress-strain relationship is highly dependent on deformation rates [36], [37]. Considering that, agglomerated cork experiences high deformation strains without significant plastic deformation it is a common approach to model this material with a hyperelastic elastomeric foam model with the Mullins effect [36]. This model is designed for cellular materials whose porosity allows very large elastic deformations (up to 90%) and can capture the compression stages of the material behaviour (linear-elastic, plateau, and densification). A brief description of the material model is given as follows:

If the current position of a material point is given by the vector \bar{x} and the reference position of the same point by \bar{X} , the deformation gradient is :

$$F = \frac{d\bar{x}}{d\bar{X}} \quad (4.3)$$

The total change in the volume is given by the Jacobian

$$J = \det(F) \quad (4.4)$$

The deviatoric stretch matrix can be written as

$$B = F \cdot F^T \quad (4.5)$$

So that the first and second strain invariants are

$$I_1 = \text{trace}(B) \quad (4.6)$$

$$I_2 = \frac{1}{2}(I_1^2 - \text{trace}(B \cdot B)) \quad (4.7)$$

For isotropic incompressible (or almost incompressible) materials an additive decomposition of the deviatoric and volumetric strain energy contributions gives the polynomial form [38]:

$$U = f(I_1 - 3, I_2 - 3) + g(J_{el} - 1) \quad (4.8)$$

This expression can be expanded using the Taylor series and the contribution of the second invariant can be neglected to obtain a reduced polynomial form:

$$U = \sum_{i=1}^N C_{i0} (I_1 - 3)^i + \sum_{i=1}^N \frac{1}{D_i} (J_{el} - 1)^{2i} \quad (4.9)$$

Where D_i determines the compressibility of the material. If D_i are zero the material is considered as fully incompressible. The elastic volume strain J_{el} is computed from the total volume strain and the volume strain due to thermal expansion J_{th}

$$J_{el} = \frac{J}{J_{th}} \quad (4.10)$$

To accurately represent the three compression stages of a typical hyperelastic foam (linear-elastic, plateau, and densification) this material model uses a strain function [39]. The strain energy is represented in an alternative polynomial form in terms of the principal stretches $\hat{\lambda}_1, \hat{\lambda}_2, \hat{\lambda}_3$ that can be fitted up to sixth order ($N=6$). Additionally since elastomeric foams are not incompressible it can be stated that $J = \lambda_1 \lambda_2 \lambda_3 \neq 1$

$$U = \sum_{i=1}^N \frac{2\mu_i}{\alpha_i^2} \left[\hat{\lambda}_1^{\alpha_i} + \hat{\lambda}_2^{\alpha_i} + \hat{\lambda}_3^{\alpha_i} - 3 + \frac{1}{\beta_i} (J_{el}^{-\alpha_i \beta_i} - 1) \right] \quad (4.11)$$

Here J_{el} is the elastic volume ratio, μ_i is shear moduli, and α_i, β_i are the curve-fitting non-integral exponents [37].

Two methods are available for specifying the material properties: the hyperfoam material coefficient can be introduced directly or up to five different kinds of test data (uniaxial, equibiaxial, shear, planar and volumetric) can be introduced for Abaqus to estimate the material coefficients. The least-squares fit is used to compute the coefficients.

4.3.1.1 Mullins Effect

Mullins effect is used to model the stress-strain softening associated with damage when the material is stretched beyond its prior maximum value. This phenomenon is observed in elastomeric materials and it is the only damage model provided by Abaqus capable of modelling stress softening associated with straining in elastomeric materials [40]. The Mullins effect describes the material behaviour through a strain energy potential function that is a function of the deformation gradient tensor F and a scalar variable that controls the material properties η [41].

$$U(F, \eta) \quad (4.12)$$

The variable η allows the material response to be governed by an energy function on unloading and allows reloading it in a path different from the initial path. Due to the

influence of η , part of the potential energy U is recovered as strain energy while the other part is dissipated due to damage. From Figure 4.38 it can be noticed that the shaded area in the stress-stretch curve corresponds to the energy dissipated by damage while the unshaded area corresponds to the recovered energy.

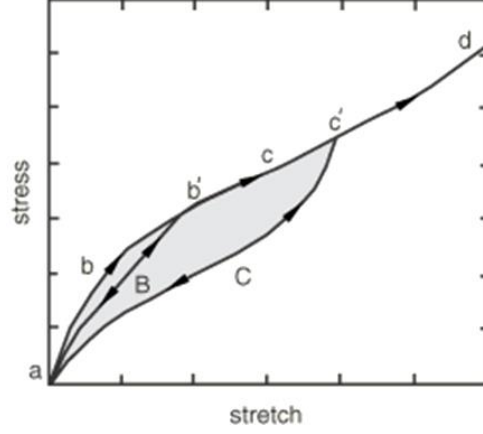


Figure 4.38. Stress vs. strain response with Mullins effect. Source: [37]

During the deformation process, the variable η may switch from inactive to active or vice versa. When η is inactive the material behaves elastically following a strain energy $U(F, \eta)$ with η being constant ($\eta=1$). However, when active η is determined from the deformation gradient tensor and the material behaves elastically but with a different strain energy function $U(F, \eta(F))$.

As a result, the Mullins Effect uses the following modified energy function

$$U(\bar{\lambda}_i, \eta) = \eta U_{dev}(\bar{\lambda}_i) + \Phi(\eta) + U_{vol}(J^{el}) \quad (4.13)$$

Where $\eta U_{dev}(\bar{\lambda}_i)$ is the deviatoric part of the strain energy of the initial (primary) material response multiplied by the scaling factor η . $\Phi(\eta)$ is a damage function and $U_{vol}(J^{el})$ is the volumetric part of the strain energy.

When $\eta = 1$ (inactive damage) it is required that $\Phi(\eta) = 0$ in such a way that the energy function is the same as the primary response

The evolution of the damage variable is controlled by:

$$\eta = 1 - \frac{1}{r} \operatorname{erf}\left(\frac{U_{dev}^m - \tilde{U}_{dev}^m}{m + \beta U_{dev}^m}\right) \quad (4.14)$$

Where U_{dev}^m is the deviatoric strain energy when maximum stretches are reached, and r, m, β are material functions. From mathematics, the error function $\operatorname{erf}(x)$ is given by:

$$\operatorname{erf}(x) = \frac{2}{\sqrt{\pi}} \int_0^x e^{-w^2} dw \quad (4.15)$$

Finally, the damage dissipation can be obtained from the following expression:

$$\Phi(\eta) = \frac{m + \beta U_{dev}^m}{r\sqrt{\pi}} e^{-\left(\frac{U_{dev}^m - \tilde{U}_{dev}^m}{m + \beta U_{dev}^m}\right)^2} + (1 - \eta)U_{dev}^m \quad (4.16)$$

The value of m can be considered as a scale of the strain energy level for the total deformation at which dissipation takes place. In the extreme case of $m=0$ dissipation occurs at low strain levels.

4.3.2 PET foam constitutive material model

Previous analytical studies in [2] suggest that hydrostatic strength in isotropic cellular materials are about three times the uniaxial strength. This is since the hydrostatic strength is governed by cell wall stretching whereas the uniaxial strength is governed by cell wall bending. Although this approximation considers the morphology of the materials it neglects morphological defects such as cell wall waviness that could significantly reduce the hydrostatic strength. Deshpande and Fleck [42] developed a constitutive model to describe the yield behaviour of metallic foams based on their observations in aluminium foams. Particularly they studied the initial yield surface and its evolution under hydrostatic and uniaxial compressive loading. These results suggest that the hardening rate under hydrostatic compression is greater than under uniaxial compression. Additionally, they found that the yield surface is fitted by a quadratic function in the mean stress and effective stress plane.

Based on their observations the authors developed a self-similar yield surface model defined by the yield function:

$$\Phi = \hat{\sigma} - Y \leq 0 \quad (4.17)$$

Where $\hat{\sigma}$ is the equivalent stress by the function:

$$\hat{\sigma}^2 = \frac{1}{1 + \left(\frac{\alpha}{3}\right)^2} (\sigma_e^2 + \alpha^2 \sigma_m^2) \quad (4.18)$$

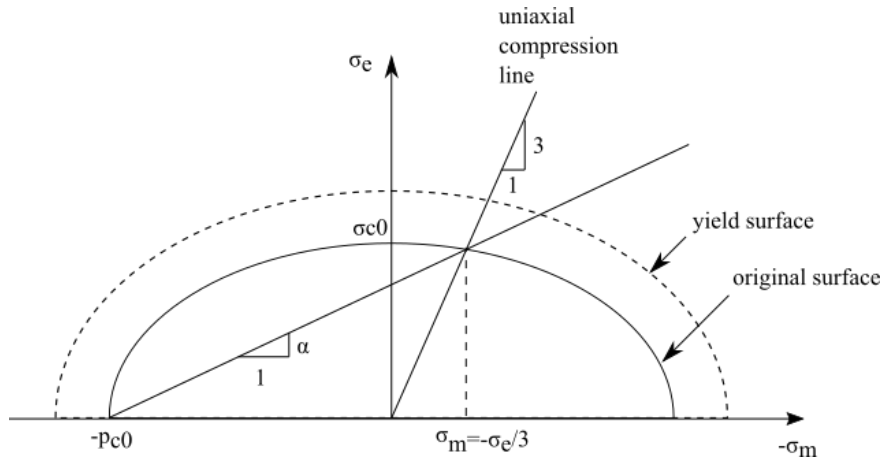


Figure 4.39. Yield surface Deshpande and Fleck model

Being σ_e the Von Mises stress, σ_m the mean stress and Y the yield strength in uniaxial compression. The parameter α defines the aspect ratio of the ellipse and can be obtained using the initial yield stress in uniaxial compression, and the initial yield stress in hydrostatic compression.

$$\alpha = \frac{3k}{\sqrt{9 - k^2}} \quad (4.19)$$

$$k = \frac{\sigma_{c0}}{p_{c0}} \quad (4.20)$$

Alternatively, the dependence of α upon the plastic Poisson ratio is given by:

$$\nu_p = -\frac{\dot{\epsilon}_{p11}}{\dot{\epsilon}_{p33}} = \frac{\frac{1}{2} - \left(\frac{\alpha}{3}\right)^2}{1 + \left(\frac{\alpha}{3}\right)^2} \quad (4.21)$$

Therefore the value of α can be obtained by measuring the plastic Poisson ratio ν_p in uniaxial compression at 20-30% strain.

The plastic flow is then given by:

$$\dot{\epsilon}_p = \frac{1}{H} \frac{d\Phi}{d\sigma} \left(\frac{d\Phi}{d\check{\sigma}} \right) \check{\sigma} \quad (4.22)$$

Where H is the hardening modulus, which is assumed independent in stress rate and $\check{\sigma}$ is the Jaumann stress rate, used to ensure objectivity to rigid body rotations.

Introducing an equivalent strain $\hat{\epsilon}$ which is a work rate conjugate to $\hat{\sigma}$.

$$\hat{\sigma} \dot{\hat{\epsilon}} = \sigma \dot{\epsilon}_p \quad (4.23)$$

Doing some algebraic manipulation the flow rule can be rewritten as:

$$\dot{\epsilon}_p = \dot{\hat{\epsilon}} \frac{d\Phi}{d\sigma} \quad (4.24)$$

Where the effective strain rate can be decomposed in terms of the Von Mises plastic strain rate $\dot{\varepsilon}_e$ and volumetric plastic strain rate $\dot{\varepsilon}_m$:

$$\dot{\varepsilon}^2 = \left[1 + \left(\frac{\alpha}{3}\right)^2\right] (\dot{\varepsilon}_e^2 + \frac{1}{\alpha^2} \dot{\varepsilon}_m^2) \quad (4.25)$$

Additionally, the experimental results revealed that the hardening modulus H varies linearly in the following manner:

$$H = \frac{\sigma_e}{\hat{\sigma}} h_\sigma + \left(1 - \frac{\sigma_e}{\hat{\sigma}}\right) h_p \quad (4.26)$$

Where h_σ and h_p are the tangent moduli under uniaxial and hydrostatic compression:

$$h_\sigma(\hat{\varepsilon}) = \frac{\dot{\sigma}_{33}}{\dot{\varepsilon}_{33}^p} \quad (4.27)$$

$$h_p(\hat{\varepsilon}) = \frac{-\alpha^2}{1 + \left(\frac{\alpha}{3}\right)^2} \frac{\dot{p}}{\dot{\varepsilon}_m} \quad (4.28)$$

4.3.3 Validation of the FEA model for dynamic compression

An explicit/dynamic FEA model in Abaqus V6.14 is proposed to capture the dynamic compressive response of agglomerated cork and PET foam based on the experimental testing explained in the previous section. In both cases, a tetrahedral testing specimen ($40 \times 40 \times 35 \text{ mm}^3$) is impacted by circular a rigid wall with a radius of 33 mm and weight of 9.13 kg of mass (16.13 kg is also studied for PET foam). An initial velocity is assigned to the impactor to analyze different impact energies (20 J, 40 J, 50 J, 60 J for agglomerated cork and 40 J, 87 J, 156 J for PET foam). Due to the high levels of deformation gravity acceleration is included in the model to account for the work done by gravity over the impactor during the deformation of the specimen. An explicit general contact with surface pairs is used for both top and bottom surfaces of the specimen with a friction coefficient of 0.1. The rigid circular bottom wall has a radius of 38 mm and it is fixed while the impactor is restrained in all DOF except in the vertical direction (Figure 4.40).

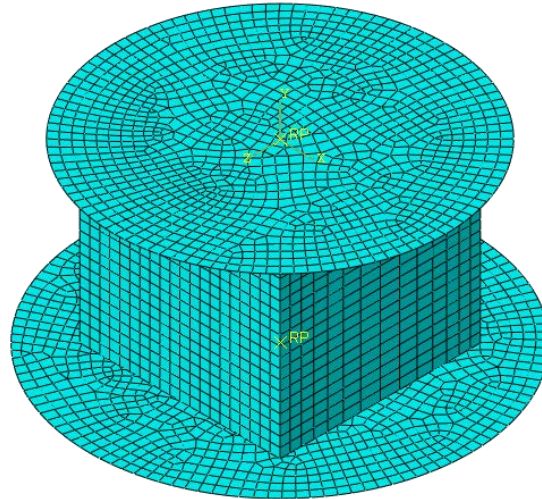


Figure 4.40 FEA Mesh (Dynamic compression)

A mesh sensitivity analysis is carried out using the residual kinetic energy as a control variable (Figure 4.41). It is found that a mesh of 7200 C3D8R elements with 2 mm overall length provides a good compromise for accuracy and computation time.

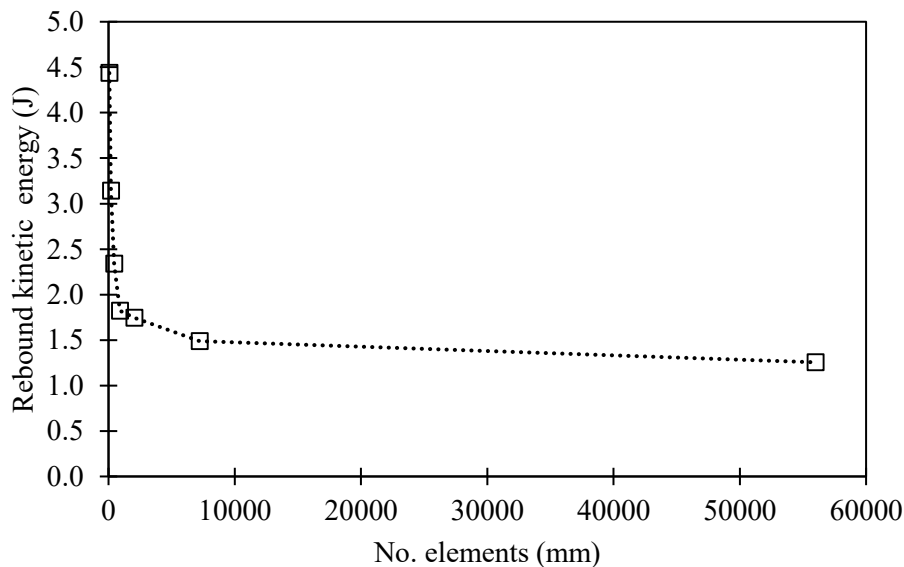


Figure 4.41. Mesh sensitivity analysis

4.3.4 Agglomerated cork

Agglomerated cork NL-10 and NL-20 [43] are modelled with a hyperelastic elastomeric foam model (Hyperfoam) using uniaxial stress-strain data taken from dynamic compression testing. Lateral strains are also included in order to account for the variable Poisson ratio. Figure 4.42 shows the values used for both agglomerated corks. A 3rd order polynomial is used to represent the strain energy potential.

BUILDING A RELIABLE MODEL FOR THE CORE

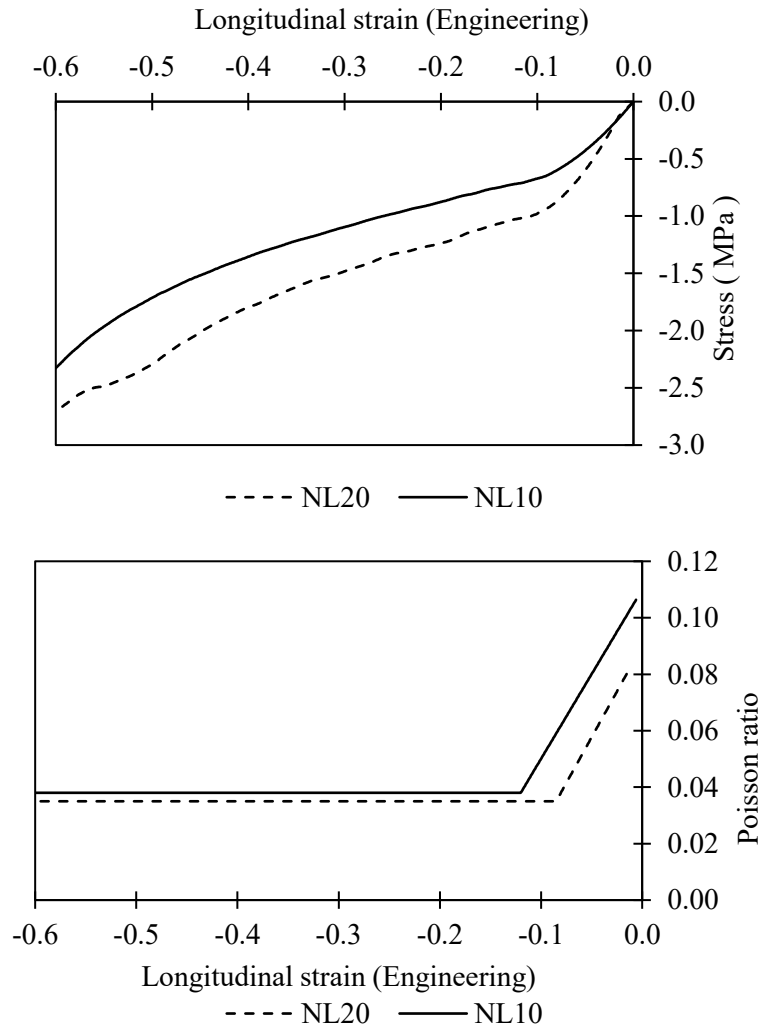


Figure 4.42. a) Stress vs. strain curve, b) Poisson ratio vs. strain curve

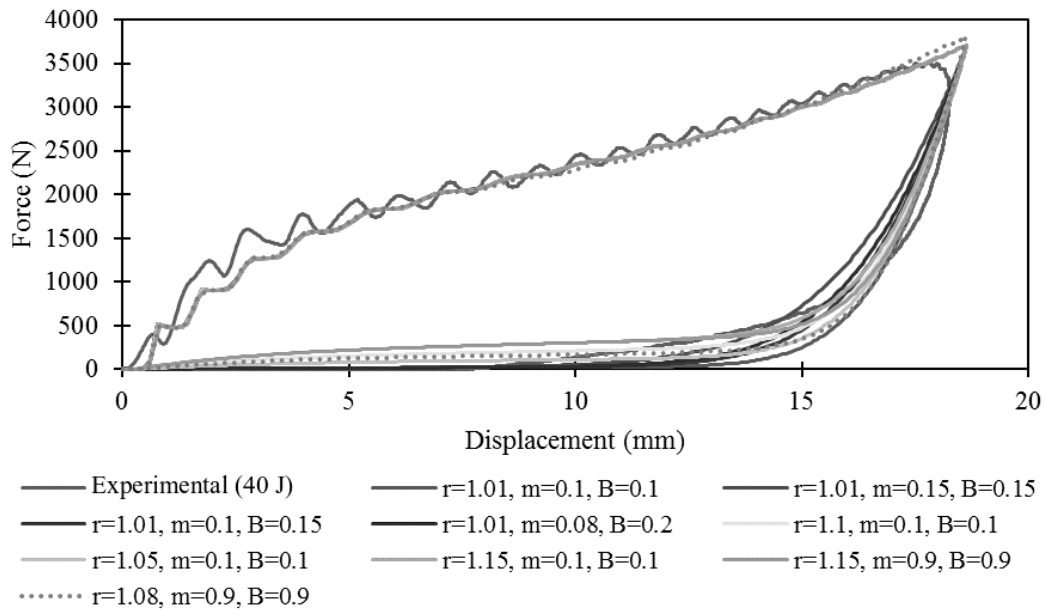


Figure 4.43. Force vs. Displacement curve for sensitivity analysis of damage parameters (r , m , β). Agglomerated cork NL-20 (40 J)

Mullins effect is used to model the stress softening and damage of the material. A sensitivity analysis of the damage variables r , m , β is carried out to find the values that best fit the energy dissipation levels reached during experimental testing. Figure 4.43 shows the force vs. displacement curve for the 40J impact with different combinations of the damage coefficients.

Table 4.4 shows the ratio of dissipated energy to initial kinetic energy for different combinations of r , m and β . It is found that $r=1.08$, $m=0.09$, $\beta=0.09$ is the combination that best fit the energy dissipation results obtained through experimental testing. This combination agrees very well with the values used in [37] for a similar agglomerated cork.

Parameters	E_{dis}/E_i (%)
Experimental (40 J)	85%
$r=1.01$, $m=0.1$, $B=0.1$	89%
$r=1.01$, $m=0.1$, $B=0.15$	86%
$r=1.01$, $m=0.15$, $B=0.15$	82%
$r=1.01$, $m=0.08$, $B=0.2$	85%
$r=1.1$, $m=0.1$, $B=0.1$	82%
$r=1.05$, $m=0.1$, $B=0.1$	86%
$r=1.15$, $m=0.1$, $B=0.1$	78%
$r=1.15$, $m=0.9$, $B=0.9$	80%
$r=1.08$, $m=0.09$, $B=0.09$	85%

Table 4.4. Energy dissipation ratio for different damage variables

Figure 4.44 shows a comparison of the force vs. displacement curves for dynamic compression of NL-20 at diverse impact energy levels. The dotted lines show the experimental results discussed in the previous section while the solid lines show the results obtained by the FEA model. A sequence of photograms at different instants of time are also included to provide a qualitative visualization of the accuracy of the model. It can be noticed that the FEA model captures with high accuracy the nonlinearity of the force-displacement curve in the loading part of the curve and can reproduce the elastic return of the material during a good part of the discharge curve. Besides this, the peak force estimated by the FEA model is slightly higher than in the experiments.

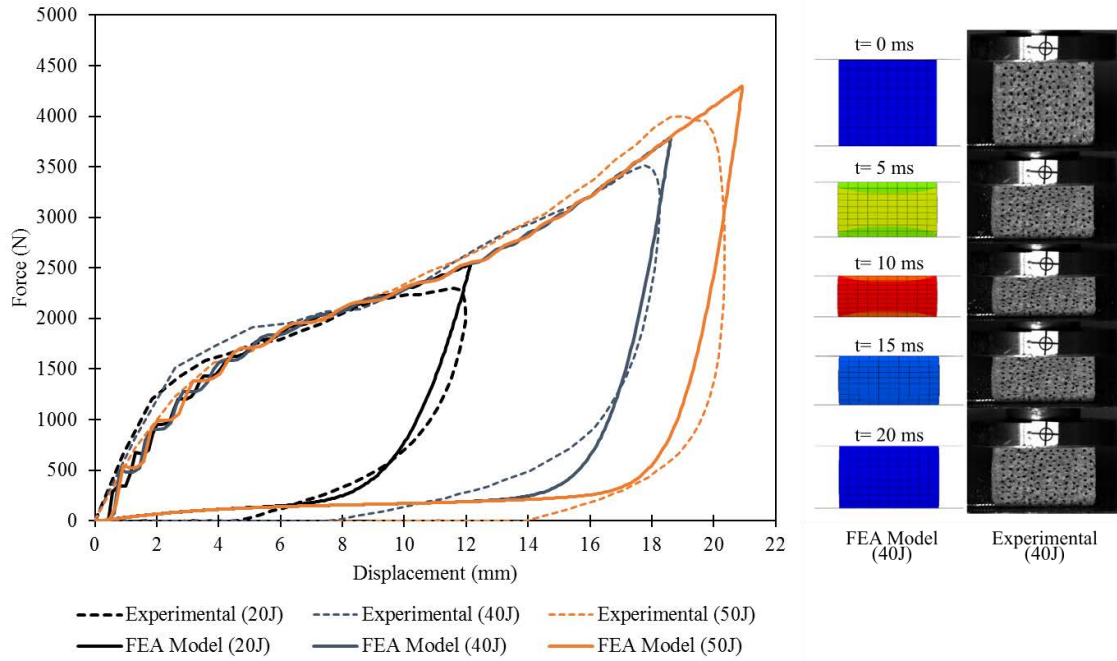
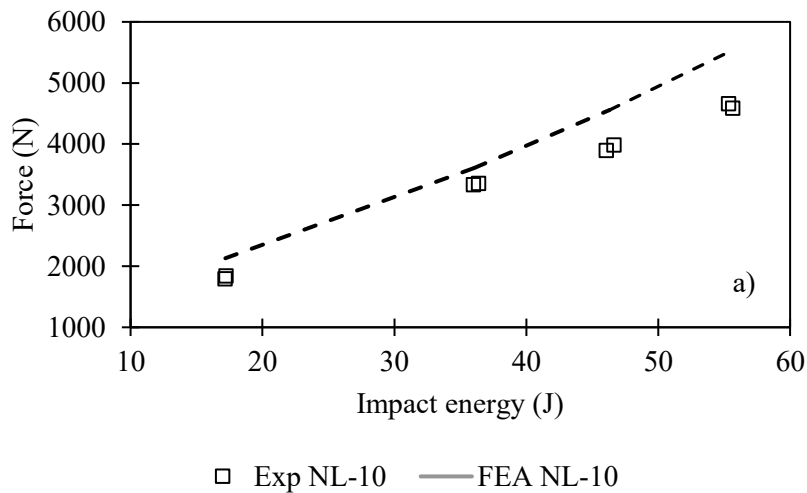


Figure 4.44. Force vs. Displacement curve at three different impact energies (NL-20). Comparison between experimental and FEA results

Figure 4.45.a) and Figure 4.46.a) shows the peak force at different impact energies for both agglomerated corks while Figure 4.45.b) and Figure 4.46.b) shows the ratio between the dissipated energy and the initial kinetic energy of the impactor (measured by the tracker) at different impact energies. In all cases, a good agreement is obtained between the results obtained through the FEA model and the experimental testing. For the peak force, the maximum relative error is 11% whilst for the energy absorption is 1.3%.



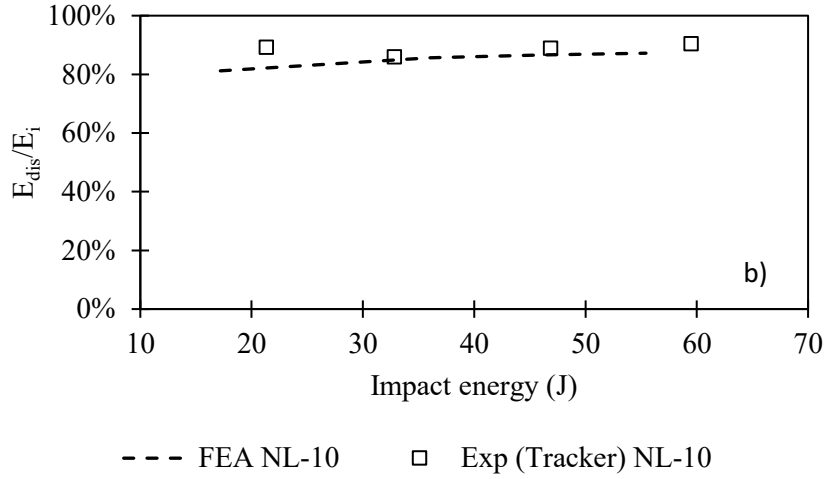


Figure 4.45. Comparison between experimental and FEA results.
 a) Peak Force NL-10, b) Energy dissipation ratio NL-10

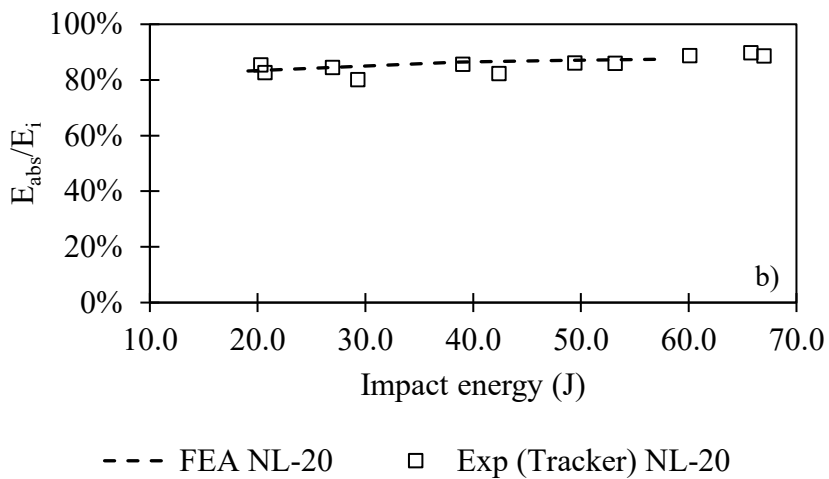
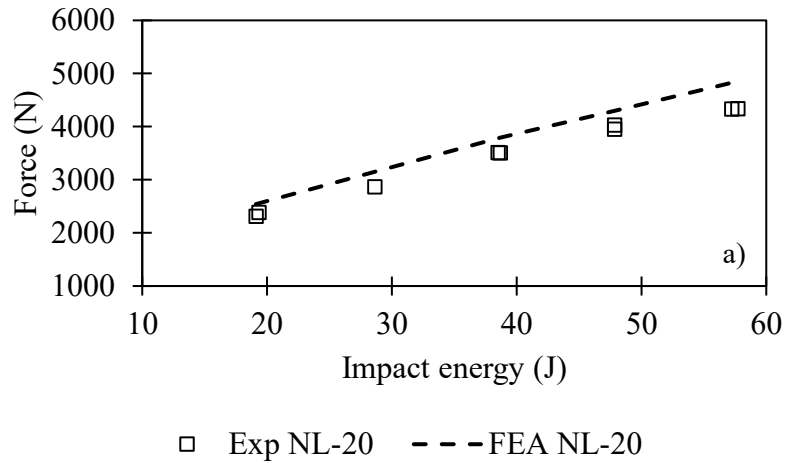


Figure 4.46. Comparison between experimental and FEA results.
 a) Peak Force NL20, b) Energy dissipation NL20

4.3.5 PET foam

The material is modelled using the isotropic hardening model for foams developed by Deshpande and Fleck commonly known in Abaqus as crushable foam. The mechanical properties of the material are obtained from the experimental compression testing discussed in the previous section. The properties used in this model are summarized in Table 4.5

Property	Value
ρ (kg/m ³)	211
E (MPa)	133
ν	0.4
ν_p	0.35
k	0.95

Table 4.5. PET foam mechanical properties

The hardening law defines the value of the yield stress in uniaxial compression as a function of the absolute value of the axial plastic strain. The hardening law is entered in the following tabular form (Table 4.6):

σ_y (MPa)	ϵ_p
3.79	0.00
4.05	0.00
4.28	0.00
4.51	0.00
4.74	0.01
4.57	0.03
4.34	0.04
4.12	0.06
3.89	0.07
3.67	0.09
3.67	0.12
3.56	0.16
3.37	0.18
3.15	0.21
3.09	0.25
2.89	0.28
2.70	0.31

2.63	0.35
2.45	0.39
2.34	0.43
2.22	0.48
2.05	0.52
1.90	0.56
1.77	0.60
1.64	0.64
1.55	0.69
1.45	0.74
1.35	0.79
1.34	0.84
1.42	0.89
1.54	0.93
1.66	0.97
1.77	1.02
1.87	1.06

Table 4.6. Hardening function PET foam

Since the mechanical behaviour of PET foam is sensitive to the strain rate a piecewise linear law is entered as a table relating the yield stress ratio R to the strain rate. Values for R are computed from dynamic compression testing using the collapse stress as the control variable.

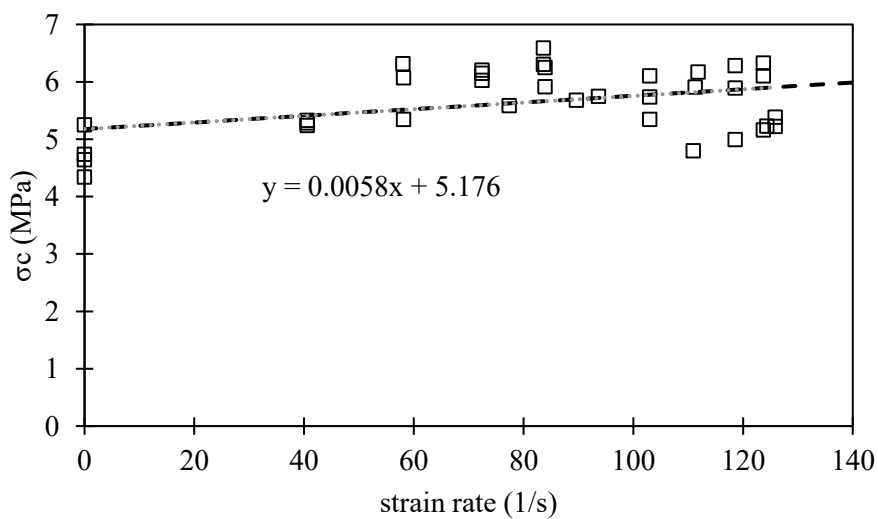


Figure 4.47. Collapse stress vs. strain ratio. Experimental testing PET foam

BUILDING A RELIABLE MODEL FOR THE CORE

R	Strain rate (1/s)
1.000	0
1.000	0.1
1.000	0.2
1.000	0.3
1.000	0.4
1.001	0.5
1.001	0.6
1.001	0.7
1.001	0.8
1.001	0.9
1.001	1
1.002	2
1.003	3
1.004	4
1.006	5
1.007	6
1.008	7
1.009	8
1.010	9
1.011	10
1.022	20
1.034	30
1.045	40
1.056	50
1.067	60
1.078	70
1.090	80
1.101	90
1.112	100
1.123	110
1.134	120
1.146	130
1.157	140
1.168	150
1.224	200
1.224	500
1.224	1000
1.224	10000

Table 4.7. Yield stress ratio R as a function of strain rate

Figure 4.48, Figure 4.49, and Figure 4.50 show a comparison in the evolution of the force and velocity of the impactor between the results obtained by the FEA model and the experimental data. Figure 4.48 shows the evolution of the impactor velocity as a function of displacement while Figure 4.49 and Figure 4.50 show the evolution of the contact force as a function of displacement and time respectively. As it can be observed from all cases the FEA model can capture with high accuracy the response of the under dynamic compression. In particular variables such as the collapse force, the maximum displacement and the impact duration shows a high correlation with experimental results.

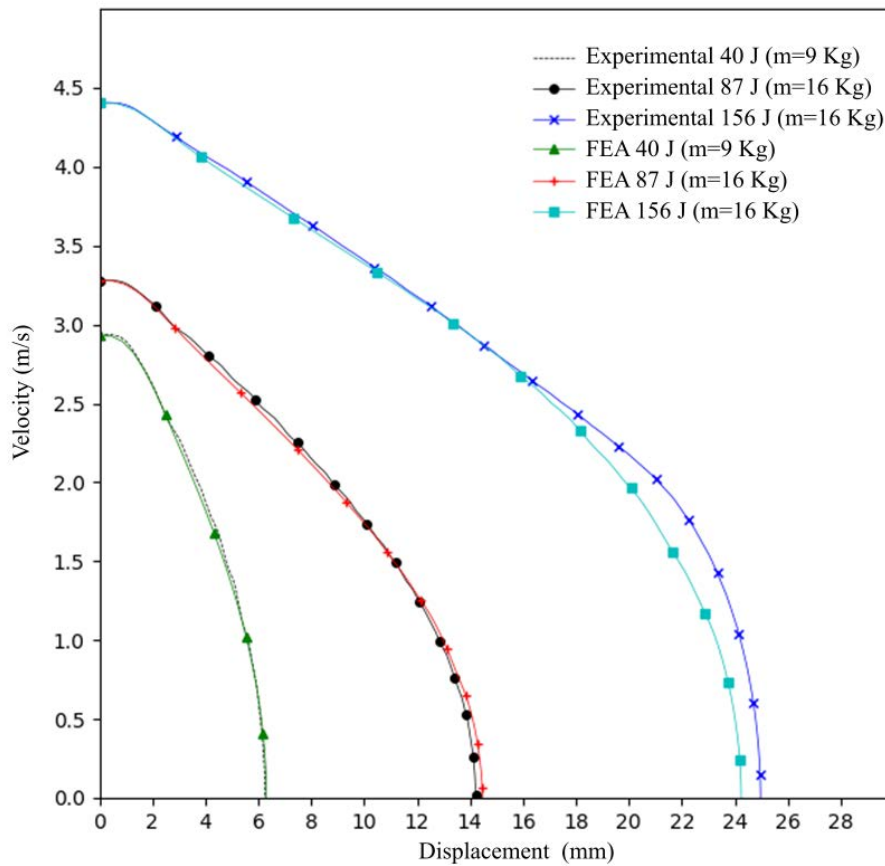


Figure 4.48. Impactor velocity vs. displacement during dynamic compression. Comparison of FEA model and experimental testing (PET foam).

BUILDING A RELIABLE MODEL FOR THE CORE

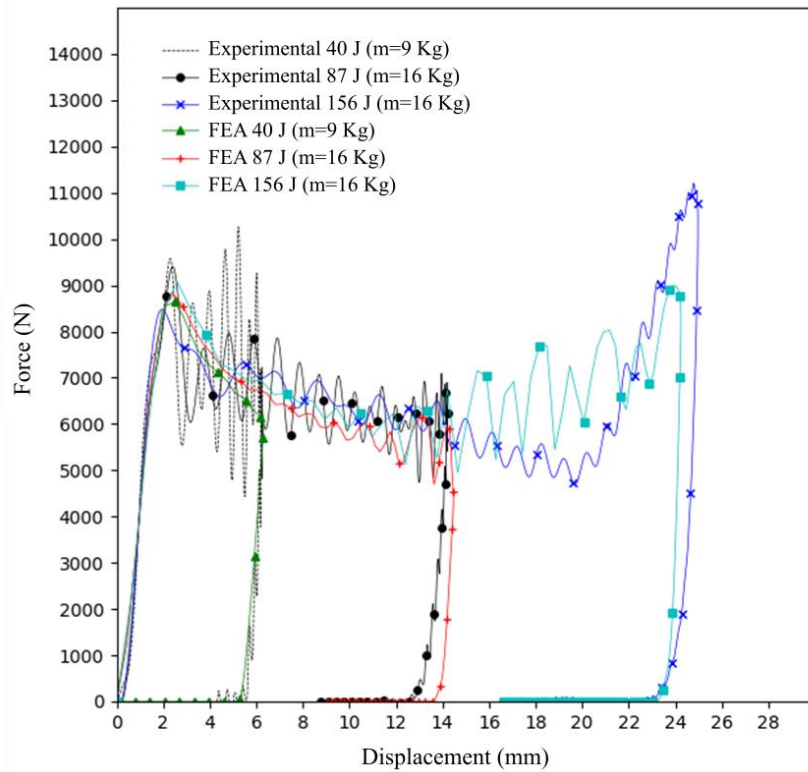


Figure 4.49. Impactor force vs. displacement curve for dynamic compression. Comparison of FEA model and experimental testing (PET foam).

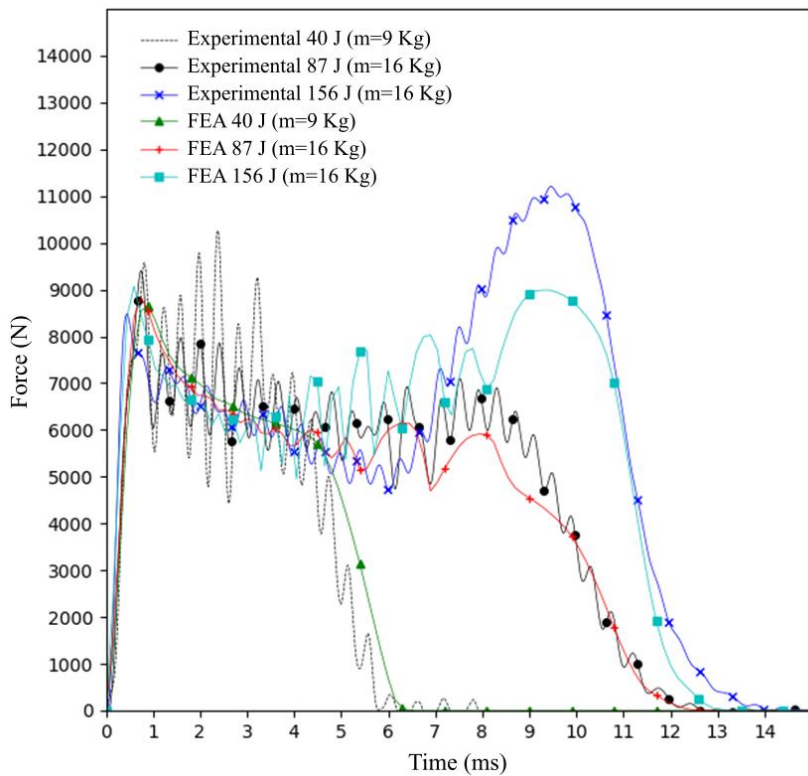


Figure 4.50. Force vs. Time curve for dynamic compression in PET foam. Comparison of FEA model and experimental testing.

From the previous discussion, it is clear that the model can predict with high accuracy the overall elastoplastic response of the material in dynamic compression as well as the strain sensitivity of the initial collapse force at moderate strain rates. However, this material model is unable to describe the localization phenomena particularly the dynamic crushing present at high impact velocities. For example, Figure 4.51 shows a frame sequence taken by a high-speed camera and those obtained by the FEA results. The overall displacement of the impactor is captured with precision at all time frames. However, the model is not able to capture the formation of a crushed layer next to the impactor surface.

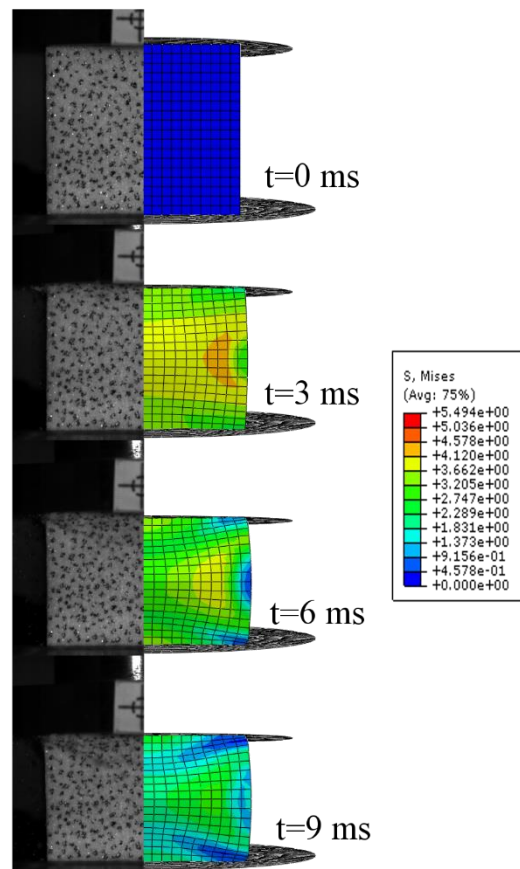


Figure 4.51. Frame sequence of the dynamic compression for 60 J impact with Von-Mises stress distribution (PET foam).

Figure 4.52 shows the maximum displacement at different impact energies while Figure 4.53 shows the ratio between the dissipated energy and the initial kinetic energy of the impactor at different impact energies. In both figures, there is a high agreement between the results obtained through the FEA model and the experimental testing.

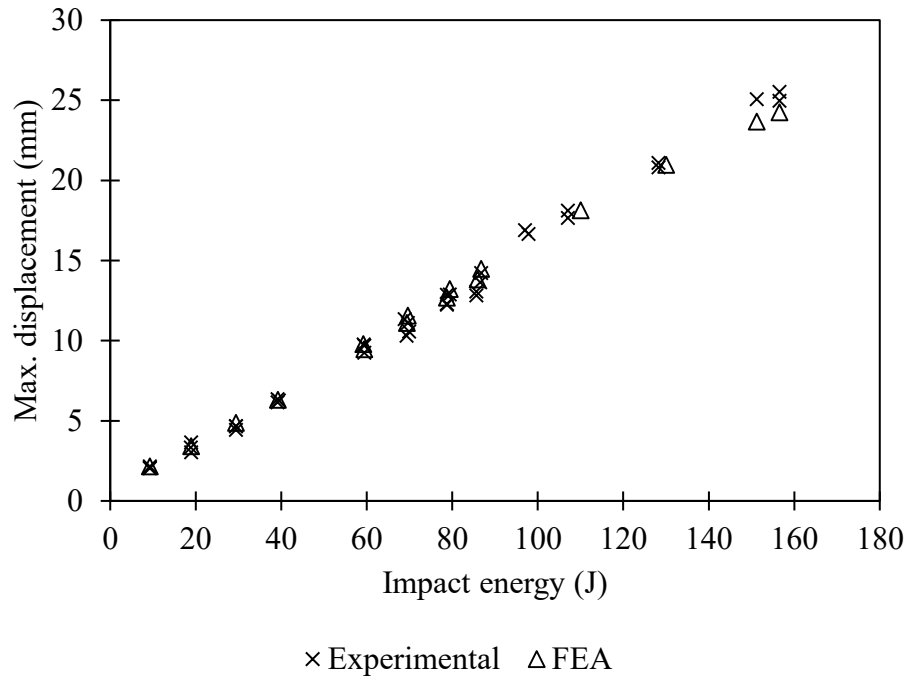


Figure 4.52. Max displacement vs. impact energy for dynamic compression. Comparison of FEA model and experimental testing (PET foam).

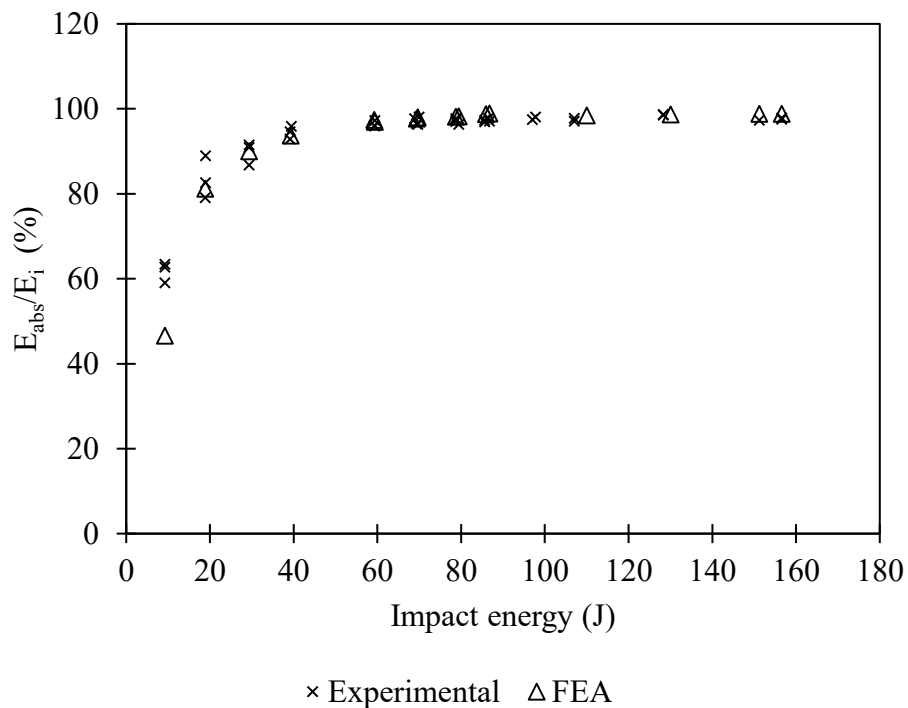


Figure 4.53. Energy dissipation ratio vs. impact energy for dynamic compression. Comparison of FEA model and experimental testing (PET foam).

References of the chapter

- [1] EASA. Notification of a Proposal to issue a Certification Memorandum: Modelling and Simulation – CS-25 2020:1–55.
- [2] Gibson LJ, Ashby MF. Cellular solids. 2nd ed. Cambridge University press; 1997.
- [3] Ouellet S, Cronin D, Worswick M. Compressive response of polymeric foams under quasi-static, medium and high strain rate conditions. *Polym Test* 2006;25:731–43. <https://doi.org/10.1016/j.polymertesting.2006.05.005>.
- [4] Sun Y, Li QM. Dynamic compressive behaviour of cellular materials: A review of phenomenon, mechanism and modelling. *Int J Impact Eng* 2018;112:74–115. <https://doi.org/10.1016/j.ijimpeng.2017.10.006>.
- [5] Tan PJ, Reid SR, Harrigan JJ, Zou Z, Li S. Dynamic compressive strength properties of aluminium foams. Part i - Experimental data and observations. *J Mech Phys Solids* 2005;53:2174–205. <https://doi.org/10.1016/j.jmps.2005.05.007>.
- [6] Silva M Da, Oleskovicz M, Coury D V. Cork: properties, capabilities and applications. *Int Mater Rev* 2005;50:345–58. <https://doi.org/10.1179/174328005X41168>.
- [7] Jardim RT, Fernandes FAO, Pereira AB, Alves de Sousa RJ. Static and dynamic mechanical response of different cork agglomerates. *Mater Des* 2015;68:121–6. <https://doi.org/10.1016/j.matdes.2014.12.016>.
- [8] Ptak M, Kaczynski P, Fernandes FAO, de Sousa RJA. Assessing impact velocity and temperature effects on crashworthiness properties of cork material. *Int J Impact Eng* 2017;106:238–48. <https://doi.org/10.1016/j.ijimpeng.2017.04.014>.
- [9] Fernandes FAO, Jardim RT, Pereira AB, Alves De Sousa RJ. Comparing the mechanical performance of synthetic and natural cellular materials. *Mater Des* 2015;82:335–41. <https://doi.org/10.1016/j.matdes.2015.06.004>.
- [10] Le Barbenchon L, Girardot J, Kopp J-B, Viot P. Multi-scale foam : 3D structure/compressive behaviour relationship of agglomerated cork. *Materialia* 2019;5:100219. <https://doi.org/10.1016/j.mtla.2019.100219>.
- [11] Sasso M, Mancini E, Chiappini G, Sarasini F, Tirillò J. Application of DIC to Static and Dynamic Testing of Agglomerated Cork Material. *Exp Mech* 2018;58:1017–33.

- <https://doi.org/10.1007/s11340-017-0369-9>.
- [12] Castro O, Silva JM, Devezas T, Silva A, Gil L. Cork agglomerates as an ideal core material in lightweight structures. *Mater Des* 2009;31:425–32. <https://doi.org/10.1016/j.matdes.2009.05.039>.
- [13] Silva JM, Gamboa P V, Nunes C, Paulo L, Franco N. Cork: Is It a Good Material for Aerospace Structures? n.d. <https://doi.org/10.2514/6.2011-2159>.
- [14] Le Barbenchon L, Kopp J-B, Girardot J, Viot P. Multi-scale foam: 3D Structure/Compressive Behaviour Relationship Of Agglomerated Cork. *Materialia* 2019;5:100219. <https://doi.org/10.1016/j.mtla.2019.100219>.
- [15] Viot P, Beani F, Lataillade JL. Polymeric foam behavior under dynamic compressive loading. *J Mater Sci* 2005;40:5829–37. <https://doi.org/10.1007/s10853-005-4998-5>.
- [16] Li QM, Magkiriadis I, Harrigan JJ. Compressive strain at the onset of densification of cellular solids. *J Cell Plast* 2006;42:371–92. <https://doi.org/10.1177/0021955X06063519>.
- [17] Sanchez-Saez S, Barbero E, Garcia-Castillo SK, Ivañez I, Cirne J. Experimental response of agglomerated cork under multi-impact loads. *Mater Lett* 2015;160:327–30. <https://doi.org/10.1016/j.matlet.2015.08.012>.
- [18] Santos PT, Pinto S, Marques PAAP, Pereira AB, Alves de Sousa RJ. Agglomerated cork: A way to tailor its mechanical properties. *Compos Struct* 2017;178:277–87. <https://doi.org/10.1016/j.compstruct.2017.07.035>.
- [19] Pires Gameiro C, Cirne J, Gary G. Experimental study of the quasi-static and dynamic behaviour of cork under compressive loading 2007. <https://doi.org/10.1007/s10853-006-0675-6>.
- [20] Sarasini F, Tirillò J, Lampani L, Sasso M, Mancini E, Burgstaller C, et al. Static and dynamic characterization of agglomerated cork and related sandwich structures. *Compos Struct* 2019;212:439–51. <https://doi.org/10.1016/j.compstruct.2019.01.054>.
- [21] Sasso M, Sarasini F, Chiappini G, Mancini E, Tirillò J. Evaluation of Stress Equilibrium in Dynamic Tests on Agglomerated Cork n.d. https://doi.org/10.1007/978-3-319-62956-8_36.

- [22] Fortes MA, Teresa Nogueira M. The poison effect in cork. *Mater Sci Eng A* 1989;122:227–32. [https://doi.org/10.1016/0921-5093\(89\)90634-5](https://doi.org/10.1016/0921-5093(89)90634-5).
- [23] Ashby MF. Materials and the environment. *Mater Environ* 2012:i–iii. <https://doi.org/10.1016/b978-0-12-385971-6.00016-6>.
- [24] Li-Na J. Study on preparation process and properties of polyethylene terephthalate (pet). *Appl Mech Mater* 2013;312:406–10. <https://doi.org/10.4028/www.scientific.net/AMM.312.406>.
- [25] Airex. Airex T92 DATA SHEET 04.2018. 2018.
- [26] Core for composites: Winds of change: *CompositesWorld* n.d. <https://www.compositesworld.com/articles/core-for-composites-winds-of-change> (accessed February 24, 2019).
- [27] Fathi A. Mechanical Properties of Strand PET Foams at Different Length Scales. ProQuest LLC, 2018.
- [28] Santo L, Bellisario D, Quadrini F. Shape memory behavior of PET foams. *Polymers (Basel)* 2018;10:1–16. <https://doi.org/10.3390/polym10020115>.
- [29] Rajput MS, Burman M, Köll J, Hallström S. Compression of structural foam materials – Experimental and numerical assessment of test procedure and specimen size effects. *J Sandw Struct Mater* 2019;21:260–88. <https://doi.org/10.1177/1099636217690500>.
- [30] Pyrzowski Ł, Sobczyk B. Local and global response of sandwich beams made of GFRP facings and PET foam core in three point bending test. *Compos Struct* 2020;241:112122. <https://doi.org/10.1016/j.compstruct.2020.112122>.
- [31] ASTM International. ASTM D 1621 Standard test method for compressive properties of rigid cellular plastics. n.d.
- [32] Sánchez-Sáez S, Barbero E, Navarro C. Analysis of the dynamic flexural behaviour of composite beams at low temperature. *Compos Sci Technol* 2007;67:2616–32. <https://doi.org/10.1016/j.compscitech.2006.12.002>.
- [33] Belingardi G, Vadori R. Low velocity impact tests of laminate glass-fiber-epoxy matrix composite material plates. *Int J Impact Eng* 2002;27:213–29. [https://doi.org/10.1016/S0734-743X\(01\)00040-9](https://doi.org/10.1016/S0734-743X(01)00040-9).

- [34] Belingardi G, Montanini R, Avalle M. Characterization of polymeric structural foams under compressive impact loading by means of energy-absorption diagram. *Int J Impact Eng* 2001;25:455–72.
- [35] Anjos O, Rodrigues C, Morais J, Pereira H. Effect of density on the compression behaviour of cork 2014. <https://doi.org/10.1016/j.matdes.2013.07.038>.
- [36] Gameiro CP. Numerical and experimental study of the dynamic behaviour of cork. *Des Use Light Weight Mater* 2005:65–84.
- [37] Fernandes FAO, Pascoal RJS, Alves De Sousa RJ. Modelling impact response of agglomerated cork. *Mater Des* 2014;58. <https://doi.org/10.1016/j.matdes.2014.02.011>.
- [38] Dassault Systèmes Simulia Corp. Abaqus 6.14 Theory Guide 2014. <http://ivt-abaqusdoc.ivt.ntnu.no:2080/v6.14/books/stm/default.htm> (accessed June 25, 2020).
- [39] Abaqus/Explicit Advanced techniques. Abaqus Analysis user’s manual 2013:Providence, Rhode Island, US. <https://www.sharcnet.ca/Software/Abaqus610/Documentation/docs/v6.10/books/usb/default.htm?startat=book01.html> (accessed August 24, 2018).
- [40] Abaqus DS. 4.7.1 Mullins effect n.d. <http://ivt-abaqusdoc.ivt.ntnu.no:2080/v2016/books/stm/default.htm?startat=ch04s07ath126.html> (accessed February 28, 2019).
- [41] Dassault Systèmes Simulia Corp. Abaqus Theory guide. Providence, RI, USA: 2014.
- [42] Deshpande VS, Fleck NA. Isotropic constitutive models for metallic foams. *J Mech Phys Solids* 2000;48:1253–83. [https://doi.org/10.1016/S0022-5096\(99\)00082-4](https://doi.org/10.1016/S0022-5096(99)00082-4).
- [43] Composites A cork. NL10/Nl20/NL25 Technical data. 2013.

5 INTERMEDIATE VELOCITY IMPACT TEST ON SANDWICH PANELS

This section presents the experimental results obtained from the intermediate velocity impact tests carried out over CFRP sandwich panels with agglomerated cork and PET foam cores. The response of the sandwich panel is assessed using non-contacting techniques such as high-speed video recording, 3D-DIC analysis, and image tracking. Additionally different damage and failure mechanisms are analysed by studying the post-impact damage of the specimens using visual inspection and X-ray computed tomography. As a result, diverse qualitative and quantitative information is acquired and diverse hypotheses about the physics involved in the impact event are suggested. Some of the results presented in this chapter are also used in chapter 6 for the validation of the proposed numerical model. Due to the complexity of this kind of experimental effort, a rigorous state of the art review is carried out in order to guide some of the experimental design decisions taken in this work. Some relevant previous studies in the field are briefly discussed in this section.

5.1 Introduction

Multiple experimental studies have been carried out in the area of composite sandwich panels subjected to impact loads. The literature review made for the present work shows that most of this research is focused on the study of sandwich panels made of metallic or composite face-sheets and metallic honeycomb cores. Besides their extended application in the aerospace industry, those results are hard to correlate with the type of sandwich panels treated in this study, and therefore they are excluded from the discussion.

Research about sandwich panels with different composite material face-sheets (e.g. CFRP, GFRP, and flax) and synthetic polymeric cores is more limited but recently is gaining interest in the research community. Despite the majority of studies deal with low-velocity impacts and blast impacts some of their results provide relevant discussions to the analysis of woven CFRP sandwich panels with agglomerated cork and PET foam.

Back in 1994 Caprino et al. [1] studied the influence of the core density and thickness in sandwich panels subjected to low-velocity impact. Sandwich panels of GFRP and PVC foam core were impacted using an instrumented drop weight tower and the specimens were visually inspected to assess the damage extension. Residual tensile strength after impact

(RTSAI) was also measured and related to the impact kinetic energy. Some interesting conclusions were obtained in this work:

- It was observed that the force history curve is not influenced by the constrain conditions but it depends only on the local rigidity of the panel. For more dense cores the contact force is higher due to the local higher rigidity
- The damage extension increases with impact energy however once perforation occurs damage extension remains unchanged. Additionally, the damage extent and residual strength seem to be independent of the core density.

A similar study was carried out by Shin et al. [2] where sandwich panels with plain woven face-sheets of diverse materials (Kevlar, graphite, polyester, polyethylene) with PVC foam cores of two different densities were subjected to drop weight impact testing. Light microscopy and electron microscope were used to study the micro-failure mechanisms. Their results suggest that the face-sheet material determines how influential the core density is in the impact response of the sandwich panel. For example, for face-sheets made from tough materials such as polyester and polyethylene fibres, the impact response is almost insensitive to the density of the foam core. On the other hand, for face-sheets made from less tough materials such as Kevlar and graphite, the response tends to be dominated by the core. Some other differences in the damage mechanisms were spotted by the authors. For example, a diamond-shaped fracture pattern along the fibre directions was reported for graphite and Kevlar face-sheets while for polyester and polyethylene panels, plastic deformation and interface debonding was observed in the top faces-sheet.

Complementary work in this area was published by Fan et al. [3] who compared multiple sandwich panels under low-velocity impact using a drop weight testing machine with a hemispherical indenter. Sandwich panels were made from rigid polyurethane foam (RPUF) core and plain woven face-sheet of different materials (Kevlar, CFRP, GFRP, Kevlar/CFRP and stitched GFRP). The authors confirmed that the evolution of the force history curve, the peak load and the damage extend are highly dependent on the face-sheet material. Panels with Kevlar face-sheets exhibit the highest peak load but the least damage, followed by the CFRP and Kevlar/CFRP face-sheets. While the GFRP showed the least peak load but the worst damage extend. Additionally, the authors observed that damaged panels show a cone crack formation in the core characterized by a damage angle that decreases with the impact energy.

A comprehensive work by Kepler [4], [5], [6] studied the penetration and damage of sandwich panels of GRFP face-sheets and PVC foam core under intermediate velocity impact (70 m/s and 93 m/s) with impactors of different tip geometry. An air gun was used for firing the impactors and a ballistic pendulum principle was used to estimate the required energy for panel penetration. This study found that the contact force and the face-sheet delamination area depends on the bluntness of the impactor showing lower values for conical tips and higher values for rounded tips. Delamination was observed to increase progressively in the impact direction. Two different core fracture patterns were observed in this study. The first is core cross-cracking that is the result of the structural level deformation of the core due to transversal shear stresses. This crack surface forms cone with an angle close to 45° to the plane. The second pattern is punching which is a localized phenomenon in which a plug of core is formed under compressive loads followed by the formation of a cylindrical mode II crack surface. Additionally, this study also describes the appearance of massive core failure in the intersection with the back face-sheet during penetration.

Ren et al. [7] analysed the response of a sandwich panel made of unidirectional carbon/epoxy face-sheets with PVC foam cores subjected to underwater impulsive loading. An underwater shock simulator consisting of a tube filled with water is struck at one end to produce a pressure pulse that travels to the other end when the structure is located. The deflection history of the panel was measured using DIC and high-speed photography. It was found that the compression of the PVC foam can reduce the deformation and damage of the sandwich panel. Core's density seems to influence the deflection of the rear face-sheets. In particular, panels with low-density core experience more core compression but less deflection of rear face-sheets.

A similar study was carried out by Rolfe et al. [8] with a full-scale blast loading over multiaxial CFRP and GFRP sandwich panels with single-core and graded cores (multilayer core with foams of different density) made of SAN (Styrene Acrylonitrile) foam. The strain history measured by strain gauges in the front and rear face sheet showed that higher levels of strain were recorded in the rear face while in the front face a combination of bending and membrane loading results in an approximately zero strain. 3D DIC is used for measuring the out of plane displacement of the rear face-sheet. It was found that panels deform into a so-called "bath shape" and panels with graded cores significantly reduce panel deflection and damage. The post-blast damage was assessed using X-ray computed

tomography. CFRP panels suffered from less out-of-plane displacement than their GFRP counterparts however they experience more damage due to a lower strain failure. It was also observed that CFRP panels show almost complete debonding between the front face-sheet and the core, and a considerable core crushing in the centre point

Little research has been carried out in regards to the use of agglomerated cork as a core material for sandwich composite structures subjected to impact loadings. A very comprehensive work presented by Sarasini et al. [9] studied and compared the low-velocity impact response of bare agglomerated cork and sandwich panels with flax/epoxy face-sheets and agglomerated cork core. Three different core densities were considered in this study finding that density affects the damage, maximum peak load and energy absorption of bare specimens. However, this effect is less visible in the case of sandwich panels since a large fraction of the impact energy is absorbed by the top face-sheet. The core damage was also studied by visual inspection of cut-sectioned specimens. The authors report the appearance of cracks across the thickness for both kinds of specimens (bare specimens and sandwich panels). From the photos presented in their work, it is appreciated that vertical cracks (impact direction aligned) appear in both cases as well as diagonal cross-cracking patterns. A detailed inspection of the core using scanning electron microscopy showed no signs of cell wall breakage for those specimens impacted up to 75% of the perforation energy.

A similar study on low-velocity impact was carried out by Prabhakaran et al. [10]. In their case sandwich panels were manufactured from bidirectional woven face-sheets made of flax, GFRP or a combination of both. The core material was agglomerated cork and three different densities were considered. The authors concluded that independently of the sandwich core density, GFRP show the highest perforation impact energy. Additionally, it was found that the perforation impact energy is dependent on the agglomerated cork density. In particular cores with higher density seem to have a higher perforation impact energy. This phenomenon is justified by the authors due to the variation of the inter-granular space and shear strength across different densities. The damage in the front and rear face-sheets was also examined showing that flax sandwich panels show a clear circular crater in the front face-sheet and a petal-shaped opening in the rear face-sheet. In contrast for GFRP sandwich panels, the clean crater opening in the front face-sheet is not present, and the rear face-sheet is characterized by large concentric delamination, and the appearance of petals is less visible.

Ivañez et al. [11] carried out an experimental study on the ballistic behaviour and damage of sandwich panels previously damaged by a low-velocity impact. Sandwich panels were made of unidirectional carbon/epoxy face-sheets and agglomerated cork core. Intact and damaged specimens were subjected to ballistic impact and the residual velocity and ballistic limit were compared with those of a monolithic laminate. It concluded that the difference in the ballistic limit (per surface density) between intact and damaged sandwich panels is not significantly altered. This indicates that the addition of agglomerated cork as a core material might improve the ballistic performance of panels previously damaged

Attwood et al. [12] conducted a 2D ballistic experiment to observe the transient failure process of ultra-high molecular weight polyethylene (UHMWPE) fibres in a polymeric matrix subjected to impact. In their work, they demonstrated that failure across the laminate occurs progressively due to tensile failure attributed to indirect tension starting with those plies in direct contact with the projectile and then propagating through the thickness. Their observations also showed that plies fail very early in the deformation history when the deflection of the laminate is much smaller than its thickness.

5.2 Materials and Methods

5.2.1 Materials

Impact testing is carried out over rectangular sandwich panels of 120 mm x120 mm with an average thickness of 8.6mm. The Spanish company AEROTECNIC is selected for manufacturing all composite sandwich panels due to its prior experience manufacturing aeronautical structures. Each face-sheets is made from plain-woven carbon/epoxy AS4/8552 plies (also called AGP193-PW) manufactured by Hexcel Corporation. The monolithic laminates are manufactured separately with a $[90^{\circ}/0^{\circ}/45^{\circ}/-45^{\circ}]_s$ layup using autoclave consolidation and following the manufacturer's curing cycle [15]. Both face-sheets are glued to a 5 mm thick core material by secondary bonding applying an epoxy-based glue. Sandwich panels are manufactured from two different core materials. The first is agglomerated cork with a density of 215 Kg/m^3 (NL20 CORECORK) manufactured by AMORIM CORK COMPOSITES. The second is Polyethylene Terephthalate (PET) foam with an average density of $\rho=211 \text{ Kg/m}^3$ manufactured by the company AIREX under the commercial name of T92.200.

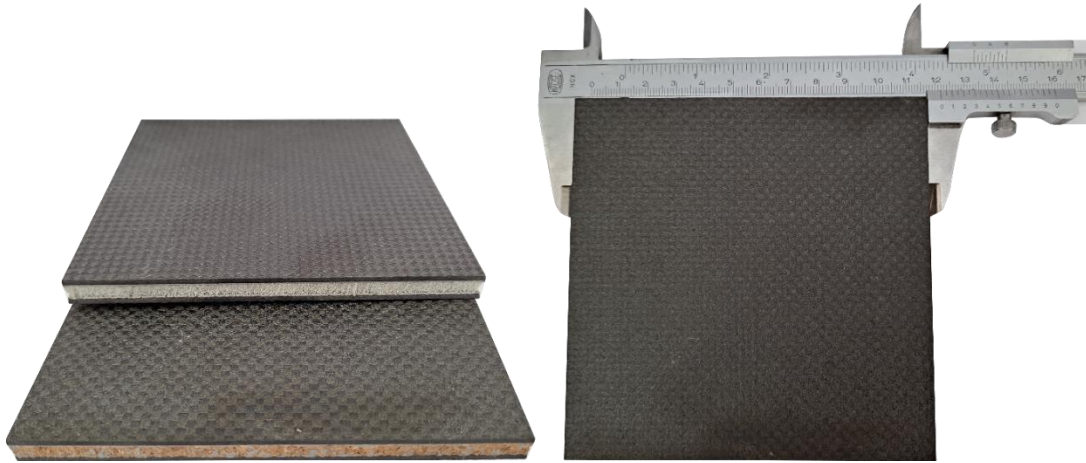


Figure 5.1. Sandwich panels. Top: PET foam core. Bottom: agglomerated cork core

5.2.2 Intermediate impact test procedure

Intermediate velocity impact (IVI) tests are carried out using a gas cannon Sabre Ballistic firing spherical steel projectiles of 7.5 mm of diameter and 7.98 gr of mass. Stargon gas (a mixture of Argon gas, CO₂ and O₂) is selected as propellant gas to achieve the desired range of impact velocities. The test specimens are retained in place using two grooves (top and bottom) that restrain the displacement of the specimen along the impact direction.

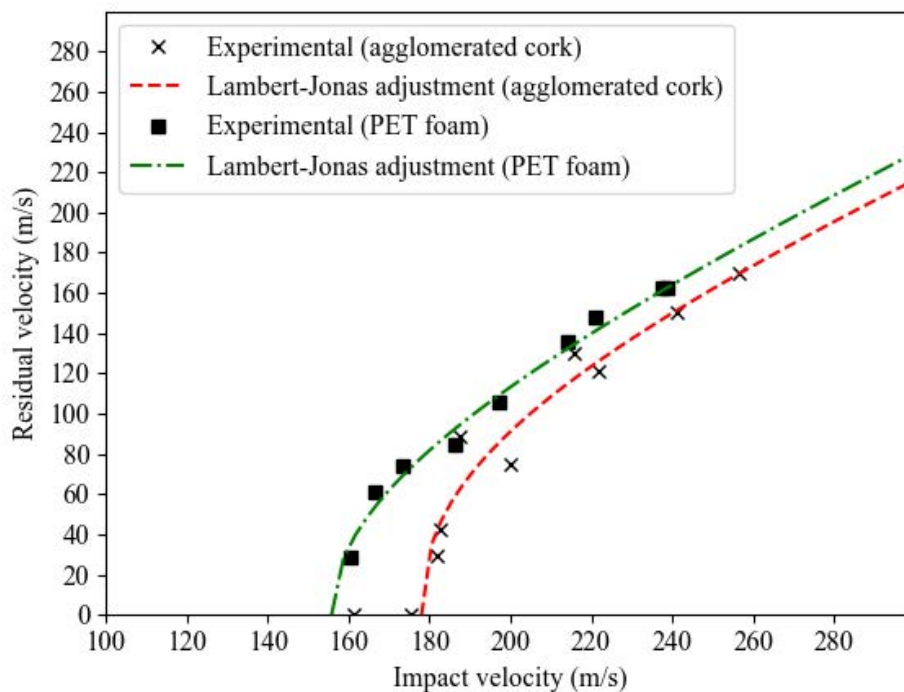


Figure 5.2. Residual velocity vs impact velocity for sandwich panels with agglomerated cork and PET foam core.

The range of velocities is carefully selected to ensure that the sandwich panels are not completely perforated. Therefore, a precise estimation of the ballistic limit for each sandwich panel is done beforehand applying the Lambert and Jonas adjustment algorithm [16]. From Figure 5.2 it is found that the ballistic limit is 156 m/s and 178 m/s for sandwich panels with PET foam core and agglomerated cork respectively. As result, the range of impact velocities studied in the present work is between 62 m/s to 170 m/s.

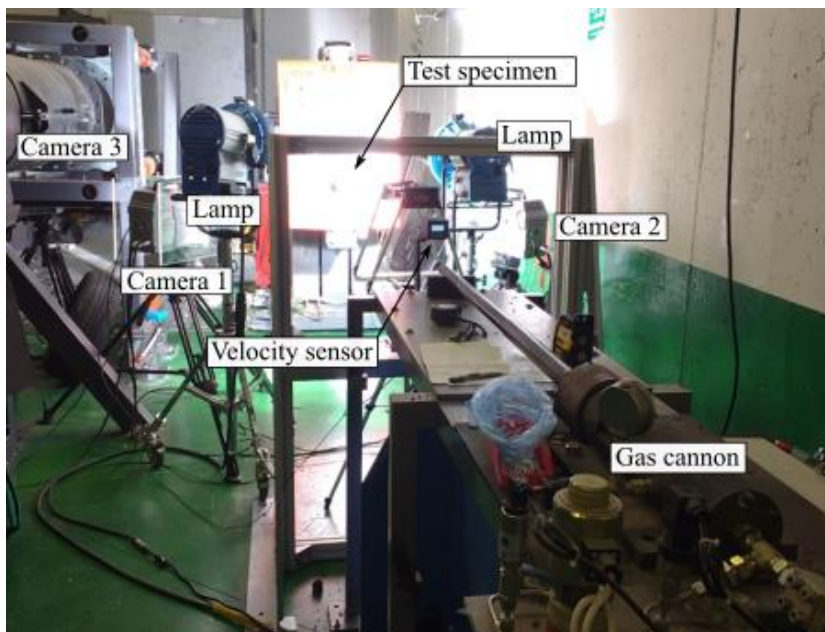
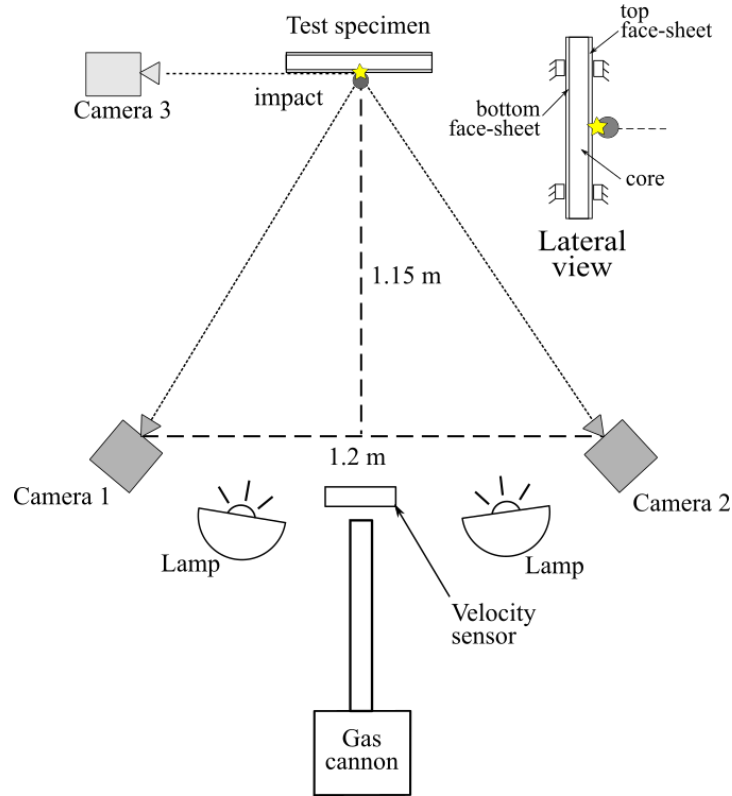


Figure 5.3. Experimental set-up. Top: schematic. Bottom: experimental set-up

Two PHOTRON FASTCAM SA-Z high-speed cameras in stereo configuration are used to record the testing at 70000 fps (time between frames 14.2 μ s) with a spatial resolution of 512 x 496 pixels and a time of exposure of 1/400 ms. Both cameras are equipped with Tokina MACRO 100 f2.8D lenses. The purpose of these cameras is to record the impact event and provide the required input frames for the stereo 3D DIC analysis. A third high-speed camera Photron Ultima is located perpendicular to the projectile path pointing over the impact location recording at the same frame rate. In this case, the camera recording is used to estimate the impact velocity as well as the rebound or residual velocity using an image-tracking algorithm. Additionally, this camera provides a perpendicular view of the impacted specimen that helps to further interpret the impact event. All cameras are synchronized and levelled with the test specimen. The cannon is also aligned to the centre of the specimen using laser levels, however, it was hard to achieve reproducibility in the impact location with deviations in the order of ± 10 mm. A schematic of the experimental set-up can be seen in Figure 5.3

The projectile impact velocity is varied by manually adjusting the cannon pressure. The impact velocity seems to approximate a logarithmic function with cannon pressure. However, there is some scattering due to the calibration of the pressure system and variability of the sabot used. This makes it hard to maintain the reproducibility of the impacts at the same impact conditions (Figure 5.6). The impact velocity is measured in two different ways. The first is by a laser velocity sensor at the cannon exit and the second estimating the impact velocity at the impact location using the video frames recorded by camera 3 (Figure 5.3) using an image tracking software (Figure 5.5). It is appreciated from Figure 5.6 that both measurements closely agree to provide confidence in the measurement of impact velocity used in this analysis. In overall, the velocity provided by the image tracking software is slightly smaller than the measured by the velocity sensor. This is expected considering that each measurement is taken at different locations and aerodynamic drag slows down the projectile while flying to reach the target. For this reason from now on in this chapter, the term “impact velocity” will refer to the velocity measured by the camera and the tracking software just before the impact takes place.

INTERMEDIATE VELOCITY IMPACT TEST ON SANDWICH PANELS

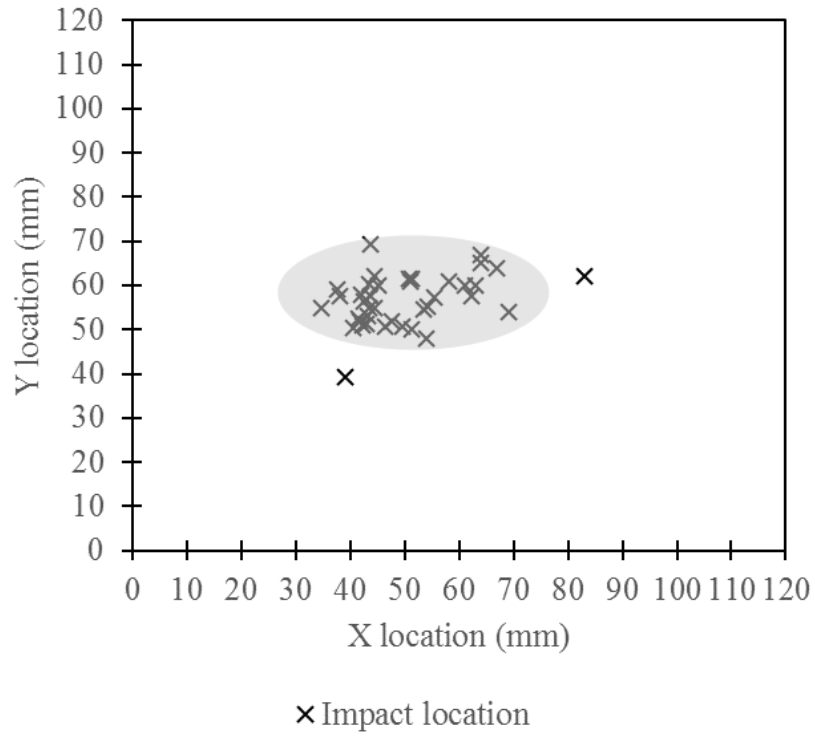


Figure 5.4. Impact location over the front face for all tests.

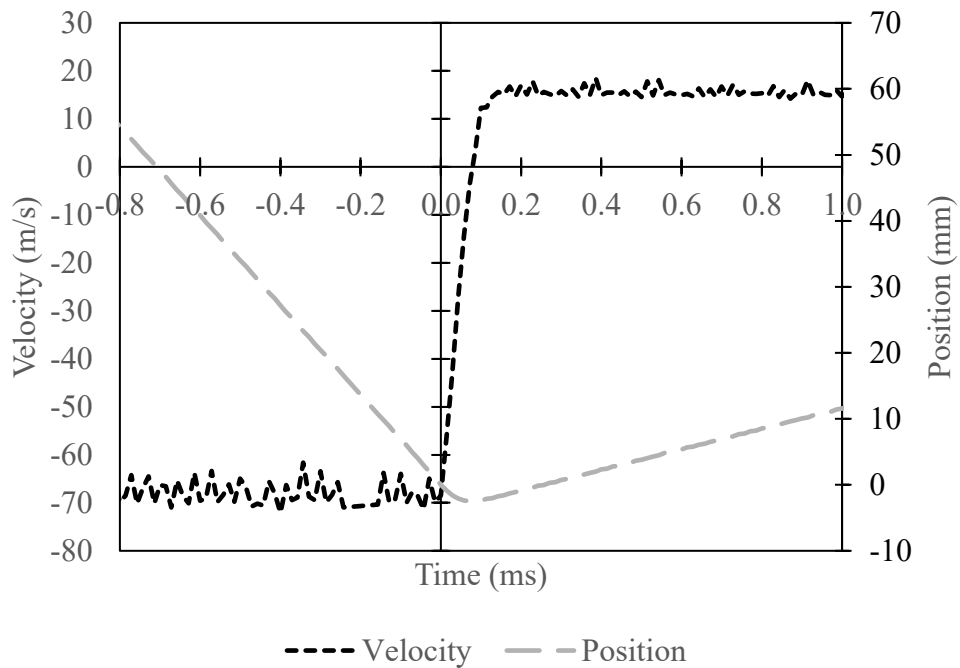


Figure 5.5. Example - Projectile position and velocity measured by the tracking software for an impact at $P=4$ bar over PET sandwich panel ($V_i=-67.4$ m/s, $V_r=15.4$ m/s)

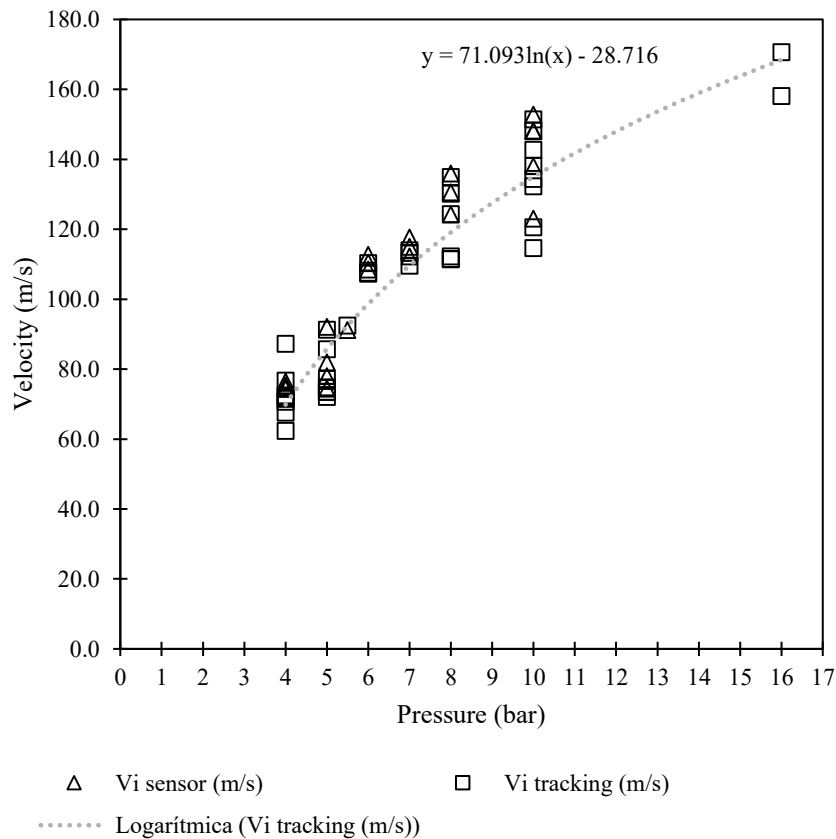


Figure 5.6. Impact velocity vs cannon pressure measured by the laser sensor and the image tracking software

5.2.3 Digital Image Correlation (DIC) Procedure

Stereo 3D-DIC is used to measure the displacements and plane strain distribution in the front face-sheet of some test specimens during the impact event. This method provides accurate identification of changes among the video frames correlating them at the pixel and subset level to find the displacement and strain field.

The speckle pattern was generated with spray paint using an airbrush as recommended in [14]. A series of different patterns are tested before selecting the definitive pattern to be used over the sandwich specimens. Different parameters are evaluated in order to optimize the contrast and the speckle size. Some of the evaluated parameters are:

- a) Airbrush nozzle size: 0.2mm, 0.3mm, 0.5 mm
- b) Airbrush pressure: 0.7 bar, 1bar
- c) Paint concentration: 50%, 66%, 100%
- d) Application time: 3 min to 15 min

Ten different patterns are analysed and the histogram of the region of interest (ROI) is obtained for each of them. The following technical observations are made during the speckle generation process:

- Low airbrush pressure in the range of 0.7 bar to 1 bar encourages speckle dots larger than 1 mm. Higher airbrush pressure decreases the speckle size encouraging blurred speckle patterns.
- The percentage of black pixels is proportional to the application time. Application times larger than 10 min seems to be necessary to obtain a percentage of black pixels larger than 30%
- A proper combination of paint concentration and nozzle size is required to avoid the blockage of the airbrush nozzle during the painting process.

The results obtained for all patterns are summarized in Table 5.1. Based in these results it is observed that pattern 8 and pattern 10 show a good compromise between black/white proportion with low grey proportion and minimum paint use.

Ref	Paint (%)	Time (min)	Nozzle (mm)	Pressure (bar)	Black (%)	White (%)	Grey (%)	Black/Grey	Black/White
1	66	5	0.5	0.7	9.1	87.9	1.2	7.6	0.10
2	100	7	0.5	0.7	9.6	88.9	0.6	16.0	0.11
3	100	3	0.5	0.7	3.2	95.4	0.6	5.3	0.03
4	50	5	0.5	0.7	19.8	75.6	1.7	11.6	0.26
5	100	5	0.5	0.7	8.3	90.3	0.5	16.6	0.09
6	100	7	0.5	1	11.3	82.3	2.7	4.2	0.14
7	100	15	0.5	0.7	40.8	46.8	4.1	10.0	0.87
8	50	10	0.5	0.7	33	43.7	3.5	9.4	0.76
9	100	15	0.2	0.7	25.1	64.1	4	6.3	0.39
10	50	15	0.3	0.7	30.6	57.9	2.9	10.6	0.53

Table 5.1. Speckle pattern candidates

After finding the proper combination of parameters, the top surface of the test specimens is painted with any of the two combinations. Little difference is found between the final painted specimens and the initially studied patterns. The histogram of two typical sandwich specimens used during testing is presented in Figure 5.7.

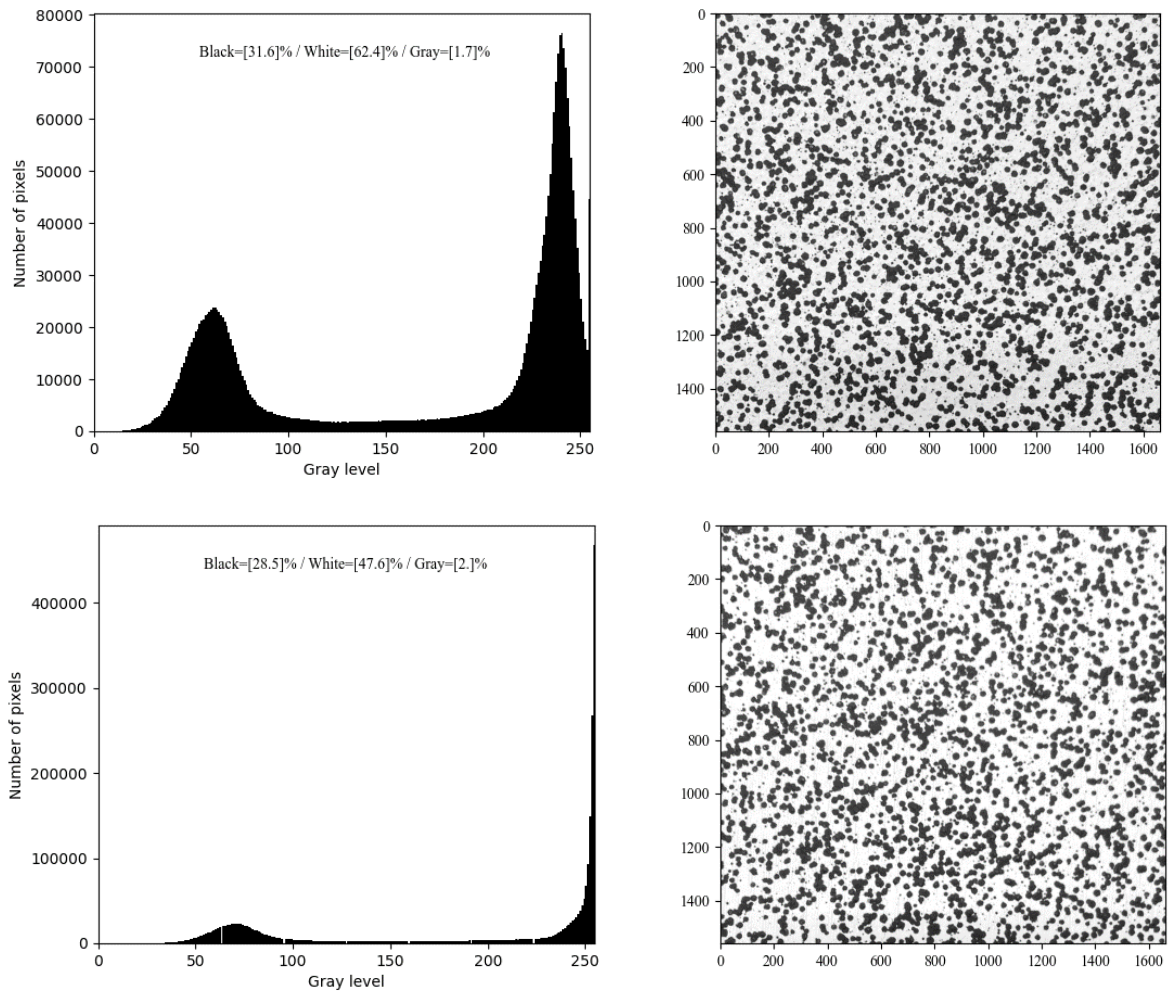


Figure 5.7. Example of a final specimen speckle pattern

The software used in this analysis is Digital Correlation Engine V.2. developed by SANDIAS NATIONAL LABORATORY in the U.S. The subset size is selected according to the speckle size ensuring that at least three speckles are covered by a single subset (Figure 5.8). Additionally, the step size is chosen to obtain enough spatial resolution and low computational time.

The average speckle size is 1 mm and since each frame has a resolution of 512 x 496 pixels a subset size of 21 pixels and a step size of 8 pixels is used. The calibration is performed taking multiple images to a dotted grid with a spacing of 8mm varying its orientation respect both cameras. The transformation matrix and the lens distortion parameters are obtained with minimum epipolar error. The same calibration file is used for all DIC analyses. All the previously mentioned parameters provide good correlation and spatial definition; the maximum correlation error was 2.9% with a measurement error lower than 2 μ m.

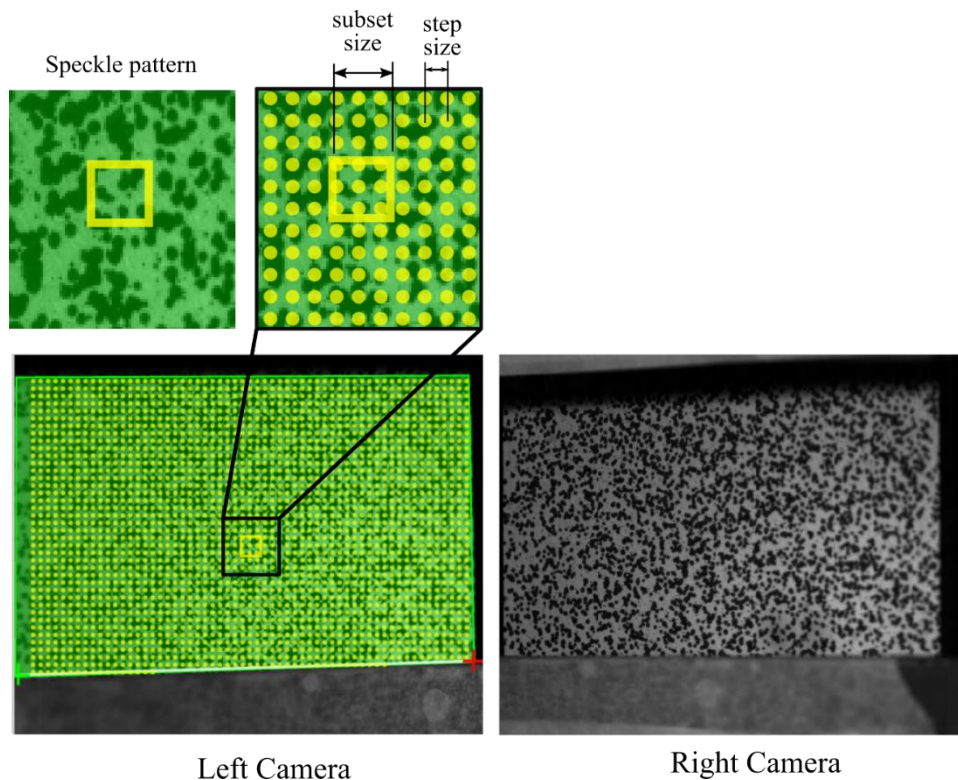


Figure 5.8. Digital image correlation speckle sub-set and step size

5.2.4 X-ray Computed Tomography (XCT)

The morphology of the post-impact damage is important to understand the mechanisms of energy dissipation and their overall importance in the panel behaviour. Additionally, it provides valuable qualitative and quantitative information to validate the FEA model proposed in the next chapter. Conventional inspection techniques for composite materials such as C-Scan ultrasound inspection and X-ray radiography are not convenient for the inspection of sandwich panels due to the dissipative effects of the sandwich core and the difficulty to visualize interior damage features in the core.

In contrast, X-ray Computed Tomography (XCT) offers the possibility to capture with detail interior features within the specimen. This technique uses a scanner consisting of a rotating X-ray tube and targets that measure the attenuation produced by materials inside the specimen. Multiple images are taken at different angles around the specimen which are processed in a computer using reconstruction algorithms to produce cross-section images of the specimen.

The post-impact XCT inspection of the specimens is contracted to IMDEA Materials Institute (Madrid, Spain). Due to the size of the specimens, the field of view (FOV) is limited to a portion of the total length, which includes the impact region. A Tungsten target

in mode 0 is used with 120 kV of voltage and 60 μ A of current. The scanner takes 3000 images per specimen with a resolution of 27.7 μ m/pixel. The lateral faces of the panels are also aligned for better analysis. All tomographic images are processed and analysed by the author using the software Image J.

5.3 Results and discussion

One of the simplest observations comes from the video sequence obtained with the third camera (perpendicular to the impact location). Both the impact velocity and core material massively influence the travel of the spherical projectile. In the case of the agglomerated cork panels, the projectile rebounds in all impact conditions in which there is no complete penetration of the panel and the projectile never are trapped inside the panel. This occurs even when the top face-sheet is penetrated (Table 5.2). In contrast, in the case of PET foam panels, the projectile rebounds only at impact velocity lower than 73 m/s in which the top face-sheet is not penetrated (Table 5.3). However, in those cases when the top face-sheet is penetrated, the projectile is unable to exit the panel and is trapped inside.

Vi tracking (m/s)	Rebound?	Trapped inside?	Penetration? (top face-sheet)	Penetration? (bottom face-sheet)
70.6	YES	NO	NO	NO
71.5	YES	NO	NO	NO
76.7	YES	NO	NO	NO
87.2	YES	NO	NO	NO
91.3	YES	NO	NO	NO
74.8	YES	NO	NO	NO
92.5	YES	NO	NO	NO
74.6	YES	NO	NO	NO
85.7	YES	NO	NO	NO
107.6	YES	NO	NO	NO
109.6	YES	NO	YES	NO
113.2	YES	NO	YES	NO
134.9	YES	NO	YES	NO
130.2	YES	NO	YES	NO
111.4	YES	NO	YES	NO
151.4	YES	NO	YES	NO
138.1	YES	NO	YES	NO
114.6	YES	NO	YES	NO
132.3	YES	NO	YES	NO
170.6	NO	NO	YES	YES

Table 5.2. Projectile travel and panel penetration (agglomerated cork sandwich panels)

INTERMEDIATE VELOCITY IMPACT TEST ON SANDWICH PANELS

Vi tracking (m/s)	Rebound?	Trapped inside?	Penetration? (top face-sheet)	Penetration? (bottom face-sheet)
72.5	YES	NO	NO	NO
72.1	YES	NO	NO	NO
67.6	YES	NO	NO	NO
62.4	YES	NO	NO	NO
72.0	YES	NO	NO	NO
77.2	YES	NO	NO	NO
73.5	YES	NO	NO	NO
73.5	YES	NO	NO	NO
110.3	NO	YES	YES	NO
107.3	NO	YES	YES	NO
114.0	NO	YES	YES	NO
124.3	NO	YES	YES	NO
111.5	YES	NO	YES	NO
112.2	NO	YES	YES	NO
120.6	NO	YES	YES	NO
134.4	NO	YES	YES	NO
148.2	NO	YES	YES	NO
142.7	NO	YES	YES	NO
158.1	NO	NO	YES	YES

Table 5.3. Projectile travel and panel penetration (PET foam core sandwich panels)

In those cases where projectile rebound occurs the projectile rebounds with a velocity lower than the initial impact velocity (Figure 5.9). As a result, the projectile recovers part of the initial kinetic energy in the spring back and its magnitude can be estimated by measuring the rebound velocity with the tracking system. Figure 5.11 shows the ratio between the projectile’s kinetic energy before and after impact as a function of impact velocity. Both sandwich panels can recover from 4% to 7% of their initial kinetic energy. PET foam sandwich panels show slightly higher kinetic energy ratios than Agglomerated cork panels. However, data scattering avoids raising a definitive conclusion about the influence of the core material in the energy dissipation ratio.

From the same figure, it is observed that the kinetic energy ratio decreases at higher impact velocities probably due to the appearance of other non-conservative energy dissipation mechanisms such as plastic dissipation and panel damage. In fact, for velocities large enough to penetrate the top face-sheet the rebound kinetic energy can drop up to 1% of the initial kinetic energy for a sandwich with an agglomerated cork core.

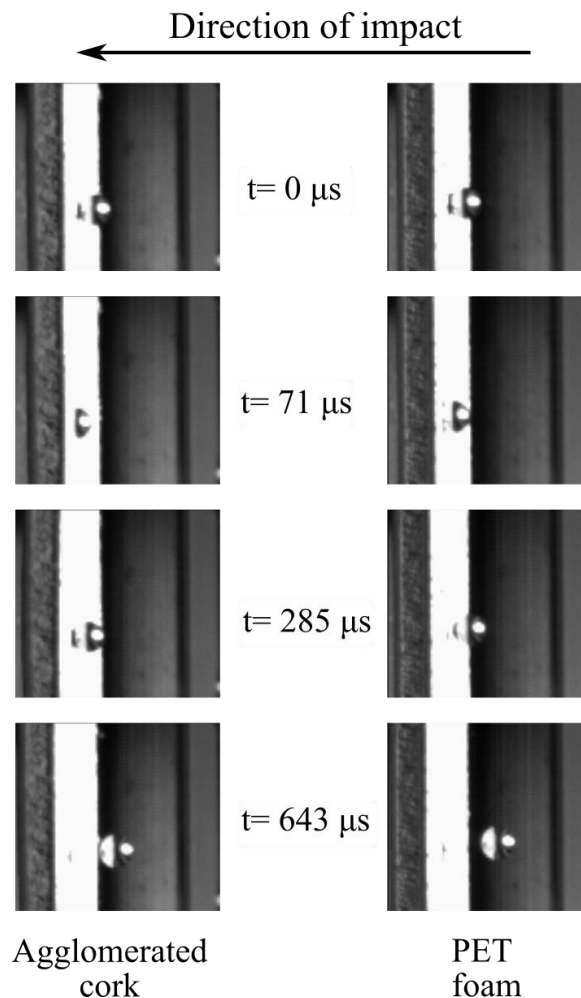


Figure 5.9. High-speed video frames showing the impact and rebound of the projectile for both sandwich panels. $P=4$ bar, $V_i=71.5$ m/s (agglomerated cork) and $V_i=72.5$ m/s (PET foam).

A significant difference is observed between sandwich panels with agglomerated cork and PET foam. In the first case independently of the impact velocity, the projectile was able to rebound (Figure 5.9 and Figure 5.10) even when there is perforation of the top face-sheet. On the other hand for PET foam sandwich panels for velocities above the penetration velocity, the projectile is trapped inside the panel (Figure 5.10). This difference in behaviour is associated with the mechanical properties of the core material. In the case of agglomerated cork, the material shows a high elastic return even after large deformations [17],[18], [19] while in the case of PET foam due to its semi-rigid nature the material response is dominated by plastic crushing with very little elastic recovery. This difference is discussed in detail in chapter 4.

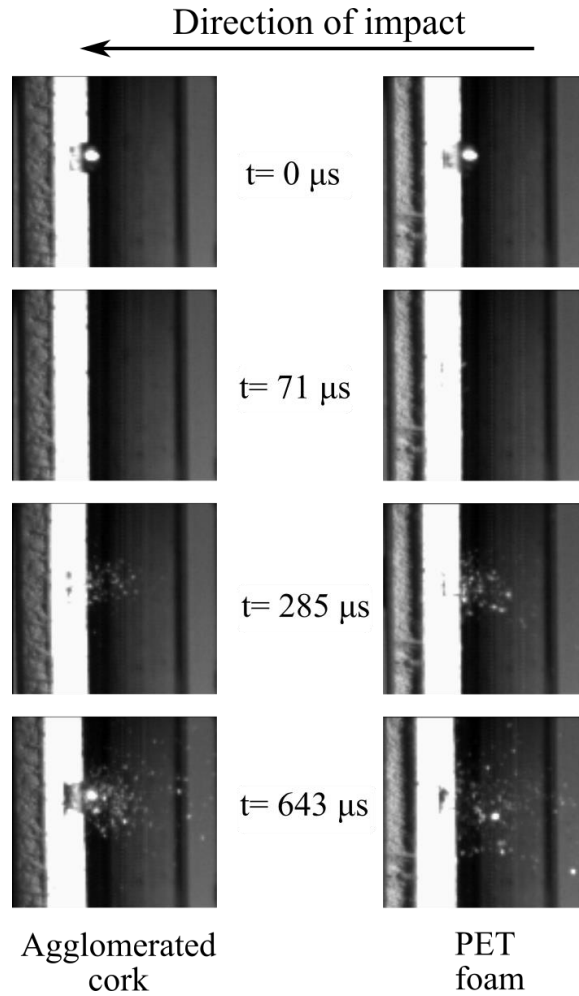


Figure 5.10. High-speed video frames showing the impact for both sandwich panels. $P=10 \text{ bar}$, $V_i=135 \text{ m/s}$ (agglomerated cork) and $V_i=138 \text{ m/s}$ (PET foam)

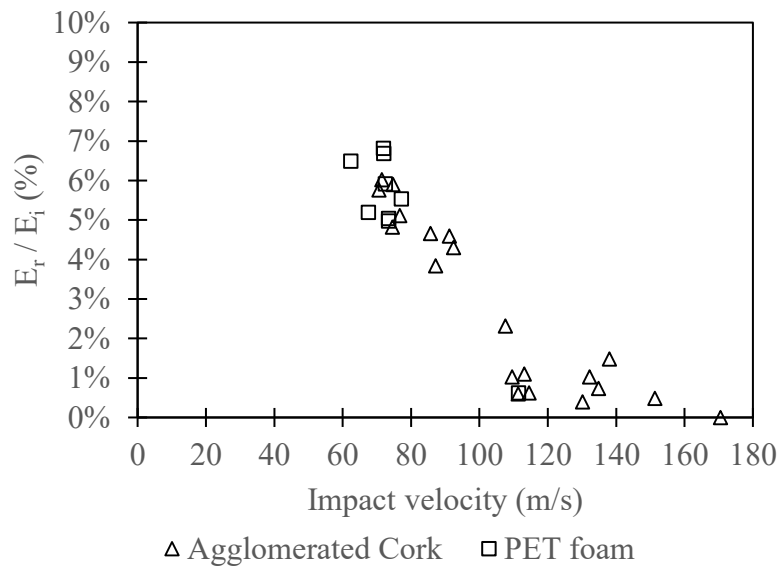


Figure 5.11. Ratio of the projectile kinetic energy before and after impact with respect to impact velocity.

The progressive out-of-plane displacement in the external surface of top face-sheet is measured during the first 120 μs after impact using the results obtained from the 3D DIC analysis. Figure 5.12 and Figure 5.13 shows the out of plane displacement field produced by the impact over both sandwich panels at two different impact velocities (73 m/s and 131 m/s). As expected, the magnitude of the disturbance is maximum at the impact location growing with time as the perturbation waves propagate radially outwards.

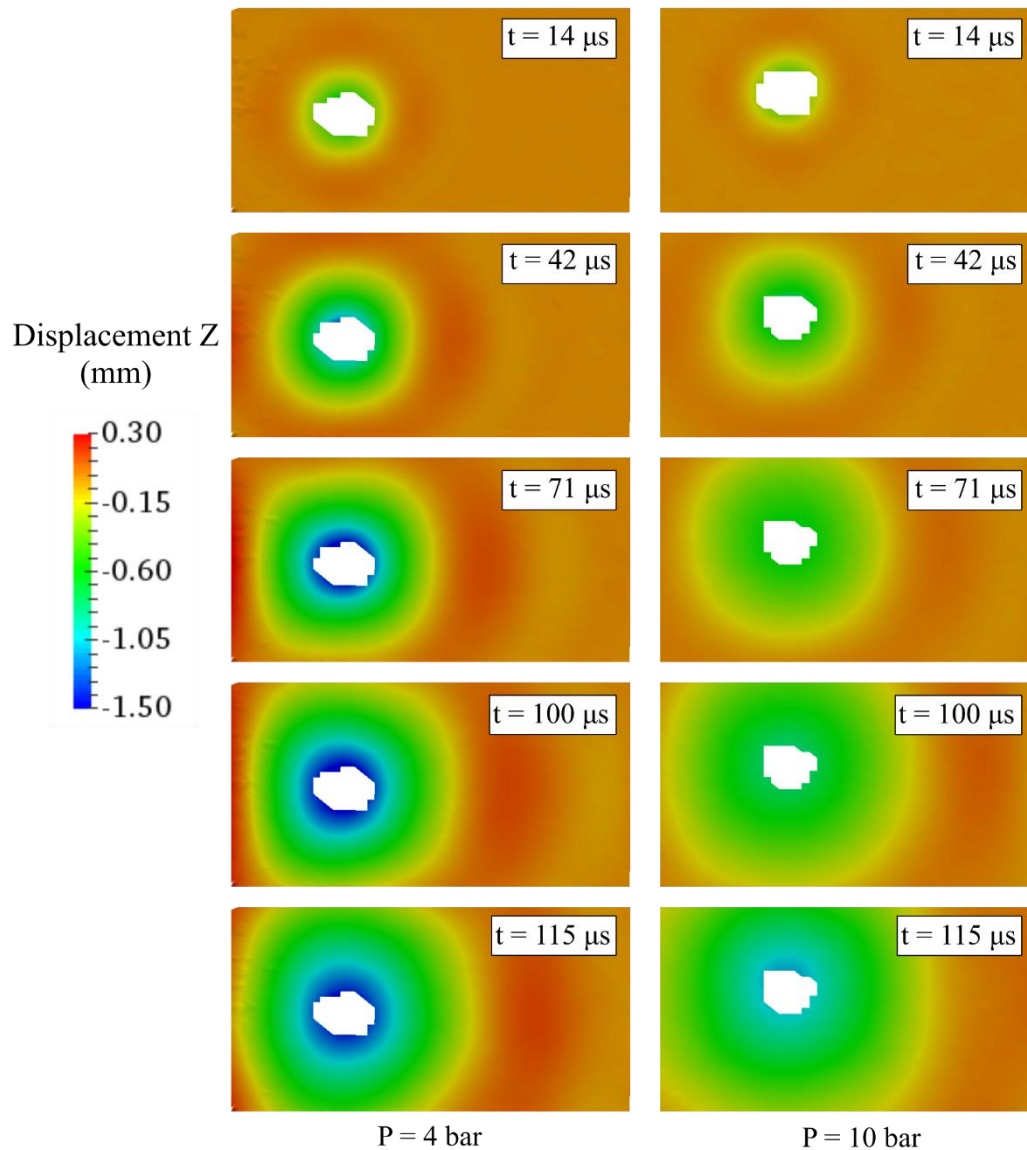


Figure 5.12. Out-of-plane displacement and propagation of the disturbance during impact. Sandwich panel with agglomerated cork core. $P=4$ bar ($V_i=71.5$ m/s), $P=10$ bar ($V_i=135$ m/s)

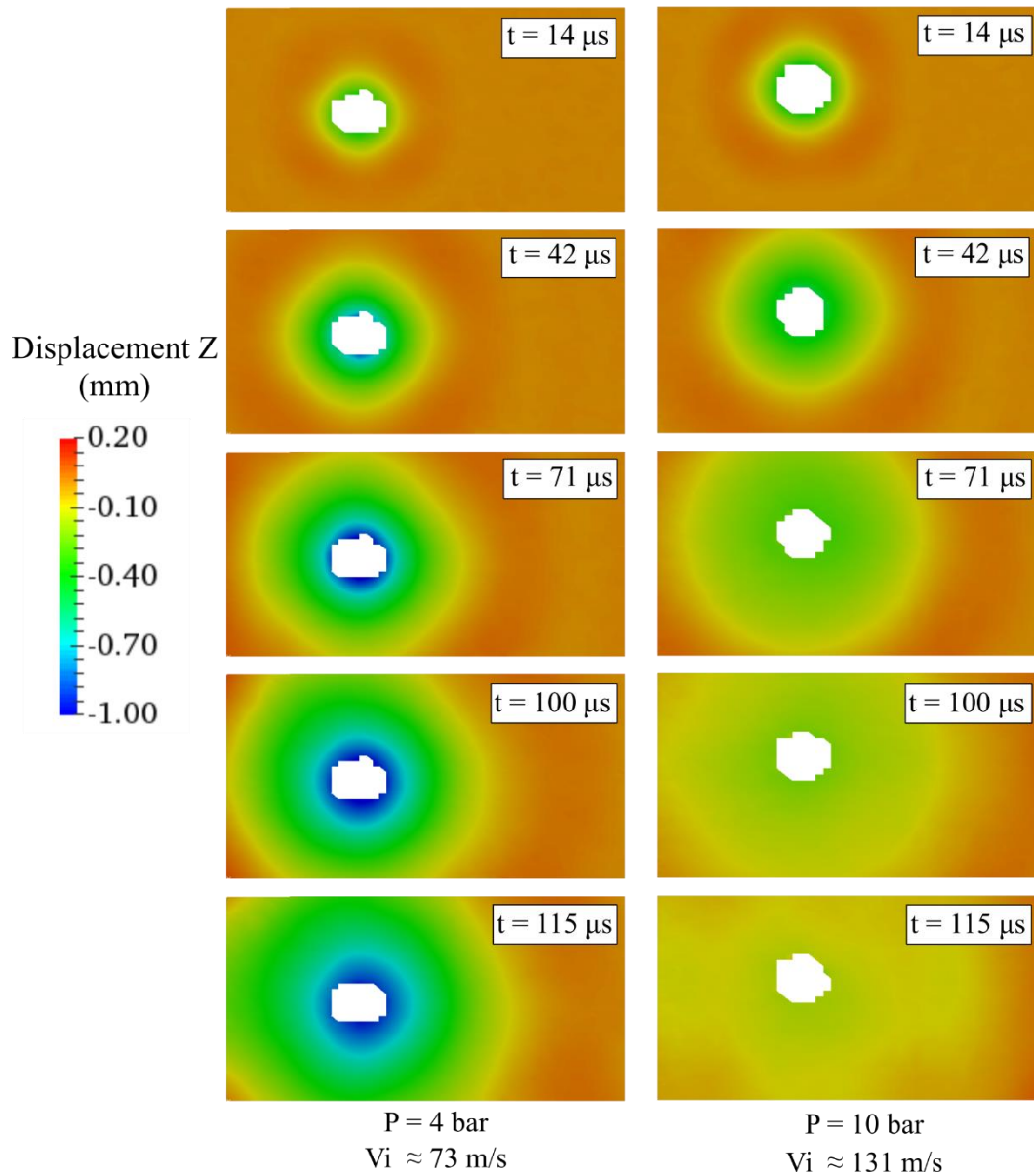


Figure 5.13. Out of plane disturbance and propagation of the disturbance after impact. Sandwich panel with an PET foam core. P=4 bar ($V_i=72.5$ m/s), P=10 bar ($V_i=138$ m/s).

Figure 5.14 depicts the displacement shape at equally spaced time intervals ($\Delta t = 14.2 \mu s$) for both sandwich panels at different impact velocities. In the impact location, it was not possible to get cross-correlation due to the shadow created by the projectile. Despite this, the deformation in the vicinity of the impact location was captured with high accuracy.

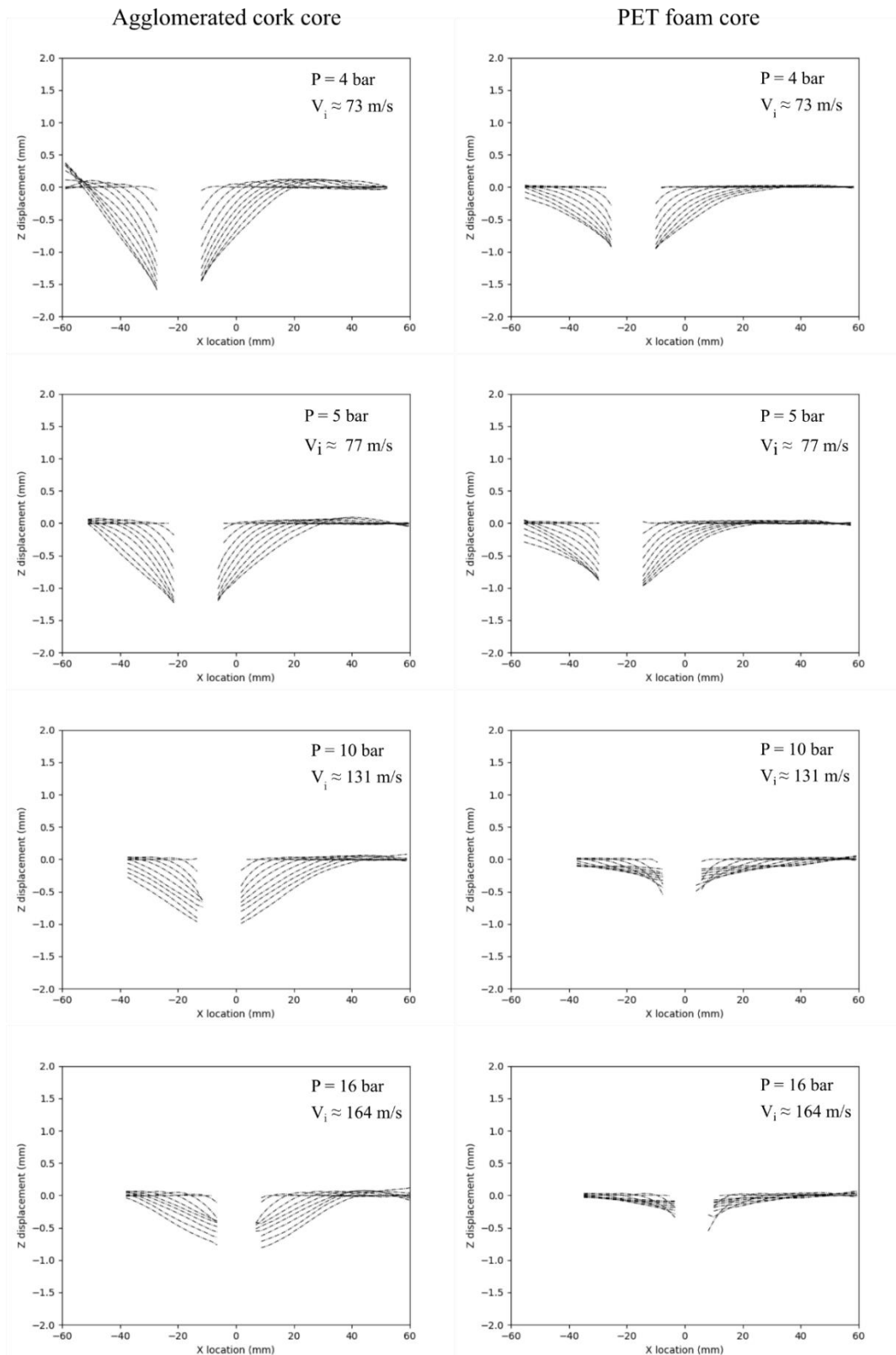


Figure 5.14. Deflection shape during the first 120 μ s after impact measured by 3D-DIC analysis. Comparison between sandwich with agglomerated cork core (left) and PET foam core (right) at different impact velocities.

It can be observed that the magnitude of the displacements changes with the impact velocity. At low impact velocities ($V_i \leq 77$ m/s), the top face-sheet shows larger overall displacements than at higher impact velocities ($V_i \geq 131$ m/s). This behaviour seems counterintuitive, however, it is observed in both sandwich panels and for all impact cases. This effect can be explained because of the influence and severity of local failure during penetration at higher impact velocities. For example, at low impact velocities, the damage and failure in the plies directly in contact with the projectile are small. Therefore, the top face-sheet behaves almost like a continuum body deflecting together with the advancing projectile. On the other hand, at higher impact velocities, the projectile produces progressive failure of the plies directly in contact. This failure propagates through the thickness and eventually breaks apart the top face-sheet into two detached regions. One small fragmented and detached plug that has roughly the size of the projectile and can keep moving together with the projectile. The other region is the remaining top face-sheet that after separation is unable to keep deflecting with the projectile and starts oscillating due to the initial disturbance.

The magnitude of the out-of-plane displacements in the top face is also dependent on the core material. As can be observed from Figure 5.14 the magnitude of displacements is larger for sandwich panels with agglomerated cork core than for those with PET foam core besides they are impacted at roughly the same impact velocities. This may be caused by the difference in the stiffness and plateau stress between both materials. Results in Chapter 4 and previous publications made by the author [17] shows that the dynamic Young modulus of the PET foam (139 MPa) is more than 10 times larger than the agglomerated cork (11.6 MPa). Similarly, the plateau stress of PET foam (5.57 MPa) is almost 5 times larger than for agglomerated cork (1.14 MPa). As a result, the front face-sheet with the PET foam is expected to have a more rigid foundation and less out-of-plane displacements.

The strain distribution around the impact region is also analyzed during the first 56 μ s after impact for both sandwich panels and at two different impact velocities (Figure 5.15 to Figure 5.18). The strain distribution is not homogeneous but instead is characterized by an orthogonal distribution in which compressive and tensile longitudinal strains are aligned with the orientation of the fibres at 0° and 90° (ϵ_{xx} , ϵ_{yy}). Meanwhile positive and negative shear strains (ϵ_{xy}) are also orthogonally distributed but are aligned 45° from the orientation of the fibres. The strain is distributed in a lobular shape around the impact point with strain levels decreasing with the distance from the impact location.

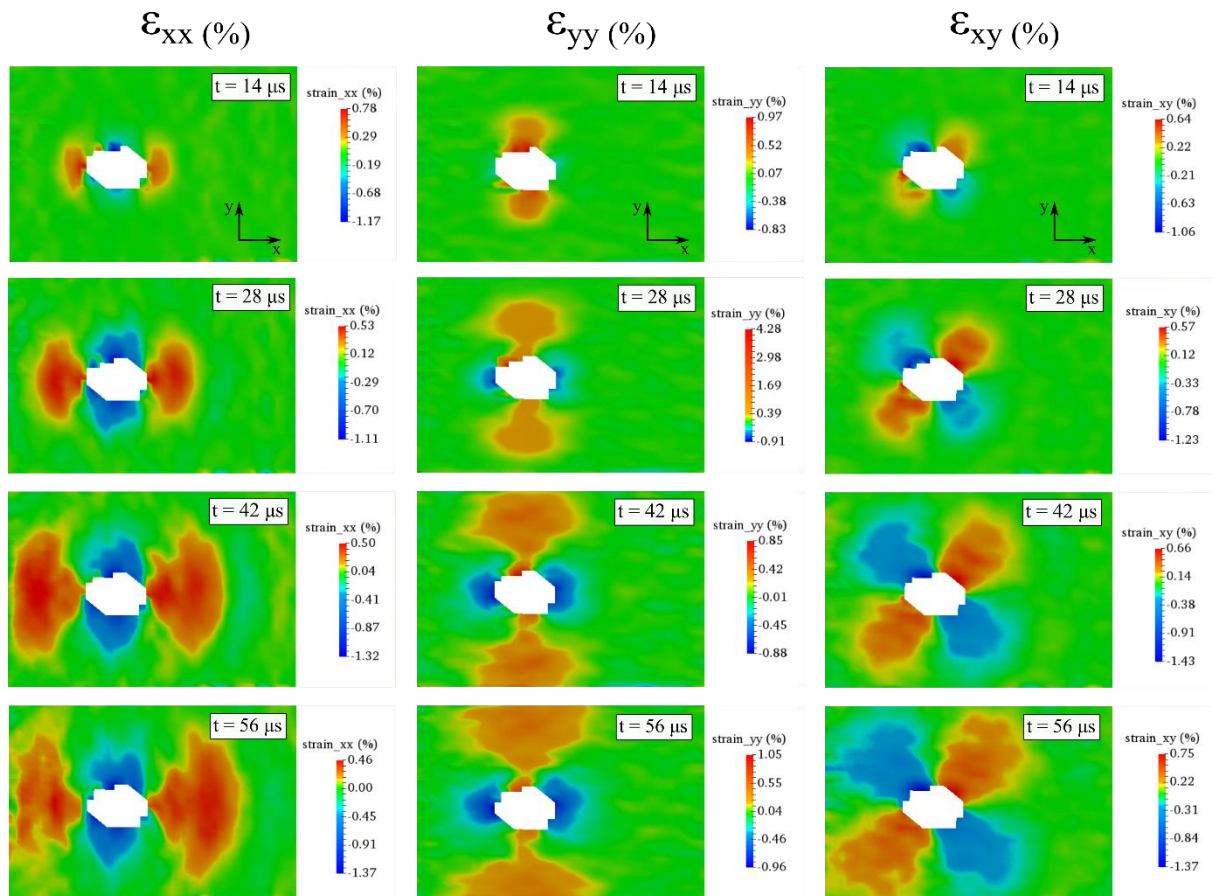


Figure 5.15. Strain distribution of the front face-sheet (ply 8) during the first instants after impact measured with DIC. Agglomerated cork sandwich, $P=4\text{bar}$, $V_i=71.5\text{ m/s}$

In Figure 5.15 and Figure 5.16 the impact velocity is not enough to perforate the top face-sheet while in Figure 5.16 and Figure 5.18 the impact velocity is higher and the projectile penetrates the face-sheet. The penetration of the front face-sheet creates a difference in the propagation of the strain field as the impact continues. For example, for no perforation condition, the strain disturbance propagates radially and continuously as the impact proceeds. However, when perforation occurs the propagation of the strain disturbance is suddenly interrupted once there is a massive fracture in the impact region. At this point, the continuity of the face-sheet is lost and no further strain is transmitted from the impact point. This effect can be visualized in both Figure 5.16 and Figure 5.18 for impact times $t=42\ \mu\text{s}$ and $t=56\ \mu\text{s}$ where disturbances of the strain field seem to stop around the impact point.

INTERMEDIATE VELOCITY IMPACT TEST ON SANDWICH PANELS

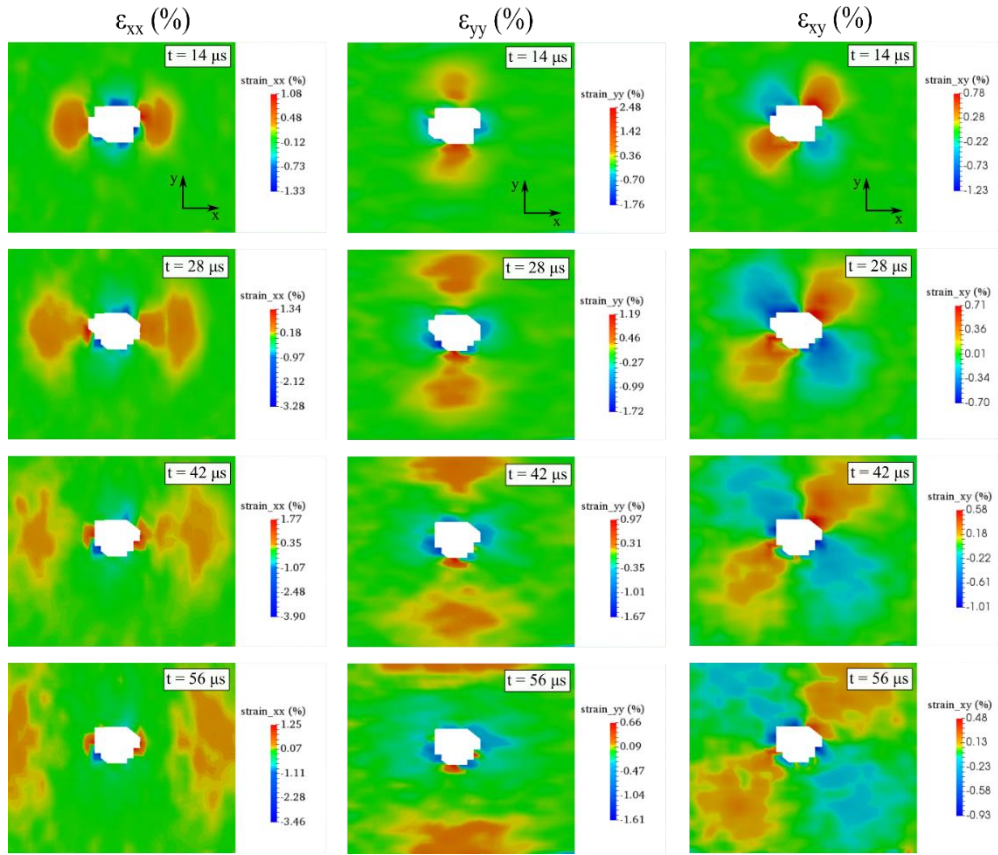


Figure 5.16. Strain distribution of the front face-sheet (ply 8) during the first instants of time after impact measured with DIC. Agglomerated cork sandwich, $P=10\text{bar}$, $V_i=135\text{ m/s}$

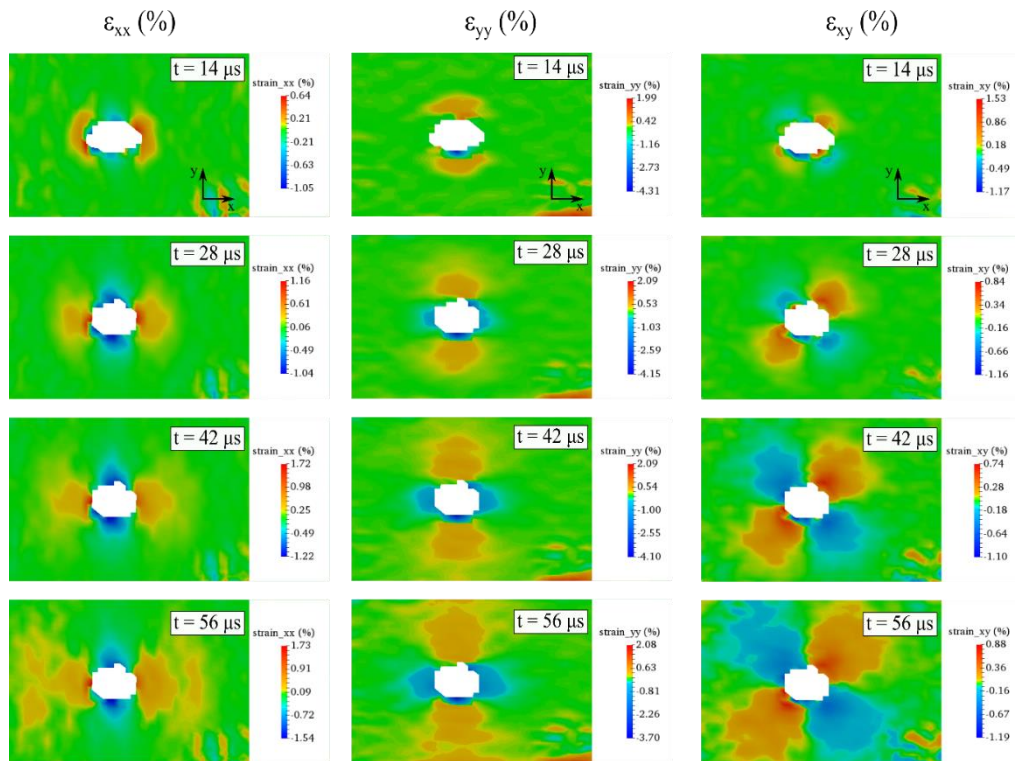


Figure 5.17. Strain distribution of the front face-sheet (ply 8) during the first instants of time after impact measured with DIC. PET foam sandwich, $P=4\text{ bar}$, $V_i=72.5\text{ m/s}$

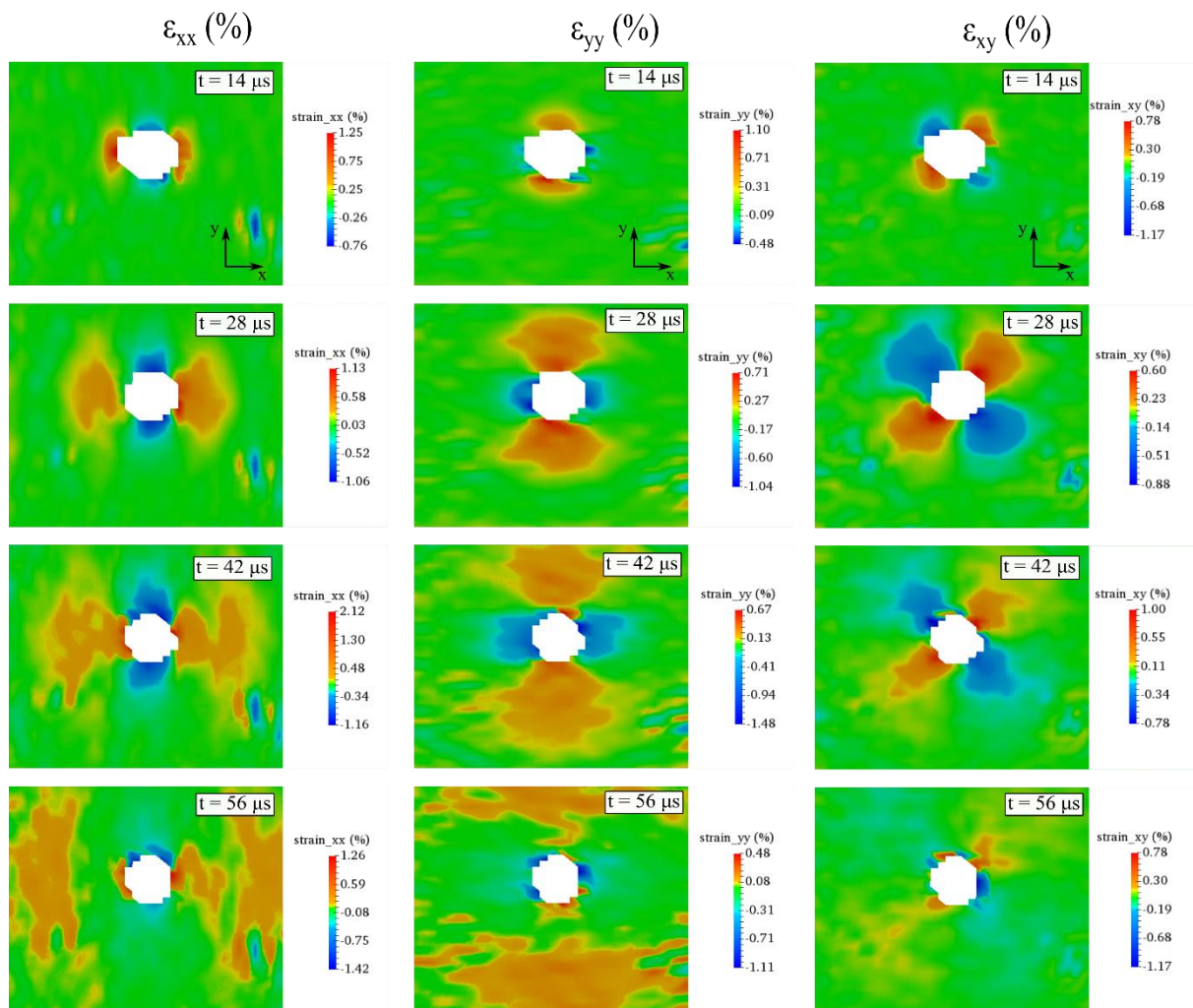


Figure 5.18. Strain distribution of the front face-sheet (ply 8) during the first instants of time after impact measured with DIC. PET foam sandwich, $P=10$ bar, $V_i=138$ m/s.

5.3.1 Damage and failure morphology

The damage and failure morphology of the sandwich panels after impact are also studied using destructive and non-destructive inspection techniques. In the first case, test specimens are sectioned across the impact point using a waterjet cutting. In the second case, computed X-ray tomography (XCT) is used to obtain a detailed internal 3D view of the specimens after impact.

5.3.1.1 Visual inspection of cut-sectioned specimens

Figure 5.19 shows the cut-section of sandwich panels of both core materials (agglomerated cork and PET foam) impacted at three different velocities. As can be observed at impact

velocities near 71 m/s both panels show indentation of the top face-sheet accompanied with a localized core compression under the impact point. In the case of PET foam core, local crushing is visible. In both cases, the top face-sheet first ply (next to the core surface) seems to have failed under fibre breakage.

At impact velocities close to 113 m/s both panels are heavily damaged with the appearance of a crater that penetrates the core. This crater is formed by failed plies in the top face-sheet (petals) that after breaking tilt inwards in the direction of the projectile advance. The formation of petals is also accompanied by delamination in the top face-sheet which extends beyond the projectile diameter and the crater region. This petal-shaped crater also squeezes the core sidewise, something that is visible by the crushed PET foam core around the crater. It is also clearly visible that the core is highly compressed by the projectile advance in the vertical direction. A key difference is observed between the two core materials: in the case of PET foam core the projectile penetration seems larger than for agglomerated cork and the crushed region seems to have densified and fragmented. In contrast, agglomerated cork is also highly compressed but can keep its integrity without fracturing or fragmenting.

PET foam core shows a brittle behaviour with the formation and growth of different cracks. For example, at $V_i = 114$ m/s a large crack appears in the intersection of the bottom face-sheet and the core extending horizontally beyond the impact region (Figure 5.19). There are signs indicating this crack propagates in the core and not in the glue layer especially noticing that strength in the core is much lower than in the glue layer. Even though, this failure mechanism must be studied in more detail in future works since debonding is also encountered in some other impact cases. Similarly at $V_i = 134$ m/s this crack is also present but is accompanied by a diagonal cross-section crack that creates a cone joining the crater to the horizontal intersection crack (Figure 5.19). At this point, it is important to highlight that none of these crack formations are observed in the case of agglomerated cork sandwich panels.

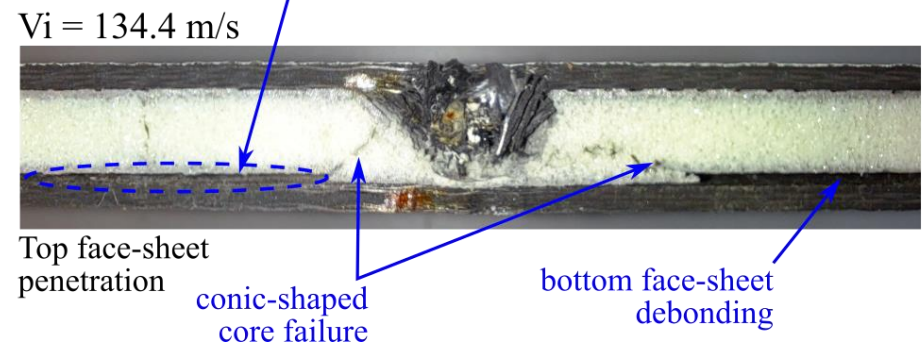
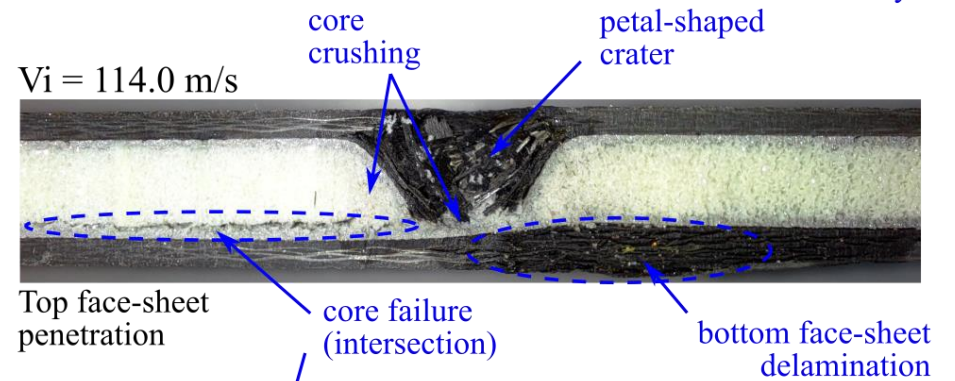
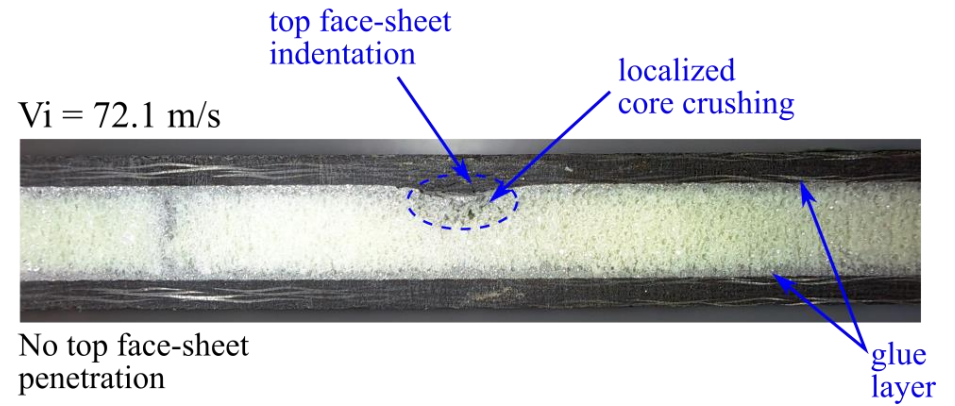
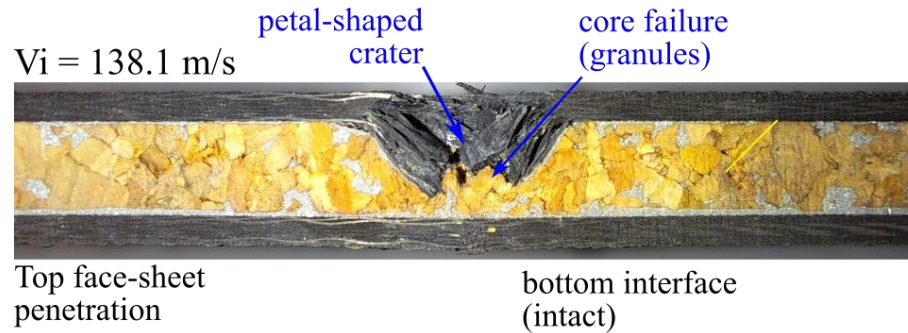
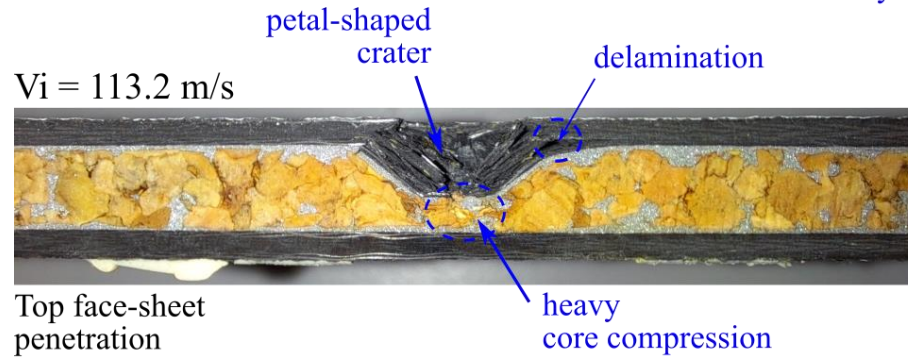
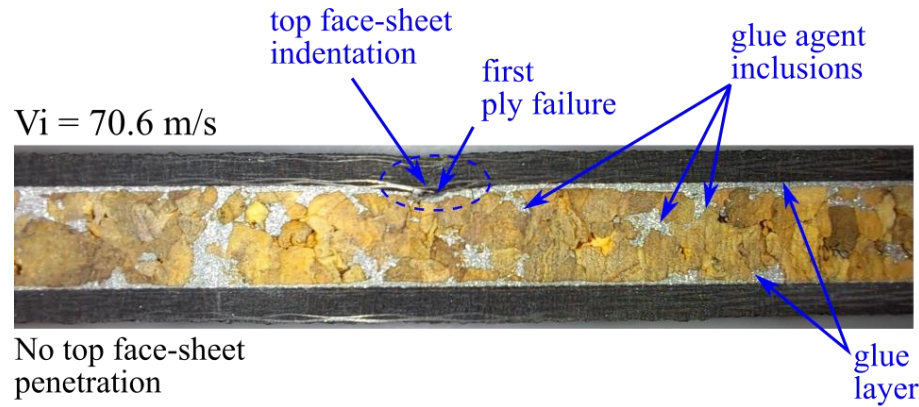


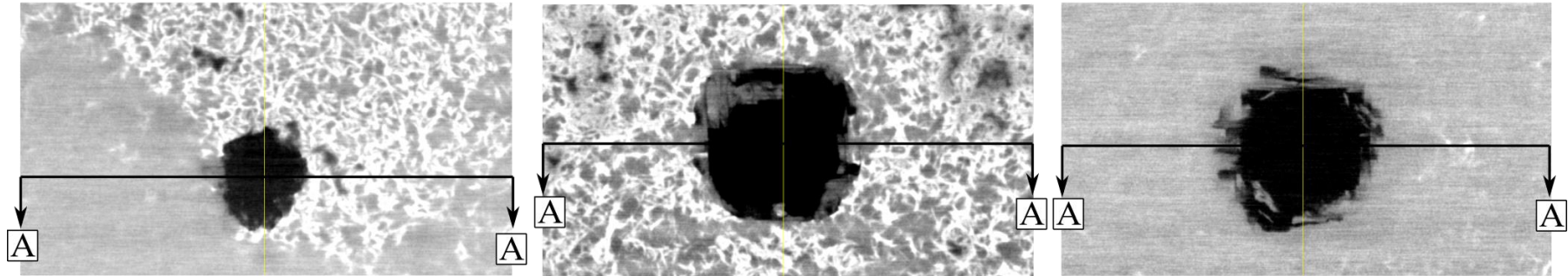
Figure 5.19. Post-impact damage. Cut-section of test specimens impacted at three different velocities. Left: Agglomerated cork sandwich panels. Right: PET foam sandwich panels.

TOP VIEW

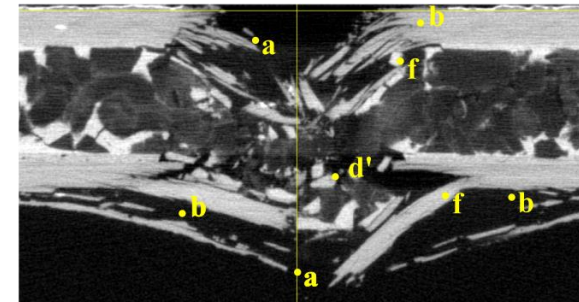
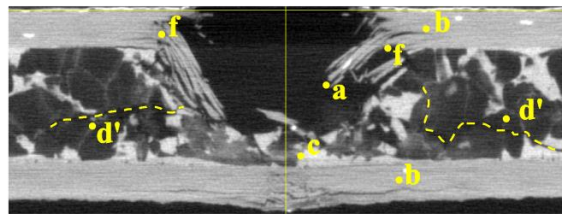
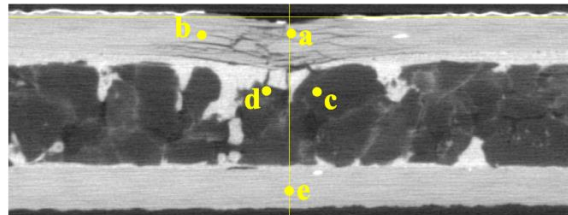
$V_i = 76.7 \text{ m/s}$

$V_i = 132.2 \text{ m/s}$

$V_i = 170.6 \text{ m/s}$



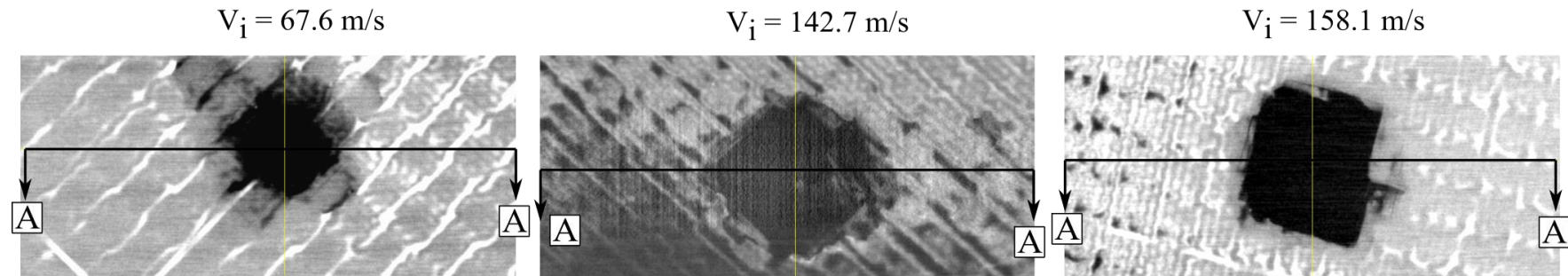
SECTION A-A (mid-section)



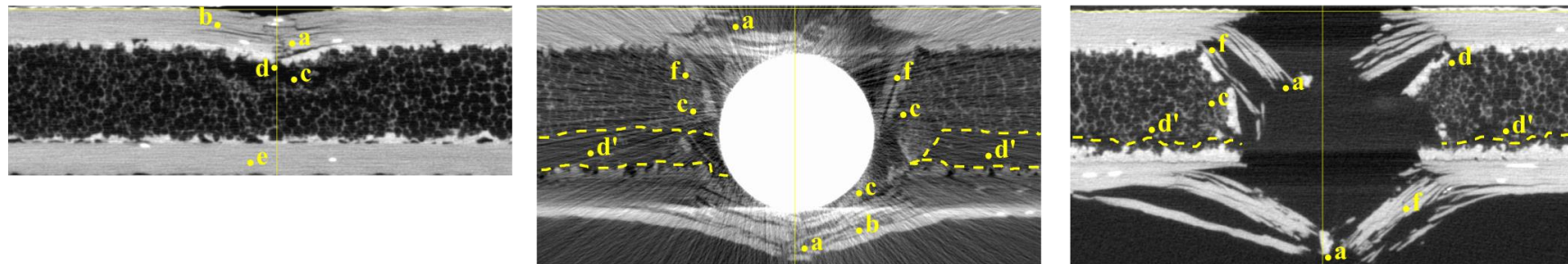
- | | |
|--------------------------|-------------------------------------|
| a. intralaminar fracture | d'. core fracture crack |
| b. delamination crack | e. bottom face-sheet
(no damage) |
| c. core compression | f. large ply bending |
| d. glue fracture | |

Figure 5.20. Post impact damage for three different impact velocities. X-ray computed tomography across the mid-section (agglomerated cork sandwich panel)

TOP VIEW



SECTION A-A (mid-section)



- | | |
|--------------------------|----------------------------------|
| a. intralaminar fracture | d'. core fracture crack |
| b. delamination crack | e. bottom face-sheet (no damage) |
| c. core crushing | f. large ply bending |
| d. glue fracture | |

Figure 5.21. Post impact damage for three different impact velocities. X-ray computed tomography across the mid-section (PET foam core sandwich panel).

5.3.1.2 X-ray computed tomography (XCT) inspection

Similar results are obtained from the XCT inspection and are shown in Figure 5.20 and Figure 5.21 for agglomerated cork and PET foam sandwich panels respectively. These figures show the top view of the impacted specimens and the mid-cross-section of the at three impact velocities.

The impact velocities are selected to show three different levels of post-impact damage. At the lowest impact velocity (76 m/s for agglomerated cork and 67 m/s for PET foam) the indentation in the top face-sheet is small (approximately 0.5 mm in both panels) and it could pass unnoticed by the naked eye. However, as shown in the midsection images there is a considerable amount of damage dominated by intra-laminar ply fracture and multiple delamination cracks in the top face-sheet that extend radially beyond the indentation crater. Glue fracture also appears in the intersection of the core to top face-sheet forming a crack that leads to debonding. Core compression is also observed in both core materials however, PET foam seems to suffer from premature crushing and fragmentation while agglomerated cork seems to sustain compression without any apparent detrimental effect. No damage is observed in the bottom face-sheet for any of the sandwich panels under the mentioned impact velocities.

At higher impact velocities (132 m/s for agglomerated cork and 142 m/s for PET foam) there is complete penetration of the top face-sheet and massive core damage for both panels. Complete ply intra-laminar failure leads to large bending of individual plies what in turn forms the petals described in the previous subsection. These petals compress the core laterally being crushed in the case of PET foam cores. Large cracked regions are observed across both core sections. Indeed, for the PET foam core, the cracked regions encouraged a massive separation of the core and bottom face-sheet as described in the previous subsection. At these impact velocities, the bottom face-sheet suffer from large delamination and some intra-laminar failure but not perforation.

Finally, at the highest impact velocities (170 m/s for agglomerated cork and 158 m/s for PET foam) there is generalized damage across the panel thickness similar to the one described for the previous velocity range. The greatest difference though is the visible intra-laminar failure in the bottom face-sheet accompanied by the formation of petals. Additionally, delamination damage in the bottom face-sheet is critically extended as will be discussed in the following paragraphs.

The delamination area in the face-sheets is estimated by projecting the pixels with the minimum intensity along the vertical direction (top view). An appropriate selection of the image slices is required to capture the delamination area of top and bottom face-sheets separately. After that, the colour balance is adjusted to define a sharp closed contour that is later measured using Image J.

Figure 5.22 and Figure 5.23 show the resulting delamination area for agglomerated cork and PET foam sandwich panels respectively at the same impact velocities discussed in the previous paragraph. It is observed that for all impact conditions and in both sandwich panels the delamination area in the top face-sheet has a semi-circular shape centred at the impact location, which extends radially beyond the crater diameters (darker pixels). From the studied specimens, the delamination area in the top face-sheet seems to increase with impact velocity. However, the trend that the delamination area follows as a function of the impact velocity is still unknown due to the few numbers of specimens inspected using XCT.

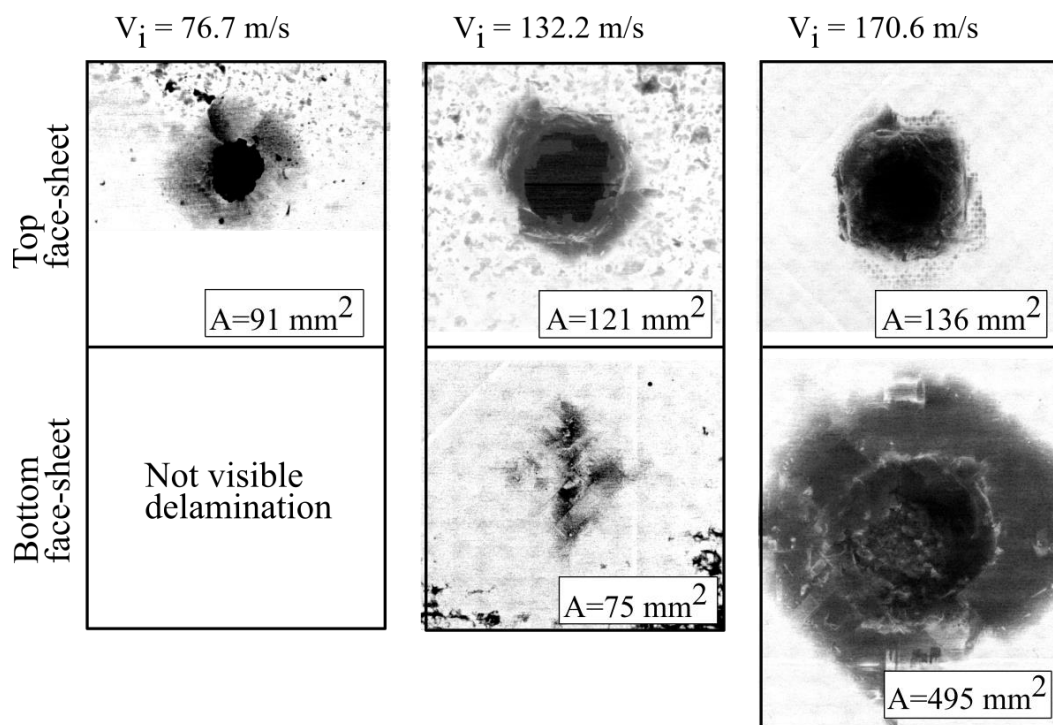


Figure 5.22. Projected delamination area in top and bottom face-sheets measured from X-ray tomography over agglomerated cork sandwich panels

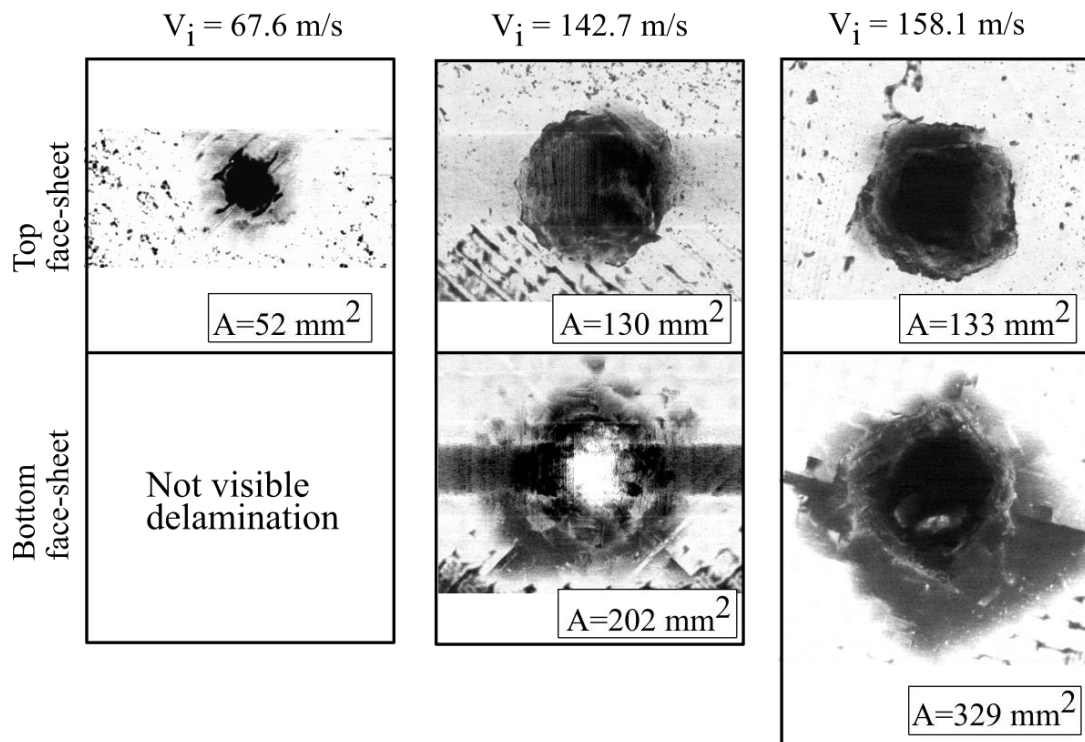


Figure 5.23. Projected delamination area in top and bottom face-sheets measured from X-ray tomography over PET foam sandwich panels

In regards to the bottom face-sheet it can be stated that if there is no penetration of the top face-sheet the delamination in the bottom face-sheet is zero (e.g. Figure 5.22 at $V_i = 76.7 \text{ m/s}$). However, if penetration occurs delamination in the bottom face-sheet is not zero and depending on the impact velocity delamination area could be many times larger than in the top face-sheet. An example of this situation is seen in Figure 5.22 at $V_i = 170.6 \text{ m/s}$. In this case, the delamination area in the top face-sheet is 136 mm^2 while in the bottom face-sheet is 495 mm^2 .

References of the chapter

- [1] Caprino G, Teti R. Impact and post-impact behavior of foam core sandwich structures. *Compos Struct* 1994;29:47–55. [https://doi.org/10.1016/0263-8223\(94\)90035-3](https://doi.org/10.1016/0263-8223(94)90035-3).
- [2] Shih WK, Jang BZ. Instrumented impact testing of composite sandwich panels. *J Reinf Plast Compos* 1989;8:270–98. <https://doi.org/10.1177/073168448900800304>.
- [3] Xia F, Wu XQ. Work on impact properties of foam sandwich composites with different structure. *J Sandw Struct Mater* 2010;12:47–62. <https://doi.org/10.1177/1099636209106256>.

- [4] Kepler J. Impact penetration of sandwich panels at different velocities - An experimental parameter study: Part I - Parameters and results. *J Sandw Struct Mater* 2004;6:357–74. <https://doi.org/10.1177/1099636204038217>.
- [5] Kepler J. Impact penetration of sandwich panels at different velocities - An experimental parameter study: Part II - Interpretation of results and modeling. *J Sandw Struct Mater* 2004;6:379–97. <https://doi.org/10.1177/1099636204038218>.
- [6] Kepler J. Equipment for Impact Testing of Sandwich Panels. *J Sandw Struct Mater* 2003;5:161–77. <https://doi.org/10.1106/109963603028495>.
- [7] Ren P, Ding C, Liu Y, Ye R, Wu J, Ma Y, et al. Dynamic response and failure of carbon/epoxy composite sandwich subjected to underwater impulsive loading. *Int J Impact Eng* 2020;143:103614. <https://doi.org/10.1016/j.ijimpeng.2020.103614>.
- [8] Rolfe E, Kelly M, Arora H, Hooper PA, Dear JP. Failure analysis using X-ray computed tomography of composite sandwich panels subjected to full-scale blast loading. *Compos Part B Eng* 2017;129:26–40. <https://doi.org/10.1016/j.compositesb.2017.07.022>.
- [9] Sarasini F, Tirillò J, Lampani L, Sasso M, Mancini E, Burgstaller C, et al. Static and dynamic characterization of agglomerated cork and related sandwich structures. *Compos Struct* 2019;212:439–51. <https://doi.org/10.1016/j.compstruct.2019.01.054>.
- [10] Prabhakaran S, Krishnaraj V, Shankar K, Senthilkumar M, Zitoune R. Experimental investigation on impact, sound, and vibration response of natural-based composite sandwich made of flax and agglomerated cork. *J Compos Mater* 2019;54. <https://doi.org/10.1177/0021998319871354>.
- [11] Ivañez I, Sánchez-Saez S, Garcia-Castillo SK, Barbero E, Amaro A, Reis PNB. High-velocity impact behaviour of damaged sandwich plates with agglomerated cork core. *Compos Struct* 2020;248. <https://doi.org/10.1016/j.compstruct.2020.112520>.
- [12] Attwood JP, Russell BP, Wadley HNG, Deshpande VS. Mechanisms of the penetration of ultra-high molecular weight polyethylene composite beams. *Int J Impact Eng* 2016;93:153–65. <https://doi.org/10.1016/j.ijimpeng.2016.02.010>.
- [13] Michael A. Suttons, Jean-Jose Orteu HWS. Image correlation for shape, motion and

- deformation measurements. Springer Science+Business Media; 2009. <https://doi.org/10.1007/978-0-387-78747-3>.
- [14] Bigger R, Blaysat B, Boo C, Grewer M, Hu J, Jones A, et al. A Good Practices Guide for Digital Image Correlation. *Int Digit Image Correl Soc* 2018;94.
- [15] HexPly® 8552 Epoxy matrix (180°C/356°F curing matrix). 2016.
- [16] Lambert JP, Jonas GH. Towards standardization in terminal ballistics testing: Velocity presentation. Aberdeen, Maryland: 1976. <https://doi.org/10.21236/ada021389>.
- [17] Gómez A, Sanchez-Saez S, Barbero · Enrique. Compression impact behaviour of agglomerated cork at intermediate strain rates. *Eur J Wood Wood Prod* 2021;79:381–96. <https://doi.org/10.1007/s00107-020-01638-2>.
- [18] Sergi C, Sarasini F, Barbero E, Sanchez-Saez S, Tirillò J. Assessment of agglomerated corks and PVC foams cores crashworthiness under multiple-impact events in different loading conditions. *Polym Test* 2021;96. <https://doi.org/10.1016/j.polymertesting.2021.107061>.
- [19] Sanchez-Saez S, Barbero E, Garcia-Castillo SK, Ivañez I, Cirne J. Experimental response of agglomerated cork under multi-impact loads. *Mater Lett* 2015;160:327–30. <https://doi.org/10.1016/j.matlet.2015.08.012>.

6 FEA MODEL OF IMPACT ON SANDWICH PANELS

This chapter presents the FEA modelling of woven CFRP sandwich panels with agglomerated cork and PET foam core subjected to intermediate velocity impacts (IVI). A nonlinear/explicit finite element model is implemented to study the problem applying the continuous damage models discussed in Chapter 3 for intra-laminar and inter-laminar damage in the face-sheets. The non-linear behaviour of the core materials is also included applying the constitutive material models discussed in Chapter 4 together with a multi-axial failure criterion. The precision of the proposed FEA model for the whole sandwich panel is assessed with experimental tests presented in Chapter 5. The phases and mechanisms of damage evolution are discussed and related to the impact history. Finally, this chapter presents a comparative analysis of different parameters such as impact velocity, core thickness, impact angle, and axial preload and how they influence the mechanical response of the sandwich panels under IVI.

6.1 Introduction

The preceding chapter highlighted the importance of experimental testing in the effort of understanding the behaviour of sandwich panels that are subjected to intermediate impact loads. However, due to the complexity of the phenomenon and the limitations of the experimental procedure, there are multiple questions still unsolved. For example: What are the dominant energy dissipation mechanisms? How do these mechanisms evolve and interact with each other during the impact event? Can we predict their behaviour and apply this knowledge to design better structures against impact vulnerability? Answers to these questions have been addressed in previous research through analytical and numerical models and their conclusions are still in under constant revision. Some of the most relevant studies up to date are briefly described below.

Analytical models have been developed since 1965 to predict the behaviour of sandwich panels under localized impact [1] [2][3][4] [5]. Most of them are focused on low-velocity impacts and fall in any of the following categories: The first category is based on a quasi-static response of the panel using spring-mass models and an empirical contact law between the sandwich panel and the indenter [1], [3], [4]. The second category uses the classical plate theory for a symmetrical laminate on an elastic foundation. And the model uses energy

balance that in recent models include different energy dissipation mechanisms such as local indentation, global deformation, shear plunging, tensile fracture, delamination and core crushing [6], [5], [6], [7].

A very detailed analytical model of the dynamics of sandwich plates was proposed by Sayir and Koller [2]. In this work, an asymptotic analysis of the 3D equations of linear elasticity for sandwich plates is used to obtain independent wave equations at different frequency ranges. For sandwich panels with core thickness much larger than the face-sheet thickness, the shear stresses in the core have a high order of magnitude and the transversal normal stresses play an important role in the transmission of inertial effects between the core and the facings. The physical mechanism dominating the response of the panel varies depending on the wavelength range that is given by the relative stiffness and the thickness of the core and the face-sheets. For large wavelengths, the rotation of the facing can be neglected and the face-sheet produces “membrane stresses” that equilibrate the shear stresses transmitted by the core but produces no net moment. Disturbances with medium wavelengths travel mainly as shear waves since in-plane displacements are much smaller than transverse displacements. In this range, the induced shear stress carries most of the inertial effects. In the case of even stiffer face-sheets, shorter wavelengths disturbances are produced. This is characterized by in-plane stresses linearly distributed over the thickness of the face-sheets, each carrying bending and torsion moments. The rotation of the face-sheets becomes important and the core behaves like a shear spring connecting both face-sheets that act individually [2]. Although these models are valid in certain specific problems, their governing equations of motion are mathematically involving and usually, they have to be solved numerically.

Multiple numerical FEA models have also been proposed in the literature to study the behaviour of sandwich panels under different kinds of impact, most of them relying on industrial codes such as ABAQUS, RADIOSS or LS-DYNA [9], [8], [9], [10], [11]. Most of them use non-linear FEA explicit/dynamic procedures and continuum damage models (CDM) to simulate the initiation, growth and interaction of different failure modes in the composite face-sheets. For example, Feng et Aymerch [8] studied the effect of core density on low-velocity impact response for a sandwich with carbon/epoxy face-sheets and PVC foam core of three different densities. In their work, an explicit FEA was developed in Abaqus implementing cohesive elements at the interface between layers to simulate delamination and face-sheet/core debonding. The numerical predictions were compared

with experimental results obtained from the drop-weight tests obtaining a good correlation. This study found that the density of the foam core affects the response of the structure particularly the force-time and force-deflection curves. In contrast, the energy dissipated during impact seems independent of the core density while the induced damage is dependent on the face-sheet layup. This difference can be attributed to the different bending stiffness of the face-sheets.

Feli et al. [6] developed an explicit/dynamic FEA model in LS-DYNA of a sandwich panel subjected to high-velocity impact to validate a proposed analytical model. The face-sheets are made of E-Glass/polyester and are modelled as a transversally isotropic material using the Chag-Chang failure criteria for fibre fracture, matrix cracking and compressive failure. The core is a Divinacell H130 foam that is modelled using the MAT_CRUSHABLE_FOAM material model. Material erosion is used once the principal strain reaches a defined value; to avoid excessive distortion in the mesh. Although the experimental correlation is limited the model can predict the ballistic limit and the residual velocity showing results that agree with the analytical method.

Pascal et al. [9] analysed the impact damage of sandwich panels made from carbon/epoxy and glass/epoxy woven fabric with polyurethane foam core subjected to low and intermediate velocity impacts. Their FEA model uses an explicit scheme in the software RADIOSS and implements a semi-continuous approach for the laminates where the behaviour of the bundles of fibres and the resin are disconnected [9], [12]. The results provided by this modelling strategy are good enough to represent the damage and the contact force history observed experimentally.

Ivañez et al. [10] compared the response of E-glass/polyester sandwich panel with PVC foam core with spaced laminates both subjected to high-velocity impact. They developed an explicit FEA model in Abaqus where the face-sheet failure was implemented through a VUMAT subroutine. This subroutine included the Hou criteria for fibre failure in the longitudinal and transverse direction and Brewer-Lagace criteria for out of plane delamination. Damage degradation and element erosion were also included and the core was modelled using a crushable plasticity foam model. The residual velocity was compared with experimental data showing good agreement. It was found that if compared to the separated laminates the core has a little effect in the ballistic limit but its effect is more pronounced in the reduction of the residual velocity and damage area.

6.2 Model description

The sandwich panel (120 mm x 120 mm) is made of two square laminate face-sheets located in the top and bottom bonded to a 5 mm thickness core (Figure 6.1). Each face-sheet laminate is made from plain-woven plies of carbon/epoxy AS4/8552 with a $[90/0/\pm 45]_s$ layup. Two different core materials are studied. The first is agglomerated cork Amorim NL-20 with a density of 215 Kg/m³ and the second PET foam Airex T92.200 with a density of 211 Kg/m³. The panels are impacted at the centre with a spherical steel projectile of 7.5 mm in diameter and 7.98 g of mass at impact velocities between 40 to 170 m/s.

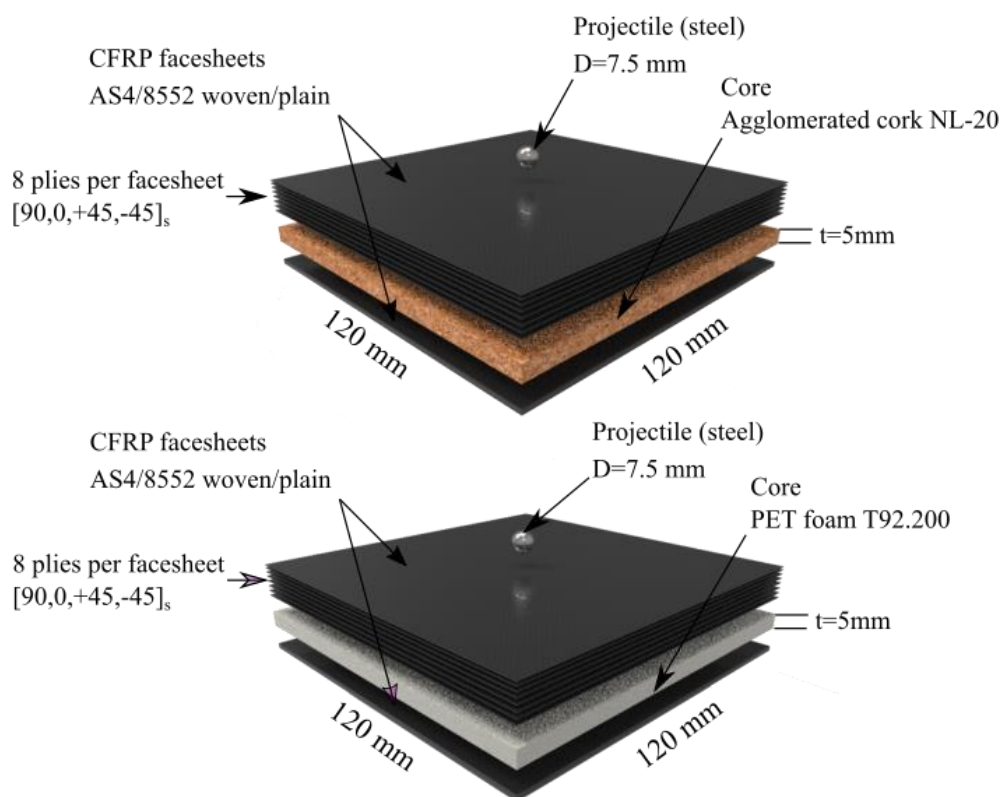


Figure 6.1. Model description (sandwich panel and projectile).
Top: Agglomerated cork core. Bottom: PET foam core

6.2.1 Mesh

The face-sheets and core are modelled as 3D deformable bodies. The front and back face-sheet laminates are modelled as a series of independent body parts to create an independent mesh for each ply and allow the definition of the cohesive interaction. All body parts are partitioned as shown in Figure 6.2 to assign a proper mesh control and create mesh refinement regions. Each ply is modelled individually using continuum shell elements with

reduced integration (SC8R) and five integration points across the thickness. The mesh is dominated by hexahedral elements and it is partitioned into five transition regions around the impact zone to improve computational efficiency. The smallest element size at the impact region is 0.5 mm while the largest element size is 4 mm at the free edges. Second-order accuracy, enhanced hourglass control and element deletion are active to avoid excessive deformations. The core is modelled in a single part using 3D hexahedral elements with reduced integration (C3DR8). The same transition regions used were used on the core plane with a 0.5 mm seed across the thickness. The smallest element size (0.5 mm) is located in the impact region while the largest element size (4 mm) is at the free edges. Enhanced hourglass control and element deletion are also used for the core elements. Finally, the projectile is also modelled with 3D hexahedral elements with reduced integration (C3DR8) with an element size of 0.5 mm.

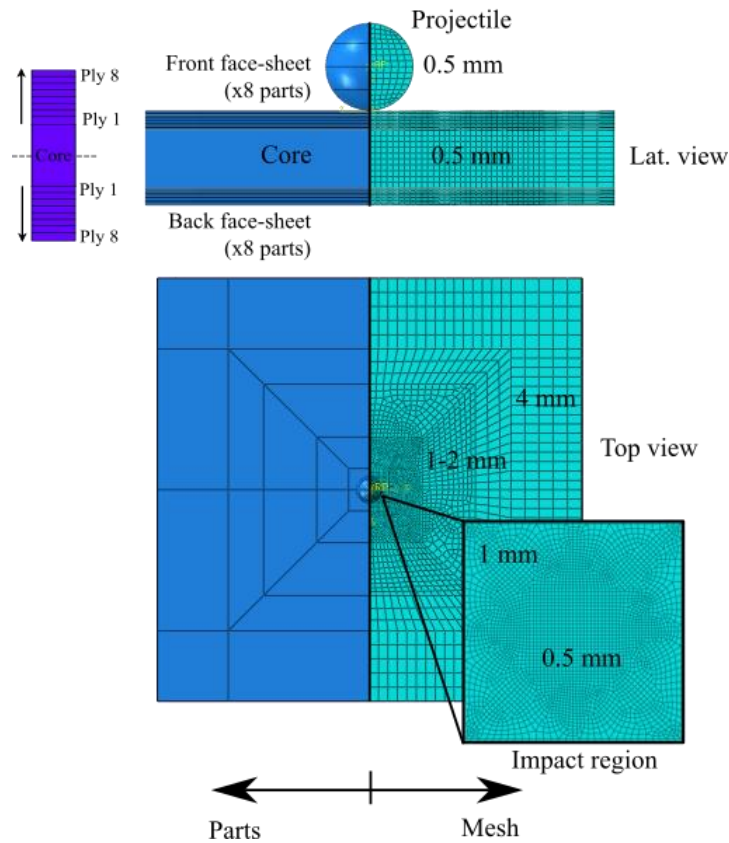


Figure 6.2. Model partitioning and mesh

6.2.2 Interactions

The general (explicit) contact algorithm is used to model all interactions in the model. Due to the complexity in the interactions the surface pairs are defined manually to ensure that

all possible interactions are included and provide a proper assignment of the different interaction properties. The following interactions are considered:

- External projectile interactions: contact interaction of the projectile surface to the ply/laminate surfaces and core external surfaces. A normal “Hard” contact property and a tangential penalty with a friction coefficient of 0.55 are used (Figure 6.3.a).
- Internal post-element deletion interactions: Contact interaction of the projectile or any ply/laminate surface to the internal mesh of the core or other ply/laminate after element deletion in a previous time step. To assign this interaction a node-based surface is created to include the internal nodes of the part. A normal “Hard” contact property and a tangential penalty with a friction coefficient of 0.75 are assigned for this interaction (Figure 6.3.b).
- Cohesive interactions: Adhesive interaction between the top laminate plies or between the core top/bottom surface to the face-sheet internal surface. Cohesive behaviour with damage is applied (Figure 6.3.c).

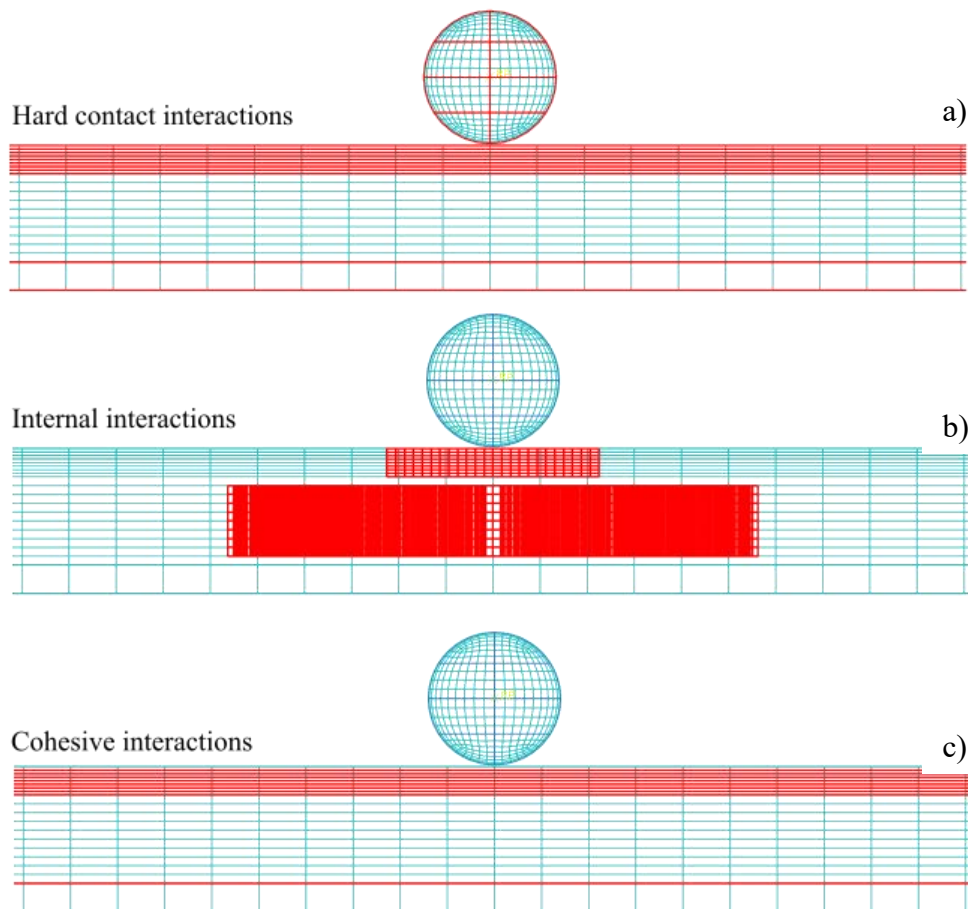


Figure 6.3. Interaction categories. a) projectile interaction, b) internal post-element deletion interaction, c) cohesive interactions

6.2.3 Boundary conditions and initial conditions

The sandwich panels are retained in place by two supports (top and bottom) that restrain the displacement of the sandwich panel along the impact direction. These supports are modelled as rigid shell geometries. An initial velocity field is applied over all projectile nodes. A reference point is tied to the internal centre nodes of the projectile to track its position and velocity. Nonlinear geometry (NLgeom) is activated and the time increment is automatically estimated by the software based on the smallest element size.

6.2.4 Materials

The constitutive material models and properties used for each component are discussed in previous chapters. The reader is encouraged to refer to the following sections for further details:

- a) Face-sheet and projectile: Same as in chapter 3 section 3.1 and 3.2.
- b) Agglomerated cork core: Same as in chapter 4 section 4.3.4
- c) PET foam core: Same as in chapter 4 section 4.3.5

Additionally, in the case of both core materials, element deletion is implemented through a VUSDFLD user subroutine using the Tsai-Wu fracture criteria (Appendix B). Uniaxial tensile and compressive strength (X , and X') are obtained from the experimental test presented in section 4.2. The shear strength (S) is obtained from the literature in [13] and [14] respectively.

Property	Agglomerated cork	PET foam
X (MPa)	1.1	3.0
X' (MPa)	13.1	12.1
S (MPa)	0.63	2.0

Table 6.1. Axial and shear strength of the core materials as implemented in the Tsai-Wu failure criteria.

6.3 Results

The analysis of results is addressed in two different subsections. The first one provides a qualitative analysis of the impact phenomena in the agglomerated cork panel focusing on two different scenarios (with and without perforation of the top face-sheet). Results suggest that the impact process occurs in different phases that are discussed together with their dependency on the top face-sheet perforation. The second subsection analyses the differences encountered in the impact response of the PET foam sandwich panel.

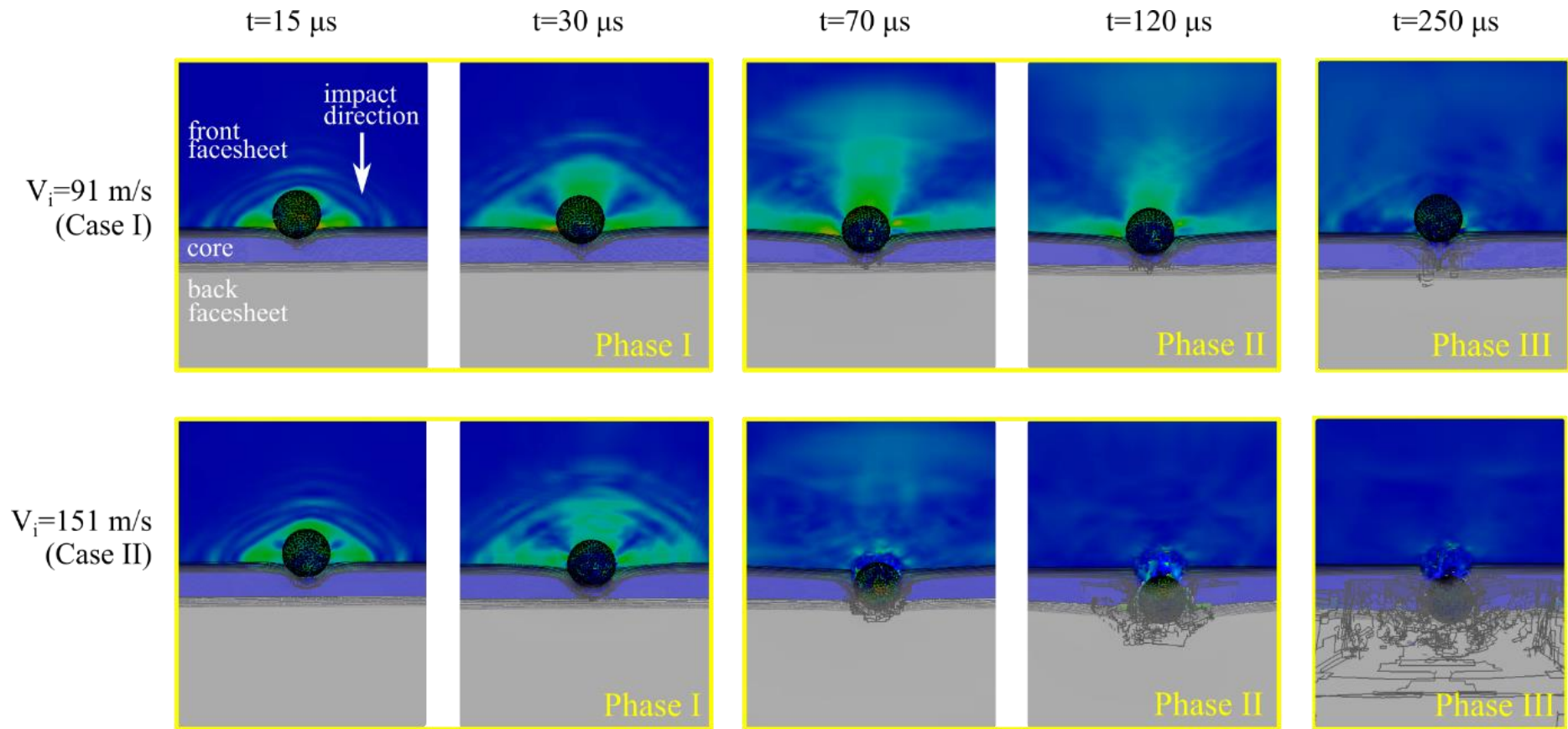


Figure 6.4. Comparison in the impact evolution without perforation (case I) and with perforation (case II) of the front face-sheet. Agglomerated cork sandwich panel

6.3.1 Impact phases in sandwich panels with an agglomerated cork core.

The dynamic response of the panel varies substantially depending on whether or not the projectile perforates the front face-sheet. For this reason, two different impact velocities below the ballistic limit are studied in detail:

Case I. The projectile does not perforate the front face-sheet ($V_i=91$ m/s)

Case II. The projectile does not perforate the back face-sheet ($V_i=151$ m/s)

The impact evolution is studied for each impact case, and three impact phases are identified and depicted in Figure 6.4. The physical mechanisms dominating each phase are discussed in the following paragraphs together with some hypotheses made by the author based on the quantitative and qualitative results obtained in each FEA model.

6.3.1.1 Phase I

This phase occurs between the time of initial contact and the time in which there is a reflection of the travelling waves across the panel thickness. For the panel discussed here, this corresponds to a time lapse between $0 \mu\text{s}$ to $30 \mu\text{s}$ in Figure 6.4. The perturbation created by the projectile propagates across the thickness and in the radial direction. The wavefront covers the whole thickness in just $30 \mu\text{s}$ while it takes $120 \mu\text{s}$ to reach the lateral edges of the panel. In this phase, the deformation is highly localized around the impact region without deformation in the back face-sheet.

In the front face-sheet, the contact force induces a high level of axial stresses around the contact region. At each ply, this level of stress produces tensile failure along the fibre direction creating a cruciform pattern that propagates radially as the impact continues (Figure 6.5). The pattern is also observed in plies with a different orientation (e.g. $\pm 45^\circ$) in which the cross-shape pattern is rotated giving an X-shape pattern. This is accompanied by the onset of delamination that appears next to the intra-laminar cracks propagating at almost the same extent as the tip of the intra-laminar cracks. The delamination area varies for different plies in the face-sheet getting larger in those plies located closer to the core (Figure 6.5). This agrees with the previous observation considering that plies closer to the core show larger intra-laminar cracks (Figure 6.5). A similar observation was found in [15] for ballistic impact over GFRP sandwich panels with PVC foam core. For the first ply in contact with the projectile, the cruciform damage pattern is not visible, but instead, the damage can be better approximated by a circular region with the size of projectile diameter.

In this ply, fibre failure and delamination are homogeneously distributed what creates premature element deletion due to the critical stress concentration.

At this point, the projectile has already deflected the impact region by 2.3 mm and has progressively indented all plies of the front face-sheet. Similar crack patterns have been reported in previous research for monolithic woven carbon/epoxy laminates and sandwich panels of graphite and Kevlar face-sheets with PVC foam core [9], [16].

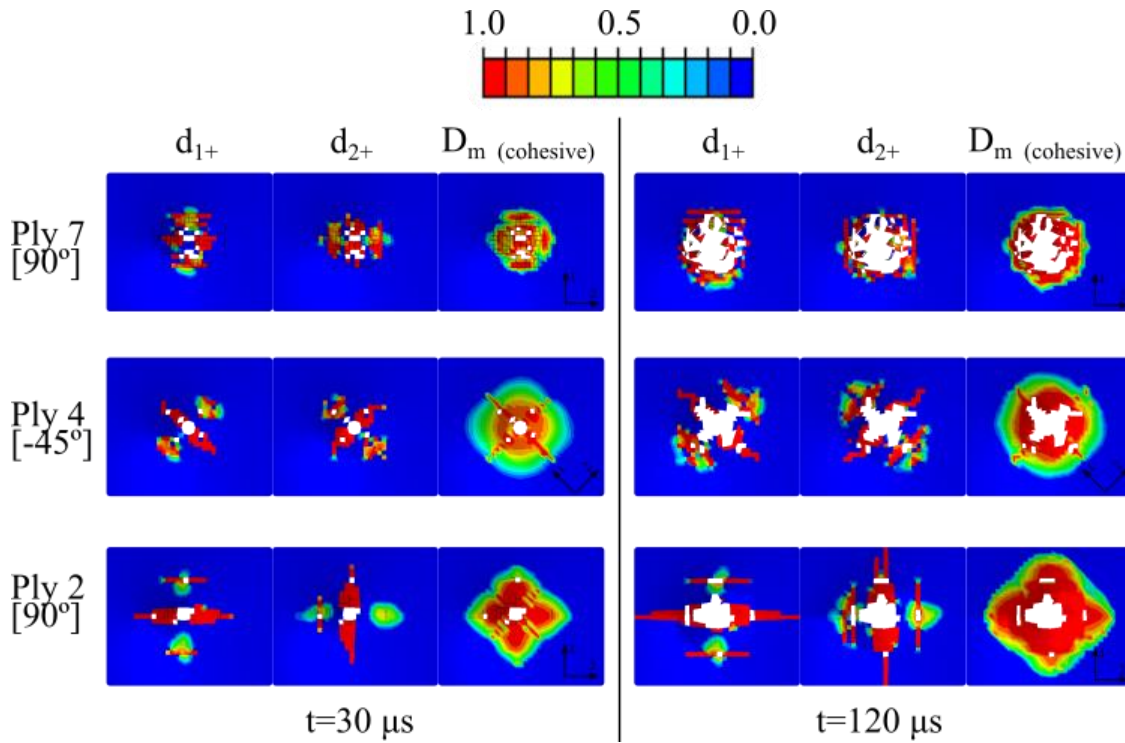


Figure 6.5. Initial intra-laminar and inter-laminar damage evolution in three different plies of the front face-sheet ($V_i=91 \text{ m/s}$)

The indentation produced by the projectile in both the face-sheet and core creates in the core a complex multi-axial 3D strain state that is dominated by compression and shear strains in the impact direction, Figure 6.6. The strain level increases dramatically in the vicinity of the impact region propagating radially and across the thickness. Initially, the response of the core is mainly elastic with large displacements and little failure. As the impact progresses the core starts fail in the vicinity of the impact region creating a cruciform crack pattern that propagates radially and through the thickness. This can be appreciated in Figure 6.9 together with the projectile travel.

The evolution of the model energies during impact is depicted in Figure 6.7. During phase-I part of the initial kinetic energy of the projectile is rapidly transformed into internal energy in the panel (elastic strain energy, damage energy, and plastic dissipation) due to projectile deceleration, panel local deformation and damage.

FEA MODEL OF IMPACT ON SANDWICH PANELS

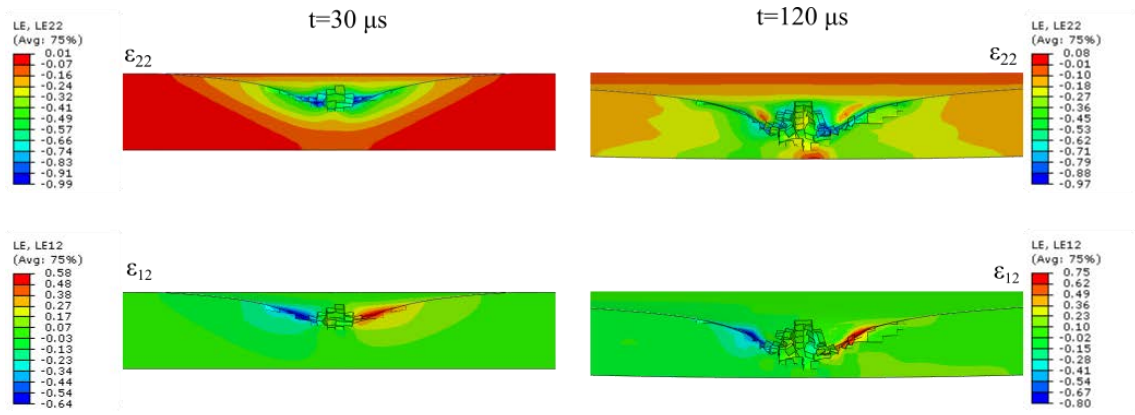


Figure 6.6. Strain distribution in the midsection of the core ($V=91$ m/s).

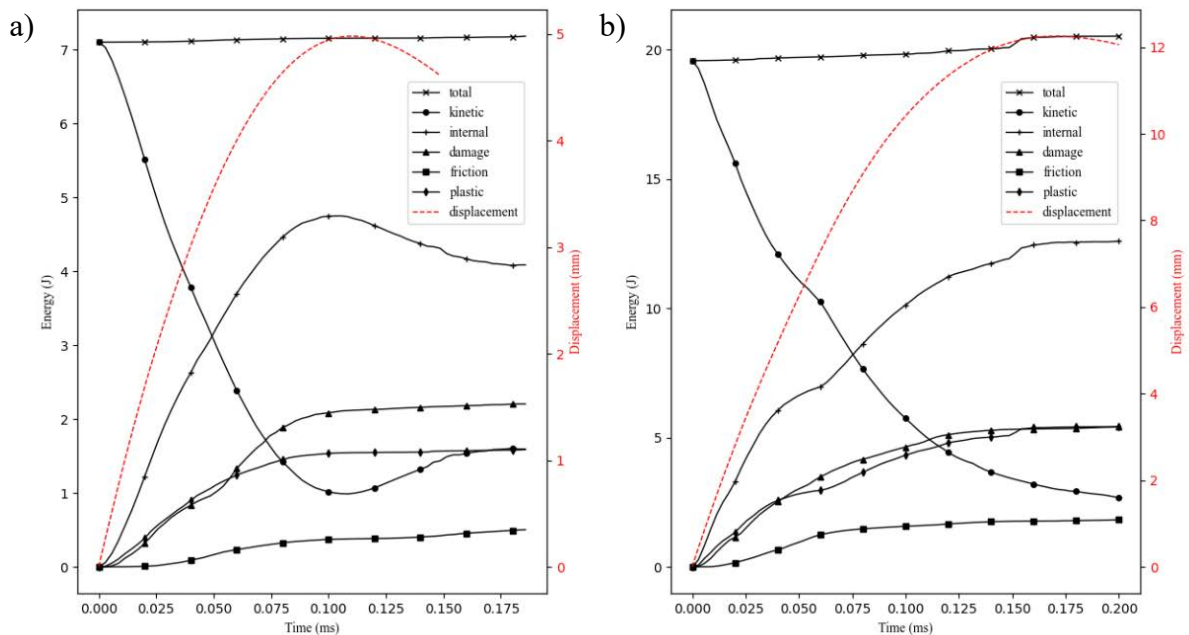


Figure 6.7. Evolution of the model energy and projectile displacement (Agglomerated cork sandwich panel). a) $V_i=91$ m/s, b) $V_i=151$ m/s impact

6.3.1.2 Phase II

Phase II occurs between the travelling wave reflection in the back face-sheet ($30 \mu\text{s}$) and the maximum projectile's displacement ($120 \mu\text{s}$ for case I and $170 \mu\text{s}$ for case II). This phase is different in both analysed cases.

a) Case I:

After the initial localized deformation of the front face-sheet, the back face-sheet starts deforming and the response of the panel is influenced by the interaction of all components of the sandwich panel. As the projectile advances the local deformation and indentation produced in the upper plies of the front face-sheet make the contacting plies take the

projectile contour. As a result, the contact area increases and moves outwards from the initial contact point reaching almost the diameter of the projectile. This effect decreases the stress concentration in the contact region in both the projectile and the laminate.

Intra-laminar damage and delamination continue increasing and eventually reach an asymptotic maximum value once the projectile reaches the maximum penetration in the panel ($t=120 \mu\text{s}$). Other non-conservative energy dissipation mechanisms such as friction and plastic dissipation show the same tendency as can be observed from the energy history plot in Figure 6.7.a.

Not all the initial kinetic energy is dissipated as internal energy in the form of strain energy, damage or plasticity dissipation. Some other energy is dissipated as a product of the momentum transfer between the projectile and the initially static panel, through the initial impulse that generates a travelling wave and propagates radially across the panel. The magnitude of the transferred kinetic energy can be estimated from the kinetic energy of the whole system at around $t=120 \mu\text{s}$ when the projectile has reached maximum penetration and its velocity is zero.

b) Case II:

For case II ($V_i=151 \text{ m/s}$), the indentation is followed by a penetration phase, from wave reflection to maximum penetration ($30 \mu\text{s}$ to $260 \mu\text{s}$).

In case II, the projectile penetrates the front face-sheet and continues damaging the core, until it contacts the back face-sheet. At $t= 50 \mu\text{s}$, the projectile penetrates with its whole diameter the front face-sheet and touches the back face-sheet at around $t=70 \mu\text{s}$, reaching the maximum displacement at $t=170 \mu\text{s}$.

During the penetration, the intra-laminar cross-shaped cracks in the front face-sheet keep growing what reduces the local stiffness of the laminate in the contact region. With cracks long enough the local stiffness of each ply is heavily reduced, and the projectile advance induces the creation of petal shape segments giving space for the projectile advance (Figure 6.8). This phenomenon is more visible in plies opposite to the initial contact point (close to the core). However, in plies next to the contact point this phenomenon is less visible due to the fragmentation of the material. Similar petal-shaped crack patterns have been observed by Lopez-Puente et al. [17] in high-velocity impacts of woven CFRP laminates.

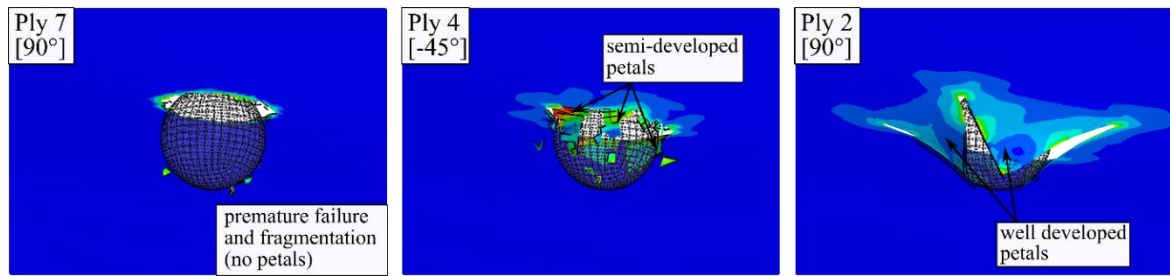


Figure 6.8. Penetration petals for different plies in the front face-sheet. $V_i=151$ m/s,
 $t=70\mu\text{s}$

From Figure 6.7.b it can be observed that the inter-laminar damage energy shows a steep increase until $t=120\ \mu\text{s}$, the moment at which the projectile has almost completely penetrated the top laminate. At this point, the delamination and the intra-laminar damage have reached a maximum and do not continue growing. It is important to notice that the damage dissipation energy accounts for a large proportion of the maximum internal energy; around 40% for both impact scenarios (Figure 6.7). When the projectile completely penetrates the front face-sheet the core becomes exposed. Since its multi-axial strength is small, further core failure appears, and the core is unable to contain the advance of the projectile but it slightly decreases its velocity. Once the projectile contacts the back face-sheet ($t=70\ \mu\text{s}$) its velocity is substantially reduced as a product of the energy dissipated in the back face-sheet due to damage and deflection. Figure 6.9 shows that the impact of the projectile on the back face-sheet tries to pull apart the front face-sheet from the back face-sheet by breaking the core that shows little resistance due to its low multi-axial strength. Two failure regions were identified in the core the first in the bond-line next to the back face-sheet and the second in the interior of the core. As the impact continues both regions will grow around the impact region reaching a longitude many times larger than the projectile diameter and eventually interacting together. The extend of the crack growth in the vicinity of the bond-line and its mechanism of failure can be appreciated in Figure 6.10 where the Tsai-Wu failure index is plotted at different times. A similar phenomenon has been described by [15] for sandwich panels with GFRP face-sheets and PVC foam core subjected to ballistic impact.

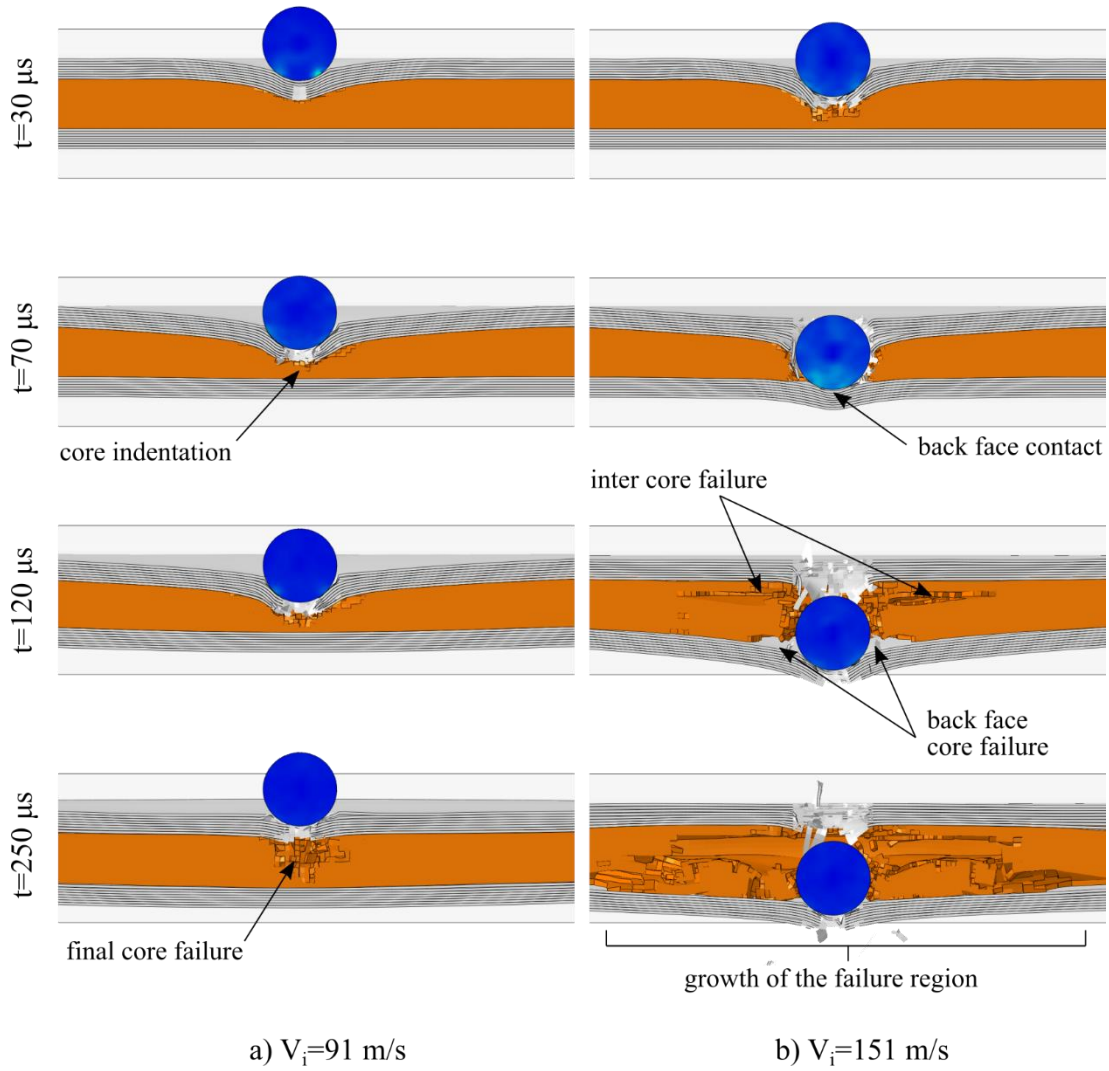


Figure 6.9. Comparison in the impact evolution a) without perforation of the front face-sheet and b) with perforation of the faces-sheet.

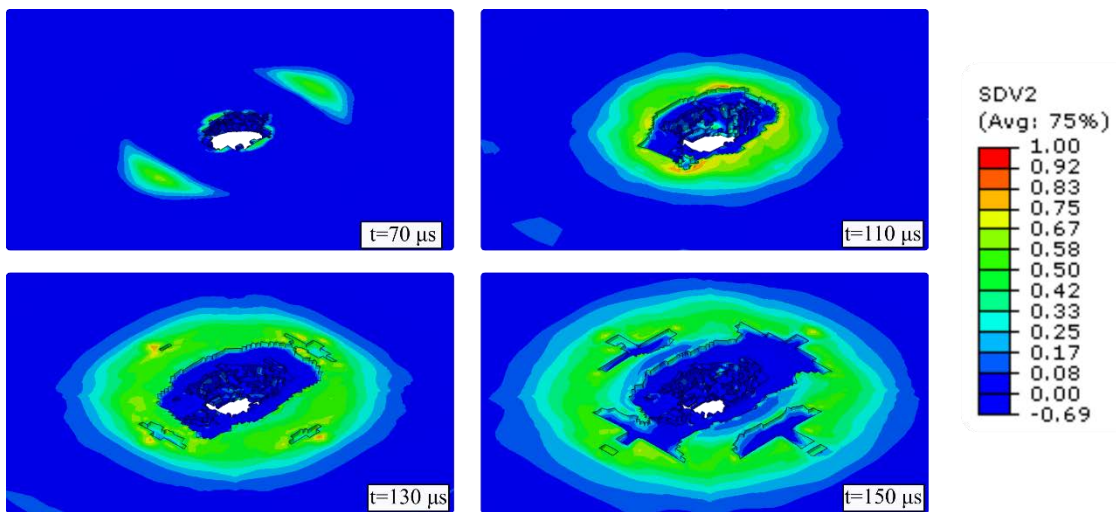


Figure 6.10. Tsai-Wu index for core failure in the bottom surface ($V_i=151 \text{ m/s}$)

6.3.1.3 Phase III

This last phase occurs between the maximum displacement of the projectile and the projectile spring back. In Case I, from 120 μs to the end of the impact while in Case II, from 170 μs to the end of the impact. With the projectile at its maximum displacement inside the panel, the stress level in the front face-sheet decreases and part of the strain energy stored as the elastic deformation of the face-sheet is released as kinetic energy to the laminate and mechanical work over the projectile. A similar phenomenon occurs in the core where the strain energy due to compression is converted into kinetic energy on the face-sheets favouring the spring back recovery of the projectile. This phenomenon occurs in both impact cases. Figure 6.7 shows how decrements in strain energy (internal energy) at the end of the impact are accompanied by increments in kinetic energy. From its stand-still position at maximum displacement to the end of the impact the projectile recovers certain kinetic energy as a product of the spring back of the front face-sheet and the core. At the end of the impact (for case I), the FEA model predicts a projectile rebound velocity of 25.3 m/s. This velocity is also measured experimentally obtaining a rebound velocity of 19.6 m/s. Although there is a small difference, the FEA model can predict the rebound velocity with an error of 6% of the initial impact velocity.

Another observation is that the elastic return of the back face-sheet is delayed with respect to the instant of time in which the projectile reaches the maximum penetration. This effect occurs in both impact cases and is associated with the delay in which the initial disturbance reaches the front and back face-sheet. Once the projectile has left the panel, the remaining strain energy and kinetic energy continue fluctuating in phase due to the oscillations taking place. However, the magnitude of these oscillations is unable to create further damage and in the case of an externally dissipative environment, these oscillations will die over time.

6.3.2 Impact phases in sandwich panels with PET foam core

The behaviour of the sandwich panels with PET foam core presents the same impact phases previously described for the agglomerated cork sandwich panels (Figure 6.11). However, a couple of important differences in its response are discussed as follows.

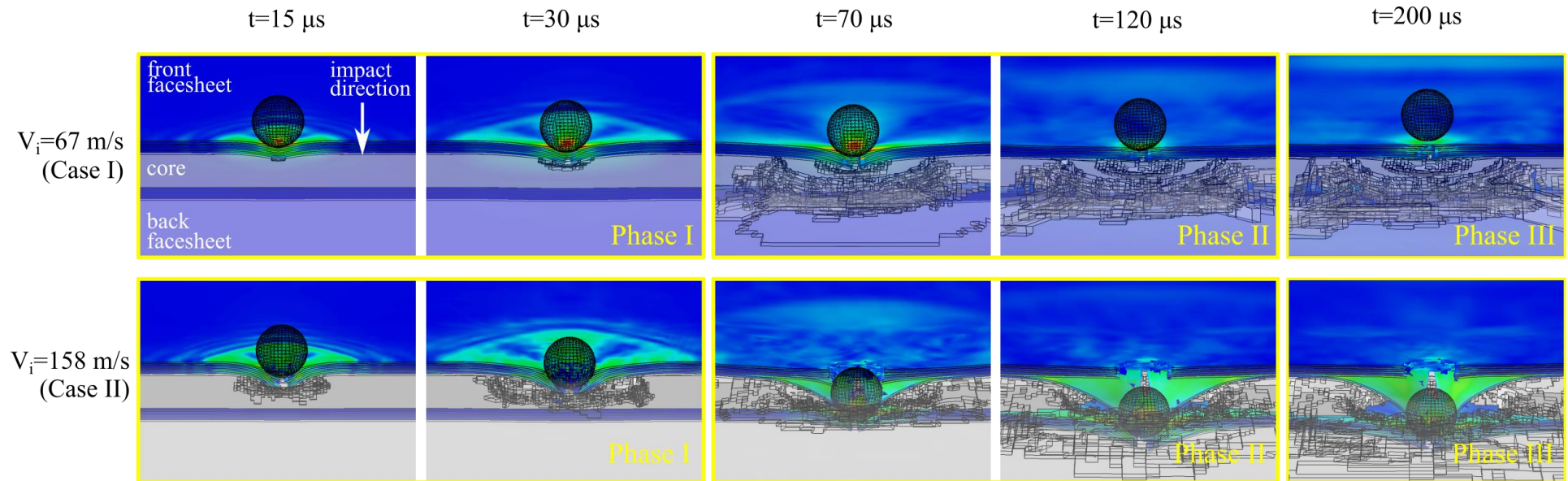


Figure 6.11. Comparison in the impact evolution without perforation (case I) and with perforation (case II) of the front face-sheet. PET foam core sandwich panel

The PET core shows a stiffer response with faster wave propagation and smaller displacements around the impact region. This phenomenon is expected since the overall stiffness of the PET foam is larger than the agglomerated cork despite having almost the same density. Additionally, its response is characterized by the early development of a fracture region in the top surface of the core next to the impact point. Figure 6.12 shows the evolution of this fracture region in the PET foam core by depicting the Tsai-Wu criteria. Element erosion due to crushing is observed below the impact point which creates a crater that grows as the impact progresses. A concentric ring of eroded elements is also formed in the core top surface. This fracture ring has a diameter larger than the projectile diameter and grows through the thickness forming a cone that eventually reaches the bottom surface of the core (Figure 6.14). This phenomenon triggers fracture in the bottom surface that grows radially extending far away from the impact location. This kind of failure mechanism is also observed in the inspected test specimens presented in chapter 5, section 5.3, and has been reported by other authors for sandwich panels of GRFP face-sheets and PVC foam core under intermediate velocity impact [15], [18]. This result contrasts the previously discussed response of the agglomerated cork panel, where the core shows an initial highly elastic response with large displacements and little fracture (section 6.3.1).

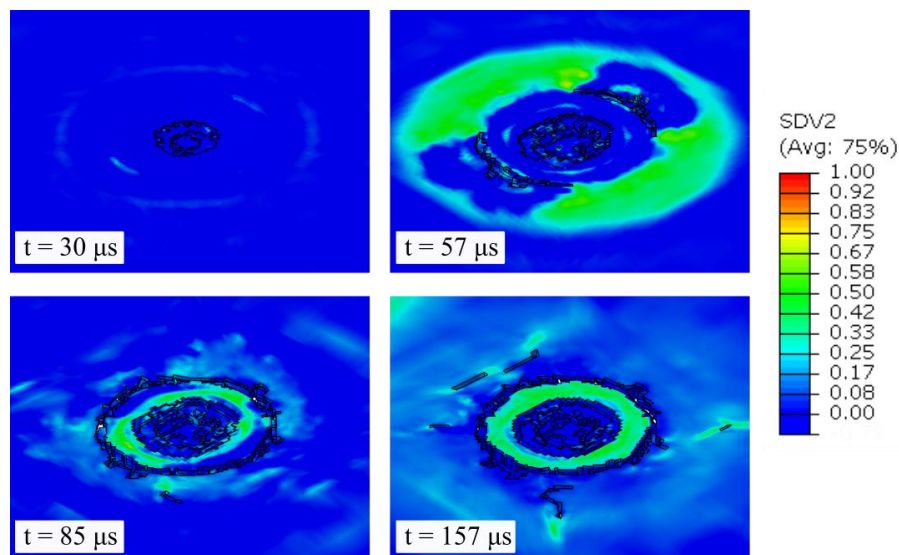


Figure 6.12. Evolution of the Tsai-Wu failure criteria in the PET foam core top surface ($V_i=67 \text{ m/s}$)

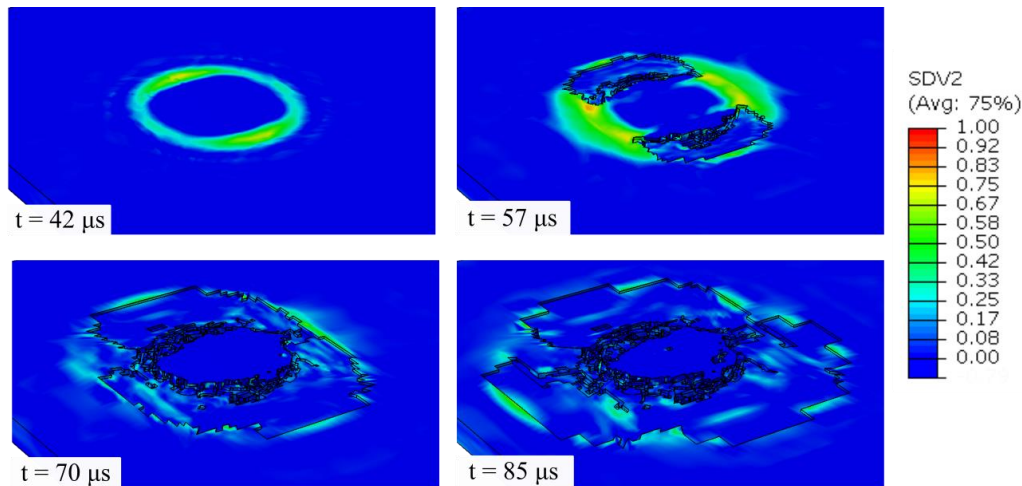


Figure 6.13. Evolution of the Tsai-Wu failure criteria in the PET foam core bottom surface ($V_i=67$ m/s)

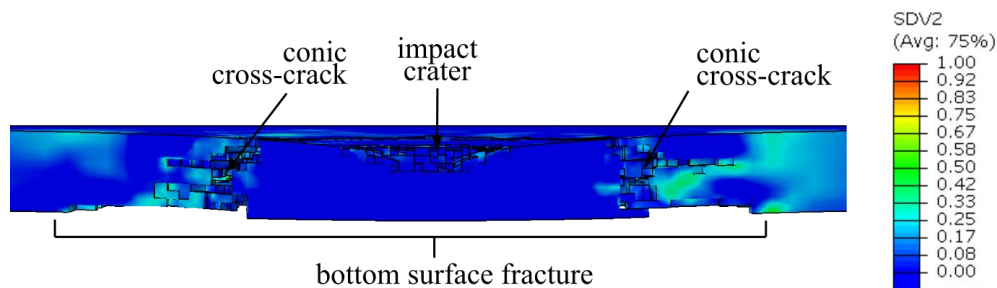


Figure 6.14. Fracture in the cross-section for the PET foam core ($V=67$ m/s, $t=85$ μ s)

In the PET panel, plastic dissipation is the main mechanism of energy dissipation contrary to the cork panel where the damage energy is the main mechanism of energy dissipation. This is observed when comparing the evolution of the energy in each model (Figure 6.7 for agglomerated cork and Figure 6.15 for PET foam). The difference in the dominant dissipation mechanism can be attributed to two reasons. First, the localized compression in the upper elements of the PET core are subjected to plastification in the plateau region until failure and element erosion occurs. Second, in PET sandwich panels damage only accounts for intra-laminar and inter-laminar damage while in the case of the agglomerated cork panel it also includes core damage due to Mullin's effect.

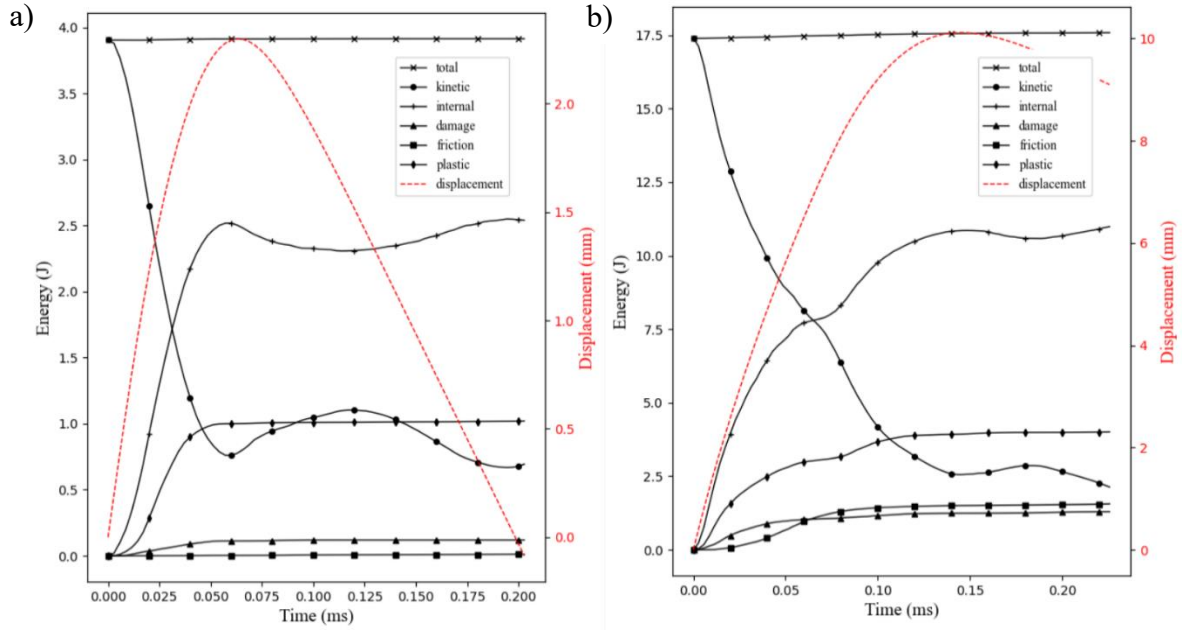


Figure 6.15. Evolution of the model energy and projectile displacement (PET foam core). a) $V_i = 67$ m/s, b) $V_i = 142$ m/s impact

6.4 Validation

6.4.1 Panel perforation

Before starting the discussion of the results, it is convenient to validate that the FEA model of both sandwich panels reproduces the experimental test presented in chapter 5. The first variable to determine the precision of the model is its ability to predict whether there is perforation of the front face-sheet and core at five different impact velocities below the ballistic limit. Table 6.2 and

V_i (m/s)	Experimental		FEA	
	Pass? (front)	Pass? (back)	Pass? (front)	Pass? (back)
67.6	NO	NO	NO	NO
73.5	NO	NO	NO	NO
111.5	YES	NO	NO	NO
142.7	YES	NO	YES	NO
158.1	YES	YES	YES	NO

Table 6.3 shows a comparison between the FEA predictions and the observations made in the experiments. Both models are able to predict whether the projectile perforates the front face-sheet.

Vi (m/s)	Experimental		FEA	
	Pass? (front)	Pass? (back)	Pass? (front)	Pass? (back)
70.6	NO	NO	NO	NO
91.3	NO	NO	NO	NO
109.6	YES	NO	YES	NO
113.2	YES	NO	YES	NO
151.4	YES	NO	YES	NO

Table 6.2. Perforation of the sandwich panel. Agglomerated cork core

Vi (m/s)	Experimental		FEA	
	Pass? (front)	Pass? (back)	Pass? (front)	Pass? (back)
67.6	NO	NO	NO	NO
73.5	NO	NO	NO	NO
111.5	YES	NO	NO	NO
142.7	YES	NO	YES	NO
158.1	YES	YES	YES	NO

Table 6.3. Perforation of the sandwich panel. PET foam core

6.4.2 Cross-section displacements

The precision of the model to predict the deformation of the structure during the impact is studied. From the experimental tests discussed in chapter 5, the out-of-plane deflection of the front face-sheet along the sandwich mid-plane is measured using 3D DIC. These results are compared with those obtained from the FEA model. Figure 6.16 and Figure 6.17 shows the panel deformation for an impact velocity of 113 m/s for the agglomerated cork panel and 134 m/s for the PET foam panel. In both cases, the model predicts with high accuracy the initial response of the sandwich, capturing the shape of the disturbance created by the projectile as well as its propagation. In both figures, there are no data in the impact region for both the DIC and FEA due to the difficulty of measuring displacements in the vicinity of the impact location. In the case of the DIC analysis, the displacements can not be measured due to the shadow created by the projectile in its path. In the FEA analysis, they are no data due to the erosion of the elements near the impact point.

FEA MODEL OF IMPACT ON SANDWICH PANELS

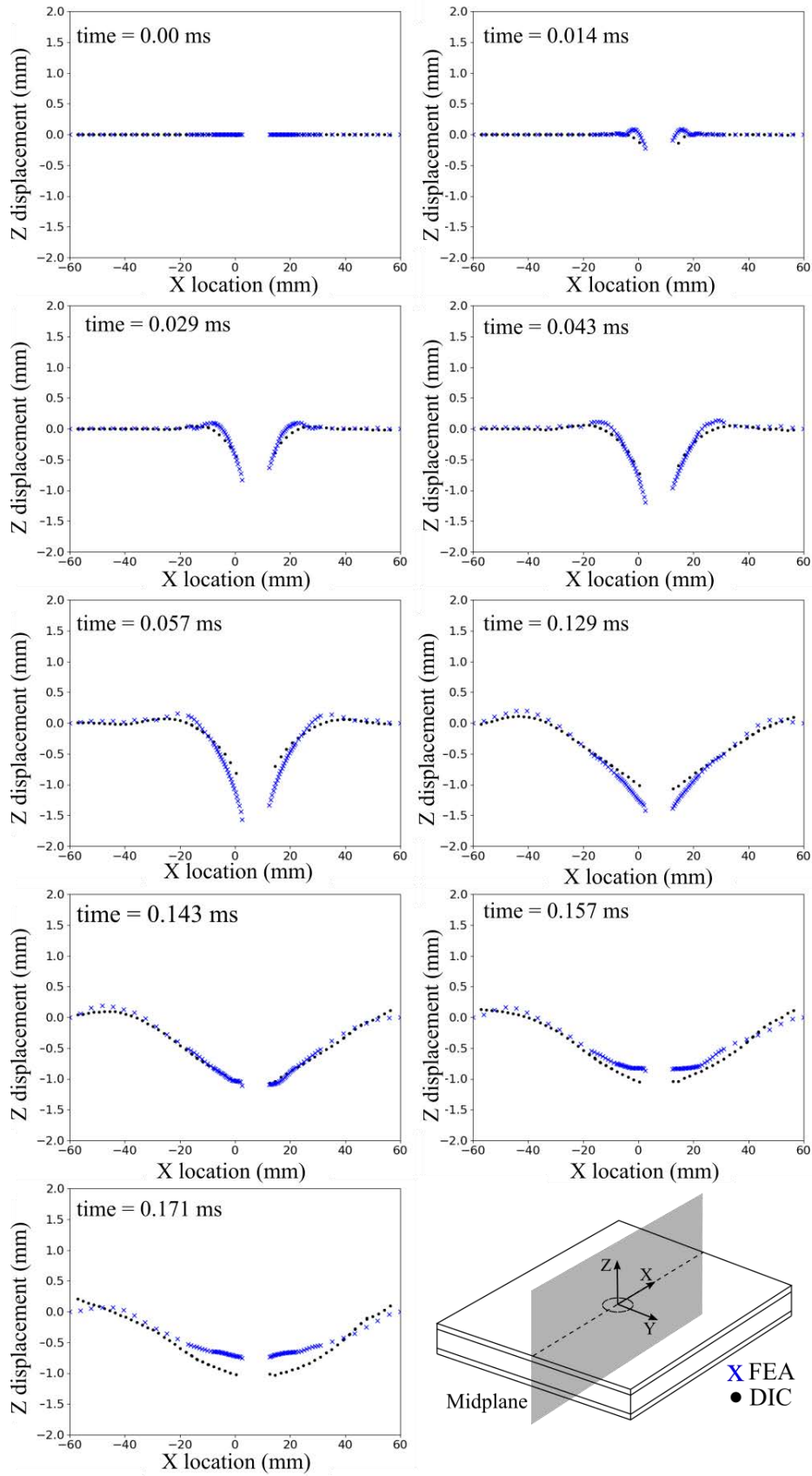


Figure 6.16. Deflection of the front face-sheet mid-plane. Comparison between FEA model results and DIC measurements. Sandwich panel with agglomerated cork core ($V_i=113$ m/s)

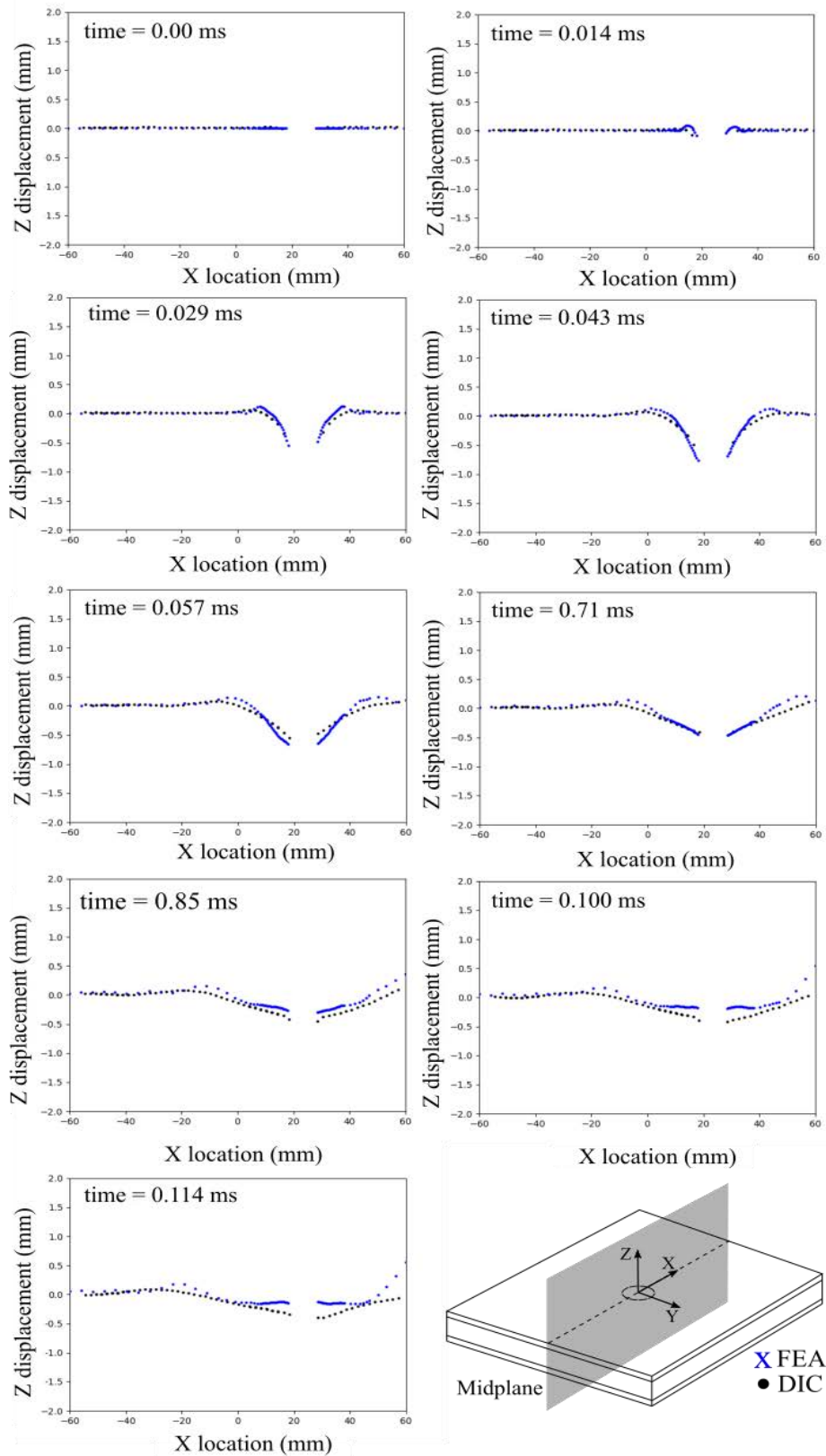


Figure 6.17. Deflection of the front face-sheet mid-plane. Comparison between FEA model results and DIC measurements. Sandwich panel with PET foam core ($V_i=134$ m/s)

6.4.3 Damage morphology

At the qualitative level, the FEA model reproduces multiple features of the damage morphology encountered during the inspection of the real-world test specimens. The first feature is the superficial damage over the front face-sheet. Figure 6.18 and Figure 6.19 show a comparison of the superficial damage for both sandwich panels at two different impact velocities. A circular dent is visible in both the FEA model and inspected specimens for those impact velocities where there is no perforation. In contrast, if perforation occurs a circular crater of roughly the same size of the projectile diameter is formed.

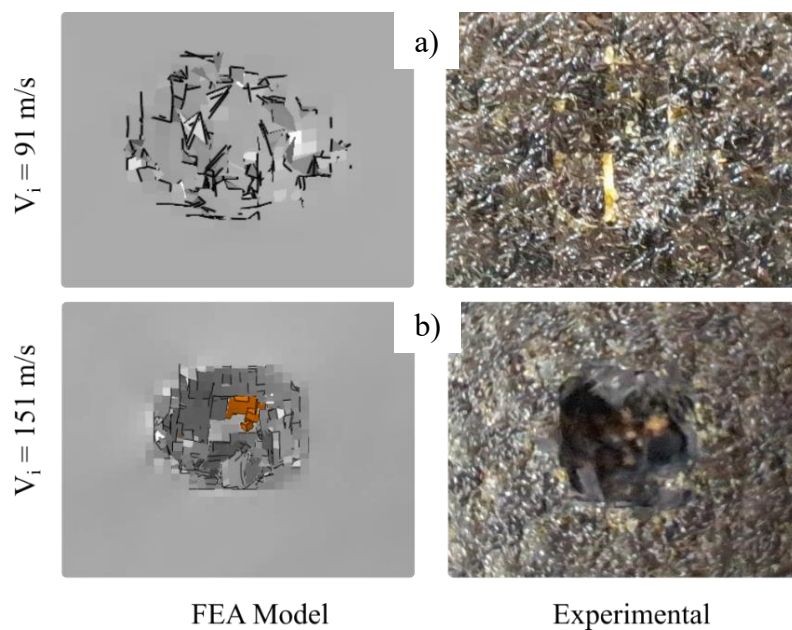


Figure 6.18. Superficial damage in the front face-sheet at two different impact velocities. Comparison FEA model and visually inspected test specimens (Agglomerated cork sandwich panel). a) circular indentation. b) circular crater.

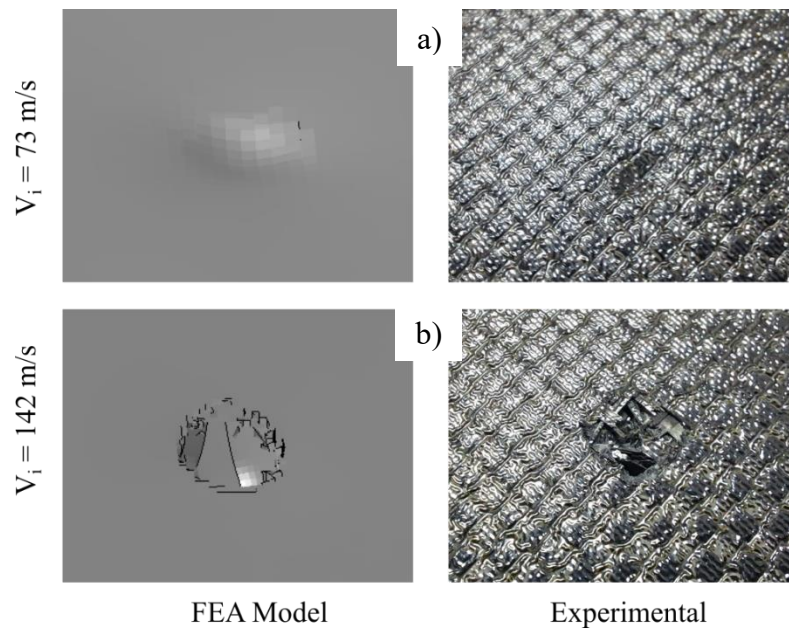


Figure 6.19. Superficial damage in the front face-sheet at two different impact velocities. Comparison of FEA model and visually inspected test specimens (PET foam sandwich panel). a) circular indentation. b) circular crater.

The model is also able to reproduce with accuracy the damage morphology in the cross-section of the sandwich panels. Figure 6.20 presents a comparison between the results obtained by the FEA model and those obtained using X-ray computed tomography (XCT) inspection. Two different impact cases are depicted, the first without penetration of the front face-sheet and the second with penetration of the front face-sheet.

From the first case ($V_i = 76$ m/s for agglomerated cork and $V_i = 67$ m/s for PET foam) it is observed that the FEA model captures the intra-laminar fracture and delamination of the front face-sheet as well as the core fracture visualized in the XCT scan. The FEA model also predicts that the back face-sheet should be intact under these impact velocities, something that is confirmed by the XCT images.

From the second case ($V_i = 170$ m/s for agglomerated cork and $V_i = 158$ m/s for PET foam) the model can reproduce the extend of the penetration, the intra-laminar damage and delamination in both face-sheets as well as the core fracture along the projectile path.

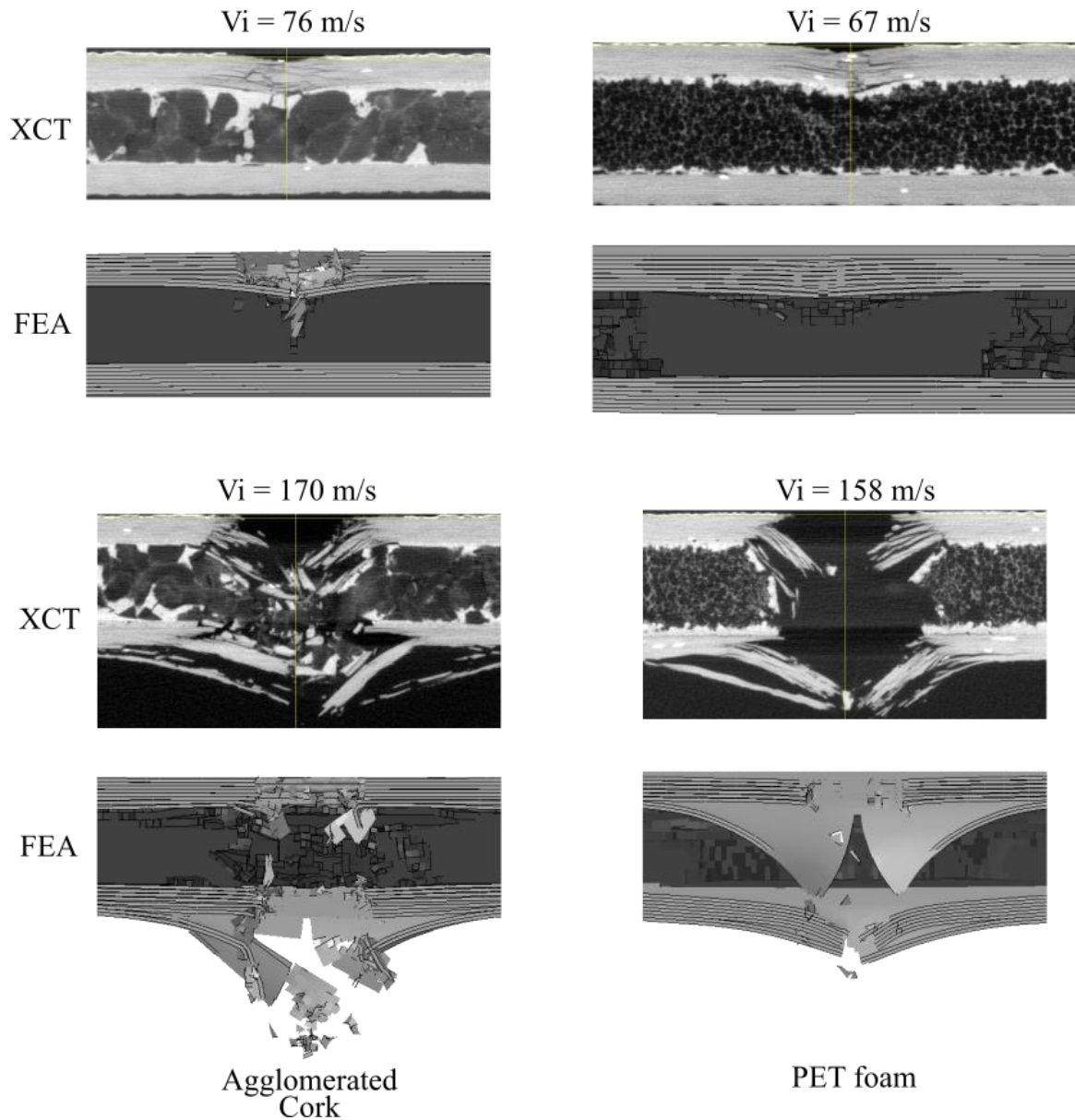


Figure 6.20. Damage morphology of the panel cross-section at two different impact velocities. Comparison of FEA model and X-ray Computed Tomography (XCT)

6.5 Comparative analysis of parameters

After understanding the steps occurring during the impact event in sandwich panels the purpose of this section is to determine the influence of different parameters in the response of the panel. The parameters analysed are four: impact velocity, core thickness, impact angle, and axial preload (Figure 6.21). They are chosen based on the relevance that they could arise to structural analysts during the early design phases of lightweight structures. This since little previous research has been carried out in the influence of these parameters on the impact behaviour of sandwich panels with CFRP face-sheets.

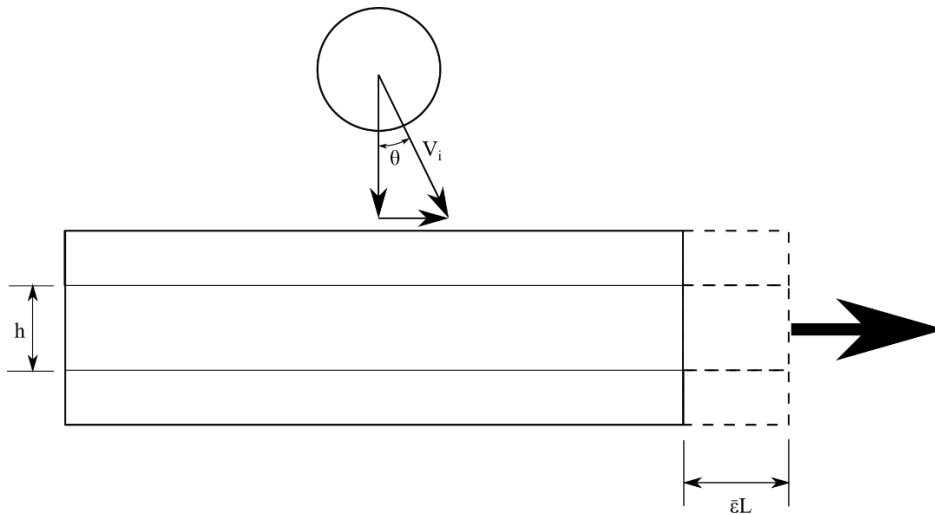


Figure 6.21. Parameters for the sensitivity analysis

The response of the sandwich panels will be analyzed using different control variables that can be compared quantitatively and qualitatively. This first set of variables are related to the projectile travel during the impact since it provides an insightful manner to differentiate the different impact phases. The deformation of the panel midsection is also analyzed to visually observe the difference in the elastic response of the panel when different parameters are changed. The damage evolution in the sandwich laminates is analyzed through the projected cohesive damaged area. Finally, the evolution of the model's energies is also studied since it provides valuable information on the evolution of the different energy dissipation mechanisms and the interaction of the internal and kinetic energy.

The definition of the FEA models presented in this section is the same than in the previous section, except for the specific changes in parameters indicated for each case. An Abaqus parametric script is developed to generate and run all FEA models of the comparative analysis. In this way, the model definition (geometry, material, mesh, boundary conditions, etc...) is the same for all cases and there is no human error that can compromise the results.

6.5.1 Impact velocity

The first parameter in this comparative study is the impact velocity. Here the sandwich panel is defined the same as in the previous section except for boundary conditions for the panel support. In this analysis and the remaining comparative analyses, all lateral faces are simply supported in order to reduce computational time and standardize the boundary. The impact location is also maintained the same at the geometrical centre point and the same impact velocities are analysed in both sandwich panels. The range of impact velocities analysed in this section is:

$$40 \text{ m/s} < V_i < 160 \text{ m/s}$$

Figure 6.22 and Figure 6.23 show the evolution of the displacement and velocity of the projectile at different impact velocities. From the figures, the projectile begins its travel at the contact point with its initial impact velocity. As the impact continues, the projectile starts losing its velocity as it advances into the panel. Eventually, the projectile loses all its velocity at the same instant of time that it reaches the maximum displacement. After that, the projectile returns to its initial position with a final negative (rebound) velocity.

A couple of interesting observations are made from these figures.

- The maximum projectile displacement increases with impact velocity (Figure 6.24). At impact velocities larger than 95 m/s the maximum displacement of the projectile seems larger for agglomerated cork panels.
- For low impact velocities ($V_i \leq 100 \text{ m/s}$) the rebound velocity seems to be a linear function of the impact velocity. For impact velocities between 60 m/s to 100 m/s, panels with agglomerated cork shows a stronger spring back than panels with PET foam (Figure 6.25)
- The duration of the impact increases with the impact velocity
- The ratio between the projectile kinetic energy at the end of impact (E_r) and the impact energy (E_i) varies linearly with respect to the impact velocity. This ratio can vary between 1% to 15% (Figure 6.26).

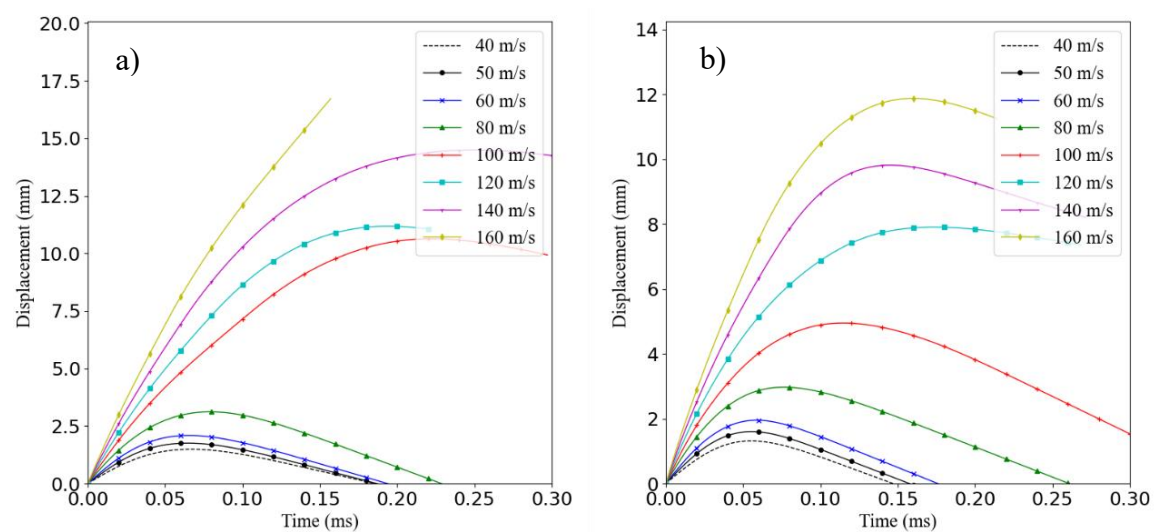


Figure 6.22. Projectile displacement vs time at different impact velocities. Comparison of sandwich panels with different core materials.
a) Agglomerated cork core. b) PET foam core.

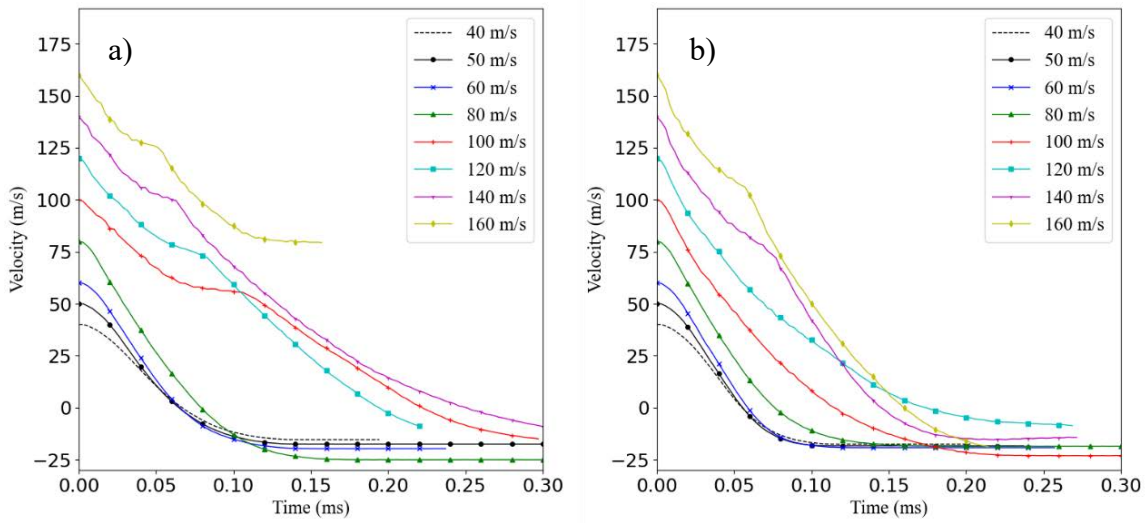


Figure 6.23. Projectile velocity vs time at different impact velocities. Comparison of sandwich panels with different core materials. a) Agglomerated cork core. b) PET foam core.

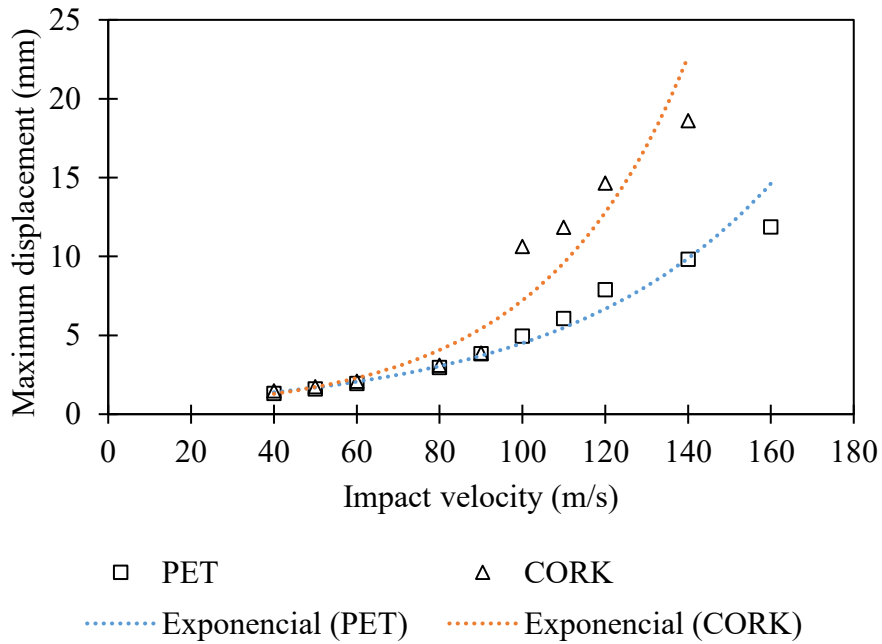


Figure 6.24. Maximum projectile displacement as a function of impact velocity. Comparison Agglomerated cork core and PET foam core.

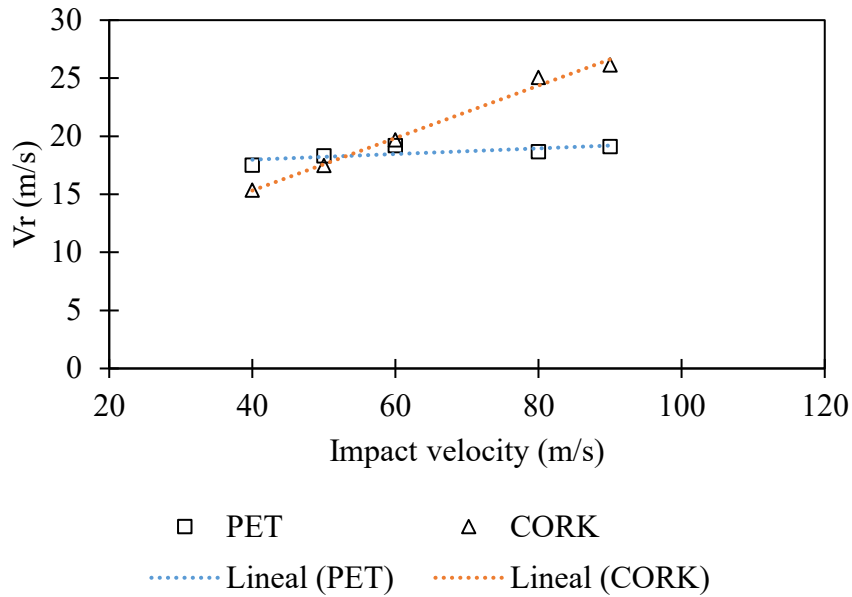


Figure 6.25. Rebound velocity at different impact velocities. Comparison Agglomerated cork core and PET foam core.

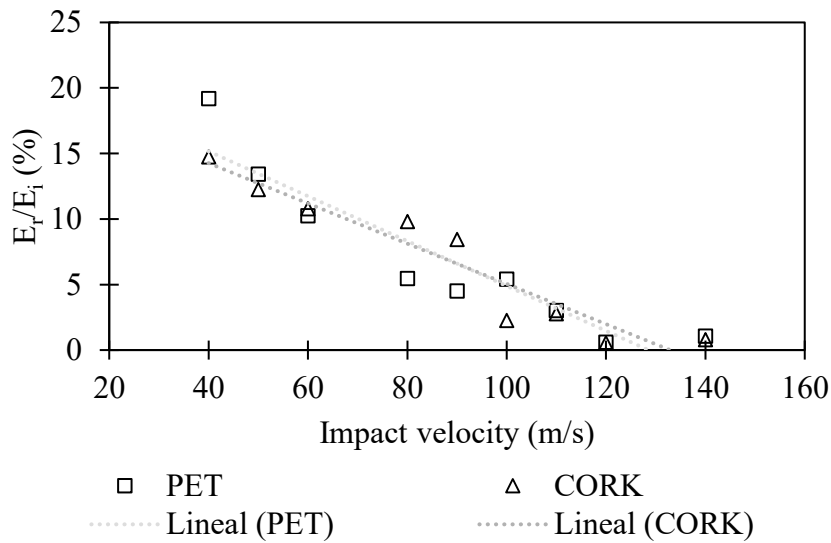


Figure 6.26. Rebound energy ratio at different impact velocities. Comparison Agglomerated cork core and PET foam core.

The deformation in the front face-sheet midsection is depicted in Figure 6.27 at different instants of time during the first 120 μ s after impact. From the figure, it is clear that the impact velocity influences the shape of the deformation. Impact velocities $V_i \leq 100$ m/s seem to have larger overall deflection curves of the face-sheet while higher velocities present more localized deformations around the impact point. No particular differences in the deformation shape are encountered between agglomerated cork panels and PET foam panels.

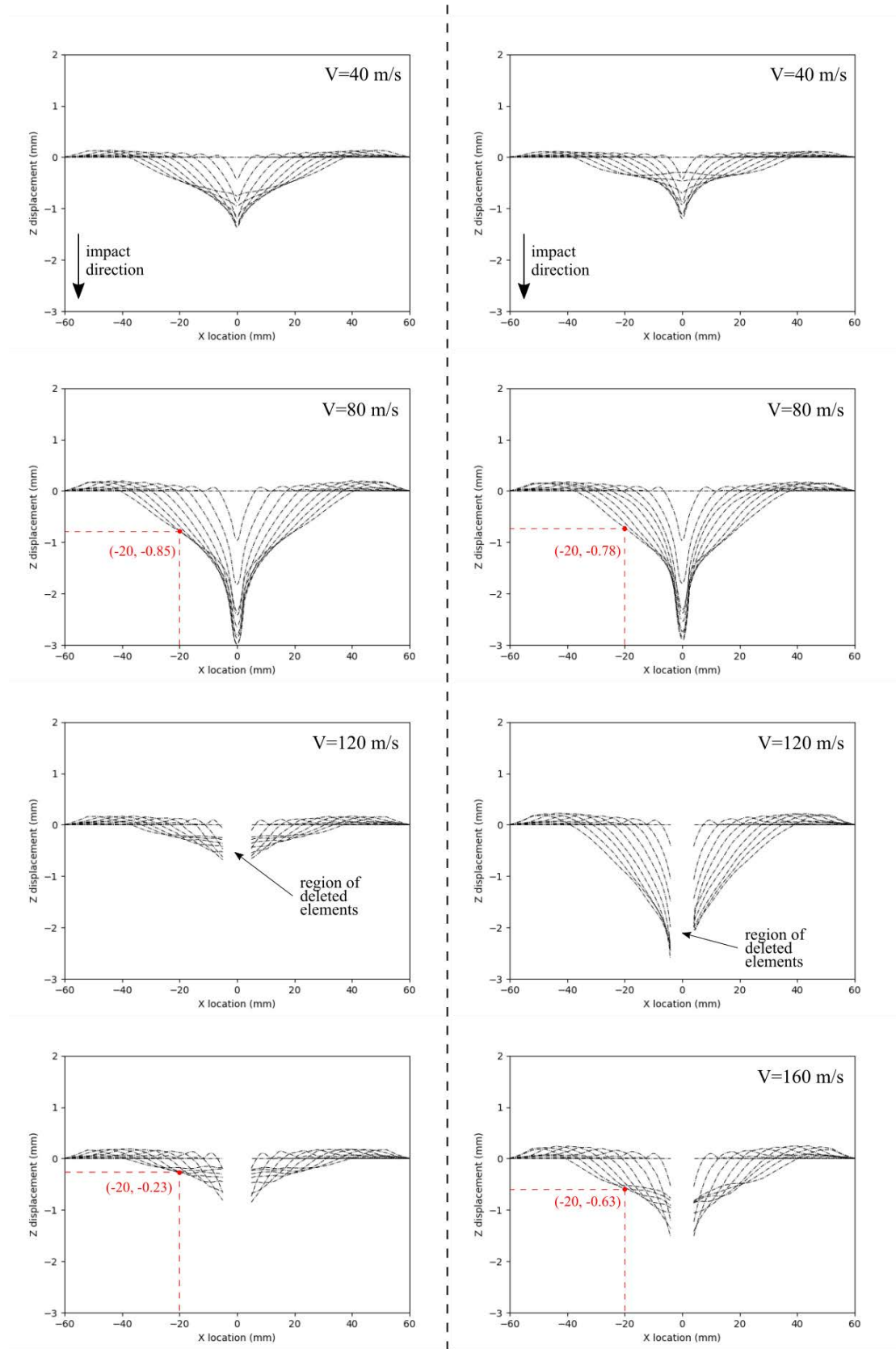


Figure 6.27. Shape deformation of the midsection (ply 8-front face-sheet) during 120 μ s after impact for different impact velocities. All lines are spaced at equal time intervals. Left: Agglomerated cork core. Right: PET foam core

The dissipation energy of the whole model is also studied and as it is expected it is found that its magnitude increases with the impact velocity due to the contributions of damage, plasticity and friction dissipation. Figure 6.28 shows the contribution of each dissipation mechanism as a percentage of the total dissipated energy. It is observed that the dominant dissipation mechanism for panels with agglomerated cork is damage while for panels with PET foam it is plastic dissipation. Let us remember that the damage dissipation energy includes the intra-laminar and inter-laminar damage in the face-sheet as well as the Mullis damage (in the cork core only). The energy dissipated by plasticity comprises the plastic dissipation energy in the laminate matrix as well as the plastic dissipation in the core (for the PET foam only). Since plastic dissipation is not included in the cork constitutive material model, it is expected to see a larger plastic dissipation in the PET foam sandwich panel than in the cork sandwich. Friction dissipation is negligible at low impact velocities (< 80 m/s) but its contribution becomes relevant at higher impact velocities where it can account for up to 36% and 29% of the total dissipated energy for agglomerated cork and PET foam respectively (Figure 6.28).

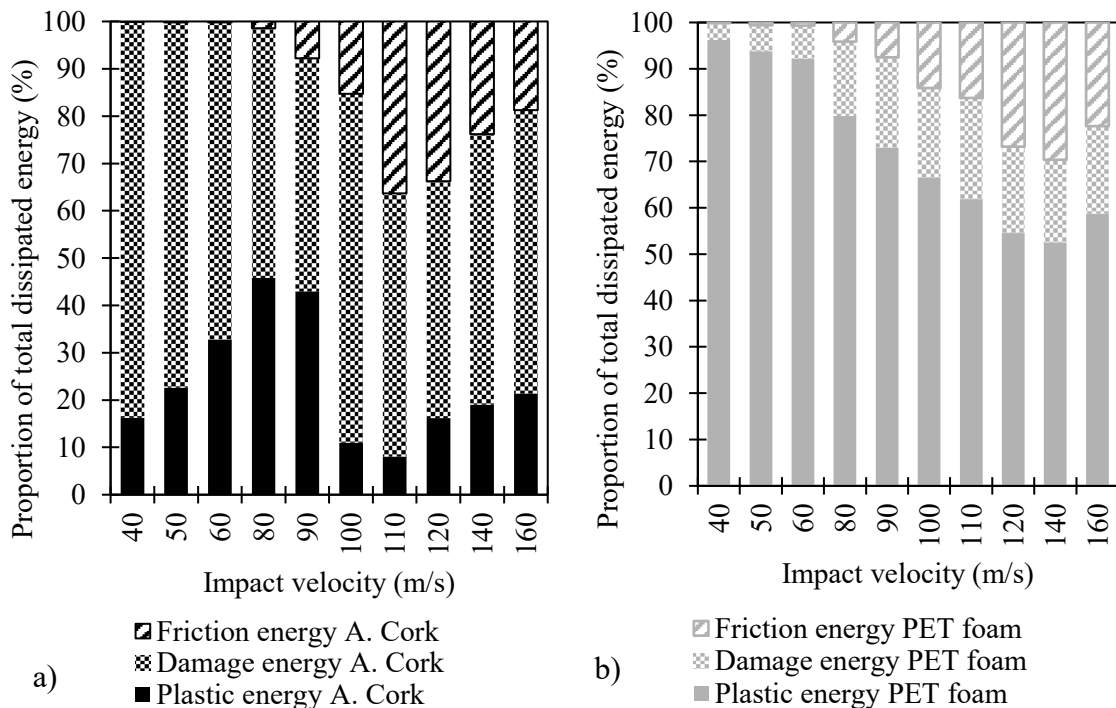


Figure 6.28. Dissipation energy at different impact velocities. Comparison agglomerated cork core (a) and PET foam core (b).

The total delamination area in the front face-sheet is estimated as the projection of the individual inter-laminar damage at each ply interface. The projected area corresponds to those mesh elements in the ply in which the inter-laminar damage variable is greater than

zero at the end of the impact. Figure 6.29 show a comparison of both sandwich panels at different impact velocities. From the figure, it can be observed that the delamination area in the front face-sheet increases with the impact velocity. Additionally, it can be noticed that panels with agglomerated cork show smaller damaged areas than their counterparts with PET foam for all impact velocities.

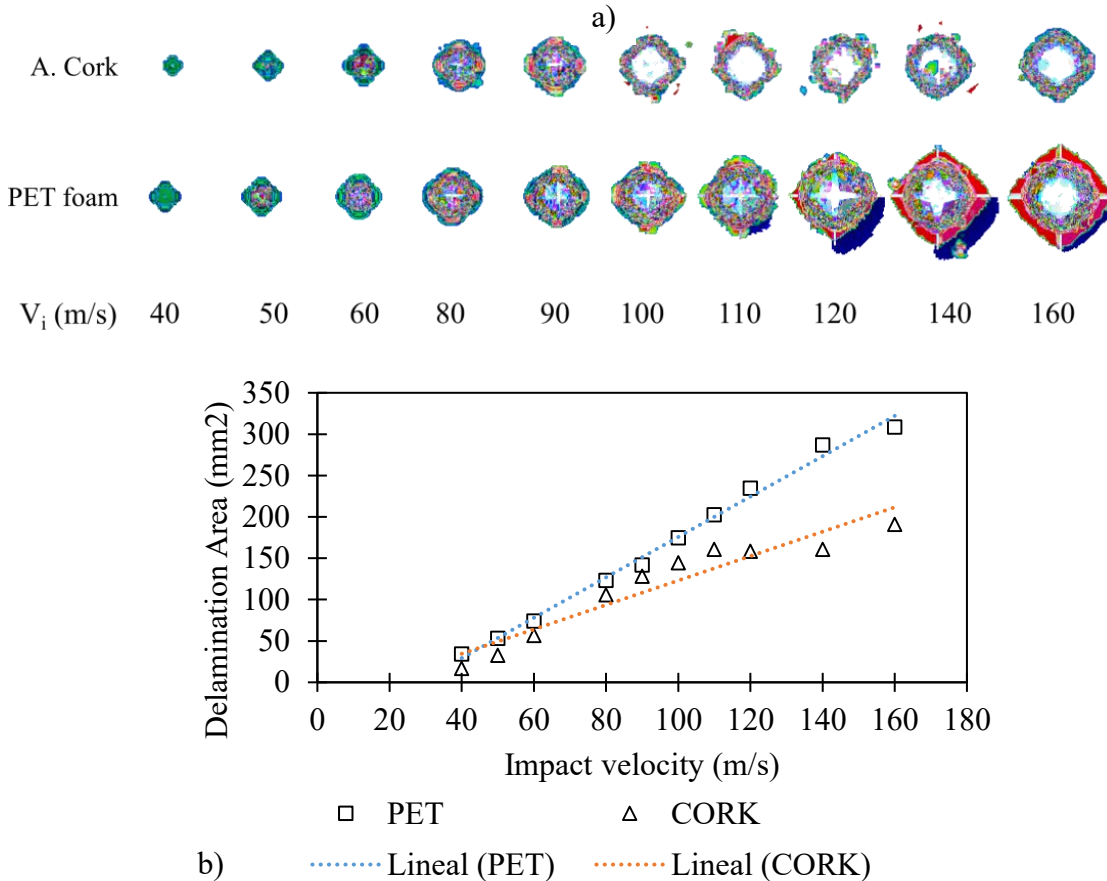


Figure 6.29. Delamination area in the front face-sheet at different impact velocities. Comparison between agglomerated cork core and PET foam core. a) Projection of the inter-laminar damage. b) Delamination area vs impact velocity

6.5.2 Core thickness

The sensitivity of the sandwich panel response to core thickness is studied using the previously described FEA models for agglomerated cork and PET foam core. Here the sandwich face-sheets are maintained as in the previous subsection but the thickness of the core is changed. For convenience, the core thickness (h) is expressed in terms of a relative thickness fraction of the previously analysed core thickness ($H=5\text{mm}$). The relative thickness fractions studied are:

$$0.25 \geq \frac{h}{H} \leq 4$$

The impact velocity is the same in all cases and is equal to 60 m/s. Figure 6.30 and Figure 6.31 show the evolution of the displacement and velocity of the projectile at different relative core thicknesses. The shape of each curve is similar to the ones presented in the previous subsection in which the projectile advance and rebound are identified. Here it can be noticed that both, duration of the impact and the rebound velocity are influenced by the core thickness.

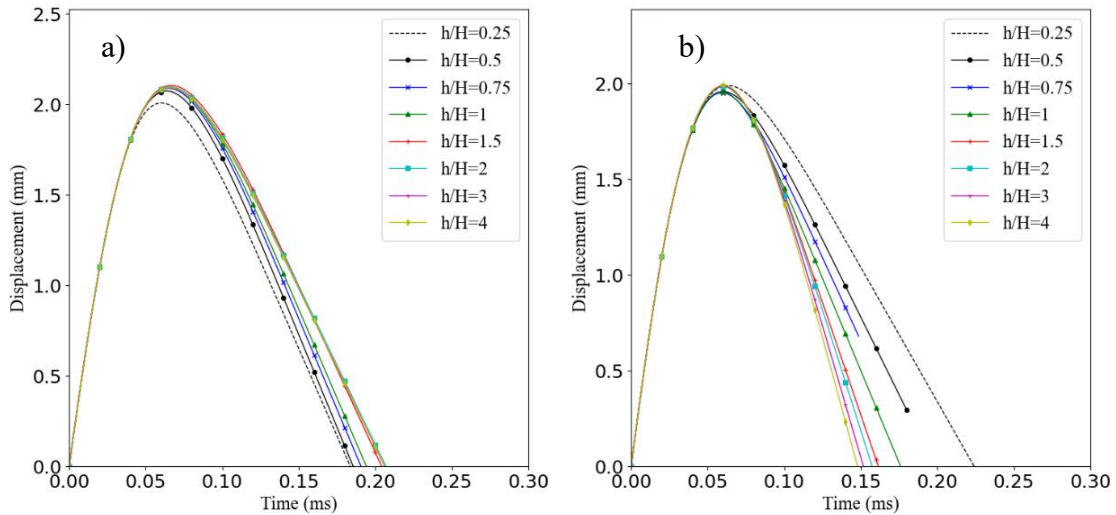


Figure 6.30. Projectile displacement vs time at different relative thicknesses ($V_i=60$ m/s). Comparison of sandwich panels with different core materials. a) Agglomerated cork core. b) PET foam core.

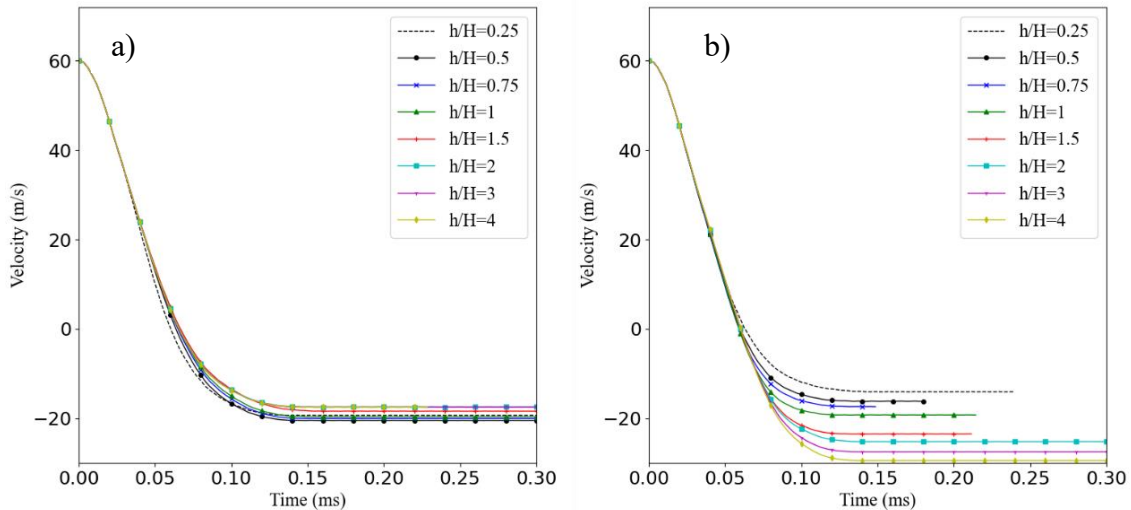


Figure 6.31. Projectile velocity vs time at different relative thicknesses ($V_i=60$ m/s). Comparison of sandwich panels with different core materials. a) Agglomerated cork core, b) PET foam core.

From Figure 6.32 it can be noticed that the maximum displacement of the projectile seems to be unaffected by the core thickness. In fact, for relative thickness greater than 1, the maximum displacement into sandwich change less than 0.05 mm. For smaller relative

thicknesses, the maximum displacement slightly varies what can be associated with a stronger interaction between the front face-sheet and back face-sheet.

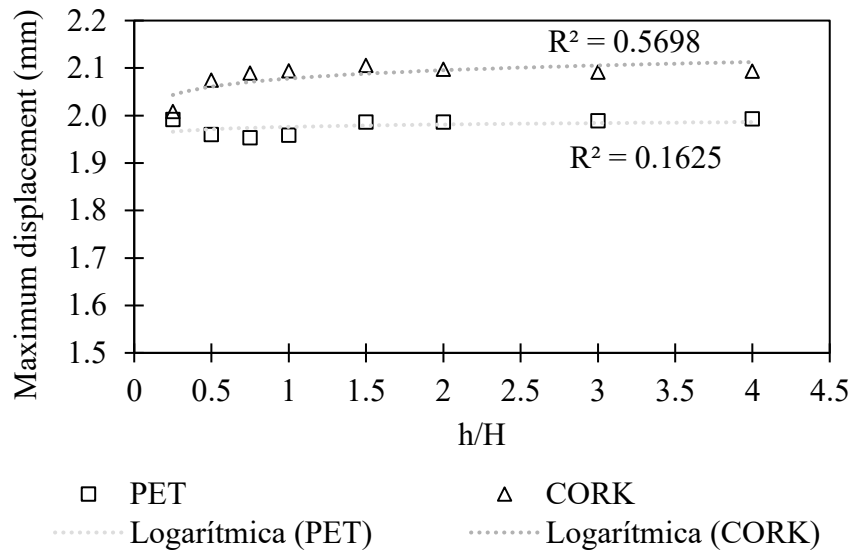


Figure 6.32. Maximum projectile penetration for different core thicknesses ($V_i=60$ m/s)

At the analysed impact velocity ($V_i= 60$ m/s) the projectile does not perforate the front face-sheet and rebounds. Figure 6.33 plots the rebound velocity (V_r) as a function of relative core thickness. The core thickness seems to affect differently both sandwich panels. Panels with PET foam core show larger rebound velocities at larger relative thickness. However, in the case of panels with agglomerated cork, this trend is not clear since the rebound velocity varies little showing a decreasing tendency with core thickness.

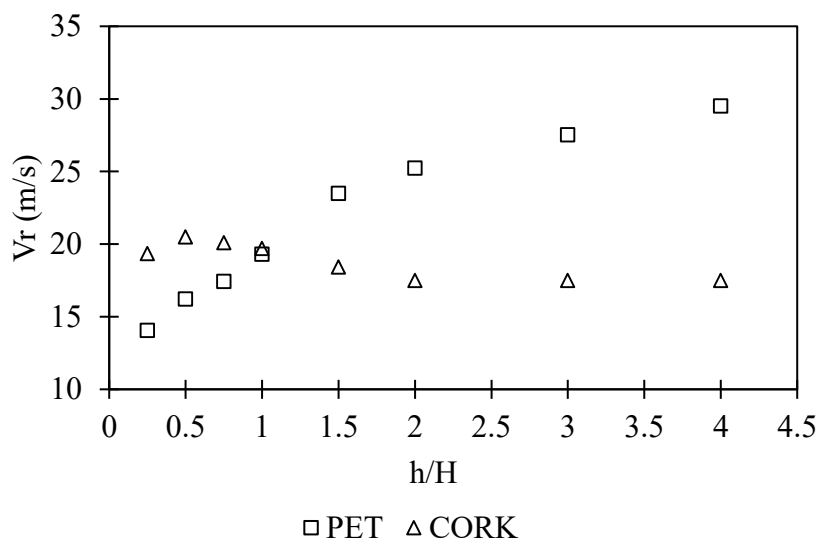


Figure 6.33. Rebound velocity at different for different core thicknesses ($V_i=60$ m/s)

One of the first observations is that for very thin cores ($h/H=0.25$ or 0.5) the perturbation created by the projectile in the front face-sheet interacts with the back face-sheet which plays an important role during the impact process. In contrast, for thick cores ($h/H>2$) the front face-sheet and the neighbouring regions of the core primarily support the projectile advance while the back face-sheet plays a minor role (Figure 6.34).

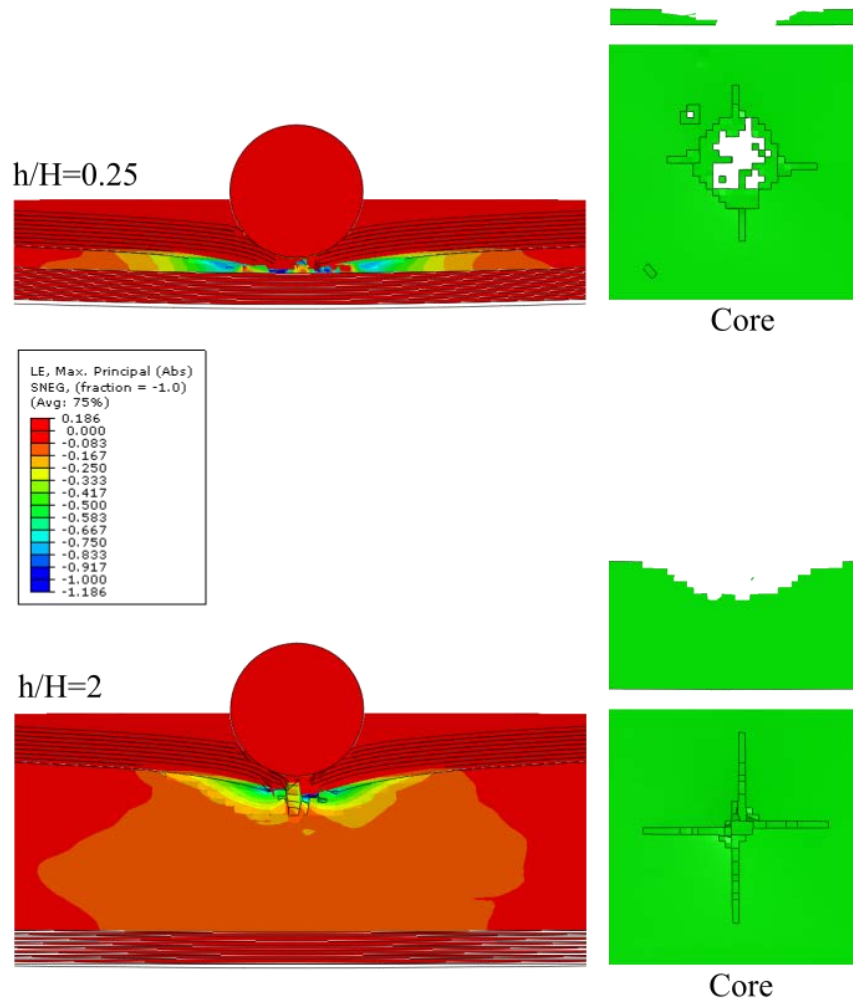


Figure 6.34. Core damage at two relative thicknesses at $V_i=60$ m/s (Agglomerated cork core) at 0.11 ms

A second observation is that the core thickness significantly influences the strain distribution and fracture in the core. Figure 6.34 shows the maximum principal strain in the core for agglomerated cork panels with two different thicknesses as well as the eroded elements that have reached the Tsai-Wu failure criteria. In both cases, there is strain concentration near the impact region that for the thicker core is smoothly dissipated across the core. Contrary to the case of the thinner core the strain concentration is squeezed

between the front and back face-sheets covering the entire thickness. This single difference seems to be enough to change the way fracture occurs. For example in the case of the thicker core, fracture occurs in a well-defined cross crack pattern that grows within the core. In the case of the thinner core, a crater of eroded elements is also formed due to core crushing and its projected area is larger. This compressive crushing seems more critical for cores of small thickness since the back face-sheet behaves like semi-rigid support encouraging larger compressive strains in the core. This effect can be identified if carefully comparing the strain concentration region of both cores in Figure 6.34. It can be observed that for $h/H=0.25$ the strain values larger than 66% (blue in the colour bar) are more extended than for the case of $h/H=2$.

The shape of the deformation at the front face-sheet at the midsection is presented in Figure 6.35 for the first 120 μs after impact. The deformation shape provides a valuable visual insight into the effect of the core thickness and material on the response of the front face-sheet. The effect of the core thickness in the shape of the deformation is minimum for the agglomerated cork. A similar observation is obtained for panels with PET foam core however in this case, larger core thicknesses seem to have a small effect on the “sharpness” of the local perturbation around the projectile, which can be visualized if comparing $h/H=0.5$ and $h/H=4$. From Figure 6.35 it is also apparent that the deformation shape is slightly different for both materials. In general panels with agglomerated cork show a more spread deformation around the impact point while panels with PET foam core show a more localized and sharp deformation around the impact point. This effect is easy to observe if comparing $h/H=2$ or $h/H=4$ for both materials and can be attributed to the difference in the stiffness of both core materials and the support they provide to the front face-sheet.

Analysis of the energies in the model shows that the contribution due to plastic dissipation is predominant in the panel with PET foam core while damage energy is dominant in the agglomerated cork panel. From relative thickness greater than one, the proportion of those energy dissipation mechanisms seems to be almost unaltered by the core thickness (Figure 6.37). As observed in Figure 6.37 the proportion of energy dissipated as damage is higher for very thin cores ($h/H=0.25$ and 0.5) while it is lower for larger relative core thicknesses. In the absence of any other observation that can explain this behaviour, this difference can be attributed to the damage suffered by the cork core when the thickness is small following the explanation given in the previous paragraphs.

FEA MODEL OF IMPACT ON SANDWICH PANELS

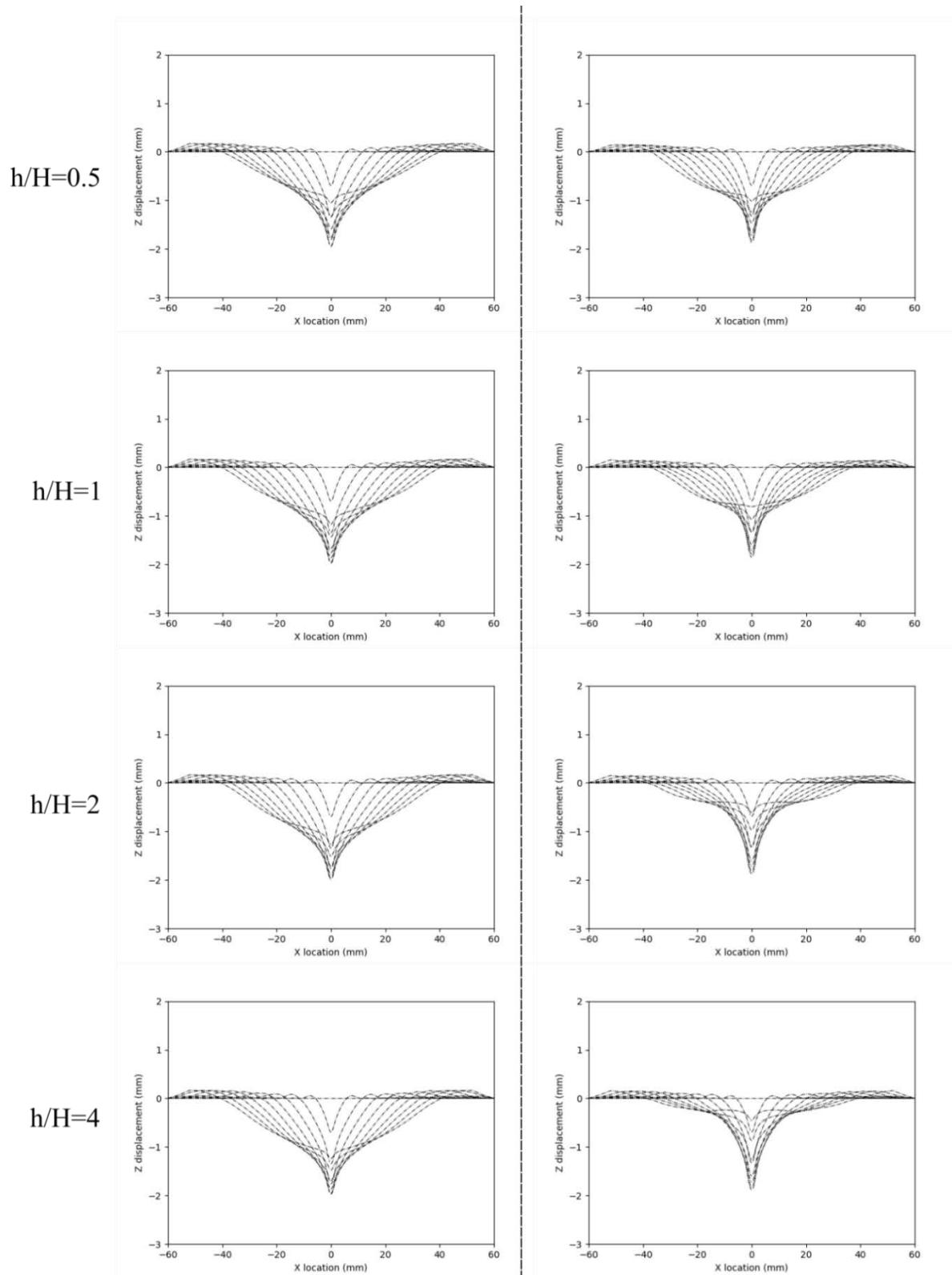


*Figure 6.35. The shape of the deformation at the midsection (ply 8-front face-sheet) during the first 120 μ s after impact for different relative thicknesses ($H=5$ mm). FEA model ($V_i=60$ m/s). All lines are spaced at equal time intervals.
Left: Agglomerated cork core. Right: PET foam core*

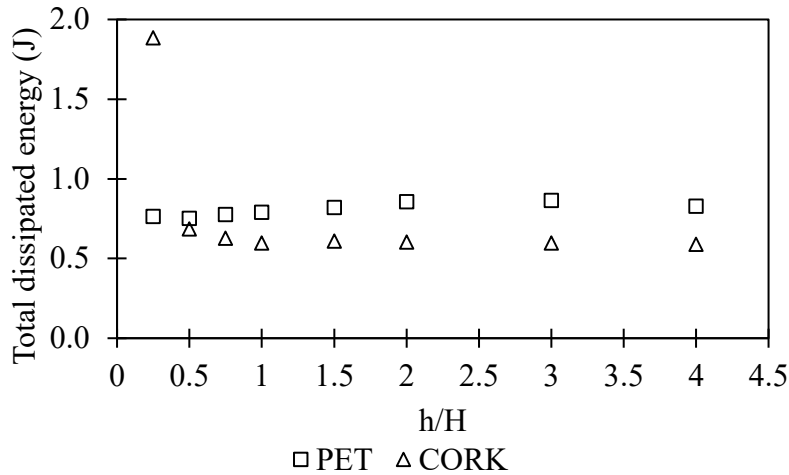


Figure 6.36. Total dissipated energy at different relative thicknesses ($V_i=60$ m/s)

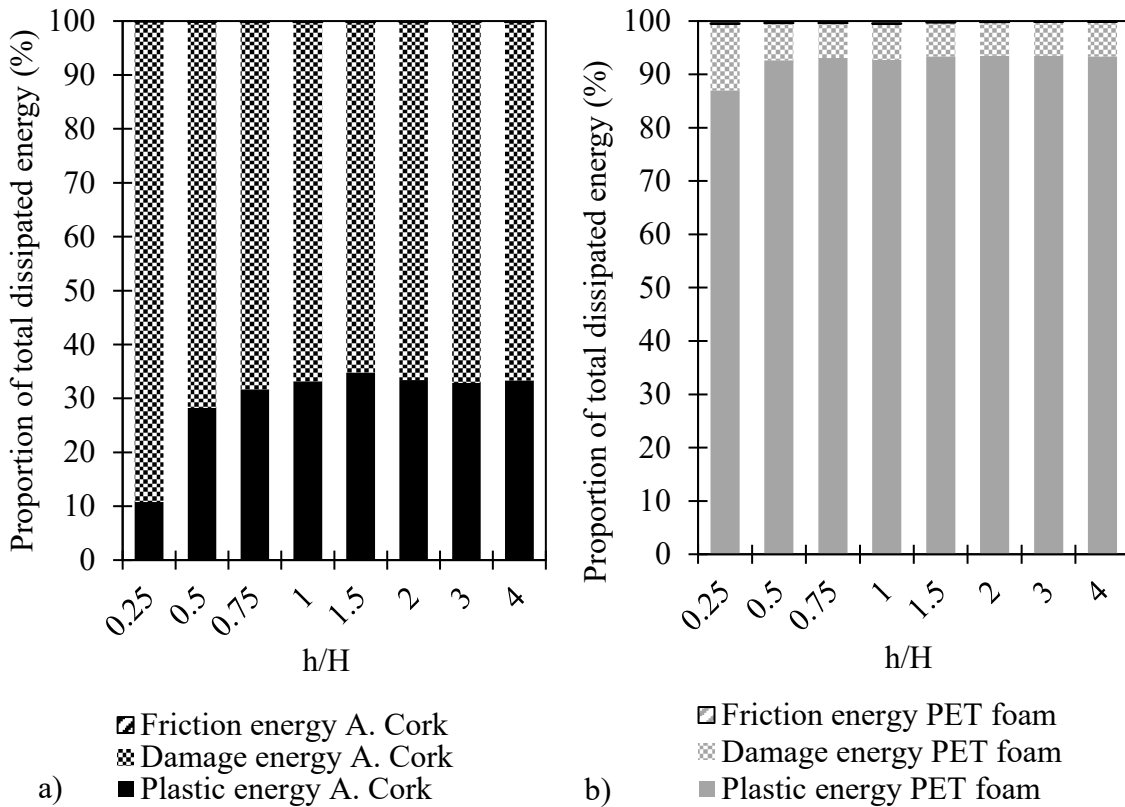


Figure 6.37. Dissipation energy at different relative core thicknesses ($V_i=60$ m/s). Comparison agglomerated cork core (a) and PET foam core (b).

The variation of the damaged area with respect to the core thickness seems to be less evident. In the case of sandwich panels with an agglomerated cork core, the damaged area is roughly constant across the range of analysed thicknesses. However, in the case of sandwich panels with PET foam core, the damage tends to slightly increase with the core thickness, this should be taken carefully since there is considerable scattering in the obtained data.

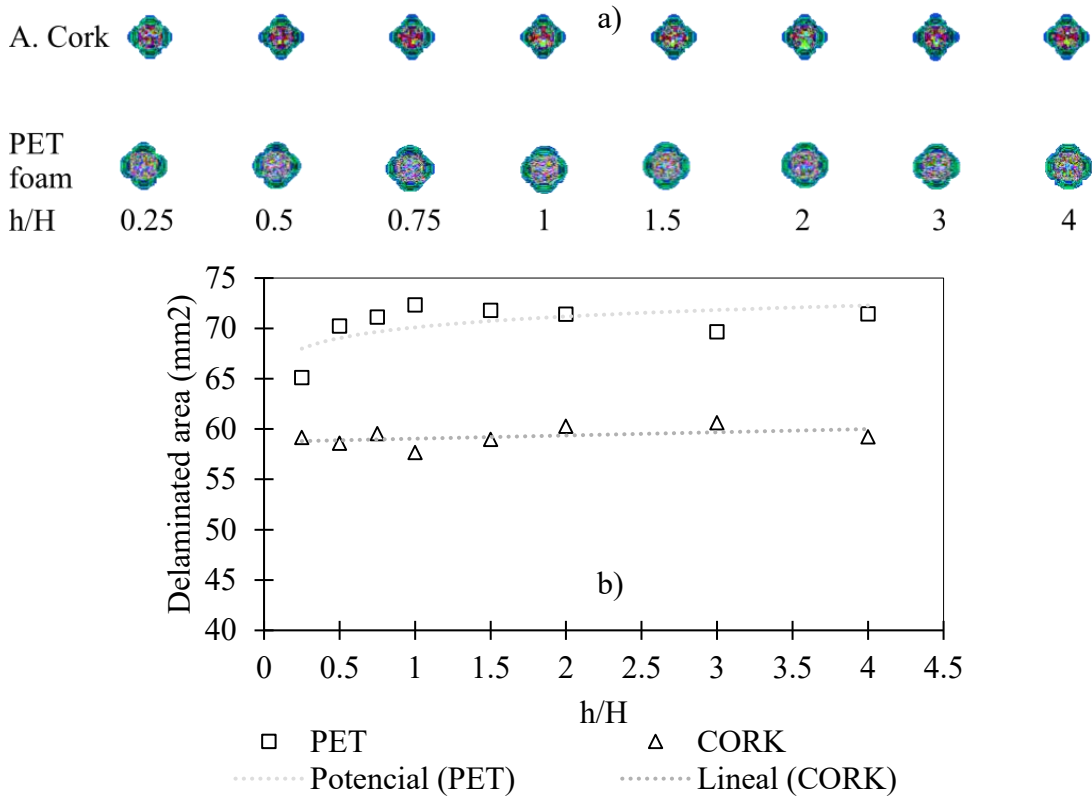


Figure 6.38. Delamination area in the front face-sheet for different relative core thicknesses ($V_i=60$ m/s). Comparison between agglomerated cork core and PET foam core. a) Projection of the inter-laminar damage. b) Delamination area vs impact velocity.

6.5.3 Impact angle

In this subsection, the sensitivity of the sandwich panel response to the impact angle is assessed using the previous FEA model. Here the sandwich face-sheets and core are equal as in section 6.2 but the impact angle θ is varied by modifying the vertical and horizontal components of the projectile velocity vector. The magnitude of the velocity vector is held constant for all cases to 60 m/s. The range of impact angles analysed in this section are shown below, where $\theta=0^\circ$ corresponds to a perpendicular impact.

$$0^\circ \geq \theta \leq 75^\circ$$

In oblique impacts, the momentum of the projectile can be decomposed into two components one perpendicular to the panel and the other parallel to the panel. Since the momentum perpendicular to the panel is the one responsible for the penetration it is expected that the displacement of the projectile decreases at higher impact angles. This tendency is identified for both sandwich panels in the displacement history plot presented in Figure 6.39.

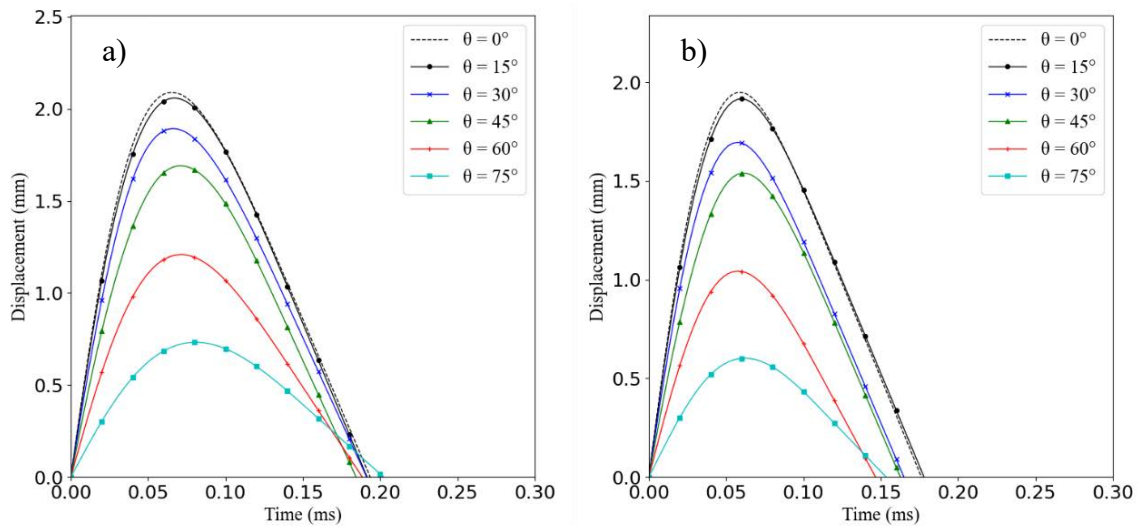
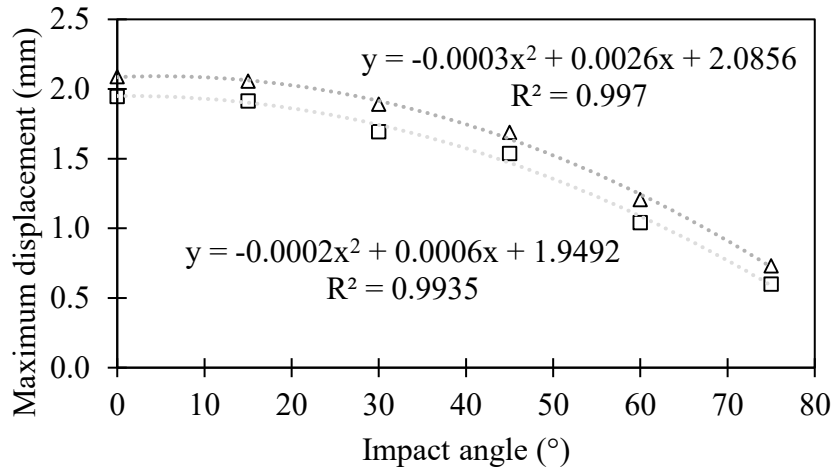


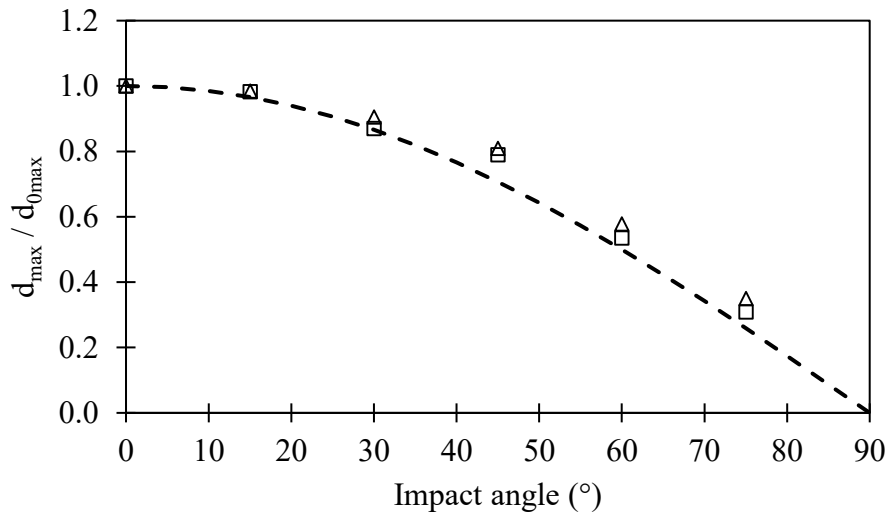
Figure 6.39. Projectile displacement vs time at different impact angles ($V_i=60$ m/s). Comparison of sandwich panels with different core materials. a) Agglomerated cork core. b) PET foam core.

Figure 6.40 shows that the maximum displacement of the projectile into the panel decreases at higher impact angles. As expected the maximum displacement of the projectile occurs when the impact angle is zero (perpendicular impact). This tendency seems to be approximately proportional to the cosine of the impact angle as can be observed in Figure 6.40. In this figure, d_{\max} is the maximum displacement at a given impact angle, while $d_{0\max}$ is the maximum displacement for the $\theta=0^\circ$ (perpendicular impact).

As it can be expected, the rebound velocity perpendicular to the face-sheet plane decreases with larger impact angles (Figure 6.41). An interesting observation is obtained when calculating the magnitude of the whole rebound velocity vector. From Figure 6.42 it is clear that the magnitude of the rebound velocity vector increases with the impact angle showing a quadratic tendency. The minimum rebound velocity occurs when the impact angle is zero (perpendicular impact) while for larger angles the rebound velocity progressively approaches the initial impact velocity (60 m/s). This observation can be interpreted in terms of the balance between initial kinetic energy and recoverable internal energy. At high impact angles, a large amount of the initial kinetic energy is recovered in the rebound while for low impact angles the recovered impact energy is less due to higher damage and plastic dissipation produced due to a higher penetration as will be explained in subsequent paragraphs.



PET
 CORK
 Polinómica (PET)
 Polinómica (CORK)



PET
 CORK
 Cos(θ)

Figure 6.40. Top: Maximum projectile penetration for different impact angles ($V_i=60$ m/s). Bottom: Non-dimensional max displacement

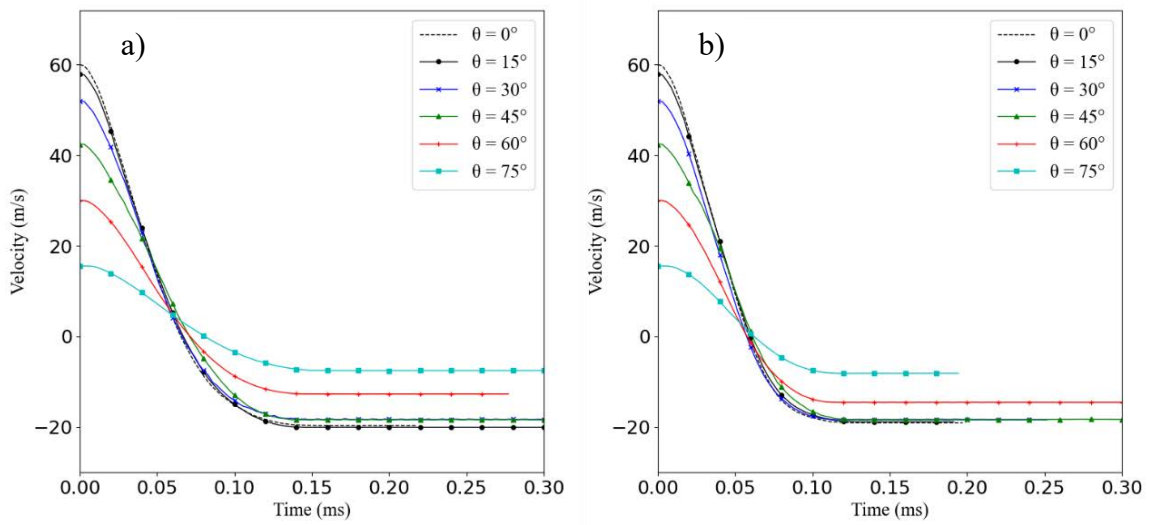


Figure 6.41. Projectile perpendicular velocity vs time at different impact angles. Comparison of sandwich panels with different core materials. a) agglomerated cork core. b) PET foam core.

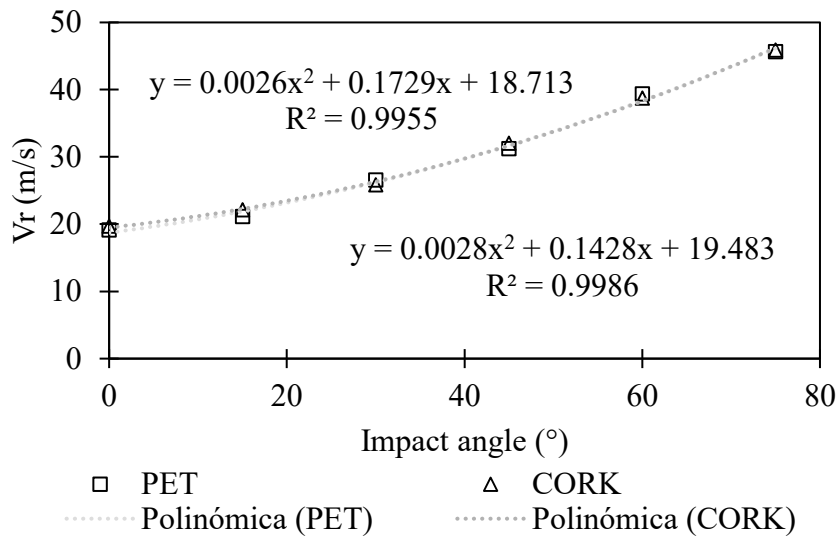


Figure 6.42. Rebound velocity at different impact angles ($V_i=60m/s$)

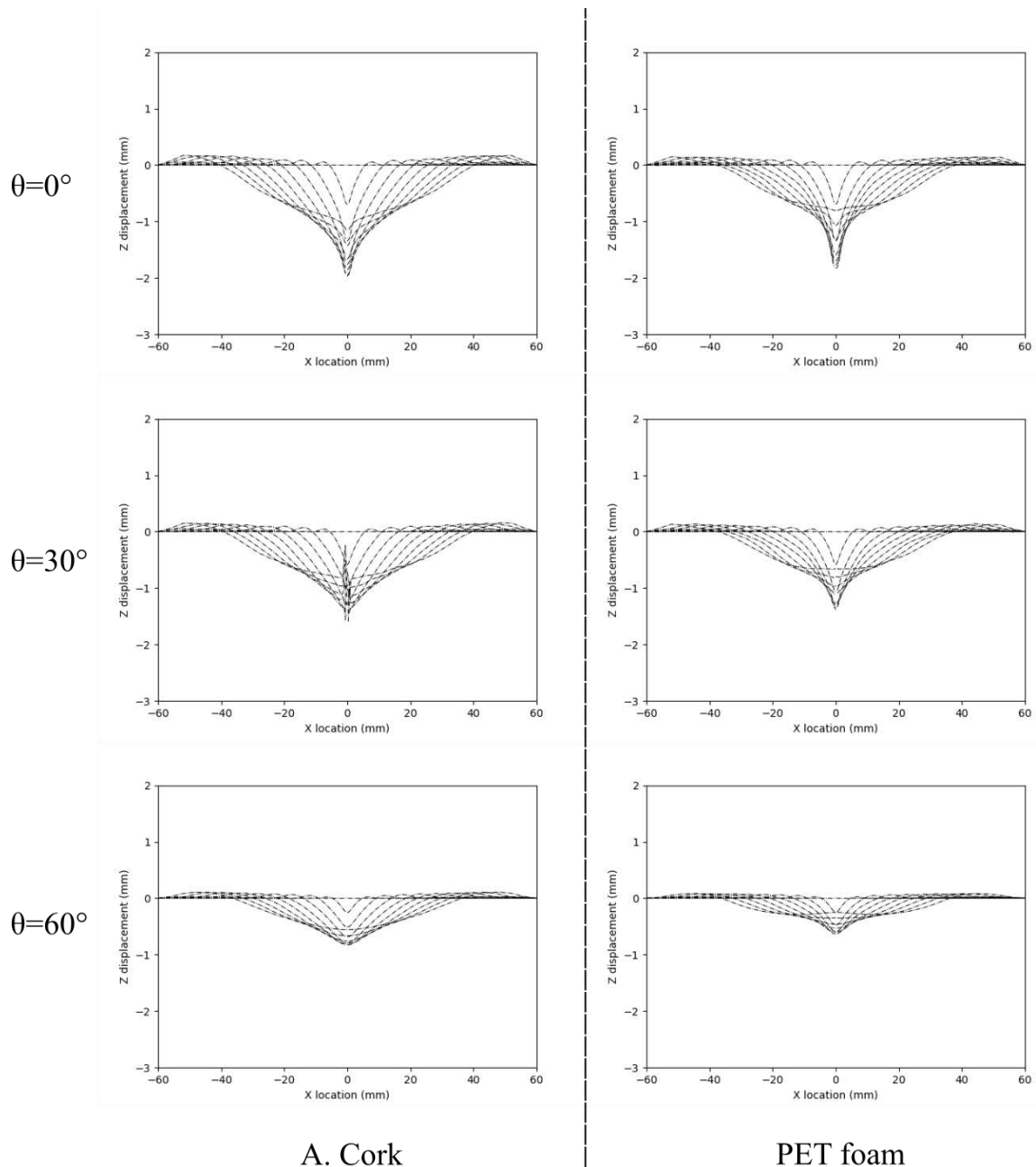


Figure 6.43. Shape deformation of the midsection (ply 8 front face-sheet) during $120 \mu\text{s}$ after impact for different impact angles. FEA model ($V_i=60 \text{ m/s}$). All lines are spaced at equal time intervals.

The overall out-of-plane deformation in the front face-sheet is affected by the impact angle as shown in Figure 6.43. The perpendicular impact creates the largest overall deformation in the front face-sheet while at higher impact angles the deformation is reduced. This result gives clues that indicate that the internal strain energy stored in the panel is reduced at higher impact angles. This statement is probed when analysing the evolution of the energies in the model. Figure 6.44 and Figure 6.45 show the different energy components at impact angles of 30° and 60° . Despite the initial impact energy (kinetic energy) being the same in

both cases the internal strain energy at the end of impact is much lower when $\theta=60^\circ$. This occurs in both sandwich panels and seems to be related to the reduced overall deformation in the panel, as indicated previously.

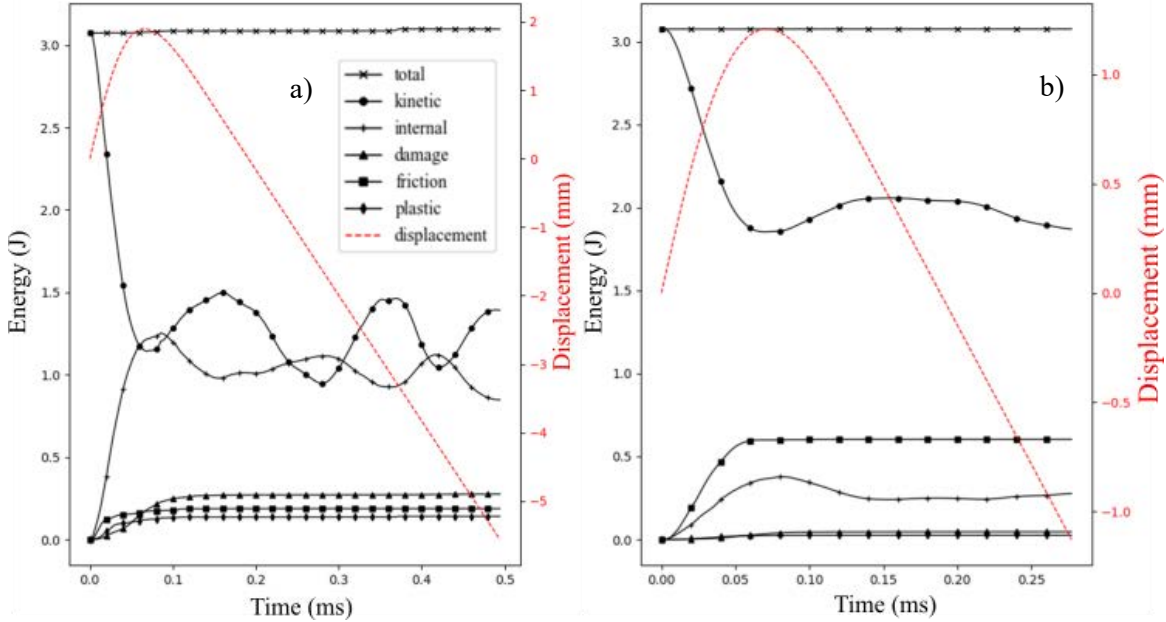


Figure 6.44. Evolution of the model energies (Agglomerated cork core panel, $V_i=60$ m/s).
 a) $\theta=30^\circ$. b) $\theta=60^\circ$.

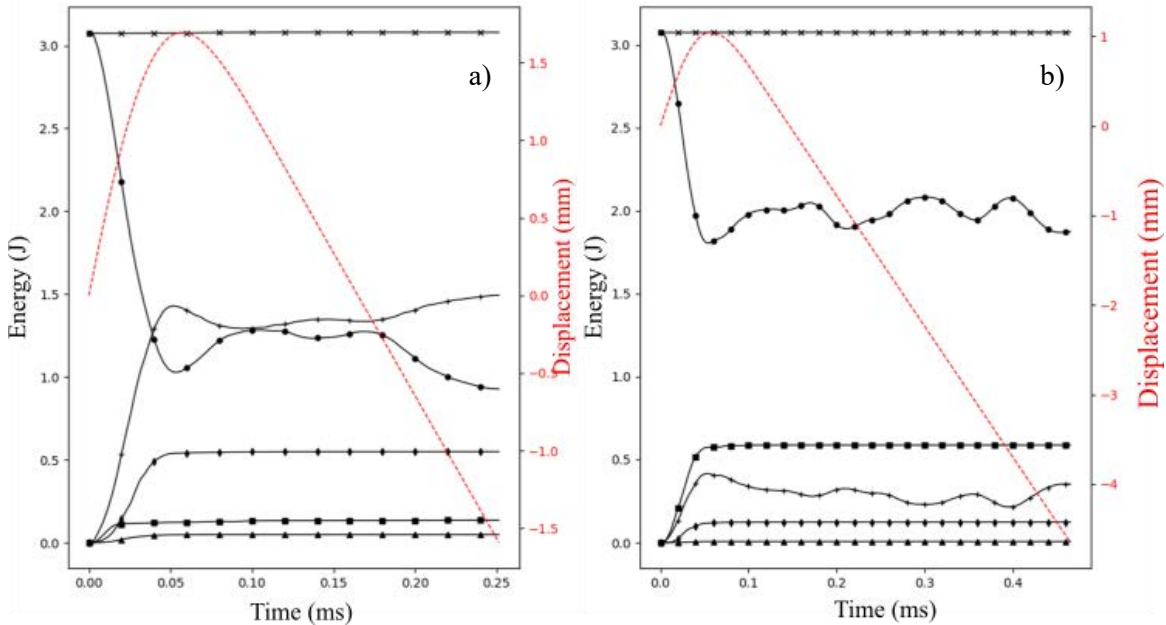


Figure 6.45. Evolution of the model energies (PET foam core panel, $V_i=60$ m/s).
 a) $\theta=30^\circ$. b) $\theta=60^\circ$.

The contribution of friction dissipation energy seems to play an important role in oblique impact. As demonstrated in Figure 6.46 friction dissipation massively increases with the

impact angle in both sandwich panels. This is the product of the friction forces exerted by projectile lateral motion (due to its non-perpendicular velocity component to the panel face). Indeed, for more tilted angles the effective friction area becomes larger what increases the work done by friction forces.

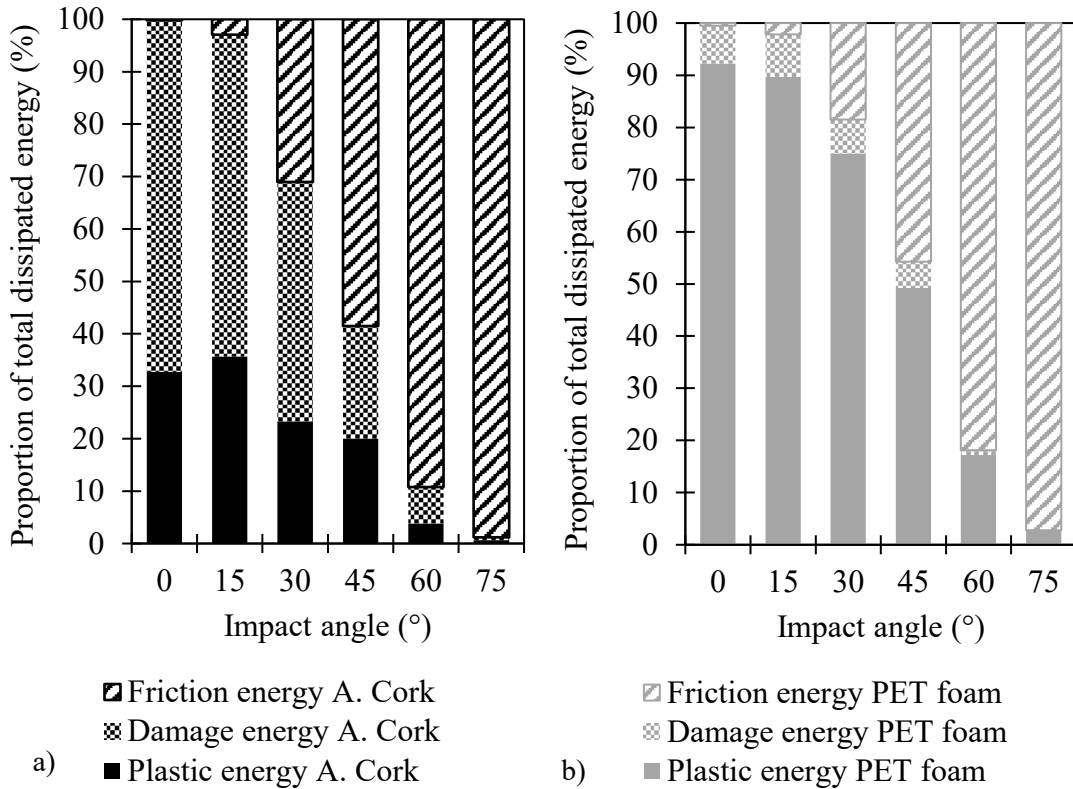


Figure 6.46. Mechanisms of dissipation energy at different impact angles ($V_i=60$ m/s). Comparison agglomerated cork core (a) and PET foam core (b).

The plastic dissipation energy is also affected by the impact angle. As depicted in Figure 6.46 the plastic dissipation decreases at higher impact angles for both core materials as a consequence of two different phenomena. First, at high impact angles the core deformation is small therefore, the plastic dissipation (in the PET foam core) is smaller. Second and probably more important, the plastic dissipation in the front face-sheet is smaller at high impact angles since the plasticity region in the laminate is smaller than for low impact angles. This effect is observed in Figure 6.47 where the plastic strain distribution in the top face-sheet is superficial for an impact angle of 60° while in the case of 0° and 30° the plastic strain is very well developed throughout the entire thickness. It is also visible that the intra-laminar damage varies at different impact angles. For small angles (0° and 15°) the intra-laminar damage in the most superficial ply (ply 8) is less critical and shows no failure while for intermediate impact angles (30° and 45°) element deletion and therefore ply failure is

reached. It can be summarized that at low impact angles the damage is propagated inside the face-sheet thickness while for large impact angles the damage is superficial but its intensity is higher since failure occurs.

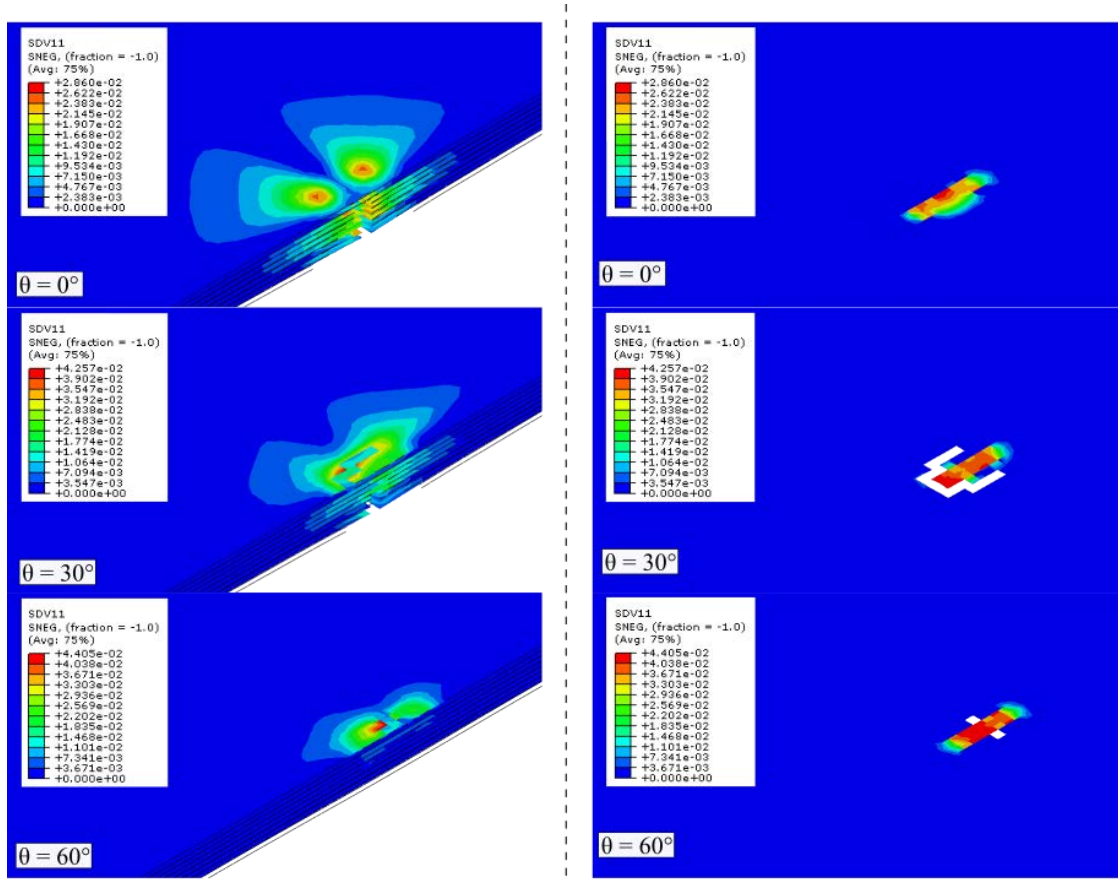


Figure 6.47. Left: Plastic strain at different impact angles (front face-sheet). Right: Compressive damage (front face-sheet ply 8) along the impact direction. PET foam core panel ($V_i=60$ m/s)

The damage dissipation energy also varies with the impact angle (Figure 6.46). However here it is important to notice that the damage energy remains almost constant up to 15° and shows a steep fall for large impact angles. This difference in the damage energy is associated to the decrease in the damaged area in an oblique impact. The analysis of the damaged area shows that both inter-laminar and intra-laminar damage are deeper (through the thickness) at lower impact angles. At higher impact angles, the damage is more superficial and does not show the characteristic cruciform petal shape but a more elongated damaged area. Figure 6.48 shows that the damaged area decreases with higher impact angles following a linear relationship. This figure also shows that the projected inter-laminar damage is elongated in the direction of the lateral velocity component while thinner in the transversal direction.

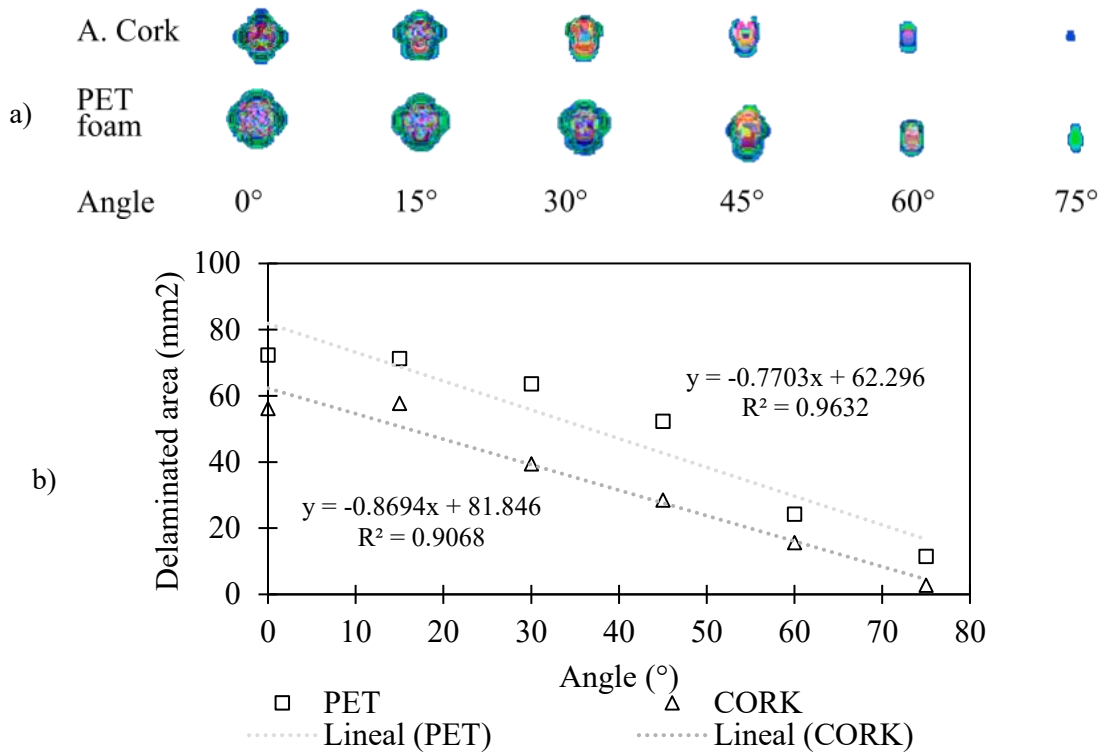


Figure 6.48. Delamination area in the front face-sheet for different impact angles ($V_i=60$ m/s). Comparison between agglomerated cork core and PET foam core. a) Projection of the inter-laminar damage. b) Delamination area vs impact velocity.

6.5.4 Axial preloading

This section studies the influence of an axial preload on the impact response of the sandwich panels. The same FEA models presented in section 6.2 are used here. However, an additional analysis step is implemented to model the axial preload occurring before the impact. In this first step, an axial displacement is applied uniformly over one of the sandwich lateral faces while the opposite face is restrained with simple support. To get a quasi-static response during the preloading step a mass scaling factor is applied to increase the explicit time increment. This technique is suitable for this first preloading step since it is assumed quasi-static and the kinetic energy is negligible. The kinetic energy and internal energy levels during the preload are monitored to ensure that no substantial kinetic energy is added by the mass scaling factor ($\Delta KE/IE < 5\%$). At this point, it is important to highlight that the mass scaling factor is only applied in the first (preload) step and is removed in the second (impact) step by reinitializing the mass matrix. This since in the impact step the kinetic energy is dominant and mass scaling can compromise the accuracy of the results.

The magnitude of the impact velocity vector is held constant for all cases to 60 m/s and the panels are preloaded in both tension and compression, ensuring that the overall axial strain

is smaller than the critical failure stress. The range of overall axial strains ($\bar{\epsilon}$) studied in this analysis is:

$$-0.5\% < \bar{\epsilon} < 0.8\%$$

The maximum displacement of the projectile showed to be sensitive to the axial preloading for both sandwich panels and in both preloading conditions (tension and compression). From Figure 6.49 it is observed that the maximum displacement shows a quadratic growth with the axial preload reaching much larger values at strain levels higher than 0.5%.

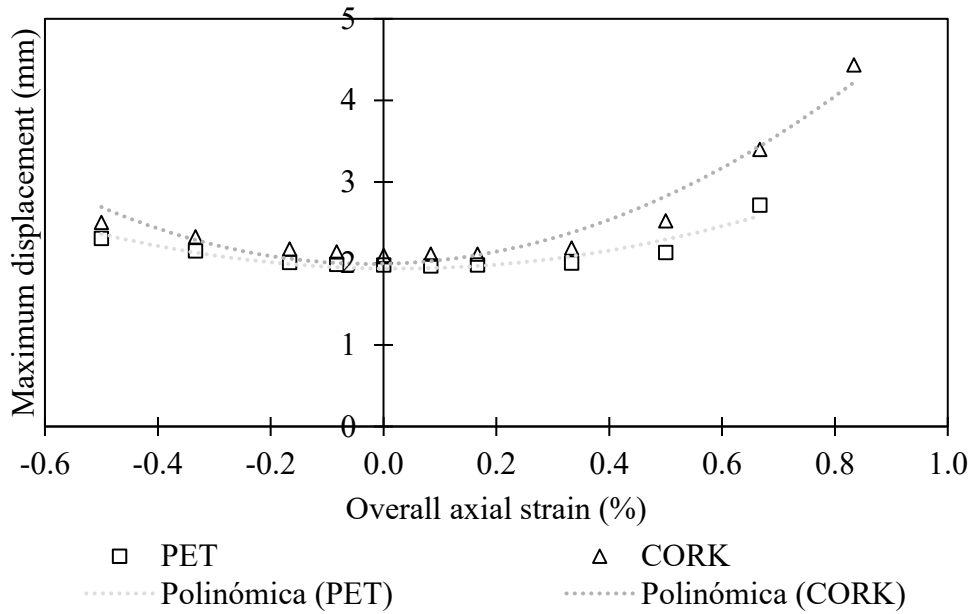


Figure 6.49. Maximum projectile displacement for different preload conditions ($V_i=60$ m/s)

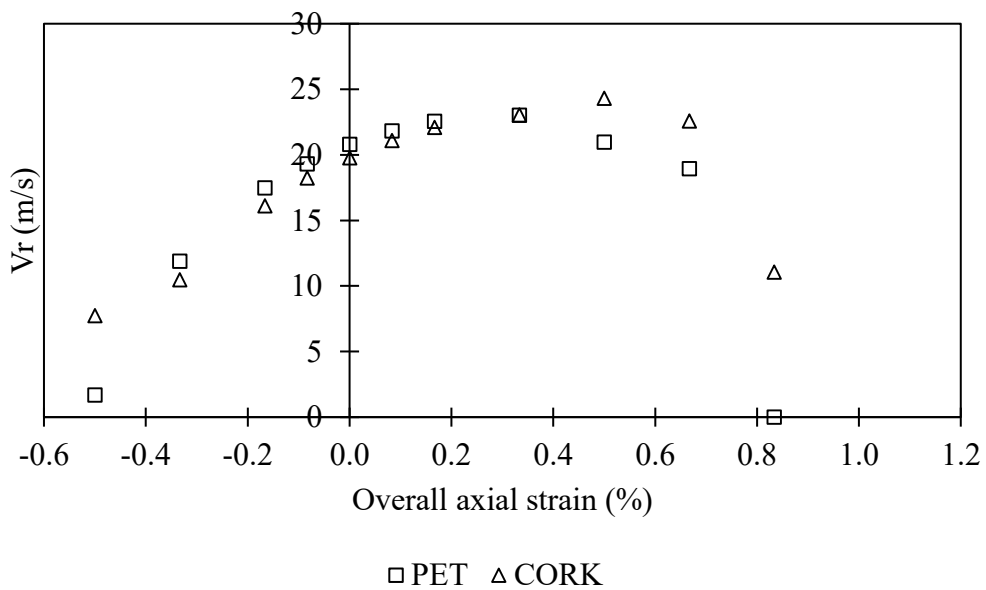


Figure 6.50. Projectile rebound velocity for different axial preloading conditions

In the case of the rebound velocity, the preload plays an important role as well. For both sandwich panels, a compressive axial preload tends to critically reduce the projectiles rebound velocity if compared with the no preloading condition (Figure 6.50). On the other hand, if a tensile preload is applied the rebound velocity is increased. However, this increment in the rebound velocity is limited when the overall strain level is high ($> 0.5\%$) after which the rebound velocity is gain reduced. This inflexion point is associated with a massive growth of a crack perpendicular to the preloading direction. This crack reduces the overall stiffness of the top face-sheet and releases some of the strain energy stored during the preloading.

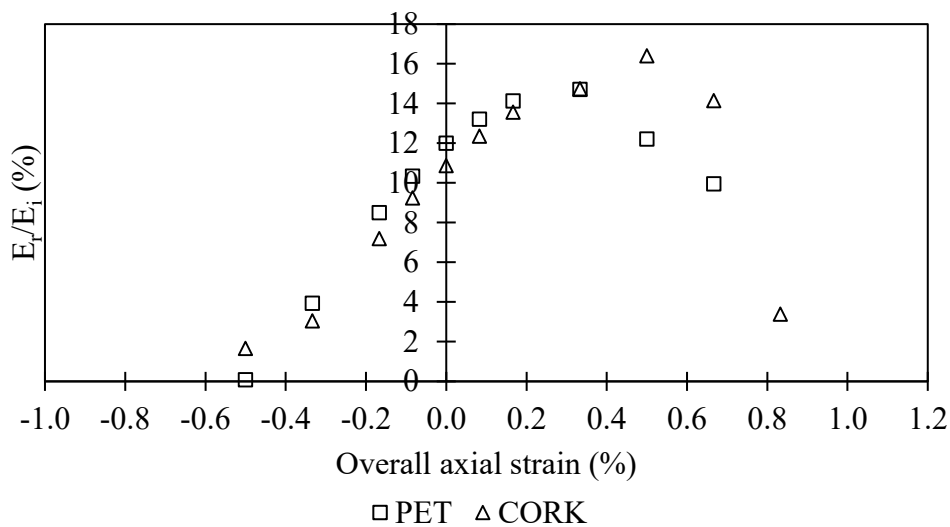


Figure 6.51. Projectile kinetic energy rebound ratio at different preload conditions ($V_i=60\text{m/s}$)

Another interesting observation on the influence of the axial preload is observed when visualizing the vertical displacement of the midsection in the most external ply (ply-8) of the front-face sheet (Figure 6.52). The axial preload applied to the panels seems to affect the propagation of the surface waves by increasing the propagation speed for tensile preloads and by decreasing its propagation speed for compressive preloads. The propagation velocity for each preloading condition is computed from the distance travelled by the wave crest in a period ($14\mu\text{s}$). For example, in agglomerated cork sandwich panels if there is no axial preloading the speed is 489 m/s while if a compressive axial strain of -0.3% is applied the wave velocity is reduced to 346 m/s . Accordingly, for a tensile axial strain of 0.3% , the propagation velocity is increased to 565 m/s . The variation in propagation speed can have an important effect on the response of the sandwich panels against impact loads since faster waves will be able to interact earlier with surrounding boundaries or constraints while slower waves would present a more localized response

limiting their effect on the impact region. It is also observed that while the propagation velocity increases with positive axial preloading the magnitude of the wave crest decreases. In the case of compressive preloading, the opposite occurs and the wave crest increases (Figure 6.52). This increment seems severe at higher compressive strains and can be associated with a coupling effect with local structural instability; however, more research is needed in this area to evaluate this hypothesis.

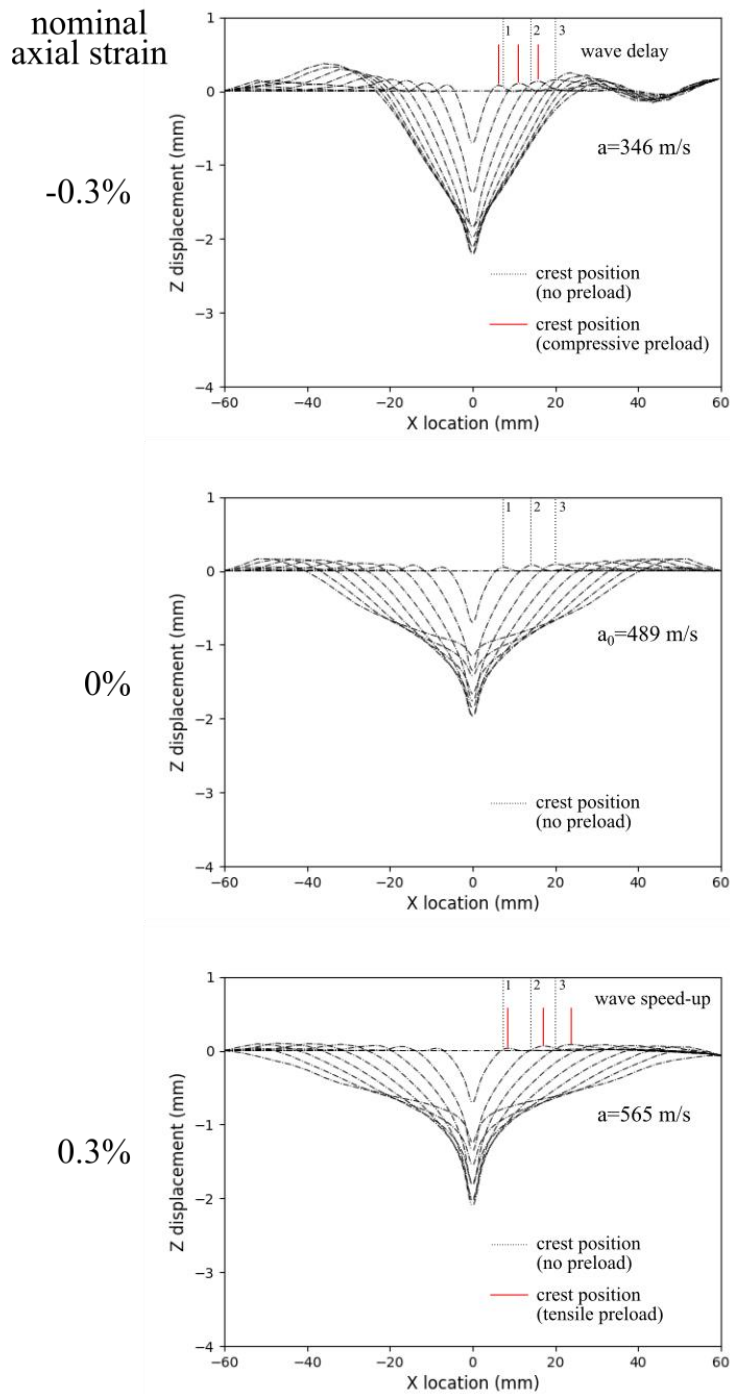


Figure 6.52. Vertical displacement of the midsection at different instants of impact for different axial preload conditions. (Agglomerated cork sandwich panel, $V_i = 60 \text{ m/s}$)

The total dissipated energy in the model increases with both tensile and compressive preloading if compared to the unloaded condition. A critical jump in the dissipation energy occurs at very large tensile and compressive overall strains (0.7 % and -0.5 % respectively). In both cases, this jump is associated with physical mechanisms induced by the preloading that are explained in the following paragraphs.

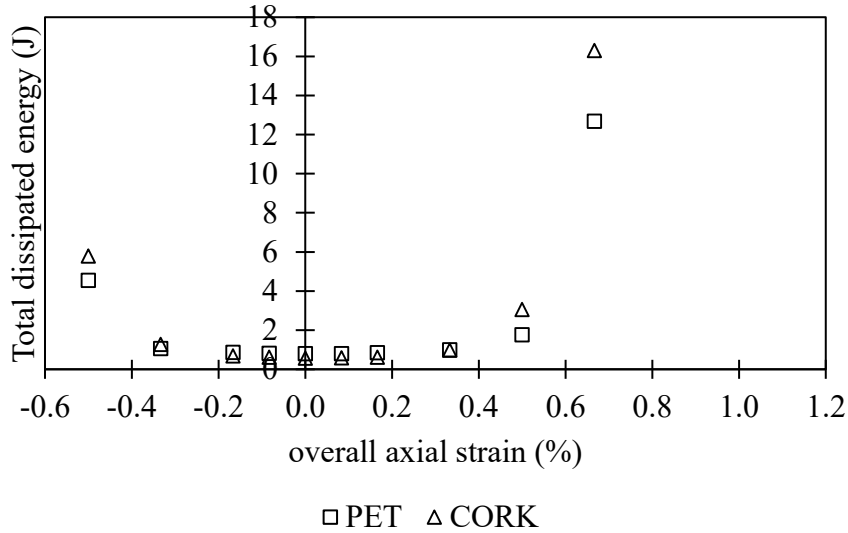


Figure 6.53. Total dissipated energy in the panel for different overall strains. Comparison between agglomerated cork core and PET foam core ($V_i=60$ m/s).

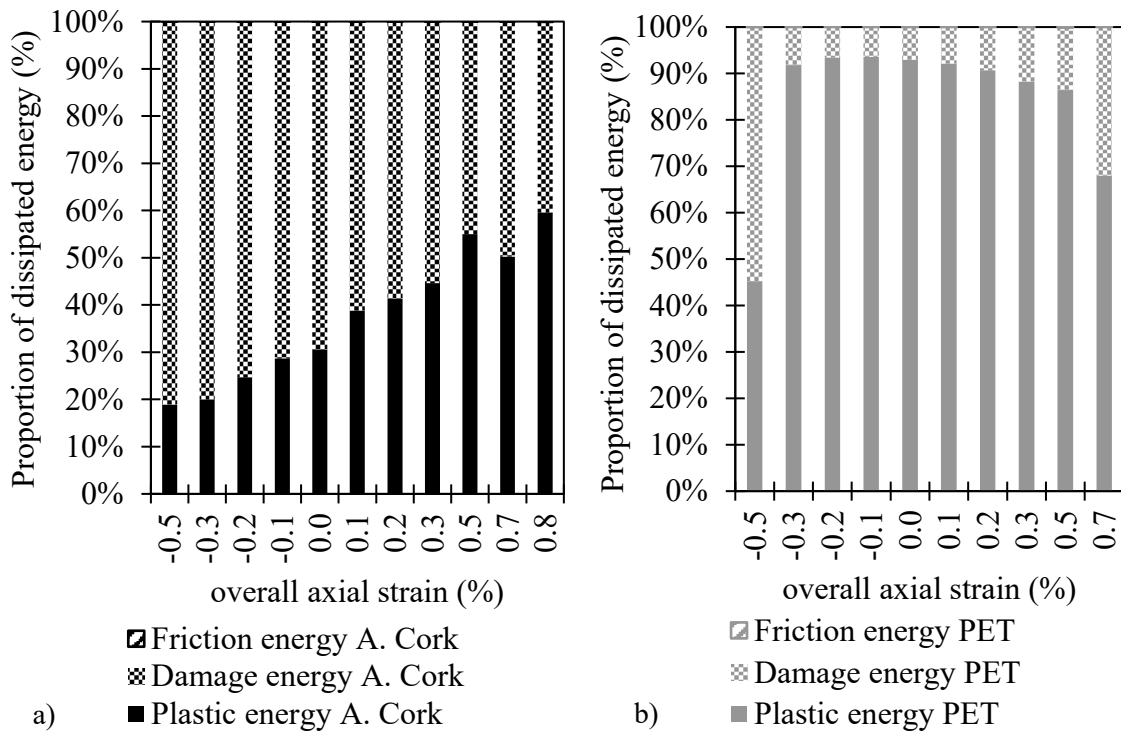


Figure 6.54. Mechanisms of dissipation energy at axial preloading conditions ($V_i=60$ m/s). Comparison agglomerated cork core (left) and PET foam core (right).

The contribution of damage energy and plastic energy as a percentage of the total dissipated energy is presented in Figure 6.54. In the case of agglomerated cork panels, there is a clear trend of the plastic dissipation component to increase with positive axial preloading while the opposite occurs for the damage energy. In the case of PET foam panels, this tendency is less clear but seems to show that damage energy increases with positive axial preloading.

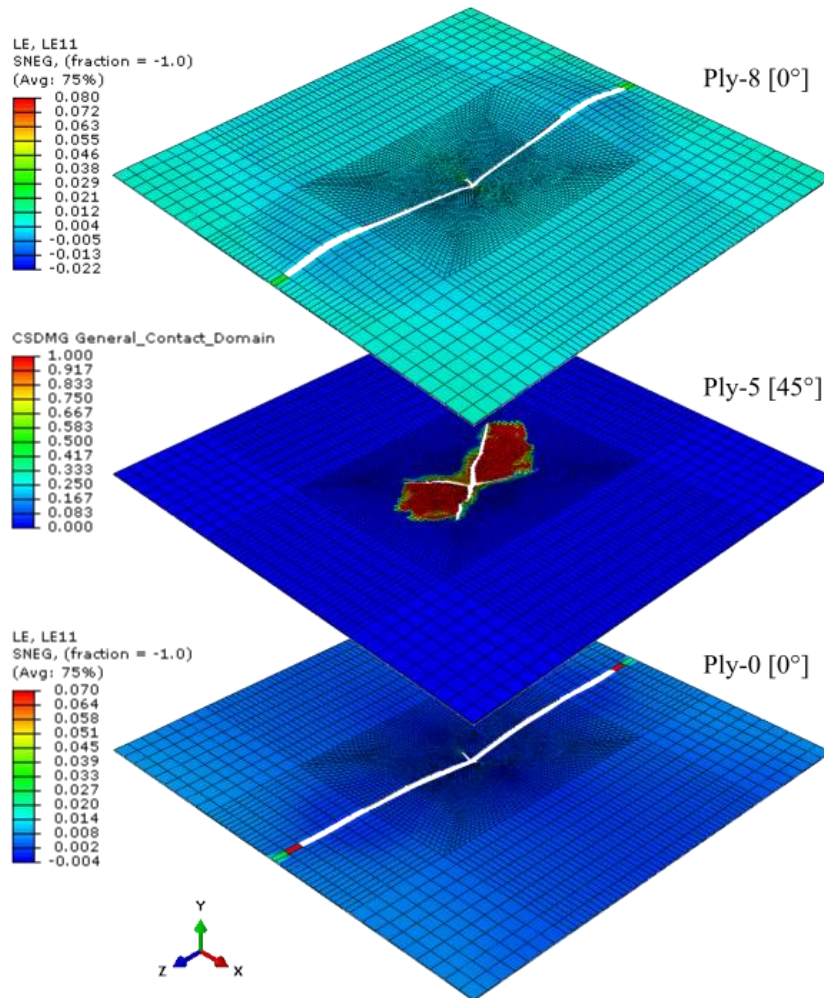


Figure 6.55. Damage extension in the front face-sheet for a high tensile preload (overall strain = 0.7%). Agglomerated cork core sandwich panel ($V_i=60$ m/s).

The variations in the total dissipated energy and their components at large tensile and compressive preloading strains seem to be dominated by two physical phenomena. The first is encountered at high tensile preload conditions ($\bar{\epsilon}=0.7\%$). In this case, the localized projectile impact compromises the integrity of the whole sandwich panel by triggering the appearance and extension of a large crack in the most exterior plies of the front face-sheet, which is aligned perpendicular to the preloading direction. An elongated cruciform crack pattern appears in the intermediate plies which are accompanied by large delamination.

(Figure 6.55). The phenomenon is observed in both sandwich panels and can be considered as a clear crash vulnerability issue for heavily loaded structures subjected to localized impact events.

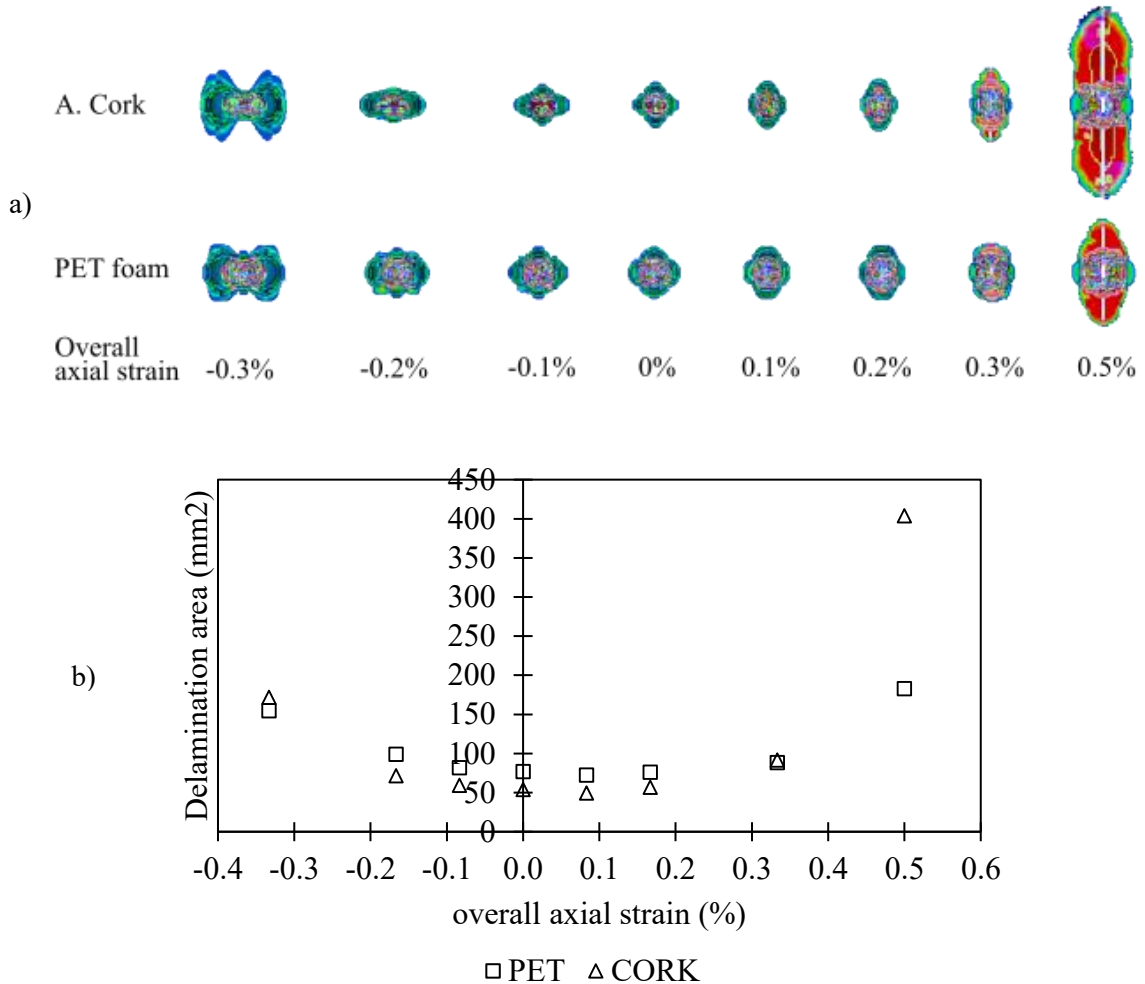


Figure 6.56. Delamination area in the front face-sheet for preloading conditions ($V_i=60$ m/s). Comparison between agglomerated cork core and PET foam core. a) Projection of the inter-laminar damage. b) Delamination area vs impact velocity.

The evolution of the initial crack pattern in ply 1 changes drastically depending on the direction of the axial preload and it is dominated by the stress field along the load direction (s_{11}). From Figure 6.57 it can be observed that when there is no axial preload the projectile produces a symmetric cruciform crack pattern that is aligned with the fibre directions 1 and 2 that grows symmetrically symmetrical during the whole impact. In contrast, when a tensile axial preload is applied the cruciform crack pattern changes. The length of the crack perpendicular to the direction of the preload is much larger than the parallel crack. This can be explained by the larger stress level around the perpendicular crack tip and the severity of the fracture in mode I produced by the axial preload.

If a compressive axial preload is applied instead, the opposite occurs. The length of the perpendicular crack is massively reduced while the crack parallel to the axial load is increased. As observed in Figure 6.57 the compressive stress due to the preload prevents Mode I fracture of the perpendicular crack. However, the stress concentration in the parallel crack increases if compared to the zero preload condition.

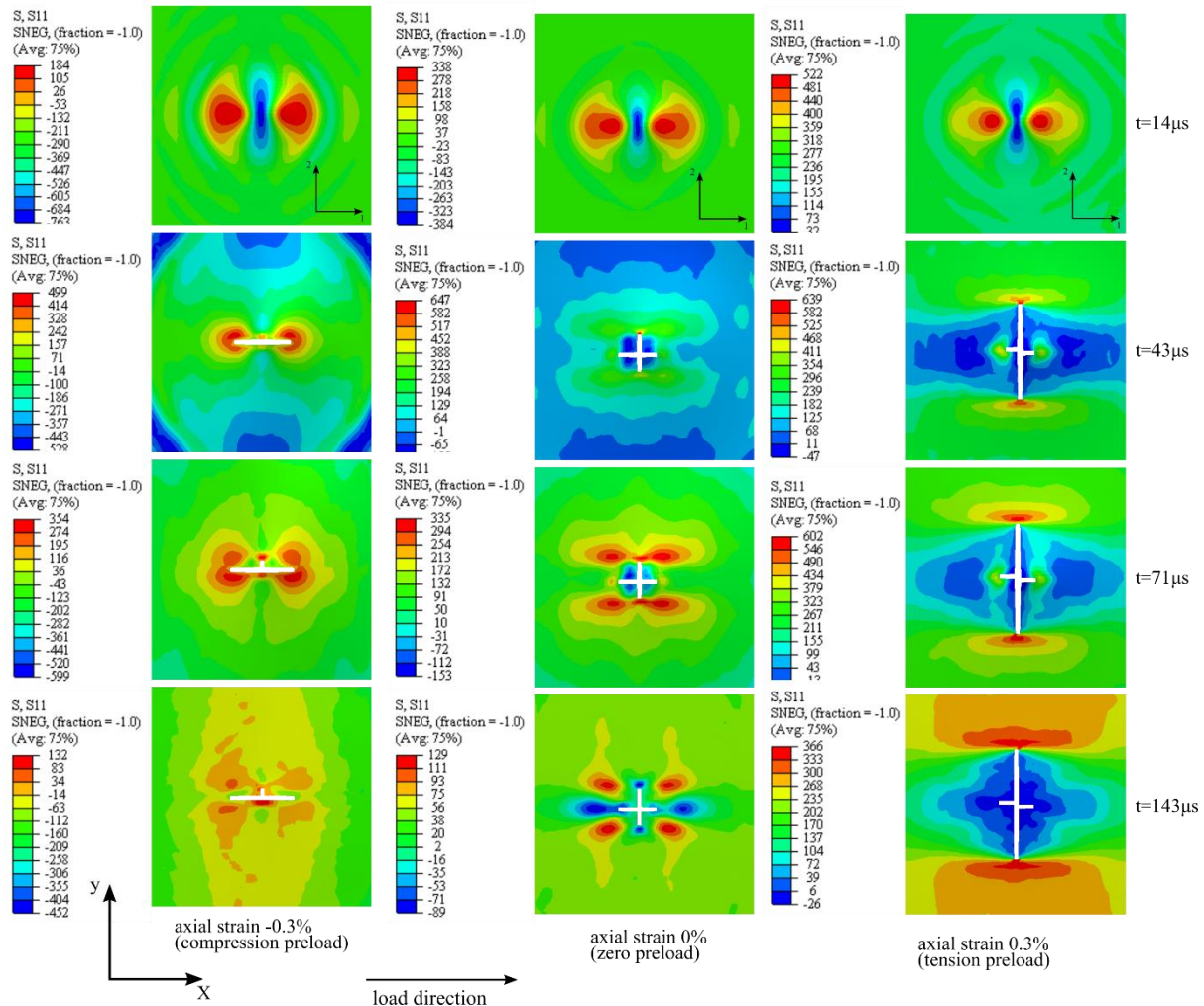


Figure 6.57. Crack pattern and axial stress distribution in ply 1 (front face-sheet) for three different preloading conditions (compression, tension, and zero preload). Agglomerated cork sandwich panel.

The total delamination area is larger when the panel is preloaded in compression than when it is non-preloaded or preloaded in tension. Additionally, the extend of the delamination region is aligned to the preload direction something opposite to the case when a tensile preload is applied (Figure 6.56). This particular behaviour can be associated with the appearance of buckling in the initially delaminated plies. Early delaminated plies have a lower local section moment of inertia than the rest of the face-sheet which makes them more susceptible to buckling. As a result, a lateral (out of plane) reaction force triggers

crack growth in mode I further increasing the delamination area in the direction of the preload (Figure 6.58).

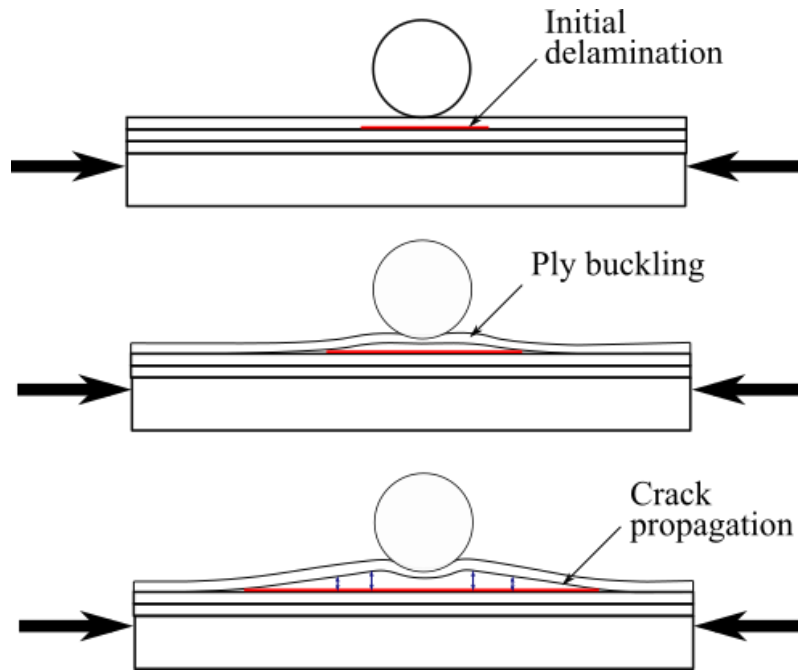


Figure 6.58. Ply buckling induced delamination growth

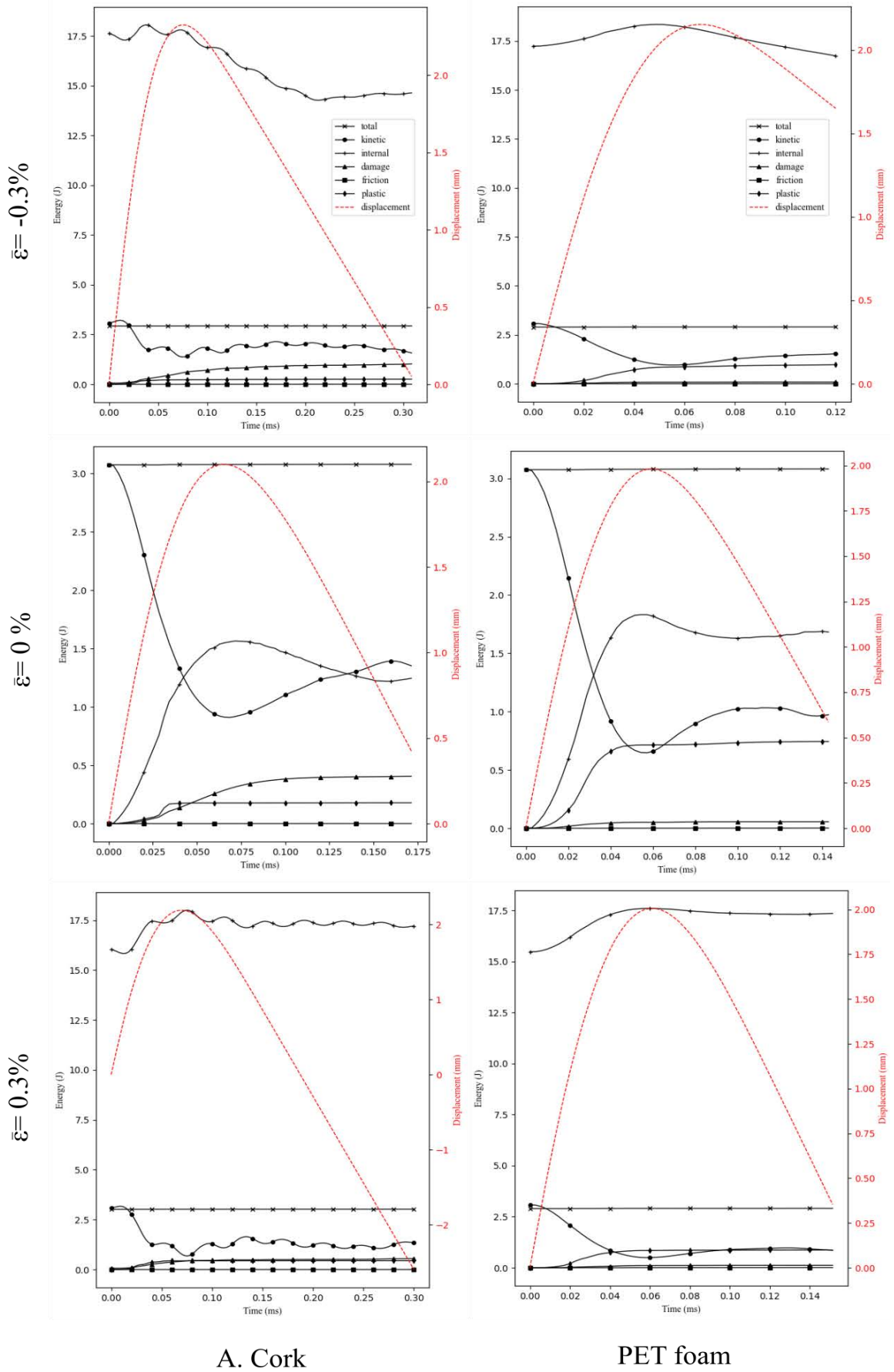


Figure 6.59. Evolution of the energies in the model at different preload levels.

Reference of the chapter

- [1] Abrate S. Localized impact on sandwich structures with laminated facings. *Appl Mech Rev* 1997;50:69–82. <https://doi.org/10.1115/1.3101689>.
- [2] Sayir M, Koller MG. Dynamic behaviour of sandwich plates. *ZAMP Zeitschrift Für Angew Math Und Phys* 1986;37:78–103. <https://doi.org/10.1007/BF00955520>.
- [3] Fatt MSH, Park KS. Dynamic Models for Low-Velocity Impact Damage of Composite Sandwich Panels-Deformation. *Compos Struct* 2001;52:335–51.
- [4] Hoo Fatt MS, Park KS. Dynamic models for low-velocity impact damage of composite sandwich panels -Part B: Damage initiation. *Compos Struct* 2001;52:353–64. [https://doi.org/10.1016/S0263-8223\(01\)00045-9](https://doi.org/10.1016/S0263-8223(01)00045-9).
- [5] Zhu Y, Sun Y. Dynamic response of foam core sandwich panel with composite facesheets during low-velocity impact and penetration. *Int J Impact Eng* 2020;139:103508. <https://doi.org/10.1016/j.ijimpeng.2020.103508>.
- [6] Feli S, Jafari · S S. Analytical modeling for perforation of foam-composite sandwich panels under high-velocity impact. *J Braz Soc Mech Sci Eng* 2017;39:401–12. <https://doi.org/10.1007/s40430-016-0489-7>.
- [7] Ivañez I, Barbero E, Sanchez-Saez S. Analytical study of the low-velocity impact response of composite sandwich beams. *Compos Struct* 2014;111:459–67. <https://doi.org/10.1016/j.compstruct.2014.01.028>.
- [8] Feng D, Aymerich F. Effect of core density on the low-velocity impact response of foam-based sandwich composites. *Compos Struct* 2020;239. <https://doi.org/10.1016/j.compstruct.2020.112040>.
- [9] Pascal F, Rogani A, Mahmoud B, Navarro P, Marguet S, Ferrero JF. Impact damage prediction in thin woven composite laminates – Part II: Application to normal and oblique impacts on sandwich structure. *Compos Struct* 2018;190:43–51. <https://doi.org/10.1016/j.compstruct.2018.02.013>.
- [10] Ivañez I, Santiuste C, Barbero E, Sanchez-Saez S. Numerical modelling of foam-cored sandwich plates under high-velocity impact. *Compos Struct* 2011. <https://doi.org/10.1016/j.compstruct.2011.03.028>.
- [11] Tang E, Yin H, Chen C, Han Y, Feng M. Simulation of CFRP/aluminum foam

- sandwich structure under high velocity impact. *J Mater Res Technol* 2020;9:7273–87. <https://doi.org/10.1016/j.jmrt.2020.04.093>.
- [12] Pascal F, Dorival O, Navarro P, Marguet S, Ferrero JF. Impact damage prediction in thin woven composite laminates – Part I: Modeling strategy and validation. *Compos Struct* 2018;190:32–42. <https://doi.org/10.1016/j.compstruct.2018.02.007>.
- [13] Sergi C, Tirill J, Sarasini F, Pozuelo EB, Saez SS, Burgstaller C. *The Potential of Agglomerated Cork for Sandwich Structures: A Systematic Investigation of Physical, Thermal, and Mechanical Properties* 2019.
- [14] Fathi A. *Mechanical Properties of Strand PET Foams at Different Length Scales*. ProQuest LLC, 2018.
- [15] Kepler J. Impact penetration of sandwich panels at different velocities - An experimental parameter study: Part I - Parameters and results. *J Sandw Struct Mater* 2004;6:357–74. <https://doi.org/10.1177/1099636204038217>.
- [16] Shih WK, Jang BZ. Instrumented impact testing of composite sandwich panels. *J Reinf Plast Compos* 1989;8:270–98. <https://doi.org/10.1177/073168448900800304>.
- [17] López-Puente J, Zaera R, Navarro C. High energy impact on woven laminates. *J Phys IV JP* 2003;110:639–44. <https://doi.org/10.1051/jp4:20020765>.
- [18] Kepler J. Impact penetration of sandwich panels at different velocities - An experimental parameter study: Part II - Interpretation of results and modeling. *J Sandw Struct Mater* 2004;6:379–97. <https://doi.org/10.1177/1099636204038218>.

7 HAILSTONE IMPACT OVER COMPOSITE SANDWICH PANELS

7.1 The hail impact vulnerability problem

7.1.1.1 Hailstone impact

Hailstones are lumps of ice, water and air in a layered structure that depending on their size can be either spherical, conical or ellipsoidal. Hail is formed by the accumulation of super-cooled liquid droplets during convective storms. The latent heating effect of the freezing droplets determines the content of air bubbles [1]. Hail density varies considerably showing values between 50 to 890 Kg/m³ for small hail sizes and 810 to 915 Kg/m³ for larger sizes [1]. Therefore, it is reasonable to assume the worst case of hailstone density as the density of solid ice (917 Kg/m³).

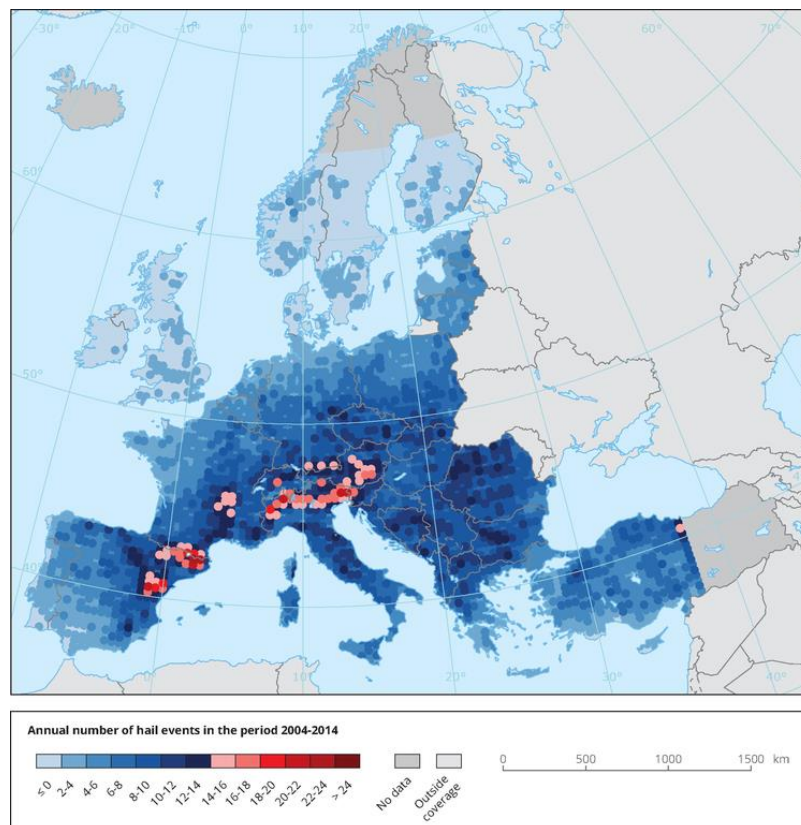


Figure 7.1. Annual hail frequency in Europe. Source: [3]

Hail is common in middle latitudes during spring and early summer. Months in which the upper atmosphere is cool enough to support ice but the surface temperature is warm enough to promote thunderstorm. Additionally, hail is more common in mountainous regions

where the elevations force the wind to deflect upwards. Court et al. [2] developed a worldwide geographical report on hail distribution and frequency per year.

Research in [4] reports the frequency of large hail in the United States from 1955 to 2002 showing that 42% of the hail reports correspond to the size of less than an inch of diameter (<25.4mm). While very large hailstones of around two inches (50.8 mm) account for 8.2% of the reports. In Europe: the Alps region, Italy, Romania, Greece and the south east of Europe are the regions with the highest frequency of hail events (Figure 7.1) with size larger than 15 mm. In these regions the density of events is in the range of 1.7 to 4.8 days of hail per year whilst in some particular areas this vale can reach up to 22 days per year [1].

The fall speed for hail has been previously estimated using the terminal fall speed equation for a sphere:

$$V_f = \sqrt{\frac{4g\rho_{hail}D}{3C_d\rho_{air}}} \quad (7.1)$$

Where g is the gravity acceleration, ρ_{hail} is the hailstone density, ρ_{air} is the air density, D is the characteristic diameter of the hailstone and C_d is the drag coefficient. Since C_d is a function of the Reynolds number (Re) and the hailstone shape, the terminal fall speed varies. However, it is commonly accepted that 10 mm particles have a fall speed in the range of 9 to 17 m/s while larger hailstones have fall speeds in the range of 20-35 m/s. Previous aircraft incidents investigations related to hail impact [5] have also shown that airplanes have encountered large hailstones with more than 50 mm of diameter.

There are numerous engineering structures using composite sandwich panels that are vulnerable to hailstone impact. Among them, the most critical situations occur with moving structures when there is a relative velocity between the hailstone and the structure. The relative impact velocity vector can be estimated by the summation of both velocity vectors measured from the same inertial reference frame. The magnitude of the impact velocity depends on the magnitude and direction of both velocity vectors whilst the impact angle also depends on the direction of the normal surface vector (Figure 7.3).

In most practical scenarios, two major simplifications can be made: the first, the direction of the hailstone falling velocity (V_f) is aligned to the vertical direction since gravity is the main acting force. Second, the magnitude of the structure's velocity is dominant since its magnitude is usually larger than the hailstone's falling speed (9-17 m/s for hailstones with diameters <10 mm and 20-35 m/s for hailstones up to 50mm) [1]. Therefore, the impact

velocity and obliquity can be approximately assessed by knowing the structure’s velocity and the normal vector of the impact surface.

A simple comparison of the operation speed of different engineering machines using sandwich construction shows that in most real applications the impact velocity of a hailstone should lay between the bounds of intermediate to high velocity impacts (Table 7.1). Based in this simple analysis, the author finds reasonable to use a velocity range between 60 m/s to 160 m/s to study the hailstone impact over sandwich structures. This in order to analyse similar impact conditions than those encountered in real life applications.

Type	Operation speed (m/s)
Medium range commercial airplane (Airbus A319)	230
Regional transport airplane (ATR 72)	142
Executive transport airplane (Beechcraft Start-ship)	158
Light jet airplane (Cirrus SF50)	157
Kit Aircraft (Lancair Legacy)	123
Light aircraft (Cirrus SR20)	80
Transport helicopter (Eurocopter EC155)	90
Rotor blade tip speed (Helicopter SA 330H Puma)	208 to 279
Rotor blade tip speed (2 MW Wind turbine Vestas V90)	87
Rotor blade tip speed (4 MW Wind turbine Vestas V112)	104
Rotor blade tip speed (8 MW Wind turbine Vestas V164)	104
High speed train (Acela Express)	74
High speed train (Siemens Velaro E)	112

Table 7.1. Operation speed of different engineering machines that could encounter hailstone impacts [27], [28], [29], [30], [31]



Figure 7.2. Hail impact damage on DC-8 aircraft operated by Scandinavian Airlines (SAS). Source: [5]

Hailstone impact should also be considered during the design phase of wind turbine blades to be installed in areas where hailstorm is common. The nacelle and the coating on the blades are especially vulnerable. However, in some critical conditions hailstone impact drives the design of the leading edge of rotor blades [6]. Early engineering handbooks in wind turbine development [7] highlight the importance of large hail impact as large as 1 to 2 in (25.4mm to 50.8mm) in geographical areas between 30N and 50N latitude. The same report also recommends for design purposes to assume a fall velocity of 20 to 30 m/s with a wind speed of 10 m/s.

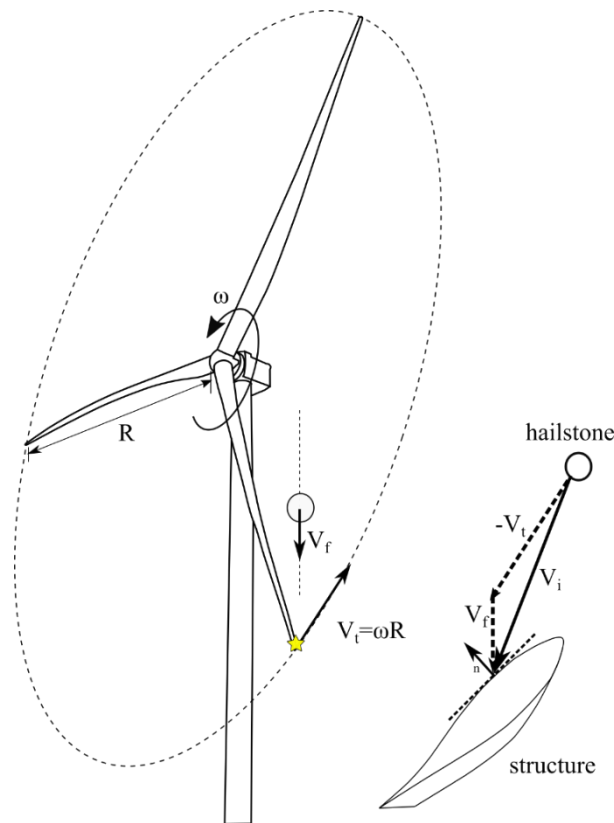


Figure 7.3. Relative impact velocity of a hailstone with an operating wind turbine blade.

Previous research in the analysis of hail impact has been carried out at the experimental and numerical level. The experimental procedure is similar in most studies and it uses a gas cannon to fire the projectile, a force transducer is used for measuring the impact force and a high-speed camera to observe the kinetic behaviour of ice during impact. Most of these studies use water ice to simulate hail-stones since the properties of hail-stones are highly variable and relatively unknown. One of the early works was carried out by Kim et al [8] using monolithic and layered ice spheres of 25.4mm and 50.8mm of diameter fired against a rigid force transducer and woven CFRP plates at speeds from 30 m/s to 213 m/s. It was observed that the ice spheres locally crush upon contact to the force transducer showing

micro-cracking through the sphere. The damage mode was classified depending on the impact velocity (Figure 7.4) and the elastic response of the composite panels was measured using strain gauges. An interesting observation made by the authors states that when there is not penetration of the panel the damage produced by a higher velocity impact is less detrimental to the structural performance than the damage produced by a lower impact velocity. In fact this finding suggest that the common industrial standard of performing a single experiment with the maximum perceived threat (or velocity) can be misleading since more severe damage modes can be present at lower impact velocities [8].

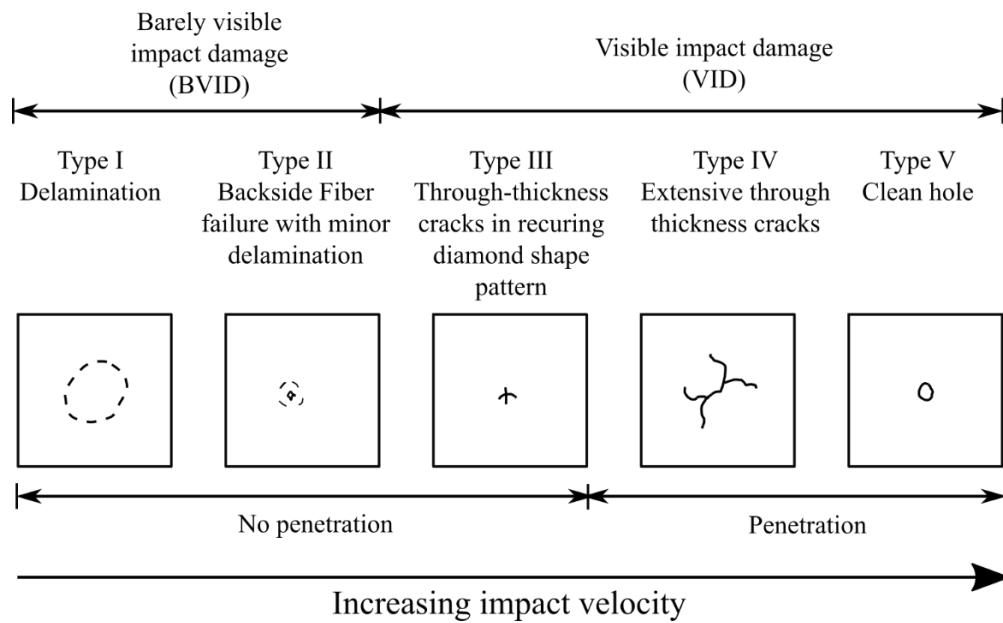


Figure 7.4. Failure modes in CFRP panels due to the impact of spherical ice projectiles. Source: [8]

In 2006 a research lead by Pereira et al. [9] at NASA evaluated the forces generated by high-velocity impact of ice (from 91 to 243 m/s) on a rigid structure. In this case, single-crystal and polycrystalline ice of two different densities were analysed. The ice projectiles were cylinders of 17.4mm of diameter and 42.6mm length. This research concluded that when the impact velocity is significantly lower than the wave propagation speed the ice projectile behaves like an agglomeration of many tiny ice particles rather than a single solid. Therefore, the mechanical properties (including density) and the crystal structure become relatively insignificant and the impact force is governed by the shape and mass of the projectile.

The repeated impact of hail ice (5mm to 20 mm of diameter) over GFRP panels was studied in [10] for speeds associated with wind turbine operation (50m/s to 95m/s). Even for a large

number of impacts, there was little evidence of surface damage and mass loss associated with erosion was minimum.

7.1.2 Mechanical behaviour of ice

The previous section outlined the variability of hail's mechanical properties. As result and in sake of simplicity it is a conservative and widely used practice to model hailstone with the properties of water frozen into a solid-state better known as ice. Depending on the pressure and temperature during the freezing process, ice can have several different crystalline structures, being the hexagonal the most commonly found in nature. These hexagonal crystals are grouped into polycrystalline grains for which its size can vary from one to tenths of millimetres [11]. Additionally, its structure can vary due to the presence of impurities such as particles or air bubbles. Therefore ice is can be better considered as a class of material rather than a single material [9].

Because of the random orientation of the granules and crystalline structure, ice is usually considered as an isotropic material [11]. Despite its importance in human life, the research about the mechanical properties of ice is less extensive than for common engineering materials and the description of the mechanical behaviour of ice is still in ongoing research.

Mechanical properties of ice are very variable and highly dependent on the strain rate, temperature and grain size. At temperatures between $-10\text{ }^{\circ}\text{C}$ to $-20\text{ }^{\circ}\text{C}$ the tensile strength of ice can be in the range of 0.7 to 3.1 MPa, commonly using the value of 1.43 MPa as an average from published scientific literature [12]. Although the tensile strength is rate-independent it decreases with increasing grain size. The elastic behaviour of ice presents small anisotropy along different directions with Young modulus between 8.6 to 10 GPa. At low strain rates ($<10^{-7}\text{ s}^{-1}$) tensile stress-strain curves show a ductile behaviour but at intermediate and high strain rate ($\sim 10^{-3}\text{ s}^{-1}$) the material is brittle [13].

In the same range of temperature, the compressive strength of ice can vary from 5 MPa to 25 MPa in quasi-static conditions showing a ductile behaviour at low and intermediate strain rates and brittle failure at strain rates in the order of 10^{-3} s^{-1} . However recent studies by Xianqian et al. [14] have observed ductile softening in the stress-strain curve and residual strength in the range of 119 to 271 s^{-1} . This ductile behaviour of ice is a dislocation-based process that raises the compressive flow stress similar to a Von Mises material were the deviatoric stress tensor is independent of the hydrostatic component [14].

The compressive properties of ice have been previously studied for quasi-static and dynamic conditions. Early research [15] carried out quasi-static compressive testing of ice at strain rates from 10^{-7} to 10^{-3} s^{-1} . This research used a regression analysis to find a power relationship between the initial yield point and the quasi-static strain rate. It was found that the tangent modulus is a good approximation for the estimation of Young's modulus. However, there is big scattering and a tendency for the apparent modulus to increase with strain rate. From the same research it was noticed that as strain becomes large the stress decreases to an asymptotical limit (residual strength) [15]. Other study was carried out on uniaxial compression of fresh and seawater ice at strain rates in the range of 10^{-1} s^{-1} to 10 s^{-1} using low and high-speed testing machines [16]. This research shows that the strength of the ice increases with strain rate within the analysed range. It was also reported that freshwater ice is about 1.4 times stronger than low salinity sea ice.

During recent years different compression testing has been carried out at high strain rates and temperatures. Shazly et al. [17] used a modified split Hopkinson Pressure Bar (SHPB) to study the dynamic response of single crystal and polycrystalline ice in the range of 60 to 1400 s^{-1} . The experimental results showed that at high strain rates there is also a positive strain rate dependency similar to other brittle materials such as ceramics and rocks. Additionally, it was reported that the effect of the microstructure is small in the analysed range. A similar study [14] also found a positive strain rate sensitivity for strain rates in the range 100 to 1350 s^{-1} showing a region of residual strength after the peak stress for a test temperature of $-15 \text{ }^\circ\text{C}$. The temperature dependence clearly shows that the peak strength increases in the range of $-15 \text{ }^\circ\text{C}$ to $-125 \text{ }^\circ\text{C}$ while it remains nearly constant in the range of $-125 \text{ }^\circ\text{C}$ to $-173 \text{ }^\circ\text{C}$. Similarly it was also observed that at low temperatures (from $-150 \text{ }^\circ\text{C}$ to $-173 \text{ }^\circ\text{C}$) the residual strength of ice is negligible.

7.2 Modelling Hail impact using FE analysis

Different numerical models have been proposed in order to model the impact behaviour of ice. Kim et al. [8] developed an explicit FE model of a spherical ice projectile impacting against a force transducer. Three projectile diameters were studied: 1 in (25.4 mm), 1.68 in (4.68 mm), and 2 in (50.8 mm). This model was implemented in DYNA3D using a Lagrangian mesh with a material Type-13 Elastic-Plastic and failure. For this material model once, the plastic failure strain is reached all shear stress components are set to zero. Additionally, once the failure pressure is reached the material is only allowed to carry

hydrostatic compressive stress behaving like a fluid. According to the author one of the disadvantages of this material model is its inability to provide any on strain rate dependency. Despite that constrain the kinetic behaviour, the peak force predictions and the elastic response of the target agreed with experimental observations in the range of velocity between 30 to 152 m/s.

A more sophisticated phenomenological model was developed by Kelly et al. [18] and the material model implemented in LS-DYNA using a multi-material Eulerian formulation. This model is able to capture the strain rate sensitivity of the flow stress and the ability of failed ice to continue carrying hydrostatic stress. Additionally, it has independent failure stress in tension and compression. At the request of NASA, this model is available in new versions of LS-DYNA as 155 MAT_PLASTICITY_COMPRESSION_TENSION_EOS.

Pernas-Sanchez et al. [19] developed a constitutive model for ice using the Drucker-Prager plasticity criteria which allows a different behaviour in tension and compression and introduces a pressure dependency for the yield surface. Additionally, this model includes a power law to account for the strain rate sensitivity observed in the experiments. The material model was implemented as a user subroutine in LS-DYNA and three different integration methods were analysed (Lagrangian, ALE and SPH) and validated with experimental testing.

Tippmann et al. [20] developed a simplified strain rate model in ABAQUS explicit. The material is modelled as an elastic-plastic material with Mises yield surface similar to the model used by Kim et al. The yield stress remains constant (zero plastic hardening) and its value is dependent on strain rate and given through a yield strength ratio obtained from the previous testing and tabulated using a linear-log fit. The tensile failure pressure (hydrostatic tension) is used for allowing failed elements to still carry hydrostatic stresses while their deviatoric component is set to zero. Comparison with experimental data shows a strong correlation in the peak impact force. The simulation was also able to predict the failure progression with the crack propagation observed in the high-speed video.

Soft body impacts can be modelled in FEA software packages using different integration approaches such as conventional Lagrangian, Eulerian, Arbitrary Lagrangian Eulerian (ALE) and Smooth Particle Hydrodynamics (SPH) [19], [21]. A Lagrangian mesh is the most conventional approach in FEA where mesh nodes are fixed to the material and the boundaries of the body are clearly defined. Because of that, large element distortions can

introduce severe numerical problems such as hourglassing, and negative volume elements [22]. In an Eulerian approach, the mesh is fixed in space and the material flows inside the mesh. As a result, the previously mentioned numerical problems do not occur but the exact geometry of the boundary can not be defined unless reducing the mesh size. Another disadvantage is that the size of the mesh domain is large since it must cover the space where the material would exist at any time. This makes this approach computationally inefficient. The ALE approach uses an Eulerian domain that is not fixed where the mesh moves and deforms with the material flowing inside. This significantly reduces the number of elements required for the simulation. However since the number of elements inside the domain is fixed the accuracy of the results is highly dependent on the mesh size and usually needs very fine meshes [22]. Finally, the SPH method is a meshless technique where the material is represented with discrete particles interacting with other neighbouring particles. Particles have their own mass, velocity and constitutive material behaviour which is evaluated through a smoothing kernel function in which a range of influence is defined. Using this approach the explicit time step is constant however large numbers of particles are required to achieve reliable numerical results

Previous works [19], [21] have analysed the aforementioned modelling approaches to model hailstone/ice impact showing that all of them accurately reproduce the ice behaviour showing that Lagrangian mesh produces the most accurate results while SPH method the most computationally efficient. In the remaining of this work, SPH is used to model the hailstone behaviour.

7.2.1 Smooth Particle Hydrodynamics (SPH)

The SPH method is a Lagrangian modelling method that allows the discretization of a set of continuum equations by interpolating the properties at a discrete set of points without using a mesh. It is useful for modelling structural problems involving severe distortions. Additionally, SPH can be linked to standard finite element Lagrangian formulations in order to be applied to a wide range of high-velocity impact problems [23].

This method is able to express a scalar or vector field at a given position of interest $A(\vec{r})$ by the use of a function that is dependent on the relative position of adjacent points and the value of the field in these adjacent locations [24].

$$A_s(\vec{r}) = \int W(\vec{r} - \vec{r}')A_s(\vec{r}')dr' \quad (7.2)$$

Where W is a function satisfying the condition

$$\int W(\vec{r})dr = 1 \tag{7.3}$$

Since $A_s(r')$ is unknown it cannot be evaluated directly. However, having a set of N points $r_1 r_2 r_3 \dots r_N$ distributed according to the density ρ , the integral can be evaluated by the Monte Carlo method.

$$A_N(r) = \frac{M}{N} \sum_{j=1}^N W(\vec{r} - \vec{r}_j) \frac{A(\vec{r}_j)}{\rho(\vec{r}_j)} \tag{7.4}$$

Where

$$M = \int \rho(\vec{r})dr \tag{7.5}$$

Since in many applications it is desired to compute the continuum derivative of the smoothed function is common to use either a Gaussian, B-spline or a Quadratic smoothing function [24], [23]:

$$W = \left(\frac{1}{\pi h^2}\right)^{\frac{3}{2}} e^{-\frac{r^2}{h^2}} \tag{7.6}$$

$$W = \frac{1}{\pi h^3} \left[1 - \frac{3}{2} \left(\frac{r}{h}\right)^2 + \frac{3}{4} \left(\frac{r}{h}\right)^3\right] \tag{7.7}$$

$$W = \frac{1}{\pi h^3} \left[\frac{5}{8} \left(\frac{r}{h}\right)^2 - \frac{3}{2} \left(\frac{r}{h}\right) + \frac{3}{2}\right] \tag{7.8}$$

Where h is a parameter with units of length that tends to zero when N tends to infinity. It is important to notice that as N increases $A_N(r)$ better approximates to $A(r)$.

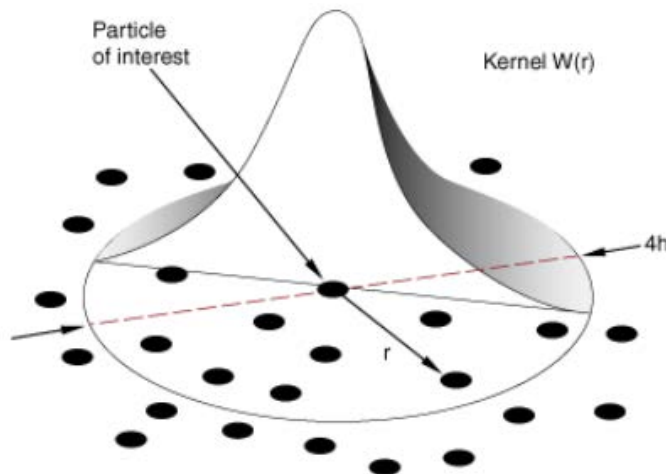


Figure 7.5. Kernel function in a group of particles. Source: [25]

The solution algorithm of SPH particles is similar than for standard elements with the exception that the computation of the strain, strain rate and nodal force is different.

Initially, a point of interest is designated as the centre node and neighbour nodes are searched in order to estimate their relative position, their mass and diameters. This time can be significant for large problems.

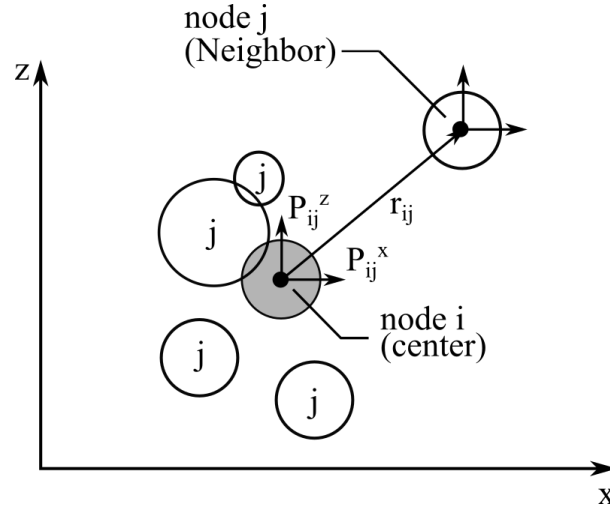


Figure 7.6. Force of a neighbour node over a centre node

Knowing the current velocities and displacements of all nodes the corresponding strain and strain rates are calculated using the previously mentioned smoothing functions W_{ij} and its derivative respect to position W'_{ij} . Here V_j is the volume of node j while \dot{u}_j, \dot{v}_j , are the velocities of node j in x and z directions (Figure 7.6). Additionally l_x, l_y, l_z represent the director cosines between nodes i and j .

$$\dot{\varepsilon}_x = - \sum_j \beta_x W'_{ij} V_j (\dot{u}_j - \dot{u}_i) l_x \quad (7.9)$$

$$\dot{\varepsilon}_y = - \sum_j \beta_y W'_{ij} V_j (\dot{v}_j - \dot{v}_i) l_y \quad (7.10)$$

$$\dot{\varepsilon}_z = - \sum_j \beta_z W'_{ij} V_j (\dot{u}_j - \dot{u}_i) l_z \quad (7.11)$$

$$\dot{\gamma}_{xy} = - \sum_j W'_{ij} V_j [\beta_y (\dot{u}_j - \dot{u}_i) l_y + \beta_x (\dot{v}_j - \dot{v}_i) l_x] \quad (7.12)$$

$$\gamma_{xz}^x = - \sum_j W'_{ij} V_j [\beta_x (\dot{w}_j - \dot{w}_i) l_x + \beta_z (\dot{u}_j - \dot{u}_i) l_z] \quad (7.13)$$

$$\gamma_{yz}^y = - \sum_j W'_{ij} V_j [\beta_z (\dot{v}_j - \dot{v}_i) l_z + \beta_y (\dot{w}_j - \dot{w}_i) l_y] \quad (7.14)$$

Where β factors are given by:

$$\beta_x = \frac{-1}{\sum_j W'_{ij} V_j r_{ij} l_x^2} \quad (7.15)$$

$$\beta_y = \frac{-1}{\sum_j W'_{ij} V_j r_{ij} l_y^2} \quad (7.16)$$

$$\beta_z = \frac{-1}{\sum_j W'_{ij} V_j r_{ij} l_z^2} \quad (7.17)$$

After the strain rates are calculated it is possible to determine the stress tensor in the standard manner. The forces P_{ij}^x , P_{ij}^y , P_{ij}^z exerted by a neighbouring particle over the central node are given as follows:

$$P_{ij}^x = W'_{ij} V_i V_j [\beta_x (\sigma_i^x - Q_{ij}) l_x + \beta_y \tau_i^{xy} l_y + \beta_z \tau_i^{xz} l_z] \quad (7.18)$$

$$P_{ij}^y = W'_{ij} V_i V_j [\beta_y (\sigma_i^y - Q_{ij}) l_y + \beta_x \tau_i^{xy} l_x + \beta_z \tau_i^{yz} l_z] \quad (7.19)$$

$$P_{ij}^z = W'_{ij} V_i V_j [\beta_z (\sigma_i^z - Q_{ij}) l_z + \beta_x \tau_i^{xz} l_x + \beta_y \tau_i^{yz} l_y] \quad (7.20)$$

Where σ_i and τ_i are the normal and shear stresses at the neighbouring particle and Q_{ij} is an artificial viscosity which depends on the relative velocities. It is used for stability purposes and keep an adjacent node from becoming too close to one another [23]. After collecting the forces from the SPH nodes, the velocity and displacements are updated for all nodes.

7.2.2 Modelling hailstone plasticity

7.2.2.1 Mises Yield Criteria

From the discussion in previous sections, it has been shown that ice can be considered as an isotropic material that exhibits a ductile behaviour and plastic flow in compression. A classical plasticity model based on a Mises yield surface is proposed in order to predict the onset of yielding. This criterion predicts that yielding occurs when the applied strain energy density exceeds the strain energy density for yield in simple uniaxial tension or compression. This yield stress criterion can be easily explained based on the relationship between the deviatoric strain energy density and effective stress (Mises) [25].

The strain energy density W (do not confuse with kernel function W) can be given in terms of the hydrostatic and deviatoric components as shown below

$$W = \frac{1}{2} \sigma_{Hyd} : \varepsilon_{hyd} + \frac{1}{2} \sigma' : \varepsilon' \quad (7.21)$$

Where the deviatoric strain energy density is given by

$$W' = \frac{1}{2} \sigma' : \varepsilon' \quad (7.22)$$

Recalling from Hook's law that the deviatoric strain is only a function of the deviatoric strain

$$\varepsilon' = \frac{1}{2G} \sigma' \quad (7.23)$$

The strain energy density can be expressed in terms of the deviatoric stress.

$$W' = \frac{1}{4G} \sigma' : \sigma' \quad (7.24)$$

Since the deviatoric strain energy is a function of the double dot product of the deviatoric stress tensor it is convenient to replace it by a representative scalar equivalent $\sigma_{Rep} = \sqrt{\sigma' : \sigma'}$

$$W' = \frac{1}{4G} \sigma' : \sigma' = \frac{1}{4G} \sigma_{Rep}^2 \quad (7.25)$$

For the case of uniaxial tension (σ) it can be shown that

$$\sigma_{Rep} = \sqrt{\frac{2}{3}} \sigma \quad (7.26)$$

For convenience, since the representative stress is $\sqrt{\frac{2}{3}}$ times the stress measured in uniaxial testing a scale factor of $\sqrt{\frac{3}{2}}$ is applied to give as a result the effective Mises stress.

$$\sigma_{VM} = \sqrt{\frac{3}{2} \sigma' : \sigma'} \quad (7.27)$$

An effective strain can also be defined

$$\varepsilon_{eff} = \sqrt{\frac{2}{3} \varepsilon' : \varepsilon'} \quad (7.28)$$

7.2.2.2 Hardening and strain rate dependency

The Mises yield surface is used to define isotropic yielding. The flow rule and the evolution law are given in terms of uniaxial yield stress that is a function of uniaxial equivalent plastic strain. Since ductile materials present large inelastic strains it is convenient to express the equivalent plastic strain as a true (logarithmic) strain [26]:

$$\varepsilon_{ln}^{pl} = \ln(1 + \varepsilon_n) - \frac{\sigma_{true}}{E} \quad (7.29)$$

Where ε_n is the nominal (engineering) strain, σ_{true} is the true stress and E is the Young's modulus. Figure 7.7. illustrates the typical example of a ductile material that is loaded twice above its yield stress (segments ABCD and DCF).

It can be noticed that each loading produces a plastic strain ε_1^{pl} , ε_2^{pl} being the total logarithmic plastic strain $\varepsilon_{ln}^{pl} = \varepsilon_1^{pl} + \varepsilon_2^{pl}$. Additionally, the total plastic strain is lower than the total logarithmic strain due to the elastic recovery $\frac{\sigma_{true}}{E} = \varepsilon_2 - \varepsilon_2^{pl}$

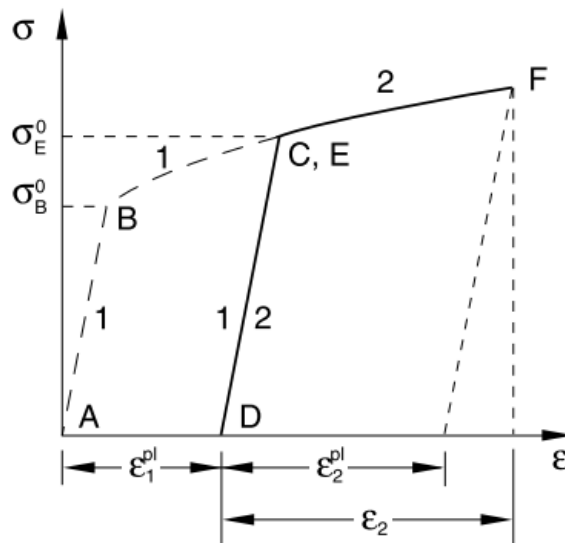


Figure 7.7. Equivalent plastic strain. Source: [25]

As discussed in previous sections the ice's strength and ductile behaviour show a high dependency with strain rate. This strain rate dependency can be implemented in the plasticity model using the yield stress ratio R that is the ratio of the yield stress at nonzero strain rate to the static yield stress (σ^0). Therefore the yield stress can be expressed in the following manner [26]:

$$\bar{\sigma} = \sigma^0(\varepsilon^{pl})R(\dot{\varepsilon}^{pl}) \quad (7.30)$$

7.2.2.3 Dynamic failure model

Failure can be implemented together with the plasticity model using a tensile failure model. This criteria uses hydrostatic pressure stress (p) as a failure quantity to model dynamic spall or a pressure cut-off. Failure occurs once the pressure stress has reached a value higher than the specified cut-off stress.

Once the element has failed, the element can be removed or assigned any of the following spall (crumbling) models [26]:

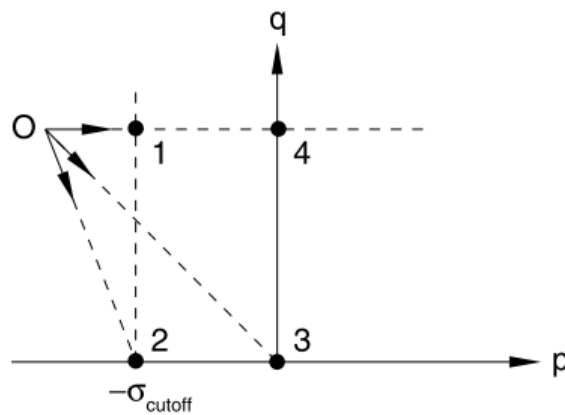


Figure 7.8. Tensile failure choices. Source: [25]

The deviatoric stress components (q) can be either unaffected or be zero, and the pressure stress can be limited by the hydrostatic cut-off stress or must be compressive (Figure 7.8).

- Ductile shear and ductile pressure (1): The deviatoric stress components are not affected and the pressure stress is limited to the hydrostatic cutoff stress.
- Brittle shear and ductile pressure (2): The deviatoric stress components are zero and the pressure stress is limited by the hydrostatic cutoff stress.
- Brittle shear and brittle pressure (3): The deviatoric stress components are zero and the pressure stress must be compressive.
- Ductile shear and brittle pressure (4): The deviatoric stress components are not affected and the pressure stress must be compressive.

7.2.3 FEA validation of the hailstone impact

A dynamic/explicit FEA model in Abaqus V6.14 is developed to validate the material model of ice. Results are compared against available scientific literature validating the model and its suitability for hailstone impact simulations.

The model consist of a spherical solid ice projectile of 50.8 mm diameter fired against a semi-rigid flat wall at three different impact velocities (60 m/s, 104 m/s, and 144 m/s). The impact force history and the maximum impact force are the main quantitative validation variables. However, the qualitative analysis of the ice fragmentation is also used to support the validation of the model.

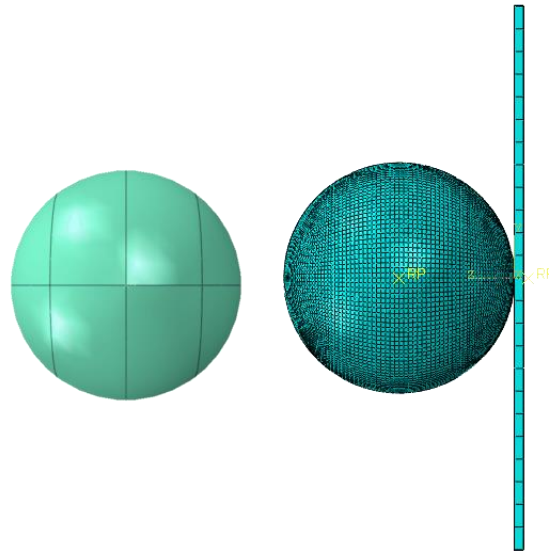


Figure 7.9. FEA model. Projectile partition and mesh.

The projectile is modelled using the SPH integration scheme with a cubic (B-spline) Kerner function. The projectile is meshed using hexahedral C3D8R elements with a nominal size of 1 mm. Due to the spherical shape of the projectile and in order to get a mesh with the desired type of element it was necessary to partition the projectile into semi-hemispherical segments (Figure 7.9). Particle conversion is applied at the initial time increment creating only one particle per element. The initial impact velocity is assigned to all nodes in the projectile mesh and a frictionless general-explicit contact definition is used.

The semi-rigid flat wall is modelled as a deformable rigid solid body made of steel using hexahedral C3D8R elements with a mesh size of 5 mm. The surface opposite to the impact face is constrained in all DOF in order to avoid bending on the wall but allow local compression of the impact region. A linear bulk viscosity parameter of 1.2 is used to reduce numerical instability produced by high-frequency noise in the explicit algorithm.

7.2.3.1 Material model

For steel, a perfect linear elastic material is used with the following properties: $\rho=7850 \text{ Kg/m}^3$, $E=200 \text{ GPa}$, $\nu=0.25$. Ice is modelled as a linear elastic material (Table 7.2) with Mises plasticity and strain rate dependency.

Property	Value
$\rho \text{ (Kg/m}^3\text{)}$	900
$E \text{ (GPa)}$	9300
ν	0.3
$\sigma_{\max} \text{ (MPa) (quasi-static)}$	-3.56
$p_{\max} \text{ (MPa)}$	1.5

Table 7.2. Basic mechanical properties of ice. Source: [20]

The plastic region is defined through a tabulated data series (Table 7.4) that contains the yield stress vs the equivalent plastic strain. This table allows to include the description of the hardening/softening “shoulder” region observed in experimental testing together with the residual strength. This characteristic curve was obtained from dynamic compression experiments carried out by [14] and scaled to a quasi-static scenario (Figure 7.10).

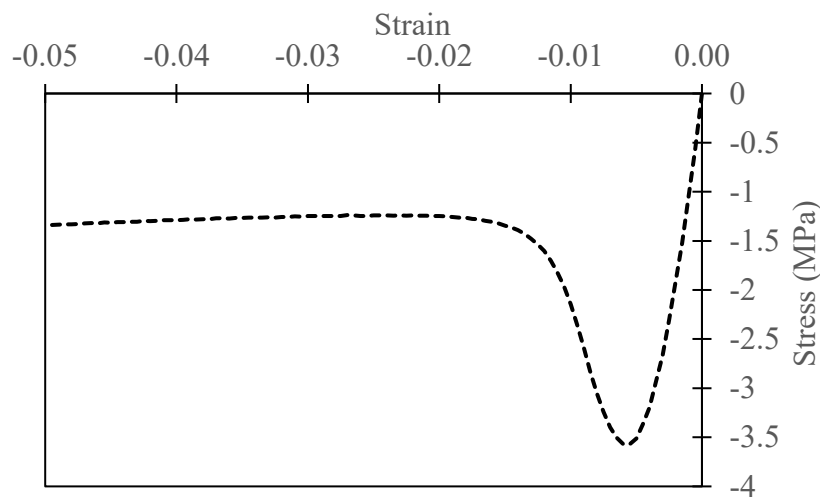


Figure 7.10. Quasi-static stress vs strain curve for ice. Reconstructed from [14]

R	strain rate (s ⁻¹)
1	0
1.01	0.1
1.4956	0.5
1.709	1
2.2046	5
2.418	10
2.9136	50
3.127	100
3.6226	500
3.836	1000
4.3316	5000
4.5451	10000
5.0406	50000
5.2541	100000
5.7496	500000
5.9631	1000000

Table 7.3. Strain rate sensitivity for ice. Yield stress ratio vs strain rate. Source: [20]

The tensile failure pressure (hydrostatic tension p_{\max}) is used for allowing failed elements to still carry hydrostatic stresses while their deviatoric component is set to zero (Table 7.2) [20]. Since the Abaqus graphic user interface (GUI) does not provide a direct method to include this failure criteria the following code lines were added to the input file in the material definition section:

```
*TENSILE FAILURE, SHEAR=BRITTLE,PRESS=DUCTILE
1.5
```

The strain rate dependency is also included in tabular form through the yield strength ratio R and the equivalent strain rate (Table 7.3). Values used were obtained from a parametric analysis carried out by Tippman et al [20].

σ_y (MPa)	ϵ_0
2.704	0.00000
2.895	0.00014
3.064	0.00024
3.234	0.00041
3.400	0.00071
3.567	0.00116
3.500	0.00265
3.339	0.00350
3.170	0.00415
3.003	0.00477
2.834	0.00532
2.665	0.00585
2.496	0.00638
2.327	0.00694
2.159	0.00754
1.991	0.00818
1.825	0.00894
1.662	0.00982
1.512	0.01108
1.387	0.01276
1.315	0.01492
1.283	0.01720
1.269	0.01950
1.272	0.02179
1.281	0.02407
1.282	0.02634
1.292	0.02861
1.304	0.03087
1.313	0.03316
1.330	0.03541
1.340	0.03769
1.352	0.03996
1.371	0.04221
1.387	0.04447
1.405	0.04673

Table 7.4. Plastic region curve for ice. True stress vs true plastic strain. Source: [14]

7.2.3.2 Mesh sensitivity

Despite the advantages in processing time of the SPH method it is observed that the computation effort required for this simulation is a critical constraint for the available computer power. Therefore, it is decided to perform a mesh sensitivity analysis in order to properly select the element size. The maximum peak force is used as a control variable and

four mesh sizes are tested ranging from 2 mm to 0.8 mm. Larger element sizes are not analysed since they are unable to accurately represent the circumference of the hailstone. In contrast, smaller element sizes overcome the memory capability of the available PC constantly generating software crash and inadmissible processing times. From Figure 7.11 it is observed that the force history is similar for all analysed meshes however, for the largest element size (2mm) there is large numerical instability and the peak force is overestimated.

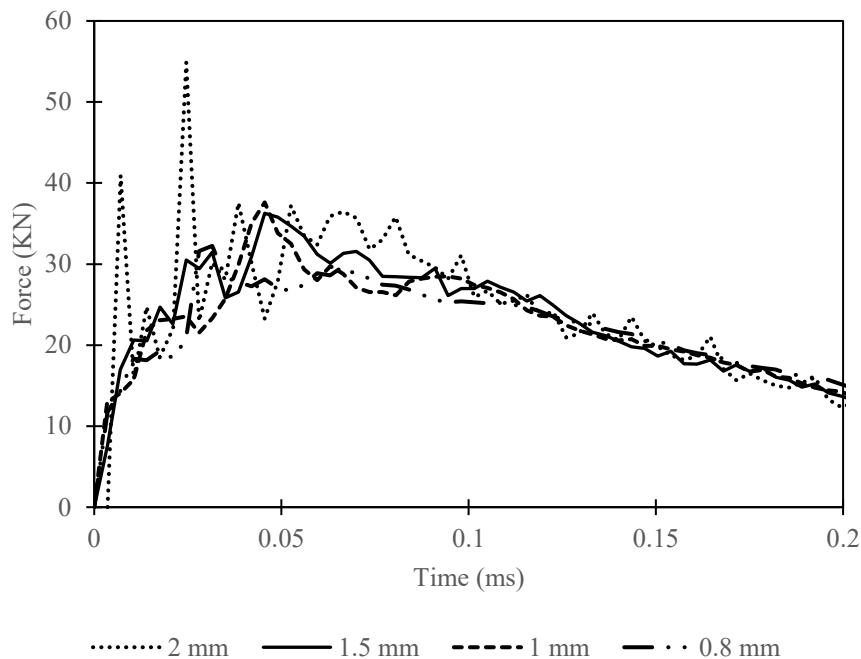


Figure 7.11. Mesh sensitivity analysis with different element sizes. Force history (Projectile $D=50.8$ mm, $V_i=104$ m/s)

Figure 7.12 shows that for element sizes between 1.5 mm to 0.8 mm the peak force is similar. However, the CPU processing time for 0.8mm is five times larger than for 1 mm. As a result it was concluded that element sizes between 1 mm to 1.5 mm offer the best compromise between numerical accuracy with an error in the order of 3% and processing time in the order of hours.

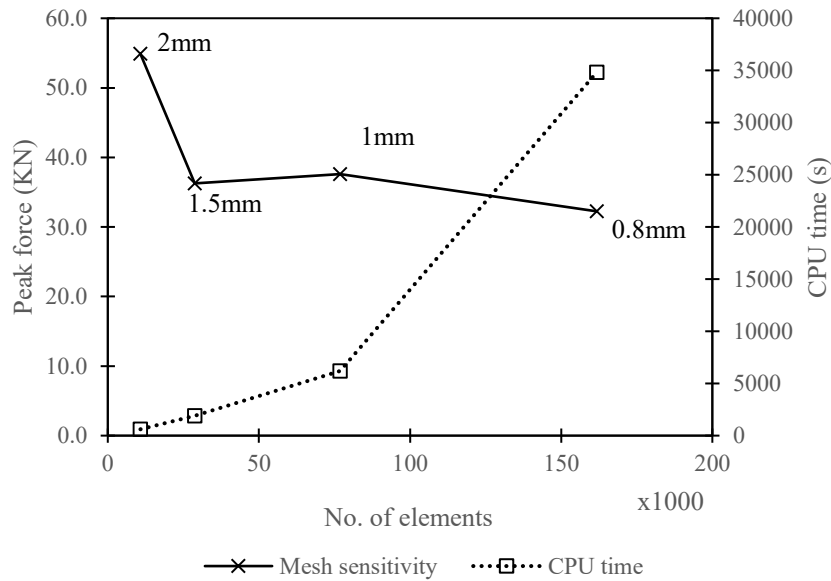


Figure 7.12. Mesh sensitivity analysis. Peak force & CPU time (Projectile $D=50.8$ mm, $V_i=104$ m/s)

7.2.3.3 Results of the hailstone model validation

From the results obtained in the FEA model, the evolution of the reaction force is analysed during the impact. Figure 7.13 plots the force history at three different impact velocities. From this figure, it can be noticed that the impact force has a steep increment during the initial instants of impact reaching a peak value followed a progressive decrease in the impact force. It is clear that the peak load is a function of the impact velocity presenting higher values at larger impact velocities. Figure 7.14 shows the stress distribution over the projectile at the instant of maximum force. It is also noticed that the stress distribution can be divided into three main regions along the impact direction. A first region next to the impact surface is dominated by plastic deformation with nearly constant stress levels in the range to 5 to 6 MPa. This plastic region is followed by a region of higher stress level in the range of 6 to 12 MPa that is dominated by the presence of longitudinal cracks created by local tensile failure. Similar longitudinal cracks were found experimentally by Tippman et al. [20]. The third region is found at the opposite end of the impact surface where the strain level is minimum and there is not plastic strain.

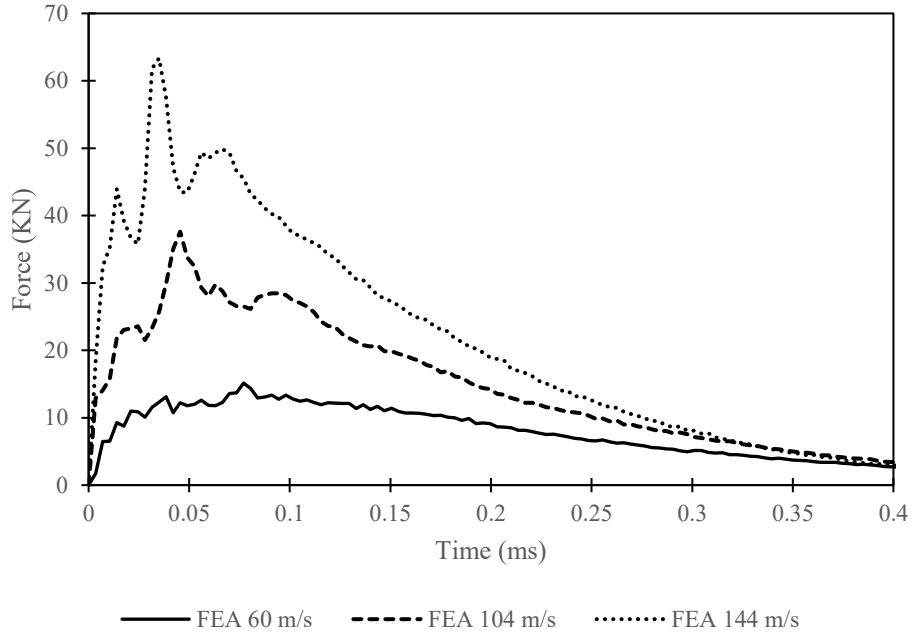


Figure 7.13. FEA model force history at different impact velocities

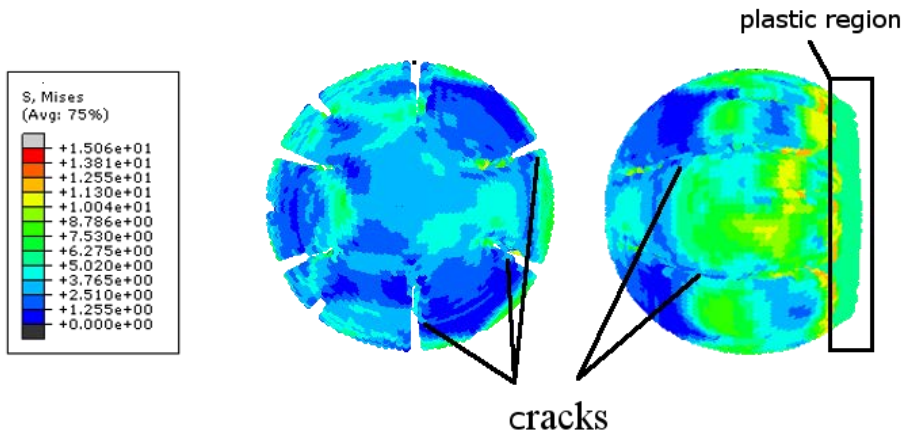


Figure 7.14. Crack propagation. $V_i=60 \text{ m/s}$ at $t=80 \mu\text{s}$

The evolution of the plastic strain region along the mid-plane of the projectile is presented in Figure 7.15. From this figure, the plastic region predominantly occurs at the centre of the projectile instead than in the free surface. This behaviour is explained from the spherical shape projectile since the centre region is the first to contact the rigid surface accumulating over time more plastic deformation than the external surface.

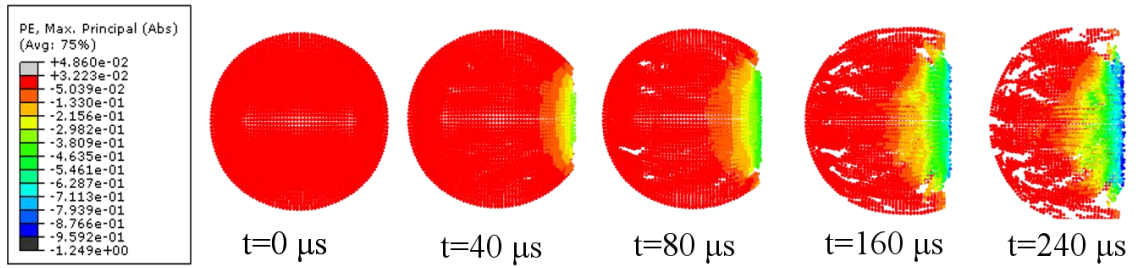


Figure 7.15. Evolution of the plastic strain region (mid-plane)

From Figure 7.16 to Figure 7.18 it can be observed the comparison of the force history for each impact velocity obtained by the FEA model and experimental testing carried out by Tippman et al. [20]. The correlation shows a good agreement particularly in the estimation of the peak force and the time it occurs. Additionally, the model is able to capture the softening region after impact as well as the kinematic evolution and fragmentation of the projectile (Figure 7.19) as reported in the literature [20].

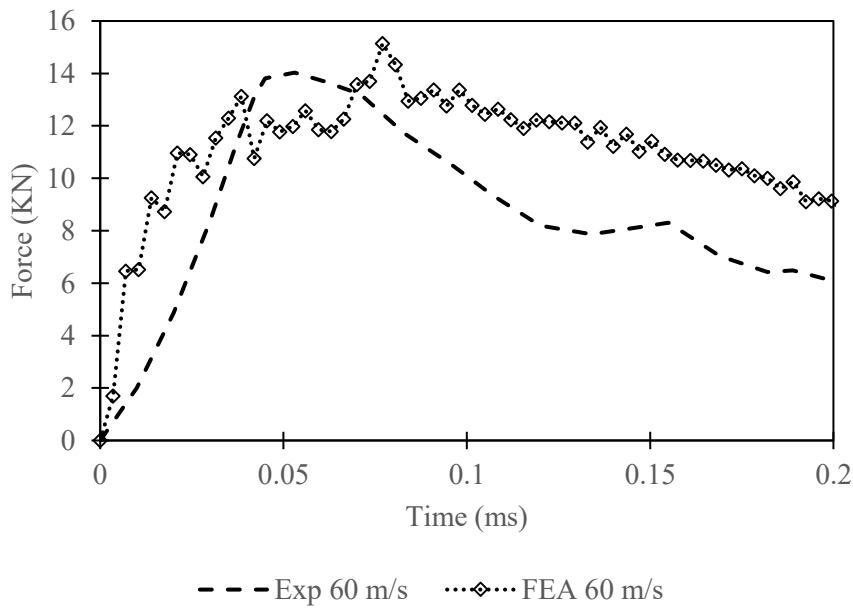


Figure 7.16. Impact force history. $V_i = 60 \text{ m/s}$

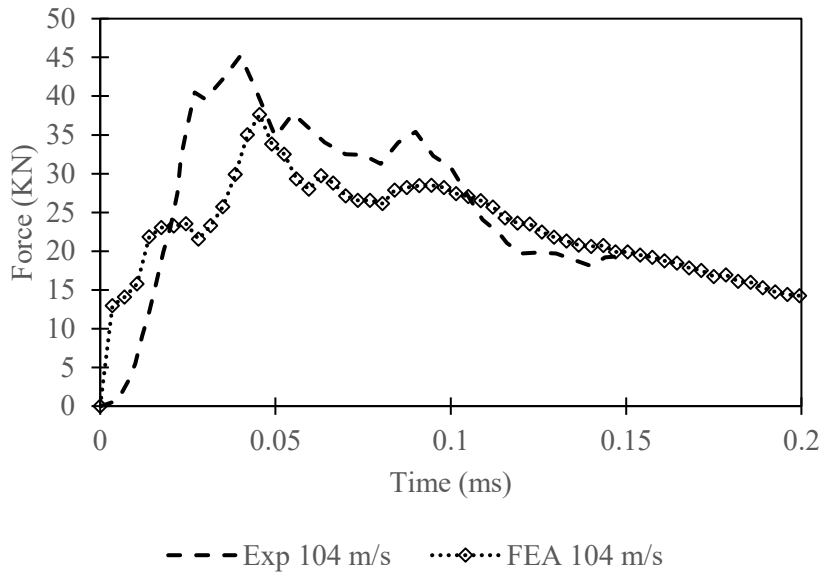


Figure 7.17. Impact force history. $V_i = 104$ m/s

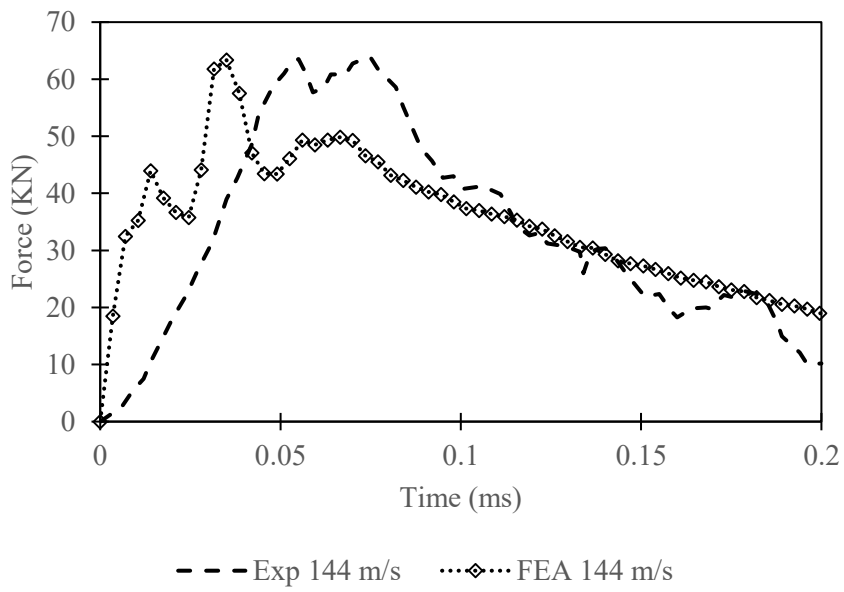


Figure 7.18. Impact force history. $V_i = 144$ m/s

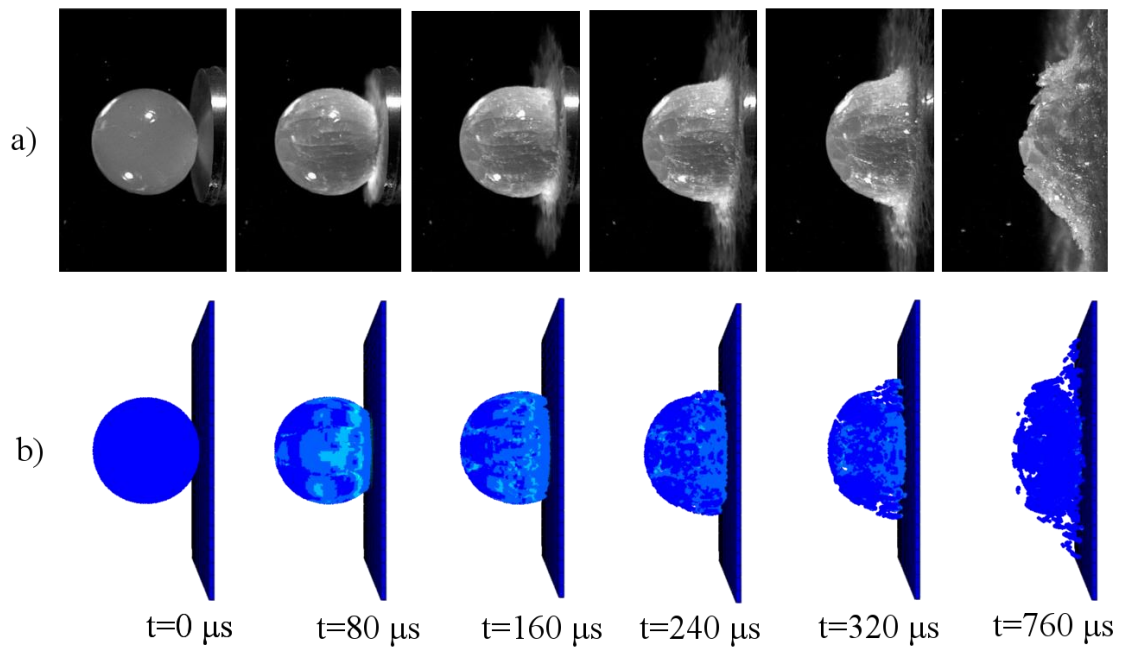


Figure 7.19. Kinematic evolution and fragmentation of the hailstone. a) Video frames source: [20], b) FEA simulation frames

7.3 Hailstone impact over CFRP sandwich panels

7.3.1 FEA model

A dynamic/explicit nonlinear FEA model in Abaqus is implemented to evaluate the behaviour of sandwich panels against hailstone impact. This model is similar to the one previously presented in chapter 6 but in this case the projectile is a hailstone instead of a steel projectile. Models with two different hailstone sizes are created ($D=25.4$ mm and $D=50.8$ mm) evaluating impact velocities between 60 to 160 m/s. The hailstone diameters are selected based on previous research from diverse authors in order to replicate two different scenarios: the first ($D=25.4$ mm), corresponds to a common size used experimental laboratory testing and represents a moderate hail size, while the second ($D=50.8$ mm) represents the largest diameter expected. Hailstones are modelled using the SPH methodology previously explained and validated in section 7.2.

Material for the sandwich panel are the same as in chapter 6. Face-sheets made from woven CFRP while the core is made from either Agglomerated cork or PET foam. The panel size is increased to 220x220mm requiring a change in the mesh size and topology to account for larger projectile sizes (Figure 7.20). This model evaluates thinner face-sheet laminates

than chapter 6 with a stacking sequence of $[0^\circ, 45^\circ, -45^\circ, 90^\circ]$ while the core thickness is maintain to 5mm.

The sandwich panel is modelled using a conventional Lagrangian approach with continuum damage models for the face-sheets whilst the core nonlinearity is modelled using an hyperelastic foam model (Agglomerated cork) and a crushable foam model (PET foam). Details of about the constitutive material models and the general modelling strategy are explained and validated in chapter 6. Due to the large processing time introduced by the hailstone SPH method only a quarter model is implemented (Figure 7.20) with symmetric boundary conditions in the symmetry planes (plane yz: $U_x=0, UR_y=0, UR_z=0$ and plane xy: $U_z=0, UR_x=0, UR_y=0$ where U_i are displacements in direction i and UR_i are rotations along the i axis).

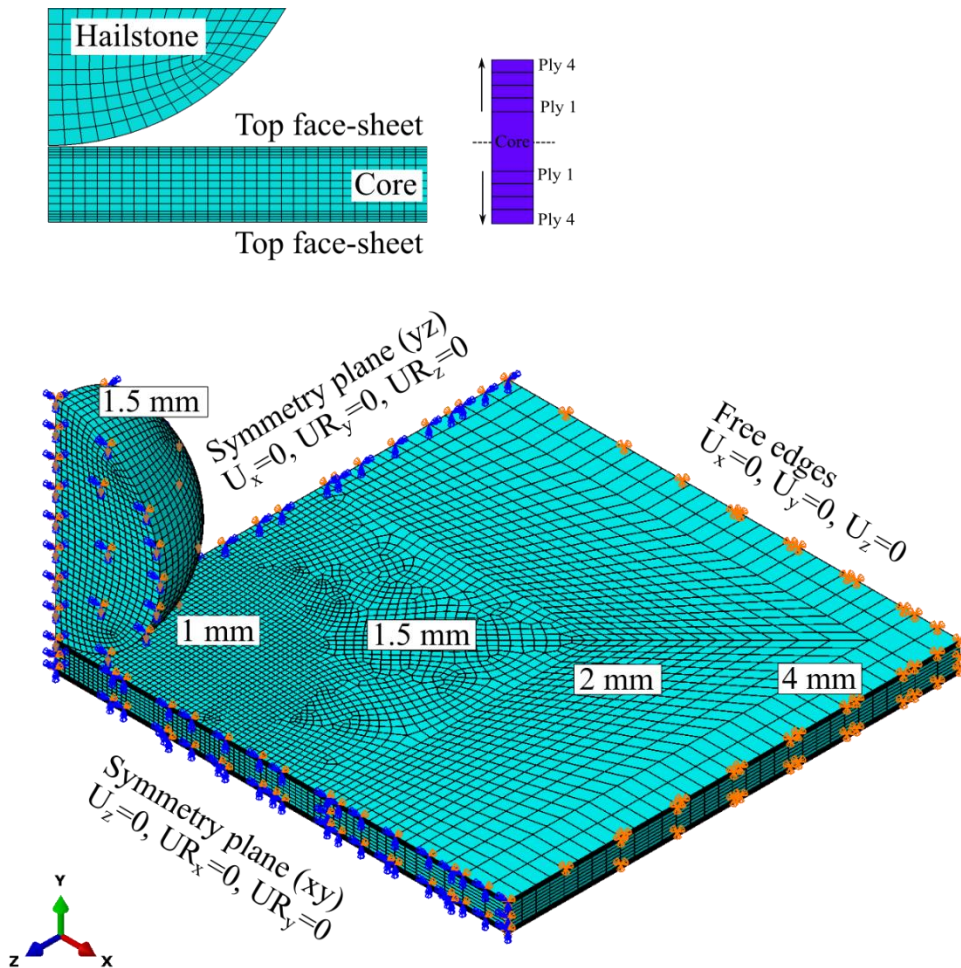


Figure 7.20. Quarter-model mesh and boundary conditions (Largest hailstone $D=50.8mm$)

7.3.2 Results of the largest hailstone (D=50.8 mm)

The behaviour of sandwich panels against the impact of the largest hailstone (D=50.8 mm) shows a progressive and complex interaction between different phenomena. In one hand permanent deformation, and fracture of the hailstone. In the other hand the elastic response of the sandwich panel and its different damage and failure mechanisms (e.g. intra-laminar and inter-laminar failure for the face-sheets and multi-axial core failure).

A sharp difference is observed between moderate-low impact velocities (60 m/s) and high impact velocities (160 m/s), with the first being characterized by minor damage while the second is characterized by panel penetration and catastrophic damage and failure. Figure 7.21 and Figure 7.23 show the evolution of the impact at 60 m/s for sandwich panels with both core materials while Figure 7.22 and Figure 7.24 does the same at 160 m/s.

At 60 m/s the impact seems to be dominated by the permanent deformation and failure of the hailstone and the out-of-plane deflection of the panel. At this impact velocity the stress intensity in the face-sheets is moderate and elastic range is not exceeded.

At 160 m/s the previously mentioned mechanisms are also present. However, a higher stress intensity triggers intra-laminar damage and failure. At this impact velocity penetration occurs in both sandwich panels with the formation of a petal shaped opening (Figure 7.22 and Figure 7.24).

The critical penetration velocity was obtained for both sandwich panels. It was found that for the agglomerated cork sandwich panel it is 127 m/s while for sandwich panel with PET foam core this value is slightly higher to 132 m/s. This result suggest that sandwich panels with PET foam provide a stronger resistance against hailstone penetration than agglomerated cork panels. This could be caused by multiple factors such as higher impact forces that encourage the hailstone fragmentation or large plasticity and fragmentation of the core. As will be shown later these advantages does not come alone bringing some disadvantages such as excessive core failure that could compromise the residual strength of the panel after impact.

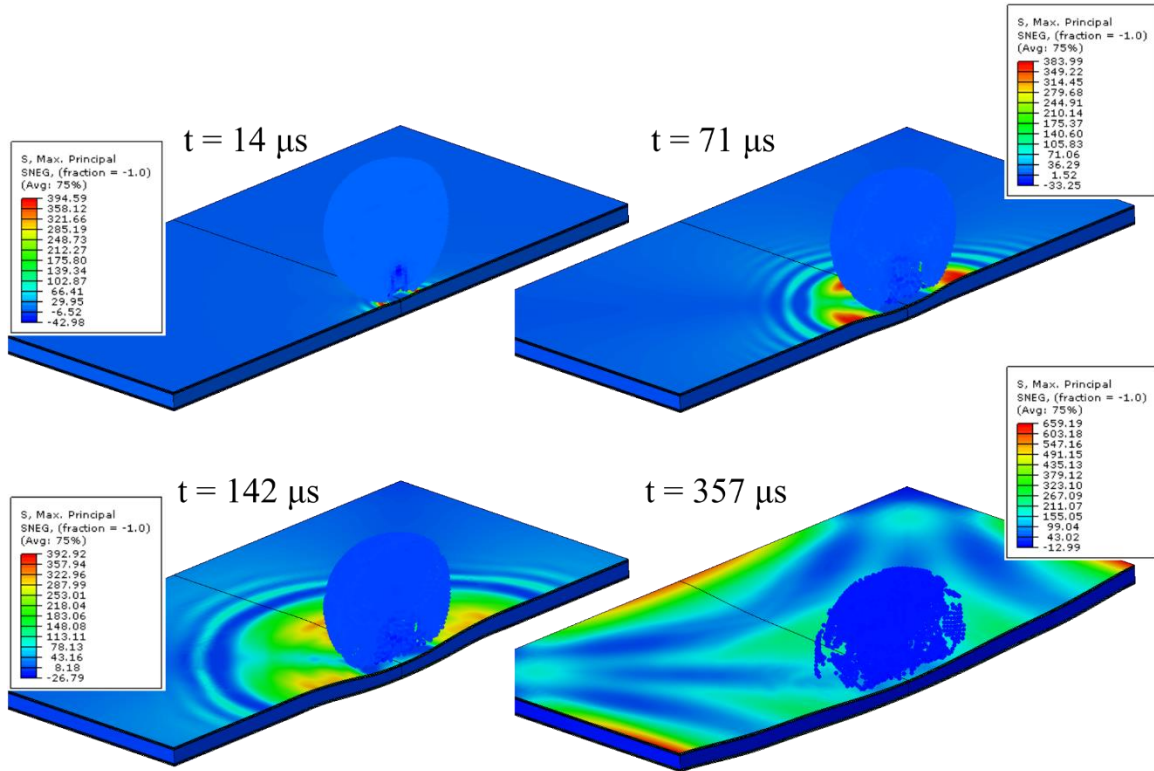


Figure 7.21. Impact evolution (mirrored quarter model). Agglomerated cork core sandwich at $V_i=60$ m/s

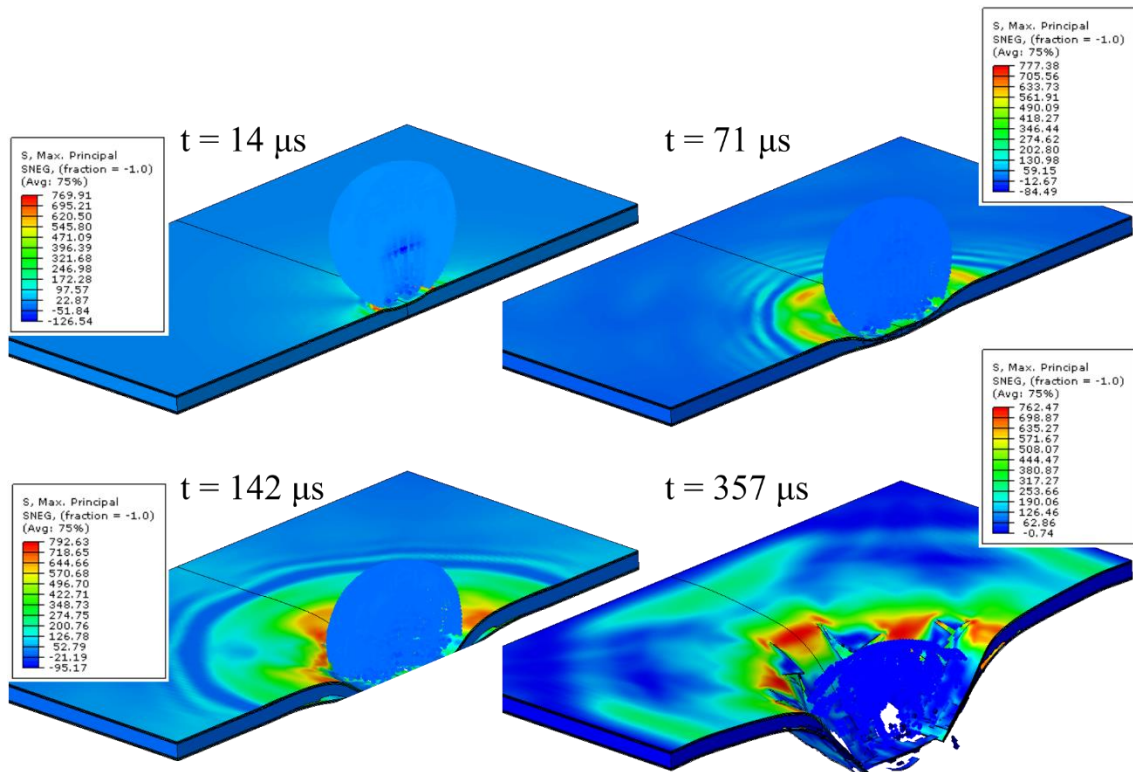


Figure 7.22. Impact evolution (mirrored quarter model). Agglomerated cork core sandwich panel at $V_i=160$ m/s. ($D=50.8$ mm)

HAILSTONE IMPACT OVER COMPOSITE SANDWICH PANELS

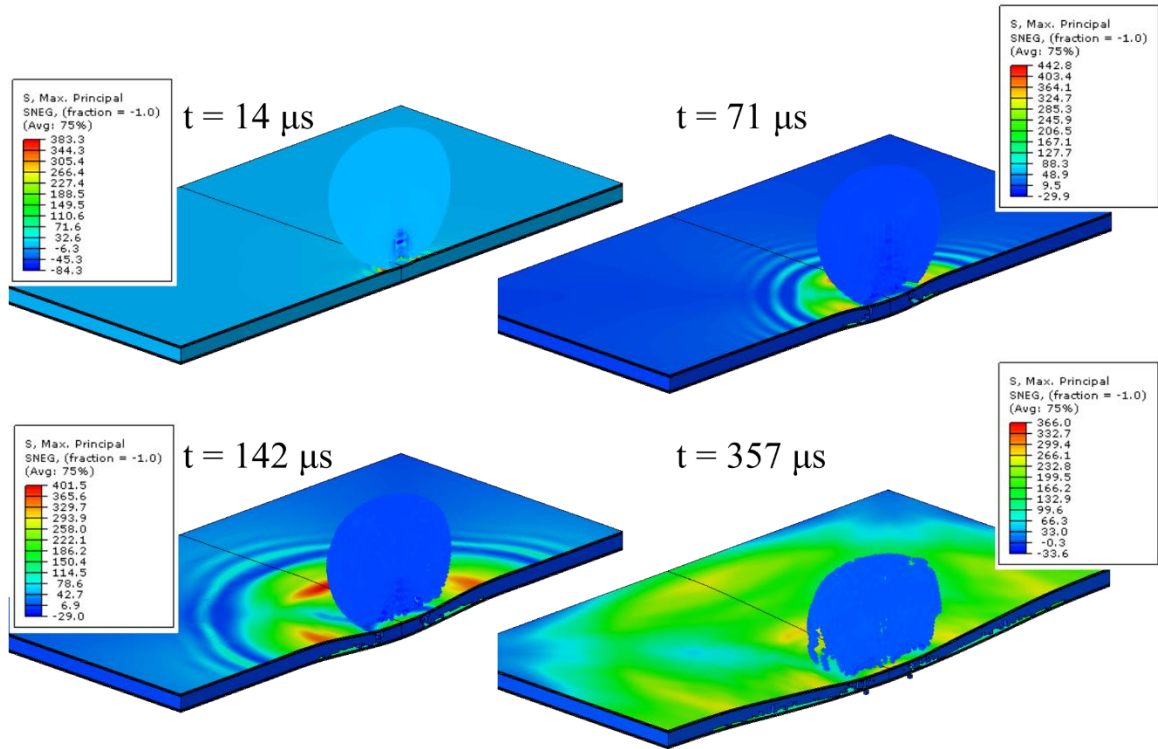


Figure 7.23. Impact evolution (mirrored quarter model). PET foam core sandwich panel at $V_i=60$ m/s. ($D=50.8$ mm)

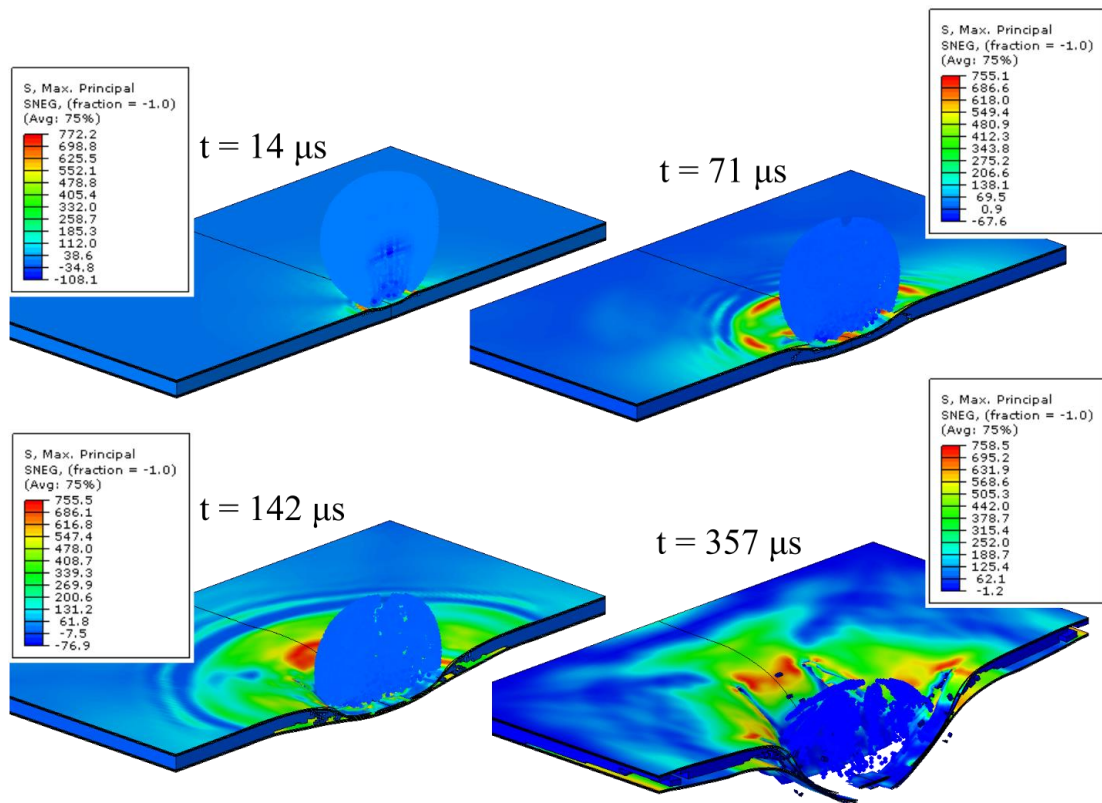


Figure 7.24. Impact evolution (mirrored quarter model). PET foam core sandwich panel at $V_i=160$ m/s. ($D=50.8$ mm)

One of the first observations made is related to the behaviour of the hailstone during the initial instants of impact and its influence in the response of the sandwich panels. Figure 7.25 shows the evolution of the hailstone and the contact pressure exerted over top face-sheet. From the figure, as the impact progress, the initially spherical hailstone starts deforming and fragmenting under the contact pressure exerted by the panel's top face-sheet. This phenomenon is encouraged by the higher strength and stiffness of the face-sheets if compared to the hailstone. In the initial instants of time ($14 \mu\text{s}$) the contact region is highly localized around the impact midpoint. Due to the small contact area the contact pressure forces are high and the hailstone starts deforming permanently eventually failing and forming a flat surface. This flat surface increases the contact area what in turn decreases the contact pressure even further ($57 \mu\text{s}$). If internal stresses are high enough, the hailstone will continues deforming and failing, increasing again the size of the contact surface. This process continues until eventually the contact area remains with the same size and there is neither new permanent deformation nor failure in the contact area (Figure 7.25).

The previous observation suggest that permanent deformation and fracture are critical mechanisms of energy dissipation that must be considered when studying the hailstone impact against composite sandwich panels. In fact the increment in the contact surface and the associate reduction in the pressure forces have an important effect in the stress distribution in the face-sheets what at the same time governs the formation of delamination and intra-laminar fracture.

The stiffness of both sandwich panels against the hailstone impact was evaluated by measuring the out of plane vertical displacements in the mid-section at different impact velocities at time intervals of $14\mu\text{s}$. Figure 7.26 shows vertical displacements in ply-4 of the top face-sheet (first ply in contact to the hailstone) while Figure 7.27 does the same for ply-4 in the bottom face-sheet (ply opposite to the hailstone). Comparison of the plots show that the overall response shape does not seem to be affected by the core material. Indeed, there is no appreciable difference in the top face-sheet displacements between both sandwich panels. Beside this a careful examination of Figure 7.27 shows that vertical displacements in the bottom face-sheet (at $x=80 \text{ mm}$) seems to be up to 12% higher for sandwich panels with agglomerated cork. This difference is expected since agglomerated cork is much less stiff than PET foam. This previous observation suggests that the shape response is dominated by the panel bending stiffness in which the face-sheets is more relevant than the core material. Besides this, the core material plays an important localized

role on transmitting and dissipating internal energy to the bottom face-sheet what in turns slightly affects the out of plane response.

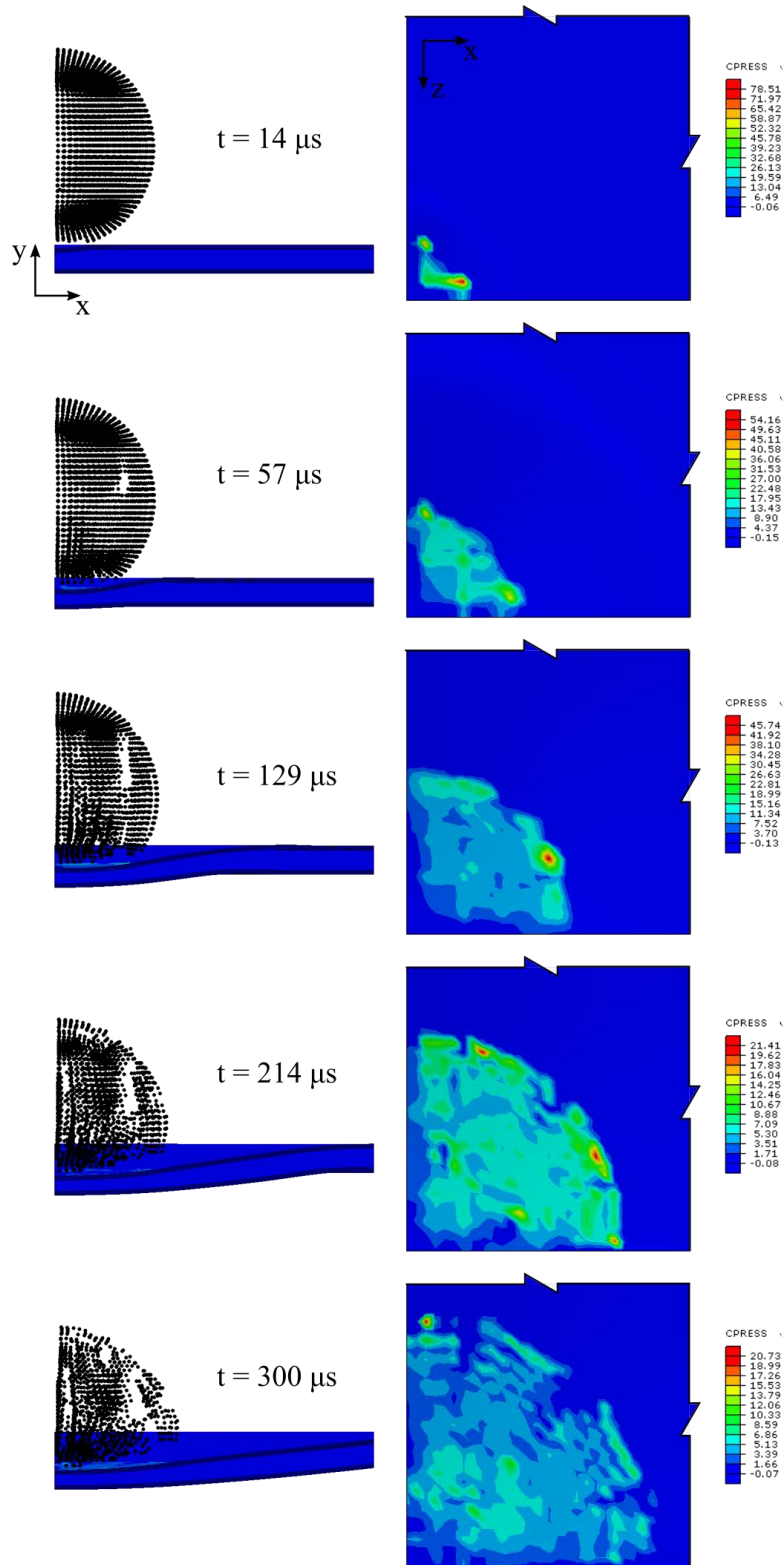


Figure 7.25. Contact pressure (quarter model) in the top face-sheet at different instants of impact ($V=100$ m/s, large hailstone $D=50.8$ mm)

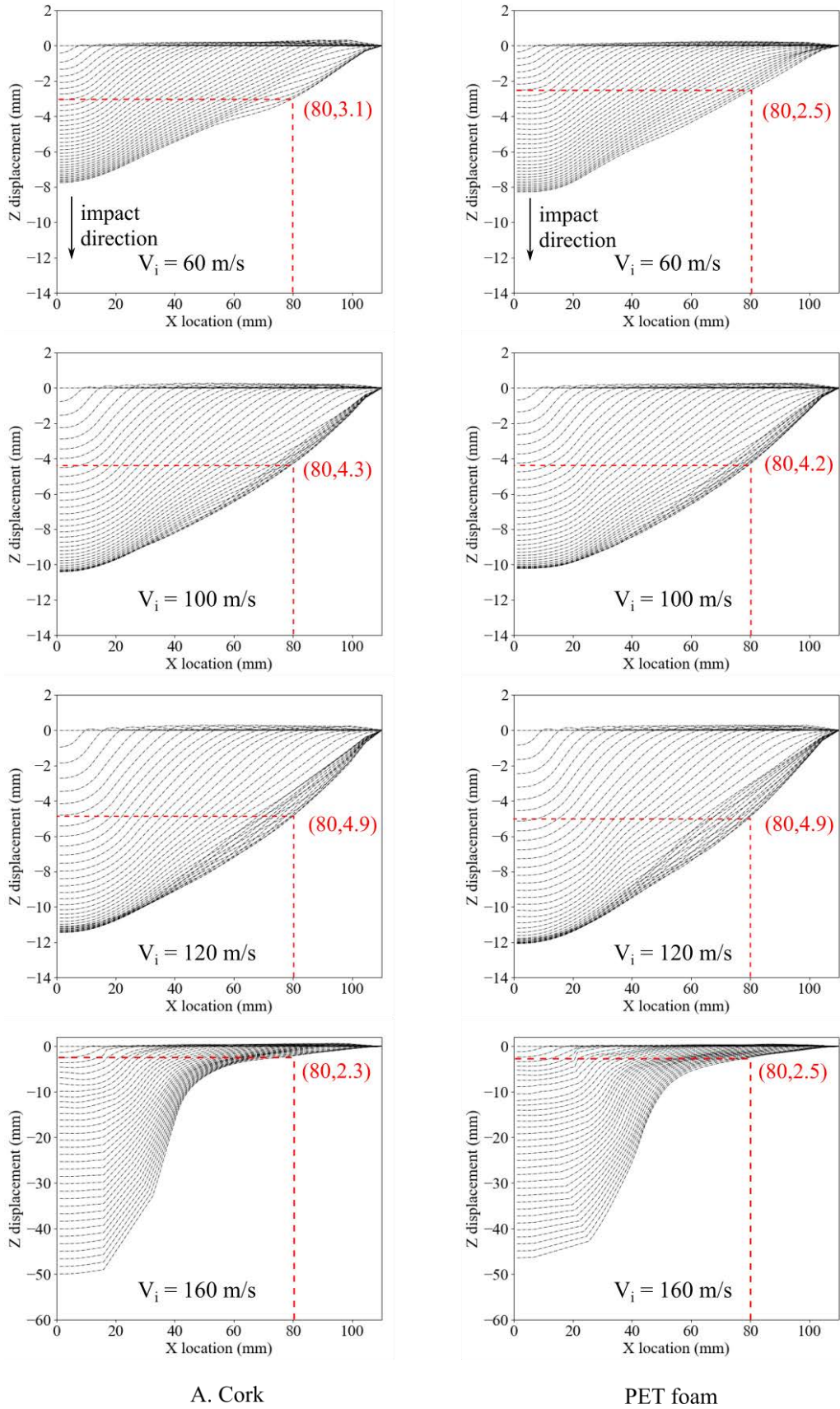


Figure 7.26. Mid-plane vertical displacement of top face-sheet (ply 4) at different instants of times (Agglomerated cork and PET foam core sandwich panels).

HAILSTONE IMPACT OVER COMPOSITE SANDWICH PANELS

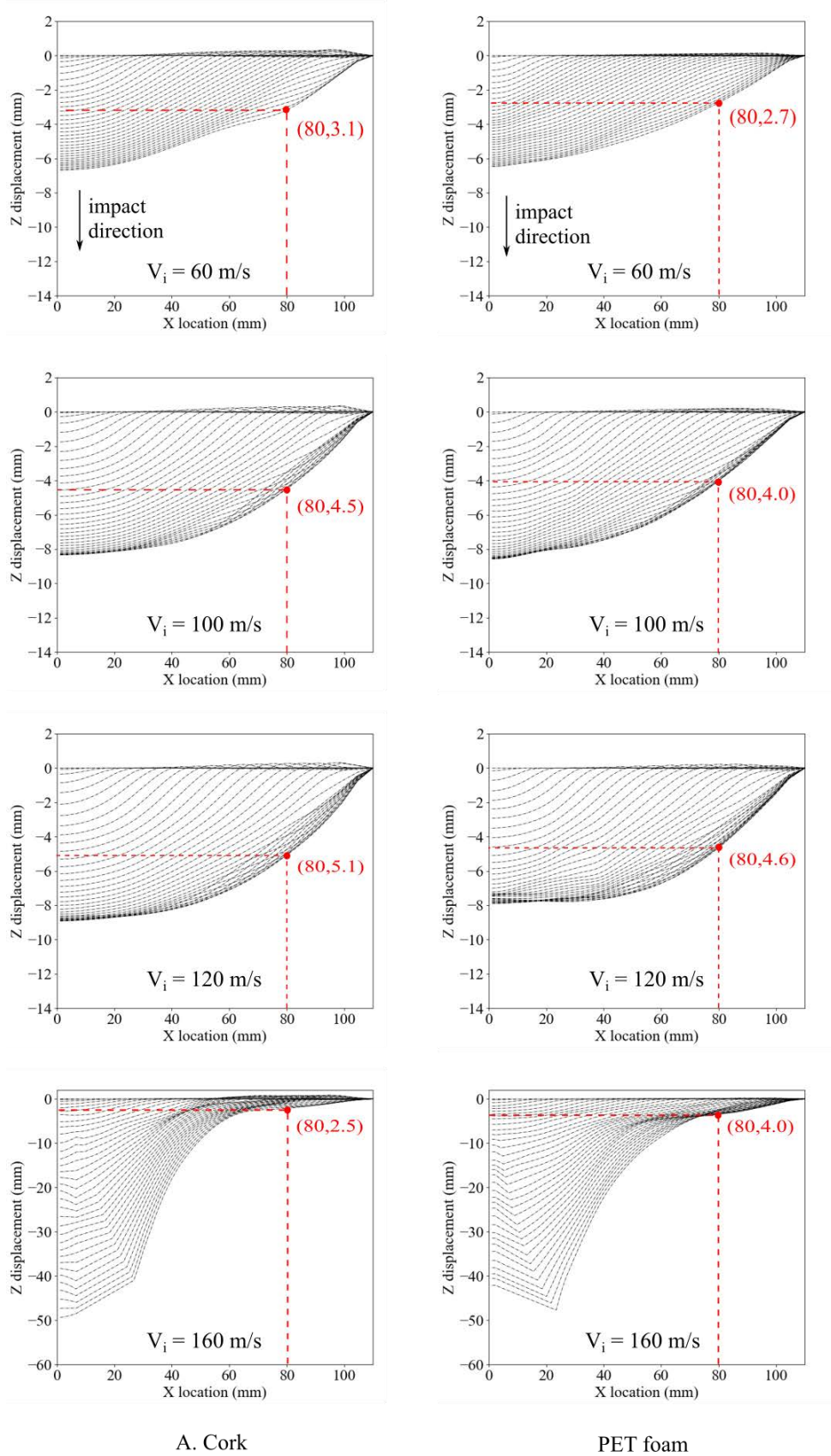


Figure 7.27. Mid-plane vertical displacement of bottom face-sheet (ply 4) at different instants of times (Agglomerated cork and PET foam core sandwich panels).

Large hailstones create different levels of damage in the sandwich panels that could go from mild to harsh damage depending on the impact velocity. Damage in the top face-sheet is one of the major concerns due to its detrimental effect in the panel's stiffness and residual strength. At impact velocities between 60 m/s to 80 m/s the delamination area around the impact region is minimum. However, at higher impact velocities (100 m/s and 120 m/s) the delamination area is much larger and its size extends up to the hailstone's diameter (Figure 7.29, Figure 7.31).

From the same figures, it is observed that an additional slender delamination is formed in the mid-axis (symmetry edge) far from the impact region. This secondary delamination was present in almost all run cases for both sandwich panels and its appearance is somehow unexpected considering the localized nature of the impact phenomena. A detail analysis suggests that it might be associated to a coupling between bending stresses in the symmetry axis and stress concentration due to the support conditions in the free edges. This particular damage mechanism is not explored further due to the mesh size in this region. However, results like this suggest that the secondary mid-axis delamination might play an important role and should be considered as a new damage mechanism in the panel face-sheet.

From impact velocities between 60 m/s to 120 m/s no intra-laminar damage or failure are present next to the impact region in any of the panel's face-sheet. This is an indication that the membrane-like stresses exerted by the hailstone contact forces are well below the ply strength. However, at higher impact velocities (from 120 m/s to 160 m/s) the damage suffered by the panel is considerable. The top face-sheet in particular shows both intra-laminar and inter-laminar damage and failure while the bottom face-sheet is only damaged if the top face-sheet is penetrated ($V_i > 140$ m/s).

In the case of the top face-sheet both inter and intra-laminar damage seems to appear simultaneously around the impact region and their growth is clearly interconnected. Intra-laminar damage is followed by failure and the formation of petal shaped crack patterns similar to those described in previous sections. However, in this case the crack petals are not cruciform but form a quadrilateral shape as depicted in Figure 7.28. It can also be noticed that crack pattern seems to have the same alignment despite the different stacking direction of both plies.

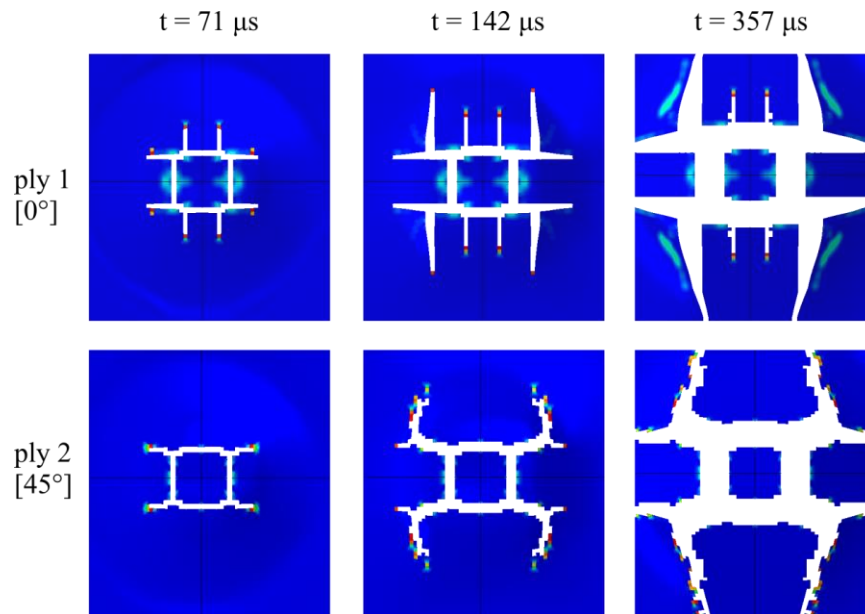


Figure 7.28. Intra-laminar crack pattern (whole panel – mirrored) in the top face-sheet (Agglomerated cork core sandwich panel, $V_i=140$ m/s)

The delaminated area is much larger than in those cases where there is not penetration and it is extended well beyond the impact region surrounding the intra-laminar cracks previously mentioned (Figure 7.29 and Figure 7.31).

The panel's core failure was also analysed and the following general observations are obtained: in both sandwich panels and in all analysed impact velocities that a core failure surface appears in the core's bottom surface (opposite to the impact) next to the intersection with the bottom face-sheet. This initial cracked surface is formed by the sudden propagation of multi-axial stresses created during the first microseconds after impact. It extends rapidly towards the edges of the panel creating a de-attached region between the core and the bottom face-sheet. This failure mode could be easily confused with deboning however after a careful review the cohesive damage indexes show to be lower than unity confirming that it is core failure and not deboning what causes this separation between core and face-sheet.

A similar failure surface is also observed in the core's top surface however, this is observed in agglomerated cork core sandwich while it is not present in PET foam sandwich.

Some other differences in the core failure mechanism were also spotted between agglomerated cork core and PET foam core sandwich panels. As observed in Figure 7.30 and Figure 7.32 agglomerated cork core suffers little or no failure around the impact region at impact velocities between 60 to 100 m/s. In contrast at same impact velocities PET foam core encounters a massive early fragmentation accompanied by the formation of multiple

cracks that could extend outward across most of the panel. This difference can be associated to the brittle nature of the PET foam and the highly elastic characteristics of agglomerated cork.

At higher impact velocities (from 120 m/s to 140 m/s) there is massive core failure characterized by and core pull out in the case of agglomerated cork and fragmentation in the case of PET foam core (Figure 7.30, Figure 7.32). In this case core failure extends not only directly ahead the impact region but it also reaches most of the panel extension.

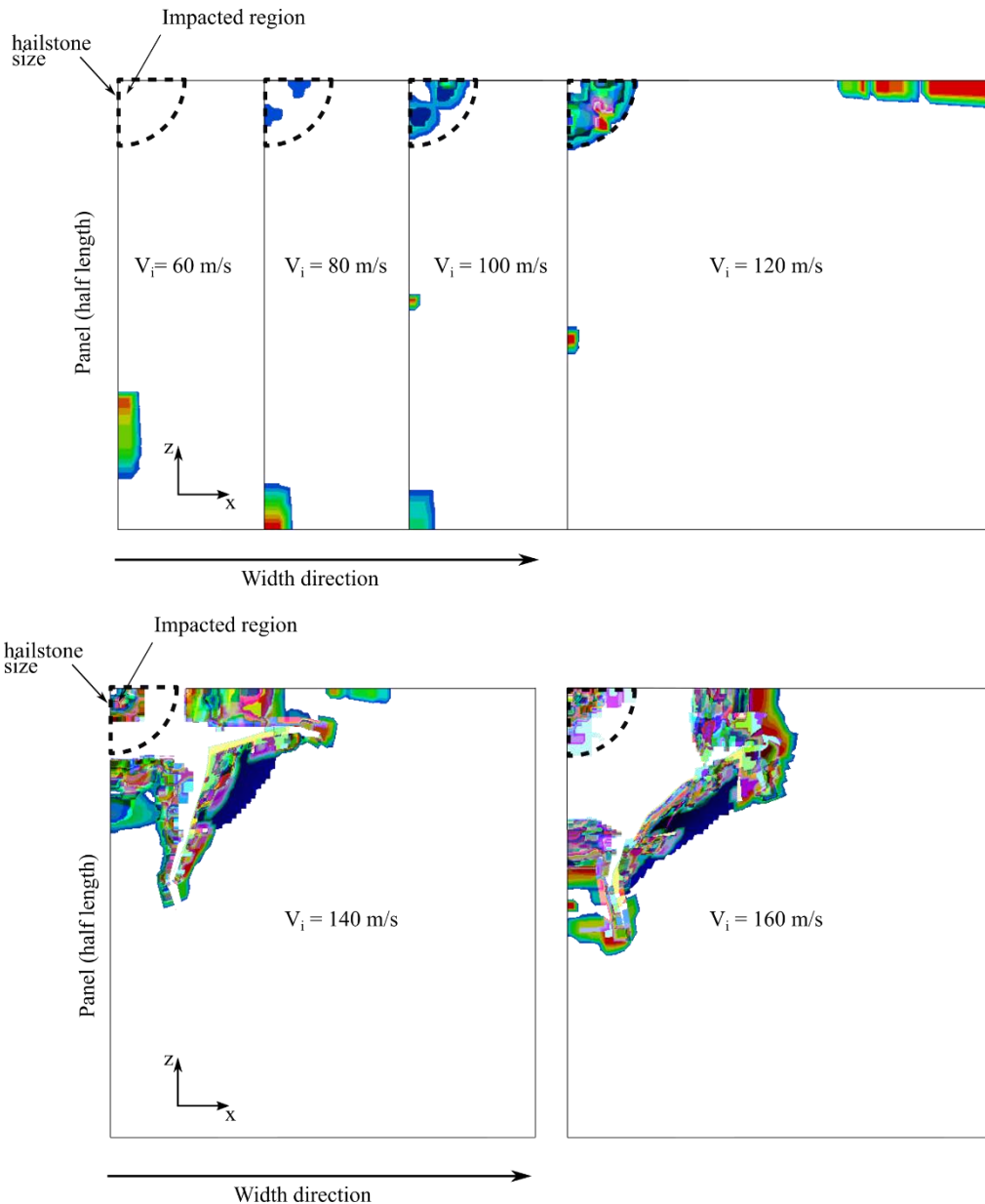


Figure 7.29. Projected delamination area (quarter panel) in the top face-sheet at different impact velocities (Agglomerated cork core – large hailstone $D=50.8$ mm)

HAILSTONE IMPACT OVER COMPOSITE SANDWICH PANELS

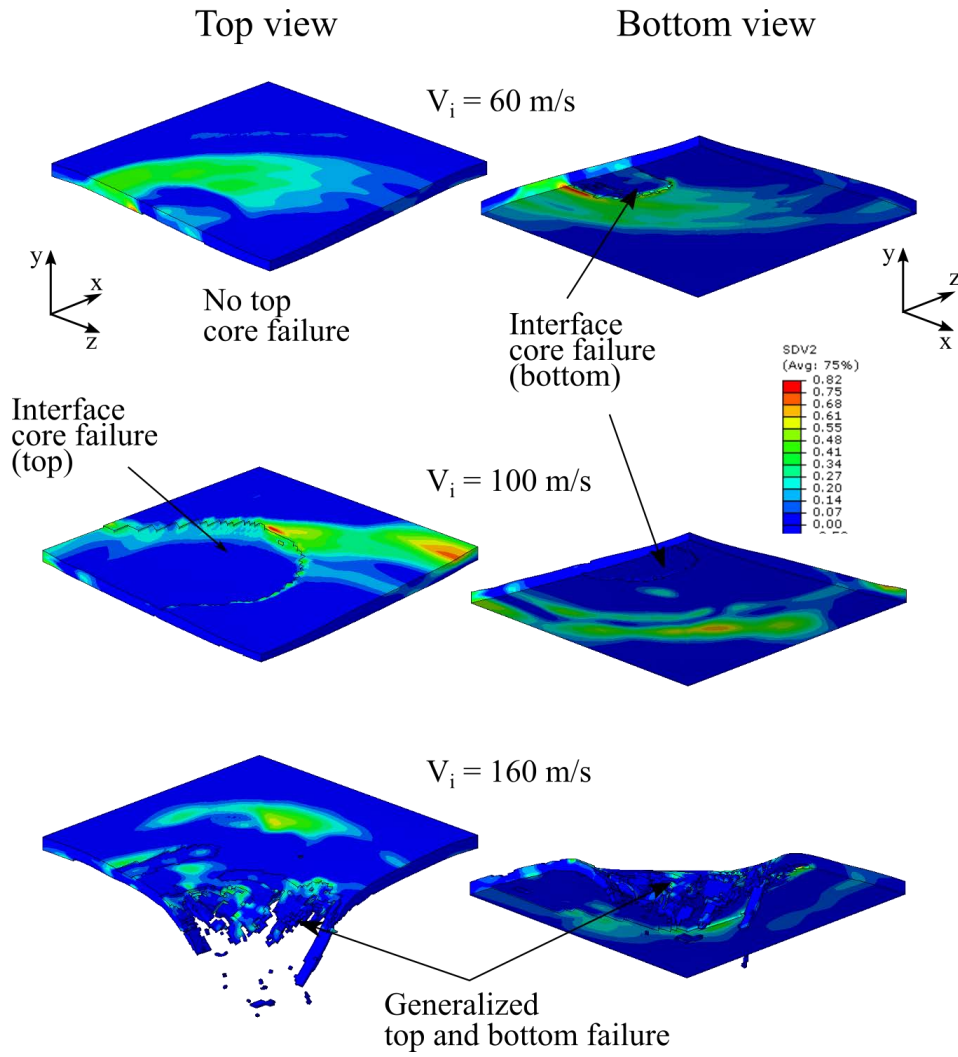


Figure 7.30. Core failure and Tsai-Wu index (quarter panel) at different impact velocities for agglomerated cork core – large hailstone $D=50.8$ mm (top and bottom view)

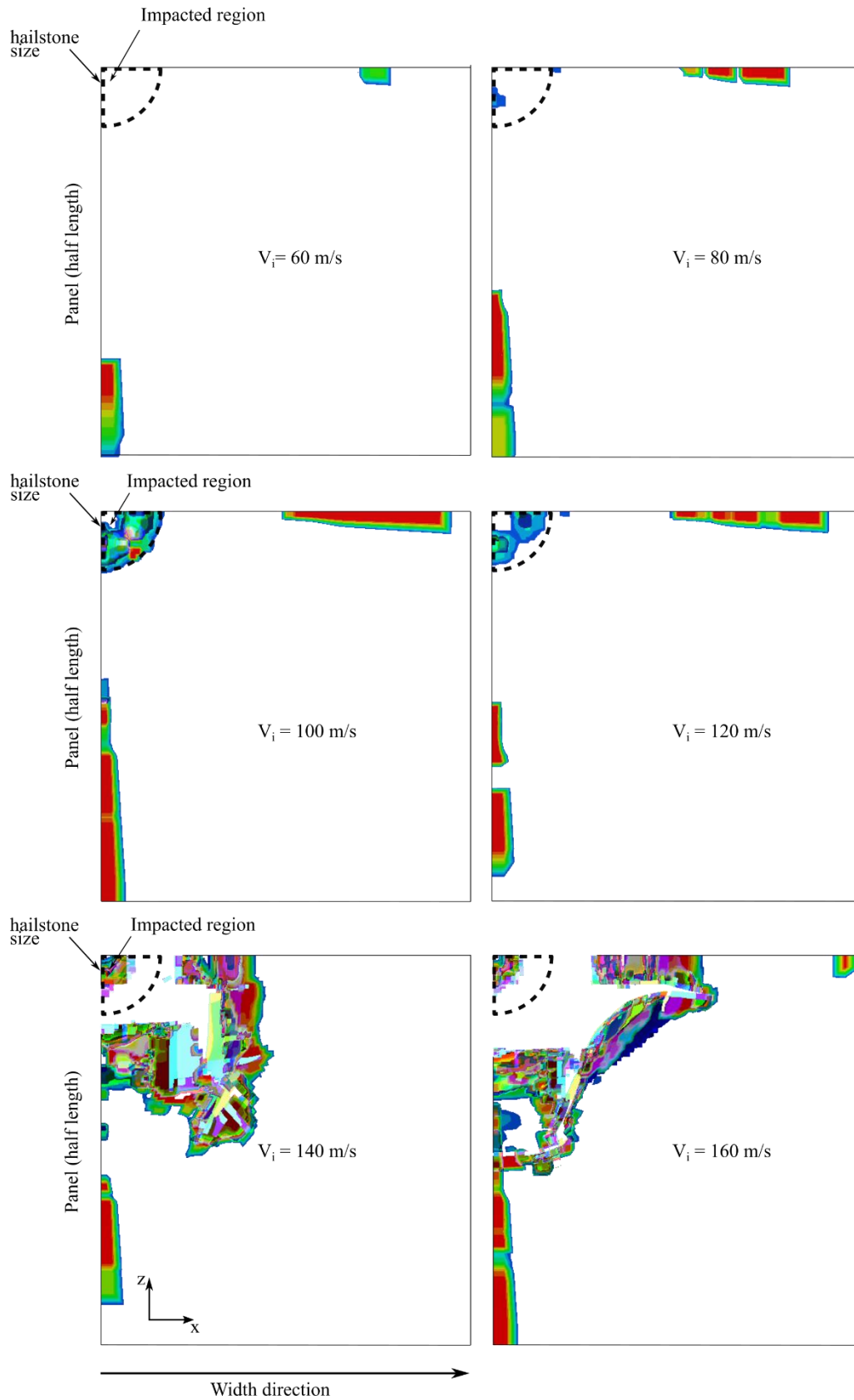


Figure 7.31. Projected delamination area (quarter model) in the top face-sheet at different impact velocities (PET foam core – large hailstone $D=50.8$ mm)

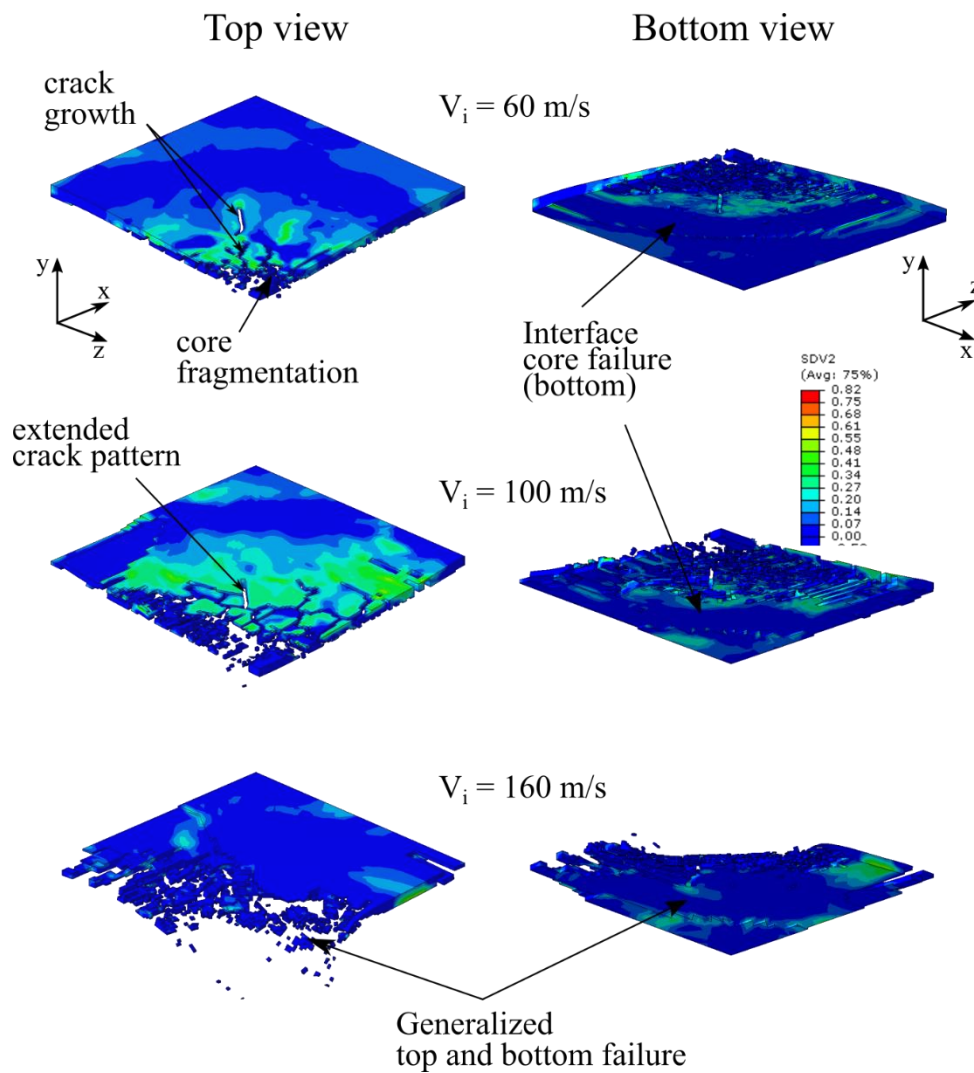


Figure 7.32. Core failure and Tsai-Wu index (quarter model) at different impact velocities for PET foam core – large hailstone $D=50.8 \text{ mm}$ (top and bottom view)

7.3.3 Results of a common hailstone ($D=25.4 \text{ mm}$)

The behaviour observed in the impact of common size hailstones is controlled by the same complex and interactions than for the largest size hailstone. However it is clearly observed from Figure 7.33 to Figure 7.36 that the severity of the damage and failure is highly reduced to the point that no perforation is observed in any sandwich panel even at the highest analysed impact velocity ($V_i=160 \text{ m/s}$).

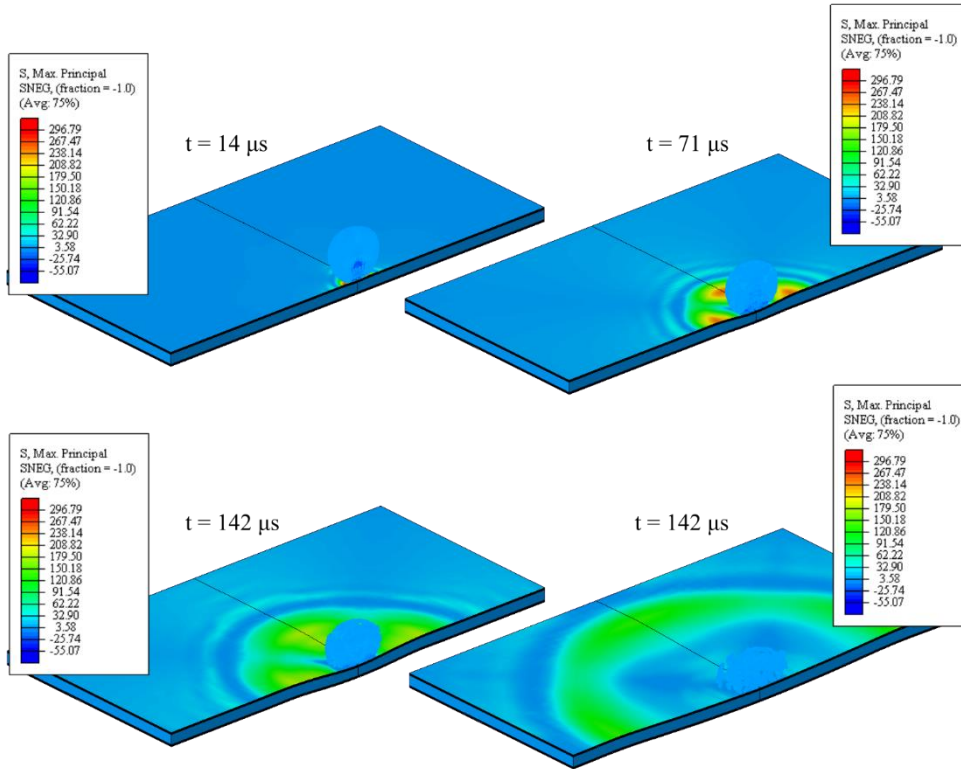


Figure 7.33. Impact evolution (mirrored quarter model). Agglomerated cork core sandwich at $V_i = 60 \text{ m/s}$ ($D=25.4 \text{ mm}$)

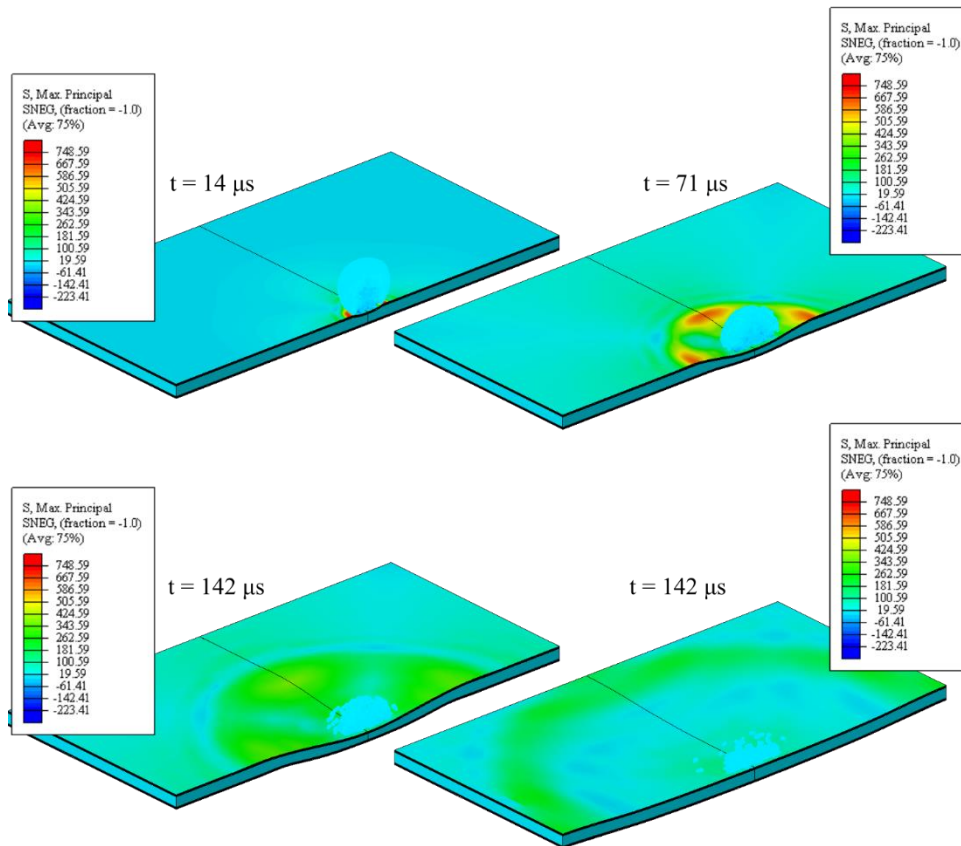


Figure 7.34. Impact evolution (mirrored quarter model). Agglomerated cork core sandwich at $V_i = 160 \text{ m/s}$ ($D=25.4 \text{ mm}$)

HAILSTONE IMPACT OVER COMPOSITE SANDWICH PANELS

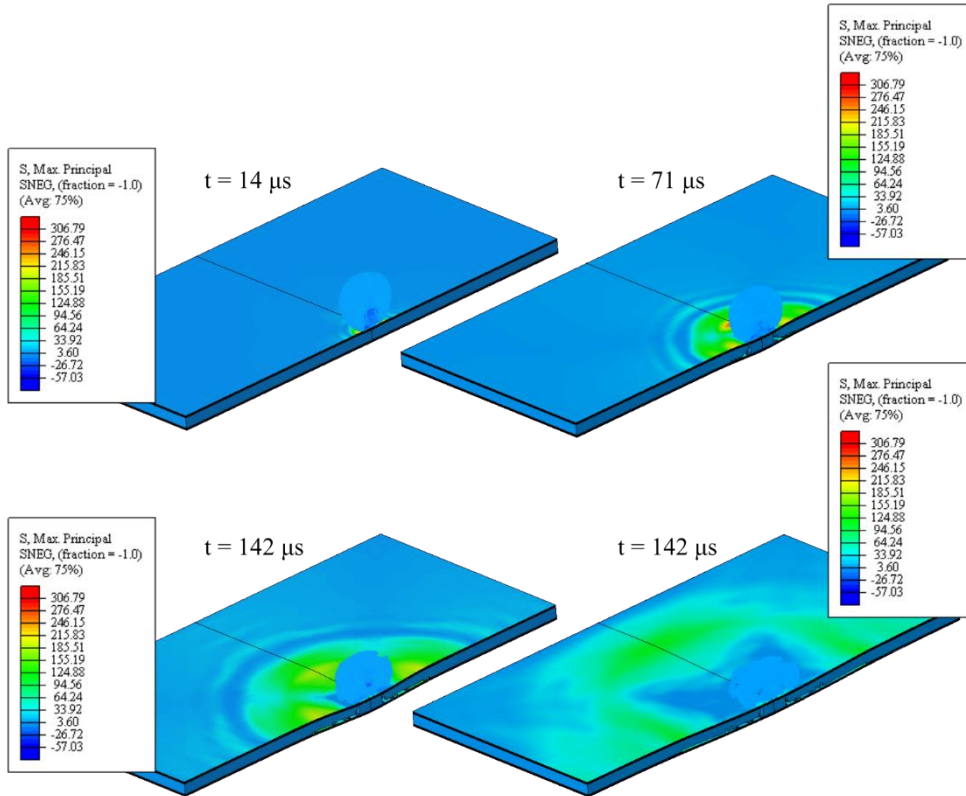


Figure 7.35. Impact evolution (mirrored quarter model). PET foam core sandwich panel at $V_i = 60$ m/s ($D=25.4$ mm)

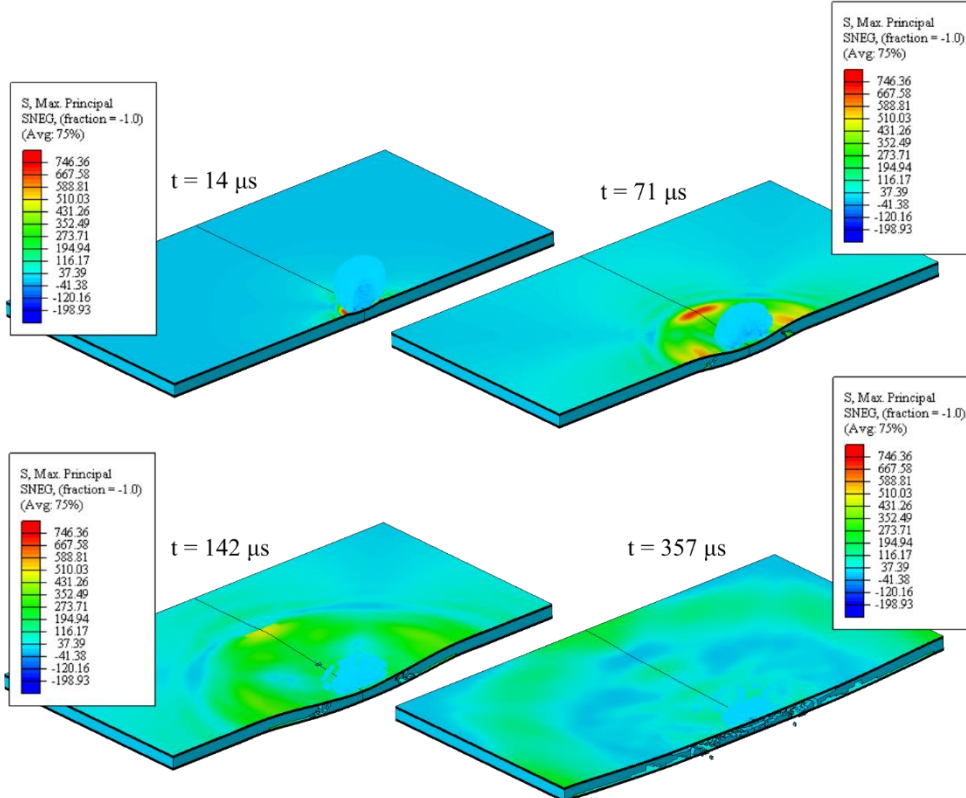


Figure 7.36. Impact evolution (mirrored quarter model). PET foam core sandwich panel at $V_i = 60$ m/s ($D=25.4$ mm)

In particular, no intra-laminar damage is observed in any of the sandwich panels at any impact velocity. This suggests that the membrane-like stresses occurring during impact are smaller than the lamina strength. Similarly, inter-laminar damage (delamination) is not present at most impact velocities. Delamination is only observed in the top face-sheet laminate at impact velocities $V_i \geq 100$ m/s for agglomerated cork core sandwich panels and $V_i \geq 140$ m/s for PET foam core sandwich panels (Figure 7.37 and Figure 7.38). This delamination is concentrated around the impact region and can extend beyond the projectile diameter.

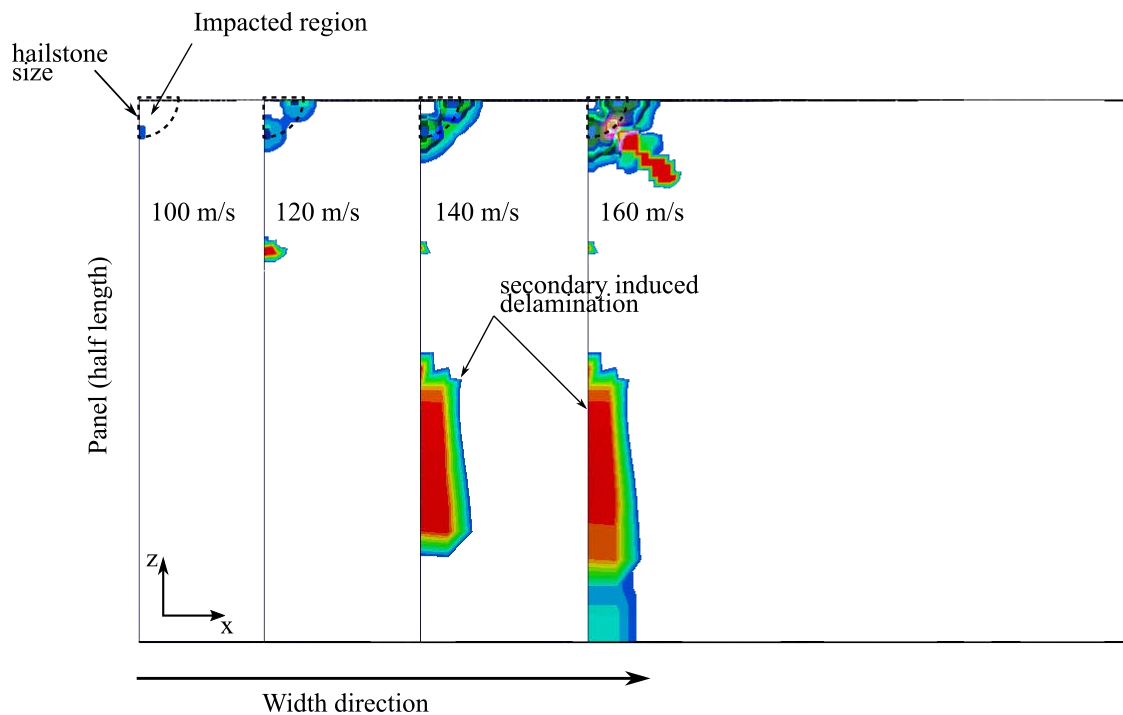


Figure 7.37. Projected delamination area in the top face-sheet at different impact velocities (Agglomerated cork core – small hailstone $D=25.4$ mm)

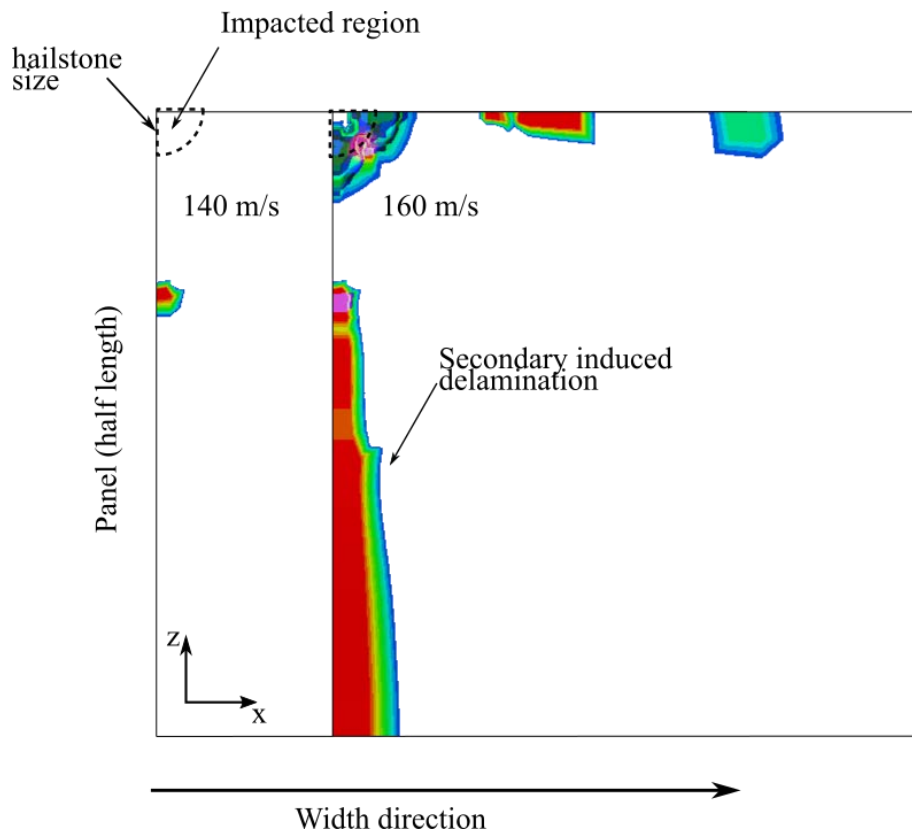


Figure 7.38. Projected delamination area in the top face-sheet at different impact velocities (PET foam core – small hailstone $D=25.4$ mm)

In the cork sandwich panel the core remains almost intact except for a region of core failure in the intersection between the core's bottom surface and the bottom face-sheet. This initial failure creates a cracked surface that extends massively reducing the load transfer capability between core and face-sheet. This type of core failure is also visible in sandwich panels with PET foam core. However, in this case the massive core failure appears accompanied by fragmentation around the impact region, which can extend in the whole panel (Figure 7.39). The same difference in the core failure is also observed in the impact of the largest hailstone ($D=50.8$ mm) at low impact velocities ($60 \text{ m/s} < V_i < 100 \text{ m/s}$) and it is reported in the previous section.

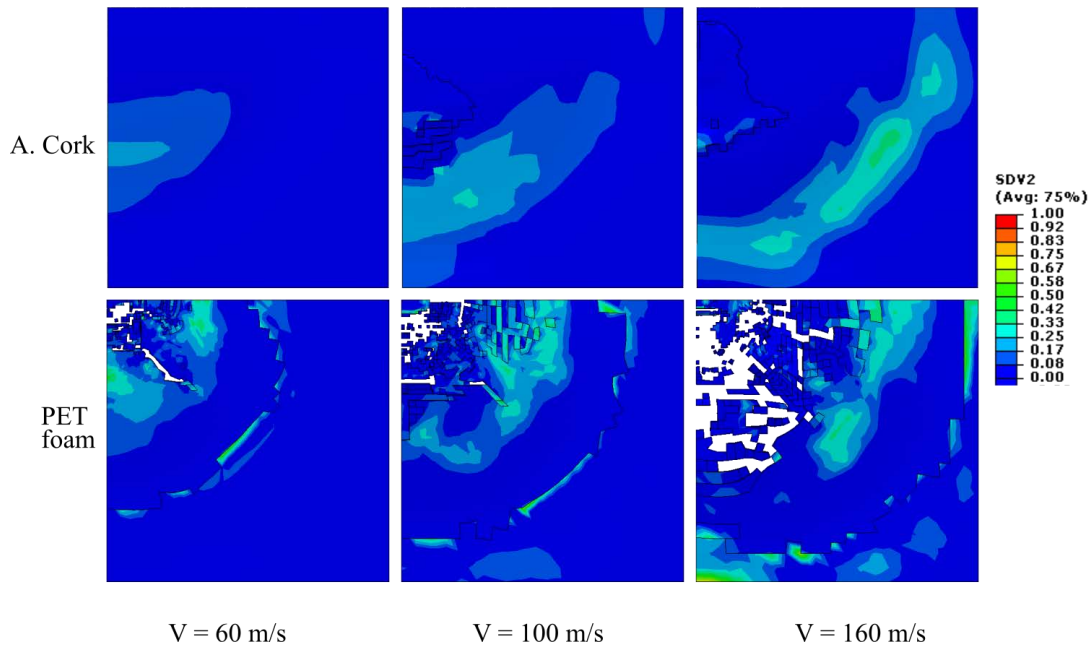


Figure 7.39. Core failure and Tsai-Wu index at different impact velocities for both core materials – common size hailstone $D=25.4$ mm (bottom view)

It can be stated that the impacts of common size hailstones ($D=25.4$ mm) at impact velocities in the range of 60 m/s to 160 m/s causes no penetration of the panel. However the integrity and residual strength of the panel can be compromised due to the presence of delamination and massive core failure in the intersection between the core and bottom face-sheet.

References of the chapter

- [1] European Aviation Safety Agency (EASA). Hail Threat Standardisation - Final Report EASA_REP_RESEA_2008_5. 2008.
- [2] Court A, Griffiths JF. 1986: Thunderstorm climatology. Thunderstorm Morphol Dyn 1986. <https://doi.org/10.1029/2008JD009982>.
- [3] Agency EE. Annual number of hail events in the period 2004-2014. <https://www.eea.europa.eu/Data-and-Maps/Figures/Annual-Number-of-Hail-Events> 2019. <https://www.eea.europa.eu/data-and-maps/figures/annual-number-of-hail-events>.
- [4] Schaefer JT, Levit JJ, Weiss SJ, McCarthy DW. THE FREQUENCY OF LARGE HAIL OVER THE CONTIGUOUS UNITED STATES. 2003.
- [5] Accident Investigation Board Finland. Aircraft damage in hailstorm west of Helsinki on 21.7.2001. Helsinki, Finland: 2002.
- [6] DNV/Risø. Guidelines for Design of Wind Turbines - 2nd Edition. vol. 29. 2002.

- [https://doi.org/ISBN 87-550-2870-5](https://doi.org/ISBN%2087-550-2870-5).
- [7] Walter Frost, B. Long RT. Engineering handbook on the atmospheric environmental guidelines for use in wind turbine generator development. 1978.
- [8] Kim H, Kedward K. Experimental and numerical analysis correlation of hail ice impacting composite structures. 40th Struct. Struct. Dyn. Mater. Conf. Exhib., Reston, Virginia: American Institute of Aeronautics and Astronautics; 1999. <https://doi.org/10.2514/6.1999-1366>.
- [9] J. Michael Pereira, Santo A. Padula, II, Duane M. Revilock and MEM. Forces Generated by High Velocity Impact of Ice on a Rigid Structure 2006.
- [10] Macdonald H, Nash D, Stack MM. Repeated impact of simulated hail ice on glass fibre composite materials. *Wear* 2019;432–433. <https://doi.org/10.1016/j.wear.2019.06.001>.
- [11] Pernas Sánchez J. Análisis y simulación de impactos de hielo sobre laminados carbono/epoxi. University Carlos III of Madrid, 2013. <https://doi.org/10.13140/RG.2.1.1086.8086>.
- [12] Petrovic JJ. Review Mechanical properties of ice and snow. *J Mater Sci* 2003;38.
- [13] Schulson EM. The structure and mechanical behavior of ice. *J Miner Met Mater Soc* 1999.
- [14] Wu X, Prakash V. Dynamic compressive behavior of ice at cryogenic temperatures. *Cold Reg Sci Technol* 2015;118:1–13. <https://doi.org/10.1016/j.coldregions.2015.06.004>.
- [15] Mellor M, Cole DM. Stress/strain/time relations for ice under uniaxial compression. *Cold Reg Sci Technol* 1983;6:207–30. [https://doi.org/10.1016/0165-232X\(83\)90043-5](https://doi.org/10.1016/0165-232X(83)90043-5).
- [16] Jones SJ. High Strain-Rate Compression Tests on Ice. n.d.
- [17] Shazly M, Prakash V, Lerch BA. High-strain-rate compression testing of ice - Tech. Mem. NASA/TM—2006-213966. 2006. <https://doi.org/NASA/TM—2006-213966>.
- [18] Carney KS, Benson DJ, DuBois P, Lee R. A phenomenological high strain rate model with failure for ice. *Int J Solids Struct* 2006;43:7820–39. <https://doi.org/10.1016/j.ijsolstr.2006.04.005>.
- [19] Pernas-Sánchez J, Pedroche DA, Varas D, López-Puente J, Zaera R. Numerical modeling of ice behavior under high velocity impacts 2012. <https://doi.org/10.1016/j.ijsolstr.2012.03.038>.

- [20] Tippmann JD, Kim H, Rhymer JD. Experimentally validated strain rate dependent material model for spherical ice impact simulation. *Int J Impact Eng* 2013;57:43–54. <https://doi.org/10.1016/j.ijimpeng.2013.01.013>.
- [21] Prato Anghileri Milanese Castelleti. FE to SPH approach applied to the analysis of soft body impact: bird strike and hail impact. n.d.:1–11.
- [22] Heimbs S. Computational methods for bird strike simulations: A review. *Comput Struct* 2011;89:2093–112. <https://doi.org/10.1016/j.compstruc.2011.08.007>.
- [23] Johnson GR, Stryk RA, Beissel SR. SPH for high velocity impact computations. *Comput Methods Appl Mech Eng* 1996;139:347–73. [https://doi.org/10.1016/S0045-7825\(96\)01089-4](https://doi.org/10.1016/S0045-7825(96)01089-4).
- [24] A. GR, J. MJ. Smoothed particle hydrodynamics and application to non-spherical stars. *Mon Not R R Astronaut Soc* 1977;181:375–89.
- [25] Dassault Systèmes Simulia Corp. Abaqus/CAE User’s Guide 2014. <http://ivt-abaqusdoc.ivt.ntnu.no:2080/v6.14/books/usi/default.htm>.
- [26] Dassault Systemes. Abaqus 6.14 Analysis user’s guide. Volume III: Materials 2014;I.
- [27] CASTANIE B, BOUVET C, Ginot M. Review of composite sandwich structure in aeronautic applications. *Compos Part C Open Access* 2020;1. <https://doi.org/10.1016/j.jcomc.2020.100004>.
- [28] Pascal F, Navarro P, Marguet S, Ferrero JF, Aubry J, Lemaire S. Study of medium velocity impacts on the lower surface of helicopter blades. *Procedia Eng* 2014;88:93–100. <https://doi.org/10.1016/j.proeng.2014.11.131>.
- [29] MASON K. Composites Aboard High-Speed Trains. *Compos World* 2004.
- [30] The Wind Power. Manufacturers and turbines 2021. <https://www.thewindpower.net/index.php> (accessed August 27, 2021).
- [31] Gething MJ, Endres G. *Jane’s Aircraft Recognition Guide*. 5th ed. 2007.

8 CONCLUSIONS AND FUTURE WORK

8.1 General conclusion

The mechanical response, impact process and damage mechanisms occurring in an intermediate velocity impact over composite sandwich panels made of carbon/epoxy face-sheets with core of agglomerated cork or PET foam are studied using a mixed numerical and experimental approach. The proposed building block methodology is successful for validating the FEA model of the sandwich panel using experimental results at all the analysed pyramid scale levels. Both numerical and experimental results allow to study the impact process in detail. At the most general level the impact process is dominated by different interacting physical mechanisms such as elastic deformation of the panel, inter-laminar and intra-laminar fracture of the face-sheets, non-linear core deformation, multi-axial core failure and core-face-sheet debonding.

Impact velocity seems to be a critical parameter that dominates the mechanical response, impact process and the damage extend. At impact velocities well below the penetration threshold (impact velocity required to penetrate the top face-sheet) most non-conservative energy dissipation mechanisms are negligible and the impact process is dominated by elastic response of the panel, and the subsequent projectile rebound. At impact velocities closer to the penetration threshold but still lower than it, delamination and face-sheet fracture start dissipating more energy. Both numerical and experimental results suggest that they do not act independently but interact to each other during the impact process. This idea is supported by the correlation between growth in intra-laminar crack length and delamination growth. Multi-axial compressive and shear deformation in the core produces local failure around the impact region triggering the formation of small internal indentations below the top-facesheet which are not easily detected from the surface of the sandwich panel. The effect of these internal core indentations could affect the post-impact performance and fatigue life of the panel under service conditions. At impact velocities higher than the penetration threshold the top face-sheet fractures in a petal (or diamond) shaped crack pattern which is associated with large delamination extend. Multi-axial core failure occurs around the impact region and in the interface between bottom face-sheet and the core. This interface failure is not visually detectable from the surface of the panel but

can be multiple times larger than the projectile diameter and constitute a risk to the post-impact integrity of the panel.

About the differences in the panel response when changing the core material it is observed that the strength and stiffness of the core seem to influence the out-of-plane displacement of the top face-sheet during impact. Panels with agglomerated cork show larger displacements than the more rigid and stiff PET foam. Indentation and core failure are visible in both core material at velocities near or higher to the penetration threshold, however the physical mechanisms are different. For example agglomerated cork is dominated by a large elastic response and fracture of the agglomerate grains while PET foam is dominated by a elasto-plastic response with dynamic crushing near the impact region. FEA results suggest that agglomerated cork provides a beneficial effect on the top face-sheet delamination area if compared to PET foam; however there is not sufficient experimental evidence to back up this hypothesis.

The influence of other impact parameters is also studied using the developed FEA model. Core thickness seems to play an important role in the rebound of the projected below the penetration threshold and influence the fracture pattern in the core. Beside this, the damage and plastic dissipation energies seem to be unaffected by the core thickness for most of the analysed relative thicknesses. The obliquity of the impact seems to influence the extend of the damage across the panel thickness, as well as the rebound velocity of the projectile and the amount of energy dissipated as friction. For small impact angles the panel response is similar to the perpendicular impact while for large impact angles the face-sheet damage is more superficial and the severity is lower due to higher tangential rebound of the projectile. Another studied impact parameter is pretension (either tensile or compressive) which is found detrimental to the impact resistance of sandwich panels since it encourages the growth of intra-laminar cracks and speeds up the extension of the delaminated area during impact.

Finally, the thesis also studies the hailstone impact over the sandwich panels applying the validated FEA model of the sandwich panel. Results suggest that there is a strong interaction between the dominant physical mechanisms in the sandwich panel (e.g. elastic response, face-sheet damage, core failure, etc...) and the fragmentation of the hailstone. Core fracture in the intersection between the core and the bottom face-sheet is a dominant failure mode that extends quickly and appear early in the impact process. Besides this damage extend is highly dependent on the impact velocity and the size of the hailstone.

A more detailed description of the conclusions obtained in each chapter is described in the following section.

8.2 Conclusions by chapters

Chapter 3: Building a reliable model for the face-sheets:

This chapter describes the implementation of an FEA model to study the damage and failure of woven CFRP laminates. The proposed material model includes an intra-laminar continuum damage model developed by Johnson [7] for orthotropic woven composites. The inter-laminar behaviour is captured by a multi-ply FEA model approach applying a cohesive zone model. When possible the parameters for the material formulation are extracted directly from the literature or otherwise calibrated directly from fracture tests reported by other authors. Results of the FEA models show that the proposed material model can reproduce with accuracy the crack growth and the load vs. displacement curves for CT tests (intra-laminar fracture) as well as DCB and ENF tests (inter-laminar fracture). The suitability and precision of the proposed material model for impact engineering applications are also assessed by modelling a set of ballistic impact tests available in the literature. The obtained results show that the material model can predict with accuracy the ballistic limit of the laminate as well as the characteristic petal-shaped fracture morphology of the laminate reported in the experiments.

The good experimental-numerical correlation obtained in both validation scenarios (fracture tests and ballistic impact) indicates that the proposed material model is appropriate to model the face-sheet laminates of the whole sandwich panel.

Chapter 4: Building a reliable model for the core

This chapter describes the experimental testing carried out to characterize the quasi-static and dynamic compression response of agglomerated cork and PET foam as well as their quasi-static tensile response. A universal testing machine and an instrumented drop weight tower are used for the quasi-static and dynamic testing respectively. Additionally, two FEA models for the dynamic compression are proposed and validated using the obtained experimental results. 2D-DIC is used to study the strain field and estimate the quasi-static and dynamic Poisson ratio. Some of the conclusions for this chapter are summarized below:

Experimental testing in agglomerated cork:

- a) Compression testing shows that agglomerated cork has the typical non-linear behaviour of cellular materials with closed cells characterized by three stages (linear-elastic, plateau, densification) in both quasi-static and dynamic regimes (until 75 s^{-1}). The plateau region occurs at a non-constant stress level but slightly increase until reaching densification.
- b) There is a considerable difference in the stress-strain curves for quasi-static and dynamic conditions. From dynamic compression (in the analysed range of strain rates) the material shows a much larger Young modulus and plateau stress than in quasi-static conditions. This trend is visible in agglomerated cork of both densities (NL-10 and NL-20).
- c) The densest agglomerated cork (NL-20) shows higher strength and stiffness than the less dense material (NL-10) for both quasi-static and dynamic compression.
- d) For dynamic compression (between 25 s^{-1} to 75 s^{-1}) no significant influence of strain rate on the mechanical properties is appreciated.
- e) After compression, agglomerated cork presents permanent deformation that could be produced by damage of the cellular structure as well as delayed strains due to viscoelastic effects (such as creeping).
- f) The onset of densification is identified using the energy absorption efficiency method. Results show that there is only a minor difference in the strain of the onset of densification for both materials, around 5%. This small dependency on density can be explained since densification is mostly dependent on the cell geometry (porosity) which is similar for both agglomerates.
- g) Agglomerated cork have good energy absorption qualities for impacts where compression is the dominant dissipation mechanism. Experimental results from dynamic compression show that the material can absorb from 77% to 99% of the initial impact energy. The energy absorption ratio is slightly higher for the NL-10 than NL-20. This difference can vary from 1% up to 13%.
- h) DIC analysis is used to explore strain distribution in the specimen during testing. It is observed that the strain field is non-uniform
- i) a non-uniform distribution in the strain field is observed in the test specimens for both agglomerated cork materials what shows the heterogeneity of agglomerated

cork at a small scale. This variation can be attributed among others to the amorphous shape and random allocation of the granules as observed in the surface analysis.

- j) A non-zero mean Poisson ratio is estimated for quasi-static and dynamic compression using DIC analysis. The mean Poisson ratio decays with the longitudinal strain reaching a plateau at higher strains. The Poisson ratio shows strain rate sensitivity with higher values at higher strain rates.
- k) Some variability in the mechanical properties of agglomerated cork is observed. This could be caused by heterogeneity.
- l) The quasi-static tensile testing result shows that agglomerated cork has a non-linear response characterized by an initial linear response followed by progressive decay of the tangent stiffness and final fracture.

Experimental testing in PET foam:

From the experimental study of the compressive behaviour of PET foam:

- a) Under the dynamic condition, the plateau region is characterized by highly unstable oscillations produced by the effects of localization during dynamic crushing. Depending on the severity of dynamic crushing the material might suffer stress hardening or stress softening in the plateau region. DIC analysis shows that oscillations in the plateau region are related to the cell collapse in the shock layer near the loading and reaction faces. Additionally, it was observed a variation in the local strain along the longitudinal axis, showing higher gradients in the vicinity of the shock layer. These results suggest that modelling dynamic compression events with PET foam requires the use of a proper dynamic stress-strain curve. The observed variation of mechanical properties with strain rate in PET foam has been found in some high-density PU foam and others such as EPS and HDPE [3].
- b) The Poisson ratio (for quasi-static and dynamic compression) is neither constant nor zero but decreases with longitudinal strain. For such a reason to develop a numerical model of the material, it is convenient to include the Poisson ratio sensitivity on strain and strain rate.
- c) The quasi-static tensile testing result shows that PET foam has a non-linear response characterized by an initial linear response followed by progressive decay of the tangent stiffness and final fracture.

Validation of FEA models of dynamic compression for agglomerated cork and PET foam:

- a) The non-linear compressive response of agglomerated cork is modelled with a hyperelastic elastomeric foam model with the Mullins effect. The comparison of the results provided by the FEA model and experimental testing shows that the constitutive model is adequate to model the response under dynamic compression. Although the Mullins effect can capture the energy dissipation with accuracy, it is unable to capture the progressive softening of the material at the maximum strain and the viscoelastic return.
- b) The non-linear compressive response of PET foam is modelled with the Deshpande-Fleck isotropic hardening material model for crushable foams. The results are compared to experimental data obtained from a dynamic compression using a drop weight tower. The overall material response is characterized and shows a good correlation with experimental data. Particularly variables such as the collapse force, the maximum displacement, impact duration and energy dissipation ratio shows a high correlation with experimental results. The material model shows limitations to replicate the localization phenomena produced by dynamic crushing, however, its effect in the overall response of the material can be adjusted through the hardening function.
- c) The author proposes as future research work a more detailed characterization of the yield surface through a hydrostatic pressure test.

Chapter 5: Intermediate velocity impact test on sandwich panels

This chapter describes the experimental testing of CFRP sandwich panels with two different core materials (agglomerated cork and PET foam) subjected to impact loads at intermediate velocities using a gas cannon. Non-contacting techniques such as high-speed video recording, 3D-DIC analysis, and image tracking are used to study the behaviour of the panels during impact. Post-impact damage and failure are assessed by visual inspection of sectioned specimens and X-ray tomography. Some of the conclusions for this chapter are summarized below:

- a) For velocities lower than the perforation velocity, the core material seems to have a minor role in the rebound energy ratio. In this context, PET foam core seems to provide slightly higher dissipation effects than the agglomerated cork counterparts.

- b) The magnitude and shape of the out-of-plane displacement of the top face-sheet are governed by the perforation process and the formation of a plug. If there is no perforation no plug in the face-sheet is formed and the out of plane displacements are larger since the face-sheet deflects together with the advancing projectile. However when perforation occurs a plug forms and detaches from the rest of the face-sheet. Consequently, the rest of the face-sheet is unable to deflect together with the advancing projectile and the overall out of plane displacement in the top face-sheet is reduced.
- c) The strength and stiffness of the core material seem to influence the out-of-plane displacement of the top face-sheet during impact. It is observed that panels with agglomerated cork sandwiches show higher displacements than the more rigid and stiff PET foam counterparts.
- d) From 3D-DIC results, it is observed that during impact a lobular shaped strain distribution is formed around the impact region. The strain level is maximum at the impact point and decreases in the radial direction. Once penetration occurs and a plug is formed, the face-sheet is unable to transfer the load from the centre region where the projectile contacts to the rest of the face-sheet.
- e) Post-impact damage and failure morphology suggest that the petal-shaped crater formed in the top face-sheet during penetration is the product of a complex interaction of different phenomena such as early intra-laminar ply failure, delamination and large bending of broken plies. These petals interact with the neighbouring core material compressing it sidewise.
- f) Both visual and XCT inspection of PET sandwich panels spotted the formation of a very large fracture surface in the interface between the bottom face-sheet and core. Crack propagation occurs radially through the core material but in some cases debonding is also observed. Its large extension along the panel and its early appearance at moderate impact velocities makes this failure mechanism a critical one on which little previous research has been focused. This particular failure mechanism is not observed in agglomerated cork sandwich panels, which show a stronger interface.
- g) XCT inspection shows that delamination in the bottom face-sheet seems to be dominated by the penetration of the top face-sheet and the impact velocity. In those scenarios when there is no penetration, the bottom face-sheet suffers no delamination. However, in those situations where the top face-sheet is penetrated,

delamination appears in the bottom face-sheet and depending on the impact velocity it could propagate even further than in the top face-sheet. As a result, once penetration occurs bottom face-sheet delamination seems to be a critical damage mechanism.

Chapter 6: FEA model of impact on sandwich panels

This chapter discusses the numerical implementation of a dynamic/explicit FEA model used to study the behaviour of sandwich panels made of woven CFRP face-sheets and two different core materials (agglomerated cork and PET foam) subjected to impact loads at intermediate velocities. The model is validated using experimental test data presented in previous chapters. From the model results, the different energy absorption mechanisms and damage evolution are estimated and analysed. Some hypotheses are made to explain the physical mechanisms interacting in the impact process. Additionally, the FEA model is used to study the sensitivity of the panel response to some critical impact parameters such as impact velocity, core thickness, impact angle, and preloading. Some of the conclusions for this chapter are summarized below:

- a) The proposed building block methodology shows to be successful for validating the FEA model of the sandwich panel using result from experimental testing. Additionally the FEA modelling approach shows to be successful in particular the use experimentally validated continuum damage models which show to be accurate to model the inter-laminar and intra-laminar fracture of the face-sheets during impact. In this regard the use of continuum 3D shells elements together with cohesive interactions shows to be accurate to model the inter-laminar behaviour of the face-sheets at a moderate computational cost.
- b) The evolution of the impact process is characterized by an initial local membrane response of the top face-sheet with an early appearance of panel indentation, tensile failure in a cruciform pattern and delamination. The core response is highly localized and dominated by compressive and shear deformation. This multiaxial loading triggers failure and the formation of a crater which is dominant in the case of PET foam core. Meanwhile, agglomerated cork core shows a highly elastic initial response with reduced fracture.
- c) The FEA model is successfully validated from experimental tests presented in chapter 5 using diverse quantitative and qualitative variables. The model can predict

with accuracy the perforation of the front face-sheet and core, as well as the out-of-plane displacements in the front face-sheet. The morphology of the damage is also compared showing a good correlation with the experimental results.

- d) After the initial response, the behaviour of the panel varies substantially depending on whether or not there is a penetration of the top face-sheet. If it is not complete, penetration of the initial local response is followed by a progressive panel bending with further intra-laminar and inter-laminar crack growth and a final stage of elastic recovery. On the other hand, if there is penetration the plies in the top face-sheet fracture into a petal shape pattern representative of failure in woven laminates. This allows the projectile to get directly in contact with the core which opposes little resistance to the projectile advance. Core failure is further increased around the impact region and an extended failure is spotted in the intersection between the core and the bottom face-sheet.

About the comparative analysis of impact velocity the following conclusions are highlighted:

- a) The maximum projectile displacement increases with impact velocity. Agglomerated cork sandwich panels show larger displacements into the panel than PET foam panels. This phenomenon can be caused by the large differences in strength and stiffness of both materials.
- b) Energy dissipation in the agglomerated cork panel is dominated by damage dissipation while for the PET foam panel it is dominated by plastic dissipation. Friction dissipation is negligible at impact velocities where the front face-sheet is not penetrated but becomes relevant at higher impact velocities where there is perforation of the front face-sheet.
- c) In both analysed sandwich panels the delamination area increases with impact velocity. Results show that the delamination area in PET foam panels is larger than in agglomerated cork panels for all the analysed impact velocities. Sandwich panels with agglomerated cork core show a top face-sheet damaged area 15% to 56% smaller than panels with PET foam core. This clearly shows the promising applications of agglomerated cork as a core material for impact engineering applications.

In relation to the comparative analysis of the core thickness, the following is concluded:

CONCLUSIONS AND FUTURE WORK

- a) The maximum displacement of the projectile seems to be almost insensitive to the core thickness while the duration of the impact and the rebound velocity are influenced. The core thickness seems to affect differently both sandwich panels. Panels with PET foam core show larger rebound velocities at larger relative thickness.
- b) Thicker cores favour the rebound of the projectile being able to reach larger rebound velocities than for thinner cores. This is associated with a larger penetration of the projectile into the sandwich and the capability of a thick core to store recoverable internal energy. The elastic response of agglomerated cork seems to favour the projectile rebound.
- c) The core thickness influences the strain distribution and fracture in the core. In the case of thicker cores, fracture occurs in a well-defined cross crack pattern while in thinner cores a crater is also formed. These effects seem to be related to the interaction of the core with the back face-sheet and how it varies with different core thicknesses.
- d) In the studies range of relative core thicknesses damage dissipation and plastic dissipation seems to be unaffected by changes in the core thickness when the $h/H > 1$. Accordingly, the delamination area seems almost unaffected by changes in the core thickness.

About the comparative analysis of the impact angle the following conclusions are highlighted:

- a) The response of the panel is highly influenced by the impact angle. At low impact angles ($\theta < 15^\circ$) the panel is expected to behave similarly to a transversal impact characterized by large displacement of the projectile into the top face-sheet and a large region of inter-laminar and intra-laminar damage as well plastic damage in the core and the face-sheet matrix. The plastic damage propagates deep into the face-sheet which explains the larger plastic dissipation in this range of angles.
- b) In contrast for large impact angles ($\theta > 15^\circ$), the response of the panel is dominated by the momentum of the projectile parallel to the face-sheet. The displacement of the projectile into the panel is reduced, and the cohesive damage in the face-sheet is lower and more superficial. The intra-laminar damage in the most superficial ply is stronger with the presence of local failure. The plastic dissipation is lower than for lower angles while the friction dissipation between the projectile and the panel

starts playing a major role. For this kind of impact, the kinetic energy recovered by the projectile's rebound is larger than in a transversal impact.

About the comparative analysis of the preloading, the following is observed:

The application of an axial preload (either tensile or compressive) is detrimental to the resistance of sandwich panels since it encourages the growth of intra-laminar cracks and speeds up the extension of the delaminated area. As a result, the displacement of the projectile into the panel as well as the damaged area are increased compared without preload.

- a) The application of axial preload changes the speed of propagation of surface waves. In the case of tensile preloads the propagation speed increases while the opposite occurs for compressive preloads.
- b) If the axial preload is large enough localized intermediate velocity impact events with small projectiles could cause total failure of an entire sandwich panel. This effect is caused by a premature intra-laminar failure in the impact region and further crack extension generated by the axial preload that is dominated by mode I fracture.

Chapter 7: Hailstone impact over composite sandwich panels

From the numerical model of a spherical hailstone impacting a semi rigid surface, it is concluded that:

- a) The impact behaviour of a hailstone can be accurately modelled as a spherical projectile of ice using the Smoothed Particle Hydrodynamic (SPH) method together with Mises plasticity model, strain rate dependency and pressure tensile failure. The impact force history is compared with previous experimental studies showing good correlation specifically in the estimation of the maximum impact force and the softening region after impact. The hailstone model also captures with accuracy the kinematic evolution of the projectile including fragmentation and the appearance of longitudinal crack.

From the numerical model of a spherical hailstone impacting CFRP sandwich panels with agglomerated cork core or PET foam core, it is concluded that:

CONCLUSIONS AND FUTURE WORK

- a) There is a progressive and complex interaction between phenomena such as permanent deformation, and fracture of the hailstone, the elastic response of the sandwich panel and its different damage and failure mechanisms (e.g. intra-laminar and inter-laminar failure for the face-sheets and multiaxial core failure). Core fracture in the intersection between the core and the bottom face-sheet is found to be a dominant failure mode that extends quickly and appear early in the impact process.
- b) For impacts with the largest hailstones ($D=50.8$ mm) at low impact velocities ($V_i=60$ m/s) intra-laminar damage is nule but minor delamination and core failure are present which increase with impact velocity until panel penetration is encountered. Results show that resistance against penetration is slightly higher for sandwich panels with PET foam core than for panels with agglomerated cork being their critical penetration velocity 132 m/s and 127 m/s respectively. At velocities higher than the critical impact velocity there is a massive intra-laminar failure and crater holes with a petal shape are formed in the front face-sheet.
- c) The core material seems to play a minor role in the response of the sandwich panel. However, it is found that the core stiffness influences the out-of-plane deformation of the bottom face-sheet. Agglomerated cork cores suffer less severe failure than PET foam cores where fracture and fragmentation are extensive. This suggests that agglomerated cork sandwich panels could have better residual strength after impact than PET foam sandwich panels giving the first material a potential use for post-impact applications. Besides this, there is no conclusive evidence that shows that the preference of one of those materials provides extra benefits for the mitigation of intra-laminar failure or delamination.
- d) The impacts of common size hailstones ($D=25.4$ mm) at impact velocities in the range of 60 m/s to 160 m/s are also studied. Results show that under this impact condition there is no penetration. However, the integrity and residual strength of the panel must be carefully evaluated due to the presence of delamination and massive core failure in the intersection between the core and bottom face-sheet.

8.3 Future work

In this subsection, some complementary works are suggested to improve the accuracy of the developed FEA model including a more detailed characterization of the materials and more complex numerical implementations of the FEA model.

- a) To characterize the cyclic shear stress-strain curve of the woven carbon/epoxy laminate to calibrate the plastic hardening function used in the ABQ_PLY material model.
- b) To implement a continuum damage model for woven laminates similar to the one used in this thesis, which incorporates a three-dimensional damage and failure criteria, that accounts for out-of-plane axial and shear stresses.
- c) To study the convenience of using more complex cohesive laws for modelling inter-laminar damage and fracture.
- d) To carry out detailed experimental testing to study fracture behaviour at the interface core-face-sheet and obtain the fracture energies for debonding.
- e) To perform a detailed experimental characterization of multiaxial fracture of the core materials that allows verifying the validity of the Tsai-Wu failure criteria and calibrating the factor due to coupling between axial and shear stresses.

Some improvements in the experimental techniques used in this thesis are also proposed:

- a) For the impact tests, it is important to ensure repeatability in the impact conditions and obtain a better correlation of the results. This can be achieved by:
 - Designing a retention system to have a constant-tight grip of the panel to ensure symmetrical boundary conditions.
 - Improving the alignment of the gas cannon's outlet and the target by the use of specialized laser pointers. Additionally, the distance between the cannon and the target can be reduced to diminish the effect of the projectile parabolic trajectory.
 - Implementing geometrically standardized sabots and the use of electronic controllers for the cannon firing pressure.

Finally from the results obtained in this thesis the following subjects are suggested for future research projects:

CONCLUSIONS AND FUTURE WORK

- a) To study the accuracy of the proposed FEA model with different impact conditions not studied in this work (e.g. face-sheet thickness, face-sheet lay-up, impactor shape and size)
- b) To study in detail the appearance of cross-cracks in the core thickness and their relation to core fracture in the interface core/bottom face-sheet. This can include a characterization of the residual strength of impacted panels that have suffered from this failure mode

APPENDIX A. RELEVANT CONCEPTS IN FINITE ELEMENT ANALYSIS

A.1 Explicit time Integration

An explicit method is an approach used in numerical analysis for obtaining numerical approximations to the solutions of time-dependent differential equations. In FEA it is used to analyse problems where there is dynamic equilibrium and the duration of the impact is very small (e.g. crash impacts, ballistic impacts, etc...). This method is based on the central difference method, which allows estimating the variation of the node displacement, velocity, and acceleration over time in situations where inertial and damping effects are not negligible.

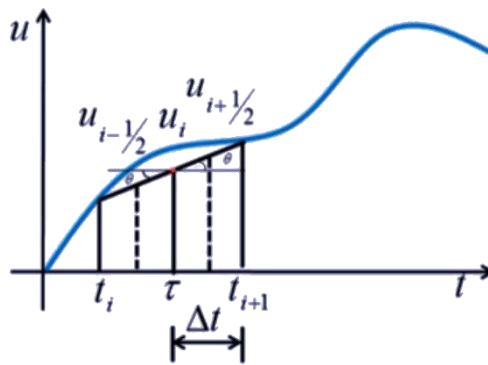


Figure A.1. Variation of the node position vs. time. Source: [1]

Considering the position $u(t)$ as a function of time. The velocity $\dot{u}(t)$ at a time $t = i\Delta t$ can be obtained from the difference in the displacement $u_{(i-1)}$ before and after $u_{(i+1)}$ a time step Δt .

$$\dot{u}_{(i)} = \frac{u_{(i+1)} - u_{(i-1)}}{2\Delta t} \quad (\text{A.1})$$

Similarly, the acceleration $\ddot{u}_{(i)}$ is obtained from the corresponding velocity at the time step $i + \frac{1}{2}$ and $i - \frac{1}{2}$

$$\ddot{u}_{(i)} = \frac{\dot{u}_{(i+\frac{1}{2})} - \dot{u}_{(i-\frac{1}{2})}}{\Delta t} \quad (\text{A.2})$$

Substituting for $\dot{u}_{(i+\frac{1}{2})}$ and $\dot{u}_{(i-\frac{1}{2})}$ in terms of the displacements

APPENDIX A

$$\dot{u}_{(i+\frac{1}{2})} = \frac{u_{(i+1)} - u_{(i)}}{\Delta t} \quad (\text{A.3})$$

$$\dot{u}_{(i-\frac{1}{2})} = \frac{u_{(i)} - u_{(i-1)}}{\Delta t} \quad (\text{A.4})$$

Therefore the acceleration at time step i is left in terms of the displacements at time steps $i - 1$ and $i + 1$.

$$\ddot{u}_{(i)} = \frac{\frac{u_{(i+1)} - u_{(i)}}{\Delta t} - \frac{u_{(i)} - u_{(i-1)}}{\Delta t}}{\Delta t} \quad (\text{A.5})$$

Simplifying:

$$\ddot{u}_{(i)} = \frac{u_{(i+1)} - 2u_{(i)} + u_{(i-1)}}{\Delta t^2} \quad (\text{A.6})$$

The dynamic equilibrium is written in terms of the nodal displacements and their derivatives:

$$M\ddot{u}_{(i)} + C\dot{u}_{(i)} + Ku_{(i)} = Q_{(i)} \quad (\text{A.7})$$

Substituting the nodal acceleration and nodal velocity from the previously obtained relations:

$$M\left(\frac{u_{(i+1)} - 2u_{(i)} + u_{(i-1)}}{\Delta t^2}\right) + C\left(\frac{u_{(i+1)} - u_{(i-1)}}{2\Delta t}\right) + Ku_{(i)} = Q_{(i)} \quad (\text{A.8})$$

Regrouping for nodal displacements at different time steps:

$$\left(\frac{M}{\Delta t^2} + \frac{C}{2\Delta t}\right)u_{(i+1)} = \left(\frac{M}{\Delta t^2} - \frac{C}{2\Delta t}\right)u_{(i-1)} - \left(K - \frac{2M}{\Delta t^2}\right)u_{(i)} + Q_{(i)} \quad (\text{A.9})$$

This method is explicit since the equilibrium equation is used at time step i to obtain the solution for time step $i + 1$. The central difference method is only conditionally stable when the time step is smaller than the smallest period in finite element assemblage T_n divided by π .

$$\Delta t \leq \frac{T_n}{\pi} \quad (\text{A.10})$$

In the nonlinear analysis, this smallest period can change over time. It becomes smaller due to the effect of large displacements and becomes larger due to material nonlinearities.

A.2 Energy conservation

The first law of thermodynamics states that the time rate of change of kinetic energy and internal energy is equal to the rate of work done by surface and body forces [2]:

$$\frac{d}{dt} \int_V \left(\frac{1}{2} \rho \bar{v} \cdot \bar{v} + \rho U \right) dV = \int_S \bar{v} \cdot \bar{t} dS + \int_V \bar{f} \cdot \bar{v} dV \quad (\text{A.11})$$

Where ρ is the density, \bar{v} is the velocity vector, U is the internal energy per unit of mass, $\bar{t} = \sigma \cdot n$ is the surface traction vector, and \bar{f} is the body force vector. Applying the Gauss theorem and the principle of virtual work the equation can be written in terms of the stress tensor σ and strain rate tensor $\dot{\epsilon}$.

$$\frac{d}{dt} \int_V \left(\frac{1}{2} \rho \bar{v} \cdot \bar{v} + \rho U \right) dV = \int_V \left[\left(\frac{\delta}{\delta \bar{x}} \cdot \sigma + f \right) \cdot \bar{v} + \sigma : \dot{\epsilon} \right] dV \quad (\text{A.12})$$

Using Cauchy's equation of motion

$$\frac{\delta}{\delta \bar{x}} \cdot \sigma + f = \rho \frac{d\bar{v}}{dt} \quad (\text{A.13})$$

Yields:

$$\frac{d}{dt} \int_V \left(\frac{1}{2} \rho \bar{v} \cdot \bar{v} + \rho U \right) dV = \int_V \left[\frac{d}{dt} \left(\frac{1}{2} \rho \bar{v} \cdot \bar{v} \right) + \sigma : \dot{\epsilon} \right] dV \quad (\text{A.14})$$

Integrating it on time

$$\int_V \rho U dV + U_0 = \int_0^t \int_V \sigma : \dot{\epsilon} dV dt \quad (\text{A.15})$$

Where U_0 is the internal energy at $t = 0$ and the rate of change of the internal energy is given as the double dot product of the stress and strain-rate tensors:

$$\rho \frac{dU}{dt} = \sigma : \dot{\epsilon} \quad (\text{A.16})$$

If the first law of thermodynamics is integrated on time and each term is separated it is found that each term:

$$\int_V \frac{1}{2} \rho \bar{v} \cdot \bar{v} dV + \int_V \rho U dV = \int_0^t \dot{E}_{WF} d\tau + constant \quad (\text{A.17})$$

APPENDIX A

$$E_K + E_U = \int_0^t \dot{E}_{WF} d\tau + constant \quad (A.18)$$

Where the first term E_K is the kinetic energy and the second term E_U is the net change in internal energy from the initial state.

$$E_k = \int_V \frac{1}{2} \rho \bar{v} \cdot \bar{v} dV \quad (A.19)$$

$$E_U = \int_V \rho U dV = \int_0^t \int_V \sigma : \dot{\epsilon} dV dt - U_0 \quad (A.20)$$

The term on the right-hand side is the work done by the external forces and friction forces. The term \dot{E}_{WF} can be decomposed by splitting the traction vector t into the distributed surface load \bar{t}^l and the friction traction load t^f .

$$\dot{E}_{WF} = \left(\int_S \bar{v} \cdot \bar{t}^l dS + \int_V \bar{f} \cdot \bar{v} dV \right) - \left(- \int_S \bar{v} \cdot \bar{t}^f dS \right) = \dot{E}_W + \dot{E}_F \quad (A.21)$$

Where \dot{E}_W is the rate of work done by external forces and \dot{E}_F is the rate of work done by friction on the different surfaces.

Replacing the above in the energy equation for the whole model

$$E_K + E_U + E_W + E_F = constant \quad (A.22)$$

The internal energy can be separated into two terms the first due to the stress derived from the constitutive equation of the material (σ^c) and the second is due to the viscous stress due to bulk viscosity, and material damping (σ^v).

$$E_U = \int_0^t \int_V \sigma : \dot{\epsilon} dV d\tau = \int_0^t \int_V (\sigma^c + \sigma^v) : \dot{\epsilon} dV d\tau \quad (A.23)$$

$$E_U = \int_0^t \int_V \sigma^c : \dot{\epsilon} dV d\tau + \int_0^t \int_V \sigma^v : \dot{\epsilon} dV d\tau \quad (A.24)$$

$$E_U = E_I + E_V \quad (A.25)$$

Being E_V the viscous dissipation energy and E_I the remaining internal energy.

The internal energy E_I can be further decomposed in terms of the elastic, plastic and creep strain rates ($\dot{\epsilon}^{el}$, $\dot{\epsilon}^{pl}$, $\dot{\epsilon}^{cr}$)

$$E_I = \int_0^t \int_V \sigma^c : \dot{\varepsilon} dV d\tau \quad (\text{A.26})$$

$$E_I = \int_0^t \int_V \sigma^c : \dot{\varepsilon}^{el} dV d\tau + \int_0^t \int_V \sigma^c : \dot{\varepsilon}^{pl} dV d\tau \quad (\text{A.27})$$

$$+ \int_0^t \int_V \sigma^c : \dot{\varepsilon}^{cr} dV d\tau$$

$$E_I = E_S + E_P + E_C \quad (\text{A.28})$$

This above indicates that the remaining internal energy is equal to the summation of the elastic strain energy E_S , the plastic strain energy E_P and the time creep/viscoelastic dissipated energy E_C .

If continuum damage models are used in the constitutive material equation at any instant of time the stress σ^c can be expressed as a function of the undamaged stress σ^u and the damage parameter d .

$$\sigma^c = (1 - d)\sigma^u \quad (\text{A.29})$$

If damage occurs not all of the elastic strain energy is recovered since upon unloading the damage parameter remains fixed at its value. Then the recoverable strain energy is [2]:

$$E_E = \int_0^t \int_V (1 - d_t)\sigma^u : \dot{\varepsilon}^{el} dV d\tau \quad (\text{A.30})$$

And the energy dissipated through damage is equal to

$$E_D = \int_0^t \int_V (d_t - d)\sigma^u : \dot{\varepsilon}^{el} dV d\tau \quad (\text{A.31})$$

After the previous discussion it is important to recall the output variable identifiers used by Abaqus for the energy balance of the whole FEA model [1]:

$$\begin{aligned} \text{ETOTAL} = & \text{ALLKE} + \text{ALLIE} + \text{ALLVD} + \text{ALLFD} - \text{ALLWK} - \text{ALLPW} \\ & - \text{ALLCW} \end{aligned} \quad (\text{A.32})$$

Being:

$$\text{ALLIE} = \text{ALLSE} + \text{ALLPD} + \text{ALLCD} + \text{ALLAE} + \text{ALLDMD} + \text{ALLDC} \quad (\text{A.33})$$

Where:

ETOTAL = Total energy

APPENDIX A

ALLKE = EK = Kinetic energy

ALLIE = Total strain energy

ALLVD = Energy dissipated by viscous effects

ALLFD = Total energy dissipated through frictional effects

ALLIHE = Internal heat energy (don't apply to the current model)

ALLWK = External work

ALLPW = Work done by contact penalties

ALLCW = Work done by constraint penalties

ALLSE = Recoverable strain energy

ALLPD = Energy dissipated by plastic deformation

ALLCD = Energy dissipated by viscoelasticity

ALLDMD = Energy dissipated by damage

ALLAE = "Artificial" strain energy associated with constraints used for hourglass control.

ALLDC = Energy dissipated for controlling excessive distortions.

A.3 Continuum shell elements and hour-glassing

Continuum shell (CS) elements can be described as an intermediate element type between conventional shell elements and 3D solid elements. CS elements are assigned to a solid 3D part, which defines the element thickness by the nodal geometry.

RELEVANT CONCEPTS IN FINITE ELEMENT ANALYSIS

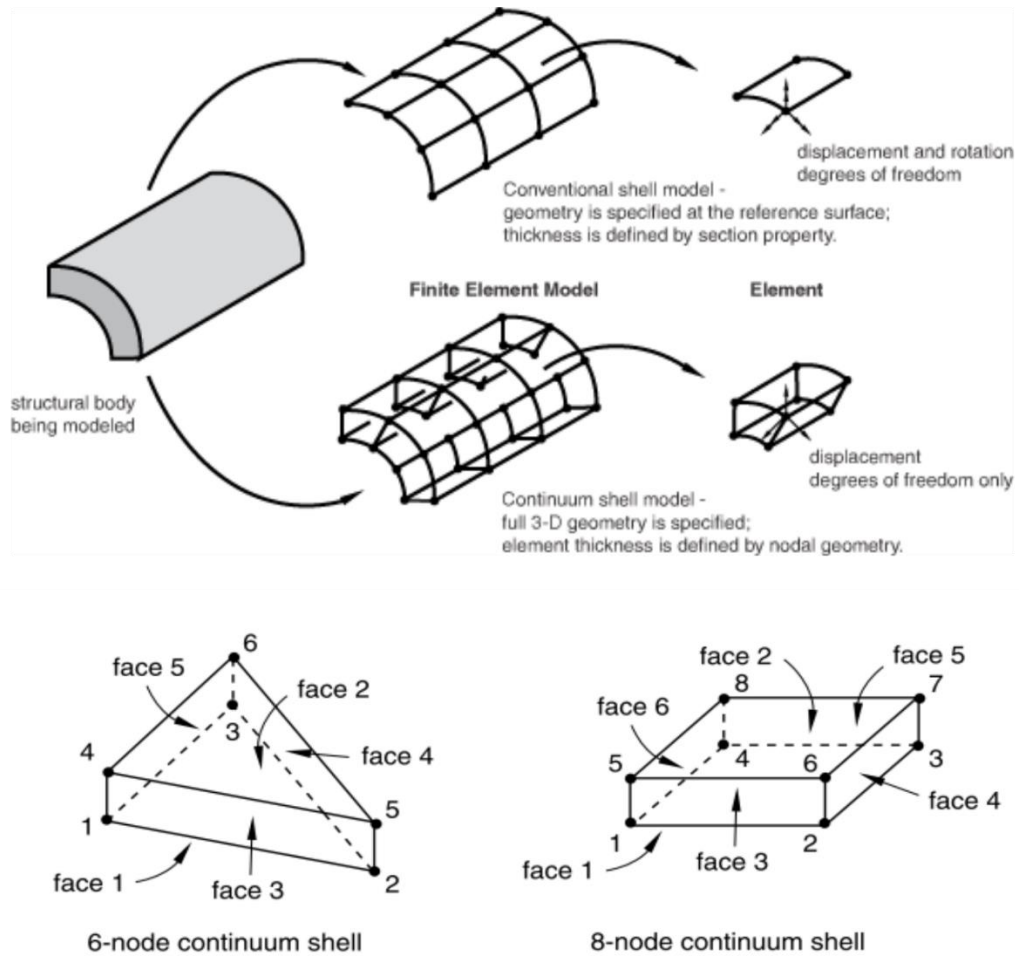


Figure A.2. Comparison conventional shell element vs continuum shell element. Source: [1]

The kinematic behaviour of CS elements is not fully 3D like in solid elements since it uses the First-Order Shear Deformation (FSDT) constraints but it is not simplified by the Kirchhoff constraint like in conventional shell elements.

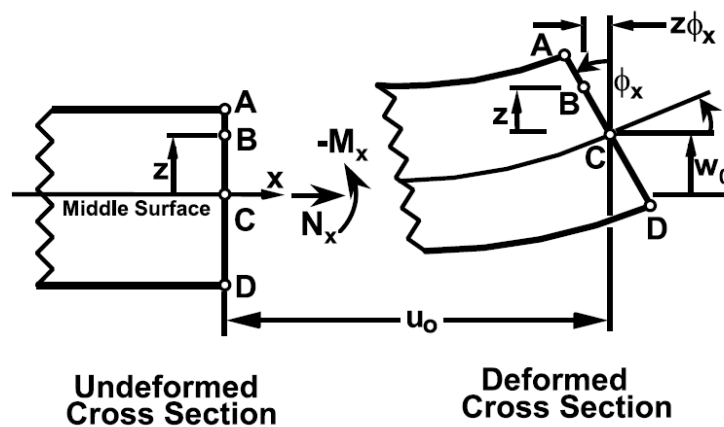


Figure A.3. FSDT assumption. Source: [3]

APPENDIX A

The first FSDT constrain for plates states that a straight line through the thickness of the plate can rotate but it remains straight after deformation. The second constrain states that the change in the shell thickness is negligible. Consequently, the 3D constitutive equations can be written in terms of 2D quantities at the mid-surface:

$$\varepsilon_x(x, y, z) = \frac{du_0}{dx} - z \frac{d\varphi_x}{dx} = \varepsilon_x^0 + z\kappa_x \quad (\text{A.34})$$

$$\varepsilon_y(x, y, z) = \frac{du_0}{dy} - z \frac{d\varphi_y}{dy} = \varepsilon_y^0 + z\kappa_y \quad (\text{A.35})$$

$$\varepsilon_z(x, y, z) = 0 \quad (\text{A.36})$$

$$\gamma_{xy}(x, y, z) = \frac{du_0}{dy} + \frac{dv_0}{dx} - z \left(\frac{d\varphi_x}{dy} + \frac{d\varphi_y}{dx} \right) = \gamma_{xy}^0 + z\kappa_{xy} \quad (\text{A.37})$$

$$\gamma_{yz}(x, y, z) = -\varphi_y + \frac{dw_0}{dy} \quad (\text{A.38})$$

$$\gamma_{xz}(x, y, z) = -\varphi_x + \frac{dw_0}{dx} \quad (\text{A.39})$$

Where ε_x^0 , ε_y^0 , γ_{xy}^0 are the membrane strains at the mid-surface, γ_{yz} , γ_{xz} are the shear strains through the thickness and κ_x , κ_y , κ_{xy} are the change in curvature. CS elements only have displacement degrees of freedom and therefore the FSDT has to be enforced by a particular interpolation function. One of the most important advantages of CS elements over conventional shell elements is that since more nodes are used to represent the thickness CS can be stacked to obtain a better representation of the shear deformation. Also, continuum shell elements are two-sided elements making them suitable for modelling contact. Finally, there is no aspect ratio problem since the strain out of the plane is zero (if compared with 3D solid elements).

A.4 Reduced integration and hour-glassing

In FEA quadrilateral and hexahedral elements can use the reduced integration approach to estimate the stiffness matrix $[k_e]$ in natural coordinates (ξ, η) .

$$[k_e] = t \int_{-1}^1 \int_{-1}^1 [B^T][C][B] \det[J] d\xi d\eta$$

Where $[B]$ is the strain-displacement matrix, $[C]$ is the material law matrix and $[J]$ is the jacobian to pass from the global coordinate system to the natural coordinate system. The

reduced integration scheme uses the Gaussian quadrature method in which a function is integrated by estimating the number of points and optimizing their positions in what is called Gaussian co-ordinates (ξ_i, η_j) . For each point, the function is multiplied by an optimized weight function $(\alpha_i \alpha_j)$ and at the end, the integral is solved by adding all these functions together. For a given two dimensional function to be integrated the Gauss quadrature method is given as follows:

$$\int_{-1}^1 \int_{-1}^1 F(\xi, \eta) d\xi d\eta = \sum_{i,j} \alpha_i \alpha_j F(\xi_i, \eta_j)$$

As expected reduced integration uses fewer integration points than full integration schemes (one integration point less in each direction) what provides a better computational time performance at the expense of accuracy in specific problems. Linear elements with reduced integration only have one single integration point located at the element centroid (Figure A.4).

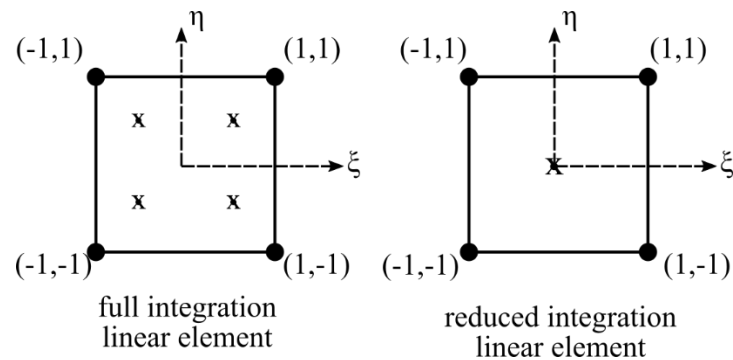


Figure A.4. Full integration element vs reduced integration element.

Reduced integration elements are also associated with a very flexible model representation in which spurious modes (which result in zero stiffness) such as Hour-glassing can occur. These are displacements that cause strains but are not captured at the integration points. In linear elements, spurious modes occur due to bending while for quadratic elements it occurs due to hour-glassing (Figure A.5).

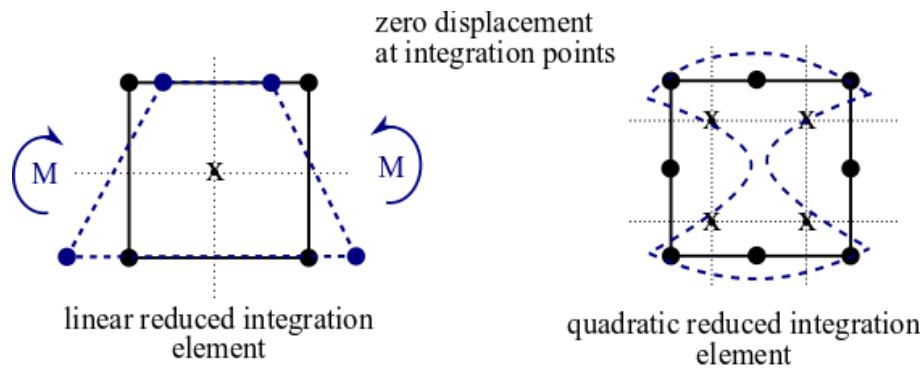


Figure A.5. Spurious modes in reduced integration elements (hour-glassing).

Excitation of these modes non-physical modes can induce severe mesh distortion since no stresses are resisting the deformation, furthermore, the element does not contribute to the energy integral. There are common reasons why hour-glassing may occur in elements with a single integration point: due to a concentrated force, boundary condition or contact at a single node, or when bending is model with too few elements. Hour-glassing can be controlled by including internal artificial nodal forces using the integral viscoelastic approach or the kelvin viscoelastic approach which are already implemented in Abaqus. Always that hourglass control is used it is advisable to verify the balance of the energy energies in the model and in particular to compare the magnitude of the artificial energy of the model (ALLAE) against the internal energy (ALLIE). For good modelling practices, a low percentage (<2%) is acceptable.

APPENDIX B. IMPLEMENTATION OF THE TSAI-WU FAILURE CRITERIA FOR ELEMENT DELETION

During impact events modelled by a fully Lagrangian approach, the mesh is sometimes subjected to excessive distortion that could potentially destroy the numerical stability of the solution. In such situations, it is a common practice to delete some elements using a criterion based on the damage and failure of real materials. Both core materials used in this thesis are highly anisotropic and are subjected to a multiaxial stress state during the impact event. For this reason, the multiaxial failure criteria proposed by Tsai et Wu [4] is used and implemented in a VUSDFLD user subroutine in Abaqus.

B.1 Tsai-Wu failure criteria

The Tsai-Wu failure criterion is based on a failure surface in the stress-space given by the following equation in contracted notation:

$$f(\sigma_k) = F_i \sigma_i + F_{ij} \sigma_i \sigma_j = 1 \quad (\text{B.1})$$

Where $i, j, k = 1, 2, \dots, 6$. F_i and F_{ij} are strength tensors

$$F_i = \begin{bmatrix} F_1 \\ F_2 \\ F_3 \\ F_4 \\ F_5 \\ F_6 \end{bmatrix} \quad (\text{B.2})$$

$$F_{ij} = \begin{bmatrix} F_{11} & F_{12} & F_{13} & F_{14} & F_{15} & F_{16} \\ \cdot & F_{22} & F_{23} & F_{24} & F_{25} & F_{26} \\ \cdot & \cdot & F_{33} & F_{34} & F_{35} & F_{36} \\ \cdot & \cdot & \cdot & F_{44} & F_{45} & F_{46} \\ \cdot & \cdot & \cdot & \cdot & F_{55} & F_{56} \\ \cdot & \cdot & \cdot & \cdot & \cdot & F_{66} \end{bmatrix} \quad (\text{B.3})$$

For orthotropic materials the terms F_4 , F_5 , and F_6 vanish and the coupling between normal and shear strength F_{16} also vanishes. With the same criterion, the shear strength for an orthotropic material is all uncoupled:

$$F_{45} = F_{56} = F_{64} = 0 \quad (\text{B.4})$$

For transversally isotropic material it can be stated that:

APPENDIX B

$$F_2 = F_3 \quad (B.5)$$

$$F_{12} = F_{13} \quad (B.6)$$

$$F_{22} = F_{33} \quad (B.7)$$

$$F_{55} = F_{66} \quad (B.8)$$

Additionally, it can be observed that the full shear stress state can be represented in terms of the principal stresses:

$$F_{44} = 2(F_{22} - F_{23}) \quad (B.9)$$

Additionally, if failure by hydrostatic stresses is assumed impossible the components of F_{ij} can be related as follows:

$$(F_{11} + F_{22} + F_{33}) + 2(F_{12} + F_{23} + F_{31}) = 0 \quad (B.10)$$

The remaining components F_i and F_{ij} can be related to the engineering strengths measured in the laboratory:

$$F_{11} = \frac{1}{XX'}; F_1 = \frac{1}{X} - \frac{1}{X'} \quad (B.11)$$

$$F_{22} = \frac{1}{YY'}; F_2 = \frac{1}{Y} - \frac{1}{Y'} \quad (B.12)$$

$$F_{33} = \frac{1}{ZZ'}; F_3 = \frac{1}{Z} - \frac{1}{Z'} \quad (B.13)$$

$$F_{44} = \frac{1}{QQ'}; F_4 = \frac{1}{Q} - \frac{1}{Q'} \quad (B.14)$$

$$F_{55} = \frac{1}{RR'}; F_5 = \frac{1}{R} - \frac{1}{R'} \quad (B.15)$$

$$F_{66} = \frac{1}{SS'}; F_6 = \frac{1}{S} - \frac{1}{S'} \quad (B.16)$$

Where:

X, X', uniaxial tensile and compressive strength in directions 1

Y, Y' uniaxial tensile and compressive strength in directions 2

Z, Z' uniaxial tensile and compressive strength in directions 3

Q, Q' shear strength in directions 2-3

IMPLEMENTATION OF THE TSAI-WU FAILURE CRITERIA FOR ELEMENT DELETION

R, R' shear strength in directions 3-1

S, S' shear strength in directions 1-2

The determination of F_{12} and F_{16} requires an experiment with combined stress. A common assumption is to write F_{12} as a function of F_{11} and F_{22} .

$$F_{12} = -\frac{1}{2}\sqrt{F_{11}F_{22}} \quad (\text{B.17})$$

This idea can be generalized to the other interactive terms giving the following simplified 3D Tsai-Wu failure criteria:

$$\begin{aligned} F_1\sigma_1 + F_2(\sigma_2 + \sigma_3) + F_{11}\sigma_1^2 + F_{22}(\sigma_2^2 + \sigma_3^2 + 2\sigma_4^2) + F_{66}(\sigma_5^2 + \sigma_6^2) \\ + 2F_{12}(\sigma_1\sigma_2 + \sigma_1\sigma_3) + 2F_{23}(\sigma_2\sigma_3 - \sigma_4^2) = 1\Delta \end{aligned} \quad (\text{B.18})$$

B.2 VUSDFLD user subroutine

```

subroutine vusdfld(
c Read only -
  * nblock, nstatev, nfieldv, nprops, ndir, nshr,
  * jElem, kIntPt, kLayer, kSecPt,
  * stepTime, totalTime, dt, cmname,
  * coordMp, direct, T, charLength, props,
  * stateOld,
c Write only -
  * stateNew, field )
c
  include 'vaba_param.inc'
c
  dimension jElem(nblock), coordMp(nblock,*),
  * direct(nblock,3,3), T(nblock,3,3),
  * charLength(nblock), props(nprops),
  * stateOld(nblock,nstatev),
  * stateNew(nblock,nstatev),
  * field(nblock,nfieldv)
  character*80 cmname
c
c Local arrays from vgetvrm are dimensioned to
c maximum block size (maxblk)
c
  parameter( nrData=6 )
  character*3 cData(maxblk*nrData)
  dimension rData(maxblk*nrData), jData(maxblk*nrData), s(nblock,nrData)
c
c
  jStatus = 1
  call vgetvrm( 'S', rData, jData, cData, jStatus )

```

APPENDIX B

```

c
  if(jStatus .ne. 0 ) then
    call xplb_abqerr(-2,'Utility routine VGETVRM '//
      'failed to get variable.',0,zero,')
    call xplb_exit
  end if
c -----
c -- This arranges the tensor from imported data
do r = 1, nblock
  do i = 1, (nrData)
    s(r,i) = rData(r+nblock*(i-1))
  end do
end do
c -- This part estimates the Tsai-Wu_index
  X_t = 1.1
  X_c = 22.1
  S_f = 0.63
c
c   call xplb_abqerr(-2,'Hello',0,zero,')
c   call xplb_exit
c
  F_1 = (1./X_t)-(1./X_c)
  F_2 = F_1
  F_11 = (1./(X_t*X_c))
  F_22 = F_11
  F_66 = (1./S_f**2.)
  F_12 = (-0.5)*sqrt(F_11*F_22)
  F_23 = F_12
  do f = 1, nblock
    term1 = F_1*s(f,1)
    term2 = F_2*(s(f,2)+s(f,3))
    term3 = F_11*(s(f,1)**2.)
    term4 = F_22*((s(f,2)**2.)+(s(f,3)**2.)+(2.*(s(f,4)**2.)))
    term5 = F_66*((s(f,5)**2.)+(s(f,6)**2.))
    term6 = 2.*F_12*((s(f,1)*s(f,2))+s(f,1)*s(f,3)))
    term7 = 2.*F_23*((s(f,2)*s(f,3))-s(f,4)**2.)
    TW_index = term1+term2+term3+term4+term5+term6+term7
c -- This stores Tsai-Wu_index in state variable
    stateNew(f,2) = TW_index
c -- Element deletion when effective_strain or strain_11 is greater than max_strain
    if ( TW_index > 1 ) then
      stateNew(f,1) = 0
    end if
  end do
c
  return
end

```

APPENDIX C. FUNDAMENTALS OF DIGITAL IMAGE CORRELATION (DIC)

As is shown in the coming sections, Digital Image Correlation (DIC) and high-speed video recording create a valuable experimental tool to study the details of the dynamic behaviour of the sandwich panel face-sheet against impact loads. The implementation of this method in the laboratory presented multiple challenges for the author particularly with the quality of the 3D stereo correlation and the calibration of the entire system. Solving these challenges successfully required a deep understanding of how the method works to take relevant decisions during the laboratory set-up assembly. This section tries to guide the reader into the fundamental concepts required to make effective use of the DIC method and obtain useful results. The whole discussion presented below is a summary of the more extended discussion found in textbooks such as [5] and [6].

The DIC method is a non-contacting method for motion and deformation analysis. This is done by obtaining digital images of an object and performing image analysis to extract the full field of deformation and/or motion. Image matching is done by the use of random patterns that are compared in sub-regions of the image.

C.1 Basics of camera optics.

Digital cameras are used to obtain the images for correlation. Therefore, it is important to understand the fundamentals of optics and image transformation in advance and some approximations made in the process. Here is some important terminology before starting:

- **Focus:** Point where light rays originated from a point on the object converge.
- **Focal length (\bar{f}):** The distance between the centre of a lens and its focus
- **Optical axis:** a line passing through the centre of curvature of a lens and parallel to the axis of symmetry.
- **Electro-optical sensor:** Electronic detectors that convert light, or a change in light, into an electronic signal.

For thin lenses or those lenses such as their thickness is neglected if compared to focal length, the Gauss or paraxial approximation assumes that an incident ray of light makes a small angle θ to the optical axis. Therefore:

$$\sin(\theta) = \tan(\theta) = \theta \quad (C.1)$$

From a pinhole camera system, as shown in Figure C.1, it is possible to obtain a transformation of an object point M into a sensor plane (M'') by using an ideal image point M' located at the optimal focus of rays.

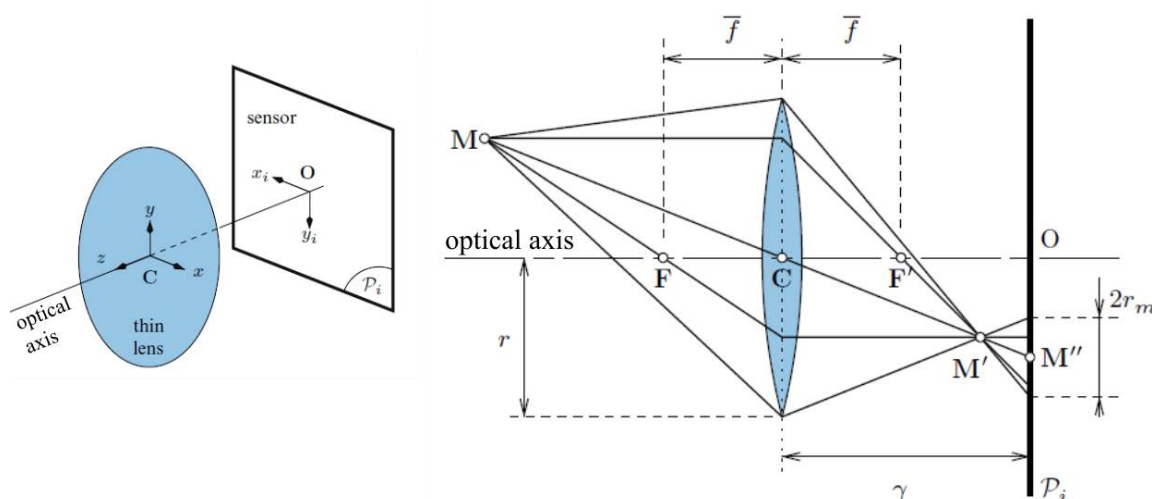


Figure C.1. Pinhole camera model for a thin lens. Source: [5]

The relationship between the coordinates in the object and the image is given by

$$\frac{y}{|CM|} = -\frac{y'}{|CM'|} \quad (C.2)$$

Where y and y' are the vertical coordinates in the object plane and image plane respectively.

Additionally, the lensmaker's equation provides a relationship between the location of the object and image plane to the focal length:

$$\frac{1}{|CM|} + \frac{1}{|CM'|} = \frac{1}{\bar{f}} \quad (C.3)$$

Knowing that for the image point to be focused on the sensor plane, the sensor plane must be located where the rays intersect. Therefore the distance γ must be equal to the z-component of the ideal image point M' leading to the definition of the focus plane.

$$z = \frac{\gamma \bar{f}}{\gamma - \bar{f}} \quad (C.4)$$

Combining the equations above the image point location in the sensor plane can be written as [5]:

FUNDAMENTALS OF DIGITAL IMAGE CORRELATION (DIC)

$$x'_i = \frac{x\gamma}{z} \quad (\text{C.5})$$

$$y'_i = \frac{y\gamma}{z} \quad (\text{C.6})$$

Since the image coordinates given by the pinhole model are non-linear due to their dependence in $(1/z)$ it is convenient to use a homogeneous coordinate system to express it as a linear model [5].

$$\alpha \begin{Bmatrix} x'' \\ y'' \\ 1 \end{Bmatrix} = \begin{bmatrix} \gamma & 0 & 0 & 0 \\ 0 & \gamma & 0 & 0 \\ 0 & 0 & 1 & 0 \end{bmatrix} \begin{Bmatrix} x \\ y \\ z \\ 1 \end{Bmatrix} \quad (\text{C.7})$$

Where α is a scale factor of the perspective projection.

In most practical occasions the ideal image point M' may not coincide with the sensor plane location, creating a region slightly blurred, enlarged and shifted. The radius of the circle increases with distance from the ideal focus, therefore the largest circle that is indistinguishable from a point is called the circle of confusion. The size of the circle of confusion is related to the radius of the lens by the following equation [5]:

$$r_{M''} = r_{lens} \left(1 + \frac{\gamma(\bar{f} - z)}{\bar{f}z} \right) \quad (\text{C.8})$$

When the circle of confusion is small enough it is indistinguishable from a point, therefore the point appears to be focused. The range of distance in which the objects seems to be in focus is called Depth of Field (DOF) and can be determined by the object distance, the focal length and the relative aperture of the diaphragm.

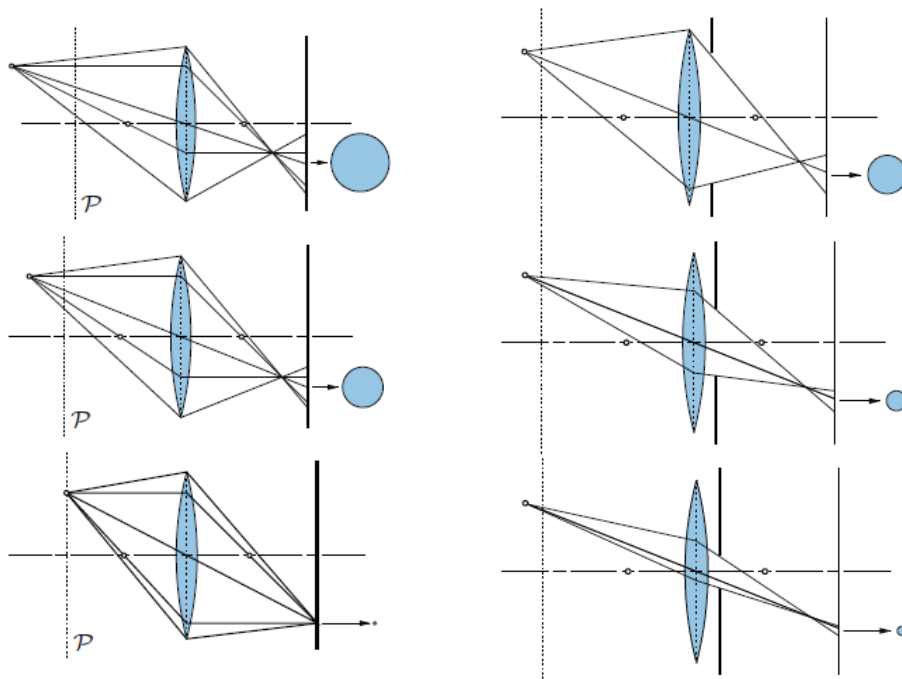


Figure C.2. Left: Effect of defocus on image blur. Right: Effect of aperture diaphragm on image blur. Source: [5]

C.2 Point image transformations

The classic pinhole camera model requires in total three transformations to represent various elements in the imaging process. The following figure shows four different reference frames: the world system R_w , (X_w, Y_w, Z_w) , the camera system R_c (x, y, z) , the image system R_r and the sensor system R_s (x_s, y_s) .

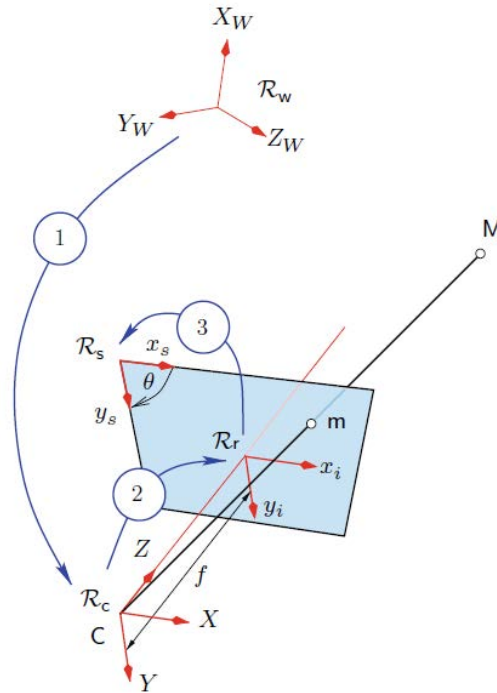


Figure C.3. Pinhole camera transformations. Source: [5]

The first transformation from the world system to the camera system requires both rotation and translation that can be achieved by applying the rotation tensor $[R]$ and the translation vector \bar{t} .

$$M = \begin{Bmatrix} x \\ y \\ z \end{Bmatrix} = [R] \begin{Bmatrix} X_W \\ Y_W \\ Z_W \end{Bmatrix} + \bar{t} \quad (\text{C.9})$$

Alternatively using homogeneous coordinates:

$$M = \begin{Bmatrix} X \\ Y \\ Z \\ 1 \end{Bmatrix} = [T] \begin{Bmatrix} X_W \\ Y_W \\ Z_W \\ 1 \end{Bmatrix} \quad (\text{C.10})$$

Where $[T]$ is the transformation matrix:

$$[T] = \begin{bmatrix} R & t \\ 0 & 1 \end{bmatrix} \quad (\text{C.11})$$

The second transformation from the camera system to the image system projects the point M on the image plane using a pure perspective projection using the homogenous form developed for the pinhole model.

APPENDIX C

$$\underline{m} = \alpha \begin{Bmatrix} x_i \\ y_i \\ 1 \end{Bmatrix} = [P] \begin{Bmatrix} x \\ y \\ z \\ 1 \end{Bmatrix} \quad (C.12)$$

Where [P] is given in terms of the image distance (f) previously defined in the previous section as (γ).

$$[P] = \begin{bmatrix} f & 0 & 0 & 0 \\ 0 & f & 0 & 0 \\ 0 & 0 & 1 & 0 \end{bmatrix} \quad (C.13)$$

The last transformation converts the position in the image system to the pixel coordinates of the sensor array. The sensor can be asymmetrical, inclined and the scale factor in the sensor coordinate directions are assumed differently. Therefore, the transformation can be given as:

$$\begin{Bmatrix} x_s \\ y_s \\ 1 \end{Bmatrix} = [A] \begin{Bmatrix} x_i \\ y_i \\ 1 \end{Bmatrix} = \begin{bmatrix} S_x & -S_x \cot \theta & -S_x(\hat{c}_x - \hat{c}_y \cot \theta) \\ 0 & S_y / \sin \theta & -S_y \hat{c}_y / \sin \theta \\ 0 & 0 & 1 \end{bmatrix} \begin{Bmatrix} x_s \\ y_s \\ 1 \end{Bmatrix} \quad (C.14)$$

Where the terms S_x, S_y are the horizontal and vertical scale factors in the sensor coordinate, the angle θ is the non-orthogonality between rows and columns in the image and \hat{c}_x, \hat{c}_y are the translations to the local origin of the sensor system.

Combining all three transformations, we can obtain an expression in terms of the global position and the parameters previously defined [5]:

$$\begin{Bmatrix} x_s \\ y_s \end{Bmatrix} = \begin{Bmatrix} c_x + f_x \left(\frac{R_{11}X_W + R_{12}Y_W + R_{13}Z_W + t_x}{R_{31}X_W + R_{32}Y_W + R_{33}Z_W + t_z} \right) + f_s \left(\frac{R_{21}X_W + R_{22}Y_W + R_{23}Z_W + t_y}{R_{31}X_W + R_{32}Y_W + R_{33}Z_W + t_z} \right) \\ c_y + f_y \left(\frac{R_{21}X_W + R_{22}Y_W + R_{23}Z_W + t_y}{R_{31}X_W + R_{32}Y_W + R_{33}Z_W + t_z} \right) \end{Bmatrix} \quad (C.15)$$

Where:

$$f_x = f S_x \quad (C.16)$$

$$f_y = \frac{f S_y}{\sin \theta} \quad (C.17)$$

$$f_s = -f S_x \cot \theta \quad (C.18)$$

$$c_x = -S_x(\hat{c}_x - \hat{c}_y \cot \theta) \quad (C.19)$$

$$c_y = -\frac{S_y \hat{c}_y}{\sin\theta} \quad (C.20)$$

Alternatively, this can be written in matrix form as

$$\bar{m} = [K] \cdot [T] \begin{Bmatrix} X_W \\ Y_W \\ Z_W \\ 1 \end{Bmatrix} \quad (C.21)$$

C.3 Fundamentals of distortion and calibration.

The homogeneous model presented in the previous subsection ideally presents a linear transformation between the object point and the image. However, in practice, lenses are not perfectly parallel. Their optical centres are not aligned and their curvature doesn't perfectly meet the Gaussian ray tracing approximation. This creates deviations in the position relative to the ideal model. A distortion model is then used after the pinhole estimation model to perform a distortion correction. The detailed description of such distortions models is beyond the scope of this work. However, a brief introduction is given to provide the reader with an insight into the subject. The reader is encouraged to refer to [5] for more detailed information about the subject. The corrected position of an image point can be expressed in terms of the ideal sensor position (pinhole model) and a 2D distortion displacement vector $D(x_s, k_i)$ that is function of the ideal sensor position and a set of distortion parameters k_i .

$$\check{m} = \bar{m} + D(x_s, k_i) \quad (C.22)$$

The distortion displacement vector can be written in terms of separate distortion components using the Seidel lens distortion model:

$$D(x_s, k_i) = D_s + D_R + D_C + D_A + D_{COF} + D_L + D_d \quad (C.23)$$

Spherical distortion (D_s): This distortion is produced by focusing error along the optical axis

Comma distortion (D_C): This distortion occurs when the lens is tilted relative to the optic axis

Astigmatism (D_A): This distortion occurs when the lens (or the object) is tilted relative to the optic axis making image points for locations offset from the centre being focused at incorrect locations, with error increasing with distance from the tilt axis.

APPENDIX C

Curvature of field (D_{COF}): Distortion model assumed symmetric relative to the optical axis and quadratic in radial position.

Linear distortion (D_L): Linear function of the radial position

De-centering distortion (D_d): Minor distortion relative to either spherical or radial distortion.

The process of finding the camera transformation parameters and the distortion coefficients is known as calibration. Among the linear calibration methods, the algorithm proposed by Ravn is attractive since it can be performed using a calibration target. Under the assumption that the calibration target is planar and that the world coordinate system is aligned with the target plane ($X_W, Y_W, 0$) the equation for the pinhole transformation can be simplified and written as two linear equations with eight unknown camera parameters.

$$x_s = \eta_1 + \eta_3 X_W + \eta_4 Y_W - \eta_7 x_s X_W - \eta_8 x_s Y_W \quad (C.24)$$

$$y_s = \eta_2 + \eta_5 X_W + \eta_6 Y_W - \eta_7 y_s X_W - \eta_8 y_s Y_W \quad (C.25)$$

$$\eta_1 = c_x + \frac{f_x t_x}{t_z} \quad (C.26)$$

$$\eta_2 = c_y + \frac{f_y t_y}{t_z} \quad (C.27)$$

$$\eta_3 = \frac{c_x R_{31} + f_x R_{11}}{t_z} \quad (C.28)$$

$$\eta_4 = \frac{c_x R_{32} + f_x R_{12}}{t_z} \quad (C.29)$$

$$\eta_5 = \frac{c_y R_{31} + f_y R_{21}}{t_z} \quad (C.30)$$

$$\eta_6 = \frac{c_y R_{32} + f_y R_{22}}{t_z} \quad (C.31)$$

$$\eta_5 = \frac{R_{31}}{t_z} \quad (C.32)$$

$$\eta_5 = \frac{R_{32}}{t_z} \quad (C.33)$$

The unknown set of parameters η_i can be obtained from each view of the target. However, it is important to consider that there are eight unknown sets of parameters therefore at least

four points $(X_{W_i}, Y_{W_i}, 0)$ from a single view of a planar target are required. It is a common practice to use more than four points creating an over-determined system of linear equations that can be solved using any of the following classical methods [5]: a) the inverse of $A^T A$, b) direct minimization or c) iterative approaches.

After obtaining, the eight parameters for each view of the calibration pattern the four intrinsic camera parameters (c_x, c_y, f_x, f_y) and the six extrinsic parameters (t_x, t_y, t_z) plus three rotation angles can be estimated using the Ravn algorithm. This method is very well known in the computer vision community and a detailed description can be reviewed in [5].

The previously mentioned linear calibration method doesn't account for non-linear distortion parameters making it necessary an adjustment technique called bundle adjustment. The bundle adjustment method is based on minimizing the difference between the model prediction (using the pinhole model) and the measured sensor location for an arbitrary 3D point. If there are $I = 1, 2, 3, \dots, N$ points and $J = 1, 2, 3, \dots, M$ views of an object then the measure of the difference is a function of the intrinsic (Int) and extrinsic (Ext) parameters as well as the points (p):

$$E(Int, Ext, p) = \sum_{J=1}^M \sum_{I=1}^N \left[|x_s^{IJ} - X_s(Int, Ext^J, p_T^I)|^2 + |y_s^{IJ} - Y_s(Int, Ext^J, p_T^I)|^2 \right] \quad (C.34)$$

Where:

$X_s(Int, Ext^J, p_T^I)$ and $Y_s(Int, Ext^J, p_T^I)$ are the distorted sensor plane prediction that are functions of both the camera parameters and distortion parameters and:

x_s, y_s are the location of the image point in the sensor for each point and each view.

To estimate the intrinsic and extrinsic camera parameters the error function is minimized using an iterative method such as Levenberg-Marquardt algorithm.

C.4 2D and 3D computer vision

In 2D computer vision, all points in a planar object are located at the same distance from the sensor plane. Therefore, each position vector O_0P is a scaled version of the image plane position vector $O_I P$. Therefore the problem is reduced to an affine projection.

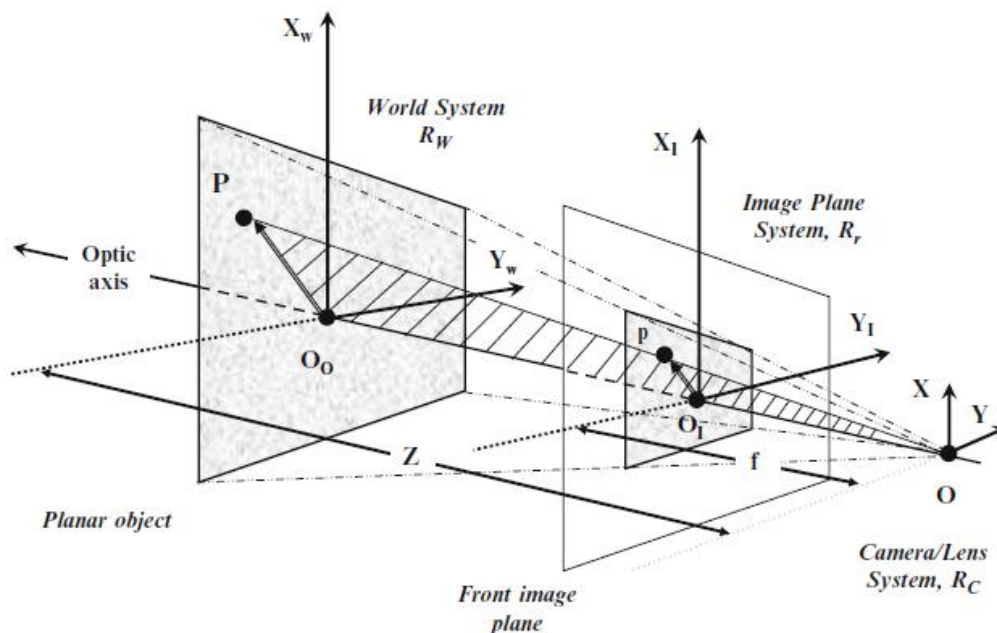


Figure C.4. 2D projection. Source: [5]

This problem can be simplified even more if the world coordinate system is assumed to be aligned to the planar object coordinate system. In such a case the rotation matrix is reduced to the identity matrix $[R] = [I]$. Additionally, if the sensor plane is orthogonal the relationship between the planar object coordinates and the sensor position are given by:

$$\begin{Bmatrix} x_s \\ y_s \end{Bmatrix} = \begin{Bmatrix} (\frac{fS_x}{Z})X_w \\ (\frac{fS_y}{Z})Y_w \end{Bmatrix} + \begin{Bmatrix} c_x \\ c_y \end{Bmatrix} \quad (C.35)$$

This equation indicates that there are just four intrinsic parameters in a 2D projection. Where the ratio (f/Z) is the image magnification factor.

In 3D computer vision, it is common to use a two cameras arrangement (stereo system) to simultaneously capture image points of the same object. A single-camera on the left can be used to perform a perspective projection of a 3D object point (R) into a 2D image point (p). However, such a projection is unable to determine the third dimension by itself since the projected point could correspond to infinite points lying in the same projective ray (C,p) at different distances (for example point Q). This problem is solved if a second camera is added to the image at the same point since only a unique point projected in the second camera plane (r') correspond to the interest point (R).

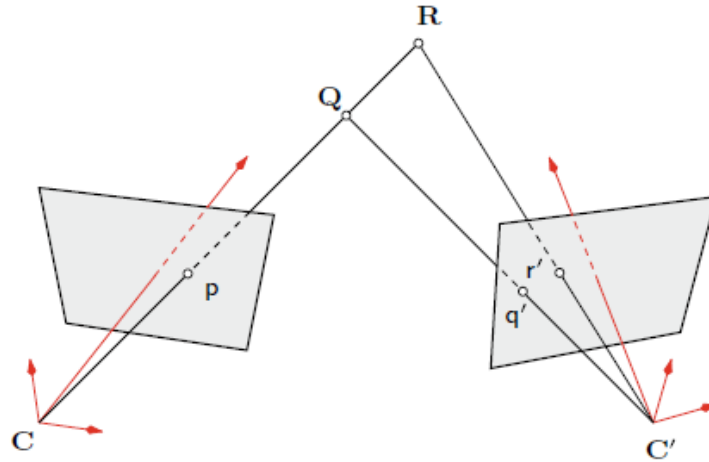


Figure C.5. Stereo-vision system. Source: [5]

The stereo vision system requires a set of coordinate transformations for each camera that include a rotation and a translation vector and can be grouped in the following matrix form:

$$[T] = \begin{bmatrix} R & t \\ 0 & 1 \end{bmatrix} \quad (C.36)$$

$$[T'] = \begin{bmatrix} R & t \\ 0 & 1 \end{bmatrix}_{C'} \quad (C.37)$$

$$[T_s] = \begin{bmatrix} R & t \\ 0 & 1 \end{bmatrix}_s \quad (C.38)$$

Where $[T]$ and $[T']$ are the transformation matrices from the world coordinates system to the coordinate system in the left and right cameras respectively. Additionally $[T_s]$ transforms the vectors in the left camera coordinate system into the right camera coordinate system.

$$[T_s][T] = [T'] \quad (C.39)$$

Using these transformations the following relation is obtained between the two image points in the left (\bar{m}) and right cameras (\bar{m}'):

$$\bar{m} = [K] \cdot [T] \cdot \bar{M} \quad (C.40)$$

And

$$\bar{m}' = [K'] \cdot [T_s] \cdot [T] \cdot \bar{M} \quad (C.41)$$

The two image points additionally are constrained by the epipolar line that is a line created by the image in one camera of a ray through the optical centre and image point in the other camera. This epipolar constrain has an important effect during the pattern matching

problem since it allows to search for coincidence along the epipolar line instead of the whole image.

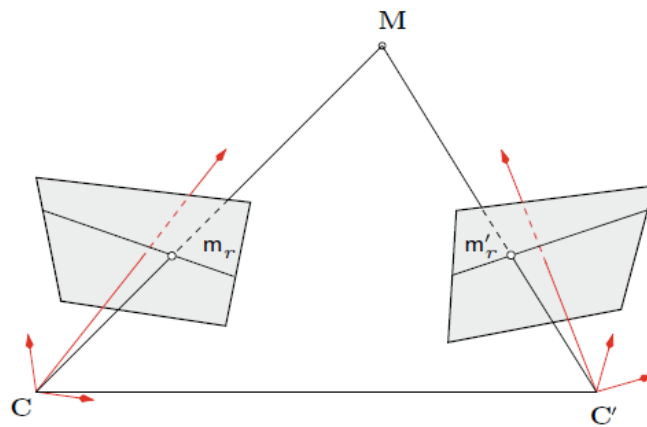


Figure C.6. Epipolar geometry. Source: [5]

C.5 Image matching

Typically, it is not possible to identify a unique correspondence of a single point of an image into another image, since the same grey value can be found in thousands of other pixels.

Therefore, it is convenient to find the correspondence of a whole neighbourhood that contains a non-periodic texture to avoid mistaken registration. The preferred texture for DIC analysis is a speckle pattern that ideally adheres to the surface and deforms with it in such a way that there is no loss in correlation. The aperture for pattern matching is usually small and is commonly referred to as a subset.

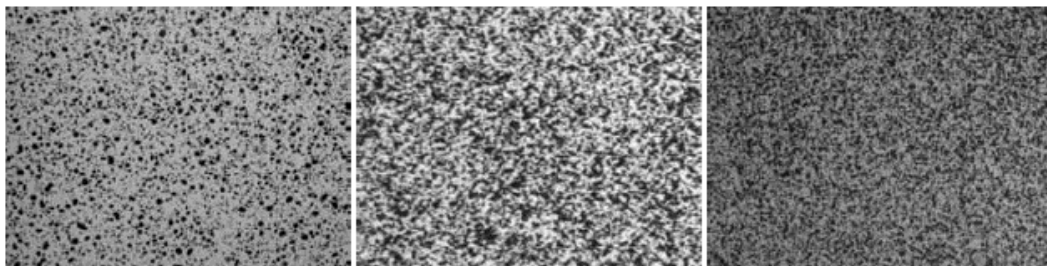


Figure C.7. Example of a speckle pattern. Source: [5]

Image matching is achieved by estimating the pattern of relative motion of image objects between two consecutive frames. Most of the methods for image matching are based on the Lucas-Kanade tracker method. Assuming that the intensity of an object is given by $G(x, t)$

for small motions, the intensity around the interest point can be expressed by a first-order Taylor expansion

$$G(x + \Delta x, t) = G(x, t) + \frac{dG}{dx} \Delta x \quad (\text{C.42})$$

When moving with a velocity \dot{u} a grey value is displaced by $\Delta x = \dot{u}\Delta t$. Therefore change in intensity after Δt is given by:

$$\Delta G = G(x, t + \Delta t) - G(x, t) \quad (\text{C.43})$$

$$\Delta G = G(x + \Delta x, t) - G(x, t) \quad (\text{C.44})$$

This change in intensity can be written in terms of the slope of intensity

$$\Delta G = -\frac{dG}{dx} \Delta x \quad (\text{C.45})$$

And the motion can be estimated by

$$\Delta x = \dot{u}\Delta t = -\frac{\Delta G}{\frac{dG}{dx}} \quad (\text{C.46})$$

Rearranging this equation and applying $\Delta t \rightarrow 0$

$$\frac{dG}{dt} + \dot{u} \frac{dG}{dx} = 0 \quad (\text{C.47})$$

Using a similar derivation, the intensity change for a two-dimensional velocity field (\vec{v}) is given by [5]:

$$\frac{dG}{dt} + \vec{v} \cdot \nabla G = 0 \quad (\text{C.48})$$

or

$$\Delta \vec{x} \cdot \nabla G = -\Delta G \quad (\text{C.49})$$

Instead of writing this equation for a single point, it can be rewritten for a neighbour image subset of points where the motion can be considered approximately constant

$$\Delta \vec{x}_1 = \Delta \vec{x}_N = \Delta \vec{x} \quad (\text{C.50})$$

$$\begin{bmatrix} \frac{dG_1}{dx} & \frac{dG_1}{dy} \\ \frac{dG_2}{dx} & \frac{dG_2}{dy} \\ \dots & \dots \\ \frac{dG_N}{dx} & \frac{dG_N}{dy} \end{bmatrix} \begin{bmatrix} \Delta x \\ \Delta y \end{bmatrix} = \begin{bmatrix} \Delta G_1 \\ \Delta G_2 \\ \dots \\ \Delta G_N \end{bmatrix} \quad (\text{C.51})$$

Being an equation system of the form $G\Delta\bar{x} = -g$ where the average motion is given by:

$$\Delta\bar{x} = -(G^T G)^{-1} G^T g \quad (\text{C.52})$$

The average motion can be estimated as long as the matrix $G^T G$ is non-singular or $\det(G^T G) = 0$. This means that motion estimation is not possible in regions of constant grey values. An extended version of the Lucas-Kanade method is used for the non-small motion vector. For this case, the motion estimation is based on minimizing the difference in the grey value intensity between the subset of an image template $F(x)$ and a displaced copy of this image $G(x + d)$.

The optimal displacement vector \bar{d}_{op} is the minimum argument to minimize the squared difference in grey values over the subset.

$$\bar{d}_{op} = \operatorname{argmin} \sum |G(x + \bar{d}) - F(x)|^2 \quad (\text{C.53})$$

The Lucas-Kanade tracker algorithm provides an iterative method for estimating the optimal displacement from a cost function of the following form.

$$\chi^2(\bar{d}_x + \Delta_x, \bar{d}_y + \Delta_y) = \sum \left| G(x + \bar{d}) - \frac{dG}{dx} \Delta_x - \frac{dG}{dy} \Delta_y - F(x) \right|^2 \quad (\text{C.54})$$

Where \bar{d}_x and \bar{d}_y are current estimates at an iteration step and Δ_x and Δ_y are incremental updates in the current iteration. For minimizing the cost function partial derivatives with respect to Δ_x and Δ_y are taken and set to zero giving as result the following equation that gives the incremental updates for each iteration:

$$\begin{bmatrix} \Delta_x \\ \Delta_y \end{bmatrix} = \begin{bmatrix} \sum \left(\frac{dG}{dx}\right)^2 & \sum \frac{dG}{dx} \frac{dG}{dy} \\ \sum \frac{dG}{dx} \frac{dG}{dy} & \sum \left(\frac{dG}{dy}\right)^2 \end{bmatrix}^{-1} \begin{bmatrix} \sum \frac{dG}{dx} (F - G) \\ \sum \frac{dG}{dy} (F - G) \end{bmatrix} \quad (\text{C.55})$$

C.6 Shape functions

In practical applications, particularly in the measurement of deformations, the specimen might experience distortion (rotation, elongation, compression, and shear). This distortion decreases the similarity between the original subset and the distorted subset.

Fortunately, the iterative matching algorithm can be extended to account for deformations. This is done by introducing a subset shape function $\xi(x, p)$ that transforms coordinates in the reference subset into coordinates in the distorted image.

Transformation functions in the 2D space can be divided into the following:

- Translation: Orientation is preserved (2 DoF)

$$x' = x + b_1 \quad (C.56)$$

$$y' = y + b_2 \quad (C.57)$$

In homogeneous coordinates:

$$\xi(\bar{x}, p) = \begin{bmatrix} 1 & 0 & b_1 \\ 0 & 1 & b_2 \\ 0 & 0 & 1 \end{bmatrix} \begin{bmatrix} x \\ y \\ 1 \end{bmatrix} \quad (C.58)$$

- Rigid motion (translation and rotation): Length is preserved (3 DoF)

$$x' = x \cos \theta - y \sin \theta + b_1 \quad (C.59)$$

$$y' = x \sin \theta + y \cos \theta + b_2 \quad (C.60)$$

In homogeneous coordinates:

$$\xi(\bar{x}, p) = \begin{bmatrix} \cos \theta & -\sin \theta & b_1 \\ \sin \theta & \cos \theta & b_2 \\ 0 & 0 & 1 \end{bmatrix} \begin{bmatrix} x \\ y \\ 1 \end{bmatrix} \quad (C.61)$$

- Affine: Parallelism is preserved

$$x' = a_1 x - a_2 y + b_1 \quad (C.62)$$

$$y' = a_3 x - a_4 y + b_2 \quad (C.63)$$

In homogeneous coordinates:

$$\xi(\bar{x}, p) = \begin{bmatrix} a_1 & a_2 & b_1 \\ a_3 & a_4 & b_2 \\ 0 & 0 & 1 \end{bmatrix} \begin{bmatrix} x \\ y \\ 1 \end{bmatrix} \quad (C.64)$$

Taking into account this transformation the cost function is re-written as:

APPENDIX C

$$\chi^2(p) = \sum |G(\xi(\bar{x}; p)) - F(\bar{x})|^2 \quad (C.65)$$

As previously explained for the non-distortion case this cost function can be minimized using an iterative algorithm with an initial estimate of p to find incremental updates Δp

$$\chi^2(p) = \sum |G(\xi(\bar{x}; p + \Delta p)) - F(\bar{x})|^2 \quad (C.66)$$

Minimizing this equation requires to compute its derivative with respect to Δp and equate it to zero:

$$2 \sum \left[\nabla G \frac{d\xi}{dp} \right]^T [G(\xi(\bar{x}; p)) + \nabla G \frac{d\xi}{dp} \Delta p - F(\bar{x})] = 0 \quad (C.67)$$

Giving

$$\Delta p = H^{-1} \sum \left[\nabla G \frac{d\xi}{dp} \right]^T [F(\bar{x}) - G(\xi(\bar{x}; p))] \quad (C.68)$$

Where H is the symmetric Hessian matrix and for the case of affine transformations is given by:

$$H^{-1} = \sum \left[\nabla G \frac{d\xi}{dp} \right]^T \left[\nabla G \frac{d\xi}{dp} \right] \quad (C.69)$$

Taking into account all the above the Kanate-Lucas-Tomasi (KLT) algorithm can be summarized in the following steps:

1. Warp G with $\xi(\bar{x}; p)$
2. Subtract the intensity of the template from the distorted image $[F(\bar{x}) - G(\xi(\bar{x}; p))]$
3. Compute the gradient ∇G
4. Evaluate the Jacobian $\frac{d\xi}{dp}$
5. Compute the steepest descent $\nabla G \frac{d\xi}{dp}$
6. Compute the inverse Hessian H^{-1}
7. Compute Δp
8. Update parameters $p \rightarrow p + \Delta p$

References of the appendices

- [1] Dassault Systèmes Simulia Corp. Abaqus/CAE User's Guide 2014. <http://ivt-abaqusdoc.ivt.ntnu.no:2080/v6.14/books/usi/default.htm>.
- [2] Dassault Systèmes Simulia Corp. Abaqus 6.14 Theory Guide 2014. <http://ivt-abaqusdoc.ivt.ntnu.no:2080/v6.14/books/stm/default.htm> (accessed June 25, 2020).
- [3] Barbero EJ. Finite Element Analysis of Composite Materials with Abaqus. Boca Raton, Florida: 2013.
- [4] Tsai SW, Wu EM. A General Theory of Strength for Anisotropic Materials. *J Compos Mater* 1971;5:58–80. <https://doi.org/10.1177/002199837100500106>.
- [5] Michael A. Suttons, Jean-Jose Orteu HWS. Image correlation for shape, motion and deformation measurements. Springer Science+Business Media; 2009. <https://doi.org/10.1007/978-0-387-78747-3>.
- [6] Bigger R, Blaysat B, Boo C, Grewer M, Hu J, Jones A, et al. A Good Practices Guide for Digital Image Correlation. *Int Digit Image Correl Soc* 2018:94.